Charakterisierung von Gastrennungseigenschaften in Mixed-Matrix-Membranen und porösen Materialien

Inaugural-Dissertation

zur Erlangung des Doktorgrades
der Mathematisch-Naturwissenschaftlichen Fakultät
der Heinrich-Heine-Universität

vorgelegt von

Alexander Nuhnen

aus Düsseldorf

Düsseldorf, April 2020

aus dem Institut für Anorganische Chemie und Strukturchemie I
der Heinrich-Heine-Universität Düsseldorf

Gedruckt mit der Genehmigung der
Mathematisch-Naturwissenschaftlichen Fakultät
der Heinrich-Heine-Universität Düsseldorf

Referent: Prof. Dr. Christoph Janiak

Korreferent: Prof. Dr. Christian Ganter

Tag der mündlichen Prüfung:

Die vorliegende Arbeit wurde in der Zeit von September 2017 bis April 2020 an der Heinrich-Heine-Universität Düsseldorf im Institut für Anorganische Chemie und Strukturchemie I im Arbeitskreis von Prof. Dr. Janiak angefertigt.

Eidesstattliche Erklärung

Ich versichere an Eides statt, dass die Dissertation von mir selbstständig und ohne unzulässige fremde Hilfe unter der Beachtung der „Grundsätze zur Sicherung guter wissenschaftlicher Praxis“ an der Heinrich-Heine-Universität Düsseldorf erstellt worden ist. Die aus fremden Quellen direkt oder indirekt übernommenen Gedanken sind als solche kenntlich gemacht. Die Arbeit wurde bisher weder im Inland noch im Ausland in gleicher oder ähnlicher Form einer anderen Prüfungsbehörde vorgelegt. Es wurden keine früheren erfolglosen Promotionsversuche unternommen.

……………………………………. ……………………………………

Ort, Datum Unterschrift

Danksagung

Ich danke Herrn Prof. Dr. Christoph Janiak für die Aufnahme in seinen Arbeitskreis und die Möglichkeit meine Arbeit dort anzufertigen. Außerdem danke ich ihm für die oft sehr langen und konstruktiven Diskussionen, die Korrekturen der Manuskripte und die vielen Freiräume während der gesamten Zeit meiner Promotion. Weiterhin möchte ich ihm für die Möglichkeit zur Teilnahme an internationalen Konferenzen und Seminaren danken.

Herrn Prof. Dr. Christian Ganter danke ich herzlich für die freundliche Übernahme des Koreferates und zahlreiche interessante Anregungen in meinen Seminarvorträgen.

Den festangestellten Mitarbeitern des Arbeitskreises danke ich für ihre Unterstützung und Kooperation während meiner Arbeit. Für die große Hilfe bei allen organisatorischen Fragen im Zuge des Universitätsalltags möchte ich mich herzlich bei Claudia Schäfer und Jutta Bourgeois bedanken. Birgit Tommes, Annette Ricken und Marcell Demandt danke ich für schnelle Messungen, die vielen Unterschriften auf allen möglichen Formularen und die Bereitstellung des Lagerschlüssels.

In besonderem Maße danke ich Simon Millan für die vielen Ideen, Anregungen und Diskussionen während meiner Arbeit und für die vielen lustigen Gespräche sowie Erlebnisse während der Institutspartys und in Lokalitäten außerhalb der Universität.

Weiterhin möchte ich mich bei meinen Kollegen aus dem Büro und Labor für die entspannte Atmosphäre bedanken. Dennis Dietrich danke ich für die Verbreitung seiner Weisheit auf jedem Themengebiet und seine Hilfe bei technischen Problemen, Sebastian Glomb für seine direkte Art und politische Diskussionen, insbesondere den Wahlomat, Yangyang Sun für die lustigen Gespräche dank leichter Verständigungsschwierigkeiten, Stefanie Bügel für die Gespräche über Membranthemen und unser gemeinsames Hobby, das Essen.

Ebenfalls möchte ich mich herzlich bei Anna Goldmann, Beatriz Gil-Hernandez, Philipp Brandt, Beatriz Giesen, Simon-Patrik Höfert, Moritz Steinert und Anna Kautz für die feucht fröhlichen Abende in der Altstadt und Umgebung bedanken.

Allen weiteren Mitgliedern des Arbeitskreises danke ich für die vielen ausgelassenen und häufig interessanten, wenn auch manchmal verstörenden Gespräche während der Mittagspause oder bei Institutsveranstaltungen.

Meiner Familie danke ich für die seelische und finanzielle Unterstützung während meines gesamten Universitätsaufenthalts und dafür, dass Ihr stets an mich geglaubt habt.

Zum Schluss möchte ich der wichtigsten Person in meinem Leben danken. Danke Seçil, dass ich dich kennen lernen durfte. Du hast mir das Leben an der Universität jeden Tag versüßt.

Kurzzusammenfassung

Metall-organische Gerüstverbindungen (MOFs) zeichnen sich durch ihre strukturelle Vielfalt und hohe potenzielle Porosität aus. Aufgrund dieser Eigenschaften wurden MOFs in den letzten Jahren in vielen Forschungsarbeiten für die anwendungsbezogenen Gebiete der Gasspeicherung und Gastrennung untersucht. Speziell für die Gastrennung wurden MOFs, neben anderen porösen Materialien, als Füllstoffe in organische Polymere eingebettet, um die Gas-Separationseigenschaften von reinen Polymermembranen zu verbessern. Die daraus hervorgehende Klasse an Materialien wird Mixed-Matrix-Membranen (MMMs) genannt. Bei der Membranherstellung müssen wichtige Parameter, wie die Füllstoffbeladung und Kompatibilität der beiden Komponenten berücksichtigt werden, da ansonsten Defekte die Trenneigenschaften der MMMs beinträchtigen.

In der vorliegenden Arbeit wurde der Einfluss von porösen und nicht-porösen Füllstoffen in MMMs mit Bezug auf die Rolle der Füllstoff-Polymer Schnittstelle, dem Grenzflächen Volumen, untersucht. Durch die Verwendung des gleichen MOFs in einem porösen und nicht-porösen Zustand, wurden Artefakte von MOF-spezifischen Eigenschaften auf die Füllstoff-Polymer Schnittstelle ausgeschlossen. Dazu wurde das poröse MOF Aluminium-Fumarat (Al-fum) und ein nicht-poröses, mit Dimethylsulfoxid (DMSO) gefülltes Aluminium-Fumarat (Al-fum(DMSO)), in das Polyimid Matrimid mit Füllstoffgehalten von 4 - 24 Gew% eingebettet. Alle Membranen wurden auf ihre Trenneigenschaften in der Gemischtgas-Separation von binären CO_2/CH_4 50/50 v:v Gasgemischen untersucht. Die Gas-Permeabilitäten für die MMMs mit den porösen Füllstoffen, sowie für die mit den nicht-porösen Füllstoffen, folgten dabei den theoretischen Vorhersagen des Maxwell Modells. Die MMMs mit dem porösen Füllstoff Al-fum zeigten erhöhte Permeabilitäten (*P*) für CO_2 und CH_4 bei einem moderaten Anstieg der Selektivität. Mit zunehmendem Massenanteil des nicht-porösen Füllstoffs Al-fum(DMSO) in den MMMs verringerten sich hingegen die Permeabilitäten der beiden Gase, wobei die Selektivität des reinen Polymers erhalten wurde. Die Auftragung von log *P* gegen das reziproke spezifische Freie Fraktionelle Volumen (sFFV) zeigte eine lineare Abhängigkeit und damit die Abwesenheit einer signifikanten Beteiligung des Grenzflächen Volumens an den Gas-Permeabilitäten der MMMs, da das sFFV nur das freie Volumen des Polymers und des Füllstoffs darstellt, jedoch nicht ein mögliches Grenzflächen Volumen einbezieht. Stattdessen beruht die Erhöhung der Permeabilität fast ausschließlich auf der Einführung des freien Volumens des porösen Füllstoffs Al-Fum. Die Verringerung des gesamten freien Volumens durch die Einbettung eines nicht-porösen Füllstoffs in Form von Al-fum(DMSO) zeigt dementsprechend auch einen Rückgang der Gas-Permeabilitäten. Berechnungen für das sFFV reichten von 0,23 $cm^3\ g^{-1}$ für die MMM mit 24 wt% Al-fum bis 0,12 $cm^3\ g^{-1}$ für die MMM mit 24 wt% Al-fum(DMSO). Der vernachlässigbare Effekt des Grenzflächen Volumen der

Schnittstellen zwischen Füllstoff und Polymer wird auch durch eine gute Übereinstimmung der theoretischen und experimentellen Dichte der MMMs belegt. Hier ergab sich ein spezifisches Grenzflächen Volumen von unter 0,02 cm^3 g^{-1} für alle MMMs.

In weiteren Studien wurden die Sorptions- und Separationseigenschaften für SO_2 an MOF-177, NH_2-MIL-125(Ti) und MIL-160 untersucht, mit dem Ziel neue Materialien für eine verbesserte Rauchgasentschwefelung zu finden. Für MOF-177 wurde die bis jetzt höchste gemessene SO_2-Aufnahme von 25,7 mmol g^{-1} (bei 298 K, 1bar) erhalten, welche mit dem sehr großen Porenvolumen von MOF-177 erklärt werden kann. NH_2-MIL-125(Ti) und MIL-160 zeigten besonders hohe SO_2-Aufnahmen bei niedrigen Drücken unter 0.01 bar. Diese Eigenschaft macht beide Materialien zu interessanten Kandidaten für die Rauchgasentschwefelung, da für die industrielle Anwendung hauptsächlich Spuren von SO_2 unter 500 ppm aus dem Rauchgas entfernt werden müssen. Insbesondere das aluminiumbasierte Furandicarboxylat MOF MIL-160 ist das vielversprechendste Material unter anwendungsorientierten Bedingungen und zeichnet sich durch hervorragende *ideal adsorbed solution theory* (IAST) Selektivitäten und überdurchschnittliche Trennleistungen bei Durchbruchsexperimenten aus. Ebenfalls zeigte MIL-160 eine hohe Stabilität sowohl unter feuchter als auch unter trockener SO_2-Exposition. Die hervorragende Sorptionsfähigkeit von MIL-160 konnte durch übereinstimmende DFT-Simulationsberechnungen in Kombination mit experimentellen Adsorptionswärmen für die Bindungsstellen erklärt werden.

Ferner wurden MMMs aus dem Polyimid 6FDA-mpD (6FDA = 4,4‘-Hexafluoroisopropyliden Diphtalsäureanhydrid, mPD= *m*-Phenylendiamin) und den zwei bekannten MOFs, MOF-199 (HKUST-1, Cu-BTC) und MIL-101(Cr), hergestellt und deren Einfluss auf die Trenneigenschaften untersucht. Permeationsstudien eines binären CO_2/CH_4 Gasgemisch (50/50) zeigten einen bemerkenswerten Anstieg der CO_2-Permeabilitäten für MIL-101(Cr)@6FDA-mPD und signifikant höhere CO_2/CH_4 Selektivitäten für MOF-199@6FDA-mPD. Die CO_2 Permeabilität erhöhte sich von 10 (reines Polymer) auf 50 Barrer für die 24 Gew% MIL-101(Cr)@6FDA-mPD-Membran (mit nahezu konstanter Selektivität) aufgrund des hohen Porenvolumens von MIL-101(Cr). Die CO_2/CH_4 Selektivität stieg von 54 auf 89 vom reinen 6FDA-mPD-Polymer bis zur 24 Gew% MOF-199@6FDA-mPD-Membran, offenbar infolge der hohen CO_2-Adsorptionskapazität von MOF-199.

Poröse Materialien, wie MOFs, sind interessante Kandidaten für die Gastrennung und Gasspeicherung. Ein wichtiger Parameter, um ein besseres Verständnis für den Adsorptionsprozess eines Adsorptivs an einem Adsorbens zu erhalten, ist die isostere Adsorptionsenthalpie (ΔH_{ads}), welche über die freigegebenen/benötigte Wärme bei der Adsorption/Desorption definiert ist. Zur indirekten Bestimmung von ΔH_{ads} müssen zunächst zwei Adsorptionsisothermen bei geringfügig unterschiedlichen Temperaturen (T_1, T_2) mit $\Delta T \approx$ 10-20 K aufgenommen werden. Diese sind die Grundlage für die Ableitung der isosteren Adsorptionsenthalpie durch den Clausius-Clapeyron-Ansatz oder die Virial Analyse, welche hier mit verwendbaren Excel-Tabellen und Origin-Dateien für die anschließende Ableitung von ΔH_{ads} vorgestellt werden. Beispielhaft wurden Adsorptionsisothermen von CO_2, SO_2 und H_2 bei zwei Temperaturen an MOFs analysiert. Die detaillierte rechnerische Beschreibung und der Vergleich des Clausius-Clapeyron-Ansatzes und der Virial Analyse zur Bestimmung von ΔH_{ads} skizzieren die Grenzen der beiden Methoden in Bezug auf die verfügbaren experimentellen Daten, insbesondere bei niedrigen Druck-/niedrigen Aufnahmewerten.

In den letzten Jahrzehnten wurden viele Anstrengungen unternommen, um CO_2 aus Verbrennungsabgasen einzufangen und abzutrennen. Als Alternative zur Aminwäsche sind poröse organische Moleküle (POMs) aufgrund ihrer maßgeschneiderten Strukturen und ihrer starken Affinität zu Molekülen wie CO_2 besonders attraktive Adsorbenzien. Die breiten Anwendungsmöglichkeiten poröser organischer Moleküle sind jedoch durch ihre labilen Gerüste, ihre geringe Oberfläche und ihren Polymorphismus begrenzt. In der vorliegenden Arbeit wurde ein neuer Ansatz zur Herstellung poröser Hybride auf POM-Basis durch Einkapselung des POMs Cucurbit[6]uril (CB6) in den Nanokäfig eines robusten MOFs dargestellt. Da das intrinsisch mikroporöse CB6-Molekül kleiner ist, als die inneren Mesoporen von MIL-101(Cr), entstehen in dem resultierenden CB6@MIL-101(Cr) Kompositmaterial mehr Affinitätsstellen für CO_2, was zu einer erhöhten CO_2-Aufnahmekapazität und zu einer höheren CO_2/N_2-Selektivität bei niedrigen Drücken führt. Die verbesserte Affinität zu CO_2 wird dabei auf die intrinsischen Poren von CB6 und die extrinsischen Poren um CB6 im Kompositmaterial zurückgeführt.

Short summary

Metal-organic frameworks (MOFs) are characterized by their structural diversity and high potential porosity. Because of these properties, in recent years MOFs have been studied in many research projects for application-related areas, such as gas storage and gas separation. Particular for gas separation processes, MOFs, among other porous materials, have been embedded as fillers into organic polymers, in order to improve the gas separation properties of pure polymer membranes. The resulting class of materials is called mixed matrix membranes (MMMs). Important parameters such as filler loading and compatibility of the two components must be taken into account, since otherwise defects will reduce the separation properties of the MMMs.

The present work deals with the influence of porous and non-porous fillers in MMMs. More specific the role of the filler-polymer interface, the so-called void volume was examined. By using the same MOF in a porous and non-porous state, artifacts from other possible properties of the filler on the filler-polymer interface were excluded. For this purpose, the porous MOF aluminum fumarate (Al-fum) and non-porous aluminum fumarate (Al-fum(DMSO)) filled with dimethyl sulfoxide (DMSO), were embedded in the polyimide Matrimid with filler contents ranging between 4 - 24 wt%. All membranes were examined for their separation properties in mixed gas studies of binary CO_2/CH_4 50/50 v: v gas mixtures. The gas permeabilities for the MMMs with the porous fillers, as well as those with the non-porous fillers, followed the theoretical predictions of the Maxwell model. The MMMs with the porous filler Al-fum showed increased permeabilities for CO_2 and CH_4 with a moderate increase in selectivity. In contrast, the permeability of both gases decreased with increasing mass fraction of the non-porous filler Al-fum(DMSO) in the MMMs, while retaining the selectivity of the pure polymer. The plot of log P against the reciprocal specific free fractional volume (sFFV) showed a linear dependency and thus, the absence of significant participation of the void volume in the permeability of the MMMs, since the sFFV includes the free volume of the polymer and the MOF, but not the filler-polymer interface volume. Instead, the increase in permeability for Al-fum@Matrmid MMMs is related entirely to the introduction of the free volume of the porous filler Al-Fum. Accordingly, the reduction in the total free volume by embedding a non-porous filler in the form of Al-fum(DMSO) is accompanied by a decrease in the permeability. Calculations for the sFFV ranged from 0.23 $cm^3\ g^{-1}$ for the MMM with 24 wt% Al-fum, to 0.12 $cm^3\ g^{-1}$ for the MMM with 24 wt% Al-fum(DMSO). The negligible effect of the void volume of the interface between filler and polymer is also evident by a good match between the theoretical and experimental density of the MMMs. In detail specific void volumes of less than 0.02 $cm^3\ g^{-1}$ were observed for all MMMs.

In further studies, the sorption and separation properties for SO_2 on MOF 177, NH_2-MIL-125(Ti) and MIL-160 were investigated, aiming for new materials for an improved flue gas desulfurization. For MOF-177 the highest measured SO_2 uptake so far of 25.7 mmol g^{-1} (at 298 K, 1 bar) was obtained, which could be explained by the enormous pore volume of MOF-177. NH_2-MIL-125(Ti) and MIL-160 showed particular high SO_2 uptake at low pressures below 0.01 bar. This property makes both materials prospective candidates for flue gas desulfurization, since for industrial use mainly traces of SO_2 below 500 ppm have to be removed from gas mixtures. In particular, the aluminum-based furandicarboxylate MOF MIL-160 is the most promising material under application-oriented conditions. MIL-160 features excellent ideal adsorbed solution theory (IAST) selectivities and outstanding separation performance in breakthrough experiments. It also showed high stability under both humid and dry SO_2 exposure. The excellent sorption capability of MIL-160 could be explained by DFT simulation calculations and matching heats of adsorption for the binding sites.

Furthermore, MMMs from the polyimide 6FDA-mpD (6FDA = 4,4'-hexafluoroisopropylidene diphthalic anhydride, mPD = m-phenylenediamine) and the two well-known MOFs, MOF-199 (HKUST-1, Cu-BTC) and MIL-101(Cr), were produced, showing excellent dispersion and compatibility between MOF particles and polymer matrix. Permeation studies of a binary CO_2/CH_4 gas mixture (50/50) showed a remarkable increase in CO_2 permeability for MIL-101(Cr)@6FDA-mPD and significantly higher selectivities for MOF-199@6FDA-mPD. The CO_2 permeability increased from 10 (pure polymer) to 50 Barrer for the 24 wt% MIL-101(Cr)@6FDA-mPD membrane (with almost constant selectivity) due to the high pore volume of MIL-101(Cr). The CO_2/CH_4 selectivity increased from 54 to 89 from the pure 6FDA-mPD polymer to the 24 wt% MOF-199@6FDA-mPD membrane, apparently due to the high CO_2 adsorption capacity of MOF-199.

Porous materials such as MOFs are interesting candidates for gas separation and storage. An important parameter to gain deeper insights into the adsorption process of an adsorptive on an adsorbent is the isosteric enthalpy of adsorption, ΔH_{ads} which is defined as the heat to be released/required when an adsorptive binds/detaches to the solid surface of an adsorbent. Two adsorption isotherms at different but close temperatures, (T_1, T_2) with $\Delta T \approx$ 10-20 K are the basis to derive the isosteric enthalpy of adsorption through the Clausius-Clapeyron approach or the virial analysis. Here the procedure of the common Freundlich-Langmuir fit/Clausius-Clapeyron approach and the virial fit of the isotherms with usable Excel sheets and Origin files for the subsequent derivation of ΔH_{ads} is presented. Exemplary adsorption isotherms of CO_2, SO_2 and H_2 at two temperatures on MOFs are analyzed. The detailed computational description and comparison of the Clausius-Clapeyron approach and the virial analysis to determine ΔH_{ads} outlines the limitations of the two methods with respect to the available experimental data, especially at low pressure/low uptake values.

During the past few decades, many efforts have been devoted to the capture and separation of CO_2 from post-combustion gases. As an alternative to amine scrubbing, porous organic molecules (POMs) are particularly attractive adsorbents for their tailored structures and strong affinity toward molecules like CO_2. However, the wide applications of porous organic molecules are limited by their labile frameworks, low surface area and polymorphism. In the present work, a new approach to prepare POM-based porous hybrids by encapsulating a POM called cucurbit[6]uril (CB6) into the nanocage of a robust MOF was depicted. Importantly, as the CB6 molecule with intrinsic micropore is smaller than the inner mesopores of MIL-101(Cr), more affinity sites for CO_2 are created in the resulting CB6@MIL-101(Cr) composites, leading to enhanced CO_2 uptake capacity and CO_2/N_2 selectivity at low pressures. The improved CO_2 affinity is attributed to the intrinsic pores of CB6 and extrinsic pores around CB6 in the composite.

Abkürzungsverzeichnis

1,4-BDC	Terephthalsäure, Benzol-1,4-dicarbonsäure
4,4‘-Bipy	4,4‘-Bipyridin
6FDA	4,4‘-Hexafluoroisopropyliden Diphtalsäureanhydrid
µm	Mikrometer
BET	Brunauer-Emmett-Teller
calc	calculated, berechnet
cm	Zentimeter
DCM	Dichlormethan
DFT	Dichtefunktionaltheorie
DMF	*N,N*-Dimethylformamid
DMSO	Dimethylsulfoxid
EDX	energy-dispersive X-ray spectroscopy, energiedispersive Röntgenspektroskopie
exp	experimentell
FFV	fractional free volume, Fraktionelles Freies Volumen
g	Gramm
HKUST	Hong Kong University of Science and Technology
H_3BBC	4,4‘,4‘‘-(Benzol-1,3,5-triyl-tris(benzol-4,1-diyl))tricarbonsäure
H_3BTB	4,4‘,4‘‘-Benzol-1,3,5-benzoltricarbonsäure
H_3BTC	1,3,5-Benzoltricarbonsäure
konz.	konzentriert
IAST	ideal adsorbed solution theory
IUPAC	International Union of Pure and Applied Chemistry
mbar	Millibar
min	Minute
mL	Milliliter

MMM	Mixed-Matrix-Membran
MOF	Metal-organic framework
mPD	*m*-Phenylendiamin
p.a.	zur Analyse
REM	Rasterelektronenmikroskopie
PXRD	Röntgenpulverdiffraktogramm
RT	Raumtemperatur
S_{BET}	BET-Oberfläche
SBU	secondary building unit
STP	Standard temperature and pressure
wt%	Gewichtsprozent

Inhaltsverzeichnis

1. Einleitung

1.1 Metall-organische Gerüstverbindungen

1.1.1 Historie und Aufbau

Schon in den 1830er Jahren wurde das Interesse für anorganisch/organische Hybridverbindungen geweckt, nachdem Zeise mit seinem später nach ihm benannten „Zeise-Salz“, mit der Summenformel ($K[PtCl_3(C_2H_4)]H_2O$), den ersten Organometallkomplex entdeckte und charakterisierte.[1] Zeise begründet damit das Feld der Organometallchemie, welches einen besonderen Fokus auf die Reaktivität der Schnittstelle zwischen Metallion und organischer Komponente legt. Im Laufe der nächsten zwei Jahrhunderte wurden zahlreiche molekulare, homogene Organometall-Verbindungen hergestellt, welche sich besonders durch ihre katalytischen Eigenschaften auszeichnen.[2] Da in dieser Zeit auch immer mehr industriell gefertigte Produkte über katalytische Prozesse hergestellt wurden, erhöhte sich das industrielle Interesse nach heterogenen Katalysatoren. Folglich wurde nach komplexeren Strukturen geforscht, deren physikalische Eigenschaften sich durch Ihren höheren Vernetzungsgrad ableiten. Dazu gehören Materialien, die eindimensionale Ketten (1D), zweidimensionale Netze (2D), oder dreidimensionale Gerüste (3D) ausbilden, sowohl kristalline als auch amorphe Strukturen.[3] Die Entwicklung von Materialien mit höherer Dimensionalität ging einher mit der Ausbildung von intrinsischer Porosität in ebendiesen. Inhärente Porosität war schon von den rein anorganischen Zeolithen und organischen Aktivkohlen bekannt und eröffnete die Möglichkeit zu neuartigen Anwendungen in der heterogenen Katalyse und der Gassorption.[4,5,6] Ein großer Nachteil der siliziumbasierten Zeolithe ist jedoch Ihre strukturelle Eindimensionalität. Zeolithe sind Alumosilikate, die nur geringe Mengen weiterer Übergangsmetallen oder Alkali/Erdalkalimetallen zur Funktionalisierung in ihrer Struktur zulassen.[7] Ferner führen die durch den Einbau an Fremdatomen entstehenden Defekte bei übermäßiger Substitution der ursprünglichen Atome zum Zusammenbruch der Struktur.[8]

Durch den Austausch der Metallionen über die vierte Hauptgruppe hinaus und die Verwendung von verbrückenden organischen Liganden wurde schließlich Anfang der 1990er Jahre eine neue Klasse an Materialien zugänglich, die Koordinationspolymere.[9] Hoskins und Robson zeigten in Ihren Veröffentlichungen, dass es möglich ist, Knotenpunkte mit tetraedrischer oder oktaedrischer Anordnung über stäbchenförmige, lineare oder tetraedrische Liganden miteinander zu verknüpfen und somit dreidimensionale Gerüste aufzubauen.[10] Durch die dadurch implizierte Strategie einer rationalen Verknüpfung verschiedener Topologien, wurde in den folgenden Jahren eine Vielzahl neuer Verbindungen synthetisiert.

Der Begriff der *metal-organic frameworks* (zu Deutsch: Metall-organische Gerüstverbindungen, MOFs) wurde zum ersten Mal von Yaghi im Jahr 1995 verwendet, um das dreidimensionale, mikroporöse Netzwerk aus $[Cu(I)(4,4'\text{-}Bipy)_{1,5}NO_3]\cdot(H_2O)_{1,25}$ zu beschreiben.[11] Zwei Jahre später wurde von der Gruppe um Kitagawa gezeigt, dass die inhärente Mikroporosität von strukturell ähnlichen dreidimensionalen Gerüstverbindungen auch für unpolare Gase (N_2, O_2 und CH_4) zugänglich ist.[12] Unter den vielen Forschungsgruppen, welche sich in den nächsten 15 Jahren mit ein- oder mehrdimensionalen Koordinationspolymeren beschäftigten, konnte jedoch keine einheitliche Terminologie für Ihre Strukturen gefunden werden. Erst als eine vorläufige hierarchische Begrifflichkeit gemäß Abbildung 1 vorgestellt wurde, stellte die IUPAC ihre eigene Definition von MOFs vor.[13,14]

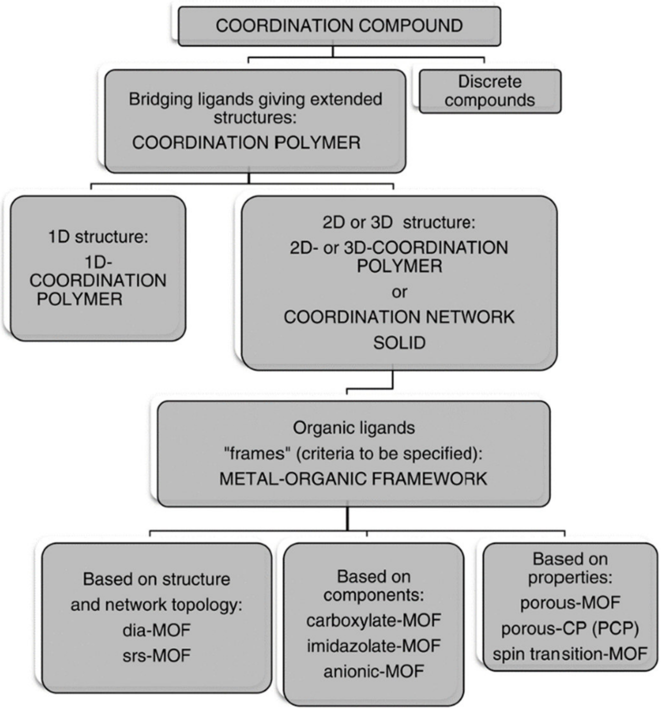

Abbildung 1: Hierarchische Unterteilung der Begriffe Koordinationsverbindung, Koordinationspolymer und Metall-organische Gerüstverbindung. Nachdruck mit Genehmigung von Ref. 13. Copyright 2012 The Royal Society of Chemistry (RSC).

Koordinationspolymere sind ein-, zwei-, oder dreidimensionale Koordinationsverbindungen aus sich wiederholenden Einheiten.

Koordinationsnetzwerke sind Koordinationsverbindungen, die sich durch wiederholende Einheiten in zwei oder drei Dimensionen erstrecken oder auch eindimensionale Verbindungen die miteinander verknüpft sind.

Metall-organische Gerüstverbindungen sind Koordinationsnetzwerke mit organischen Liganden und potentiellen Hohlräumen.

Explizit nicht genannt in dieser Definition für MOFs sind das Vorliegen von Kristallinität und der zwingende Nachweis der Porosität durch Gassorptionen. Dies ist auf die Vielzahl an dynamischen Änderungen der Strukturen abhängig von Lösungsmittel, Temperatur, Druck oder anderen externen Stimulationen zurückzuführen.[14] Der Aufbau von Koordinationspolymeren, Koordinationsnetzwerken und MOFs erfolgt über Metall-haltige Knotenpunkte, welche mittels Koordinationsbindungen über organische Liganden miteinander verknüpft sind (Abbildung 2).[15]

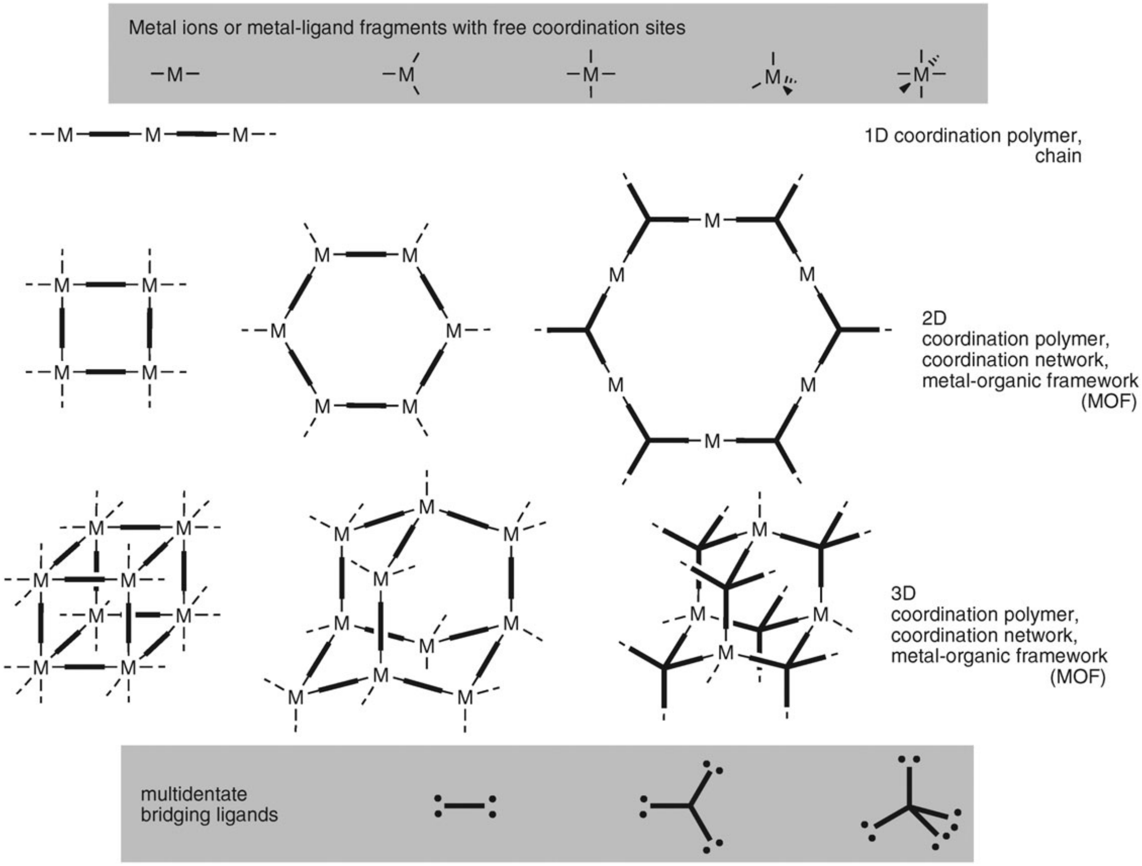

Abbildung 2: Schematische Darstellung über den Aufbau von Koordinationspolymeren, Koordinationsnetzwerke und MOFs. Nachdruck mit Genehmigung von Ref. 15. Copyright 2010 The Royal Society of Chemistry (RSC).

Anhand der oben vorgestellten Definition ist deutlich erkennbar, dass die Porosität eine zentrale Rolle im Bereich der MOFs spielt. Folgerichtig kann eine Einteilung poröser Materialien über den Porendurchmesser erfolgen. Dabei zeigen ungeordnete, (meist) nicht kristalline poröse Festkörpermaterialien, wie Aktivkohlen oder Kieselgele, eine breite Porengrößenverteilung, im Gegensatz zu den geordneten, kristallinen Materialien, wie den Zeolithen oder den MOFs. Standardisiert wurde die Einteilung poröser Materialien durch die IUPAC anhand ihrer Porengröße bzw. ihres Porendurchmessers, bestimmt durch Physisorption von Gasen an Feststoffen.[16] Bis zu einem Porendurchmesser von $Ø < 2$ nm gelten Materialien als mikroporös, bei einem Porendurchmesser zwischen Ø 2 – 50 nm spricht man von mesoporösen Materialien und Porendurchmesser $Ø > 50$ nm zeigen die makroporösen Materialien.[16]

Ende der 1990er Jahre wurden von Williams mit dem MOF HKUST-1 $[Cu_3(BTC)_2]$ und Yaghi mit MOF-5 $[Zn_4O(1,4\text{-}BDC)_3]$ zwei der heute bekanntesten MOFs synthetisiert.[17,18] Beide MOFs zeigten bis dato nicht erreichte permanente Porositäten (Porenvolumen > 0,7 $cm^3 \cdot g^{-1}$), wenn gleich die Verbindungen nur geringfügige (MOF-5) bis mäßige (HKUST-1) chemische Stabilität zeigten. Obwohl viele neue kationische, anionische und neutrale MOFs mit einzigartigen Porenstrukturen und Funktionen dargestellt wurden, gab es zunächst keine effektive Strategie zur Syntheseplanung für neue Materialien.[19] Infolge der stetig zunehmenden Porosität neuer MOFs trat zunehmend das Phänomen der Interpenetration ein-, zwei-, und dreidimensionaler Netzwerke ineinander auf, wobei allgemein bei eindimensionalen Netzwerken nicht von Interpenetration sondern von Verflechtung gesprochen wird (Abbildung 3).[20]

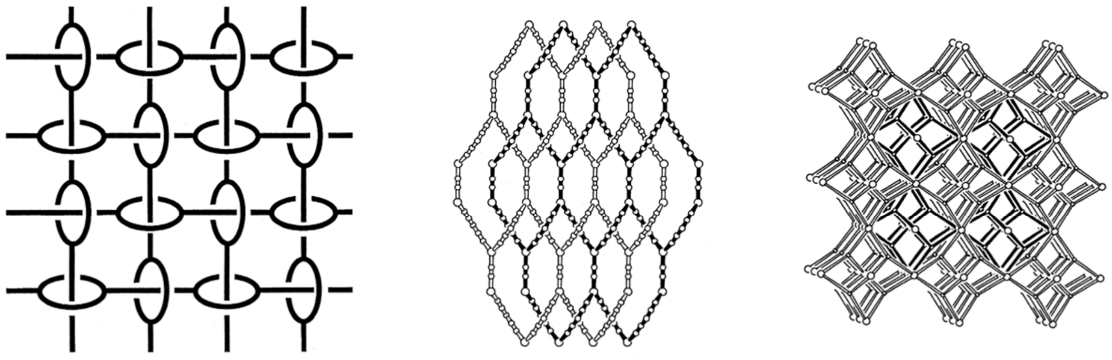

eindimensional zweidimensional dreidimensional

Abbildung 3: Schematische Darstellung der Interpenetration/Verflechtung ein-, zwei-, und dreidimensionaler Netzwerke. Nachdruck mit Genehmigung von Ref. 20. Copyright 1998 John Wiley and Sons.

Da die Entropie von Materialien mit geringer Dichte (hohe Porosität) niedriger ist als jene von Materialien höherer Dichte, kommt es zu dem natürlichen Ziel der Reduktion von Hohlräumen. Die interpenetrierten Netzwerke sind dabei untereinander nicht kovalent gebunden, können jedoch nur durch Brechen einer Bindung voneinander getrennt werden.[21]

Im Jahr 2000 schließlich übertrug Férey das Konzept der *building unit* (BU), welches schon bei den Zeolithen in Form der Interpenetration ihrer Netzwerke durch die Verknüpfung von Si/AlO$_4$-Tetraedern Anwendung fand, auf das Feld der MOF-Chemie.[22,23] *Building units* werden dabei als kleinste mögliche Anordnung von Atomen, Ionen oder Molekülen beschrieben, bei deren Bindungsbildung mit sich selbst oder anderen BUs, die Struktur des Feststoffs gebildet wird. Ein großer Vorteil der BUs ist, dass diese meist triviale geometrische Körper (Dreieck, Tetraeder, Oktaeder, Würfel, etc.) darstellen. Die BUs können gewissermaßen als Bausteine einer bestimmten Form gesehen werden, mit deren Hilfe Strukturen anderer Geometrie und Größe errichtet werden können.[23] Ferner führte Férey den Begriff der *scale chemistry* ein. Gemeint ist damit, dass die räumliche Anordnung der BU nicht von der Größe der Struktur abhängt und sich nur die Zellgröße ändert (Abbildung 4).

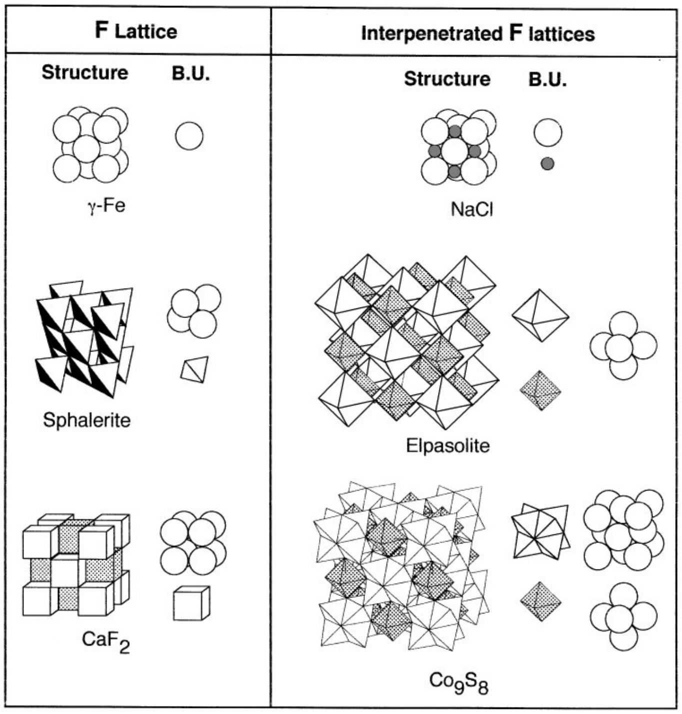

Abbildung 4: Darstellung der gleichen Ausrichtung der building units in verschiedenen Strukturen der Kristallgitter des Typs F und des Typs interpenetriert F. Nachdruck mit Genehmigung von Ref. 23. Copyright 2000 Elsevier.

Mit Hilfe dieses Designkonzepts hatte man nun ein Werkzeug, um aus den Strukturinformationen der bereits synthetisierten MOFs neue Topologien zu entwerfen.

Der Durchbruch bezüglich des Designs neuer MOFs gelang jedoch Eddaoudi, O'Keeffe und Yaghi durch die Entwicklung der modularen MOF-Chemie und die Einführung der *secondary build units* (SBU).[24,25] Dieser Ansatz ist besonders effektiv für die Synthese von porösen Netzwerken, die auf diskreten molekularen Einheiten und rigiden Liganden aufgebaut sind, und bei moderaten Temperaturen verlaufen. Sowohl die Metallknotenpunkte, als auch die Liganden bilden ihre eigenen SBUs, je nach Koordinationsumgebung des Metalls und Struktur des Liganden. Abbildung 5 zeigt typische SBUs der anorganischen Metallcluster und der organischen Brückenmoleküle.

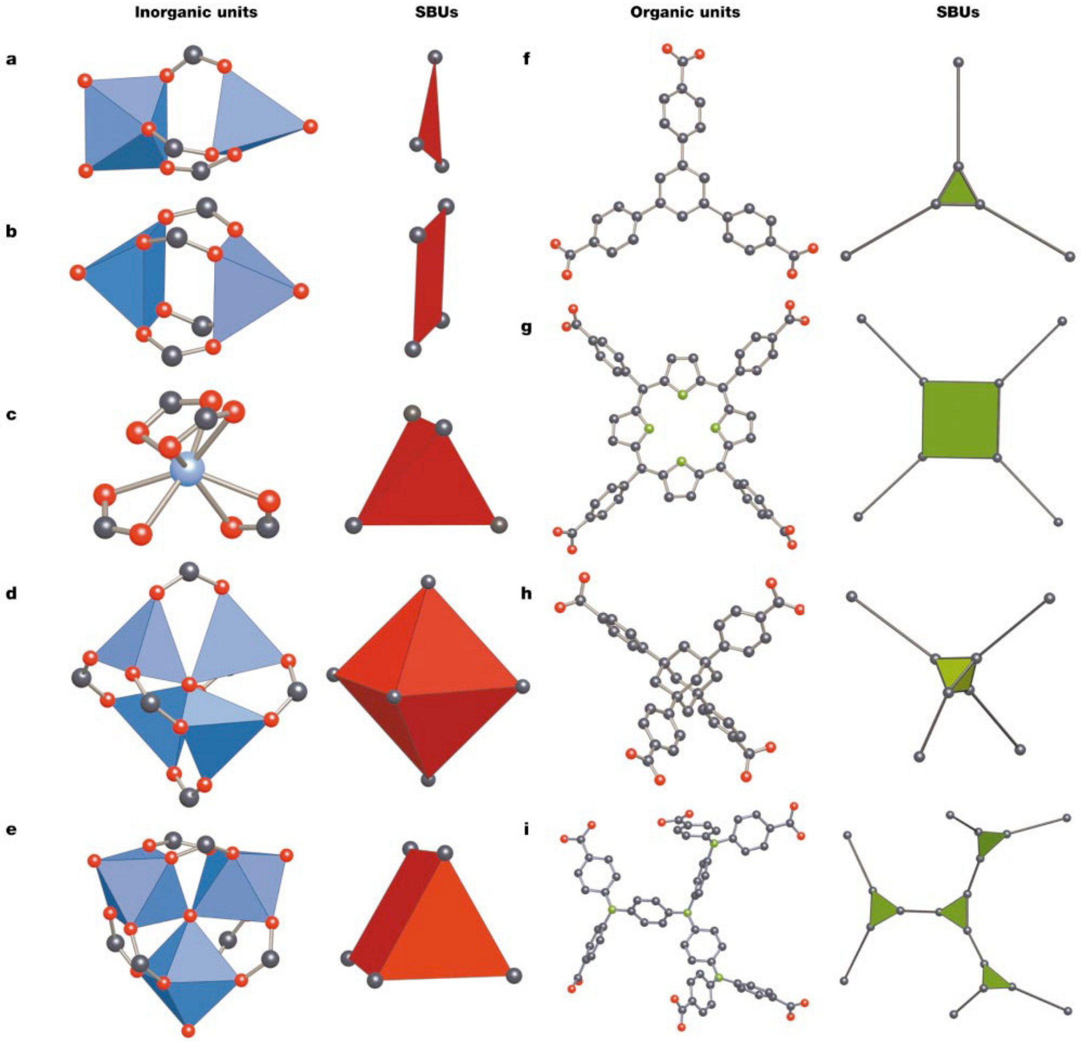

Abbildung 5: Beispiele für SBUs von Carboxylat-MOFs. O, rot; N, grün; C, schwarz. Anorganische Einheiten Metall-Sauerstoff Polyeder in blau und Polygone oder Polyeder aufgespannt von den Carboxylat Kohlenstoffatomen (SBUs) in rot. In den organischen SBUs sind die verbrückenden Polygone oder Polyeder in grün gezeigt. Nachdruck mit Genehmigung von Ref. 25. Copyright 2003 Springer Nature.

Um nun eine Vorhersage zur Bildung der Topologie der Gerüstverbindungen zu treffen, geht man von den geometrischen Eigenschaften der Linker- und Metall-SBUs aus. Welche Geometrie die Metallknoten und Linker aufweisen wird durch den sogenannten *point of extension* (Ausdehnungspunkt) definiert. Man sucht also in dem Metallknoten und dem Liganden die Geometrie, von der aus die Ausbreitung des Netzes in alle Dimensionen beschrieben werden kann. Für einen Metallknoten eines Carboxylat MOFs ist dieser entsprechend durch die Kohlenstoffatome der bindenden Carboxylgruppe repräsentiert (Abbildung 5). Die Syntheseplanung und Analyse von Netzwerken mit Hilfe des SBU-Ansatzes wird auch retikuläre (netzartige) Synthese genannt.[25] Diese Form von *crystal engineering* ist jedoch nur möglich, wenn die Eduktmaterialien ihre Struktur während der Synthese beibehalten. Deshalb sind gut definierte, starre Einheiten von essenzieller Bedeutung für die erfolgreiche retikuläre Synthese über den SBU-Ansatz.

Kombiniert man den Drang der Forscher nach Netzwerken mit immer höheren Porositäten zu streben, mit dem Konzept der retikulären Synthese, kommt man zwangsläufig zu der Vorstellung, dass allein durch Verlängerung des Linkers, bei gleichzeitigem Erhalt der Netzwerktopologie, die Porosität zunehmen sollte. Diese Strategie wird isoretikuläre Synthese genannt. Gezeigt werden konnte dies 2002 von Yaghi für die isoretikuläre Synthese der IRMOF-Serie.[26] Ausgehend von dem Prototypen MOF-5 (IRMOF-1), welches über oktaedrisch angeordnete $\{ZnO(-COO)_6\}$ Metallcluster aufgebaut ist und mittels Phenylgruppen der Terephthalatliganden verbrückt wird, wurden zahlreiche weitere MOFs mit der gleichen **pcu**-Topologie synthetisiert (Abbildung 6).[27]

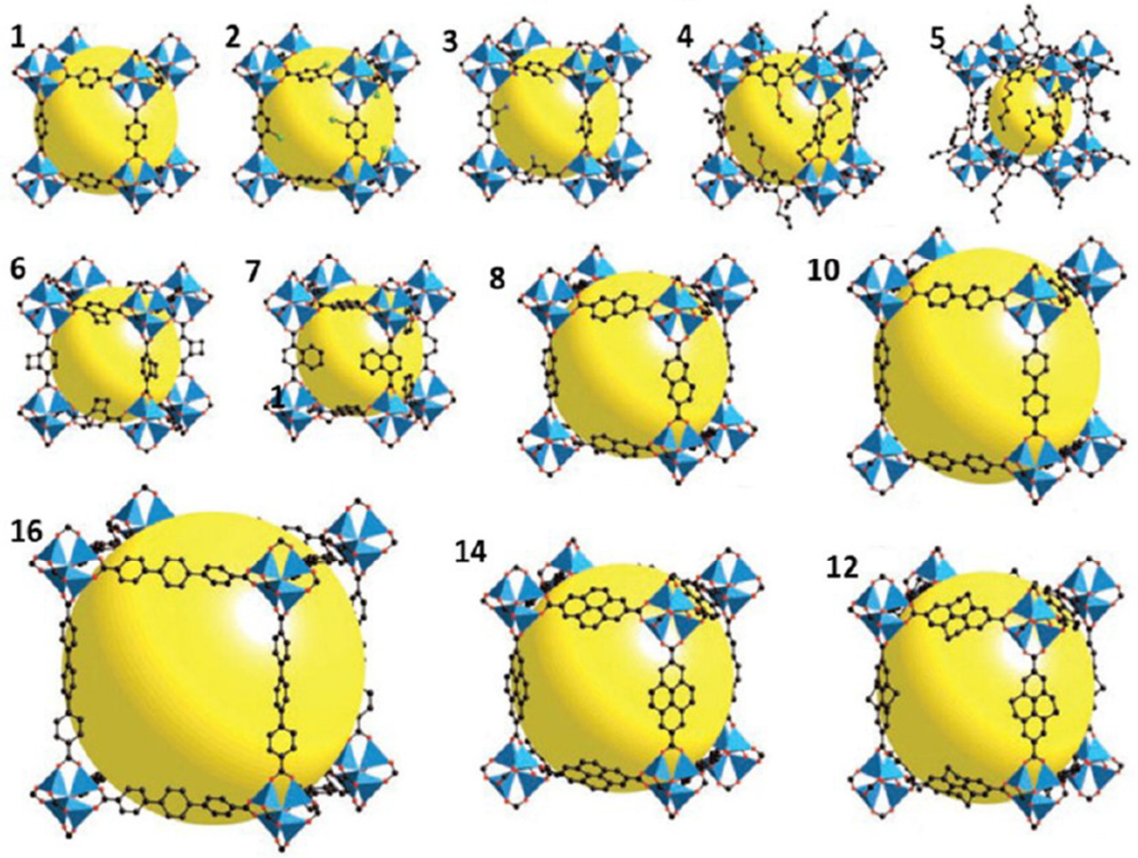

Abbildung 6: Darstellung der IRMOFs-n (n = 1-8, 10, 12, 14, 16) ohne Interpenetration. Nachdruck mit Genehmigung von Ref. 27. Copyright 2019 American Chemical Society.

.

Das freie Volumen der IRMOFs konnte je nach eingebautem Linker zwischen 55.8 % (IRMOF-5) und 91.1 % (IRMOF-16) variiert werden. Dabei kann zu großen Teilen eine Proportionalität zwischen Länge des Linkers, freiem Volumen und Porengröße festgestellt werden. Für die Kristalldichte wird dementsprechend ein antiproportionaler Zusammenhang gefunden. IRMOF-5 zeigt für poröse Materialien eine relativ hohe Kristalldichte von 1,00 $g \cdot cm^{-3}$ im Vergleich zu der sehr geringen Kristalldichte von 0,21 $g \cdot cm^{-3}$ von IRMOF-16.[26]

Ein weiteres Beispiel für die isoretikuläre Synthese ist hier anhand des bekannten MOFs HKUST-1 gezeigt.[28] Dabei wird der organische Linker im HKUST-1, die Trimesinsäure (H_3BTC), durch eine (H_3BTB) oder zwei (H_3BBC)-Phenyleinheiten als zusätzlichen Abstandshalter an allen Ausbreitungspunkten/Achsen entlang der SBU verlängert und somit die Elementarzelle und das Porenvolumen signifikant erhöht (Abbildung 5).

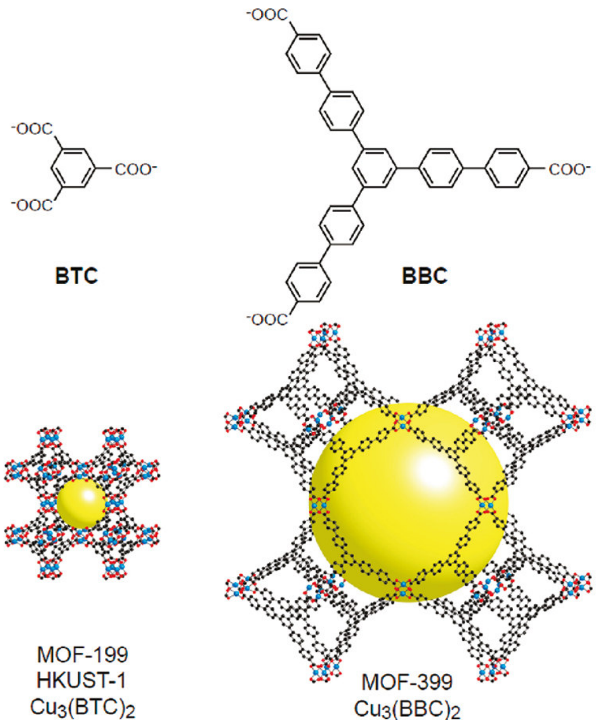

Abbildung 7: Molekülstrukturen der organischen Linker (oben). Einkristallstrukturen von HKUST-1 und MOF-399 (unten). Nachdruck mit Genehmigung von Ref. 28. Copyright 2011 American Chemical Society.

In den nächsten Jahren erzielten MOF-Publikationen, in denen neuartige MOFs mit extrem hohen inneren Oberflächen und Porenvolumina dargestellt wurden, eine hohe Aufmerksamkeit.[29] Mit dem Ziel der Wasserstoffspeicherung entwickelten die Arbeitsgruppen um Yaghi und Hupp im Jahr 2010 die Materialien MOF-210 und NU-100 mit inneren Oberflächen von ca. 6200 $m^2\ g^{-1}$.[30,31] Darauf folgte mit der Publikation des MOFs DUT-60 durch Kaskel et al. 2018 die Darstellung des Materials mit der bis heute höchsten inneren Oberfläche (7840 $m^2\ g^{-1}$) und dem größten Porenvolumen (5,02 $cm^3\ g^{-1}$).[32] Alle Materialien die eine solch hohe Porosität aufweisen, zeigen eine Verbrückung der Metallknoten über vergleichsweise lange Linker, welche wiederum zu einer mesoporösen Struktur der Materialien führt. Der Zusammenhang von Linker Beschaffenheit und Porosität wurde bereits in der retikulären Synthese der IRMOFs beobachtet.

Neben der Auswahl an Metallsalz und Linker haben auch die Synthesebedingungen einen signifikanten Einfluss auf die Struktur und Morphologie der MOFs. Bei der klassischen MOF-Synthese wird die benötigte Energie durch elektrisches Heizen zugeführt. Dabei wird in einer solvothermalen bzw. hydrothermalen (mit Wasser als Lösungsmittel) Synthese die Reaktion in einem gasdicht geschlossenen Gefäß unter autogenem Druck durchgeführt, um über dem Siedepunkt des verwendeten Lösungsmittels arbeiten zu können. Bei den nicht-solvothermalen Reaktionen wird entweder bei erhöhter Temperatur (bis zum Siedepunkt des Lösungsmittels, Rückflusssynthese) oder bei Raumtemperatur gearbeitet (Abbildung 8).[33]

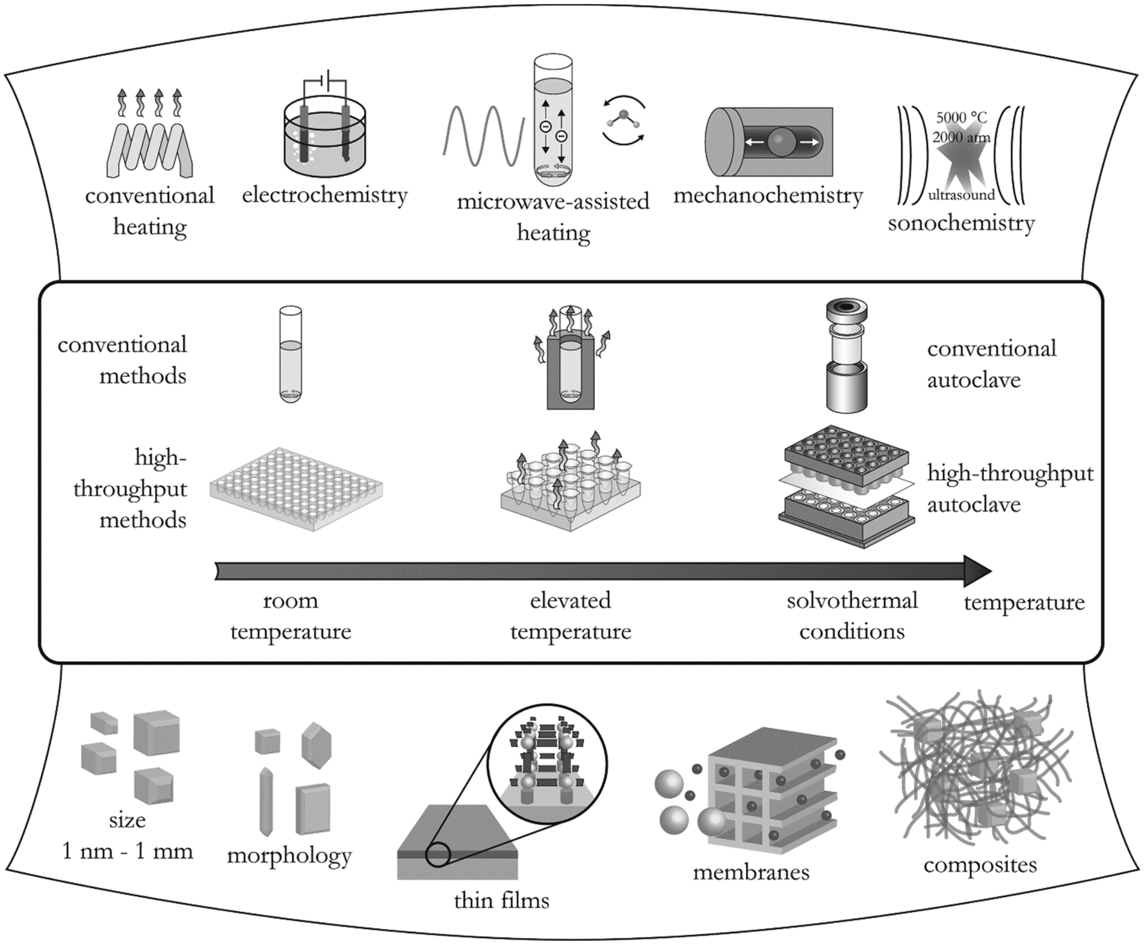

Abbildung 8: Übersicht der Synthesemethoden (oben), möglicher Reaktionstemperaturen (mittig) und Reaktionsprodukte in der MOF-Synthese (unten). Nachdruck mit Genehmigung von Ref. 33. Copyright 2012 American Chemical Society.

Im Laufe der meistens als Eintopfreaktion ablaufenden Synthese bilden die gelösten Metallsalze mit den gelösten organischen Liganden unter Selbstassemblierung der eingesetzten bzw. in situ gebildeten SBUs die sogenannte *as-synthesized* (nach Synthese) Struktur des MOFs aus. Um die Zugänglichkeit der Poren zu gewährleisten muss nun in einem weiteren Schritt das MOF aktiviert werden. Unter Aktivierung versteht man folglich das Entfernen von Gastmolekülen aus den Poren der MOFs.[34] Bei den Gastmolekülen kann es sich um unkoordinierte Liganden, Metallsalze oder Lösungsmittelmoleküle handeln. Die erfolgreichsten Methoden zur Aktivierung sind der Austausch des meist hochsiedenden ursprünglichen Lösungsmittels (DMF, DEF, DMSO, H_2O) gegen ein flüchtigeres Lösungsmittel

(MeOH, EtOH, Acteon, CH_2Cl_2), gefolgt von einer thermischen Aktivierung unter vermindertem Druck.[35,36]

Die Synthesebedingungen müssen entsprechend der gewünschten Eigenschaften (Größe, Morphologie, Kristallqualität) des herzustellenden MOFs angepasst werden. Zur Strukturaufklärung eines neuartigen MOFs wird bevorzugt die Einkristallstrukturanalyse angewendet. Dafür werden jedoch Einkristalle guter Qualität und einer Größe von ca. 100 µm benötigt. Um Einkristalle von dieser Größe zu synthetisieren muss die Kristallwachstumsgeschwindigkeit bis zur kritischen Nukleationskonzentration kontrolliert werden, da erst ab diesem Zeitpunkt das Kristallwachstum beginnt. Wichtige Faktoren dafür sind die Temperatur, Konzentration, molares Verhältnis der Edukte, das Lösungsmittel und der pH-Wert. Außerdem wird besonders in der klassischen Synthese über extrem langsame Heizraten bzw. Abkühlungszeiten (bis zu mehreren Tagen) eine hohe Kristallqualität ermöglicht.[37]

Neben der klassischen Synthese ist die mikrowellen-assistierte Synthese eine weit verbreitet eingesetzte Synthesetechnik. Die Energiezufuhr erfolgt hierbei durch das oszillierende elektrische Feld, das molekulare Rotationen von allen in der Synthese verwendeten Molekülen mit einem Dipolmoment erzeugt, welche anschließend durch Reibung in Wärme umgewandelt wird. Dadurch kommt es zu einer gleichmäßigen, sehr schnellen Erhitzung der flüssigen Phase. Neben einer drastisch verkürzten Reaktionszeit von oft mehreren Tagen hin zu wenigen Minuten oder Stunden, können zudem sehr enge Partikelgrößenverteilungen und durch eine schnelle Kristallisation sehr kleine Partikelgrößen erreicht werden.[38,39] Ähnliche Auswirkungen auf die Kristallmorphologie und die Reaktionsgeschwindigkeit zeigt die Ultraschallsynthese von MOFs. Bei der Ultraschallsynthese liegt aufgrund der großen Wellenlänge der mechanischen Schwingung keine Wechselwirkung mit den Molekülen selbst vor, stattdessen bilden sich innerhalb der flüssigen Phase Hochdruck- und Niederdruckregionen aus. In der Niederdruckphase bilden sich unterhalb des Dampfdrucks des Lösungsmittels Bläschen aus, die auf bis zu 10 µm anwachsen können, bevor sie platzen. Dieser Prozess wird Kavitation genannt. Dadurch können lokal Temperaturen vom bis zu 5000 K und Drücke bis 1000 bar entstehen, was auch bei der Ultraschallsynthese zu einem extrem schnellen Heizen mit gleichmäßigem Kristallwachstum führt.[33,40]

Weitere eher selten angewandte Synthesemethoden sind die elektrochemische und mechanochemische Synthese. Bei der elektrochemischen Synthese werden die Metallionen nicht über Salze bereitgestellt, sondern an einer Anode kontinuierlich in Lösung gebracht, um dort mit den bereits gelösten Linkermolekülen zu reagieren. Durch protische Lösungsmittel wird eine Metallanreicherung an der Kathode vermieden, es entsteht jedoch Wasserstoff. Als

Vorteil gilt auch, das die elektrochemische Synthese kontinuierlich durchgeführt werden kann.[41] Der mechanische Bindungsbruch von intramolekularen Bindungen gefolgt von chemischen Transformationen ist die Basis der mechanochemischen Synthese. Aufgrund der lösungsmittelfreien Synthese, welche oft bei Raumtemperatur stattfindet und mit geringen Reaktionszeiten abläuft könnte die mechanochemische Synthese in Zukunft jedoch noch an Bedeutung gewinnen.[42]

Durch die Auswahl geeigneter Synthesebedingungen in Verbindung mit der Vielfalt der Ausgangsmaterialien werden für MOFs eine Vielzahl von potentiellen Anwendungsgebieten diskutiert. Dabei steht häufig die charakteristische Porosität als herausragende Eigenschaft der MOFs im Vordergrund (Abbildung 9).

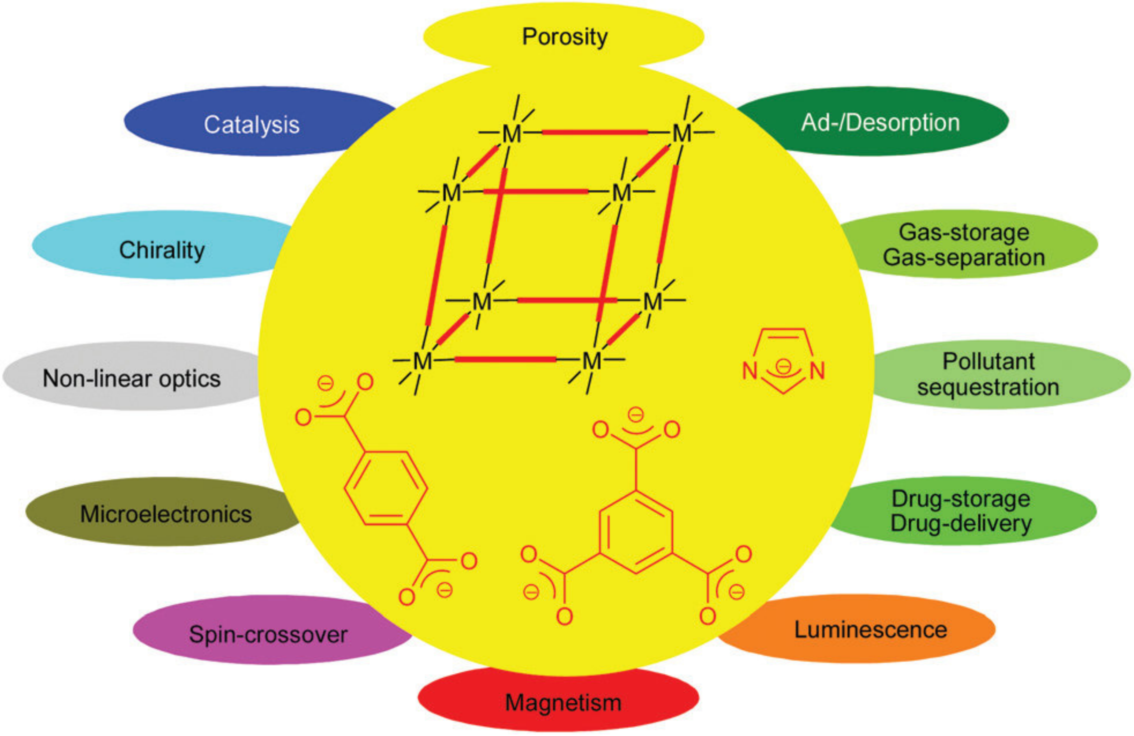

Abbildung 9: Schematische Darstellung eines MOFs, sowie wichtiger Eigenschaften und potentieller Anwendungsgebiete von MOFs. Nachdruck mit Genehmigung von Ref. 43. Copyright 2012 The Royal Society of Chemistry (RSC).

Aufgrund Ihrer Porosität können MOFs Gase reversibel oder irreversibel adsorbieren und damit in der Gasspeicherung oder der Gastrennung eingesetzt werden.[44,45,46] Auch eine potentielle Anwendung in sorptionsgetriebenen Kältemaschinen oder bei der Abgabe von Wirkstoffen in der Medizin ist möglich. [47,48] Ferner können MOFs im Bereich der heterogenen Katalyse verwendet werden.[49] Sie verfügen durch Ihre Porenstruktur über einen Größenausschlusseffekt, eine hohe Anzahl an katalytisch aktiven Zentren und große chemische Vielfalt durch ihren Aufbau.[50] Außerdem können MOFs auch als Sensoren für externe Parameter, wie zum Beispiel Druck oder Temperatur, verwendet werden.[51]

1.1.2 Porosität und Sorptionseigenschaften

Die essenzielle Eigenschaft der Porosität in MOFs, spezifischer die Mikro- und Mesoporosität von MOFs, wird mittels Gasadsorptionsmethoden nachgewiesen und charakterisiert. Die grundlegenden Prozesse der Gassorption an der festen Phase sind in Abbildung 10 dargestellt.

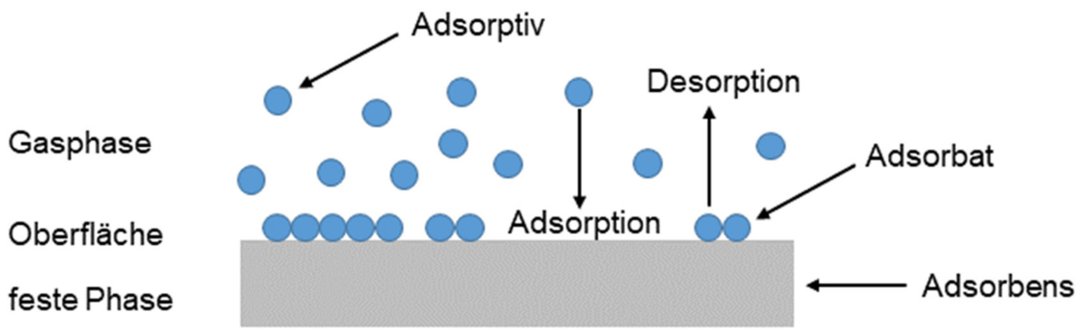

Abbildung 10: Schematische Darstellung ausgewählter Prozesse bei der Gassorption an festen Phasen.

Die Anlagerung gasförmiger Moleküle (Adsorptiv) an einer festen Phase, dem Adsorbens, wird als Adsorption bezeichnet. Nach der Anlagerung werden die Gasteilchen als Adsorbat benannt. Den gegenläufigen Prozess beschreibt die Desorption. Dabei lösen sich die Gasmoleküle von der Oberfläche des Adsorbens und gehen in die freie Gasphase über. Für die meisten Systeme liegt ein dynamisches Gleichgewicht zwischen beiden Prozessen vor. Die Adsorption kann im Allgemeinen auf zwei Arten erfolgen. Bei der Physisorption handelt es sich um eine reversible physische Adsorption mit geringen Bindungsenergien über Van-der-Waals-Kräfte. Die Adsorption ist stark temperaturabhängig, nicht spezifisch, kann Multilagen ausbilden und zeigt geringe Adsorptionswärmen bei der Anlagerung. Das zweite Phänomen beschreibt die Chemisorption, eine chemische Adsorption der Gasmoleküle an der Oberfläche des Feststoffs. Hierbei handelt es sich um starke, irreversible Bindungen mit hohen Adsorptionswärmen. Es kommt nur zu der Ausbildung einer einzigen Adsorptionsschicht (Monolage), die temperaturunabhängig und spezifisch nach den Oberflächencharakteristiken des Adsorbens verläuft.

Praktisch kann die Aufnahme von Gassorptionsisothermen (Gassorption bei gleichbleibender Temperatur) über zwei unterschiedliche Messprinzipien erfolgen. Das Standardmessprinzip ist die statisch volumetrische Messmethode. Dabei wird bei einem konstanten Volumen der Probenkammer die Menge an adsorbiertem/desorbiertem Gas an einem Festkörper bei Gleichgewichtsdruck quantifiziert. Die Quantifizierung geschieht über inkrementelle Zugabe/Entfernung einer bestimmten Menge an Adsorptiv, die zu einer Druckabnahme/zunahme führt. Dementsprechend ändert sich der Druck bis der Gleichgewichtszustand erreicht ist. Deutlich seltener wird die gravimetrische Messmethode in der Gassorption angewandt. Dabei wird die aufgenommene Menge an Gas mit der Gewichtsänderung im Gleichgewicht korreliert.

Die Analyse von mikro- und mesoporösen Festkörperstrukturen mit Hilfe der Gassorption war schon vor der Entdeckung der MOFs im Feld der Zeolithe eine anerkannte und weit verbreitete Technik.[52,53] Eine erste grundlegende Zusammenfassung und Klassifizierung der Physisorptionsdaten von Gas/Festkörpersystemen wurde von Sing et al. in Ihrem Report im Rahmen der IUPAC 1985 veröffentlicht.[54] Thommes et al. publizierten 2015 eine Aktualisierung und Erweiterung des Reports mit besonderem Augenmerk auf die Anwendung der Physisorption für mikroporöse Materialien und deren Charakterisierung.[55] Das Kernstück der beiden Publikationen beinhaltet die Klassifizierung der Physisorptionsisothermen, welche Aussagen über die spezifische Porenstruktur der Materialien treffen, in zunächst sechs (1985) und schließlich acht (2015) unterschiedliche Typen (Abbildung 11).

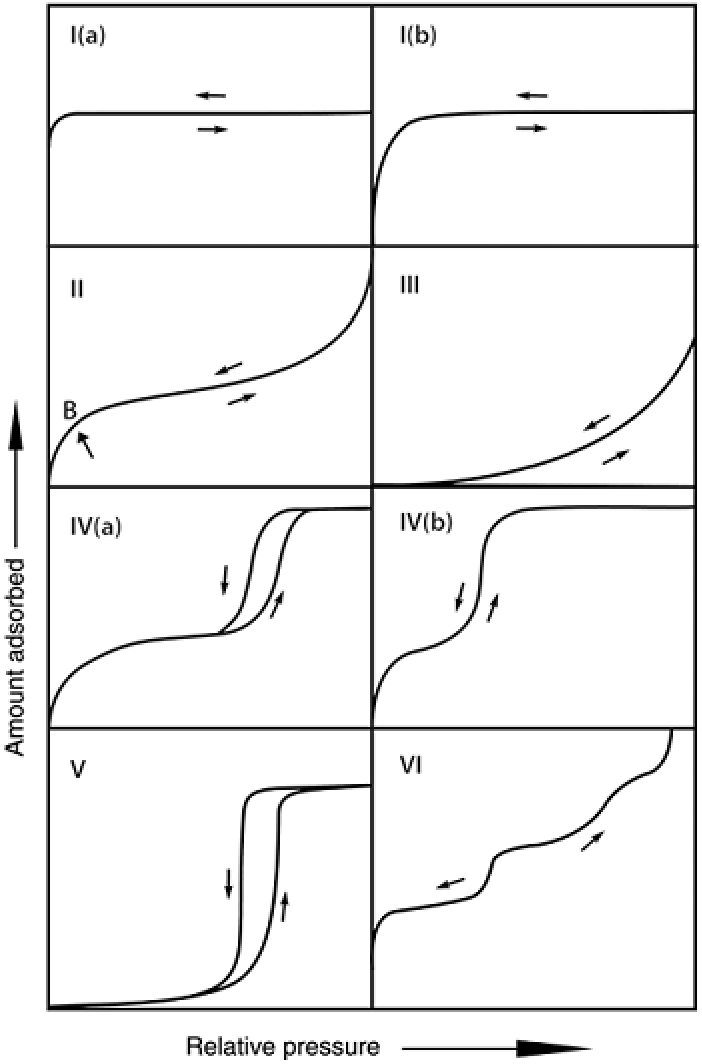

Abbildung 11: Klassifizierung der Isothermentypen nach IUPAC. Nachdruck mit Genehmigung von Ref. 55. Copyright 2015 De Gruyter, IUPAC.

Die Typen I(a) und I(b) beschreiben reversible Isothermen von mikroporösen Feststoffen mit sehr geringen äußeren Oberflächen. Charakteristisch für Typ I-Isothermen ist die rapide Gasaufnahme bei geringen relativ Drücken, die der vergleichsweise hohen Adsorbent-Adsorptiv-Wechselwirkung aufgrund der schmalen Mikroporen zugerechnet wird. Anhand der Größenrelationen zwischen Adsorptiv und Porendurchmesser kann man sich erklären, dass Anhand der Größenrelationen zwischen Adsorptiv und Porendurchmesser kann man sich erklären, dass es zwangsläufig zu einer Wechselwirkung zwischen Porenwand und Adsorptiv kommen muss. Das immer noch am häufigsten verwendete Adsorptiv zur Porencharakterisierung ist Stickstoff (im Folgenden mit N_2 bezeichnet) mit einem kinetischen Durchmesser von 0,32 - 0,36 nm (je nach Ausrichtung), die Porendurchmesser für den Typ I(a) liegen bei bis zu 1 nm und für den Typ I(b) bis zu 2 nm in der gleichen Größenordnung. Durch die größeren Poren in den Materialien mit Typ I(b)-Isothermen verschiebt sich die Aufnahme zu geringfügig höheren Relativdrücken. Eine Gemeinsamkeit beider Isothermen typen ist jedoch, dass sich nach der Monolagenbildung sofort die Mikroporenfüllung anschließt und ein Plateau erreicht wird.

Makroporöse und nicht poröse Materialien zeigen bei der Physisorption Isothermen des Typs II und III (Abbildung 11). Die Differenz zwischen den Isothermen typen lässt sich durch unterschiedlich starke Wechselwirkungen zwischen Adsorbens und Adsorbat erklären. So zeigen Materialien mit relativ starken/schwachen Wechselwirkungen zum Adsorbat eine frühere/spätere Gasaufnahme (Typ II/Typ III). Außerdem kann bei der Ausbildung einer Monolage teilweise ein scharfer Knick in der Isotherme erkannt werden (Punkt B, Abbildung 11). Liegt dieser nicht vor, überschneiden sich Monolagenbildung und Multilagenadsorption. Es wird in beiden Fällen auch bei hohen relativen Drücken kein Plateau erreicht.

Typ IV-Isothermen sind charakteristisch für mesoporöse Materialien. Bei der Gassorption laufen in diesen Materialien zwei gut voneinander trennbare Schritte ab, die im Weiteren für die mathematische Auswertung in Bezug auf die innere Oberfläche von porösen Materialien von großer Bedeutung sind. Der erste Anstieg in der Gasaufnahme bei niedrigeren

Relativdrücken kann man ausschließlich der Monolagen- und Multilagenadsorption zuordnen. Im Gegensatz zu den mikroporösen Materialien erfolgt die Porenfüllung in einem zweiten, separaten Schritt bei höheren Relativdrücken und bildet das Plateau der Gasaufnahme. Für Typ IV(a)-Isothermen folgt der Porenfüllung bei der Desorption eine charakteristische Hysterese, bedingt durch die Kapillarkondensation bei der Adsorption, dessen Auftreten abhängig von der Temperatur, dem Adsorptiv und der Porengröße (meist ab Porendurchmesser > 4 Å) ist. Für Materialien mit Mesoporen < 4 Å wird dagegen eine komplett reversible Isotherme beobachtet (Typ IV(b)).

Typ V-Isothermen treten bei geringen Wechselwirkungen zwischen Adsorbens und Adsorbat auf, ähnlich zu den Isothermen des Typs III. Die Gasaufnahme wird jedoch durch das Porenvolumen begrenzt wodurch auch hier ein Plateau ausgebildet wird. Charakteristisch ist dieser Isothermentyp auch für Wassersorption an hydrophoben Materialien.

Die am häufigsten verwendete Methode zur Bestimmung der spezifischen inneren Oberfläche von porösen Materialien erfolgt nach Brunauer, Emmett und Teller und wird BET-Methode abgekürzt.[56] Sie basiert auf dem von Langmuir 1918 vorgestellten Modell zur mathematischen Beschreibung von Sorptionsisothermen unter Ausbildung einer Monolage.[57] Mit der BET-Methode ist es jedoch ebenfalls möglich Multischichtenausbildungen bei der Adsorption zu beschreiben.

Die BET-Theorie basiert auf folgenden Annahmen:

(a) Alle Adsorptionsstellen sind energetisch identisch und können besetzt werden

(b) Keine Wechselwirkung zwischen dem Adsorptiv untereinander (ideales Gas)

(c) Die Adsorptionswärmen für Monolagen sind unabhängig vom Bedeckungsgrad

(d) Die Adsorptionswärmen für Multilagen entsprechen der Kondensationswärme des Adsorptivs

Für die Anwendung der BET-Theorie muss zunächst die allgemeine Form der Gleichung (1) linearisiert werden.

$$\frac{n}{n_m} = \frac{C\left(\frac{P}{P_0}\right)}{\left(1-\left(\frac{P}{P_0}\right)\right)\left(1-\frac{P}{P_0}+C\left(\frac{P}{P_0}\right)\right)} \tag{1}$$

Wobei *n* die spezifische Gasaufnahme beim Relativdruck *P/P₀* und n_m die spezifische Monolagenkapazität darstellt. Der Parameter *C*, die BET-Konstante, ist exponentiell abhängig von der Energie der Monolagenadsorption und somit ein direkter Indikator für die Stärke der Adsorbens-Adsorbat-Wechselwirkungen. Gleichung 2 zeigt die linearisierte Form.

$$\frac{1}{n\left(\left(\frac{P_0}{P}\right)-1\right)} = \frac{1}{n_m C} + \frac{C-1}{n_m C}\left(\frac{P}{P_0}\right) \tag{2}$$

Bei einer Auftragung von $1/[n(P_0/P) -1]$ gegen P/P_0 zeigen mesoporöse Materialien (Typ IV) einen linearen Zusammenhang für den relativen Druckbereich P/P_0 von 0,05 bis 0,30. Die Kapazität der Monolage eines Adsorbates n_m kann aus der Steigung *m* und dem Achsenabschnitt *b* aus Gleichung 2 wie folgt berechnet werden:

$$m = \frac{C-1}{n_m C} \tag{3}$$

$$b = \frac{1}{n_m C} \tag{4}$$

Nach Einsetzen und Umformen:

$$n_m = \frac{1}{m+b} \tag{5}$$

Abschließend kann nun die spezifische BET-Oberfläche $a_s(BET)$ der Materialien bestimmt werden. Dazu wird neben der Monolagenkapazität n_m die Querschnittsfläche σ_m der Adsorbatmoleküle, die Avogadrokonstante N_A und das Gewicht des Adsorbens *m* benötigt.

$$a_s(BET) = \frac{n_m\, N_A\, \sigma_m}{m} \tag{6}$$

Für die Bestimmung der spezifischen inneren Oberfläche von mikroporösen Materialien ist die BET-Theorie nicht ohne weiteres geeignet. Wie bereits beschrieben ist es für mikroporöse Typ I-Isothermen nicht möglich die Monolagen-Multilagenadsorption von der Porenfüllung zu unterscheiden, da beide Prozesse bei gleichen Relativdrücken ablaufen. Das BET-Modell leistet jedoch keine theoretische Grundlage für den Prozess der Porenfüllung. Daher sollte laut IUPAC die erhaltene BET-Oberfläche für mikroporöse Stoffe nicht als Absolutwert betrachtet werden, sondern nur als Vergleichswert in Bezug auf andere mikroporöse Materialien.[55] Um wenigstens eine Vergleichbarkeit zwischen mikroporösen Materialien zu gewährleisten, sollten neben einem linearen BET-Plot (es gibt oft mehrere lineare Bereiche) folgende weitere Kriterien erfüllt werden:

(a) Eine positive C-Konstante (positiver Achsenabschnitt)

(b) Der Term $n(1-P_0/P)$ sollte zusammen mit P/P_0 kontinuierlich steigen

(c) Der Wert für P/P_0 entsprechend der Monolagenkapazität n_m sollte im BET-Bereich liegen

Mit Hilfe dieser Einschränkungen können nach Rouquerol et al. reproduzierbare und vergleichbare Werte der BET-Oberfläche für mikroporöse Materialien erhalten werden.[58] Für MOFs mit diversen Porengrößen und Porenstrukturen wurde die Anwendbarkeit dieser Methode in den letzten Jahren durch theoretische Berechnungen belegt.[59] Beispielhaft sind in Abbildung 12 der BET-Plot und der Plot $n(1-P_0/P)$ gegen P/P_0 für Argon an Zeolithe 13 X bei 87 K dargestellt.

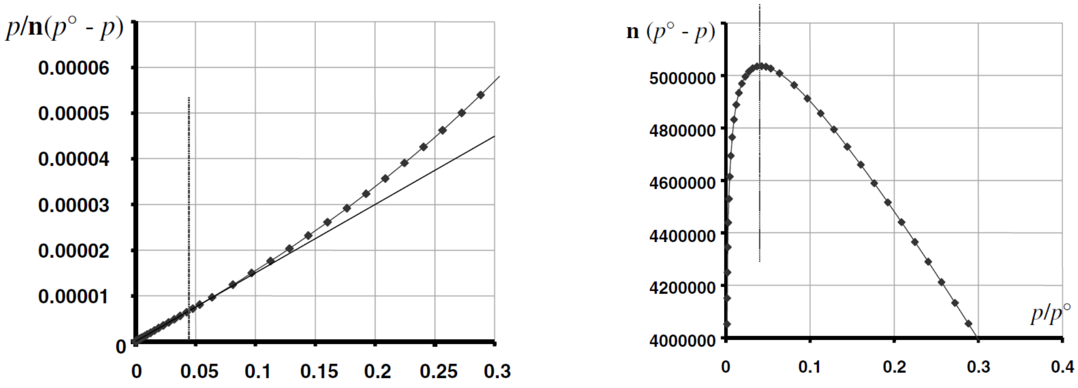

Abbildung 12: BET-Plot (links) und $n(1-P_0/P)$ gegen P/P_0 (rechts) für Argon an Zeolithe 13 X bei 87 K. Nachdruck mit Genehmigung von Ref. 58. Copyright 2007 Elsevier.

Die Auftragung von $n(1-P_0/P)$ gegen P/P_0 wird in der Literatur häufig als Rouquerol-Plot bezeichnet und wird heutzutage in den Softwarepaketen aller führenden Gassorptionsgeräteherstellern für die Auswertung der BET-Oberfläche bereitgestellt.

Die Qualität der Sorptionsisotherme und Ihre Auswertung nach dem BET-Modell werden signifikant vom verwendeten Adsorptiv beeinflusst. Das Standardverfahren der letzten Jahrzehnte war die Stickstoffsorptionsmessung bei 77 K, dem Siedepunkt von Stickstoff. Vorteilhaft bei diesem Aufbau ist, dass flüssiger Stickstoff fast überall auf der Welt zu moderaten Preisen erwerblich ist und kein besonderes Equipment benötigt wird. Von Nachteil ist jedoch, dass Stickstoff ein elektrisches Quadrupolmoment besitzt, was zu minimalen inter- und intramolekularen Wechselwirkungen führt. Die intermolekularen Wechselwirkungen zum Adsorbens bedingen eine vergleichsweise frühe Adsorption bei sehr geringen Relativdrücken.[60] Außerdem führt die Stäbchenform des Stickstoffmoleküls dazu, dass dessen Durchmesser abhängig von der Orientierung bei der Adsorption ist. Wechselt man nun das Adsorptiv und damit die Temperatur von Stickstoff bei 77 K auf Argon bei 87 K, sind die Vor- und Nachteile exakt konträr. Flüssiges, teures Argon oder spezielles Equipment wird benötigt, um bei 87 K messen zu können Argon besitzt jedoch kein elektrisches Quadrupolmoment und liegt als Kugelform vor. Ebenfalls erlaubt Argon eine schnellere Messung der Sorptionsisotherme, da besonders bei Mikroporen im Vergleich zu Stickstoff als Adsorptiv die Adsorption zu höheren Relativdrücken verschoben wird.[61]

Neben der Bestimmung der inneren Oberfläche bzw. BET-Oberfläche, kann mittels Gassorption auch eine Aussage über das Mikro- und Mesoporenvolumen von porösen Materialien getroffen werden. Häufig wird auch von einem totalen Porenvolumen (Englisch: total pore volume) gesprochen, wobei es sich hierbei um das kombinierte Mikro- und Mesoporenvolumen handelt. Makroporen mit Porengrößen über 50 nm können nicht über Gassorption charakterisiert werden, da die Poren am Ende der Sorptionsisotherme noch nicht komplett gefüllt sind und somit die Gasaufnahme noch nicht abgeschlossen ist (siehe Isothermentyp II und III, Abbildung 11). Für alle Isothermen, die ein Plateau am Ende der Isotherme zeigen (Typ: I, IV, V), kann das totale Porenvolumen V_p über die aufgenommene Menge an Gasvolumen V_{ads} berechnet werden, unter der Annahme, dass das kondensierte Adsorbat sich im flüssigen Zustand ρ_{liq} befindet (Gurvich-Regel).[62] Gleichung (7) zeigt die Berechnung des Porenvolumens über das molare Volumen V_m und die Molmasse M:

$$V_p = \frac{V_{ads}}{V_m} \times \frac{M}{\rho_{liq}} \tag{7}$$

Das Mikroporenvolumen entspricht für perfekt mikroporöse Materialien mit einer idealen Typ I-Isotherme dem totalen Porenvolumen. In der Realität kommt es durch Adsorption an der äußeren/externen Oberfläche, oder durch mesoporöse Anteile in den Adsorbenzien, häufig zu keiner perfekten Plateauausbildung. Daher wurden andere Methoden entwickelt, um das reine Mikroporenvolumen zu erhalten. Makroskopisch kann man einen Vergleich mit einem nicht porösen Referenzmaterial mit bekannter BET-Oberfläche durchführen. Dabei wird nach de Boer oder Halsey ein linearer Zusammenhang zwischen der Schichtdicke t einer Adsorptionsschicht des Adsorptivs und dem Relativdruck P/P_0 hergestellt.[63,64] Anschließend wird das adsorbierte Gasvolumen V_{ads} gegen die Schichtdicke t aufgetragen. Bei dem nicht porösen Referenzmaterial verläuft die Gerade dieser Auftragung durch den Achsenursprung, für mikroporöse Materialien wird aus dem Schnittpunkt der Geraden (im Druckbereich von $P/P_0 = 0{,}2\text{-}0{,}5$ der Sorptionsisotherme) mit der Ordinate das Mikroporenvolumen berechnet. In einer aktuellen Arbeit konnten jedoch Galarneau et al. zeigen, dass die Schichtdicke für poröse Materialien mit einem Porendurchmesser $< 10\ \sigma$ (σ = Durchmesser des Adsorptivs) nicht nur vom Relativdruck P/P_0, sondern auch vom Porendurchmesser abhängt.[65] Dadurch wird das Mikroporenvolumen mit zunehmenden Mikroporenanteil systematisch zu gering bestimmt.

Neben den makroskopischen Methoden können die Ermittlung des Mikroporenvolumens und der Porenverteilung über molekulare Berechnungen erfolgen. Dazu wird das Verhalten von Flüssigkeiten in engen Poren über nicht-lokale Dichte-Funktional-Theorie (NLDFT) oder Grand Canonical Monte Carlo (MC)-Simulationen modelliert.[66,67] Dazu müssen Modelle von verschiedenen Porenstrukturen (Schlitz-, Sphärischen-, Zylinder- oder Hybridporen) für verschiedene Materialklassen (Kohlenstoffe, Zeolithe, Silikate) entwickelt werden. Nun können für verschiedene Adsorptiv/Adsorbens paare theoretische Isothermen mit unterschiedlichen Porenstrukturen und Porengrößen berechnet werden, sogenannte Kernels. Für die Materialklasse der MOFs sind jedoch aufgrund der extremen Vielfalt der Materialien noch keine Kernels entwickelt worden, wodurch die Auswertung von MOFs bezüglich Ihrer Porenstruktur bestenfalls qualitativ erfolgen sollte. Sowohl makroskopische Methoden als auch molekulare Berechnungen sind in den meisten kommerziellen Softwarepaketen zur Charakterisierung von Sorptionsisothermen enthalten.

Sorptionsisothermen können neben der Charakterisierung der Porosität von Materialien auch Aussagen über deren Kapazität zur Gasspeicherung und Gasseparation liefern. Im Folgenden wird dies am Beispiel zur selektiven Gassorption und Gastrennung von CO_2 dargestellt.

Seit dem Beginn der industriellen Revolution Mitte des 18. Jahrhunderts basiert die Energiegewinnung hauptsächlich auf der Verbrennung von fossilen Brennstoffen (Kohle, Gas, Öl), welche beim Verbrennungsprozess CO_2 und andere Treibhausgase freisetzen. CO_2 macht dabei mit ca. 80 % in den Vereinigten Staaten den größten Anteil an Treibhausgasen aus.[68] Durch die Emission von Treibhausgasen ist die durchschnittliche Temperatur der Erde bereits um ca. 1 °C im Vergleich zum vorindustriellen Zeitalter gestiegen, bei einem gleichzeitigen

Anstieg der CO_2 Konzentration um knapp 50 % auf über 400 ppm.[69] Um den weiteren Anstieg der CO_2 Emissionen kurzfristig einzudämmen werden Möglichkeiten zur CO_2-Erfassung und Speicherung diskutiert (Carbon Capture and Storage, CCS).[70] Eine große Vielfalt an Methoden zur CO_2-Abtrennung umfassen unter anderem physische Adsorption, Membrantechnologie, Kryo-Destillation und Absorptionsprozesse.[71,72,73] Für konventionelle Kraftwerke ist die Abgasreinigung durch einen Absorptionsprozess mittels Monoethanolaminen (MEAs) oder Triethanolaminen (TEAs) bereits eine gängige Praxis (Abbildung 13).[74]

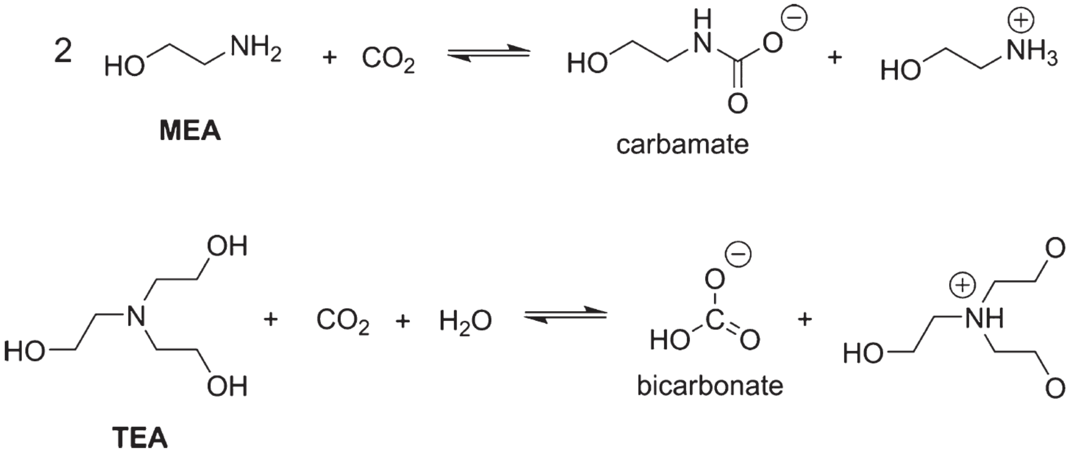

Abbildung 13: Reaktion von CO_2 mit Monoethanolamin (MEA) und Triethanolamin (TEA). Nachdruck mit Genehmigung von Ref. 74. Copyright 2012 American Chemical Society.

Dabei reagieren die Amine selektiv mit CO_2 unter Bildung wasserlöslicher Carbamatverbindungen oder Bicarbonaten.[75] Trotz hoher Selektivität und effizienter CO_2-Entfernung stellen Aminwäschen durch ihren hohen Verbrauch an Chemikalien und deren schlechte Regenerierbarkeit ein großes Problem dar. Eine deutlich leichtere Regenerierbarkeit durch schwächere Bindungen zwischen CO_2 und Substrat erfolgt bei Adsorptionsprozessen, wodurch hochporöse MOFs potenziell Anwendung finden könnten. Die Stärke der Wechselwirkungen zwischen Adsorbens und Adsorptiv können durch die oben erwähnte Adsorptionswärme dargestellt werden. Dabei weisen Adsorptionswärmen von mehr als der dreifachen Kondensationswärme auf Chemisorption hin. Geringere Adsorptionswärmen (~ 2-fache Kondensationswärme) sprechen für Physisorption. Abbildung 14 zeigt Adsorptionswärmen für CO_2 in MEAs, Zeolithen und MOFs.[76]

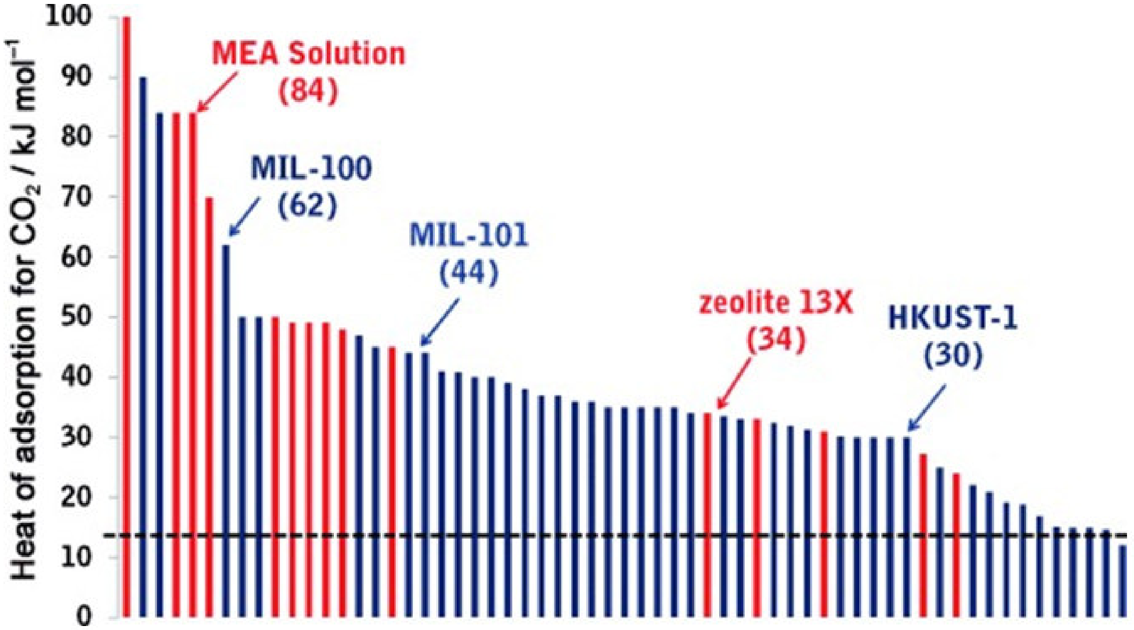

Abbildung 14: Adsorptionswärmen für CO_2 in MOFs (blau) und anderen Materialien (rot) bei Umgebungsbedingungen. Die schwarze Linie zeigt die Kondensationswärme von flüssigem CO_2 bei 17 kJ mol^{-1}. Nachdruck mit Genehmigung von Ref. 76. Copyright 2010 John Wiley and Sons.

Die strukturelle Vielfalt der MOFs ermöglicht es, Adsorptionsstellen für CO_2 in der Gerüststruktur zu verankern und damit maßgeschneiderte Bindungsstellen für das polare CO_2 anzubieten. Beispiele für solche Strukturelemente sind folgende funktionalisierte, meist polare Gruppen an den organischen Liganden: $-NH_2$ -OH, $-SO_3$, -Hal, $-NO_2$, oder freie Bindungsstellen an den Metallzentren.[77] Neben der möglichst selektiven und reversiblen Aufnahme von CO_2 ist ein weiterer Parameter von signifikanter Bedeutung, die Adsorptionskapazität.

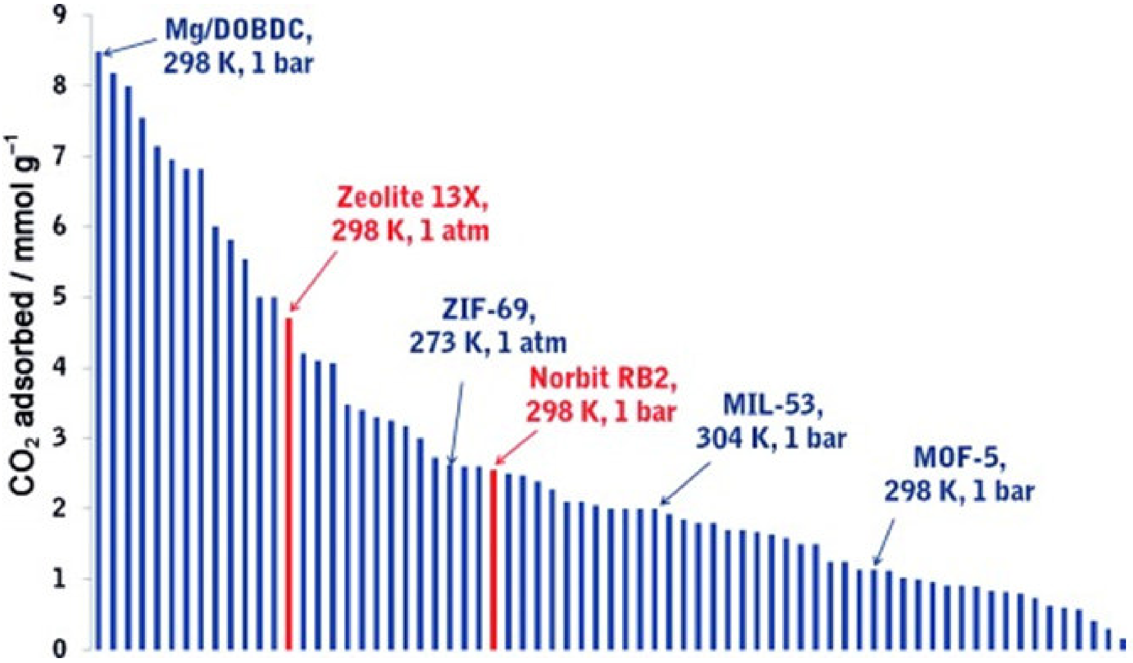

Abbildung 15: Menge an aufgenommenem CO_2 für diverse MOFs (blau) und Zeolithe 13X, Norbit RB2 (rot) bei Umgebungsbedingungen. Nachdruck mit Genehmigung von Ref. 76. Copyright 2010 John Wiley and Sons.

Für Adsorptionsprozesse bei Standardbedingungen wird die Adsorptionskapazität hauptsächlich über die Affinität des Adsorptivs zum Adsorbens bestimmt (Abbildung 15). Folglich konnte durch Einführung einer Aminfunktionalisierung im Linker des MOFs UiO-66 die CO_2-Aufnahme von ~ 2 mmol g^{-1} auf knapp 6 mmol g^{-1} in NH_2-UiO-66 gesteigert werden (303 K, 1bar).[78,79] HKUST-1 ist das klassische Beispiel für ein MOF mit freien Koordinationsstellen am Metallzentrum nach Aktivierung und auch hier zeigt sich eine hohe CO_2-Aufnahme von über 5 mmol/g bei 298 K und 1 bar.[80] Das Magnesium-MOF Mg/DOBDC (Mg-MOF-74, CPO-27-Mg) vereint die beiden vorher genannten positiven Eigenschaften. Der Linker besitzt zwei Hydroxylgruppen und gleichzeitig liegt eine hohe Dichte an koordinativ ungesättigten Metallzentren vor, was zu sehr hohen CO_2-Aufnahmen von über 8 mmol/g bei 298 K und 1 bar führt.[81] Neben freien Koordinationsstellen und funktionellen Gruppen ist auch die Porengröße der MOFs von Bedeutung. CO_2-selektive MOFs sind häufig mikroporös, wodurch die Gasmoleküle leichter in Kontakt mit den präferierten Adsorptionsstellen kommen. Da industrielle Prozesse jedoch häufig bei erhöhten Drücken ablaufen, werden auch vermehrt Hochdruckadsorptionsisothermen von interessanten MOFs ausgewertet. Dabei korreliert die CO_2-Aufnahmekapazität in den meisten Fällen mit dem totalen Porenvolumen der untersuchten MOFs.[74]

1.2 Membrantrennverfahren

Membrantrennverfahren haben über die letzten vierzig Jahre in vielfältigen Anwendungsbereichen der chemischen Industrie Einzug erhalten. Dabei basieren alle Trennprozesse mittels Membranen auf der Kontrolle der Permeationsrate chemischer Spezies durch die Membran. Membranprozesse werden heutzutage als sehr effektive Technologie beschrieben aufgrund ihrer hohen Effizienz, einfacher Bedienung und geringer Kosten. Die heutigen Stärken der Membrantechnologie galten jedoch lange Zeit als große Schwächen: zu teuer, zu geringer Fluss, geringe Selektivität und Stabilität. Mit der Entwicklung einer ultradünnen, defektfreien, Hochdurchflussmembran für die Osmose verhalfen Loeb-Sourirajan der Membrantechnologie zum Durchbruch.[82] Der hohe Durchfluss bei hinreichender Selektivität wurde durch einen dünnen Oberflächenfilm erreicht, der über einen mikroporösen Träger stabilisiert wurde. Aufbauend auf der Arbeit von Loeb und Sourirajan wurde auch die Gastrennung mittels Membranen ökonomisch interessant, sodass im Jahr 1980 die erste Membran zur Gastrennung von Monsanto unter dem Namen Prism® eingesetzt wurde.[83] Es handelte sich dabei um eine neuartige Hohlfasermembran zur Trennung von Wasserstoff, H_2 und Stickstoff, N_2 (Abbildung16).

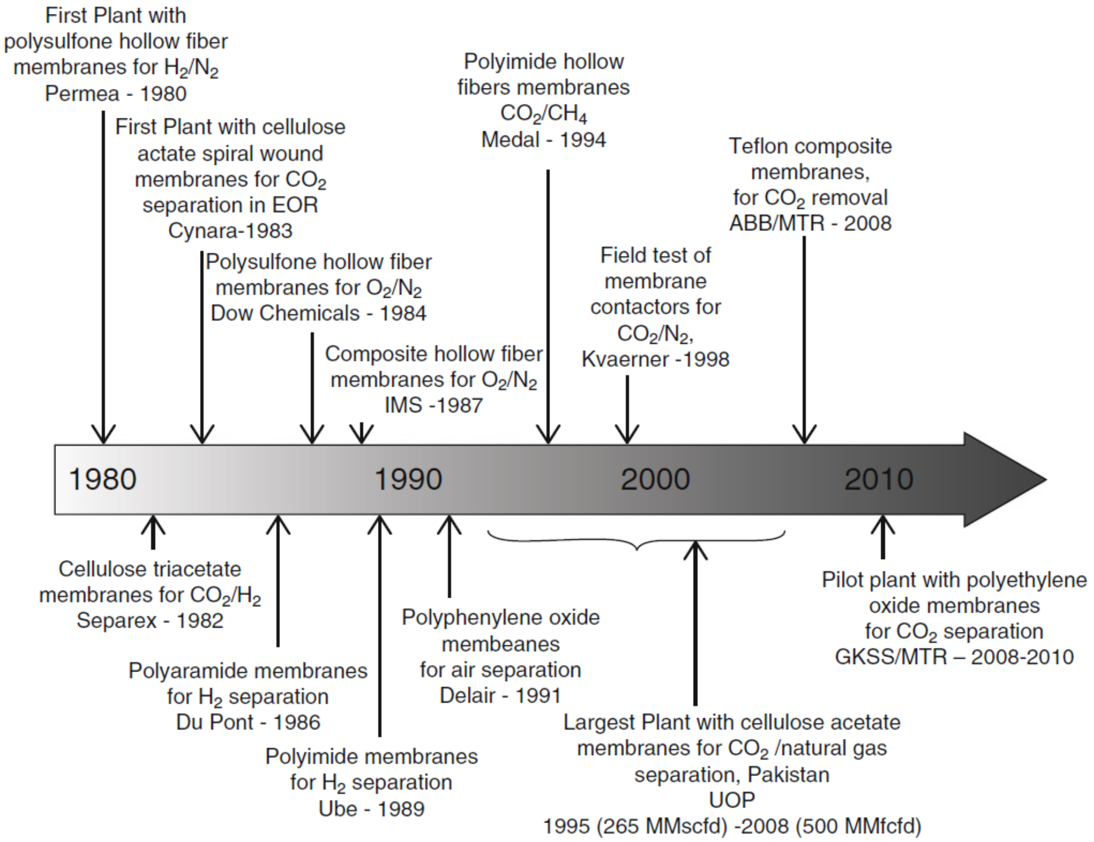

Abbildung 16: Meilensteine der Gastrennung in industriellen Anwendungen. Nachdruck mit Genehmigung von Ref. 84. Copyright 2013 Italian Association of Chemical Engineering, AIDIC.

Kurz darauf wurden Verfahren zu Gasabscheidung von N_2 aus der Luft von Dow entwickelt und Cyanara gelang die erfolgreiche Trennung von CO_2 aus Erdgas (hauptsächlich Methan, CH_4). Die in den folgenden Jahren erreichten Meilensteine der Gastrennung mittels Membranen in der Industrie zeigt Abbildung 16. Besonders bemerkenswert ist die größte Aufreinigungsanlage durch Membrantechnologie für Erdgas in Pakistan, die 1995 errichtet wurde und ein gutes Beispiel für die leichte Skalierung der Membrantechnologie darstellt. Die Überlegenheit von Membrantrennprozessen gegenüber konventionellen Verfahren ist hauptsächlich über die Vermeidung einer energieintensiven Phasenumwandlung zu erklären.[85] Aktuelle Herausforderungen für die Membrantechnik liegen in erster Linie in der degradierenden Leistungsfähigkeit über längere Zeitspannen. Der Leistungsverlust resultiert entweder aus Verunreinigungen und partieller Zersetzung der Membranen durch korrosive, schwefelhaltige Gase wie H_2S und SO_2 oder durch Anreicherung langsam permeierender Spezies in der Membran, wodurch geringere Transportraten für alle Gase verzeichnet werden.[85]

Der Stofftransport durch Membranen hängt fundamental von dem verwendeten Membrantyp ab. Dabei wird zwischen porösen und nicht porösen (dichten) Membranen unterschieden. Die porösen Membranen werden anschließend noch aufgrund ihres Transportmechanismus in weitere Unterklassen aufgeteilt. In Abbildung 17 sind die relevantesten Diffusionsmechanismen in mikroporösen Membranen dargestellt.[86]

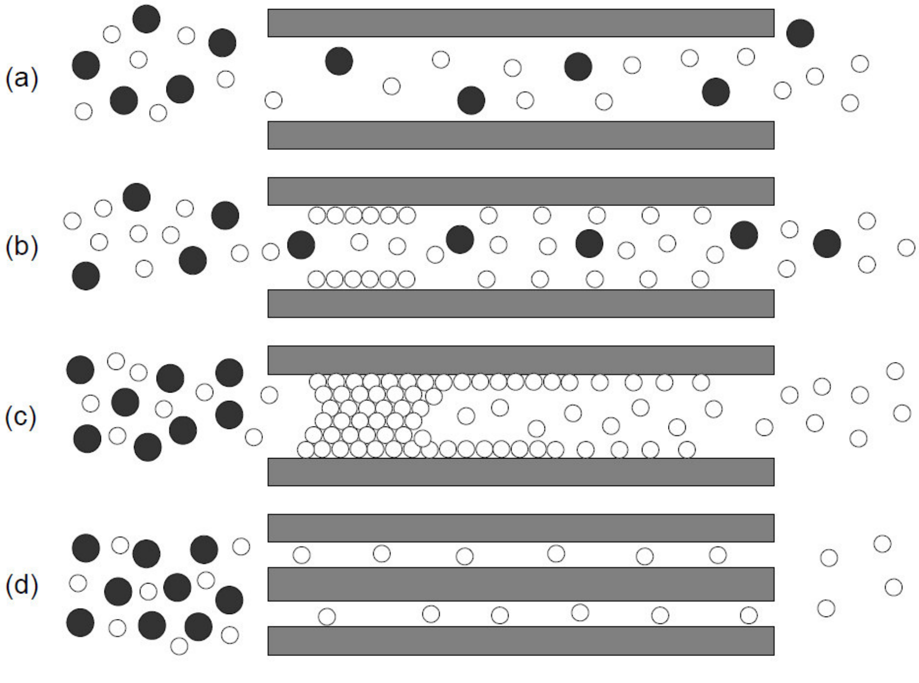

Abbildung 17: Schematische Darstellung des Transportmechanismus in porösen Membranen: (a) Knudsen-Diffusion, (b) Oberflächendiffusion, (c) Kapillarkondensation, (d) molekulares Sieb.

Fall (a) beschreibt die Knudsen-Diffusion durch poröse Membranen, in denen die Transportgeschwindigkeit der Gasmoleküle durch Stöße mit der Porenwand bestimmt wird und nicht durch Stöße zwischen den Gasteilchen. Die Diffusionsrate (*a, b*) bzw. der Separationsfaktor (α) kann nach Graham's Gesetz direkt aus der Wurzel der Molekulargewichte (M_a, M_b) der beiden Gasmoleküle wie folgt berechnet werden:

$$\alpha = \frac{Rate\ a}{Rate\ b} = \sqrt{\left(\frac{M_b}{M_a}\right)} \tag{8}$$

Die Oberflächendiffusion ist in Fall (b) dargestellt und läuft häufig simultan mit der Knudsen-Diffusion ab. Gasmoleküle werden über physikalische Wechselwirkungen an der Membranwand adsorbiert und wandern durch alternierende Adsorption und Desorption an der Oberfläche entlang. Dementsprechend wird die Permeabilität der adsorbierten Komponente erhöht und gleichzeitig der effektive Porendurchmesser verringert wird, wodurch zusätzlich die Selektivität erhöht werden kann. Kapillarkondensation (c) erfolgt nach Kondensation eines Gases in einem Teil der Membranporen. Sie geht einher mit einem hohen Fluss der kondensierten Phase unter Ausschluss aller nicht löslichen Gase in der kondensierten Phase. Das Auftreten von Kapillarkondensation in einer porösen Membran hängt von der Porengröße, Porenverteilung und der Gaskomposition ab. Im letzten Fall (d) handelt es sich um einen Gastransport unter Größenausschluss, dem sogenannten *molecular sieving*. Bei Porengrößen der Membranen im Größenbereich der kinetischen Moleküldurchmesser der permeierenden Gase kann es zu einem kompletten Ausschluss der größeren Gasmoleküle kommen.

Der Transportmechanismus für dichte, nicht poröse Membranen wird in der Literatur allgemein als Lösungs-Diffusions-Prozess beschrieben.[87] Der Stofftransfer durch die Membran läuft in drei Schritten ab (Abbildung 18).

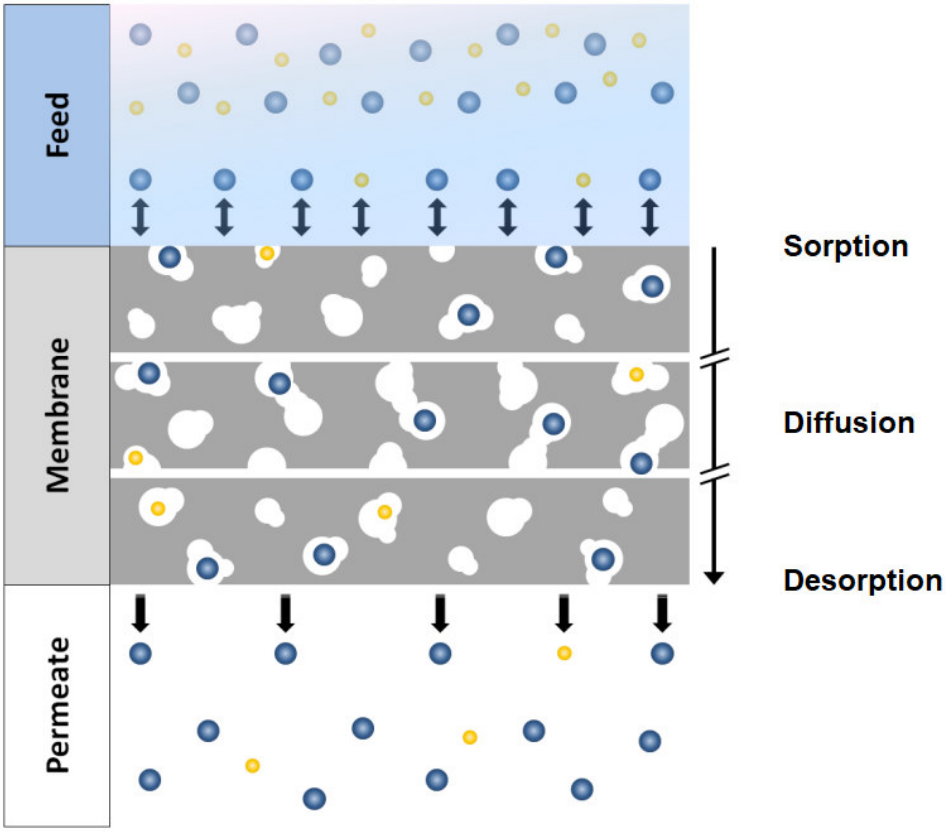

Abbildung 18: Schematische Darstellung des Transportmechanismus mittels Lösungs-Diffusion durch dichte Membranen. Basierend auf der Darstellung aus Ref. 88.

Zunächst werden die Gasmoleküle an der Membranoberfläche auf der Hochdruckseite (Upstream, Feed) adsorbiert. Anschließend diffundieren die Gasmoleküle durch die Polymermatrix hindurch, bevor sie Im letzten Schritt an der Niederdruckseite (Downstream, Permeat) der Membran desorbieren. Die Triebkraft für die beschriebenen Prozesse ist ein Gradient in Druck, Temperatur oder Konzentration. In Übereinstimmung mit dem Lösungs-Diffusions-Modell ist die Permeabilität *P* eines Gases *i* abhängig von zwei Faktoren, dem Diffusionskoeffizienten *D* und dem Löslichkeitskoeffizienten *S*:

$$\mathrm{P}_i = \mathrm{D}_i \times \mathrm{S}_i \tag{9}$$

Die Diffusion der Gasmoleküle, spezifischer die thermische induzierte Bewegung der Polymerketten durch die Gasmoleküle, ist meistens der geschwindigkeitsbestimmende Schritt in der Permeation durch eine dichte Membran. Hierbei wird, wie in Abbildung 18 durch die weißen Stellen um die Gasmoleküle angedeutet, das freie Volumen in der Polymermatrix durch die Gasmoleküle entlang des Gradienten verschoben. Die Permeabilität *P* einer Komponente *i* kann außerdem auch als Fluss *flux* normiert auf die Dicke der Membran *l* und dem angelegten Druckunterschied *Δp* zwischen Feed und Permeat formuliert werden, wie Gleichung 10 zeigt:

$$\mathrm{P}_i = \frac{(\mathrm{flux}_i \times \mathrm{l})}{(\Delta p_i)} \tag{10}$$

Die Permeabilität wird in beiden Fällen in der Einheit Barrer ausgedrückt, wobei 1 Barrer = 10^{-10}·cm³(STP)·cm/(cm²·s·cmHg) entspricht. Falls die Dicke der Membran nicht bestimmt werden kann (asymmetrische Membran, siehe unten) wird die Durchlässigkeit (*permeance*) in *gas permeation units* (1 GPU = 10^{-6} cm³ (STP)/(cm² s cmHg)) angegeben. Durch die Multiplikation der Dicke der Membran *l* in µm kann aus der Einheit GPU die Einheit Barrer erhalten werden.

Das Verhältnis der Permeabilität *P* zweier Gase *i, j* gibt die ideale Permselektivität bzw. Selektivität *α* der Membran an:

$$\alpha_{i/j} = \frac{P_i}{P_j} \tag{11}$$

Dichte Membranen zeigen häufig eine geringe Permeabilität (langsame Diffusion), dafür jedoch eine hohe Selektivität im Vergleich zu den porösen Membranen. Aufgrund dessen ist hier im Gegensatz zu der mikroporösen Membran auch eine Trennung von Molekülen mit nahezu gleicher Größe und gleichem Molekulargewicht möglich, wenn sich deren Löslichkeit im Membranmaterial deutlich voneinander unterscheidet. Anders ausgedrückt entscheidet hauptsächlich die Löslichkeit der Gase über die mögliche Trennleistung der Membran im Hinblick auf die Selektivität. Die Dicke der Membran wiederum entscheidet über die Durchlässigkeit bzw. den effektiven Fluss. Aus diesem Grund sind besonders Asymmetrische Membranen vorteilhaft und in der Industrie weit verbreitet. asymmetrische Membranen kombinieren hohe Flussraten mit guter mechanischer Stabilität. Strukturell sind sie aus einer dichten, selektiven Schicht (0,1–1 µm, in der Dicke) unterstützt durch ein poröses Substrat (50-200 µm) aufgebaut. In dem selektiven Teil der Membran verläuft die Permeation nach dem Lösungs-Diffusion Modell und in dem porösen Abschnitt nach der Knudsen Diffusion. Die bevorzugte Form solcher Membranen ist die Hohlfaser, um noch höhere Durchflussraten zu ermöglichen.

Neben der Struktur spielen chemische und physikalische Eigenschaften der Membran eine wichtige Rolle für die Separationseigenschaften. Membranen sollten defektfrei, selektiv, hoch permeabel sein, sowie eine hohe thermische, mechanische und chemische Stabilität zeigen. Klassifiziert man Membranen aufgrund ihres Materialtyps, unterscheidet man typischerweise zwischen Polymermembranen und anorganischen Membranen. Anorganische Materialien umfassen unter anderem Metalloxide, Silikate und Zeolithe, welche sich durch ihre hohe thermische und chemische Stabilität bei gleichzeitig hoher Permselektivität auszeichnen.[89,90]

Besonders amorphe anorganische Membranen zeigen jedoch eine geringe mechanische Stabilität und sind oft zu brüchig für gängige Formgebungsverfahren.[91] Nichtsdestotrotz zeigen besonders mikroporöse anorganische Membranen mit Porendurchmessern < 1 nm aufgrund ihres molekularen Siebeffekts, kombiniert mit hohen Flussraten, ein hohes Potential für die Anwendung in der Gasseparation. Ihre mechanische Belastbarkeit kann durch poröse Supportmaterialien deutlich gesteigert werden.

Polymerbasierte Membranen sind heutzutage die am häufigsten in der Industrie verwendeten Membrantypen zur Gastrennung, wobei deren kommerzielle Verwendung noch immer begrenzt ist.[92]

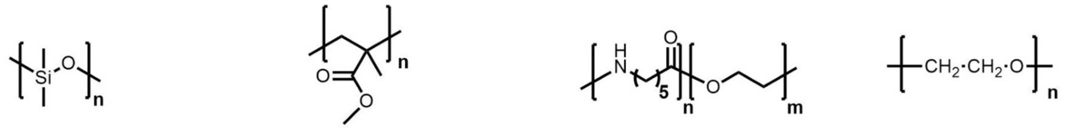

Poly(dimethylsiloxan) (PDMS)

Poly(methyl methacrylat) (PMMA)

Poly(amid-b-ethylenoxid) (Pebax 1657)

Poly(ethylenoxid) (PEO/PEG)

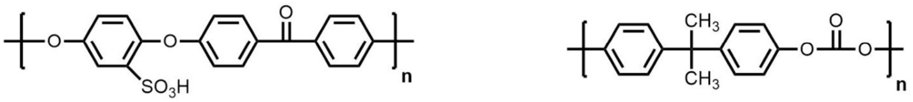

Sulfoniertes poly(ether ether keton) (SPEEK)

Poly(carbonat) (PC)

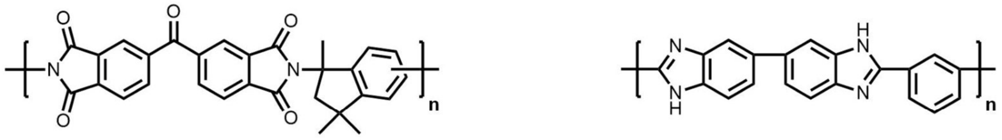

Polyimid (Matrimid)

Poly(benzimidazolat) (PBI)

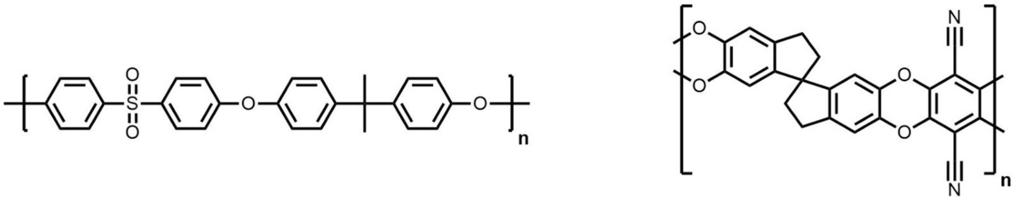

Polysulfon (PSF) (S6010)

PIM-1

6FDA-mPD

6FDA-DAM

Abbildung 19: Chemische Struktur häufig verwendeter Polymere zur Membranherstellung für die Gastrennung.

Abbildung 19 zeigt Beispiele für chemische Strukturen von Polymermaterialien zur Herstellung von Membranen für die Gasseparation. Innerhalb der Polymermaterialien für Membranen kann man weiterhin zwischen gummielastischen (rubber) und glasartigen (glassy) Polymeren unterscheiden. Wie der Name der gummielastischen Polymere schon andeutet, sind diese Polymere aufgrund ihrer Knäuelstruktur und ihrem geringen Verknüpfungsgrad verformbar und gehen nach der Deformation in ihren Ausgangszustand zurück (Elastomere). Glasartige Polymere sind hingegen nicht verformbar, sondern haben eine starre Struktur. Erst mit Überschreitung der Glastemperatur (T_g) werden die sogenannten (teilkristallinen) Thermoplaste weichelastisch. Stark vernetzte Duroplaste sind auch oberhalb der Glastemperatur weiterhin starr. Die Gasseparationseigenschaften von gummielastischen und glasartigen Polymeren verhalten sich bezogen auf die beiden Parameter Permeabilität und Selektivität diametral. Rubber-Polymere zeichnen sich durch hohe Permeabilität und geringe Selektivität für unterschiedliche Gaspaare (O_2/N_2, H_2/CH_4, CO_2/CH_4) aus, während glasartige Polymere hoch selektiv sind, jedoch nur geringe Flussraten aufweisen.[93,94] Die hohe Permeabilität der elastischen Polymere wird auf die höhere Flexibilität der Polymerketten im Vergleich zu den glasartigen Polymeren zurückgeführt, welche sich in einer niedrigeren Glastemperatur wiederspiegelt. Der Einfluss des freien Volumens innerhalb des Polymers auf die Gasseparationseigenschaften ist umstritten und nicht eindeutig belegt.[95,96] Das freie Volumen innerhalb eines Polymers wird synonym mit dem fraktionellen freien Volumen (FFV) v_f verwendet, welches dimensionslos ist (cm³ cm^{-3}) und wie folgt berechnet werden kann:

$$v_f = \frac{v - 1{,}3 \cdot v_0}{v} \tag{12}$$

wobei v das spezifische Volumen des Polymers (cm³ g^{-1}), also die reziproke Dichte, ist und v_0 das belegte Volumen der Moleküle des Polymers darstellt (cm³ g^{-1}). Das belegte Volumen der Moleküle kann anhand der von Bondi und Van Krevelen berechneten Van-der-Waals-Radien für bestimmte chemische Gruppen und anschließender Division durch die Molmasse eben dieser erhalten werden (Tabelle im Anhang).[97,98] Das so berechnete Volumen ist um den Faktor 1,3 höher als die Van-der-Waals Volumen der chemischen Gruppen, da sogar bei 0 K freies Volumen zwischen den Polymermolekülen vorliegt.

Der Kompromiss zwischen Permeabilität und Selektivität für polymerbasierte Membranen in der Gastrennung wurde von Robeson 1991 graphisch aufgearbeitet.[99,100] Dazu wird nach Robeson die Selektivität eines Gaspaares gegen die Permeabilität des schneller permeierenden Gases logarithmisch aufgetragen, wodurch der *trade-off* zwischen Permeabilität und Selektivität für Polymermembranen noch deutlicher wird und die limitierte Anwendung in der Industrie verständlich macht (Abbildung 20).

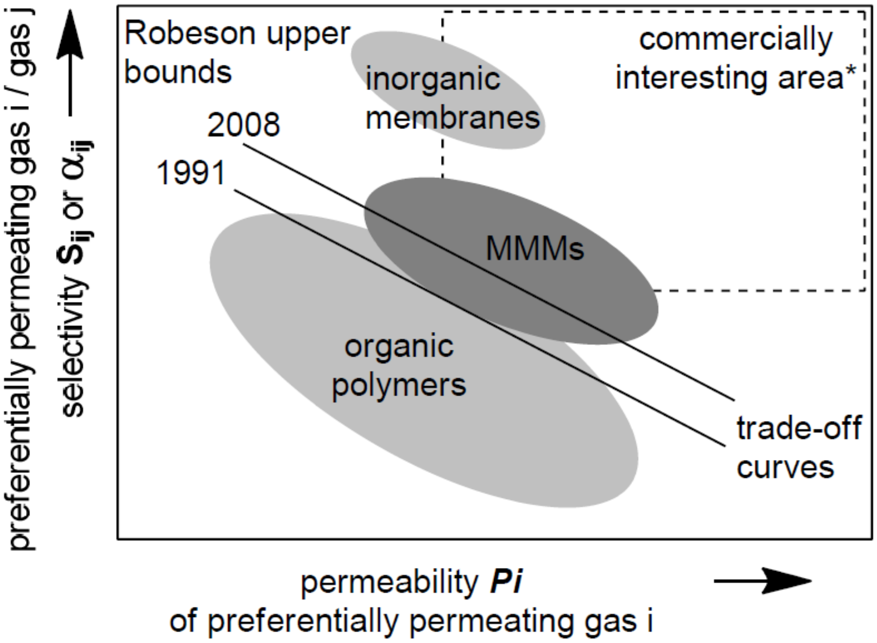

Abbildung 20: Schematische Darstellung der Robeson Grenzkurven von 1991 und 2008 (*Distanz oder Position relativ zur Grenzkurve kann je nach Trennproblem variieren). Nachdruck mit Genehmigung von Ref. 101. Copyright 2017 John Wiley and Sons.

Kommerziell ermöglicht eine höhere Permeabilität die Verkleinerung der Membranoberfläche für einen gegebenen Gasfluss und damit die Reduzierung von Investitionskosten in die Membraneinheit. Eine erhöhte Selektivität resultiert wiederum in einer höheren Reinheit des gewünschten Produkts. Je nach Trennproblem muss für Polymermembranen ein geeigneter Kompromiss zwischen Permeabilität und Selektivität gefunden werden. Der in Abbildung 20 eingezeichnete kommerziell interessante Bereich für die Gastrennung wird bereits von anorganischen Materialien, wie den Zeolithen, erreicht.[89,91] Jedoch sind anorganische Materialien oft spröde und besitzen schlechte Formgebungseigenschaften. Weiterhin konzentriert sich die Forschung auf das Design von Kompositmembranen, den sogenannten Mixed-Matrix-Membranen (MMMs), um den Kompromiss zwischen Permeabilität und Selektivität zu überwinden und in den industriell interessanten Bereich vorzustoßen.

1.3 Mixed-Matrix-Membranen

Mixed-Matrix-Membranen (MMMs) sind Kompositmembranen bestehend aus einer organischen Polymermatrix, die kontinuierliche Phase, und anorganischen oder organisch/anorganischen Materialien, welche als Füllstoffe die dispergierte Phase der Membran bilden. Der schematische Aufbau von MMMs ist in Abbildung 21 dargestellt.

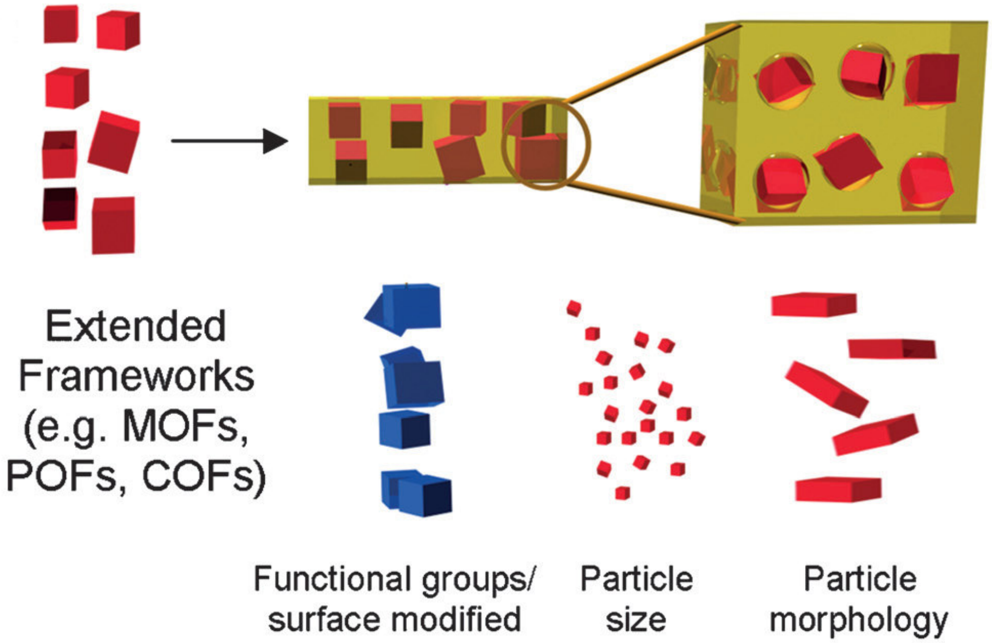

Abbildung 21: Schematischer Aufbau von MMMs mit relevanten Füllstoffeigenschaften. Nachdruck mit Genehmigung von Ref. 101. Copyright 2017 John Wiley and Sons.

Das Konzept der Mixed-Matrix-Membranen (MMMs) dient auf dem Feld der Gastrennung dazu, die positiven Eigenschaften beider Materialtypen miteinander zu verbinden, und um den Kompromiss zwischen Permeabilität und Selektivität für Polymermembranen einerseits und die begrenzte Verformbarkeit der Füllmaterialien andererseits zu überwinden. Die erste Untersuchung zu Kompositmembranen wurde in den 1970er Jahren von Paul und Kemp durchgeführt.[102] Sie entdeckten, dass der *time lag*, also die Zeitspanne, die ein Gas ursprünglich braucht um durch die Membran zu permeieren, durch Einlagerung des Zeolithes 5A in Polydimethylsiloxan (PDMS) für vier verschiedene Gase deutlich erhöht wurde. Die erhöhte Diffusionszeit lässt sich durch Adsorption der Gase in den aktivierten Poren des Füllstoffs erklären. Einen Einfluss auf die Gaspermeation im Gleichgewichtszustand (*steady state*) wurde nicht festgestellt. Die erste Arbeit mit Hinweisen auf verbesserte Permeationseigenschaften von MMMs geht auf Studien von Kulprathipanja et al. in den 80er Jahren zurück.[103] Sie konnten die Selektivität von reinen Celluloseactetatmembranen für die O_2/N_2-Gastrennung von 3,0 auf 4,3 durch Einlagerung von Silikatpartikeln erhöhen.

Die Einlagerung von Füllstoffen in eine Polymermatrix kann, abhängig von deren Eigenschaften, unterschiedliche Auswirkungen auf die Permeabilität von Gasen haben. Allgemein kann man zunächst zwischen porösen und nicht porösen Füllstoffen unterscheiden. Poröse Füllstoffe, mit Porengrößen nahe dem kinetischen Durchmesser der Gasmoleküle, können als molekulare Siebe agieren und so eine Selektion über Größenausschluss fördern.[104] Eine Einbettung solcher Füllstoffe ist daher besonders für die Abtrennung der kleineren

Komponenten von Vorteil. Weiterhin können poröse Füllstoffe den selektiven Transport von leichter kondensierbaren Molekülen fördern. Erreicht wird dies durch eine höhere Affinität der Füllstoffe zu der leichter kondensierbaren Komponente, wodurch deren Löslichkeit und/oder Transport durch den Füllstoff bevorzugt wird. Speziell für die Trennung von leicht polarisierbaren Molekülen, wie CO_2 mit seinem Quadrupolmoment, und schlecht polarisierbaren Gasen (N_2, CH_4) kann über den Einbau von funktionellen Gruppen in Füllstoffen die Affinität zu polarisierbaren Gasen gesteigert werden.[105,106] Liegen keine besondere Wechselwirkung zwischen Füllstoff und Gasmolekülen vor, so erhöht sich mit dem Einbau der porösen Füllstoffe lediglich das freie Volumen in der MMM, wodurch es mit ansteigendem Volumen der diskreten Phase simultan zu einer Erhöhung der Permeabilität kommt. Die Selektivität verbleibt in diesem Fall jedoch auf dem Niveau der reinen Polymermembran. Nicht poröse Partikel zeigen zwei entgegengesetzte Eigenschaften, abhängig von der Natur des Polymers. Zum einen können sie die Polymerketten, besonders von teilkristallinen, glasartigen Polymeren, zerrütten und dadurch die Permeabilität der MMM im Vergleich zum reinen Polymer erhöhen.[107,108] Zum anderen können sie als Barriere für die Gasmoleküle fungieren, hindern diese an der Permeation durch die Membran und verringern dadurch die Permeabilität.[109]

Eine mathematische Beschreibung und Vorhersage der Permeationseigenschaften von Kompositmembranen P_{eff} für geringe Beladungen mit einem sphärischen Füllstoff kann anhand des Maxwell-Modells basierend auf Gleichung 13 erfolgen.[110]

$$P_{eff} = P_c \times \frac{P_d + 2P_c - 2\phi_d \times (P_c - P_d)}{P_d + 2P_c + \phi_d \times (P_c - P_d)} \tag{13}$$

Hierbei steht P_c für die Permeabilität der kontinuierlichen, reinen Polymerphase, P_d bezeichnet die Permeabilität der dispergierten Phase und ϕ_d die Volumenfraktion der dispergierten Phase.

Die Volumenfraktion ϕ_d des Füllstoffs kann wie folgt über die Dichte ρ_d und ρ_c, die Einwaage in Gewichtsprozent w_d und w_c des Füllstoffs und des Polymers berechnet werden (Gleichung 14).

$$\phi_d = \frac{w_d/\rho_d}{\frac{w_c}{\rho_c} + \frac{w_d}{\rho_d}} \tag{14}$$

Für poröse und nicht poröse Füllstoffe kann man für das Maxwell-Modell Grenzfälle definieren. Mit Gleichung 15 kann die relative Permeabilität der Kompositmembran (P_{eff}/P_c) für poröse Füllstoffe, deren Permeabilität deutlich höher ist als die des reinen Polymers ($P_d >> P_c$), berechnet werden.

$$P_d \gg P_c;\ \frac{P_{eff}}{P_c} = \frac{1 + 2\phi_d}{1 - \phi_d} \tag{15}$$

Für nicht poröse Füllstoffe mit der Eigenschaft $P_d << P_c$, also eine signifikant geringere Permeabilität des Füllstoffs gegenüber dem Polymer, errechnet sich die Permeabilität der Kompositmembran nach Gleichung 16.

$$P_d \ll P_c;\ \frac{P_{eff}}{P_c} = \frac{(2 - 2\phi_d)}{(2 + \phi_d)} \tag{16}$$

Das Maxwell-Modell berücksichtigt keine Wechselwirkungen zwischen den einzelnen Füllstoffpartikeln und ist daher nur für geringe Beladungen geeignet. Stattdessen geht man von isolierten nebeneinander vorliegenden Partikeln aus. Bei höheren Füllstoffbeladungen können sich jedoch Inseln von verbundenen Partikeln bilden, die schließlich zu durchgängigen Kanälen anwachsen und somit einen alternativen Mechanismus des Gastransports auslösen (Abbildung 22).

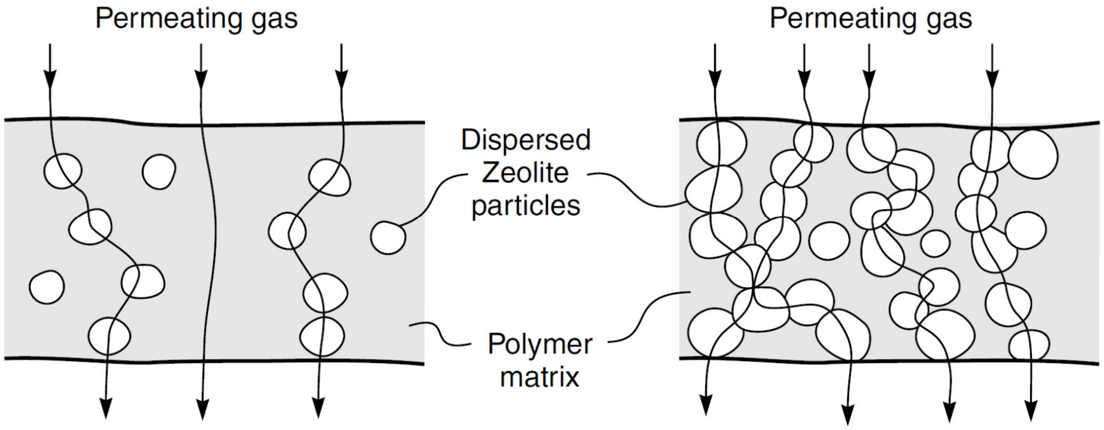

Abbildung 22: Gaspermeation durch Mixed-Matrix-Membranen mit unterschiedlichen Beladungen an Zeolithe Partikeln. Nachdruck mit Genehmigung von Ref. 96. Copyright 2004 John Wiley and Sons.

Die Perkolationsschwelle ist für jedes Kompositmaterial unterschiedlich, liegt jedoch häufig im Bereich von 30 vol.% des Füllstoffs. Für die Vorhersage der Permeabilität von MMMs mit höheren Beladungen können andere Modelle, wie zum Bespiel das Bruggeman-Modell verwendet werden, da hierbei auch Wechselwirkungen zwischen den Füllstoff Partikeln berücksichtigt werden.[111,112]

Ein wesentlicher Faktor bei der erfolgreichen Herstellung von MMMs ist die geeignete Kombination von Polymer und Füllstoff unter Berücksichtigung der physikalischen Eigenschaften des anorganischen Füllstoffs und der Schnittstelle zwischen Polymer und Partikel. Gasmoleküle wählen beim Transport durch eine Membran naturgemäß immer die

Route mit dem geringsten Widerstand. Folglich werden Gasmoleküle bei einer MMM aus einer Kombination von hochpermeablem aber nur mäßig selektivem Silikonkautschuk und einem Zeolith mit hoher Selektivität und durchschnittlicher Permeabilität, die Diffusion durch die Polymermatrix bevorzugen. Dadurch wird ein möglicher positiver Effekt des Füllstoffs verhindert. Das diese theoretische Überlegung tatsächlich in der Praxis zu beobachten ist, konnte Duval anhand der Einlagerung des Zeoliths 5A in PDMS zeigen.[113] PDMS/5A-MMMs zeigten nahezu keine Verbesserung der Trenneigenschaften, aufgrund der extrem schnellen Permeation durch das Polymer. Andererseits konnten die Separationseigenschaften für diverse Gaskomponenten von dem glasartigen, mäßig permeablen Polymer Polyethersulfon (PES) durch die Zugabe von 5A als Füllstoff signifikant verbessert werden.[114] Daher sollte schon bei der Auswahl der Komponenten auf eine ähnlich hohe Permeabilität für das schneller permeierende Gas geachtet werden.

Einen weiteren wichtigen Parameter in Kompositmembranen stellt die Partikelgröße des Füllstoffs dar. So haben sowohl kleine als auch große Partikel Vor- und Nachteile. Zum einen erlauben kleine Partikel die Herstellung von dünneren Kompositmembranen, was besonders bei Membranen, in denen die Diffusion die geschwindigkeitslimitierende Zeitspanne ist, einen höheren Durchfluss zur Folge hat. Außerdem erhöhen sich mit der Reduzierung der Partikelgröße die Polymer/Partikel-Schnittstellen, wodurch aufgrund von Sekundäreffekten (Polymerkettenversteifung oder Disruption) die Trenneigenschaften positiv aber auch negativ beeinflusst werden können. So zeigte die Untersuchung von unterschiedlich großen Zeolithe Partikeln (0,1, 0,4, 0,7, 0,8, 8 µm) in PDMS eine Abnahme der Permeabilität mit abnehmender Größe der Zeolithpartikel.[115] Ebenfalls beobachteten Cao et al. eine Abweichung im Vergleich zum Bruggeman Modell zu höheren Permeabilitäten mit steigender Partikelgröße der hier jedoch unterschiedlichen MOF-Füllstoffe.[116] Ein häufig auftretendes Phänomen ist die Sedimentation besonders von größeren Füllstoffpartikeln. Dabei setzen sich die Partikel während der Membranpräparation am Boden der Membran ab. Die Sedimentation wird durch unterschiedliche physikalische Eigenschaften zwischen Polymer und Füllstoff, hauptsächlich aufgrund unterschiedlicher Dichten, ausgelöst. Ein ähnliches Problem stellt die Agglomeration von Partikeln in Kompositmembranen da. Bei beiden Phänomenen entstehen Nadelöhre, in welche die Polymerketten nicht vordringen können und dadurch nicht selektive Hohlräume entstehen, sogenannte Mikrodefekte. Bei Anhäufung solcher Mikrodefekte kann es zum teilweisen oder kompletten Verlust der Selektivität der MMM kommen. Eine Möglichkeit, diesen Effekten entgegenzuwirken, ist die Erhöhung der Konzentration in der Polymerlösung vor dem Ausgießen der Membranen, um damit die Viskosität zu erhöhen und eine Sedimentation zu verlangsamen.[117] Zur Förderung einer besseren Polymer/Füllstoff-Interaktion haben Vu et al. die Füllstoffpartikel zunächst mit einer dünnen Schicht an Polymer überzogen und mit Ultraschall behandelt, bevor die vollständige Menge an Polymer hinzugegeben wurde.[104] Ferner ist auch eine Verringerung der Partikelgröße des Füllstoffs hilfreich, um auf diesem Weg eine Sedimentation zu verhindern.

Wie bereits mehrfach erwähnt, hängen die Transporteigenschaften der Kompositmembranen in einem hohen Maße von der Struktur der Schnittstelle zwischen Füllstoff und Polymer ab. Aus den in Abbildung 23 dargestellten vier möglichen Morphologien der Schnittstellen lassen sich unterschiedliche Auswirkungen auf die Permeationseigenschaften folgern.[118]

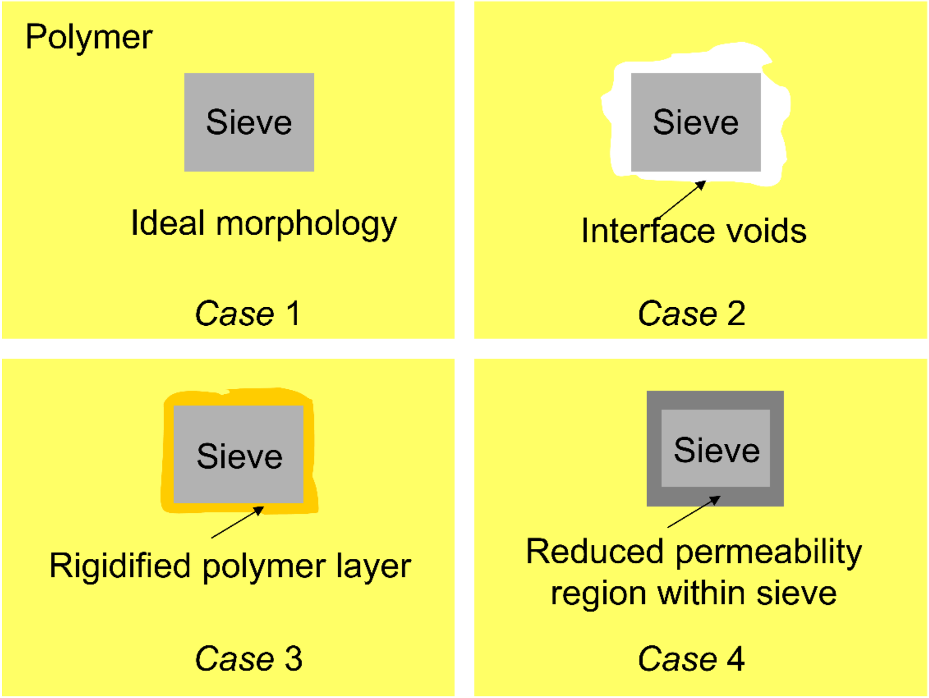

Abbildung 23: Schematische Darstellung unterschiedlicher Morphologien der Schnittstelle zwischen Polymer und Füllstoff. Nachdruck mit Genehmigung von Ref. 118. Copyright 2007 Elsevier.

In dem ersten Fall ist der Füllstoff perfekt in die Polymermatrix eingebettet. Bei einer solch idealen Morphologie sollten die Permeationseigenschaften, bei geringen Volumenfraktionen des Füllstoffs, dem Maxwell-Modell folgen und nur von den Eigenschaften der jeweiligen Komponenten abhängen. Im zweiten Fall liegen Hohlräume zwischen den beiden Phasen vor. Dieser Effekt kann insbesondere durch abstoßende Wechselwirkungen zwischen Füllstoff und Polymer zustande kommen, wie Barrer und James für die Mischung von Polymer und Zeolithpulvern anhand von elektrostatischen Widerstandsmessungen gezeigt haben.[119] Die schlechte Adhäsion zwischen beiden Phasen führt demnach zu freiem Volumen um die Partikel, welches eine erhöhte Permeabilität bei gleichzeitigem Verlust der Selektivität zur Folge hat. Für glasartige Polymere tritt dieser Fall besonders häufig auf, im Vergleich zu den elastischen kautschukartigen Polymeren. Daher wird davon ausgegangen, dass in glasartigen, steifen Polymeren, bei der Einbettung von Partikeln während der Kristallisation aufgrund von fehlender Flexibilität der Polymerketten Hohlräume in der nahen Umgebung der Partikel entstehen.[120] Ein experimenteller Nachweis für die Bildung von Hohlräumen, neben dem Verlust der Selektivität, ist schwierig. Bei einem möglichen Ansatz wird die Zunahme des freien Volumens mit einer Abnahme der Dichte in der Kompositmembran korreliert. So versuchten Paul et al. und Ahn et al. eine Quantifizierung der Hohlräume zu leisten, indem sie das Verhältnis der idealen Dichte zu der gemessenen Dichte der MMMs bestimmten.[121,122]

Die letzten beiden Typen setzten eine gewisse Affinität zwischen Polymer und Füllstoff voraus, da hierbei attraktive Wechselwirkungen zwischen kontinuierlicher und dispergierter Phase entweder eine Versteifung der Polymerketten auslösen oder die Poren des Füllstoffs durch Polymerketten blockiert werden. Wird, wie in Fall drei dargestellt, die Mobilität der Polymerkette durch Adsorption an der Oberfläche des Füllstoffs reduziert, führt dies, wie in den Arbeiten von Koros et al. und Kulprathipanja et al. gezeigt, zu einer erhöhten Selektivität der Kompositmembranen.[123,124] Die versteiften Polymerketten weisen eine verringerte Diffusion auf, besonders für die schlechter diffundierende Komponente, wodurch insgesamt die Permeabilität abnimmt. Experimentell kann man eine Versteifung der Polymerketten durch Bestimmung der Glastemperatur nachweisen. So spricht eine im Vergleich zum reinen Polymer erhöhte Tg der MMM für eine schlechtere Mobilität der Polymerketten und damit für eine Polymerkettenversteifung.[124] Eine Verwendung von porösen Füllstoffen zur Herstellung von MMMs kann, abhängig von der Porengröße der Partikel, eine teilweise oder komplette Blockade der Poren durch Polymerstränge mit sich führen. Eine komplette Verstopfung der Poren führt dementsprechend zu einer Abnahme der Permeabilität, da sich der Füllstoff nun wie ein nicht poröser Füllstoff verhält. So führte die Einlagerung des porösen Zeoliths NaX, mit Porengrößen zwischen 7 und 13 Å, in eine PDMS-Matrix, zu einem erheblichen Verlust der Permeabilität mit zunehmendem Volumenanteil an NaX, bei gleichbleibender Selektivität.[125] Eine teilweise Blockade der Porenstrukturen von Füllstoffen mit Porendurchmessern nahe dem kinetischen Durchmesser der zu trennenden Gasmoleküle ist durchaus von Vorteil. Dadurch können die Füllstoffe mit ursprünglich zu großen Poren nun als *molecular sieves* agieren, was eine erhöhte Selektivität der Kompositmembran zur Folge hat.[118]

Das hauptsächliche Ziel der Herstellung von MMMs ist die Verbesserung der Separationseigenschaften gegenüber Polymermembranen durch den Einfluss anorganischer Partikel. Daher sollte die Morphologie einer idealen MMM den Transport durch die anorganische dispergierte Phase fördern. Allgemein können MMMs entweder symmetrisch oder asymmetrisch aufgebaut sein (Abbildung 24).

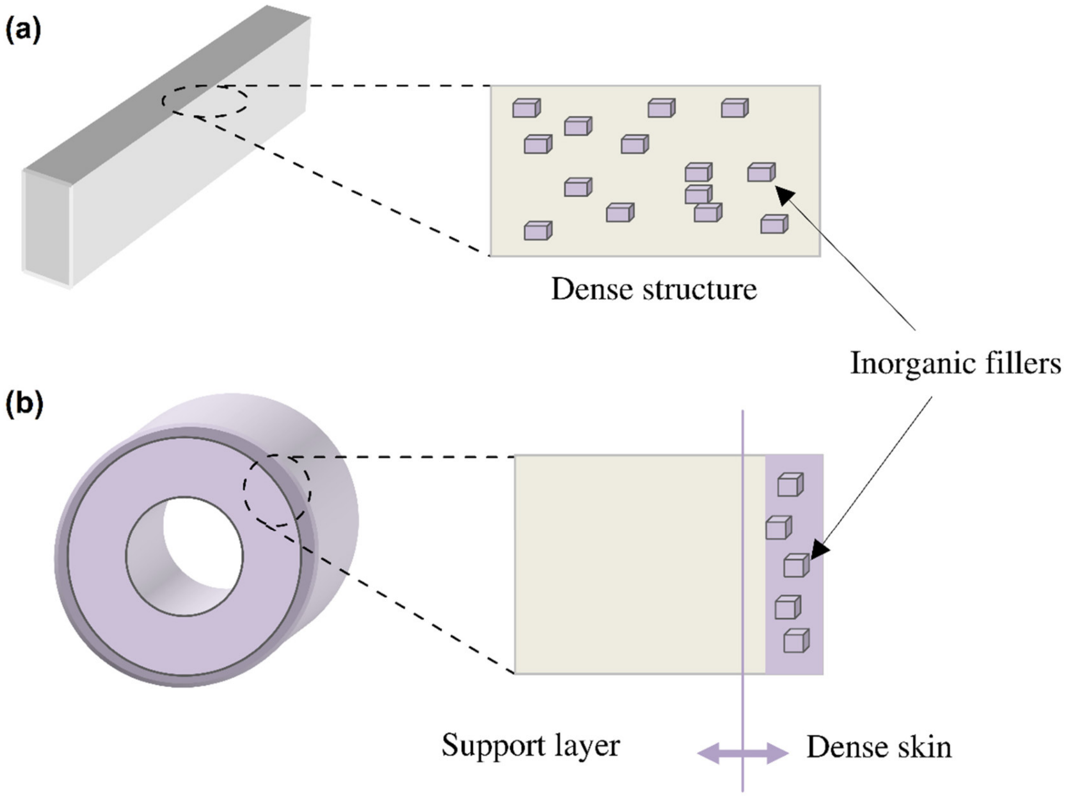

Abbildung 24: Schematische Darstellung von dichten, symmetrischen MMMs (a) und asymmetrischen MMMs (b). Nachdruck mit Genehmigung von Ref. 126. Copyright 2011 Elsevier.

Der Vorteil von symmetrischen Membranen ist deren einfache Herstellung und Charakterisierung. Sie ist daher die deutlich bevorzugte Geometrie in der Forschung der letzten Jahre.[127] Da aufgrund von einsetzender Brüchigkeit der MMMs, spätestens ab einer Beladung von über 40 %, die Perkolationsschwelle meist nicht erreicht werden kann, ist deren Potenzial in der Gastrennung begrenzt. In der Industrie ist es jedoch von höchster Bedeutung, die Produktivität von Membranen erheblich zu steigern. Dieses Ziel ist nur mit asymmetrischen Membranen zu erreichen, wie Loeb und Sourirajan mit der ursprünglichen Entwicklung der asymmetrischen Membran, die zur ersten Anwendung von Membranen in der Industrie führten, bereits gezeigt haben.[82] Generell sind asymmetrische Membranen aus einer dünnen, selektiven Schicht, die auf einen porösen Träger aufgetragen wird, aufgebaut. Asymmetrische Membranen können sowohl als flache Membranen, als auch in der Konfiguration einer Hohlfaser hergestellt werden (Abbildung 24). Die Hohlfaser bietet durch einen nochmals erhöhten Gasfluss die besten Eigenschaften für eine Anwendung in der Industrie.[128]

.

2. Aufgabenstellung

Im Rahmen dieser Arbeit sollten ausgewählte MOFs oder MOF-Polymer-Gemischtmatrix-Membranen (MOF-MMMs), auf ihre Gastrennungseigenschaften untersucht werden.

Im Speziellen sollten zunächst MMMs aus einer Polymermatrix und einem MOF als Füllstoff hergestellt werden. Dabei sollte der Füllstoff im Hinblick auf seine Porosität so modifiziert werden, dass unter Erhalt der Morphologie ein poröses und ein nicht-poröses, aber ansonsten identisches MOF entsteht, um daraufhin beide MOFs in die gleiche Polymermatrix einzubetten. Mit Hilfe der Charakterisierung der Gas-Permeationseigenschaften beider MMMs sollte der Einfluss des eingebrachten freien Volumens durch den porösen Füllstoff ermittelt werden.

Ferner sollten MOFs gesucht werden, die für eine mögliche Aufnahme und Abtrennung von (toxischen) SO_2-Restgehalten (< 500 ppm) aus Rauchgasen verwendet werden können. Dazu sollten Sorptionsisothermen von bekannten MOFs mit unterschiedlichen Eigenschaften (Porengröße, Porenvolumen, Stabilität, Metallkation, etc.) aufgenommen werden. Ferner sollte deren Stabilität unter Einfluss von SO_2 untersucht werden und die selektive SO_2-Aufnahme unter Anwendungsbedingungen, also bei Konzentration unter 500 ppm und in Gegenwart von Feuchtigkeit bestimmt werden.

In einer anschließenden Arbeit sollte die Entwicklung von neuartigen MMMs zur Gastrennung von CO_2/CH_4 erfolgen. Dazu sollten die prototypischen MOFs MOF-199 (HKUST-1) und MIL-101(Cr) in das interessante Polymer 6FDA-mPD (siehe Abbildung 19) eingebettet werden. Ferner sollte der Einfluss der charakteristischen Eigenschaften der MOFs (sehr hohes Porenvolumen von MIL-101Cr; bemerkenswert hohe Affinität von MOF-199 zu CO_2) auf die MMMs untersucht werden.

Außerdem sollte die indirekte Bestimmung der isosteren Adsorptionsenthalpie anhand von Adsorptionsisothermen bei zwei unterschiedlichen Temperaturen untersucht werden. Im Besonderen sollten mögliche Fehlerquellen sowie Vor- und Nachteile bei dem üblichen Freundlich-Langmuir-Fit/Clausius-Clapeyron-Ansatz und der Virial Analyse erarbeitet werden.

Abschließend sollte nach einer Möglichkeit zur Einlagerung von molekularen, porösen organischen Molekülen in die Poren von MOFs gesucht werden, um die hohe Affinität von porösen organischen Molekülen zu Gasen wie CO_2 mit der guten chemischen Stabilität von ausgewählten MOF-Materialien zu kombinieren und dadurch eine neue Klasse verbesserter poröser Materialen zu erhalten.

Alle relevanten Ergebnisse sollten aufgearbeitet werden und in wissenschaftlichen Journalen publiziert werden.

3. Kumulativer Teil

In den folgenden Kapiteln 3.1 – 3.6 werden die Ergebnisse, welche in Form einer Publikation in internationalen Journalen veröffentlicht wurden, in kumulativer Form präsentiert. Die Publikationen werden so dargestellt, wie sie auch in den jeweiligen Journalen veröffentlicht wurden. Daher beinhaltet jede Veröffentlichung ein separates Quellenverzeichnis. Außerdem wird zunächst für jede Publikation sowohl eine kurze Einordnung in den Kontext der Dissertation dargelegt, als auch der Anteil der Autoren an der jeweiligen Publikation beschrieben.

3.1 Role of Filler Porosity and Filler/Polymer Interfaces Volume in Metal-Organic Framework/Polymer Mixed-Matrix Membranes for Gas Separation

Alexander Nuhnen, Dennis Dietrich, Simon Millan, Christoph Janiak

ACS Appl. Mater. Interfaces, **2018**, 10, 39, 33589–33600.

DOI: 10.1021/acsami.8b12938

In der Forschung zur Gastrennung mittels Membranen wurden in den letzten Jahren die Vorteile von Mixed-Matrix-Membranen gegenüber reinen Polymermembranen durch eine Vielzahl an Publikationen belegt. Dabei wurden diverse Füllstoffe in unterschiedlichste Polymermatrizen eingebettet und besonders bei porösen Füllstoffen konnte eine Erhöhung der Permeabilität mit Zunahme an eingesetztem Füllstoff gezeigt werden. Jedoch fehlte in der Literatur eine gezielte Untersuchung, ob die Zunahme der Permeabilität in den Mixed-Matrix-Membranen eine Folge der Erhöhung des freien Volumens durch die porösen Füllstoffe ist, oder freies Volumen zwischen den Füllstoffpartikeln und den Polymerketten entsteht. In dieser Arbeit konnte durch den Einbau des porösen MOFs Aluminium Fumarat und einer nicht porösen Modifikation des gleichen MOFs der positive Effekt der inhärenten Porosität des Füllstoffs auf die Separationseigenschaften der Mixed-Matrix-Membranen belegt werden. Da die beiden Füllstoffe sich nur in ihrer Porosität unterscheiden, jedoch strukturell identisch sind, konnte ein Einfluss anderer Eigenschaften auf die Permeation, wie zum Beispiel Polymer/Füllstoff-Wechselwirkungen oder Partikelform und Partikelgröße, ausgeschlossen werden. Es konnte gezeigt werden, dass die Permeabilität der Kompositmembranen sich entsprechend des Maxwell-Modell für poröse bzw. nicht poröse Füllstoffe entwickelt. Der Einfluss des freien Volumens zwischen Füllstoffpartikel und Polymer war nicht signifikant. Voraussetzung für ein geringes freies Volumen zwischen Füllstoff und Polymer ist eine gute Kompatibilität zwischen beiden Komponenten.

Anteile an der Veröffentlichung:

- Die Entwicklung des Konzepts, die experimentellen Arbeiten im Labor, die Durchführung der Analytik, mit Ausnahme der REM/EDX Messungen und CO_2 und CH_4 Sorptionsmessungen, die Auswertung der Ergebnisse, das Erstellen von Abbildungen und Tabellen und die Verfassung des Manuskripts. Korrekturen wurden von Herrn Prof. Dr. Janiak vorgenommen.
- Die REM/EDX-Messungen wurden von Herrn Dr. Dennis Dietrich durchgeführt.
- Die CO_2 und CH_4 Sorptionsmessungen hat Herr Simon Millan ausgeführt.

ACS APPLIED MATERIALS & INTERFACES
Research Article
Cite This: ACS Appl. Mater. Interfaces 2018, 10, 33589−33600
www.acsami.org

Role of Filler Porosity and Filler/Polymer Interface Volume in Metal–Organic Framework/Polymer Mixed-Matrix Membranes for Gas Separation

Alexander Nuhnen, Dennis Dietrich, Simon Millan, and Christoph Janiak*

Institut für Anorganische Chemie und Strukturchemie, Heinrich-Heine-Universität, Universitätsstraße 1, D-40225 Düsseldorf, Germany

Supporting Information

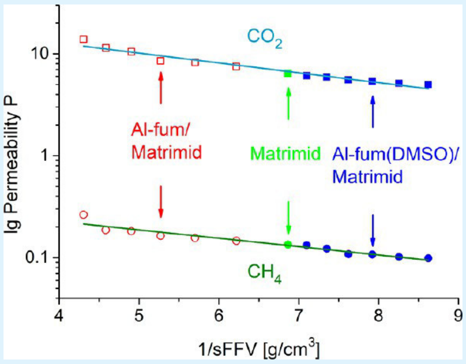

ABSTRACT: Metal−organic frameworks (MOFs) and inorganic fillers are frequently incorporated into mixed-matrix membranes (MMMs) to overcome the traditional trade-off in permeability (*P*) and selectivity for pure organic polymer membranes. Therefore, it is of great interest to examine the influence of porous and nonporous fillers in MMMs with respect to the possible role of the polymer−filler interface, that is, the void volume. In this work, we compare the same MOF filler in a porous and nonporous state, so that artifacts from a different polymer−filler interface are excluded. MMMs with the porous MOF aluminum fumarate (Al-fum) and with a nonporous dimethyl sulfoxide solvent-filled aluminum fumarate (Al-fum(DMSO)), both with Matrimid as polymer, were prepared. Filler contents ranged from 4 to 24 wt %. Gas separation performances of both MMMs were studied by mixed gas measurements using a binary mixture of CO_2/CH_4 with gas permeation following the theoretical prediction by the Maxwell model for both porous and nonporous dispersed phase (filler). MMMs with the porous Al-fum filler showed increased CO_2 and CH_4 permeability with a moderate rise in selectivity upon increasing filler fraction. The MMMs with the nonporous Al-fum(DMSO) filler displayed a reduction in permeability while maintaining the selectivity of the neat polymer. A linear dependence of log *P* versus the reciprocal specific free fractional volume (sFFV) rules out a significant contribution from a void volume. The sFFV includes the free volume of the polymer and the MOF, but not the polymer−filler interface volume (so-called void volume). The sFFV for the MMM was calculated between 0.23 cm^3/g for a 24 wt % Al-fum/Matrimid MMM and 0.12 cm^3/g for a 24 wt % Al-fum(DMSO)/Matrimid MMM. The negligible effect of an interface volume is supported by a good matching of theoretical and experimental density of the Al-fum and Al-fum/(DMSO) MMMs which gave a specific void volume below 0.02 cm^3/g, often even below 0.01 cm^3/g.

KEYWORDS: *MOFs, metal−organic frameworks, Matrimid, mixed-matrix membrane, nonporous filler, free fractional volume, void volume, gas separation*

INTRODUCTION

Membrane science and technology has attracted continuous attention over the last few decades due to its superior separation properties in comparison to conventional methods, such as crystallization, distillation, or adsorption processes.[1−3] Since purification processes based on membranes feature high energy efficiency, low production costs, and simple process conditions, they are very attractive for industrial application.[4,5]

Gas separation efficiency through dense polymer membranes is generated through a unique separation process as no high energy phase transformation is needed, unlike in the conventional separation processes. Separation through membranes is dependent instead on size, shape, and interaction of the molecules with the membrane material.[6] Membranes therefore can be characterized by two main properties to determine their efficiency. The permeability describes the velocity in which the gases travel through the membrane, and the selectivity exhibits the separation potential between two or more gases.[7]

At the current state low flux polymeric membranes are widely used in industrial processes because of their high flexibility, easy processing, low costs, and mechanical strength.[8] Yet, polymeric membranes display a major disadvantage since they exhibit an inverse relation, a trade-off between high gas permeation or good selectivity.[9] This inverse relation between permeation and selectivity is illustrated in the so-called Robeson upper bound.[9,10] A possible way to overcome this trade-off is realized by embedding inorganic or organic−inorganic hybrid materials as fillers into the polymer matrix to receive mixed-matrix membranes (MMMs).[11−14]

Received: July 30, 2018
Accepted: September 7, 2018
Published: September 7, 2018

DOI: 10.1021/acsami.8b12938
ACS Appl. Mater. Interfaces 2018, 10, 33589−33600

The used fillers can generally be divided into two groups: porous and nonporous fillers. In the field of porous fillers zeolites and highly porous metal organic frameworks (MOFs) are the most studied materials in MMMs.[15−17] Because of their high tuneability and structural diversity MOFs can be customized for different polymer matrices to obtain microdefect free MMMs or enhance their separation properties.[18,19] Usually it is found that the permeability of defect free MMMs increases with the loading of the MOF and the selectivity remains unaltered or raises only in a moderate way in comparison to the neat polymer.[20] The increase of permeability is either associated with the porous nature of the MOFs, which therefore increases the free fractional volume (FFV) of the MMMs, or to the presence of isolated voids in the interface between the MOF and the polymer.[21,22] Free fractional volume refers to the inherent porosity within the polymer and the porous filler, here the MOF. The FFV does not include any voids formed around the filler particles due to phase incompatibility. However, a consequence of voids, which become connected through a membrane because of high filler loading, will be that these MMMs show an increased permeability and a partial or complete loss of selectivity as such connected voids would be nonselective.[23,24]

Exemplary for this behavior Basu et al. studied the permeation properties of MIL-53(Al)/Matrimid, Cu-BTC/Matrimid, and ZIF-8/Matrimid MMMs for CO_2 and CH_4 and found a continuous increase in CO_2 and CH_4 permeation with growing amount of MOF. Thereby CO_2 permeation enhancement was slightly higher in relation to CH_4, resulting in a moderate rise of their selectivity.[25] A way to enhance the selectivity in a significant manner was specified by Zornoza et al., using the amino modified NH_2-MIL-53(Al) embedded in a polysulfone matrix.[13] The characterization of the MMMs showed a doubling in selectivity for the MMMs with 25 wt % MOF including a minor raise in CO_2 permeability, before losing their separation properties with higher loadings up to 40 wt % MOF.

Studies of nonporous fillers in MMMs mostly focus on nanoparticles based on fumed silica or other oxides.[14,26] As nonporous fillers are not permeable for gases, they should lower the permeability of the MMMs with increasing amount of the filler, as long as one obtains an ideal MMM. This behavior was shown by Sadeghi et al. when they incorporated silica nanoparticles into a polyether polymer matrix. The MMMs show a reduction of permeability for several gases with increasing amount of silica.[27] Nevertheless Merkel et al., Ahn et al., and Ahmadpour et al. experienced an increase of the permeability for their MMMs with nonporous nanoparticles in comparison to the neat polymer.[14,26,28] Ahn et al. explained the rise in permeability as a result of interfacial voids between nanoparticles and polymer. They quantified the resulting voids by comparing the actual density of the MMMs with the theoretically calculated density and could therefore determine the void volume of the MMMs.[28] The interfacial voids were associated with poor interactions of the inorganic nanoparticles with the polymer phase.[29] With porous fillers the determination of interfacial voids is rarely done. It was shown that there is a correlating increase between FFV and permeability, but no such correlation could be seen between void volume and permeability.[21]

With porous fillers an increase in permeability is seen as normal and viewed as an expected property. However, it cannot automatically be deduced that this increase is due to the porosity of the filler. With the formation of interfacial voids, such an increase could also derive therefrom.[23,24]

To the best of our knowledge, the relative role of porosity in the filler and interfacial voids between filler and polymer have not been clearly elucidated. Understandably it is not straightforward to conceive how the chemically same filler material could be prepared in a porous and nonporous way. Therefore, we prepared for the first time (to the best of our knowledge) a porous and a nonporous filler based on the same MOF, with the same properties as particle size, structure, and interaction with the polymer, only differing in their porosity. By embedding both fillers in the polymer Matrimid one should see which influence porosity and interfacial voids have, respectively. If the void volume is responsible for a higher permeability in MMMs, compared to the neat polymer, then one would expect a rise in permeability for both kinds of filler. If, however, the porosity is responsible for an increase in permeability, then one would expect a rise in permeability only for the MMMs with the porous filler.

RESULTS AND DISCUSSION

Al-fum and Al-fum(DMSO) Characterization. In this study the properties of porous and nonporous fillers in MMMs, based on the MOF aluminum fumarate as filler and Matrimid as polymer, is examined. Aluminum fumarate (Al-fum) was synthesized according to a recently described procedure which yields submicrometre particles of the MOF.[30] Particle size and morphology of fillers have great influence on the distribution of MOF particles in the polymer matrix. Thus, they affect phenomena such as sedimentation and agglomeration of the filler and ultimately reduce or increase microdefects in MMMs which affects permeation results.[13,31,32] Here, the obtained Al-fum particles had a size of about 250 nm, characterized by SEM (Figure S2 of the Supporting Information, SI), which is in good agreement with the literature.[30] Furthermore, the successful synthesis of aluminum fumarate was shown by a positive matching of the experimental PXRD to the simulated pattern (Figure 1). The synthesis of aluminum fumarate-(DMSO) (Al-fum(DMSO)), that is, pore filling of Al-fum by dimethyl sulfoxide, was achieved by stirring Al-fum in dimethyl sulfoxide at 180 °C overnight. DMSO-filling did neither alter the Al-fum particle size of about 250 nm (Figure S2) nor the crystallinity (Figure 1). The PXRD in Figure 1 shows slightly

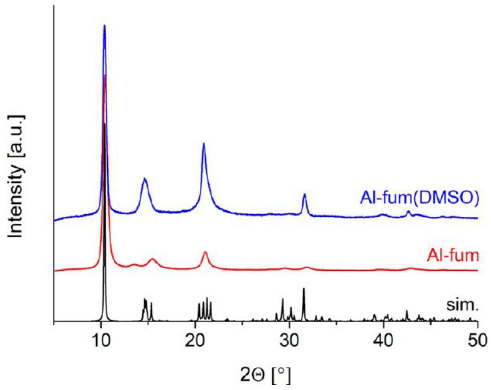

Figure 1. Powder X-ray diffractograms for Al-fum in red and Al-fum(DMSO) in blue in comparison with the simulated diffractogram (sim., based on the X-ray data refinement, CCDC number: 1051975)[37] in black.

higher intensities for reflections after 11° 2θ for Al-fum(DMSO), in comparison to the activated Al-fum. The enhancement is induced by DMSO inside the pores of Al-fum(DMSO) which contributes to the scattering. This behavior was already observed by Thoma et al. for incorporated DMSO in NH_2-MIL-53(Al).[33,34] The broadening of the reflections for both Al-fum and Al-fum(DMSO), in comparison to the simulated pattern, is due to the small crystallite size.[35,36] Following the Scherrer equation (eq 5) the crystallite size from the (0 1 1) reflection at 2θ = 10.45° was calculated to 20 nm. Note that the crystallite size is not comparable to the particle size, as particles can be made up of several different crystallites or crystallite domains or consist of a crystalline and amorphous fraction.

Besides the morphology, other crucial characteristics for the synthesized MOF, used as a filler for MMMs, are sorption properties of the very compound. Recent studies of Kanehashi et al. showed a linear dependence between the gas permeability and the fractional free volume (FFV) of the MMMs.[21] Therefore, Brunauer, Emmett, Teller (BET) surface area and pore volume for Al-fum and Al-fum(DMSO) were determined from a nitrogen sorption isotherm at 77 K (Figure 2). Al-fum shows as a first approximation a Type I nitrogen adsorption isotherm, typical for microporous materials,[38] yielding a BET surface area of 1100 m^2 g^{-1} and a total pore volume of 0.47 cm^3 g^{-1}. The micropore volume, given by the V-t-plot method according to DeBoer, is 0.37 cm^3 g^{-1}. For comparison BET surfaces areas and pore volumes of several Al-fum literature reports are collected in Table S1.

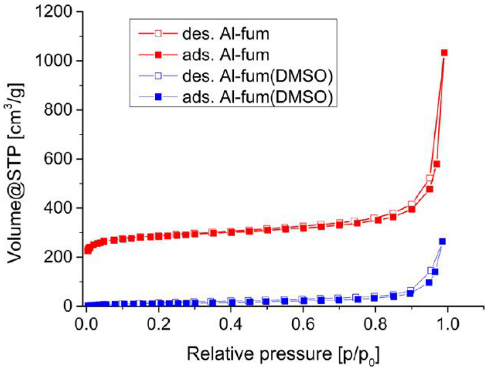

Figure 2. Nitrogen sorption isotherms of Al-fum (red) and Al-fum(DMSO) (blue) at 77 K.

In contrast Al-fum(DMSO) shows no nitrogen uptake upon low relative pressures, hence displays no micropore volume. The calculated BET surface area of Al-fum(DMSO) of 40 m^2 g^{-1} represents primarily the external surface area due to the small particle size of the MOF. Both N_2 sorption isotherms for Al-fum and Al-fum(DMSO) show a continuous slight increase in gas uptake above p/p_0 = 0.4 with increasing relative pressure. A strong rise in gas uptake above p/p_0 = 0.9 gives the isotherms a Type II or Type III isotherm appearance and high nitrogen uptake for both compounds toward the saturation pressure (i.e., at p/p_0 = 1). This curvature can be explained by interparticle condensation in the macropores formed by the particle aggregates, which is showing here because of the intentionally prepared submicrometer particles.[39,40] Al-fum samples of larger particle size, porous or nonporous (DMSO-filled), do not show this continuous gas uptake with increasing relative pressure (Figure S3 in the SI). Hence, the MOF-pore volume determination must be limited to the MOF-inherent micro- and mesoporosity. A comparison of Figures 2 and S3 in SI shows that at p/p_0 > 0.4 the interparticle volume between submicrometer particles and concomitant pore condensation leads to a nitrogen uptake, which would then include this external volume. We decided to take the total pore volume at p/p_0 = 0.4 in order not to overestimate the micro- and mesopore volume inside the framework.

IR spectra of Al-fum(DMSO) showed an additional peak which can be assigned to the stretching vibration of the sulfur–oxygen double bond (1040–1060 cm^{-1}) (Figure S4).

Thermogravimetric analysis (TGA) and elemental analysis were conducted to determine the exact amount and ratio of the loaded DMSO to the MOF.

From TGA (Figure 3), Al-fum exhibits its typical degradation at around 400 °C with a mass loss of 59% associated with the decay of the organic linker. In comparison Al-fum(DMSO) shows a continuous mass loss of 31% from 100 °C to 280 °C, where the Al-fum material starts to degrade, followed by the mass loss for the linker decay. The presence and loss of 0.31 g DMSO per g Al-fum(DMSO) with 0.69 g Al-fum sample correlates with a liquid DMSO density of 1.1 g/cm^3, hence the volume of 0.28 cm^3 in the pore volume of 0.47 cm^3/g × 0.69 g = 0.32 cm^3. Since the continuous mass loss occurs after thorough drying at 1 × 10^{-3} mbar at room temperature, it can be attributed to the desorption of DMSO from inside the pores other than just free solvent. The mass ratio of 0.31 g DMSO and 0.69 g Al-fum yields a molar ratio of approximately 0.8:1. Elemental analysis for Al-fum and Al-fum(DMSO) are represented in Table S2 and show a ratio of about 0.8:1 for DMSO to Al-fum. The slight difference in calculated and experimental elemental analysis can result from water retained in DMSO or in the MOF itself, which is in good agreement with the higher amount of hydrogen and the fewer amount of sulfur in comparison to the calculated value for both samples.

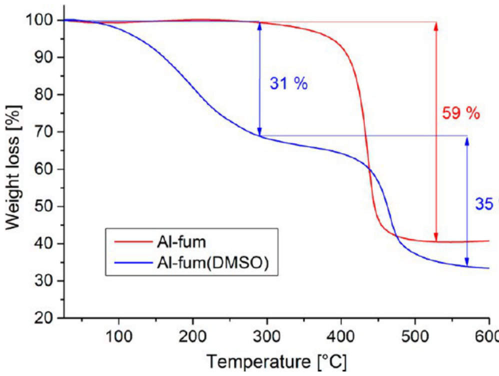

Figure 3. Thermogravimetric analysis (TGA) curves of Al-fum (red) and Al-fum(DMSO) (blue) under synthetic air at a heating flow of 2 K/min.

The porous filler material of MMMs is usually thought to contribute to the gas separation properties of the MMMs and could even enhance the selectivity of the MMMs compared to the neat polymer membrane.[41,42] Here the separation of CO_2 and CH_4 is used to test for this effect (Figure S5). The gas uptake in the porous Al-fum for CO_2 and CH_4 at 870 mmHg was 3.8 mmol/g and 1.4 mmol/g, respectively. The selectivity of 3.98 was obtained by the Henry plots of the adsorption isotherms (Figure S6) and is in good agreement with the literature for gas adsorptions measurements with a neat microsized Al-fum powder.[43] Note that the value of the selectivity for single-gas adsorption has little to do with the selectivity for neat or mixed-matrix membranes made from this MOF.[44,45]

Membrane Preparation and Gas Permeation Experiments. For the MMMs Matrimid 5218 (Figure 4) was chosen as a polymer due to its high thermal and chemical stability as well as its widespread implementation in MMMs so far. Matrimid has shown good interaction capability with MOFs as filler materials caused by polar carbonyl and imide groups which can interact with the MOF crystallites.[46,47]

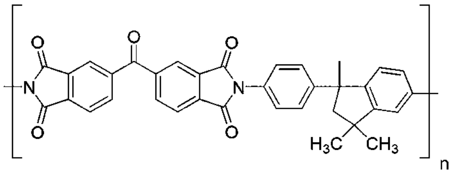

Figure 4. Structure of Matrimid.

All MMMs were prepared in the same procedure using a priming protocol in combination with multiple ultrasonication steps to receive uniform dispersed MOF particles in the polymer matrix. To determine the MOF particle distribution and embedment in the MMMs, SEM images of the cross sections in combination with an energy-dispersive X-ray spectroscopic (EDX) mapping of aluminum and sulfur were realized.

Figure 5 shows typical SEM images of cross sections for MMMs of Al-fum/Matrimid MMMs with different MOF loadings, prepared by freeze fracturing. The SEM images together with EDX depict an excellent particle distribution throughout all membranes. Close-up images of the cross section endorse a good compatibility between MOF and polymer, marked by no significant interfacial void formation around the filler particles.

EDX mapping of aluminum confirms homogeneous distribution of the filler despite minor sedimentation for various MMMs with different MOF loadings, shown by locally increased intensity of the mapped aluminum (Figure 6). Most important is to point out that even with higher loadings of Al-fum, the sedimentation of the filler remains in a reasonable scope and therefore uniformly homogeneous, dense MMMs are formed.

In the same manner MMMs of Al-fum(DMSO)/Matrimid were analyzed. Overviews and close-ups of the cross section of MMMs loaded with 4 and 24 wt % Al-fum(DSMO) are shown in Figure 7. They show equally good particle distribution across the whole MMMs. Close-up images are rather similar to the MMMs of Al-fum/Matrimid MMMs and show no interfacial void formation around the filler particles and the polymer. Figure 8 displays EDX-mapping of aluminum in red and sulfur in blue of the same cross sections shown in Figure 7. Aluminum as well as sulfur are detected homogeneously throughout the MMMs and in a similar intensity, which indicates a uniform distribution and high loading of DMSO in the pores of Al-fum. Moreover, EDX-mapping reveals minimal sedimentation for MMMs with 24 wt % MOF.

Mixed gas permeation experiments were carried out from a 50:50 v:v CO_2/CH_4 mixture at 25 °C and a transmembrane pressure of 3 bar. CO_2 and CH_4 gas permeabilities of the neat polymer and Al-fum/Matrimid MMMs are presented in Table S5 and Figure 9.

In general gas permeability increases with the increase of Al-fum loading. The selectivity increases slightly up to a loading of 20 wt %. Only for a loading of 24 wt % the selectivity drops again due to emerging microdefects, like agglomeration of MOF particles, resulting in connected nonselective voids between polymer and MOF or MOF particles themselves.[23] The 24 wt % membrane is also mechanically sensitive and quite brittle. Al-fum/Matrimid MMMs with 20 wt % performed the best with an improvement of 63% in CO_2 permeation and 28% in selectivity compared to the neat polymer. The observed trend of higher MOF loading resulting in an increased permeability is intrinsic for porous fillers in MMMs and is frequently observed.[48−50] The gas permeability and selectivity enhancement can be traced back to improved gas diffusivity and adsorption of the MMMs. Diffusivity is either influenced by the free fractional volume (FFV) of the polymer and the MOF or by interfacial voids between polymer and MOF (void volume).[21,28] The influence of both FFV and void volume is discussed in a following section. Adsorption properties of Al-fum affect the selectivity of MMMs in a desired way. The adsorption properties of Al-fum with a near 4:1 selectivity of CO_2 over CH_4, calculated from the initial Henry plot of the CO_2 and CH_4 adsorption isotherms (Figures S5 and S6), cause an improvement of selectivity with increasing MOF loading. Due to its quadrupole moment CO_2 is more likely to interact and adsorb on Al-fum causing its superior selectivity of CO_2 over CH_4.

Likewise mixed gas permeation experiments with Al-fum(DMSO)/Matrimid MMMs were carried out. The results are presented in Table S6 and in Figure 10. An Al:S quantification of the Al-fum(DMSO)/Matrimid MMMs before and after the gas permeation studies gave the same molar ratio within experimental error (Tables S3 and S4 in the SI). This ensured that no DMSO was removed upon gas permeation, hence, the nonporous nature of Al-fum(DMSO) was retained.

For the membrane with the nonporous Al-fum(DMSO) filler both CO_2 and CH_4 permeabilities are reduced in similar proportion with increased loading of Al-fum(DMSO). Consequently, the selectivity stays largely constant for the different MMM loadings. CO_2 permeabilities decrease constantly from about 6.6 Barrer of the neat polymer to 5.0 Barrer in the MMMs with 24 wt % MOF loading (24% reduction). Equally CH_4 permeability reduces from 0.14 Barrer to 0.10 Barrer (28% reduction), respectively. As described in the Introduction, compared to the effect of porous fillers, nonporous fillers have shown diverse impacts in MMMs. Either nonporous fillers increase the permeability while mostly reducing the selectivity due to the formation of defects,[25] or to the contrary nonporous fillers lead to a decrease in permeability while retaining the selectivity of the polymer.[28,51] In this work the latter is observed, which emerges out of the nature of the used filler. Usually inorganic oxides were used as nonporous fillers, showing poor interactions with most polymers. MOFs on the other hand are known to develop favorable interactions with the polymer, which leads to fewer microdefects in the MMMs. Therefore, it is not surprising that MMMs consisting of nonporous Al-fum(DMSO) and Matrimid show a reduction in permeability with increasing filler loading, as the FFV of the MOF is essentially zero and the volume of the polymer is constantly reduced.

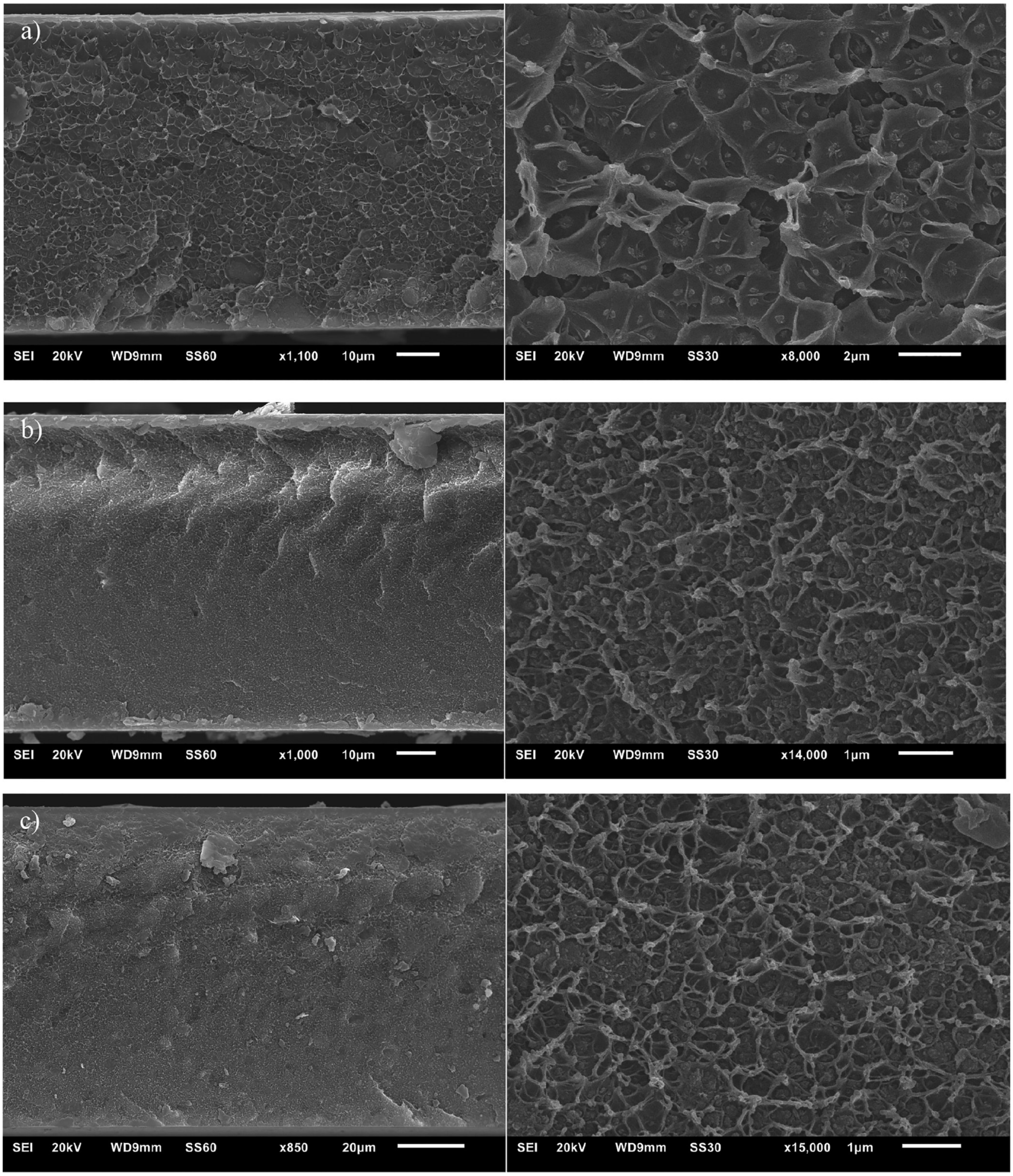

Figure 5. SEM images of cross section of Matrimid with different loadings of Al-fum as filler a) 8 wt %, b) 16 wt %, and c) 24 wt %.

Modeling of Gas Permeation. *Maxwell Model.* The Maxwell model can be applied to both porous and nonporous fillers in composite membranes to predict the permeability of the composite membrane. Prior works have shown poor or only qualitative trend agreements for porous and nonporous fillers compared to the predicted values of the Maxwell model.[51−54] The values for the observed permeability could often not be reproduced with the model. The discrepancy between model and experiment can result from stronger deviations between assumptions and reality, for example, for particle geometry, dispersion, or maximum filler loading, which are essential for the model, or the unaccounted presence of microdefects due to poor interaction between filler and polymer. Figure 11 shows the comparison between predicted

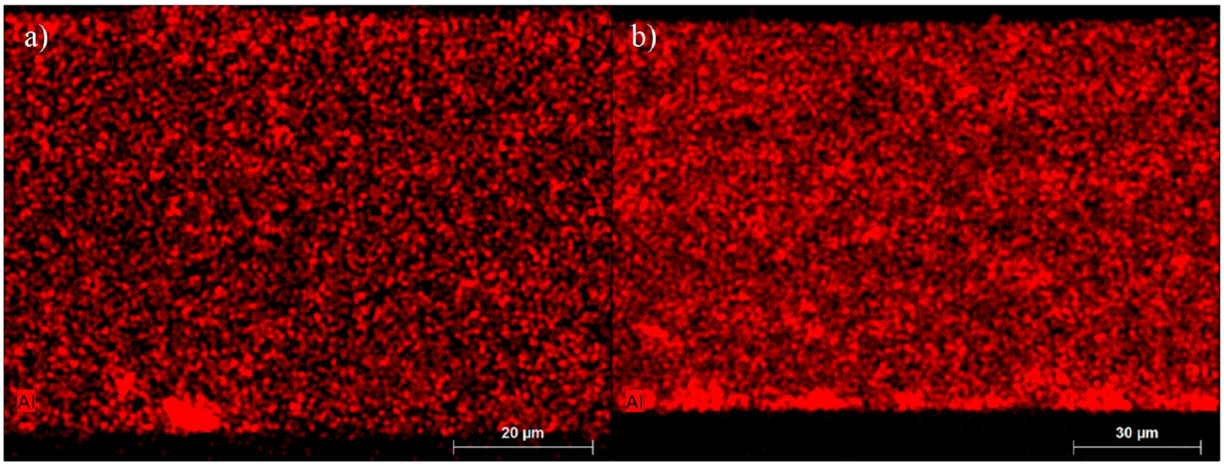

Figure 6. EDX-mapping of aluminum (red) in MMM cross sections of a) 4 wt % Al-fum and b) 24 wt % Al-fum. The bottom of the images corresponds to the bottom of the membrane when casted.

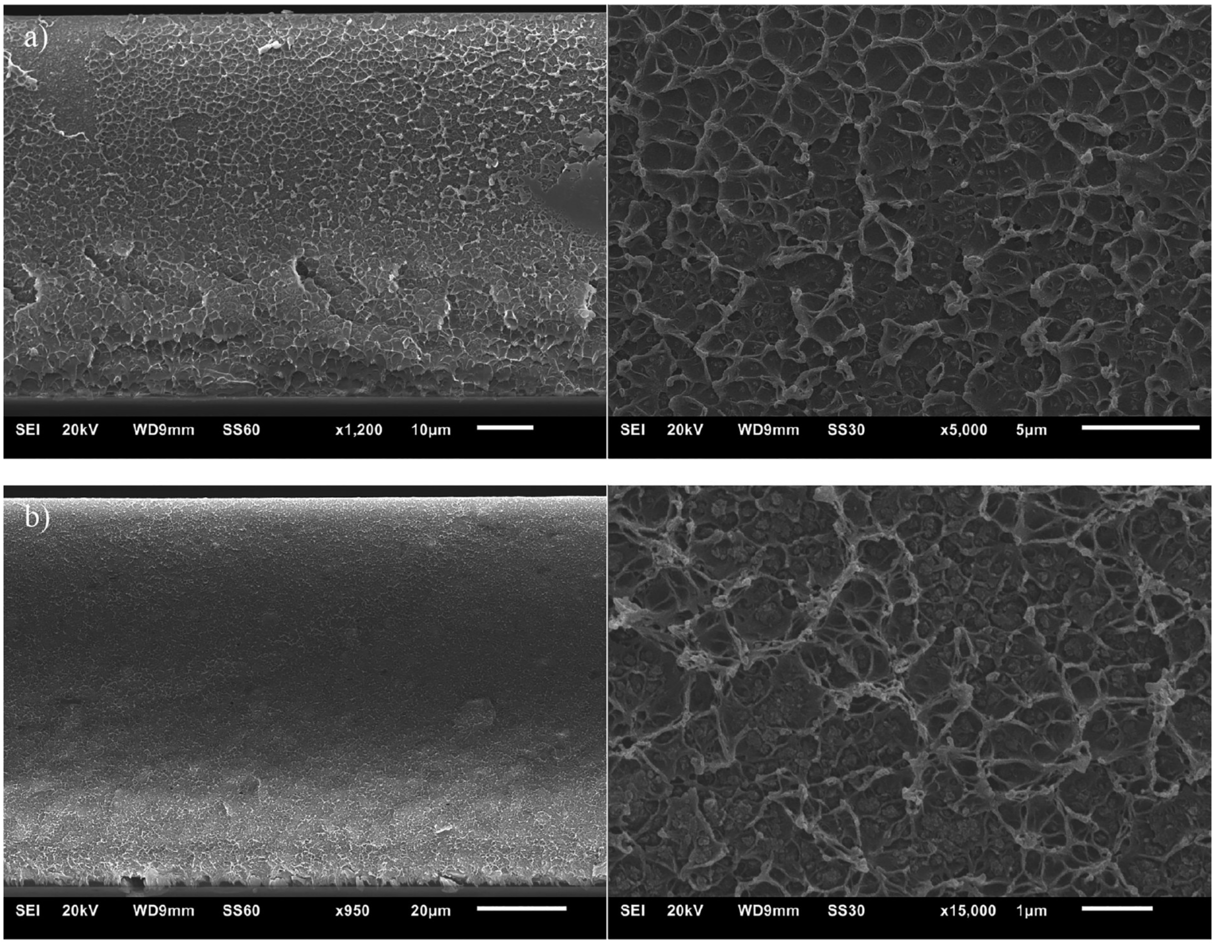

Figure 7. SEM images of cross-section of Matrimid with different loadings of Al-fum(DMSO) as filler a) 4 wt %, b) 24 wt %.

(Maxwell model) and experimental relative CO_2 permeabilities for MOF−Matrimid composite membranes with porous Al-fum and nonporous Al-fum(DMSO) fillers.

Relative experimental CO_2 permeabilities for Al-fum/Matrimid MMMs are in good agreement with the theoretical values from the Maxwell model for porous fillers ($P_d \gg P_c$). The reduction of the relative experimental CO_2 permeability for Al-fum(DMSO)/Matrimid MMMs is a good indicator for homogeneous dispersed filler particle and good interactions between polymer and MOF. Otherwise interparticular, non-selective voids should result in increased permeabilities and reduced selectivity.

Similarly, the relative CH_4 permeabilities were plotted against the filler volume in Figure S7. For CH_4 the experimental permeabilities also follow the theoretical prediction albeit with a slightly larger deviation than for CO_2.

Free Fractional Volume (FFV). In the literature, the (total) FFV was defined as the sum of the volume-weighted specific

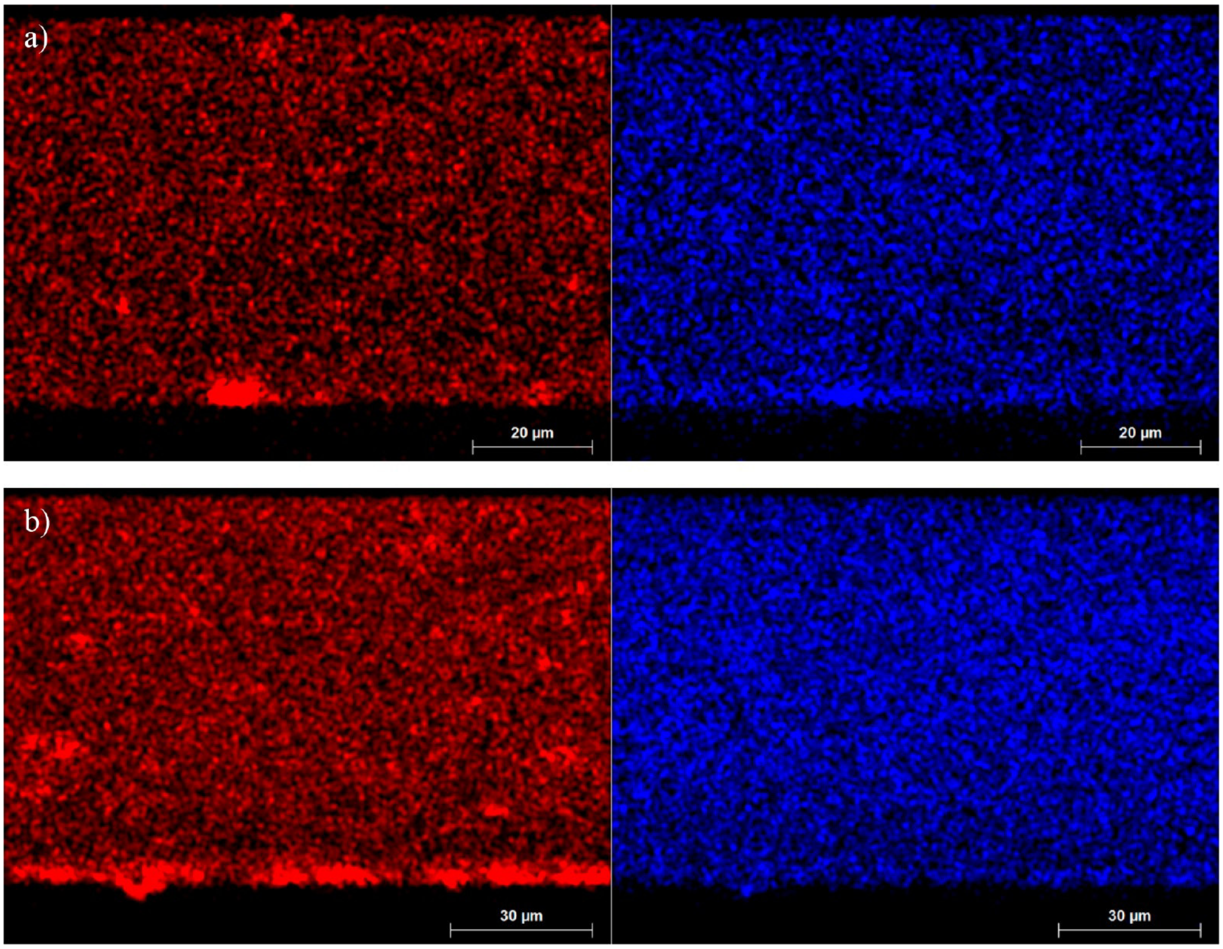

Figure 8. EDX-mapping of aluminum (red) and sulfur (blue) in MMM cross sections of a) 4 wt % Al-fum(DMSO) and b) 24 wt % Al-fum(DMSO). The molar Al:S quantification in Al-fum(DMSO) by EDX spectroscopy is given in Tables S3 and S4.

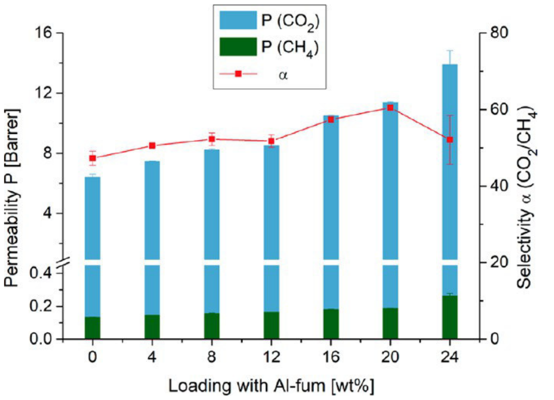

Figure 9. Performance of Al-fum/Matrimid MMMs with different Al-fum loadings in the separation of CO_2 and CH_4. The 24 wt % membrane was prepared and measured four times to ensure reproducibility and significance of the selectivity drop.

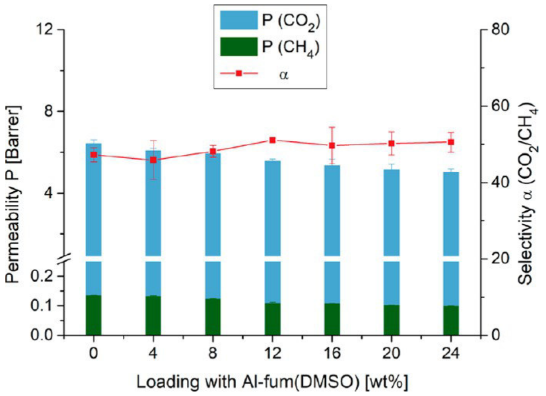

Figure 10. Performance of Al-fum(DMSO)/Matrimid MMMs with different Al-fum loadings in the separation of CO_2 and CH_4.

pore volumes (in cm^3/g) multiplied with the specific densities (in g/cm^3) of the materials (polymer, filler) in the MMM. Thereby, the FFV became a dimensionless entity (see Section S10 in the SI). Multiplication of pore volume with density was done to allow for comparison of the correlated permeability for different fillers.[21]

Here we want to elucidate the possible relative role of the FFV of the polymer, the MOF, and the void volume of the MOF−polymer interface. Therefore, we need to elucidate and compare actual specific free volumes (in units cm^3/g).

Thus, we define here a (total) specific free fractional volume sFFV as the sum of the volume-weighted (ϕ_c, ϕ_d) specific free volumes (sFV) of the polymer and the filler (eq 1). The sFV of the neat polymer Matrimid (density 1.167 g/cm^3) was reported to approximately 0.146 cm^3/g.[21,55] The sFV of the MOF is usually taken as equal to the total specific pore volume V_p determined by nitrogen sorption (Table S1).[21]

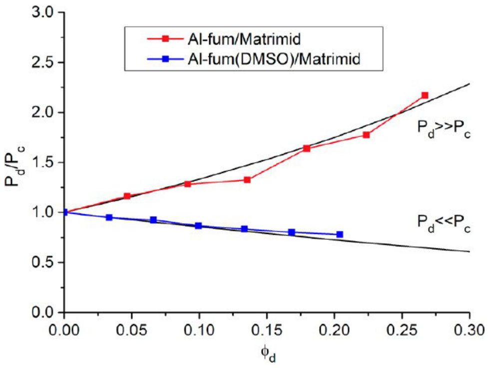

Figure 11. Relative experimental CO_2 permeabilities (referenced to the permeability P_c of the pure polymer membrane) for Al-fum/Matrimid (red curve) and Al-fum(DMSO)/MMMs (blue curve) with different filler volume fraction ϕ_d. The black lines give the relative theoretical CO_2 permeabilities for porous (filler permeability $P_d \gg P_c$) and nonporous ($P_d \ll P_c$) fillers. Note that for the same wt % of MOF the higher density of nonporous Al-fum(DMSO) leads to a lower filler volume fraction.

$$\text{(total) sFFV} = \text{sFV}_{\text{polymer}} \times \phi_c + \text{sFV}_{\text{MOF}} \times \phi_d \quad (1)$$

A listing of the sFFV values for the MMMs with different filler fractions is given in Table S7 and Table S8 in the SI. The sFFV ranges from 0.23 cm^3/g for a 24 wt % Al-fum/Matrimid MMM to 0.12 cm^3/g for a 24 wt % Al-fum(DMSO)/Matrimid MMM.

The FFV includes only the porosity in the polymer and filler and does not include any voids formed around the filler particles due to phase incompatibility. For the FFV the correlation with permeability P is given by the following:

$$P = A_p \times \exp^{(-B_p/\text{FFV})} \quad (2)$$

which is linearized to

$$\lg P = \lg A_p - \frac{B_p}{2.303\text{FFV}} \quad (3)$$

with A_p and B_p being gas- and temperature-dependent constants.[56]

Thus, if indeed the FFV determines the permeability a plot of lg P versus 1/FFV should give a straight line with slope $-B_p/2.303$ and intercept lg A_p.

A plot of lg P versus the inverse of the specific free fractional volume sFFV, is given in Figure 12 for the two gases CO_2 and CH_4 which were tested with the porous and nonporous Al-fum/Matrimid MMMs.

The plot of lg P versus 1/sFFV shows for both gases a very good linear correlation over the Al-fum and Al-fum(DMSO)/Matrimid MMMs. As the sFFV rises with decreasing nonporous Al-fum(DMSO) filler and increasing filler volume of porous Al-fum, the inverse sFFV decreases.

This illustrates that the sFFV is not only applicable for composite membranes with porous fillers, but is also usable for composite membranes with nonporous fillers. The values for A_p and B_p, calculated from the linear regression of the lg P versus 1/sFFV (1/FFV) plot (Figures 12 and S12), are presented in Table S9 (SI). Similar to previous studies the values for B_p are relatively similar for CO_2 and CH_4 for both FFV and sFFV. A_p values differ highly between CO_2 to CH_4 which is also in good agreement with the literature.[56,57] The difference in A_p, in unit Barrer, could be a result of the smaller kinetic diameter of CO_2 (3.3 Å) compared to CH_4 (3.8 Å) which leads to a faster motion within the free volume of the polymer lamellar and MOF. Furthermore, CO_2 is more likely to get adsorbed in the MOF and therefore may travel faster through the fractional free volume introduced by the MOF.

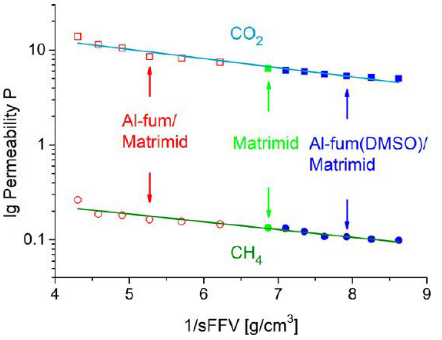

Figure 12. Combined experimental CO_2 and CH_4 permeabilities of porous and nonporous Al-fum and Al-fum(DMSO)/Matrimid MMMs as a function of the inverse (total) specific free fractional volume, sFFV. The neat polymer Matrimid has 1/sFFV = 6.9, the 24 wt % Al-fum/MMM 4.3, and the 24 wt % Alfum(DMSO)/MMM has 8.6. The straight lines are only intended as a guide to the eye.

Void Volume (VV). Besides the sFFV, which focuses on the free volume inside the polymer and the MOF, one can likewise determine the interface volume (void volume) between the polymer and the embedded MOF particles and its impact on the gas permeability. Takahashi and Paul showed that excess free volume between polymer and silica filler particles can lead to an increase in permeability, even for nonporous fillers due to poor interactions of the inorganic nanoparticles with the polymer phase and contrary to the Maxwell model. They obtained the excess void volume from a lower measured density than the theoretically determined one.[28,29] Further they described various possible morphologies of interparticular voids in composite membranes and acknowledged that the effect of the voids will be highly dependent on their distribution throughout the system.

In the literature, the void volume was derived from the difference between theoretical (D_{theo}) and measured density (D_{exp}) of the MMM according to ($[1 - D_{\text{exp}}/D_{\text{theo}}] \times 100\%$). Thereby, the void volume became a dimensionless entity.[23,29] As we want to elucidate the relative role of the FFV of the polymer, the MOF and the void volume of the MOF–polymer interface, we need to elucidate and compare actual specific free and void volumes (in units cm^3/g).

The possible specific void volume (sVV) between continuous and dispersed phase is determined according to eq 4:

$$\text{specific void volume, sVV} = \frac{1}{D_{\text{exp}}} - \frac{1}{D_{\text{theo}}} \quad (4)$$

The results for the specific void volume determination of Al-fum/Matrimid MMMs are depicted in Figure 13.

The deviation in theoretical and measured density is very small and mostly within the error bar. Thus, none of the MMMs show significant specific void volume formation. Overall there is no apparent trend for an increasing void volume formation with increasing filler volume observed. This is in contrast to the continuous rise of the permeability with increasing filler volume for the composite membranes. Hence,

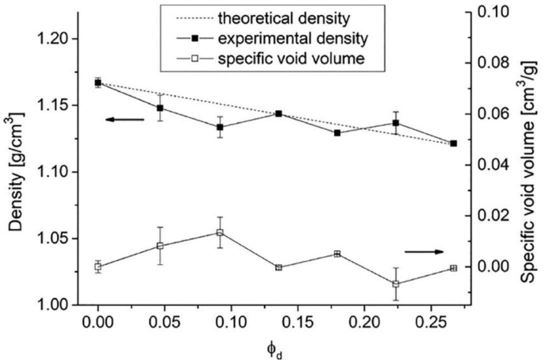

Figure 13. Specific void volume (eq 4) for Al-fum/Matrimid MMMs with different filler volumes. MMMs with 24 wt % MOF were no longer included in the presentation.

the void volume seems to have at most only a slight influence on the performance of the prepared MMMs.

Similar results for Al-fum(DMSO)/Matrimid MMMs are shown in Figure 14. The overall void volume is approximately the same as for the MMMs with the porous filler, but this time there might be a trend to higher specific void volume formation for MMMs with higher filler volumes. But since the CO_2 and CH_4 permeability for Al-fum(DMSO)/Matrimid MMMs decreases with higher MOF loadings (Table S6) there clearly is no correlation between void volume formation and separation performance in this case.

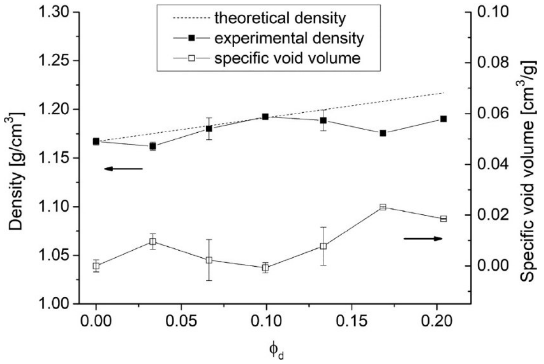

Figure 14. Specific void volume (eq 4) derived by the difference between theoretical and measured density for Al-fum(DMSO)/Matrimid MMMs with different filler volumes.

CONCLUSIONS

In this work porous, submicrometer sized Al-fum was synthesized according to the literature.[30] Nonporous Al-fum(DMSO) was obtained by heating Al-fum in DMSO and characterized with various methods. Both porous and nonporous aluminum fumarate fillers were embedded in a Matrimid matrix, thereby leading to the same polymer–filler interface. SEM images in combination with EDX-mapping revealed a mostly homogeneous filler distribution throughout all MMMs. CO_2/CH_4 separation performances showed reverse effects for porous and nonporous fillers. MMMs with the porous filler showed a continuous increase in CO_2 and CH_4 permeability while MMMs with the nonporous filler displayed a decrease in CO_2 and CH_4 permeability with rising filler content. These results are in good agreement with the Maxwell model, which predicts an increase in gas permeability for porous fillers and a decrease for nonporous fillers, respectively. The increase and decrease in gas permeability in general seems to be traceable to the difference in FFV, that is, the increased and decreased free volume of the polymer and filler. The interfacial void volume between filler and polymer contributes roughly only 10% to the available free volume in the MMM. This is most obvious regarding the gas permeation results of the MMMs with the nonporous filler compared to the measured void volume. Despite a constant to slightly growing void volume for higher nonporous filler loadings the gas permeabilities decrease. This clearly shows the negligible effect of an interfacial volume, both in absolute as in relative terms to the FFV. The organic/inorganic hybrid nature of the MOF filler certainly allowed for good compatibility with the polymer which is crucial to obtain defect free MMMs. As the free fractional volume, introduced by both the polymer and the MOF is decisive for the permeability both materials should be chosen accordingly. An increase in permeability requires high free volumes in both polymer and MOF. Thus, for MOFs a high pore volume is decisive for high permeable MMMs. In comparison to other porous fillers like zeolites MOFs should not only be advantageous because of their better compatibilities with organic polymers but also because of their higher pore volumes. Furthermore, a loss of linearity between FFV and permeability in MMMs would be a good indicator for an insufficient compatibility of the MOF and polymer which then probably results in void volume formation, with rise in permeability and partial loss of selectivity.

EXPERIMENTAL SECTION

Materials and Methods. All starting materials and solvents were obtained from commercial sources and used without further purification unless otherwise mentioned in the experimental description. Sodium aluminate (calculated as Al_2O_3 50−56%) was received from VWR chemicals, fumaric acid (99%) was obtained from TCI, dichloromethane (99%), *N*,*N*-dimethylformamide (99.99%) and dimethyl sulfoxide (99%) were purchased from Fisher Chemicals. Ethanol (99.99%) was obtained from Sigma-Aldrich. The polymer Matrimid 5218 was kindly supplied by Huntsman Advanced Materials.

Aluminum fumarate was synthesized according to the literature with the aim to obtain particles around 250 nm in size.[30] In a 100 mL round-bottom flask 0.45 g (5.49 mmol) of sodium aluminate and 0.9 g (7.76 mmol) of fumaric acid were dissolved in 50 mL of water and heated in a 90 °C preheated water bath for 30 min. After cooling down to room temperature the precipitate was collected by filtration and washed with water and ethanol for 1 day each. The collected product was dried at 150 °C in vacuum (50 mbar) overnight (yield 0.81 g, 94% based on sodium aluminate). The product was positively characterized as the MOF aluminum fumarate by powder X-ray diffraction, thermogravimetric analysis, and nitrogen sorption measurements as is detailed in the Results and Discussion.

Aluminum fumarate(DMSO) was synthesized by suspending 0.8 g aluminum fumarate in 100 mL dimethyl sulfoxide and then refluxed at 180 °C bath temperature overnight. The product was collected by filtration and dried at room temperature in vacuum (1×10^{-3} mbar) for 24 h. The pore filling and the amount of DMSO was determined by thermogravimetric analysis and elemental analysis as is detailed in the Results and Discussion.

Matrimid was dried at 80 °C for several days to remove the adsorbed moisture. All MMMs were prepared using a prime protocol to reduce agglomeration of the MOF particles and ensure a successful preparation. In the following the procedure for MMMs with 4 wt % MOF is described as an example of all prepared MMMs. The amount of 0.4 g of Matrimid was dissolved in 3.5 mL of dichloromethane and stirred for 24 h. At the same time 17 mg of the MOF was suspended

DOI: 10.1021/acsami.8b12938
ACS Appl. Mater. Interfaces 2018, 10, 33589−33600

in 4.5 mL of dichloromethane and also stirred for 24 h. Then the MOF suspension was ultrasonicated three times for 15 min with an amplitude of 20% at an ultrasonic liquid processor (VCX 750 Sonics, Microtip 630−0419) to homogenize the suspension. Between the ultrasonication steps, the suspension was stirred for 30 min. Afterward 0.16 mL of the polymer solution were added to the MOF suspension to receive an equal polymer/MOF mass ratio. After another 24 h of stirring and the same homogenization procedure, the remaining polymer was added to the MOF/polymer mixture and stirred further for 1 h. Afterward this mixture was casted into a metal ring, which was placed on a flat glass plate. To ensure slow evaporation of the solvent and to protect the membranes from dust the metal rings were immediately covered with inverted funnels. The membranes were left to dry for 3 h at room temperature and then taken off the glass plate by immersing in water and afterward dried at 150 °C overnight in the vacuum oven (50 mbar). The MMMs with 8, 12, 16, 20, 24 wt % MOF were prepared in the same way with 35 mg, 54.5 mg, 76 mg, 100 mg, and 126.5 mg MOF, respectively. The added polymer solution was adapted as follows: 0.33 mL, 0.52 mL, 0.72 mL, 0.95 mL, and 1.20 mL, respectively.

Powder X-ray diffraction (PXRD) patterns were obtained on a Bruker D2 Phaser powder diffractometer equipped with a flat silicon, low background sample holder using Cu−K_α radiation ($\lambda = 1.5418$ Å, 30 kV, 10 Ma, ambient temperature). With this sample holder at $2\theta <$ ~10° the beam spot is strongly broadened so that only a fraction of the reflected radiation reaches the detector; hence lower relative intensities are measured in this range. All samples were measured with a scan speed of 2s/step and a step size of 0.028° (2θ). Simulated patterns of aluminum fumarate were calculated with CCDC Mercury 3.9 program using the single crystal data of Basolite A520 obtained by Rietveld refinement (CCDC no. 1051975, Refcode DOYBEA).[37] The Bruker D2 Phaser had been calibrated with an LaB_6 NIST standard sample of known crystallite size (0.8 μm) for calculating the Al-fum crystallite size with the Scherrer equation (eq 5). The full width at half-maximum ($\Delta(2\theta)$) of the reflexes depends inversely on the crystallite size (L), which results in broadened reflexes for small crystallite sizes as seen in Figure 1.

$$\Delta(2\theta) = \frac{K \times \lambda}{L \times \cos(\theta_0)} \qquad (5)$$

SEM images were recorded with a Jeol JSM-6510LV QSEM Advanced electron microscope with a LAB-6 cathode at 20 keV. The microscope was equipped with a Bruker Xflash 410 silicon drift detector and the Bruker ESPRIT software for EDX analysis. The membrane cross sections were prepared through freeze-fracturing after immersion in liquid nitrogen and then coated with gold by a Jeol JFC 1200 fine-coater at an approximate current of 20 mA for 20−30 s.

Thermogravimetric analysis (TGA) were carried out with a Netzsch TG 209 F3 Tarsus in the range of 25 °C to 600 °C with a heating rate of 2 K min^{-1} under oxygen atmosphere.

Infrared (IR) spectra were obtained with a Bruker FT-IR Tensor 37 as attenuated total reflection. The scanning frequency range was 4000−500 cm^{-1}.

Nitrogen sorption measurements at 77 K were carried out on a Quantachrome NOVA 4000e gas sorption analyzer and evaluated with the AsiQwin V3 software. For activation the sample was degassed in a vacuum of 5×10^{-2} mbar at 150 °C for 3 h. The Brunauer−Emmett−Teller (BET) surface areas were calculated in the p/p_0-range of 0.01−0.05. Total pore volumes were calculated from nitrogen adsorptions isotherms at $p/p_0 = 0.4$. Micropore analysis was done with DeBoer thickness method via V-t-Plot method in the pressure range of p/p_0 0.25−0.5 of the adsorption isotherm. Adsorption isotherms for aluminum fumarate with CO_2 and CH_4 were recorded on a Micromeritics ASAP 2020 gas sorption analyzer equipped with oil-free vacuum pumps and valves, which guaranteed contamination free measurements. CO_2 and CH_4 isotherms were measured at 0 °C (ice/deionized water bath). All gases were of ultrapure grades (99.999%) supplied by Air Liquide Germany and used as-received.

Binary gas separation experiments were performed with a continuous flow permeation system (OSMO inspector, provided by Convergence Industry B.V., 7532 SM Enschede, The Netherlands) with helium as sweep gas and an Agilent 490 μGC gas chromatograph to measure the gas concentration in the permeate. The membranes were cut in a round sheet, placed in the permeation module (4.5 cm diameter) and covered by a rubber mask to provide an effective inner diameter of 3.6 cm with an area of 11.3 cm^2. All permeation experiments were conducted at 25 °C and with 3 bar transmembrane pressure. The feed gases were mixed in a 50/50 volume flow mixture of CO_2 and CH_4 by two Bronkhorst Coriolis-flow controllers as well as the helium gas stream with a total upstream flow of 160 mL min^{-1}. The downstream is swept with helium at a rate of 1 mL min^{-1} at ambient pressure. The gas concentration in the permeate stream was measured with an Agilent 490 μ gas chromatograph with thermal conductivity detector and a Pora PLOT Q column every 30 min until steady state (up to 8 h). Each membrane sample was produced twice to ensure reproducibility. Permeability of the membranes was calculated according to the following equation:

$$P_A = \frac{x_{1A} \times S_{Fl} \times d}{x_{He}^{p} \times A \times (p_2 \times x_{2A} - p_1 \times x_{1A})} \qquad (6)$$

where P_A is the permeability of the gas A in Barrer (1 Barrer = $10^{-10}\cdot$ $\text{cm}^3(\text{STP})\text{cm}/(\text{cm}^2\cdot\text{s}\cdot\text{cmHg})$), x_{1A} the molar fraction of the gas A, S_{Fl} the flow of the sweep gas in $\text{cm}^3\ \text{s}^{-1}$, d the thickness of the membrane, x_{He}^{p} the molar fraction of the sweep gas in the permeate, A the membrane area in cm^2, x_{2A} the molar fraction of the gas A in the feed and p_1, and p_2 the permeate and feed pressure in cmHg, respectively. The error bars in the permselectivity diagrams mark the range of values obtained from the independent measurement of two membranes.

Density (ρ) of the membranes was determined by measuring their volume and mass (eq 8). The membranes were measured 3 times on an analytical balance (d = 0.1 mg) to receive the mean mass. The volume (V) was derived with the formula of a cylindric body (eq 7). Both diameter ($2r$) and thickness (h) were measured at 10 different sites to receive an average diameter and thickness.

$$V = \pi \times r^2 \times h \qquad (7)$$

$$\rho = \frac{\text{mass}}{\text{volume}} \qquad (8)$$

Equations for the gas transport in polymeric membranes and the Maxwell model are given Section S12 in the SI.

■ ASSOCIATED CONTENT

S Supporting Information

The Supporting Information is available free of charge on the ACS Publications website at DOI: 10.1021/acsami.8b12938.

> Structure description of aluminum fumarate, SEM images of aluminum fumarate and aluminum fumarate-(DMSO); additional N_2 sorption isotherms of micrometer sized aluminum fumarate particles; IR spectra and elemental analysis of both compounds; Al:S quantification of various MMMs by EDX spectroscopy; CO_2 and CH_4 sorption of aluminum fumarate; gas separation performances of all MMMs; relative experimental CH_4 permeabilities compared to the Maxwell model; additional theoretical and experimental properties of all MMMs regarding the FFV, sFFV, and void volume; and equations for the gas transport in polymeric membranes and the Maxwell model (PDF)

AUTHOR INFORMATION

Corresponding Author

*Tel.: +49 211 81 12286. Fax: +49 211 81 12287. E-mail: janiak@hhu.de (C.J.).

ORCID

Christoph Janiak: 0000-0002-6288-9605

Notes

The authors declare no competing financial interest.

ACKNOWLEDGMENTS

The authors acknowledge the financial support of the Federal German Ministry of Education and Research (BMBF) in the project Optimat under grant no. 03SF0492C. We thank Mrs. Alexa Schmitz and Mr. Moritz Steinert for the thermogravimetric analyses.

ABBREVIATIONS

Al-fum = aluminum fumarate
DMSO = dimethyl sulfoxide
FVV = free fractional volume
fum = fumarate
MMM = mixed-matrix membrane
MOF = metal−organic framework
VV = void volume

REFERENCES

(1) Bernardo, P.; Drioli, E.; Golemme, G. Membrane Gas Seperation: A review/State of the Art. *Ind. Eng. Chem. Res.* **2009**, *48*, 4638−4663.

(2) Moulijn, J. A.; Makkee, M.; van Diepen, A. *Chemical Process Technology*; John Wiley & Sons: Chichester, England, 2001.

(3) Tobin, J.; Shambaugh, P.; Mastrangelo, E. *Energy Information Administration, Office of Oil and Gas*, January 2006. http://www.dnr.louisiana.gov/assets/docs/oilgas/naturalgas/ngprocess_20060131.pdf (assessed July 30, 2018).

(4) Davis, J. C.; Valus, R. J.; Eshraghi, R.; Velikoff, A. E. Facilitated Transport Membrane Hybrid Systems for Olefin Purification. *Sep. Sci. Technol.* **1993**, *28*, 463−476.

(5) Koros, W. J.; Mahajan, R. J. Pushing the limits on possibilities for large-scale gas separation: which strategies? *J. Membr. Sci.* **2000**, *175*, 181−196.

(6) Coronas, J.; Santamaría, J. Separations Using Zeolite Membranes. *Sep. Purif. Methods* **1999**, *28*, 127−177.

(7) Baker, R. W. Future Directions of Membrane Gas Separation Technology. *Ind. Eng. Chem. Res.* **2002**, *41*, 1393−1411.

(8) Koros, W. J.; Fleming, G. K. Membran-based gas separation. *J. Membr. Sci.* **1993**, *83*, 1−80.

(9) Robeson, L. M. Correlation of separation factor versus permeability for polymeric membranes. *J. Membr. Sci.* **1991**, *62*, 165−185.

(10) Robeson, L. M. The upper bound revisited. *J. Membr. Sci.* **2008**, *320*, 390−400.

(11) Zimmerman, C. M.; Singh, A.; Koros, W. J. Tailoring mixed matrix composite membranes for gas separations. *J. Membr. Sci.* **1997**, *137*, 145−154.

(12) Tanh Jeazet, H. B.; Staudt, C.; Janiak, C. Metal-organic frameworks in mixed-matrix membranes for gas separation. *Dalton Trans* **2012**, *41*, 14003−14027.

(13) Zornoza, B.; Martinez-Joaristi, A.; Serra-Crespo, P.; Tellez, C.; Coronas, J.; Gascon, J.; Kapteijn, F. Functionalized flexible MOFs as fillers in mixed matrix membranes for highly selective separation of CO_2 from CH4 at elevated pressures. *Chem. Commun.* **2011**, *47*, 9522−9524.

(14) Merkel, T. C.; Freeman, B. D.; Spontak, R. J.; He, Z.; Pinnau, I.; Meakin, P.; Hill, A. J. Ultrapermeable, reverse-selective nanocomposite membranes. *Science* **2002**, *296*, 519−522.

(15) Caro, J.; Noack, M. Zeolite membranes − Recent developments and progress. *Microporous Mesoporous Mater.* **2008**, *115*, 215−233.

(16) Zornoza, B.; Tellez, C.; Coronas, J.; Gascon, J.; Kapteijn, F. Metal organic framework based mixed matrix membranes: An increasingly important field of research with a large application potential. *Microporous Mesoporous Mater.* **2013**, *166*, 67−78.

(17) Kosinov, N.; Gascon, J.; Kapteijn, F.; Hensen, E. J. M. Recent developments in zeolite membranes for gas separation. *J. Membr. Sci.* **2016**, *499*, 65−79.

(18) Sorribas, S.; Zornoza, B.; Téllez, C.; Coronas, J. Mixed matrix membranes comprising silica-(ZIF-8) core−shell spheres with ordered meso−microporosity for natural- and bio-gas upgrading. *J. Membr. Sci.* **2014**, *452*, 184−192.

(19) Furukawa, H.; Cordova, K. E.; O'Keeffe, M.; Yaghi, O. M. The chemistry and applications of metal-organic frameworks. *Science* **2013**, *341*, 1230444.

(20) Dechnik, J.; Sumby, C. J.; Janiak, C. Enhancing Mixed-Matrix Membrane Performance with Metal−Organic Framework Additives. *Cryst. Growth Des.* **2017**, *17*, 4467−4488.

(21) Kanehashi, S.; Chen, G. Q.; Scholes, C. A.; Ozcelik, B.; Hua, C.; Ciddor, L.; Southon, P. D.; D'Alessandro, D. M.; Kentish, S. E. Enhancing gas permeability in mixed matrix membranes through tuning the nanoparticle properties. *J. Membr. Sci.* **2015**, *482*, 49−55.

(22) Dong, G.; Li, H.; Chen, V. Challenges and opportunities for mixed-matrix membranes for gas separation. *J. Mater. Chem. A* **2013**, *1*, 4610−4630.

(23) Takahashi, S.; Paul, D. R. Gas permeation in poly(ether imide) nanocomposite membranes based on surface-treated silica. Part 1: Without chemical coupling to matrix. *Polymer* **2006**, *47*, 7519−7534.

(24) Zhang, Y.; Feng, X.; Yuan, S.; Zhou, J.; Wang, B. Challenges and recent advances in MOF−polymer composite membranes for gas separation. *Inorg. Chem. Front.* **2016**, *3*, 896−909.

(25) Basu, S.; Cano-Odena, A.; Vankelecom, I. F. J. MOF-containing mixed-matrix membranes for CO_2/CH_4 and CO_2/N_2 binary gas mixture separations. *Sep. Purif. Technol.* **2011**, *81*, 31−40.

(26) Ahmadpour, E.; Sarfaraz, M. V.; Behbahani, R. M.; Shamsabadi, A. A.; Aghajani, M. Fabrication of mixed matrix membranes containing TiO2 nanoparticles in Pebax 1657 as a copolymer on an ultra-porous PVC support. *J. Nat. Gas Sci. Eng.* **2016**, *35*, 33−41.

(27) Sadeghi, M.; Semsarzadeh, M. A.; Barikani, M.; Pourafshari Chenar, M. Gas separation properties of polyether-based polyurethane−silica nanocomposite membranes. *J. Membr. Sci.* **2011**, *376*, 188−195.

(28) Ahn, J.; Chung, W.-J.; Pinnau, I.; Guiver, M. D. Polysulfone/silica nanoparticle mixed-matrix membranes for gas separation. *J. Membr. Sci.* **2008**, *314*, 123−133.

(29) Takahashi, S.; Paul, D. R. Gas permeation in poly(ether imide) nanocomposite membranes based on surface-treated silica. Part 2: With chemical coupling to matrix. *Polymer* **2006**, *47*, 7535−7547.

(30) Zhou, L.; Zhang, X.; Chen, Y. Facile synthesis of Al-fumarate metal−organic framework nano-flakes and their highly selective adsorption of volatile organic compounds. *Mater. Lett.* **2017**, *197*, 224−227.

(31) Dechnik, J.; Nuhnen, A.; Janiak, C. Mixed-Matrix Membranes of the Air-Stable MOF-5 Analogue [Co4(μ4-O)(Me2pzba)3] with a Mixed-Functional Pyrazolate-Carboxylate Linker for CO_2/CH_4 Separation. *Cryst. Growth Des.* **2017**, *17*, 4090−4099.

(32) Sabetghadam, A.; Seoane, B.; Keskin, D.; Duim, N.; Rodenas, T.; Shahid, S.; Sorribas, S.; Le Guillouzer, C.; Clet, G.; Tellez, C.; Daturi, M.; Coronas, J.; Kapteijn, F.; Gascon, J. Metal Organic Framework Crystals in Mixed-Matrix Membranes: Impact of the Filler Morphology on the Gas Separation Performance. *Adv. Funct. Mater.* **2016**, *26*, 3154−3163.

(33) Thoma, R.; Kärger, J.; de Sousa Amadeu, N.; Niessing, S.; Janiak, C. Assessing Guest-Molecule Diffusion in Heterogeneous Powder Samples of Metal-Organic Frameworks through Pulsed-Field-

Gradient (PFG) NMR Spectroscopy. *Chem. - Eur. J.* **2017**, *23*, 13000−13005.

(34) Glomb, S.; Woschko, D.; Makhloufi, G.; Janiak, C. Metal-Organic Frameworks with Internal Urea-Functionalized Dicarboxylate Linkers for SO_2 and NH_3 Adsorption. *ACS Appl. Mater. Interfaces* **2017**, *9*, 37419−37434.

(35) Loiseau, T.; Serre, C.; Huguenard, C.; Fink, G.; Taulelle, F.; Henry, M.; Bataille, T.; Ferey, G. A rationale for the large breathing of the porous aluminum terephthalate (MIL-53) upon hydration. *Chem. - Eur. J.* **2004**, *10*, 1373−1382.

(36) Gaab, M.; Trukhan, N.; Maurer, S.; Gummaraju, R.; Müller, U. The progression of Al-based metal-organic frameworks − From academic research to industrial production and applications. *Microporous Mesoporous Mater.* **2012**, *157*, 131−136.

(37) Alvarez, E.; Guillou, N.; Martineau, C.; Bueken, B.; Van de Voorde, B.; Le Guillouzer, C.; Fabry, P.; Nouar, F.; Taulelle, F.; de Vos, D.; Chang, J. S.; Cho, K. H.; Ramsahye, N.; Devic, T.; Daturi, M.; Maurin, G.; Serre, C. The structure of the aluminum fumarate metal-organic framework A520. *Angew. Chem., Int. Ed.* **2015**, *54*, 3664−3668.

(38) Thommes, M.; Kaneko, K.; Neimark, A. V.; Olivier, J. P.; Rodriguez-Reinoso, F.; Rouquerol, J.; Sing, K. S. W. Physisorption of gases, with special reference to the evaluation of surface area and pore size distribution (IUPAC Technical Report). *Pure Appl. Chem.* **2015**, *87*, 1051−1069.

(39) Jiang, D.; Burrows, A. D.; Edler, K. J. Size-controlled synthesis of MIL-101(Cr) nanoparticles with enhanced selectivity for CO_2 over N_2. *CrystEngComm* **2011**, *13*, 6916−6919.

(40) Zamidi Ahmad, M.; Navarro, M.; Lhotka, M.; Zornoza, B.; Téllez, C.; Fila, V.; Coronas, J. Enhancement of CO 2 /CH 4 separation performances of 6FDA-based co-polyimides mixed matrix membranes embedded with UiO-66 nanoparticles. *Sep. Purif. Technol.* **2018**, *192*, 465−474.

(41) Yang, S.; Sun, J.; Ramirez-Cuesta, A. J.; Callear, S. K.; David, W. I.; Anderson, D. P.; Newby, R.; Blake, A. J.; Parker, J. E.; Tang, C. C.; Schroder, M. Selectivity and direct visualization of carbon dioxide and sulfur dioxide in a decorated porous host. *Nat. Chem.* **2012**, *4*, 887−894.

(42) Jacques, N. M.; Rought, P. R. E.; Fritsch, D.; Savage, M.; Godfrey, H. G. W.; Li, L.; Mitra, T.; Frogley, M. D.; Cinque, G.; Yang, S.; Schroder, M. Locating the binding domains in a highly selective mixed matrix membrane via synchrotron IR microspectroscopy. *Chem. Commun.* **2018**, *54*, 2866−2869.

(43) Rubio-Martinez, M.; Leong, T.; Juliano, P.; Hadley, T. D.; Batten, M. P.; Polyzos, A.; Lim, K.-S.; Hill, M. R. Scalable simultaneous activation and separation of metal−organic frameworks. *RSC Adv.* **2016**, *6*, 5523−5527.

(44) Bux, H.; Liang, F.; Li, Y.; Cravillon, J.; Wiebcke, M.; Caro, J. Zeolitic Imidazolate Framework Membrane with Molecular Sieving Properties by Microwave-Assisted Solvothermal Synthesis. *J. Am. Chem. Soc.* **2009**, *131*, 16000−16001.

(45) Guo, H.; Zhu, G.; Hewitt, I. J.; Qiu, S. Twin Copper Source Growth of Metal-Organic Framework Membrane: $Cu_3(BTC)_2$ with High Permeability and Selectivity for Recycling H_2. *J. Am. Chem. Soc.* **2009**, *131*, 1646−1647.

(46) Hwang, S.; Chi, W. S.; Lee, S. J.; Im, S. H.; Kim, J. H.; Kim, J. Hollow ZIF-8 nanoparticles improve the permeability of mixed matrix membranes for CO2/CH4 gas separation. *J. Membr. Sci.* **2015**, *480*, 11−19.

(47) Venna, S. R.; Lartey, M.; Li, T.; Spore, A.; Kumar, S.; Nulwala, H. B.; Luebke, D. R.; Rosi, N. L.; Albenze, E. Fabrication of MMMs with improved gas separation properties using externally-functionalized MOF particles. *J. Mater. Chem. A* **2015**, *3*, 5014−5022.

(48) Ordoñez, M. J. C.; Balkus, K. J.; Ferraris, J. P.; Musselman, I. H. Molecular sieving realized with ZIF-8/Matrimid® mixed-matrix membranes. *J. Membr. Sci.* **2010**, *361*, 28−37.

(49) Zhang, Y.; Musselman, I. H.; Ferraris, J. P.; Balkus, K. J. Gas permeability properties of Matrimid® membranes containing the metal-organic framework Cu−BPY−HFS. *J. Membr. Sci.* **2008**, *313*, 170−181.

(50) Etxeberria-Benavides, M.; David, O.; Johnson, T.; Łozińska, M. M.; Orsi, A.; Wright, P. A.; Mastel, S.; Hillenbrand, R.; Kapteijn, F.; Gascon, J. High performance mixed matrix membranes (MMMs) composed of ZIF-94 filler and 6FDA-DAM polymer. *J. Membr. Sci.* **2018**, *550*, 198−207.

(51) Shen, Y.; Lua, A. C. Theoretical and experimental studies on the gas transport properties of mixed matrix membranes based on polyvinylidene fluoride. *AIChE J.* **2013**, *59*, 4715−4726.

(52) Rafiq, S.; Maulud, A.; Man, Z.; Mutalib, M. I. A.; Ahmad, F.; Khan, A. U.; Khan, A. L.; Ghauri, M.; Muhammad, N. Modelling in mixed matrix membranes for gas separation. *Can. J. Chem. Eng.* **2015**, *93*, 88−95.

(53) Sadeghi, Z.; Omidkhah, M.; Masoumi, M. E.; Abedini, R. Modification of existing permeation models of mixed matrix membranes filled with porous particles for gas separation. *Can. J. Chem. Eng.* **2016**, *94*, 547−555.

(54) Jeazet, H. B.; Koschine, T.; Staudt, C.; Raetzke, K.; Janiak, C. Correlation of Gas Permeability in a Metal-Organic Framework MIL-101(Cr)-Polysulfone Mixed-Matrix Membrane with Free Volume Measurements by Positron Annihilation Lifetime Spectroscopy (PALS). *Membranes (Basel, Switz.)* **2013**, *3*, 331−353.

(55) Huang, Y.; Wang, X.; Paul, D. Physical aging of thin glassy polymer films: Free volume interpretation. *J. Membr. Sci.* **2006**, *277*, 219−229.

(56) Kanehashi, S.; Nagai, K. Analysis of dual-mode model parameters for gas sorption in glassy polymers. *J. Membr. Sci.* **2005**, *253*, 117−138.

(57) Park, J. Y.; Paul, D. R. Correlation and prediction of gas permeability in glassy polymer membrane materials via a modified free volume based group contribution method. *J. Membr. Sci.* **1997**, *125*, 23−39.

Supporting Information for

On the role of filler porosity and filler/polymer interface volume in metal-organic framework/polymer mixed-matrix membranes for gas separation

*Alexander Nuhnen, Dennis Dietrich, Simon Millan, Christoph Janiak**

Institut für Anorganische Chemie und Strukturchemie, Heinrich-Heine-Universität, Universitätsstr. 1, D-40225 Düsseldorf, Germany.

Email: alexander.nuhnen@uni-duesseldorf.de, dennis.dietrich@uni-duesseldorf.de, simon.millan@uni-duesseldorf.de, janiak@uni-duesseldorf.de

Content

1. Aluminum fumarate (Al-fum)

Aluminum fumarate (Al-fum) was first described in the patent literature, there it was named by BASF SE as Basolite™ A520.[1,2] Figure S1 shows the structural features of aluminum fumarate with respect to bonding situations and cavities.

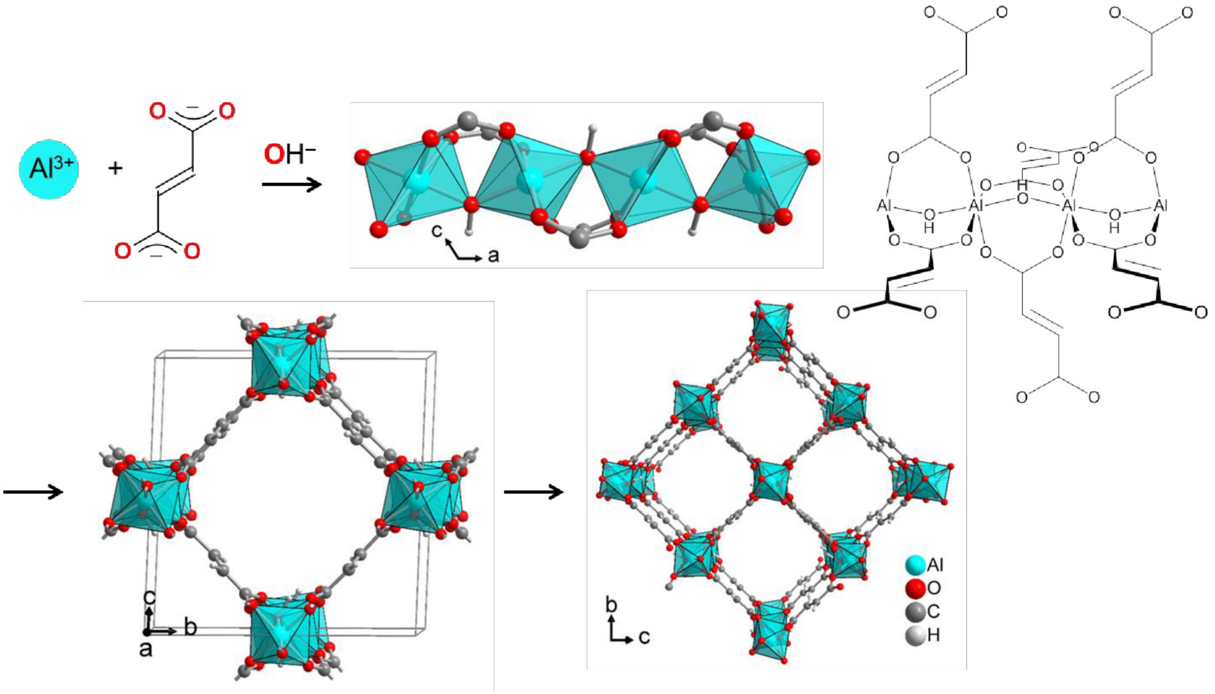

Figure S1. Al-fum resembles the monoclinic MIL-53(Al) structure (i.e. with benzene-1,4-dicarboxylate as linker) with infinite Al-OH-Al chains connected by fumarate linkers. It has the chemical formula [Al(OH)(O2C-CH=CH-CO2)]n and displays microporous, rhombohedral channels with circa 5.7 x 6.0 Å2 free dimensions.[3] The illustration was taken from ref. [4] Graphic produced by software Diamond from cif-file for Basolite A520 (CSD-Refcode DOYBEA, CCDC no. 1051975).[5]

2. SEM images of Al-fum and Al-fum(DMSO)

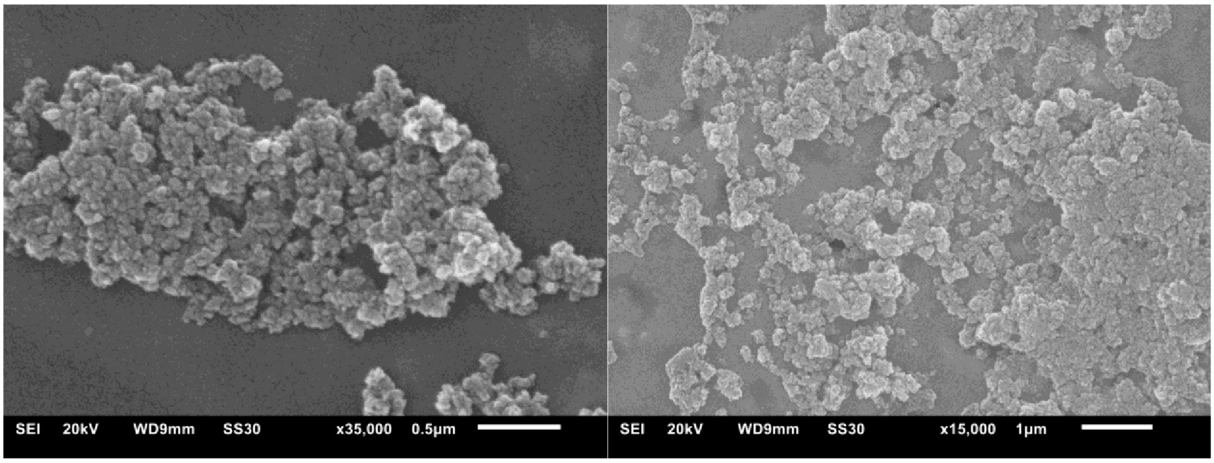

Figure S2. SEM images of Al-fum (left) and Al-fum(DMSO) (right).

3 N_2 sorption data of various Al-fum synthesis

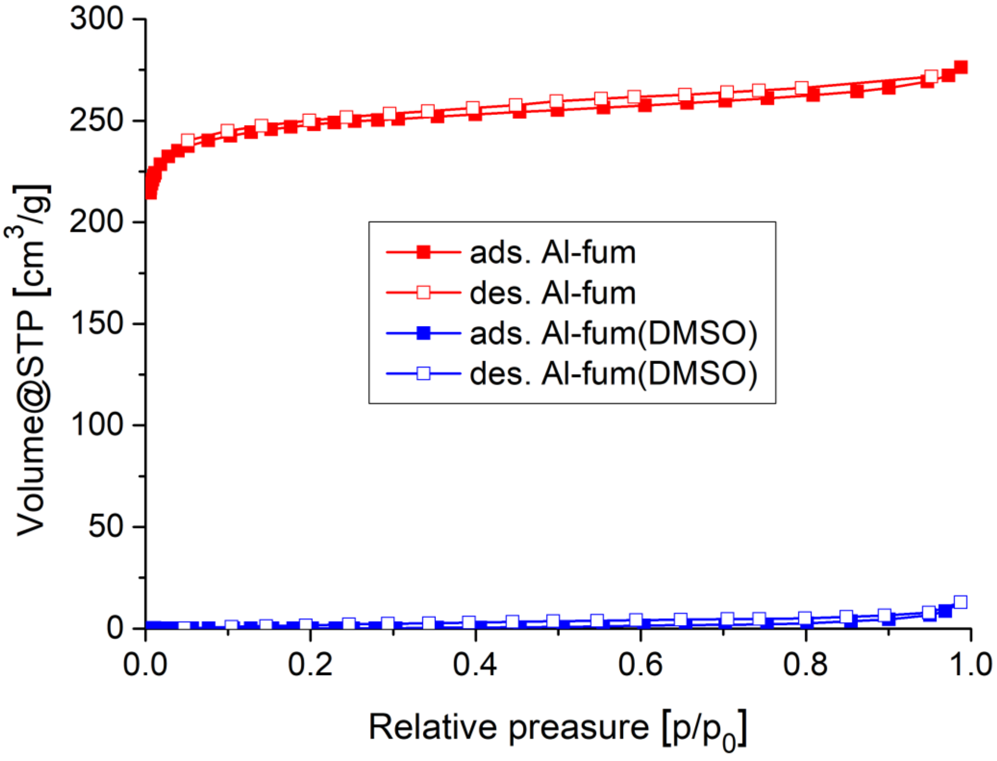

Figure S3. Nitrogen adsorption isotherm of micrometer sized Al-fum (red) and Al-fum(DMSO) (blue) at 77 K.

Table S1. Comparison of surface areas and pore volumes for various Al-fum synthesis.

reference	MBET [m^2g^{-1}]	total pore volume [cm^3g^{-1}]	micropore volume [cm^3g^{-1}]
this work	1100	0.47 [a]	0.37
4	1021	n.a.	0.48
6	1156	n.a.	n.a.
7	925	0.65 [b]	n.a.
8	1080	n.a.	n.a.
9	971	0.85 [c]	0.38

[a] calculated at $p/p_0 = 0.4$; [b] calculated at $p/p_0 = 0.98$; [c] calculated at $p/p_0 = 0.99$. At $p/p_0 > 0.4$ nitrogen uptake starts in the interparticle volume (compare Figure 2 and Figure S3 in SI) which then leads to an overestimation of the micro- and mesopore volume inside the framework.

4. IR spectra of Al-fum and Al-fum(DMSO) and DMSO

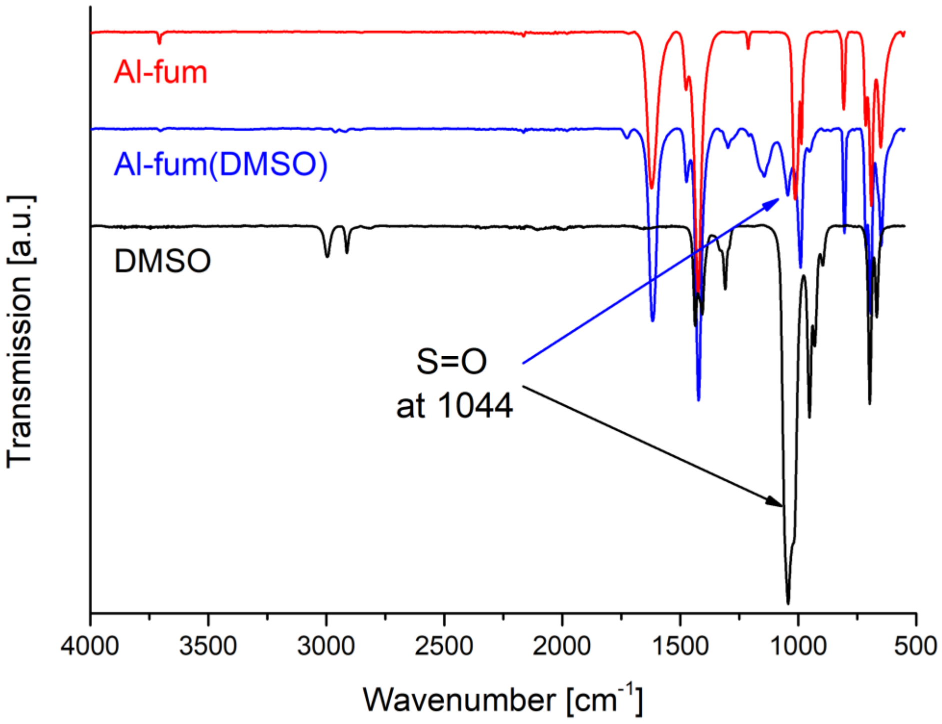

Figure S4. IR spectra of Al-fum (red) Al-fum(DMSO) (blue) and pure DMSO (black).

5. Elemental analysis for Al-fum and Al-fum(DMSO)

Table S2. Elemental analysis of Al-fum and Al-fum(DMSO)

Aluminum fumarate			Aluminum fumarate(DMSO)		
element	calc.	exp.	element	calc.[a]	exp.
% C	30.40	29.42	% C	30.50	30.47
% H	1.91	2.32	% H	3.56	4.26
% N	–	–	% N	–	–
% S	–	–	% S	11.63	11.43

[a] calculated for a 0.8 : 1 ratio DMSO : MOF

6. Molar Al:S quantification of various wt % of Al-fum(DMSO)/Matrimid MMMs by EDX spectroscopy

Table S3. Molar Al:S quantification in Al-fum(DMSO)/Matrimid MMMs before gas separation experiments by EDX spectroscopy.

	norm. At. %		molar ratio	
MMM	S	Al	S	Al
4 wt %	0.27	0.33	0.82	1.00
16 wt %	0.85	1.09	0.78	1.00
24 wt %	1.56	1.92	0.81	1.00

Table S4. Molar Al:S quantification in Al-fum(DMSO)/Matrimid MMMs after gas separation experiments by EDX spectroscopy.

	norm. At. %		molar ratio	
MMM	S	Al	S	Al
4 wt %	0.24	0.30	0.80	1.00
16 wt %	1.12	1.38	0.82	1.00
24 wt %	1.31	1.72	0.76	1.00

7. Gas selectivity from CO_2 and CH_4 sorption isotherms of Al-fum

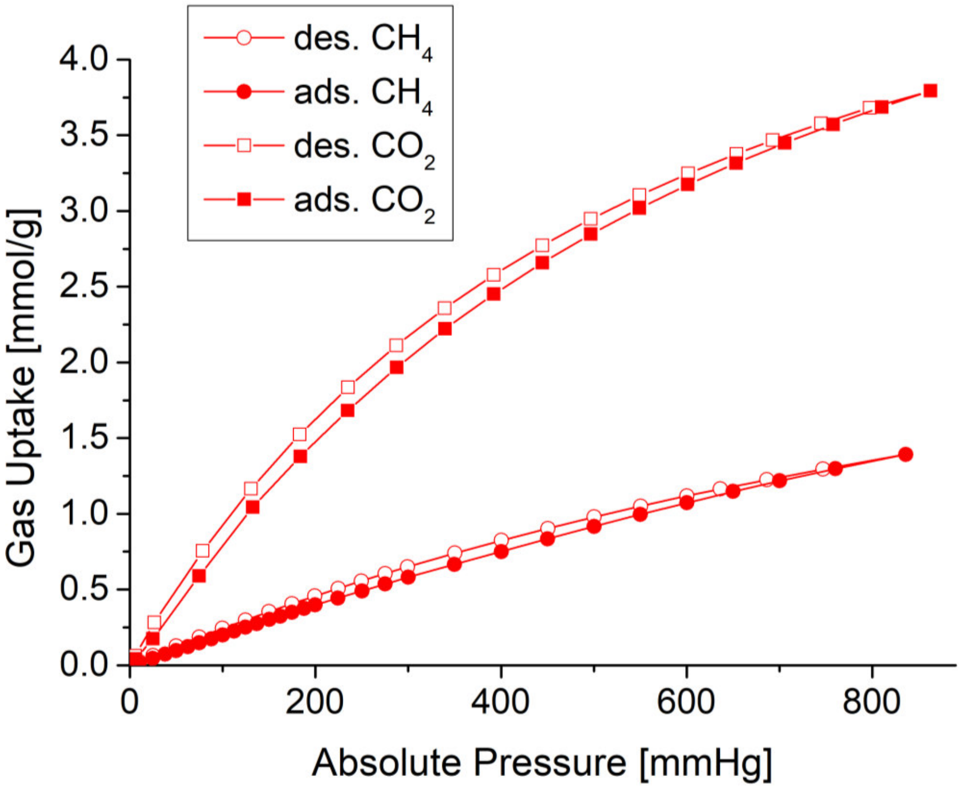

Figure S5. CO_2 and CH_4 sorption isotherms of Al-fum at 273 K.

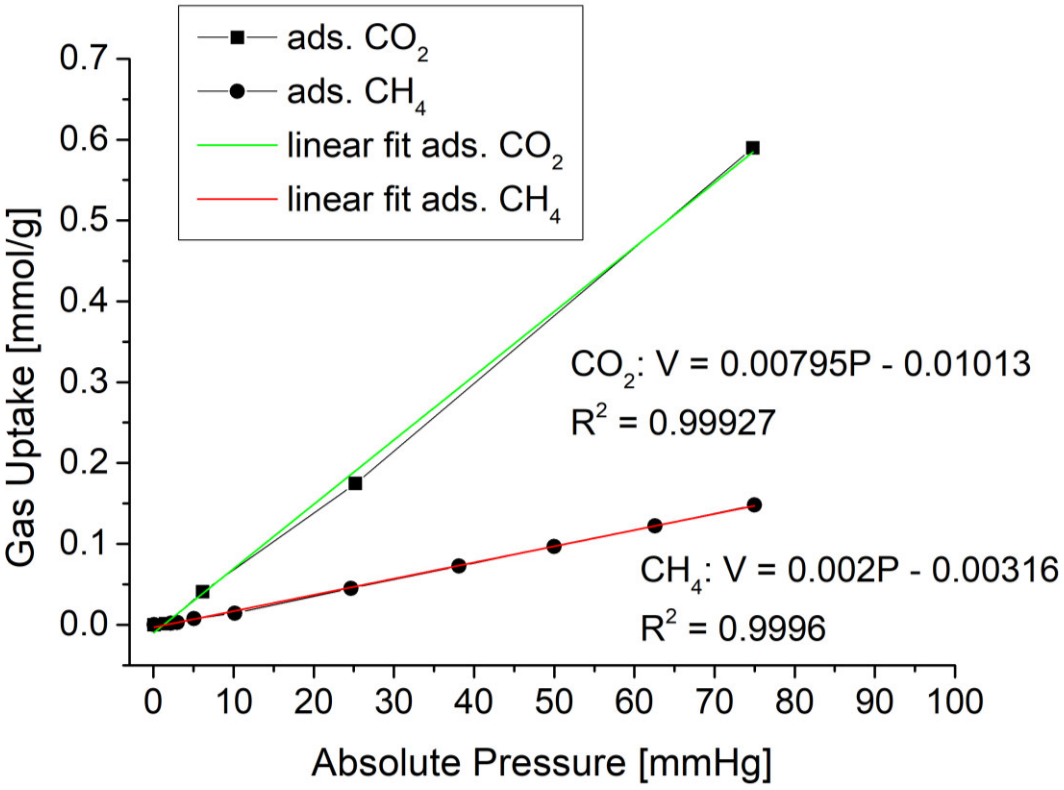

Figure S6. Initial slope in the Henry region of the adsorption isotherms of CO_2 and CH_4 of Al-fum.

8. Gas separation performance of Al-fum/Matrimid MMMs and Al-fum(DMSO)/Matrimid MMMs

Table S5. Summary of mixed gas separation performances of Al-fum/Matrimid MMMs for CO_2 and CH_4.

membrane				
MOF-loading [wt %]	membrane thickness [µm]	P (CO_2) [Barrer]	P (CH_4) [Barrer]	α (CO_2/CH_4)
0	58 – 60	6.4 ± 0.1	0.14 ± 0.00	47.3 ± 1.8
4	53 – 63	7.5 ± 0.0	0.15 ± 0.00	50.6 ± 0.2
8	64 – 67	8.2 ± 0.1	0.16 ± 0.00	52.2 ± 1.7
12	69 – 70	8.5 ± 0.2	0.16 ± 0.00	51.8 ± 1.6
16	67 – 74	10.5 ± 0.0	0.18 ± 0.00	57.4 ± 0.7
20	74 – 76	11.4 ± 0.1	0.19 ± 0.00	60.5 ± 0.6
24	73 – 75	13.9 ± 0.9	0.26 ± 0.01	52.1 ± 6.3

Table S6. Summary of mixed gas separation performances of Al-fum(DMSO)/Matrimid MMMs for CO_2 and CH_4.

membrane				
MOF-loading [wt %]	membrane thickness [µm]	P (CO_2) [Barrer]	P (CH_4) [Barrer]	α (CO_2/CH_4)
0	58 – 60	6.4 ± 0.1	0.14 ± 0.00	47.3 ± 1.8
4	62 – 66	6.1 ± 0.1	0.13 ± 0.00	45.9 ± 5.1
8	67 – 68	5.9 ± 0.1	0.12 ± 0.00	48.2 ± 1.6
12	62 – 63	5.5 ± 0.1	0.13 ± 0,00	42.2 ± 1.5
16	67– 71	5.4 ± 0.3	0.11 ± 0.00	49.7 ± 4.8
20	70 – 75	5.1 ± 0.3	0.10 ± 0.00	50.3 ± 3.1
24	68 – 77	5.0 ± 0.2	0.10 ± 0.00	50.6 ± 2.6

9. Relative experimental CH_4 permeabilities compared to the Maxwell model

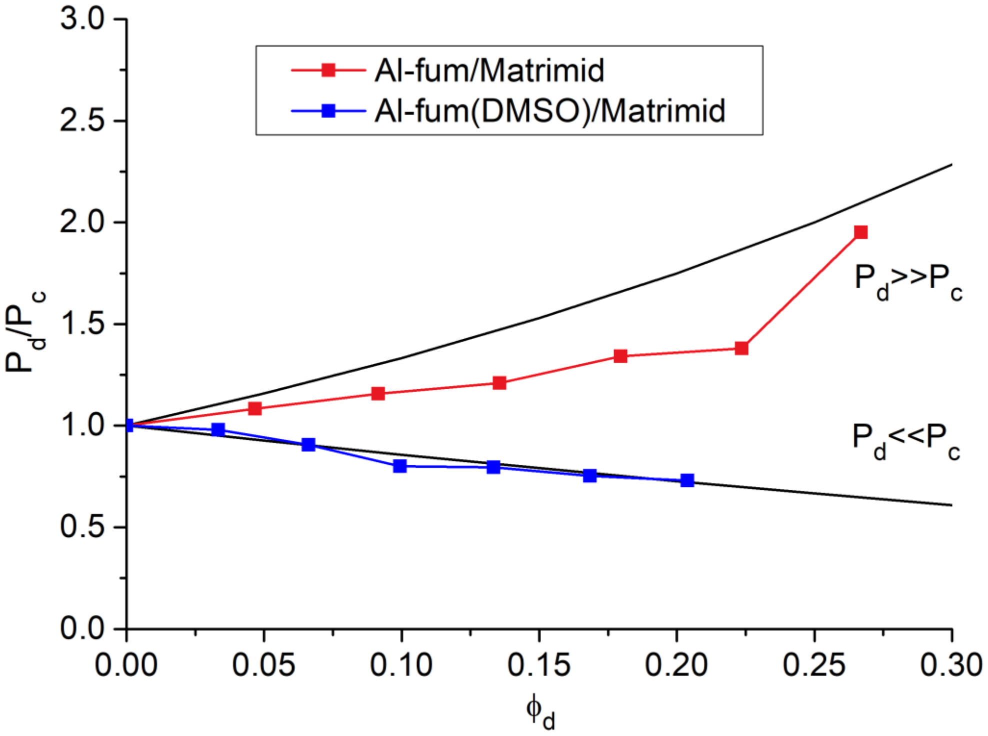

Figure S7. Relative experimental CH_4 permeabilities (referenced to the permeability P_c of the pure polymer membrane) for Al-fum/Matrimid (red curve) and Al-fum(DMSO)/MMMs (blue curve) with different filler volume fraction ϕ_d. The black lines give the relative theoretical CH_4 permeabilities for porous (filler permeability $P_d >> P_c$) and nonporous ($P_d << P_c$) fillers. Note that for the same wt % of MOF the higher density of nonporous Al-fum(DMSO) leads to a lower filler volume fraction.

10. FFV and sFFV

The (total) FFV of a composite membrane according to the literature was obtained by equation (S1). The (total) FFV was defined as the sum of the products of the volume-weighted specific pore volumes (in cm^3/g) and the specific densities (in g/cm^3) of the materials (polymer, filler) which were combined. Thereby, the FFV became a dimensionless entity. Multiplication of pore volume with density was done to allow comparison of the correlated permeability for different filler.

$$(Total)\ FFV = FFV_{polymer} \cdot \phi_c + FFV_{filler} \cdot \phi_d \tag{S1}$$

The FFV of the neat polymer Matrimid was reported to approximately 0.17. The FFV for Al-fum was 0.47 based on its density of 0.993 g/cm^3 and its pore volume of 0.47 cm^3/g (Table 1).

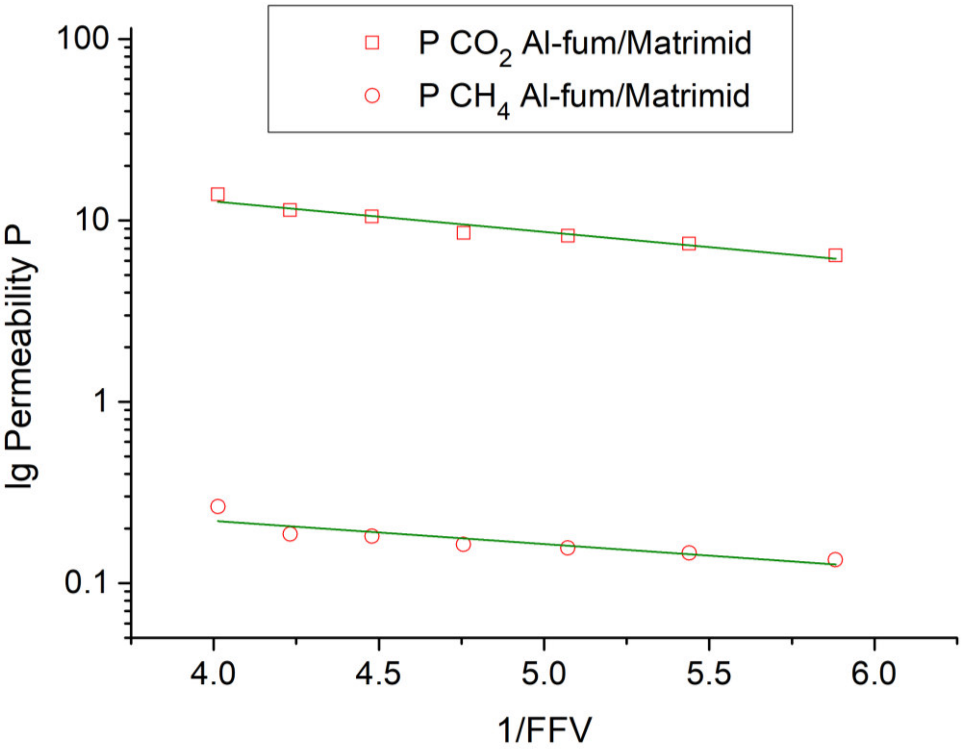

Figure S8. Experimental CO_2 and CH_4 permeabilities of Al-fum/Matrimid MMMs as a function of the inverse total FFV with the FFV calculated according to **eq. S1**. The neat polymer has 1/FFV = 5.9 the 4 wt % MMM corresponds to 1/FFV = 5.4, the 24 wt % MMM 4.0. The straight lines are only intended as a guide to the eye.

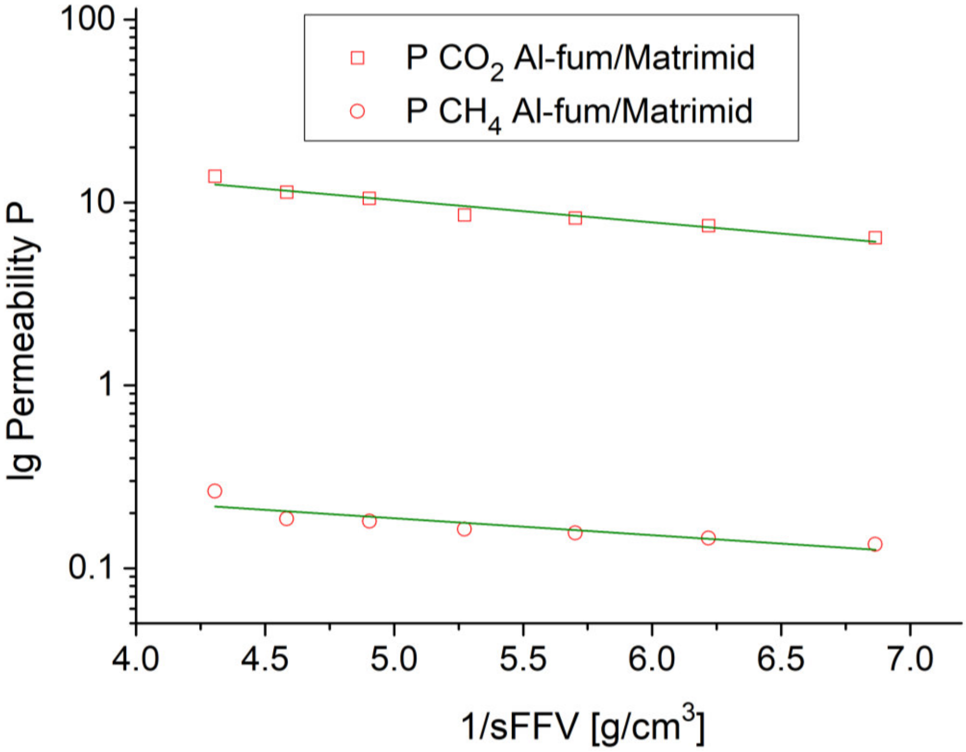

Figure S9. Experimental CO_2 and CH_4 permeabilities of Al-fum/Matrimid MMMs as a function of the inverse total specific FFV (sFFV) calculated according to **eq. 1**. The neat polymer has 1/sFFV = 6.9, the 4 wt % MMM corresponds to 1/sFFV = 6.2, the 24 wt % MMM 4.3. The straight lines are only intended as a guide to the eye.

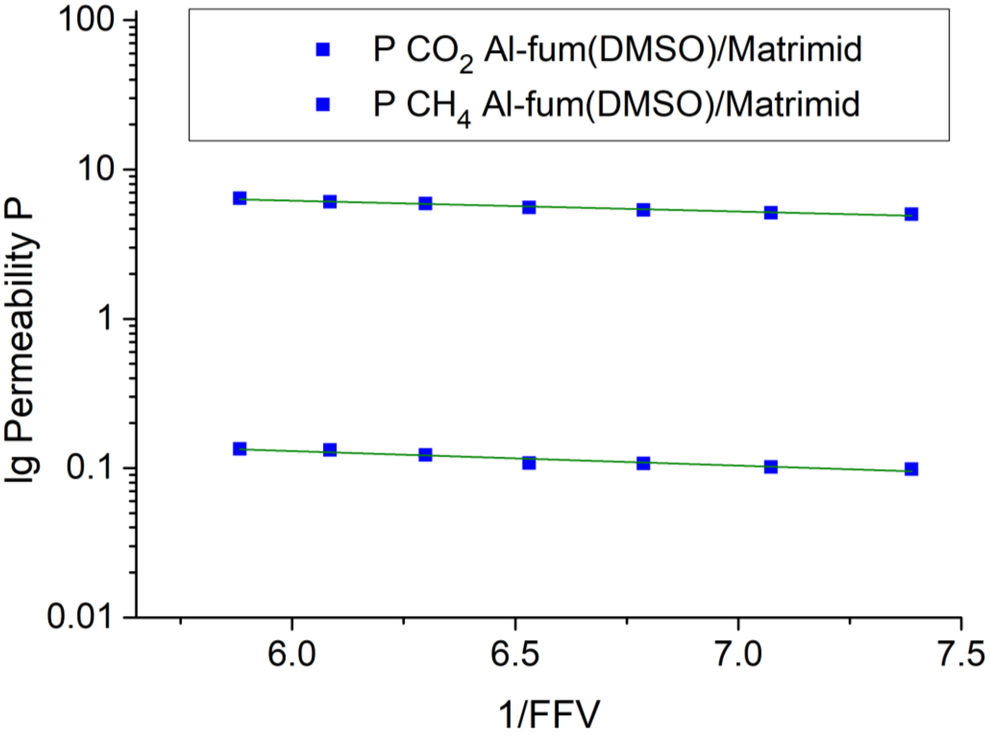

Figure S10. Experimental CO_2 and CH_4 permeabilities of Al-fum(DMSO)/Matrimid MMMs as a function of the inverse total FFV calculated according to **eq. S1**.The neat polymer has 1/FFV = 5.9, the 4 wt % MMM corresponds to 1/FFV = 6.1, the 24 wt % MMM 7.4. The straight lines are only intended as a guide to the eye.

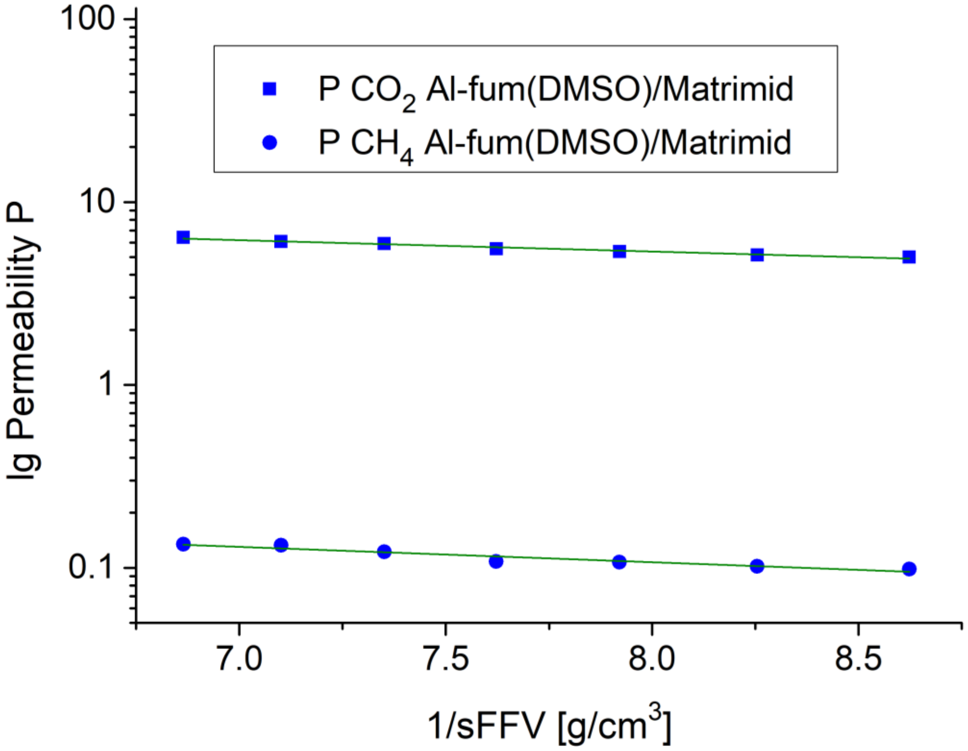

Figure S11. Experimental CO_2 and CH_4 permeabilities of Al-fum(DMSO)/Matrimid MMMs as a function of the inverse total specific FFV (sFFV) calculated according to **eq. 1**. The neat polymer has 1/sFFV = 6.9, the 4 wt % MMM corresponds to 1/sFFV = 7.1, the 24 wt % MMM 8.6. The straight lines are only intended as a guide to the eye.

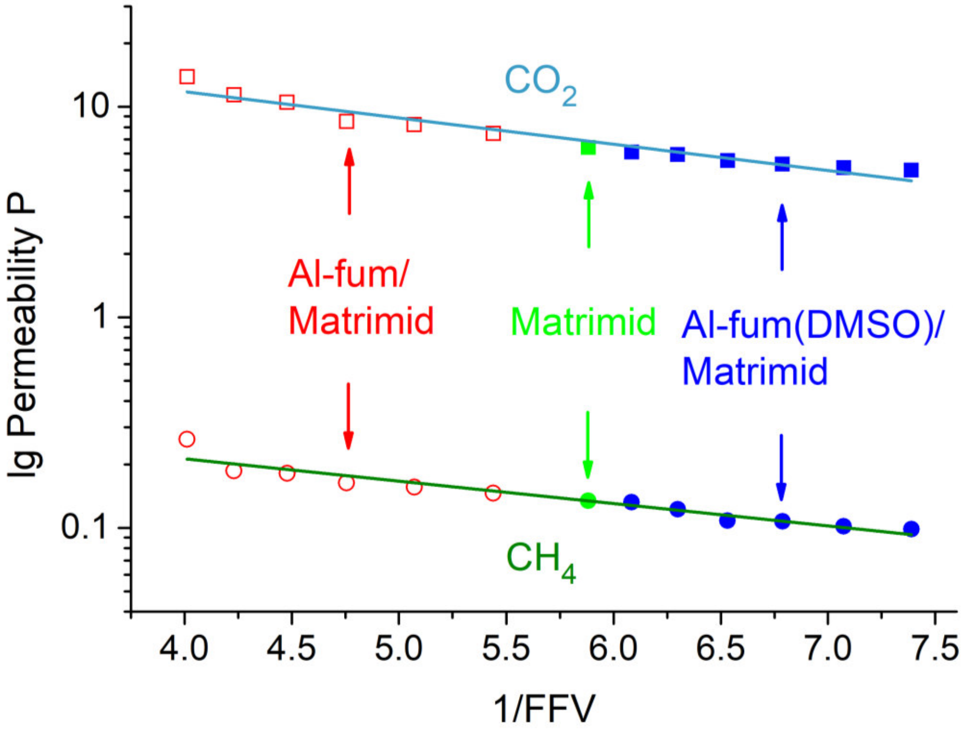

Figure S12. Combined experimental CO_2 and CH_4 permeabilities of porous and nonporous Al-fum and Al-fum(DMSO)/Matrimid MMMs as a function of the inverse (total) free fractional volume, FFV calculated according to **eq. S1**. The neat polymer Matrimid has 1/FFV = 5.9, the 24 wt % Al-fum/MMM 4.0, the 24wt % Alfum(DMSO)/MMM has 7.4. The straight lines are only intended as a guide to the eye.

Table S7. Matrimid and Al-fum contribution to the sFFV in Al-fum/Matrimid MMMs

ϕ_c	ϕ_d	$sFV_{polymer} \times \phi_c$ [cm³/g][a]	$sFV_{MOF} \times \phi_d$ [cm³/g][b]	total sFFV [cm³/g]
1.00	0.00	0.146	0.000	0.146
0.95	0.05	0.139	0.022	0.161
0.91	0.09	0.132	0.043	0.175
0.86	0.14	0.126	0.064	0.190
0.82	0.18	0.120	0.084	0.204
0.78	0.22	0.113	0.105	0.218
0.73	0.27	0.107	0.125	0.232

[a] $sFV_{polymer} = 0.146$ cm³/g; [b] $sFV_{MOF} = V_p = 0.47$ cm³/g.

Table S8. Matrimid and Al-fum(DMSO) contribution to the sFFV in Al-fum(DMSO)/Matrimid MMMs

ϕ_c	ϕ_d	$sFV_{polymer} \times \phi_c$ [cm³/g][a]	$sFV_{MOF} \times \phi_d$ [cm³/g][b]	total sFFV [cm³/g]
1.00	0.00	0.146	0.000	0.146
0.97	0.03	0.141	0.000	0.141
0.93	0.07	0.136	0.000	0.136
0.90	0.10	0.131	0.000	0.131
0.87	0.13	0.126	0.000	0.126
0.83	0.17	0.121	0.000	0.121
0.80	0.20	0.116	0.000	0.116

[a] $sFV_{polymer} = 0.146$ cm³/g; [b] $sFV_{MOF} = V_p = 0.0$ cm³/g.

Table S9. Comparison of A_p and B_p values.[a]

Gas	A_p [Barrer]	B_p	linear correlation coefficient (r^2)	reference
CO_2 FFV [b]	3.73×10^1	0.054	0.940	this work
CO_2 sFVV [b]	3.15×10^1	0.043	0.950	this work
CO_2 [c]	1.75×10^3	0.860	-	10
CO_2 [c]	2.41×10^5	1.62	0.802	11
CH_4 FFV [b]	0.567	0.046	0.919	this work
CH_4 sFFV [b]	0.489	0.037	0.920	this work
CH_4 [c]	1.14×10^2	0.967	-	10
CH_4 [c]	2.85×10^3	1.43	0.720	11

[a] Derived by linear regression from lg *P* versus 1/sFFV (1/FFV) plot and compared with other literature values. [b] At 25 °C, 4 bar feed pressure, 3 bar pressure difference. [c] At 35 °C, 10 atm feed pressure for glassy polymers.

11. Void volume

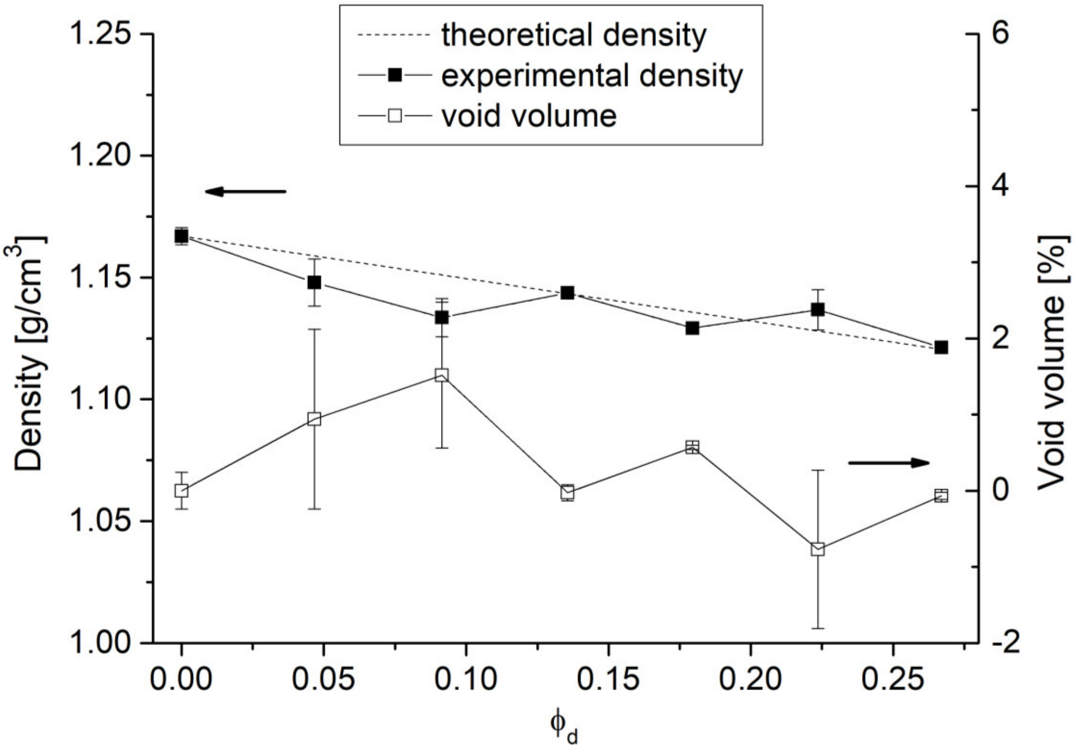

Figure S13. Void volume ([1 – D_{exp}/D_{theo}]×100%) for Al-fum/Matrimid MMMs with different filler volumes.

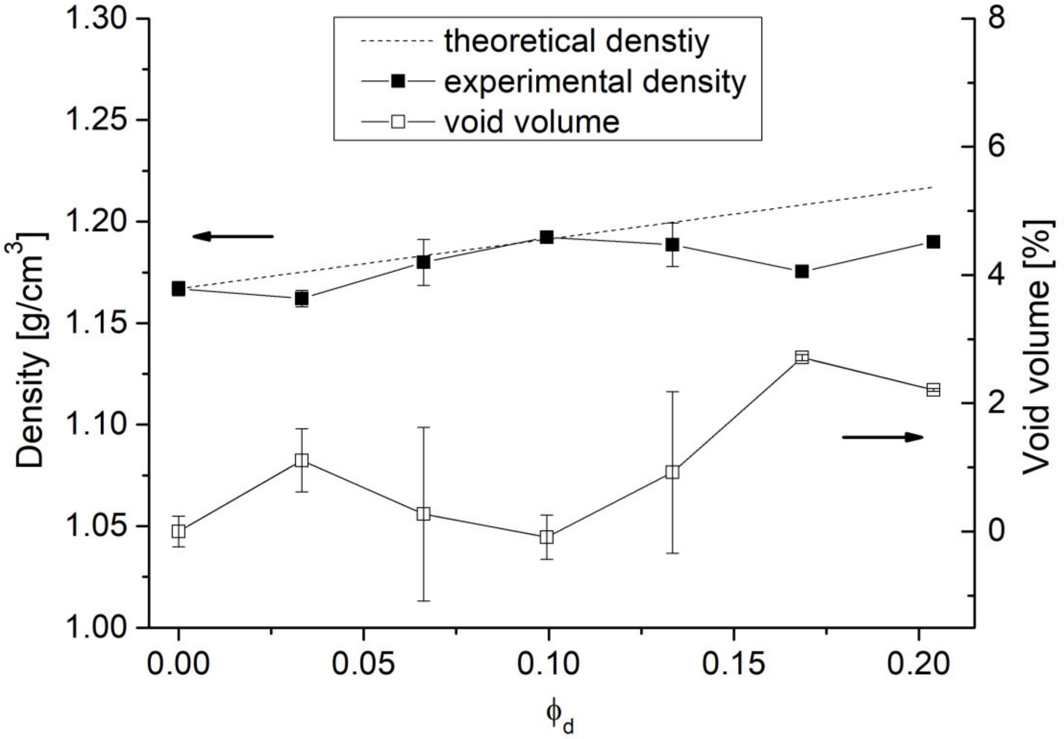

Figure S14. Void volume ([1 – D_{exp}/D_{theo}]×100%) for Al-fum(DMSO)/Matrimid MMMs with different filler volumes.

12. Equations for the gas transport in polymeric membranes and the Maxwell model

Gas transport in polymeric membranes. Gas transport in dense membranes follows the solution diffusion mechanism. Hence the gas transport can be described as follows:

$$P_i = D_i \cdot S_i \tag{S2}$$

Where P_i is the gas permeability, D_i and S_i are the diffusion and solubility coefficients of the component i.

The ideal selectivity of two gases is defined over the ratio of the permeability of the more permeable (i) compound to the permeability of the less permeable (j) compound and can be obtained by single-gas permeation measurements:

$$\alpha_{i,j}^{ideal} = \frac{P_i}{P_j} = \frac{D_i \cdot S_i}{D_j \cdot S_j} \tag{S3}$$

The ideal selectivity can differ from the real selectivity due to interaction between the gases themselves or between the gas and the dense membrane.

In experiments with binary gas mixtures the real selectivity can also be calculated from the ratio of the mole fractions w of the components i and j in the permeate (p) and the feed (f) stream:

$$\alpha_{i,j}^{real} = \frac{w_i^p / w_j^p}{w_i^f / w_j^f} \tag{S4}$$

Maxwell model. The Maxwell model was originally developed to describe electrical conductivity of particulate composites but can also be used for gas permeation through a dense composite membrane.[12]

For spherical particles the permeability of the composite membrane P_{eff} can be estimated as follows:

$$P_{eff} = P_c \frac{P_d \cdot (1 + 2\phi_d) + P_c \cdot (2 - 2\phi_d)}{P_d \cdot (1 - \phi_d) + P_c \cdot (2 + \phi_d)} \tag{S5}$$

where P_c is the continuous phase permeability, P_d is the dispersed phase permeability and ϕ_d is the volume fraction of the filler.

The volume fraction of the filler in the dispersed phase can be calculated as follows:

$$\phi_d = \frac{w_d/\rho_d}{\left(\frac{w_c}{\rho_c}\right) + \left(\frac{w_d}{\rho_d}\right)} \tag{S6}$$

where w_d and w_c are the weight percentages, ρ_d and ρ_c the densities of the filler and the polymer, respectively.

Equation (S5) can be simplified in such cases where the filler shows a distinctly higher ($P_d \gg P_c$) or lower ($P_d \ll P_c$) permeability in comparison to the continuous phase:

$$P_d \gg P_c; \frac{P_{eff}}{P_c} = \frac{(1 + 2\phi_d)}{(1 - \phi_d)} \tag{S7}$$

$$P_d \ll P_c; \frac{P_{eff}}{P_c} = \frac{(2 - 2\phi_d)}{(2 + \phi_d)} \tag{S8}$$

A general assumption within the Maxwell model is that the gas flow around the filler particles is not affected by the presence of the filler. Thus it is clear that this model is only reliable for low filler loadings up to a volume fraction of around 0.2 for the filler (ϕ_d).[12,13] Additionally the Maxwell model does not account for agglomeration of the particles and therefore demands an ideal filler distribution across the whole membrane without any microdefects.

---

[1] Leung, E.; Müller, U.; Trukhan, N.; Mattenheimer, H.; Cox, G.; Blei, S. *Process for preparing porous metal-organic frameworks based on aluminum fumarate*, U.S. Patent No. 8,524,932, BASF SE, 3 Sep. **2013**.

[2] Kiener, C.; Müller, U.; Schubert, M. *Method of using a metal organic frameworks based on aluminum fumarate*, U.S. Patent No. 8,518,264, BASF SE, 27 Aug. **2013**.

[3] Loiseau, T.; Serre, C.; Huguenard, C.; Fink, G.; Taulelle, F.; Henry, M.; Bataille, T.; Ferey, G., A rationale for the large breathing of the porous aluminum terephthalate (MIL-53) upon hydration. *Chem. Eur. J.* **2004**, *10*, 1373-1382.

[4] Jeremias, F.; Fröhlich, D.; Janiak, C.; Henninger, S. K., Advancement of sorption-based heat transformation by a metal coating of highly-stable, hydrophilic aluminum fumarate MOF. *RSC Advances* **2014**, *4*, 24073-24082.

[5] Alvarez, E.; Guillou, N.; Martineau, C.; Bueken, B.; Van de Voorde, B.; Le Guillouzer, C.; Fabry, P.; Nouar, F.; Taulelle, F.; de Vos, D.; Chang, J. S.; Cho, K. H.; Ramsahye, N.; Devic, T.; Daturi, M.; Maurin, G.; Serre, C., The structure of the aluminum fumarate metal-organic framework A520. *Angew. Chem. Int. Ed.* **2015**, *54*, 3664-3668.

[6] Karmakar, S.; Dechnik, J.; Janiak, C.; De, S., Aluminium fumarate metal-organic framework: A super adsorbent for fluoride from water. *J. Hazard. Mater.* **2016**, *303*, 10-20.

[7] Zhou, L.; Zhang, X.; Chen, Y., Facile synthesis of Al-fumarate metal–organic framework nano-flakes and their highly selective adsorption of volatile organic compounds. *Mater. Lett.* **2017**, *197*, 224-227.

[8] Alvarez, E.; Guillou, N.; Martineau, C.; Bueken, B.; Van de Voorde, B.; Le Guillouzer, C.; Fabry, P.; Nouar, F.; Taulelle, F.; de Vos, D.; Chang, J. S.; Cho, K. H.; Ramsahye, N.; Devic, T.; Daturi, M.; Maurin, G.; Serre, C., The structure of the aluminum fumarate metal-organic framework A520. *Angew. Chem. Int. Ed. Engl.* **2015**, 54, 3664-3668.

[9] Coelho, J. A.; Ribeiro, A. M.; Ferreira, A. F. P.; Lucena, S. M. P.; Rodrigues, A. E.; Azevedo, D. C. S. d., Stability of an Al-Fumarate MOF and Its Potential for CO_2 Capture from Wet Stream. *Ind. Eng. Chem. Res.* **2016**, *55*, 2134-2143.

[10] Park, J.Y.; Paul, D. R., Correlation and prediction of gas permeability in glassy polymer membrane materials via a modified free volume based group contribution method. *J. Membr. Sci.* **1997**, *125*, 23-39.

[11] Kanehashi, S.; Nagai, K., Analysis of dual-mode model parameters for gas sorption in glassy polymers. *J. Membr. Sci.* **2005**, *253*, 117-138.

[12] Bouma, R. H. B.; Checchetti, A.; Chidichimo. G.; Drioli, E. Permeation through a heterogenous membrane: the effect of the dispersed phase. *J. Membr. Sci.* **1997**, *128*, 141-149.

[13] Pal, R., Permeation models for mixed matrix membranes. *J. Colloid. Interface Sci.* **2008**, *317*, 191-198.

3.2 Metal-Organic Frameworks with Potential Application for SO_2 Separation and Flue Gas Desulfurization

Philipp Brandt, Alexander Nuhnen, Marcus Lange, Jens Möllmer, Christoph Janiak

ACS Appl. Mater. Interfaces, **2019**, 11, 19, 17350–17358.

DOI: 10.1021/acsami.9b00029

Schwefeldioxid (SO_2) ist ein toxisches Gas, welches durch die Verbrennung von fossilen Energieträgern oder andere chemische Prozesse in die Umwelt emittiert wird. SO_2 reizt schon bei sehr geringen Konzentrationen die Schleimhäute und Atemwege eines Menschen und kann bei höheren Konzentrationen zum Tod führen. Für eine mögliche Anwendung der Gastrennung von SO_2/CO_2 wurden drei bereits bekannte MOFs aufgrund unterschiedlicher Eigenschaften (chemische Stabilität, thermische Stabilität, großes Porenvolumen, etc.) ausgewählt. NH_2-MIL-125(Ti) und MOF-177 erwiesen sich bei Einzelgassorptionen von SO_2 und CO_2 bzw. bei den durchgeführten Stabilitätstests als nicht vielversprechend. MIL-160 hingegen zeigte sowohl eine außergewöhnliche Stabilität, als auch eine bemerkenswerte Selektivität gegenüber SO_2 (IAST Selektivität von 124-128 bei 293 K, 1 bar). Die ausgezeichnete Affinität zu SO_2 konnte durch die hohe isostere Adsorptionswärme von SO_2 von ca. 42 kJ/mol bei *zero coverage* (bis zu ca. 60 kJ/mol bei maximaler Beladung) erklärt werden. Ferner konnten entsprechend der Werte der Adsorptionswärme Bindungsenergien zwischen SO_2 und dem MOF-Gerüst von ca. 40-60 kJ/mol gefunden werden. Daraufhin wurden für MIL-160 *Breakthrough*-Experimente und-Simulationen durchgeführt. Auch bei diesen dynamischen Experimenten zeigte sich eine exzellente Trennleistung von SO_2 gegenüber CO_2 und N_2, welche MIL-160 zu einem vielversprechenden Kandidaten für die Rauchgasentschwefelung machen.

Anteile an der Veröffentlichung:

- Idee, Konzept experimentelle Arbeiten, Analytik und Manuskript wurden zu gleichen Teilen von Herrn Philipp Brandt und Herrn Alexander Nuhnen erarbeitet/durchgeführt/angefertigt.
- Theoretische Berechnungen und Mathematische Auswertung.
- Korrekturen am Manuskript erfolgten von Herrn. Prof. Dr. Janiak.
- Breakthrough Experimente und Auswertung wurden von Herrn Dr. Marcus Lange und Herrn Dr. Jens Möllmer durchgeführt.
- Anfertigung von DFT Berechnungen von Herrn Dr. Oliver Weingart

ACS APPLIED MATERIALS & INTERFACES
Research Article
Cite This: ACS Appl. Mater. Interfaces 2019, 11, 17350−17358
www.acsami.org

Metal−Organic Frameworks with Potential Application for SO_2 Separation and Flue Gas Desulfurization

Philipp Brandt,[†,‡] Alexander Nuhnen,[†,‡] Marcus Lange,[∥] Jens Möllmer,[∥] Oliver Weingart,[§] and Christoph Janiak*,[†,⊥]

[†]Institut für Anorganische Chemie und Strukturchemie and [§]Institut für Theoretische Chemie und Computerchemie, Heinrich-Heine-Universität Düsseldorf, Universitätsstraße 1, Düsseldorf 40225, Germany

[∥]Institut für Nichtklassische Chemie, Permoserstraße 15, Leipzig 04318, Germany

[⊥]Hoffmann Institute of Advanced Materials, Shenzhen Polytechnic, 7098 Liuxian Blvd., Nanshan District, Shenzhen 518055, China

Supporting Information

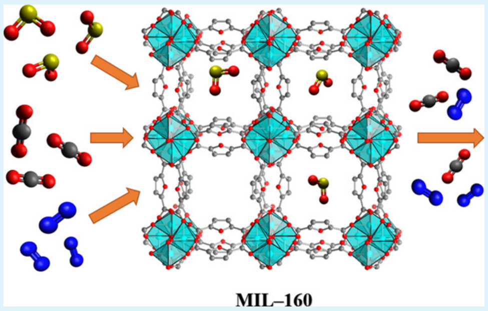

ABSTRACT: Sulfur dioxide (SO_2) is an acidic and toxic gas and its emission from utilizing energy from fossil fuels or in industrial processes harms human health and environment. Therefore, it is of great interest to find new materials for SO_2 sorption to improve classic flue gas desulfurization. In this work, we present SO_2 sorption studies for the three different metal−organic frameworks MOF-177, NH_2-MIL-125(Ti), and MIL-160. MOF-177 revealed a new record high SO_2 uptake (25.7 mmol·g^{-1} at 293 K and 1 bar). Both NH_2-MIL-125(Ti) and MIL-160 show particular high SO_2 uptakes at low pressures ($p < 0.01$ bar) and thus are interesting candidates for the removal of remaining SO_2 traces below 500 ppm from flue gas mixtures. The aluminum furandicarboxylate MOF MIL-160 is the most promising material, especially under application-orientated conditions, and features excellent ideal adsorbed solution theory selectivities (124−128 at 293 K, 1 bar; 79−95 at 353 K, 1 bar) and breakthrough performance with high onset time, combined with high stability under both humid and dry SO_2 exposure. The outstanding sorption capability of MIL-160 could be explained by DFT simulation calculations and matching heat of adsorption for the binding sites $O_{furan}\cdots S_{SO2}$ and $OH_{Al\text{-}chain}\cdots O_{SO2}$ (both ~40 kJ·mol^{-1}) and $O_{furan/carboxylate}\cdots S_{SO2}$ (~55−60 kJ·mol^{-1}).

KEYWORDS: *metal−organic framework, sulfur dioxide sorption, gas selectivity, breakthrough, DFT simulation, flue gas desulfurization*

■ INTRODUCTION

Constant economic growth leads to ever increasing energy consumption and thus to new environmental burdens and hazards for human health.[1] Hence, the development of new methods to capture air pollutants such as CO_2, NO_x, and SO_2 is an important scientific challenge.[2] The majority of anthropogenic SO_2 emission emerges from combustion of coal and heavy oil or is caused by industrial processes.[3,4] The SO_2 content in flue gases is already relatively low, with around 500−3000 ppm, and large parts of it (85−95%) can be scrubbed with classic flue gas desulfurization, using limestone as an absorbent.[5,6] However, this still leaves up to 150−450 ppm of SO_2, which are emitted to the atmosphere, contributing largely to 80 Mt of worldwide anthropogenic SO_2 emissions from energy-related sources in 2015.[3] There are substantial reasons to envision the target of a complete removal of SO_2 from flue gas. On the one hand, SO_2 emissions damage the environment, with effects such as acid rain, and lead to pulmonary diseases and premature deaths of humans caused by declining air quality.[7−9] On the other hand, it is important to note that even traces of SO_2 can significantly reduce other flue gas purification processes by inactivating sorbents for CO_2 removal or catalysts for selective reduction of NO_x.[10−12] This is why the stepwise purification of flue gases, starting with selective and quantitative removal of SO_2, would be highly desirable.[13] Porous materials with high uptake capacity, selectivity, and stability for SO_2 are therefore of major interest to decrease the global emission of anthropogenic pollutants. Metal−organic frameworks (MOFs) are a promising material class to fulfill these specific requirements.[14−17] These organic−inorganic hybrid compounds show remarkable sorption capability including selective capture of a series of toxic and polluting gases.[18−22] However, in comparison to other adsorptives such as N_2, H_2, CO_2, or CH_4, in the past, there are only a few experimental studies dealing with SO_2 adsorption in MOFs.[13,20,23−29] Currently, the research of SO_2 sorption in MOFs is receiving increasing interest for SO_2−CO_2 separation applications.[30−34]

In this study, we examine the three MOFs: MOF-177, NH_2-MIL-125(Ti), and MIL-160 (see Scheme 1 and Section 1 of the Supporting Information for their short structure descrip-

Received: January 8, 2019
Accepted: April 19, 2019
Published: April 19, 2019

DOI: 10.1021/acsami.9b00029

Scheme 1. Linker and Metal Ion in MOF-177, NH_2-MIL-125(Ti), and MIL-160

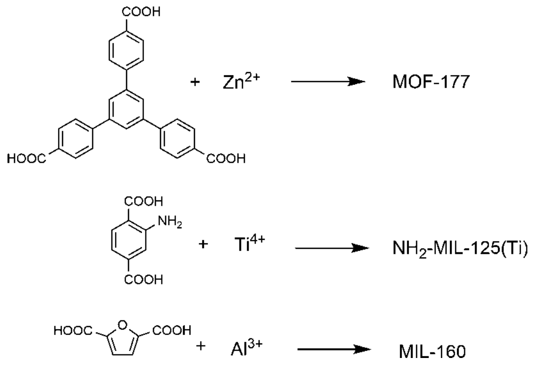

tion).[35−38] Our investigations include single gas sorption, heat of adsorption, IAST selectivity, DFT-calculated binding sites, breakthrough experiments and simulations, and stability tests under dry and humid SO_2 exposure conditions. The selected materials feature a wide range of different properties (BET surface area, total pore volume, pore window size, functionality, etc.).

For the ultrahigh surface framework MOF-177, an unusual SO_2 isotherm shape and incredible high SO_2 uptakes of ∼38 mmol·g^{-1} were theoretically predicted.[15]

Schröder et al. previously examined gas-binding interactions of amine-functionalized materials with the hydroxy-functionalized MFM-300. Here, the amine-functionalized materials showed increased heats of adsorption in comparison to the hydroxy-functionalized MFM-300 aluminum framework.[25]

MIL-160 and NH_2-MIL-125(Ti) had been examined thoroughly for their water sorption properties and showed remarkably high H_2O vapor uptake at low partial pressures and high water stability.[17,36,37] We assume that these H_2O sorption properties should be relevant for the SO_2 sorption properties because SO_2 sequestration applications take place under humid conditions. Therefore, water stability is highly important for any MOF, which is studied for SO_2 adsorption. Further, Walton et al. already performed comprehensive stability tests for MIL-125(Ti) and NH_2-MIL-125(Ti) under aqueous, humid, and dry SO_2 exposure in which the amino-functionalized MOF showed sufficient robustness.[17] An additional aspect, which led to the choice of MIL-160 over other MOFs, is that it can be synthesized in large quantities under green (aqueous) and mild conditions in a single step from readily commercially available compounds.[36] These are especially important factors regarding a possibly larger-scale industrial MOF usage in the future.

RESULTS AND DISCUSSION

Detailed information and description about the examined structures and their characterization (BET and PXRD) can be found in the Supporting Information.

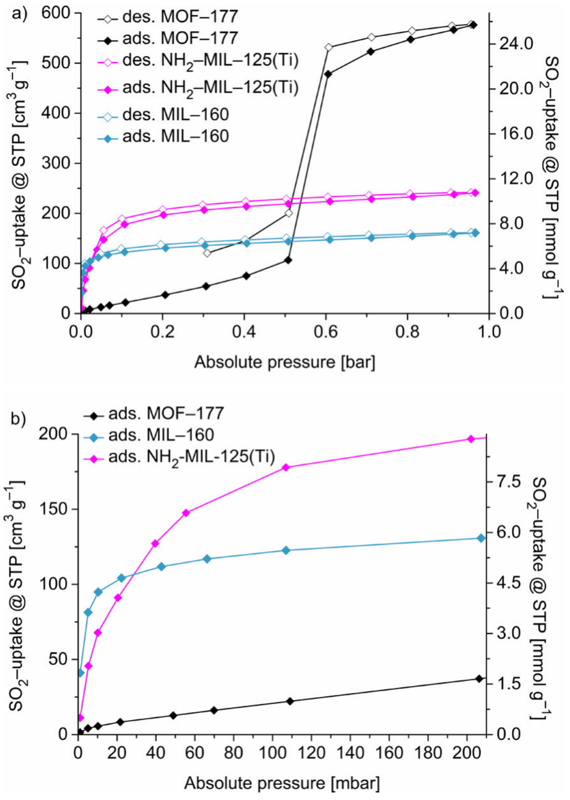

Figure 1. (a) Experimental SO_2 isotherms (0−1 bar) at 293 K; (b) low pressure area (up to 210 mbar) of experimental SO_2 isotherms at 293 K. For the nonclosure of the desorption isotherm for MOF-177 in (a), see the section on SO_2 adsorption in the Supporting Information.

SO_2 Sorption. MOF-177 showed by far the highest SO_2 capacity with a maximum uptake of 25.7 mmol·g^{-1} at 0.97 bar and 293 K (20 °C) (Figure 1). To the best of our knowledge, this is the highest reported value, measured from experimental SO_2 isotherms, in the literature so far.[20,27,30] A comparison with SO_2 capturing MOFs from the literature can be found in Table S5 of the Supporting Information. The SO_2 adsorption isotherm of MOF-177 at 293 K shows an "S"-shape or type V isotherm, which can be attributed to relatively weak adsorbent−adsorbate interactions. For such adsorbent−adsorbate pairs, molecular adsorbate clustering only occurs at higher p/p_0, followed by pore filling.[39] Such type V isotherms are typical for water adsorption on hydrophobic microporous and mesoporous (MOF) adsorbents. A similar "S"-shape or type V isotherm behavior for SO_2 sorption has been predicted for a few other materials with non-functionalized linkers, large pore sizes, and high total pore volume (IRMOF-1, IRMOF-8, and IRMOF-15).[15,16] The SO_2 gas uptake in MOF-177 starts slow, with an uptake of 4.8 mmol·g^{-1} at 0.5 bar, rises sharply to 21.3 mmol·g^{-1} at 0.6 bar and reaches a maximum of 25.7 mmol·g^{-1} at 0.97 bar. The desorption isotherm shows a significant hysteresis below 0.5 bar. The SO_2 desorption of MOF-177 had to be aborted at 0.3 bar due to the comparatively slower adsorption and desorption kinetics leading to a long measurement time for this high capacity MOF (see explanation on maximum SO_2 measuring time in Section 2 in the Supporting Information). This sorption performance together with changes in the crystallinity (Figure S22, Supporting Information) and significant decrease of BET surface area (Figure S18, Table S4, Supporting Information) suggests at least partially chemisorption, that is, strong interaction of SO_2 and the MOF-177 framework. The gas uptake at high partial pressures is attributed to the relatively large pore diameter (10.6−11.8 Å).[40] Combined with a high Brunauer−Emmett−Teller (BET) surface area of 4100 m^2·g^{-1} and a total pore volume of 1.51 cm^3·g^{-1}, this leads to the exceptional high maximum uptake. The insignificant adsorption at low partial pressures also suggests that MOF-177 is no effective adsorbent for selective SO_2 capture because in potential applications, adsorbents have to deal with low SO_2 concentrations of 500 ppm and less. These results are in accordance

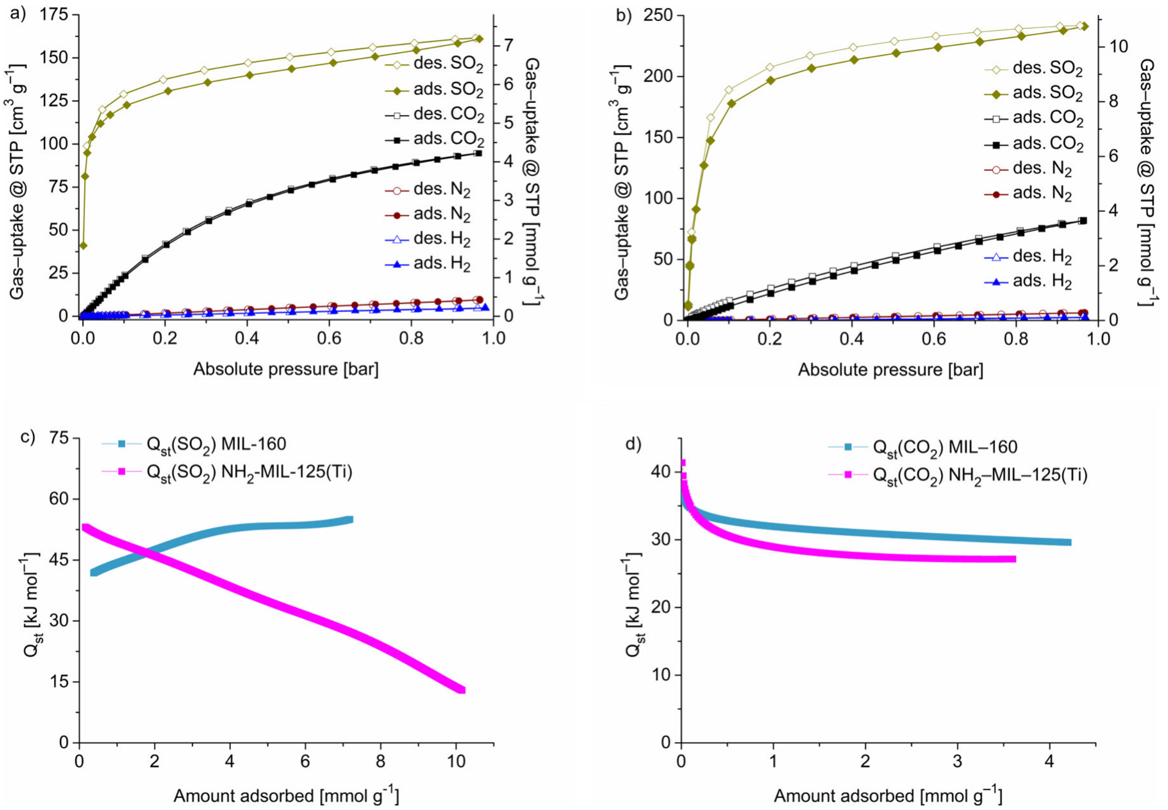

Figure 2. (a) Comparison of single gas sorption isotherms (SO_2, CO_2, N_2, and H_2) for MIL-160 at 293 K. (b) Comparison of single gas sorption isotherms (SO_2, CO_2, N_2, and H_2) for NH_2-MIL-125(Ti) at 293 K. (c) Isosteric heat of adsorption of SO_2 for MIL-160 and NH_2-MIL-125(Ti). (d) Isosteric heat of adsorption of CO_2 for MIL-160 and NH_2-MIL-125(Ti).

with breakthrough experiments performed previously by Yaghi and Brit in which MOF-177 showed no significant retention of 1.0% SO_2 in N_2.[18] Therefore, and also because of the low stability of MOF-177 (see below), no further SO_2 sorption investigations for MOF-177 were considered. In comparison to the simulated SO_2 adsorption isotherms of MOF-177, published by Song et al.[15] and Sun et al.[16] at 298 K and 313 K, respectively, it has to be noted that the high maximum SO_2 uptake of MOF-177 from experimental measurements of 25.7 mmol g^{-1} at 0.97 bar stays below the predictions of ~34 mmol·g^{-1} (298 K) or of ~28 mmol·g^{-1} (313 K) from the simulated isotherms. The adsorption isotherm with "S" or type V shape of MOF-177 at 293 K is in good agreement with the simulations done by Song et al. at 298 K, where a steep SO_2 uptake is predicted at around 0.5 bar,[15] whereas in the simulation of Sun et al. (at 313 K), the steep SO_2 uptake is shifted to higher pressures starting at 0.9 bar.[16]

NH_2-MIL-125(Ti) exhibits a compromising performance in both reasonable SO_2 capacity and good SO_2 uptake at low pressures. The SO_2 adsorption of NH_2-MIL-125(Ti) at 293 K showed a steep rise up to 0.1 bar (7.9 mmol·g^{-1}) while the further uptake proceeds with a lower rise up to the end of the adsorption at 0.95 bar (10.8 mmol·g^{-1}). The uptake agrees with the one reported by Walton et al. at 298 K.[17] The isotherm can be assigned as type Ib.

MIL-160 showed specific high SO_2 uptake at low pressures. The SO_2 adsorption isotherm at 293 K is of type I, shows a steep rise up to 0.01 bar (4.2 mmol·g^{-1}), and quickly approaches the limiting value. Already at 0.1 bar (5.5 mmol·g^{-1}), 76% of the maximum measured uptake at 0.97 bar (7.2 mmol·g^{-1}) is reached. For microporous MIL-160 and NH_2-MIL-125(Ti) with the functionalized and more hydrophilic furan and amino benzene moiety, respectively, in the linker, the interaction with polar adsorbents is increased, and physisorption and micropore filling occurs at lower pressures.[39]

Selectivity of MIL-160 and NH_2-MIL-125(Ti). To further compare the selective sorption capabilities of MIL-160 and NH_2-MIL-125(Ti), we performed sorption experiments, with SO_2, CO_2, N_2, and H_2 as adsorptives at 293 K in a pressure range of 1×10^{-3}–1 bar (Figure 2a,b). Both MOFs have similar adsorption properties, with insignificant adsorption of N_2 and H_2 and a slow rise of CO_2 adsorption across the entire pressure range (1×10^{-3}–1 bar), whereas the majority of the SO_2 adsorption occurs at low pressures of ≤0.1 bar. This encourages that MIL-160 and NH_2-MIL-125(Ti) should be able to separate SO_2 selectively from CO_2, N_2, and H_2 at low partial pressures.

We measured adsorption isotherms at two additional temperatures (313 and 373 K for SO_2 and 273 and 373 K for CO_2) for MIL-160 and NH_2-MIL-125(Ti) and applied several commonly used models on our isotherm data. The best fits for our isotherms were given for the Sips and DSLAI fitting models, which we compare in Figures S4–S7 in the Supporting Information. This enabled us to simulate adsorption isotherms for any given temperature within the interval of the measurement temperatures for this specific gas (Figures S4–S7, Supporting Information). For all fitting and simulation calculations, the "3P sim" software was used.[41] Detailed sets of fitting parameters for Sips and DSLAI models are given in Tables S1 and S2 of the Supporting Information.

Adsorption isotherms measured at 273 and 293 K were used to calculate isosteric heats of adsorption (Q_{st}) of SO_2 and CO_2 for MIL-160 and NH_2-MIL-125(Ti), respectively (Figure 2c,d).

In case of SO_2, we used virial analysis, whereas for CO_2, the Sips analysis combined with Clausius−Clapeyron calculations (Figures S8−S11, Supporting Information) was applied on isotherm data. For a detailed explanation including equations, fits, and parameters, see the Heat of Adsorption section of the Supporting Information.

The heat of adsorption for SO_2 near zero coverage (Q_{st}^0) in MIL-160 is ∼42 $kJ \cdot mol^{-1}$, whereas the amino-functionalized MOF NH_2-MIL-125(Ti) exhibits Q_{st}^0 values of ∼53 $kJ \cdot mol^{-1}$. For CO_2, both MIL-160 and NH_2-MIL-125(Ti) show similar Q_{st}^0 values with ∼37 $kJ \cdot mol^{-1}$ and ∼41 $kJ \cdot mol^{-1}$, respectively. The higher heat of adsorption for the amine-functionalized MOF is in agreement with previous work by Schröder et al.[25]

Normally, a decrease in the heat of adsorption is observed with increased loading as the higher energy binding sites are occupied first. For MIL-160, we see here an unexpected increase in Q_{st} with SO_2 loading. At the same time, we note an agreement in the measured Q_{st} value near a zero loading of ∼42 $kJ \cdot mol^{-1}$ with the calculated binding energies for the $O_{furan} \cdots S_{SO2}$ and $OH_{Al\text{-}chain} \cdots O_{SO2}$ sites (∼40 $kJ \cdot mol^{-1}$) and in the measured Q_{st} values for the maximum loading (∼55 $kJ \cdot mol^{-1}$) with the calculated energy for the $O_{furan/carboxylate} \cdots S_{SO2}$ site (60 $kJ \cdot mol^{-1}$) (see below). Although the close match of experimental and calculated values may be somewhat coincidental, we would rationalize the trend by a phase transition in MIL-160 from an activated empty phase I, where the $O_{furan/carboxylate} \cdots S_{SO2}$ site is not accessible, to a guest-loaded phase II with the accessible $O_{furan/carboxylate} \cdots S_{SO2}$ site. Thus, in the initial phase I, only the lower energy binding sites can be occupied. In this aspect, we point to studies on the water sorption in MIL-160 where a phase transition upon water loading was concluded.[42]

Next, we applied ideal adsorbed solution theory (IAST) calculations on dual-site Langmuir (DSLAI)-fitted isotherms to determine selectivities for mixed gas adsorption in binary SO_2/CO_2 mixtures (10:90−50:50 v/v) (Figure 2c). Note that for meaningful IAST calculations, adsorption capacities of the adsorbates should not differ substantially.[43] Here, we applied IAST calculations on the mixed gas adsorption process of SO_2 versus CO_2, two polar molecules, up to only 1 bar pressure. Known limitations for IAST simulations, that is, high pressure and different polarity, are not present in our case. Therefore, we expect IAST calculations to give a first and sufficiently reliable estimation of the selectivity, and indeed, IAST calculations, albeit with different concentrations, are in good agreement to the experimental breakthrough experiments (see below).

The results from the IAST calculations show that MIL-160, compared to NH_2-MIL-125(Ti), has increased selectivity toward SO_2. The SO_2/CO_2 IAST selectivities at 293 K and 1 bar are between 124−128 and 42−55 for MIL-160 and NH_2-MIL-125(Ti), respectively (Figure 3a). In comparison to the leading MOF materials with regard to SO_2/CO_2 separation, IAST selectivities between 32 and 100 at ambient temperatures are reported.[13,26,27,33] MIL-160 surpasses these values. Using the same method on SO_2/N_2 gas mixtures leads to no quantifiable values because of low N_2 affinities for both frameworks.

As most of the potential SO_2 adsorption applications (e.g., flue gas desulfurization) take place at elevated temperatures, it is important to characterize material properties at these temperatures. A common temperature for flue gas desulfurization is at around 353 K (80 °C) to condense the water vapor before the desulfurization.[44,45] For both MIL-160 and NH_2-MIL-125(Ti), the gas uptake for SO_2 and CO_2 decreases with increasing temperatures. Note that for MIL-160, the SO_2 adsorption curve in the simulation (353 K) and measurement (373 K) remains type Ib (Figure S4, Supporting Information). At the same time, the CO_2 adsorption isotherm for both materials converts to an almost linear uptake curve with low gas uptakes at these elevated temperatures (Figures S5 and S7, Supporting Information). Even though the SO_2/CO_2 IAST selectivities at 353 K and 1 bar, in comparison to 293 K, are decreasing for MIL-160 and NH_2-MIL-125(Ti) to values between 79−95 and 47−55, respectively, for both materials, a significant selectivity remains (Figure 3b).

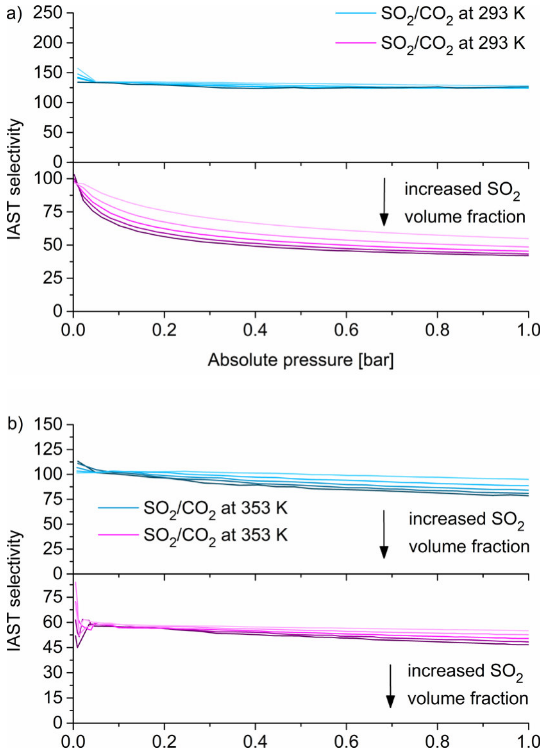

Figure 3. (a) IAST selectivities of MIL-160 (top) and NH_2-MIL-125(Ti) (bottom) with SO_2/CO_2, 10:90 (light)−50:50 (dark) (v/v) at 293 K. (b) IAST selectivities of MIL-160 (top) and NH_2-MIL-125(Ti) (bottom) with SO_2/CO_2, 10:90 (light)−50:50 (dark) (v/v) at 353 K.

Breakthrough Performance for Potential FGD Application. For the most promising material MIL-160, experimental breakthrough experiments were performed to ensure its separation capability not only under equilibrated but also under dynamic conditions. For MOF-177, previous breakthrough experiments with 1.0% SO_2 in N_2 showed no significant retention of SO_2 vapor.[18]

For MIL-160, we measured breakthrough curves of the ternary gas mixture N_2/CO_2/SO_2 (84.9:15.0:0.1 v/v/v) at 293 and 353 K and a ternary gas mixture with increased SO_2 concentration with N_2/CO_2/SO_2 (84.0:15.0;1.0 v/v/v) at 293 K (Figure 4a,b and Figure S13, Supporting Information). The 0.1% SO_2 ternary gas mixture was also employed in the simulations. The sample was pretreated at 373 K under continuous nitrogen flow (16.6 $mL \cdot min^{-1}$) until no other gas than nitrogen was detected. The composition of the ternary gas mixture was chosen according to the typical flue gas composition from the air-fired coal combustion.[46] The breakthrough plot in Figure 4a shows an immediate rise of the N_2 and CO_2 concentrations in the outlet. Under the chosen experimental conditions, this immediate rise indicates almost no N_2 adsorption and a rapid saturation for CO_2 inside the MOF, which can be assigned to a spontaneous breakthrough for CO_2.

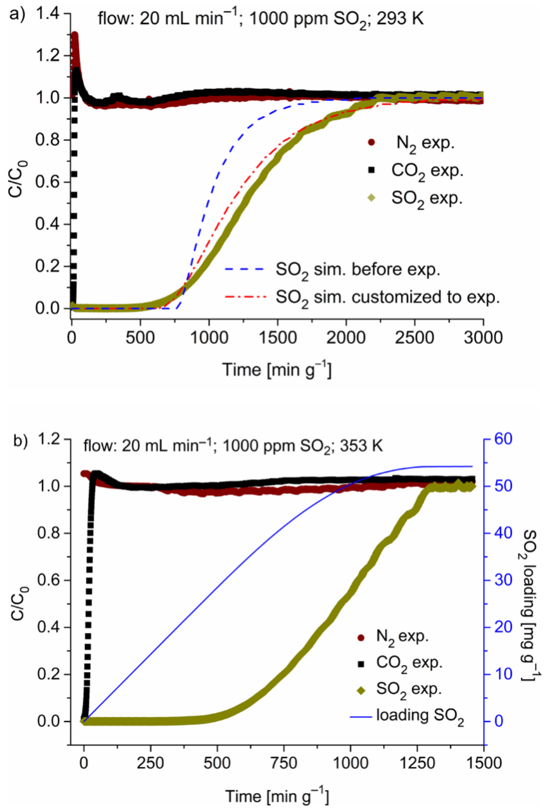

Figure 4. (a) Experimental and simulated breakthrough curves for MIL-160 at 293 K. (b) Experimental breakthrough curve for MIL-160 at 353 K.

In contrast, SO_2 could be retained for about ~600 min·g^{-1} and shows no significant loss in retention time in the second run after identical activation of the MIL-160 material (Figure S12, Supporting Information). Subsequently, to the second run, we investigated regenerability of MIL-160 in purging the column under N_2 flow (16.6 mL·min^{-1}) at 293 K for 12 h. This experiment shows that the MIL-160 material is a fully reversible SO_2 adsorber, which recovers easily at low temperatures and without the need of vacuum (Figure S14, Supporting Information).

At an elevated temperature of 353 K (Figure 4b) or with a 10-fold higher SO_2 concentration of 10,000 ppm SO_2 (Figure S13, Supporting Information), MIL-160 still shows remarkable capability to retain SO_2, with retention times of ~350 and ~500 min·g^{-1}. As expected, the total SO_2 loadings at dynamic conditions (breakthrough experiment, 293 K, 0.1% SO_2, 1.17 mmol·g^{-1}) are lower than SO_2 loadings under equilibrium conditions (sorption isotherm, 293 K, 0.001 bar, 1.8 mmol·g^{-1}). However, the maximal loading of SO_2 increases with rising SO_2 concentration in our breakthrough experiment (293 K, 1% SO_2, 3.65 mmol·g^{-1}).

Note that at 353 K, the dynamic loading of SO_2 for MIL-160 is still 0.85 mmol·g^{-1}. This comparatively high SO_2 loading can be explained by the SO_2 adsorption isotherm at 373 K (Figure S4, Supporting Information), which shifts from type Ia (293 K) to type Ib (373 K), and does not flatten completely, compared to the CO_2 adsorption under the same conditions. For a comparison of maximum loadings under equilibrium or dynamic conditions at selected partial pressures, see Table S3 of the Supporting Information.

Breakthrough Simulations. In addition, we simulated breakthrough curves with an identical gas mixture to our breakthrough experiments with a gas mixture of $N_2/CO_2/SO_2$ (84.9:15.0:0.1 v/v/v) at 293 K (Figure 4a) and further simulated CO_2/carrier gas/SO_2 (90/9.75/0.25) gas mixtures in a style of oxyfuel combustion[46] at 293 and 353 K for MIL-160 and NH_2-MIL-125(Ti), respectively (Figures S15−S17, Supporting Information). The simulated breakthrough curves were calculated from Sips-fitted isotherm data of MIL-160 and NH_2-MIL-125(Ti) (Figures S4−S7 and Tables S4 and S5, Supporting Information).

We would like to point out that breakthrough simulations (Figure 4a, blue dashed line), which were performed ahead of breakthrough experiments, gave already a good estimate for the breakthrough onset time of SO_2 in MIL-160 under identical conditions. These simulations could be further refined by taking into account experimental breakthrough data and slight deviations in the experiment from which we obtained optimized parameters for the mass transfer coefficient and axial flow (Figure 4a, red dashed line). Slight deviations in the experimental and simulated curvature slope are caused by the small particle size of MIL-160 combined with a marginal pressure drop (inlet to outlet) and the low flow rate for the gas mixture.

The simulations based on oxyfuel combustion with strongly increased CO_2 concentration as well show solid separation capability of SO_2 versus CO_2 at 293 K for MIL-160 and NH_2-MIL-125(Ti) with retention times of about 200 min·g^{-1} (Figures S15 and S16, Supporting Information). Even though the retention times are decreased at higher temperatures (353 K) for both materials, it is still worth mentioning that a separation of CO_2 and SO_2 is predicted for both materials (Figures S15 and S16, Supporting Information).

DFT Calculations. To better understand the exceptional good adsorption performance of MIL-160, we used DFT simulation calculations to investigate the possible binding sites for SO_2 in the framework. Geometry optimization of SO_2 within MIL-160 yielded at least three different possibilities for SO_2 binding: First, in one structure (Figure 5a), SO_2 is oriented with sulfur toward the ether oxygen of a furan linker ($O_{furan}\cdots S_{SO2}$ distance 3.27 Å, distances to other nearby oxygens from 3.91 to 4.48 Å). A second binding site is provided by the O−H bridge, where SO_2 associates with one oxygen toward hydrogen (Figure 5b, $OH_{Al\text{-}chain}\cdots O_{SO2}$ distance 2.10 Å). These two binding sites, $O_{furan}\cdots S_{SO2}$ and $OH_{Al\text{-}chain}\cdots O_{SO2}$, exhibit similar binding energies of 39.3 and 40.6 kJ·mol^{-1}, respectively. In a third configuration, SO_2 sits above the plane spanned by two furan units (Figure 5c), with $O_{furan/carboxylate}\cdots S_{SO2}$ distances of 3.15 and 3.36 Å toward the ether oxygens and between 3.22 and 3.68 Å to the carboxylate oxygens. This latter configuration has the largest binding energy of 60.4 kJ·mol^{-1} and may provide a model for low-concentration SO_2 binding. In this geometry, however, SO_2 has much closer proximity to ether and carboxylate oxygens as in the structure Figure 5a, suggesting that at higher loadings, the binding site in Figure 5a is displaced to the binding site in Figure 5c when more SO_2 molecules enter the channel to occupy binding sites. For MFM-300, Schröder et al. located preferred binding sites of SO_2 at the Al−OH groups from the $AlO_4(OH)_2$ chain by in situ inelastic neutron scattering (INS) and DFT calculations.[25]

MIL-160 was also studied profoundly by Maurin et al.,[47] where the preferred binding sites for various guest molecules (H_2O, CO_2, CH_4, CO, N_2, and H_2) to the MIL-160 framework

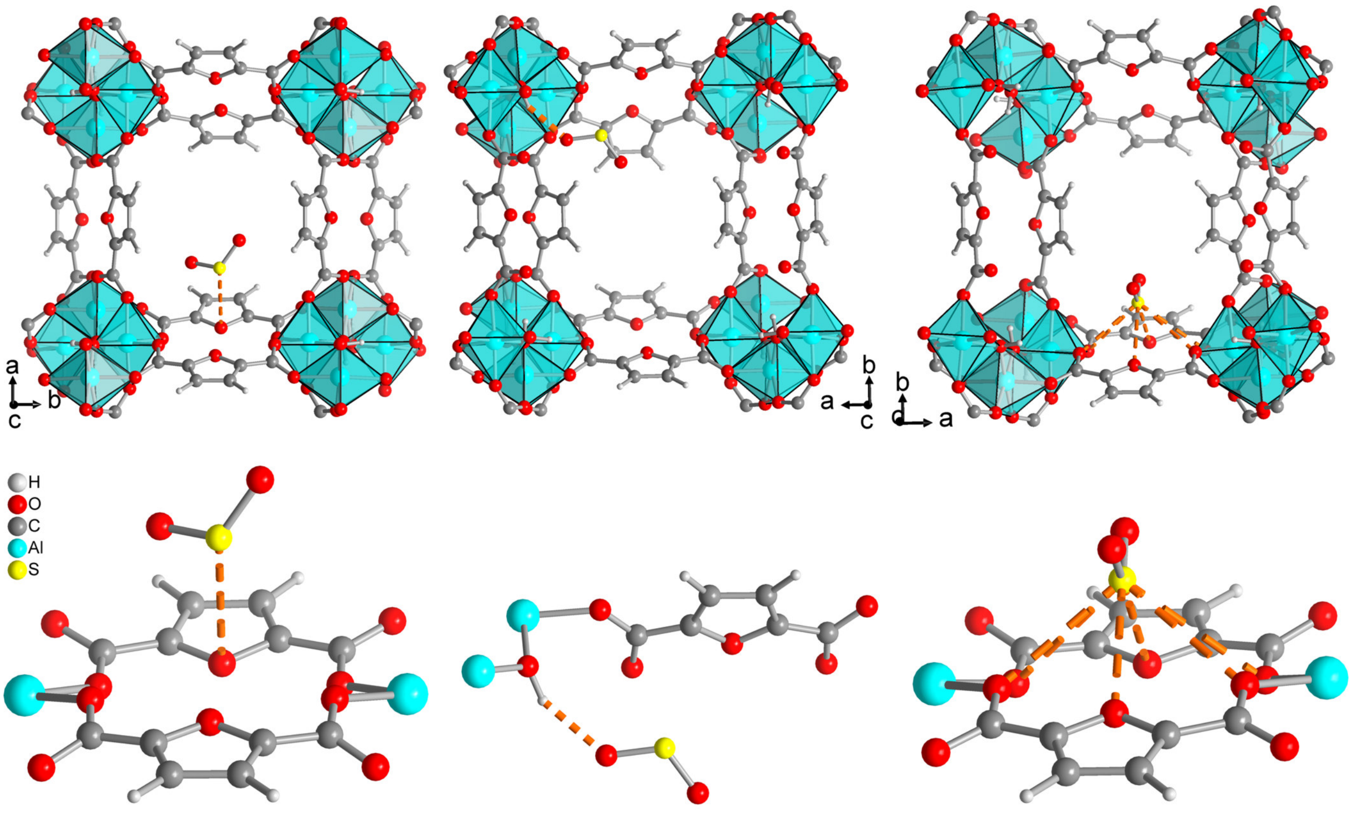

(a) (b) (c)

Figure 5. DFT-simulated binding sites of SO_2 in MIL-160. (a) $O_{furan}\cdots S_{SO2}$ interaction, (b) $OH_{Al\text{-}chain}\cdots O_{SO2}$ interaction, and (c) $O_{furan/carboxylate}\cdots S_{SO2}$ interaction. The closest contacts (as given in the text) from the SO_2 molecule to nearby framework atoms are depicted by orange dashed lines. The upper row shows the full channel cross section; the lower row gives an enlarged view of the SO_2 binding site.

were predicted by applying density functional theory (DFT), force field-based grand canonical Monte Carlo (GCMC) simulations, and radial distribution function (RDF). In these studies, CO_2 showed preferred binding to the heteroatom of the furan ligand with a distance of 3.1 Å and a binding energy of 32.5 kJ·mol^{-1} for the $O_{furan}\cdots O_{CO2}$ interaction. Thus, we rationalize the selectivity toward SO_2 by its higher binding energies. We also note that the exceptional selectivity and breakthrough performance of MIL-160 correlate with its small pore size of 5 Å diameter,[36] which is close to the kinetic diameter of SO_2 (4.11 Å)[48] and thus suitable for a selective adsorption of SO_2 under kinetic control.

Stability under Dry and Humid SO_2 Exposure. The stability of MOF materials was tested by SO_2 exposure experiments under dry (SO_2 sorption measurement) and humid conditions (SO_2 humidity chamber). For the experiment under humid conditions, we used a similar setup to Walton et al. (see the Supporting Information for details).[17] To assess the (in)stability, BET surface area and PXRD before and after exposure were measured to see whether porosity and crystallinity were preserved (Figures S18–S20 and S22–S24 and Table S4, Supporting Information).

For MOF-177, the BET surface significantly decreased from 4100 to 2270 m^2·g^{-1} (55%) under dry SO_2 conditions. Changes in the powder diffractogram (Figure S22, Supporting Information) also support the conclusion that MOF-177 undergoes a partial destruction under SO_2 exposure. Regardless of the low stability of MOF-177, we note again that this MOF is not practical for SO_2 adsorption applications at low concentrations where MOF-177 exhibits no uptake due to its "S"-shaped isotherm.

For NH_2-MIL-125(Ti), the BET surface decreased from 1560 to 1270 m^2·g^{-1} (81%) and 1250 m^2·g^{-1} (80%) under dry and humid conditions. Contrarily, MIL-160 showed no significant degradation in the BET surface under the same conditions (1170 m^2·g^{-1} a.s., 1120 m^2·g^{-1} after dry SO_2 exposure, 1130 m^2·g^{-1} after 175 ppm·h SO_2, and 75% relative humidity). PXRD patterns for NH_2-MIL-125(Ti) and MIL-160 remained unchanged.

Both MIL-160 and NH_2-MIL-125(Ti) were further investigated by measuring multiple individual SO_2 sorption runs of the same sample to evaluate SO_2 stabilities (Figure S21, Supporting Information). MIL-160 showed excellent stability with insignificant reduction of the gas uptake over five runs. In contrast, NH_2-MIL-125(Ti) displayed a reduced SO_2 uptake in the second run and then stabilized its adsorption capacity at the third run. This supports the assumption of a partial irreversible adsorption of SO_2 in the pores of NH_2-MIL-125(Ti).

The dry and humid stability tests show MOF-177 is unsuitable, and NH_2-MIL-125(Ti) is only of limited suitability for applications in flue gas desulfurization, where only a highly humid SO_2 stable adsorbent will be feasible. In contrast, MIL-160 showed remarkable stability under both dry and humid SO_2 conditions. These results expand previous studies in which Al-MOFs have shown extraordinary hydrothermal stability[49−51] and thus indicate that Al-MOFs (e.g., MIL-160 and MFM-300[24]) can be considered among the most promising MOF

DOI: 10.1021/acsami.9b00029
ACS Appl. Mater. Interfaces 2019, 11, 17350−17358

materials with regard to application under chemical aggressive conditions.

CONCLUSIONS

MOF-177 showed a record maximum SO_2 uptake of 25.7 mmol·g^{-1} at 293 K and 1 bar but turned out to be unsuitable for flue gas desulfurization (FGD) applications due to its chemical instability and low adsorption at low partial pressures of SO_2. NH_2-MIL-125(Ti) showed promising properties in IAST selectivity and breakthrough simulations for SO_2 but not as good as MIL-160, which exhibited outstanding performances in terms of SO_2/CO_2 selectivity, onset breakthrough time, and stability toward SO_2 under dry and humid conditions. In breakthrough experiments, MIL-160 could retain SO_2 for at least 500 min·g^{-1} from a typical flue gas composition of air-fired coal combustion, even at elevated temperatures. Further, MIL-160 could be easily regenerated at low temperatures (293 K) after breakthrough experiments. We would like to emphasize that for practical separation applications, it is essential for the material to feature an early gas uptake at very low partial pressure rather than a high total uptake at higher pressures. Especially so, if the gas, which ought to be separated, is present in a low volume fraction, such as SO_2 with less than 500 ppm remaining after limestone scrubbing in flue gas. The IAST-based SO_2 selectivity of MIL-160 over other gases (CO_2 and N_2) is on the level of leading benchmark MOFs. Further, MIL-160 features extraordinary stability under both dry and humid SO_2 exposure conditions, which together with the established low cost, green, and easily up scalable synthesis routes make MIL-160 a promising material for FGD applications.

EXPERIMENTAL SECTION

Materials. All reagents were commercially purchased and used without any further purification.

MOF-177. MOF-177 was synthesized by a solvothermal reaction according to the literature.[35] $Zn(NO_3)_2\cdot 6H_2O$ (0.124 g, 0.41 mmol) and H_3BTB (0.031 g, 0.07 mmol) were dissolved in DEF (3 mL) and transferred into a glass vial. The mixture was then heated to 90 °C, kept at 90 °C for 24 h, and cooled down to 30 °C in 10 h. The resulting crystals were washed with DEF (three times, 3 mL each) and CH_2Cl_2 (three times, 3 mL each). Afterward, the sample was dried under vacuum (1×10^{-3} mbar) for 24 h at room temperature.

MIL-160. The synthesis of MIL-160 was performed according to the literature.[36] $Al(OH)(CH_3COO)_2$ (1.037 g, 6.40 mmol) and 2,5-furandicarbocylic acid (0.999 g, 6.40 mmol) were added to a round-bottom flask (100 mL) and dispersed in ultrapure water (40 mL). The mixture was then stirred and refluxed for 24 h, giving a white precipitate. The solid was washed with water (three times, 50 mL each) and then dried under vacuum at 60 °C for 24 h.

NH_2-MIL-125(Ti). The synthesis of NH_2-MIL-125(Ti) was performed according to the literature.[37] NH_2-benzenedicarboxylic acid (1.086 g, 6.00 mmol) was dissolved in a 50:50 v/v mixture of DMF (3.5 mL) and MeOH (3.5 mL) under sonication. $Ti(iPrO)_4$ (0.44 mL, 1.5 mmol) was added to the solution, which was then transferred in a stainless steel autoclave with a Teflon inlay and was heated in an oven at 150 °C for 16 h. After cooling down to room temperature, the yellow precipitate was at first washed with DMF (7 mL) and secondly washed two times with MeOH (7 mL). The solid was dried under vacuum at 60 °C for 24 h.

Material Characterization. BET and PXRD characterizations were performed on a Quantachrome Autosorb 6 and a Bruker D2 phaser, respectively. SO_2 isotherms were measured with a Quantachrome Autosorb iQ MP (for detailed description see the Supporting Information). Breakthrough curves were determined on an inhouse apparatus. Experimental details for humid SO_2 exposure are also given in the Supporting Information.

ASSOCIATED CONTENT

Supporting Information

The Supporting Information is available free of charge on the ACS Publications website at DOI: 10.1021/acsami.9b00029.

> Brief MOF structure description, additional gas sorption isotherms and measurement details, isotherm fitting and simulation parameters, virial analysis, additional breakthrough experiments and simulations, powder X-ray diffractograms, and comparison of SO_2 sorption literature data (PDF)

AUTHOR INFORMATION

Corresponding Author

*E-mail: janiak@uni-duesseldorf.de.

ORCID

Christoph Janiak: 0000-0002-6288-9605

Author Contributions

‡P.B. and A.N. contributed equally to this work. The manuscript was written through contributions of all authors. All authors have given approval to the final version of the manuscript.

Notes

The authors declare no competing financial interest.

ACKNOWLEDGMENTS

We thank Dr. Andreas Möller from 3P Instruments, Germany and Mr. Simon Millan for helpful discussion. We are indebted to the Deutsche Forschungsgemeinschaft for support through grant Ja466/29-1.

ABBREVIATIONS

BET, Brunauer−Emmett−Teller
DFT, density functional theory
FGD, flue gas desulfurization
IAST, ideal adsorbed solution theory
IRMOF, isoreticular MOF
MFM, Manchester framework material
MIL, Matériaux de l′Institut Lavoisier
MOF, metal−organic framework
PXRD, powder X-ray diffraction

REFERENCES

(1) Laurent, A.; Espinosa, N. Environmental Impacts of Electricity Generation at Global, Regional and National Scales in 1980−2011: What can we Learn for Future Energy Planning? *Energy Environ. Sci.* **2015**, *8*, 689−701.

(2) Rezaei, F.; Rownaghi, A. A.; Monjezi, S.; Lively, R. P.; Jones, C. W. SO_x/NO_x Removal from Flue Gas Streams by Solid Adsorbents: A Review of Current Challenges and Future Directions. *Energy Fuels* **2015**, *29*, 5467−5486.

(3) International Energy Agency *World Energy Outlook 2016*; Iea Publications: Paris, 2016.

(4) Fioletov, V. E.; McLinden, C. A.; Krotkov, N.; Li, C.; Joiner, J.; Theys, N.; Carn, S.; Moran, M. D. A Global Catalogue of large SO_2 Sources and Emissions Derived from the Ozone Monitoring Instrument. *Atmos. Chem. Phys.* **2016**, *16*, 11497−11519.

(5) Lee, J.-Y.; Keener, T. C.; Yang, Y. J. Potential Flue Gas Impurities in Carbon Dioxide Streams Separated from Coal-Fired Power Plants. *J. Air Waste Manage. Assoc.* **2012**, *59*, 725−732.

(6) Srivastava, R. K.; Jozewicz, W. Flue Gas Desulfurization: The State of the Art. *J. Air Waste Manage. Assoc.* **2011**, *51*, 1676−1688.

(7) Likens, G. E.; Driscoll, C. T.; Buso, D. C. Long-Term Effects of Acid Rain: Response and Recovery of a Forest Ecosystem. *Science* **1996**, *272*, 244−246.

(8) Gregory, K.; Webster, C.; Durk, S. Estimates of Damage to Forests in Europe due to Emissions of Acidifying Pollutants. *Energy Policy* **1996**, *24*, 655−664.

(9) Rall, D. P. Review of the Health Effects of Sulfur Oxides. *Environ. Health Perspect.* **1974**, *8*, 97−121.

(10) Rao, A. B.; Rubin, E. S. A Technical, Economic, and Environmental Assessment of Amine-Based CO2 Capture Technology for Power Plant Greenhouse Gas Control. *Environ. Sci. Technol.* **2002**, *36*, 4467−4475.

(11) Ding, S.; Liu, F.; Shi, X.; Liu, K.; Lian, Z.; Xie, L.; He, H. Significant Promotion Effect of Mo Additive on a Novel Ce−Zr Mixed Oxide Catalyst for the Selective Catalytic Reduction of NO_x with NH_3. *ACS Appl. Mater. Interfaces* **2015**, *7*, 9497−9506.

(12) Goo, J. H.; Irfan, M. F.; Kim, S. D.; Hong, S. C. Effects of NO_2 and SO_2 on Selective Catalytic Reduction of Nitrogen Oxides by Ammonia. *Chemosphere* **2007**, *67*, 718−723.

(13) Savage, M.; Cheng, Y.; Easun, T. L.; Eyley, J. E.; Argent, S. P.; Warren, M. R.; Lewis, W.; Murray, C.; Tang, C. C.; Frogley, M. D.; Cinque, G.; Sun, J.; Rudić, S.; Murden, R. T.; Benham, M. J.; Fitch, A. N.; Blake, A. J.; Ramirez-Cuesta, A. J.; Yang, S.; Schröder, M. Selective Adsorption of Sulfur Dioxide in a Robust Metal-Organic Framework Material. *Adv. Mater.* **2016**, *28*, 8705−8711.

(14) Han, S.; Huang, Y.; Watanabe, T.; Nair, S.; Walton, K. S.; Sholl, D. S.; Carson Meredith, J. MOF Stability and Gas Adsorption as a Function of Exposure to Water, Humid Air, SO_2, and NO_2. *Microporous Mesoporous Mater.* **2013**, *173*, 86−91.

(15) Song, X.-D.; Wang, S.; Hao, C.; Qiu, J.-S. Investigation of SO_2 Gas Adsorption in Metal−Organic Frameworks by Molecular Simulation. *Inorg. Chem. Commun.* **2014**, *46*, 277−281.

(16) Sun, W.; Lin, L.-C.; Peng, X.; Smit, B. Computational Screening of Porous Metal-Organic Frameworks and Zeolites for the Removal of SO_2 and NO_x from Flue Gases. *AIChE J.* **2014**, *60*, 2314−2323.

(17) Mounfield, W. P., III; Han, C.; Pang, S. H.; Tumuluri, U.; Jiao, Y.; Bhattacharyya, S.; Dutzer, M. R.; Nair, S.; Wu, Z.; Lively, R. P.; Sholl, D. S.; Walton, K. S. Synergistic Effects of Water and SO_2 on Degradation of MIL-125 in the Presence of Acid Gases. *J. Phys. Chem. C* **2016**, *120*, 27230−27240.

(18) Britt, D.; Tranchemontagne, D.; Yaghi, O. M. Metal-Organic Frameworks with High Capacity and Selectivity for Harmful Gases. *Proc. Natl. Acad. Sci. U. S. A.* **2008**, *105*, 11623−11627.

(19) Bobbitt, N. S.; Mendonca, M. L.; Howarth, A. J.; Islamoglu, T.; Hupp, J. T.; Farha, O. K.; Snurr, R. Q. Metal-Organic Frameworks for the Removal of Toxic Industrial Chemicals and Chemical Warfare Agents. *Chem. Soc. Rev.* **2017**, *46*, 3357−3385.

(20) Wang, H.; Lustig, W. P.; Li, J. Sensing and Capture of Toxic and Hazardous Gases and Vapors by Metal-Organic Frameworks. *Chem. Soc. Rev.* **2018**, *47*, 4729−4756.

(21) Han, X.; Yang, S.; Schröder, M. Porous Metal-Organic Frameworks as Emerging Sorbents for Clean Air. *Nat. Rev. Chem.* **2019**, *3*, 108−118.

(22) Glomb, S.; Woschko, D.; Makhloufi, G.; Janiak, C. Metal-Organic Frameworks with Internal Urea-Functionalized Dicarboxylate Linkers for SO_2 and NH_3 Adsorption. *ACS Appl. Mater. Interfaces* **2017**, *9*, 37419−37434.

(23) Fernandez, C. A.; Thallapally, P. K.; Motkuri, R. K.; Nune, S. K.; Sumrak, J. C.; Tian, J.; Liu, J. Gas-Induced Expansion and Contraction of a Fluorinated Metal−Organic Framework. *Cryst. Growth Des.* **2010**, *10*, 1037−1039.

(24) Grant Glover, T.; Peterson, G. W.; Schindler, B. J.; Britt, D.; Yaghi, O. MOF-74 Building Unit has a direct Impact on Toxic Gas Adsorption. *Chem. Eng. Sci.* **2011**, *66*, 163−170.

(25) Yang, S.; Sun, J.; Ramirez-Cuesta, A. J.; Callear, S. K.; David, W. I. F.; Anderson, D. P.; Newby, R.; Blake, A. J.; Parker, J. E.; Tang, C. C.; Schröder, M. Selectivity and Direct Visualization of Carbon Dioxide and Sulfur Dioxide in a Decorated Porous Host. *Nat. Chem.* **2012**, *4*, 887−894.

(26) Yang, S.; Liu, L.; Sun, J.; Thomas, K. M.; Davies, A. J.; George, M. W.; Blake, A. J.; Hill, A. H.; Fitch, A. N.; Tang, C. C.; Schröder, M. Irreversible Network Transformation in a Dynamic Porous Host Catalyzed by Sulfur Dioxide. *J. Am. Chem. Soc.* **2013**, *135*, 4954−4957.

(27) Cui, X.; Yang, Q.; Yang, L.; Krishna, R.; Zhang, Z.; Bao, Z.; Wu, H.; Ren, Q.; Zhou, W.; Chen, B.; Xing, H. Ultrahigh and Selective SO_2 Uptake in Inorganic Anion-Pillared Hybrid Porous Materials. *Adv. Mater.* **2017**, *29*, 1606929.

(28) Tan, K.; Canepa, P.; Gong, Q.; Liu, J.; Johnson, D. H.; Dyevoich, A.; Thallapally, P. K.; Thonhauser, T.; Li, J.; Chabal, Y. J. Mechanism of Preferential Adsorption of SO_2 into Two Microporous Paddle Wheel Frameworks $M(bdc)(ted)_{0.5}$. *Chem. Mater.* **2013**, *25*, 4653−4662.

(29) Thallapally, P. K.; Motkuri, R. K.; Fernandez, C. A.; McGrail, B. P.; Behrooz, G. S. Prussian Blue Analogues for CO_2 and SO_2 Capture and Separation Applications. *Inorg. Chem.* **2010**, *49*, 4909−4915.

(30) Carter, J. H.; Han, X.; Moreau, F. Y.; da Silva, I.; Nevin, A.; Godfrey, H. G. W.; Tang, C. C.; Yang, S.; Schröder, M. Exceptional Adsorption and Binding of Sulfur Dioxide in a Robust Zirconium-Based Metal-Organic Framework. *J. Am. Chem. Soc.* **2018**, *140*, 15564−15567.

(31) Hungerford, J.; Bhattacharyya, S.; Tumuluri, U.; Nair, S.; Wu, Z.; Walton, K. S. DMOF-1 as a Representative MOF for SO_2 Adsorption in Both Humid and Dry Conditions. *J. Phys. Chem. C* **2018**, *122*, 23493−23500.

(32) Han, X.; Godfrey, H. G. W.; Briggs, L.; Davies, A. J.; Cheng, Y.; Daemen, L. L.; Sheveleva, A. M.; Tuna, F.; McInnes, E. J. L.; Sun, J.; Drathen, C.; George, M. W.; Ramirez-Cuesta, A. J.; Thomas, K. M.; Yang, S.; Schröder, M. Reversible Adsorption of Nitrogen Dioxide within a Robust Porous Metal-Organic Framework. *Nat. Mater.* **2018**, *17*, 691−696.

(33) Mon, M.; Tiburcio, E.; Ferrando-Soria, J.; Gil San Millán, R.; Navarro, J. A. R.; Armentano, D.; Pardo, E. A Post-Synthetic Approach Triggers Selective and Reversible Sulphur Dioxide Adsorption on a Metal-Organic Framework. *Chem. Commun.* **2018**, *54*, 9063−9066.

(34) Zhang, Y.; Zhang, P.; Yu, W.; Zhang, J.; Huang, J.; Wang, J.; Xu, M.; Deng, Q.; Zeng, Z.; Deng, S. Highly Selective and Reversible Sulfur Dioxide Adsorption on a Microporous Metal-Organic Framework via Polar Sites. *ACS Appl. Mater. Interfaces* **2019**, 10680−10688.

(35) Li, X.; Cheng, F.; Zhang, S.; Chen, J. Shape-Controlled Synthesis and Lithium-Storage Study of Metal-Organic Frameworks Zn_4O(1,3,5-benzenetribenzoate)$_2$. *J. Power Sources* **2006**, *160*, 542−547.

(36) Permyakova, A.; Skrylnyk, O.; Courbon, E.; Affram, M.; Wang, S.; Lee, U.-H.; Valekar, A. H.; Nouar, F.; Mouchaham, G.; Devic, T.; De Weireld, G.; Chang, J.-S.; Steunou, N.; Frère, M.; Serre, C. Synthesis Optimization, Shaping, and Heat Reallocation Evaluation of the Hydrophilic Metal-Organic Framework MIL-160(Al). *ChemSusChem* **2017**, *10*, 1419−1426.

(37) Sohail, M.; Yun, Y.-N.; Lee, E.; Kim, S. K.; Cho, K.; Kim, J.-N.; Kim, T. W.; Moon, J.-H.; Kim, H. Synthesis of Highly Crystalline NH_2-MIL-125(Ti) with S-Shaped Water Isotherms for Adsorption Heat Transformation. *Cryst. Growth Des.* **2017**, *17*, 1208−1213.

(38) Jeremias, F.; Lozan, V.; Henninger, S. K.; Janiak, C. Programming MOFs for Water Sorption: Amino-Functionalized MIL-125 and UiO-66 for Heat Transformation and Heat Storage Applications. *Dalton Trans.* **2013**, *42*, 15967−15973.

(39) Thommes, M.; Kaneko, K.; Neimark, A. V.; Olivier, J. P.; Rodriguez-Reinoso, F.; Rouquerol, J.; Sing, K. S. W. Physisorption of Gases, with Special Reference to the Evaluation of Surface Area and Pore Size Distribution (IUPAC Technical Report). *Pure Appl. Chem.* **2015**, *87*, 1051−1069.

(40) Saha, D.; Deng, S. Hydrogen Adsorption on Metal-Organic Framework MOF-177. *Tsinghua Sci. Technol.* **2010**, *15*, 363−376.

(41) 3P INSTRUMENTS, 3P sim, Version 1.1.0.7, *Simulation and Evaluation Tool for mixSorb*, 3P INSTRUMENTS 2018.

(42) Wahiduzzaman, M.; Lenzen, D.; Maurin, G.; Stock, N.; Wharmby, M. T. Rietveld Refinement of MIL-160 and Its Structural Flexibility Upon H_2O and N2Adsorption. *Eur. J. Inorg.Chem.* **2018**, *2018*, 3626−3632.

(43) Cessford, N. F.; Seaton, N. A.; Düren, T. Evaluation of Ideal Adsorbed Solution Theory as a Tool for the Design of Metal-Organic Framework Materials. *Ind. Eng. Chem. Res.* **2012**, *51*, 4911−4921.

DOI: 10.1021/acsami.9b00029

(44) Liu, C.-F.; Shih, S.-M.; Lin, R.-B. Kinetics of the Reaction of $Ca(OH)_2$/fly Ash Sorbent with SO_2 at low Temperatures. *Chem. Eng. Sci.* **2002**, *57*, 93−104.

(45) Chu, P.; Rochelle, G. T. Removal of SO_2 and NO_X from Stack Gas by Reaction with Calcium Hydroxide Solids. *JAPCA* **1989**, *39*, 175−179.

(46) Jia, L.; Tan, Y.; Anthony, E. J. Emissions of SO_2 and NO_x during Oxy−Fuel CFB Combustion Tests in a Mini-Circulating Fluidized Bed Combustion Reactor. *Energy Fuels* **2010**, *24*, 910−915.

(47) Damasceno Borges, D.; Normand, P.; Permiakova, A.; Babarao, R.; Heymans, N.; Galvao, D. S.; Serre, C.; de Weireld, G.; Maurin, G. Gas Adsorption and Separation by the Al-Based Metal−Organic Framework MIL-160. *J. Phys. Chem. C* **2017**, *121*, 26822−26832.

(48) Li, J.-R.; Kuppler, R. J.; Zhou, H.-C. Selective Gas Adsorption and Separation in Metal-Organic Frameworks. *Chem. Soc. Rev.* **2009**, *38*, 1477−1504.

(49) Lenzen, D.; Bendix, P.; Reinsch, H.; Fröhlich, D.; Kummer, H.; Möllers, M.; Hügenell, P. P. C.; Gläser, R.; Henninger, S.; Stock, N. Scalable Green Synthesis and Full-Scale Test of the Metal−Organic Framework CAU-10-H for Use in Adsorption-Driven Chillers. *Adv. Mater.* **2018**, *30*, 1705869.

(50) Jeremias, F.; Fröhlich, D.; Janiak, C.; Henninger, S. K. Advancement of Sorption-Based Heat Transformation by a Metal Coating of Highly-Stable, Hydrophilic Aluminium Fumarate MOF. *RSC Adv.* **2014**, *4*, 24073−24082.

(51) Fröhlich, D.; Pantatosaki, E.; Kolokathis, P. D.; Markey, K.; Reinsch, H.; Baumgartner, M.; van der Veen, M. A.; de Vos, D. E.; Stock, N.; Papadopoulos, G. K.; Henninger, S. K.; Janiak, C. Water Adsorption Behaviour of CAU-10-H: a Thorough Investigation of its Structure−Property Relationships. *J. Mater. Chem. A* **2016**, *4*, 11859−11869.

Supporting Information

Metal-Organic Frameworks with Potential Application for SO_2-Separation and Flue Gas Desulfurization

Philipp Brandt [a,‡], *Alexander Nuhnen* [a,‡], *Marcus Lange* [b], *Jens Möllmer* [b], *Oliver Weingart* [c], *Christoph Janiak* [a,d]*

[a] Institut für Anorganische Chemie und Strukturchemie, Heinrich-Heine-Universität Düsseldorf, Universitätsstraße 1, 40225 Düsseldorf, Germany

[b] Institut für Nichtklassische Chemie, Permoserstr. 15, 04318 Leipzig, Germany

[c] Institut für Theoretische Chemie und Computerchemie, Heinrich-Heine-Universität Düsseldorf, Universitätsstraße 1, 40225 Düsseldorf, Germany

[d] Hoffmann Institute of Advanced Materials, Shenzhen Polytechnic, 7098 Liuxian Blvd, Nanshan District, Shenzhen, China

[‡] These authors contributed equally.

Email addresses: p.brandt@hhu.de; alexander.nuhnen@hhu.de; lange@inc.uni-leipzig.de; moellmer@inc.uni-leipzig.de; oliver.weingart@hhu.de; janiak@hhu.de

Table of contents

1 Synthesis

All reagents were commercially purchased and were used without further purification. MOF-177, MIL-160 and NH_2-MIL-125(Ti) were synthesized according to the literature.[1,2,3]

1.1 MOF-177

The Zn-based MOF-177 contains the tetranuclear and tetrahedral $\{Zn_4(\mu_4\text{-}O)\}$ secondary building unit, SBU as in MOF-5. The linker is benzene-1,3,5-trisbenzoic acid, $btbH_3$ {5'-(4-carboxyphenyl)-[1,1':3',1"-terphenyl]-4,4"-dicarboxylic acid}. The compound is synthesized from $Zn(NO_3)_2\cdot(H_2O)_6$ and $btbH_3$ in DEF under solvothermal conditions, to yield the MOF formula $[Zn_4(\mu_4\text{-}O)(btb)_3]$.[1] The linker and SBU connectivity are depicted in Figure S1. The material exhibits a surface area of 4050 $m^2\ g^{-1}$ and a pore volume of 1.51 $cm^3\ g^{-1}$.

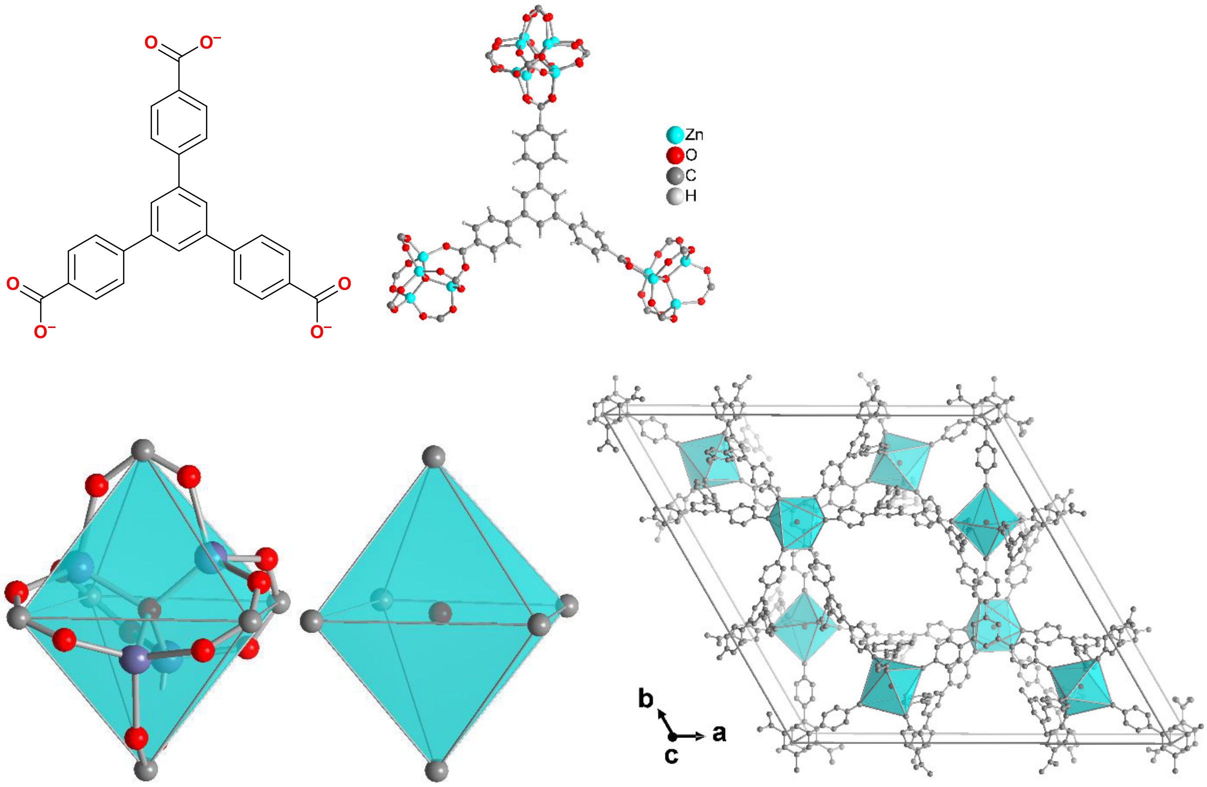

Figure S1. Structural elements in the framework of MOF-177. Top row: Linker and linker connectivity. There are two crystallographically independent SBUs which are both disordered, with one of them disordered about a special position. Bottom row: Due to this disorder, the SBUs were depicted as octahedra, with the carboxylate carbon atoms as vertices, to illustrate a view the trigonal unit cell of the framework in space group $P\text{–}31c$. Graphic produced by software Diamond[4] from cif-file for MOF-177 (CSD-Refcode BABRII).[5]

1.2 MIL-160

The Al-MOF MIL-160 (*Matériaux Institut Lavoisier*), was described by Cadiau *et al.* in 2015.[6] They obtained the MOF by applying reflux conditions for aqueous solutions of 2,5-furandicarboxylic acid, sodium hydroxide and aluminum chloride. MIL-160 is constructed identical to CAU-10-H [7,8] by cis-μ-OH-connected, vertex-sharing $\{AlO_6\}$ octahedra, that form helical chains, which are then joined by the linker 2,5-furandicarboxylate (Fig. S2).

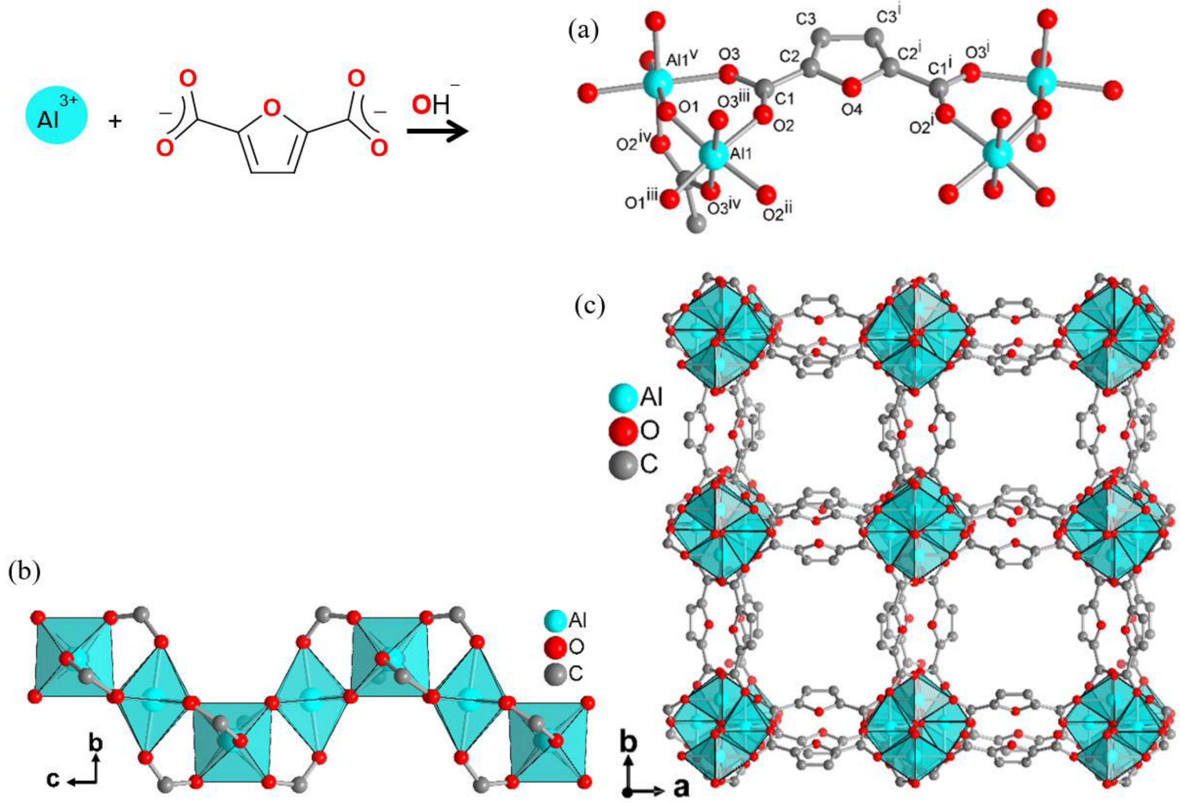

Figure S2. Structural elements in the framework of MIL-160: (a) Extended asymmetric unit with full Al coordination spheres and full ligand bridging mode. Symmetry transformations i = 1–x, y, z; ii = x, –y, –z; iii = 0.25+y, 0.25–x, –0.25+z; iv = 0.25+y, –0.25+x, 0.25–z; v = 0.25–y, –0.25+x, 0.25+z. (b) Helical chains of cis vertex-bridged {AlO_6}-polyhedra and (c) surrounded by the carboxylates ligands, to yield square-shaped one dimensional channels. Graphic produced by software Diamond[4] from cif-file for MIL-160 (CSD-Refcode PIBZOS).[9]

MIL-160 is reported to be isostructural to CAU-10-H, having chains of {AlO_6}-polyhedra that are surrounded by linker molecules.[6] This results in a chemical formula of [$Al(OH)(O_2C\text{-}C_4H_2O\text{-}CO_2) \cdot n\ H_2O]_m$ and microporous square-shaped channels of 5 Å edge length.[6,10] The material exhibits a surface area of 1070 $m^2\ g^{-1}$ and a pore volume of 0.40 $cm^3\ g^{-1}$ from $AlCl_3$ and NaOH (theoretically: 1250 $m^2\ g^{-1}$, 0.48 $cm^3\ g^{-1}$),[6] respectively 1150 $m^2\ g^{-1}$ and 0.46 $cm^3\ g^{-1}$, from $Al(OH)(CH_3COO)_2$,[10] although very recent theoretical calculations suggested a surface area of 776 $m^2\ g^{-1}$ and a pore volume of 0.45 $cm^3\ g^{-1}$.[11]

1.3 NH_2-MIL-125(Ti)

The structure of 3D-[$Ti_8O_8(OH)_4(NH_2\text{-bdc})_6$] is based on the structure of titanium terephthalate MIL-125.[12] The SBU is an eight-membered ring of edge- and vertex-sharing TiO_6 octahedra, which is connected to 12 neighboring SBUs in a body-centered cubic (bcc) packing arrangement (Fig. S3).

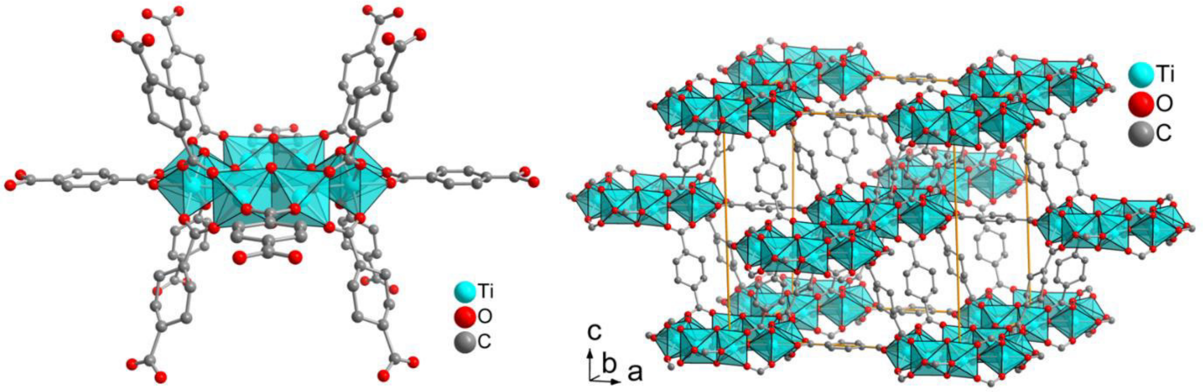

Figure S3. Structural elements in the framework of NH_2-MIL-125(Ti) aka MIL-125: Left the secondary building unit of eight edge- and vertex-sharing TiO_6 octahedra with the twelve surrouding terephthalate ligands. Right the unit cell with the body-centered cubic arrangement of the SBUs. The structure is drawn from the deposited cif-file under CCDC 751157 (MIL-125).[12]

2 Gas sorption experiments

Before each experiment samples were activated for at least 3 hours and at a minimum of 373 K under vacuum $< 5 \cdot 10^{-3}$ mbar. All used gases (He, SO_2, CO_2, N_2, H_2) were of ultra-high purity (UHP grade 5.0, 99.999%) and the STP volumes at 293.15 K and 101.325 kPa are given according to the NIST standards. If not described differently, Sorption experiments were performed on an *Autosorb iQ MP* (QUANTACHROME, Odelzhausen, Germany) instrument within a pressure range of $1 \cdot 10^{-3}$-1 bar. For safety precautions of toxic SO_2 a *Dräger Pac 6000* SO_2-detector (0-100 ppm in 0.1 ppm steps) was used in close range to the sorption-device.

SO_2-sorption experiments with our setup involve some limitations emerging from the corrosive nature of the SO_2 adsorptive. Each SO_2 sorption run had to be completed within a maximal time of 10 h. This time limit was specified by the company Quantachrome to prevent damage to the gaskets. After this time the system had to be regenerated by flushing with nitrogen. Irreversible swilling of the SO_2 adsorbing gaskets in the measurement device, which could cause leaks in the system, had to be prevented by setting the measurement time to this maximum (10 h) to meet safety precautions and to protect the device. Then, after each measurement the gas line was flushed with N_2 several times and remained under N_2 atmosphere for at least 12 h to regenerate the gaskets. In the case of long equilibration times upon adsorption and desorption we decided to collect the adsorption data points as complete as possible with long-enough equilibration times at the expense that for desorption, fewer data points could be measured. This compromise then led to incomplete, i.e. not-closed desorption branches, which however are solely due to the experimental boundary conditions and cannot be interpreted in terms of decomposition or chemisorption.

2.1 Isotherm-fitting

Fitting-simulations were calculated using 3P sim software.[13] We applied several commonly used models on our isotherm data. The best fits for our isotherms were given for the Sips and DSLAI fitting models, which we compare in Figure S4-S7.

The Sips model is a combination of Langmuir and Freundlich isotherms with the following equation:

$$q_{eq} = \frac{q_{max} \cdot K \cdot p^t}{1 + K \cdot p^t} \qquad (1)$$

Where q_{eq} is the amount adsorbed (mg/g), q_{max} is the maximum adsorption capacity (mg/g), K is the affinity constant for adsorption (L/mg), p is the equilibrium concentration of the adsorbate (mg/L) and t is the index of the heterogeneity.[14]

If K or p approaches 0 the fitting of the model is reduced to a Freundlich equation (eq. 2), whereas for homogeneous materials with $t = 1$ concentrations it is reduced to the Langmuir equation (eq. 3).[15]

$$q_{eq} = K \cdot p^t \qquad (2)$$

$$q_{eq} = \frac{q_{max} \cdot K \cdot p}{1 + K \cdot p} \qquad (3)$$

The dual-site Langmuir model is based on the following equation:

$$q_{eq} = q_{max1} \cdot \frac{K_1 \cdot p}{1 + K_1 \cdot p} + q_{max2} \cdot \frac{K_2 \cdot p}{1 + K_2 \cdot p} \qquad (4)$$

By fitting isotherms of the same adsorptive at three different temperatures the software is able to calculate any given temperature for this specific gas (here 353 K, red line).

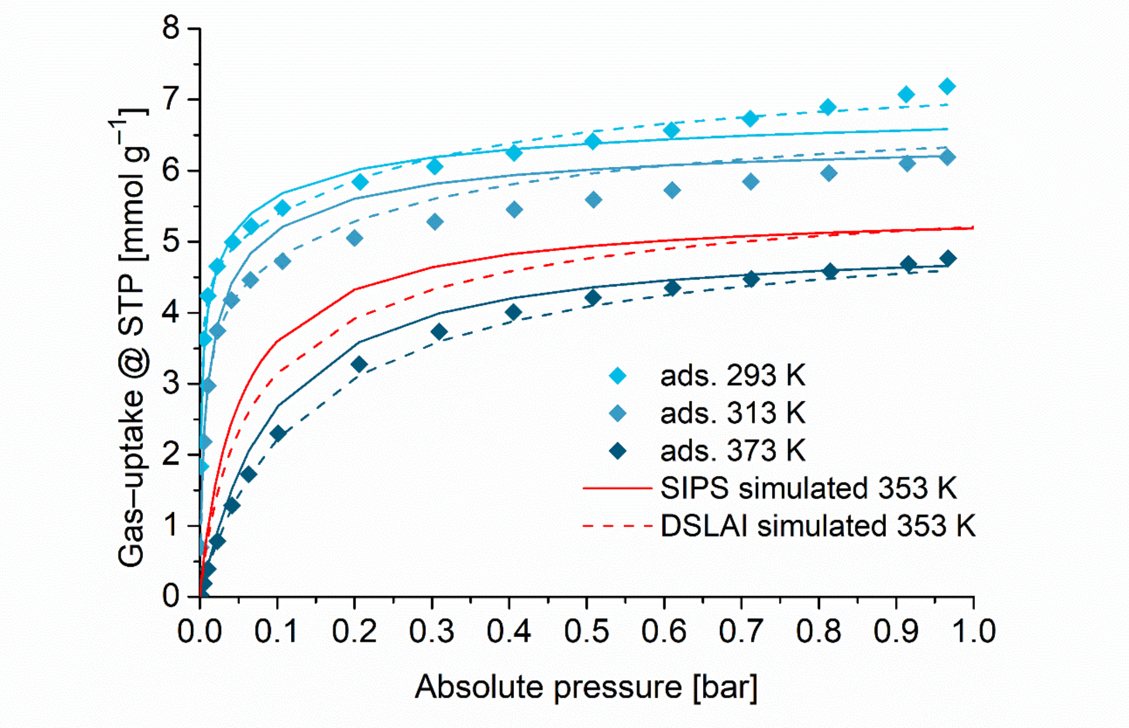

Figure S4. Experimental SO_2-adsorption isotherms (squares) and simulated adsorption isotherms with different models (lines and dashed lines) of MIL-160 at 293 K, 313 K and 373 K. The simulations at 353 K (red) are shown here as this is a common temperature for flue gas desulfurization processes.

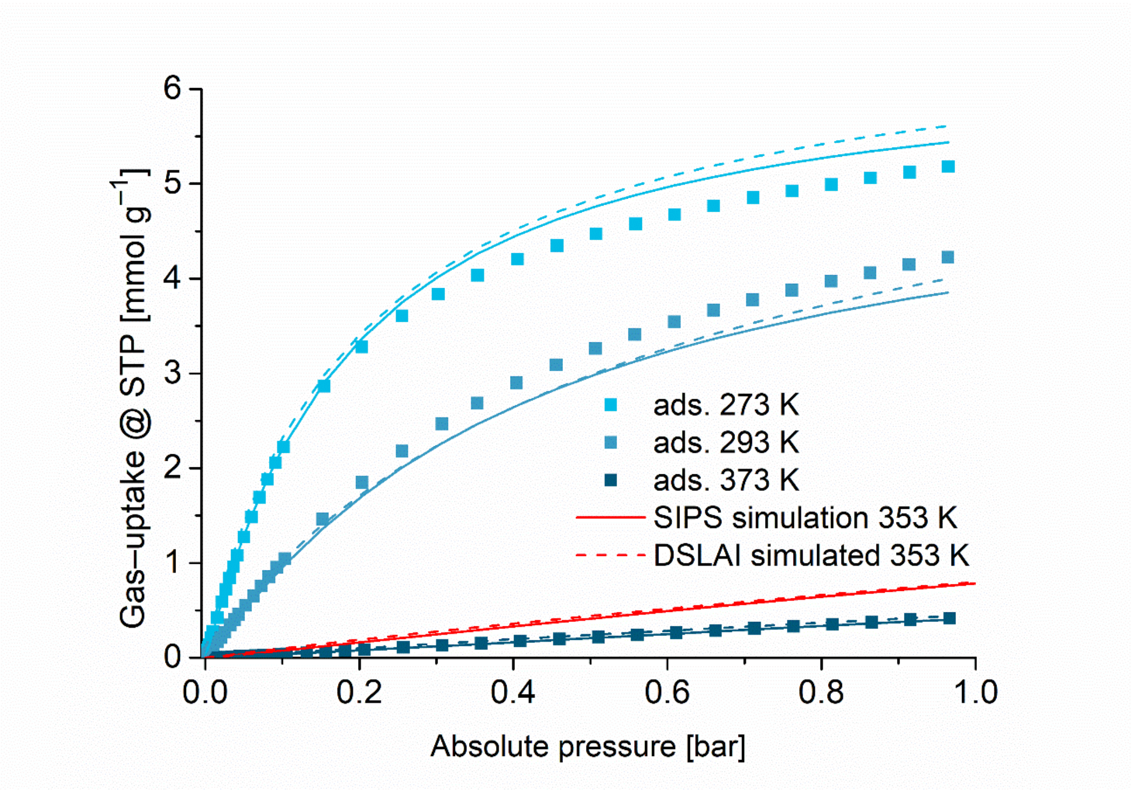

Figure S5. Experimental CO_2-adsorption isotherms (squares) and simulated adsorption isotherms with different models (lines and dashed lines) of MIL-160 at 273 K, 293 K and 373 K. The simulations at 353 K (red) are shown here as this is a common temperature for flue gas desulfurization processes.

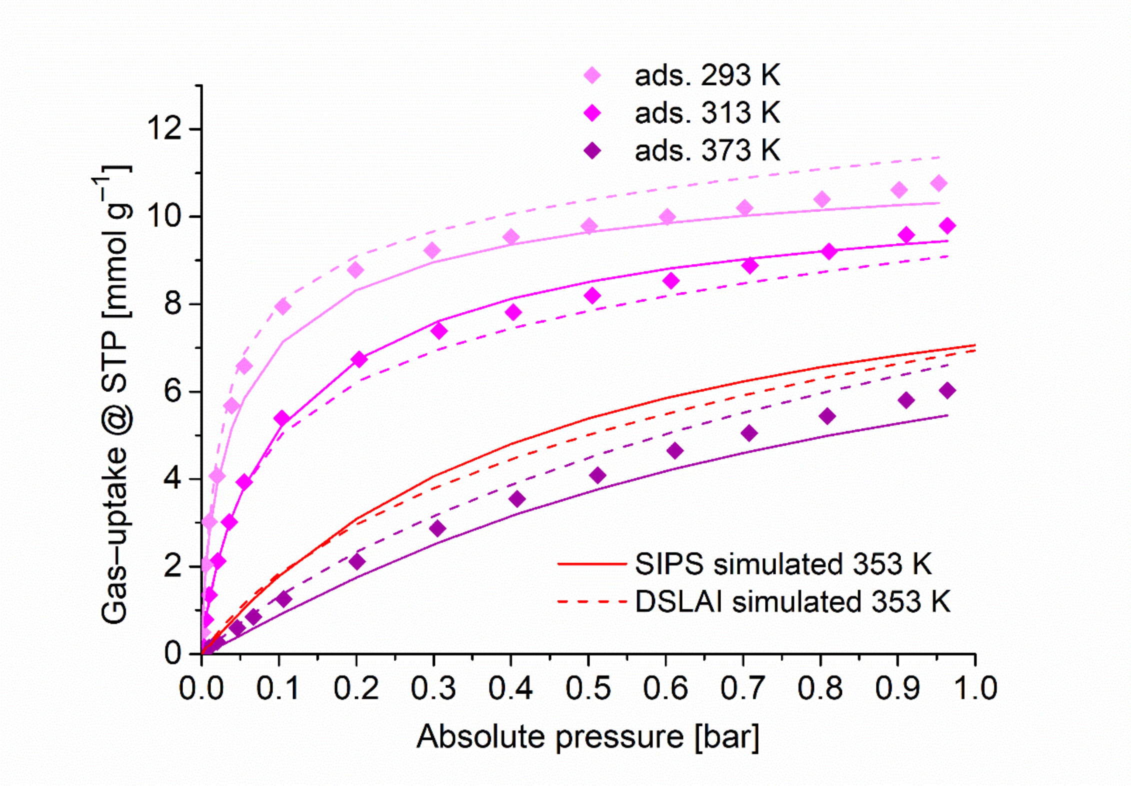

Figure S6. Experimental SO_2-adsorption isotherms (squares) and simulated adsorption isotherms with different models (lines and dashed lines) of NH_2-MIL-125(Ti) at 293 K, 313 K and 373 K. The simulations at 353 K (red) are shown here as this is a common temperature for flue gas desulfurization processes.

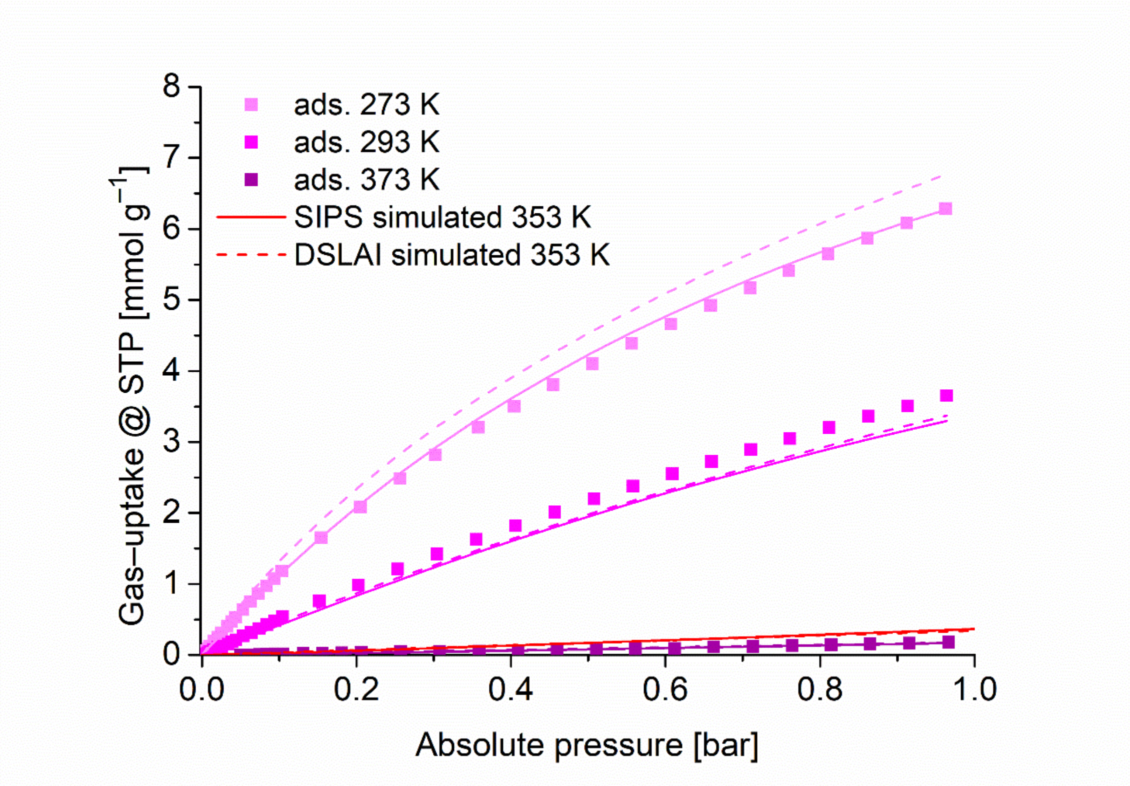

Figure S7. Experimental CO_2-adsorption isotherms (squares) and simulated adsorption isotherms with different models (lines and dashed lines) of NH_2-MIL-125(Ti) at 273 K, 293 K and 373 K. The simulations at 353 K (red) are shown here as this is a common temperature for flue gas desulfurization processes.

Heat of adsorption

2.2 Virial analysis for SO_2

To calculate the isosteric heat of adsorption (Q_{st}) for SO_2 isotherm data virial method was used. Equation (eq. 5) was used to fit the adsorption data simultaneously at 273 K and 293 K in Origin.[16]

$$\ln(P) = \ln(n) + \frac{1}{T}\sum_{i=0}^{n} a_i n^i + \sum_{j=0}^{m} b_j m^j \tag{5}$$

In equation (4), P is the pressure in kPa, n is the total amount adsorbed in mmol/g, T is the temperature in K (here 273K, 293K), a_i and b_i are virial coefficients, and n, m represent the number of coefficients required to adequately fit the isotherms.

Then Q_{st} can be calculated from equation (eq. 6), where R is the universal gas constant.

$$Q_{st} = -\mathrm{R}\sum_{i=0}^{n} a_i n^i \tag{6}$$

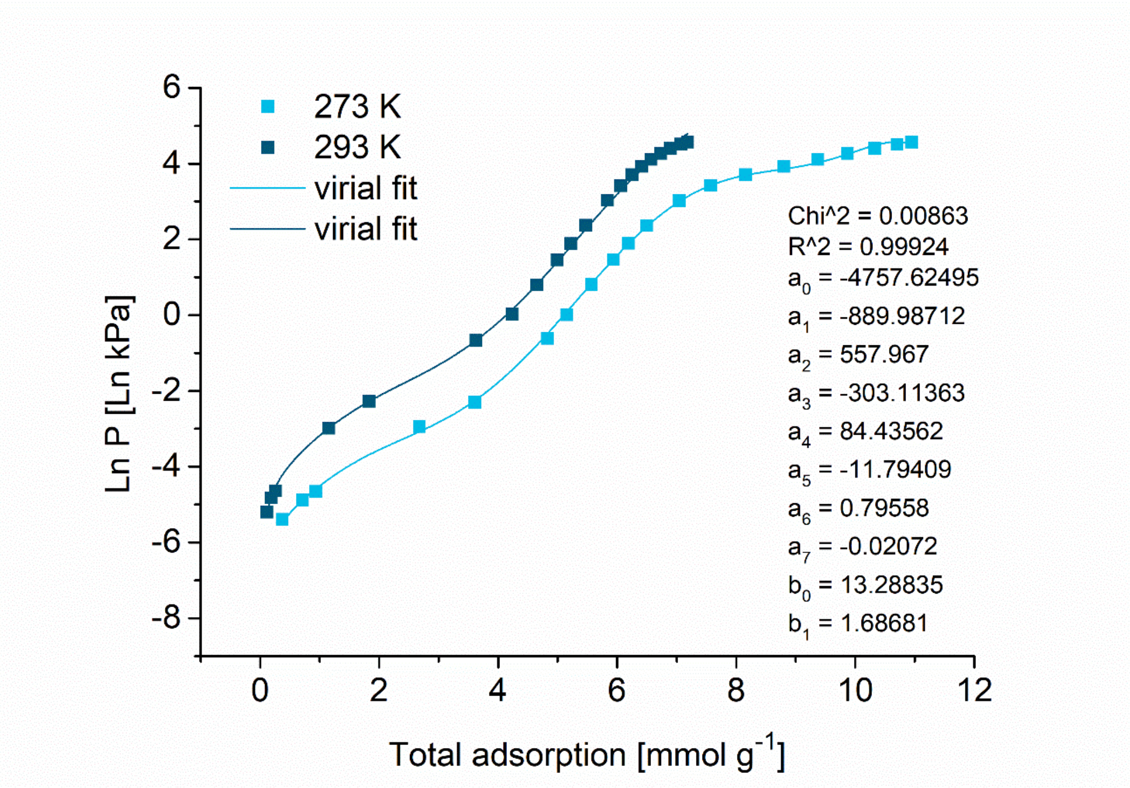

Figure S8. Virial analysis for heat of adsorption of SO_2 and MIL-160 at 273 K and 293 K.

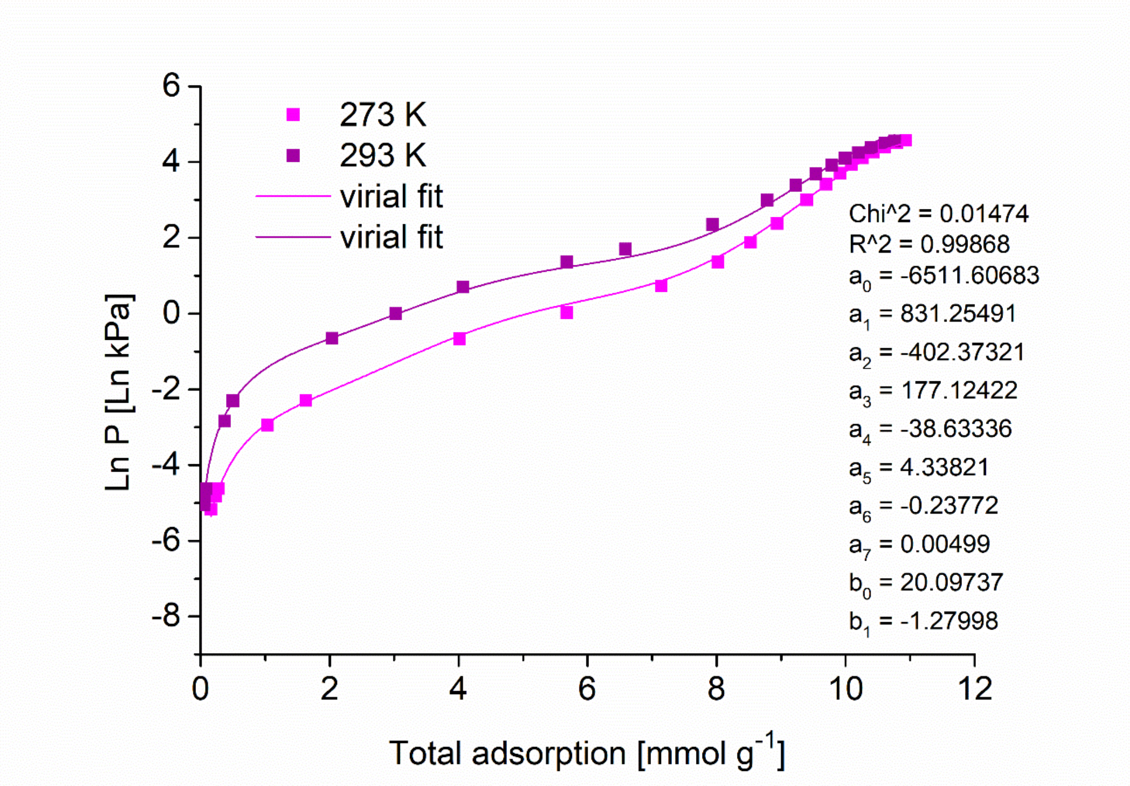

Figure S9. Virial analysis for heat of adsorption of SO_2 and NH_2-MIL-125(Ti) at 273 K and 293 K.

2.3 Sips analysis for CO_2

To calculate the isosteric heat of adsorption (Q_{st}) for CO_2 both isotherms at 273 K and 293 K were fitted according to the Sips equation (eq. 1), to be able to calculate CO_2 loadings for both temperatures at the same pressure.

By applying the Clausius-Clapeyron equation one can now calculate the isosteric heat of adsorption at any loading (eq. 7)

$$Q_{st} = -R \ln\left(\frac{p_2}{p_1}\right) \frac{T_1 T_2}{(T_2 - T_1)} \tag{7}$$

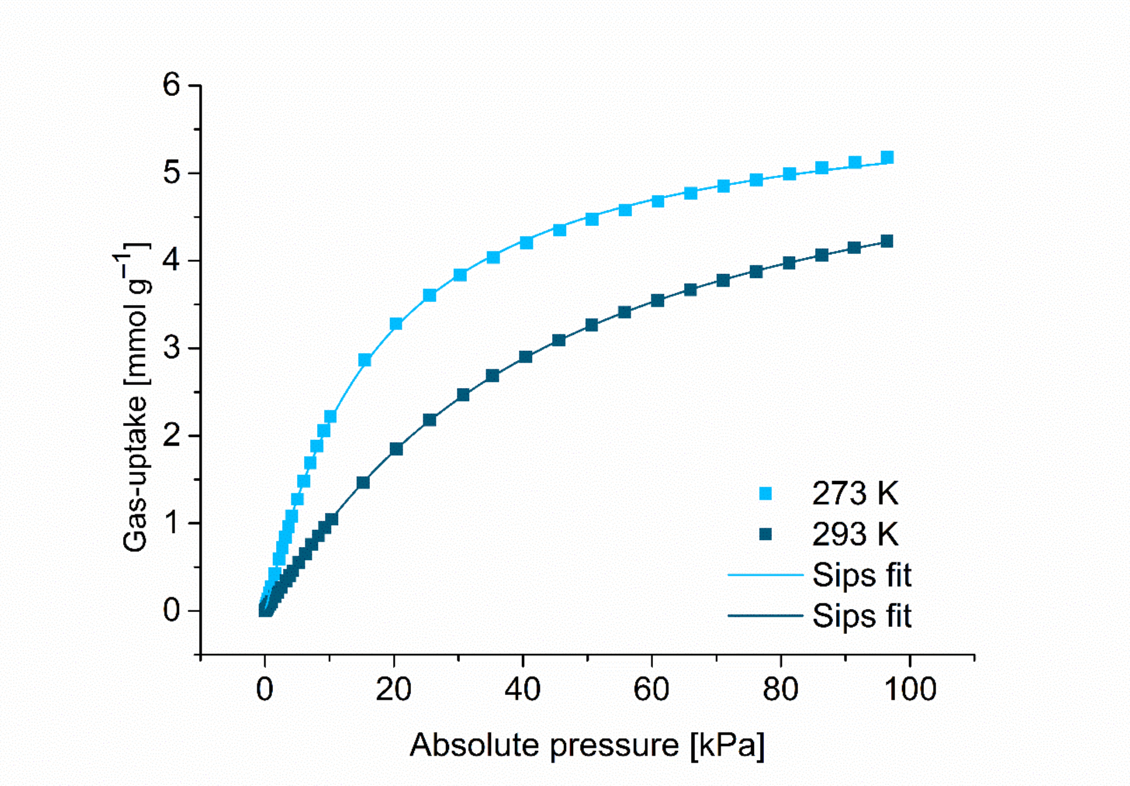

Figure S10. Sips fit of CO_2 for MIL-160 at 273 K and 293 K.

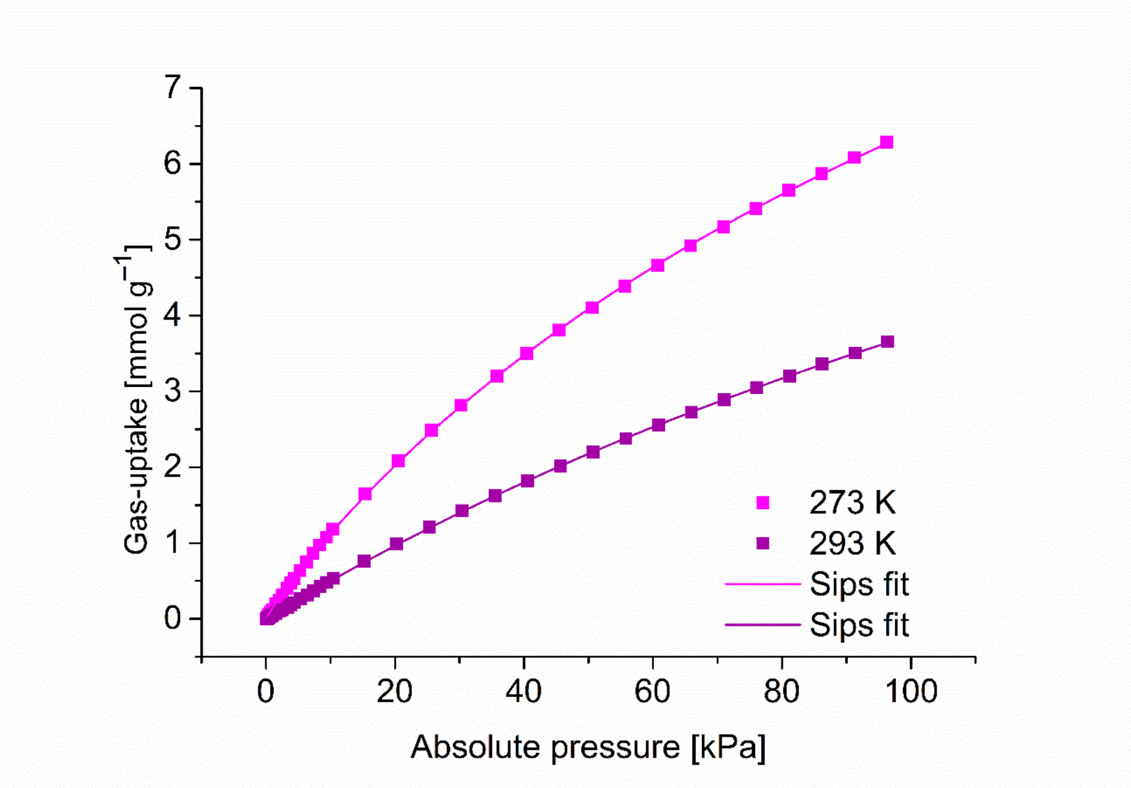

Figure S11. Sips fit of CO_2 for NH_2-MIL-125(Ti) at 273 K and 293 K.

IAST calculations

Selectivities of SO_2 over CO_2 and N_2 of MIL-160 and NH_2-MIL-125(Ti) were calculated from the dual-site Langmuir (DSLAI) (eq. 4) fitted isotherm data.

The 3P sim software (3P Instruments, Germany, version 1.1.0.7) calculates the maximal loadings of each gas depending on the given mole fraction.

IAST selectivities *S* of binary gas mixtures were calculated using equation 8, where x_i represents the absorbed gas amount and y_i the mole fraction of each adsorptive.

$$S = \frac{x_1/x_2}{y_1/y_2} \tag{8}$$

Table S1: Parameters for SIPS modeling and following simulation calculations.

				fit of isotherm				from fits simulated isotherm			
MOF	**Gas**	**Temp. [K]**	**Model**	**R²**	**affinity const. [1/bar]**	**max. loading [mmol/g]**	**heterogenity exponent**	**R²**	**affinity const. [1/bar]**	**max. loading [mmol/g]**	**heterogenity exponent**
MIL-160	SO_2	293	SIPS	0.972	108.281	7.623	0.443	0.954	157.829	7.242	0.458
	SO_2	313	SIPS	0.985	72.091	6.164	0.669	0.954	72.091	6.600	0.648
	SO_2	373	SIPS	0.999	8.532	5.084	1.090	0.988	11.372	4.998	1.096
	SO_2	353	SIPS	–	–	–	–	–	19.629	5.484	0.964
	CO_2	273	SIPS	0.999	5.892	5.931	1.056	0.985	5.515	6.353	1.066
	CO_2	293	SIPS	0.999	2.399	5.893	1.095	0.977	2.399	5.408	1.015
	CO_2	373	SIPS	0.999	0.220	2.792	1.125	0.956	0.210	2.841	1.128
	CO_2	353	SIPS	–	–	–	–	–	0.348	3.337	1.118
NH_2-MIL-125	SO_2	293	SIPS	0.997	22.359	11.775	0.706	0.985	17.855	11.760	0.693
	SO_2	313	SIPS	0.997	8.284	11.122	0.807	0.997	8.284	11.141	0.826
	SO_2	373	SIPS	0.998	1.610	9.478	1.143	0.973	1.356	9.474	1.138
	SO_2	353	SIPS	–	–	–	–	–	2.315	10.000	1.045
	CO_2	273	SIPS	0.999	1.086	12.013	1.040	0.999	0.997	12.812	1.018
	CO_2	293	SIPS	0.999	0.502	11.301	1.033	0.977	0.502	10.427	1.063
	CO_2	373	SIPS	0.992	0.072	4.501	1.204	0.989	0.067	4.574	1.196
	CO_2	353	SIPS	–	–	–	–	–	0.102	5.620	1.168

Table S2: Parameters for DSLAI modeling and following simulation calculations.

				fit of isotherm					from fits simulated isotherm				
MOF	**Gas**	**Temp. [K]**	**Model**	**R²**	**affinity const. 1 [1/bar]**	**max. loading 1 [mmol/g]**	**affinity const. 2 [1/bar]**	**max. loading 2 [mmol/g]**	**R²**	**affinity const. 1 [1/bar]**	**max. loading 1 [mmol/g]**	**affinity const. 2 [1/bar]**	**max. loading 2 [mmol/g]**
MIL-160	SO_2	293	DSLAI	0.994	691.984	4.622	3.363	3.123	0.934	787.437	4.638	3.834	2.914
	SO_2	313	DSLAI	0.997	217.734	4.222	3.016	2.481	0.910	217.734	4.203	3.834	2.722
	SO_2	373	DSLAI	0.999	9.535	3.123	5.123	2.272	0.999	10.523	3.127	3.834	2.220
	SO_2	353	DSLAI	–	–	–	–	–	–	25.766	3.451	3.834	2.376
	CO_2	273	DSLAI	0.999	3.155	4.696	13.949	1.792	0.986	3.889	5.017	9.939	1.823
	CO_2	293	DSLAI	0.999	1.306	5.866	4.859	1.226	0.989	1.306	5.400	4.859	1.200
	CO_2	373	DSLAI	0.994	0.046	7.128	0.763	0.225	0.982	0.053	7.246	0.598	0.226
	CO_2	353	DSLAI	–	–	–	–	–	–	0.104	6.733	0.923	0.343
NH_2-MIL-125	SO_2	293	DSLAI	0.998	45.054	9.069	0.560	5.210	0.969	184.670	9.258	4.629	2.055
	SO_2	313	DSLAI	0.999	20.598	7.002	0.648	7.717	0.981	48.410	7.938	3.587	2.563
	SO_2	373	DSLAI	0.999	3.098	2.500	0.484	13.017	0.993	0.960	4.291	1.700	6.207
	SO_2	353	DSLAI	–	–	–	–	–	–	2.166	5.004	1.985	4.976
	CO_2	273	DSLAI	0.999	1.924	5.063	0.176	20.151	0.984	2.082	5.471	0.177	21.385
	CO_2	293	DSLAI	0.999	0.536	6.732	0.063	24.221	0.984	0.536	6.110	0.063	22.487
	CO_2	373	DSLAI	0.999	0.010	9.318	0.003	27.086	0.975	0.010	9.501	0.003	27.491
	CO_2	353	DSLAI	–	–	–	–	–	–	0.023	8.508	0.006	26.144

3 Breakthrough experiments

Breakthrough curves were determined on an inhouse apparatus. The adsorbing unit consists of a stainless-steel column, which holds the adsorbent sample. The column is a ¼" Swagelok®-type tube with a length of max. 10 cm. The dosing unit consist of three different mass flow controllers (Bronkhorst High-Tech B.V., Netherlands, EL-Flow Prestige Series, max. flow 5 ml_N min^{-1}), each for the carrier gas (Nitrogen, Air Products, Purity 5.2, 99.9992%), CO_2 (Air Products, Purity 4.5, 99.995%) and a testing gas mixture of SO_2 in N_2 (Linde, 5 Vol.-% SO_2). An additional H_2O-bubbling system can be added to the carrier gas dosing unit. The adsorbing unit can be temperated by a thermostat (Julabo GmbH, Germany, Series F25) or by an electrical heating system. The gas phase could be analyzed in a bypass unit after the exit of the adsorber by an on-line mass selective detector (Pfeiffer Vacuum GmbH, Germany, Prisma QMS 200).

Around 110 mg of the sample were filled into the adsorber tube equipped with a stainless-steel seal and embedded in glass wool. The adsorbent material was regenerated at ~ 400 K until no other gas than nitrogen was detected. The sample was purged with 16.6 ml_N min^{-1} of carrier gas nitrogen during the regeneration time for the removal of preadsorbed fluids. After the regeneration step, the adsorber column was cooled down to the measurement temperature.

After regeneration, the adsorber was purged with the carrier gas nitrogen and the desired gas mixture was dosed into the system and the gas composition at the outlet of the adsorber was recorded. The measurements were finished after reaching steady state conditions with no significant change in gas composition and temperature. Between each breakthrough experiment the samples were regenerated again to ensure well defined starting conditions for the next experiment. All samples were weighted after the last regeneration step to get the amount of activated samples for further evaluations.

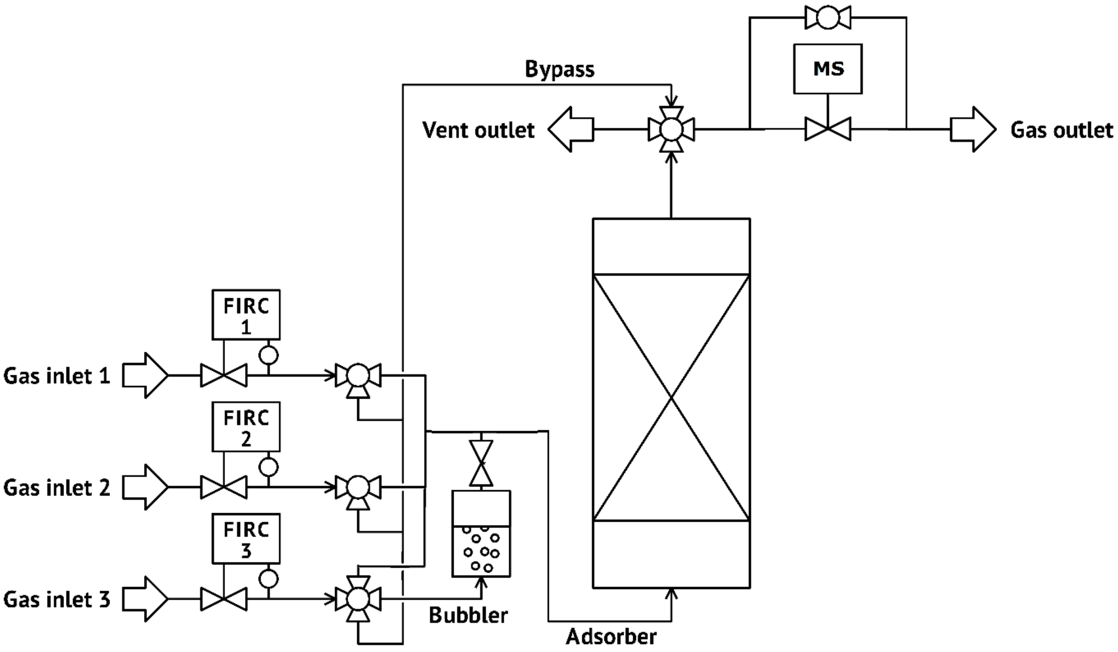

Scheme S1. Schematic of the apparatus used for breakthorguh curve measurements. The dosing unit consist of three mass flow controllers for three independent gas inlets. The carrier gas (gas inlet 3) could also be used for dosing different humidities to the adsorbing unit.

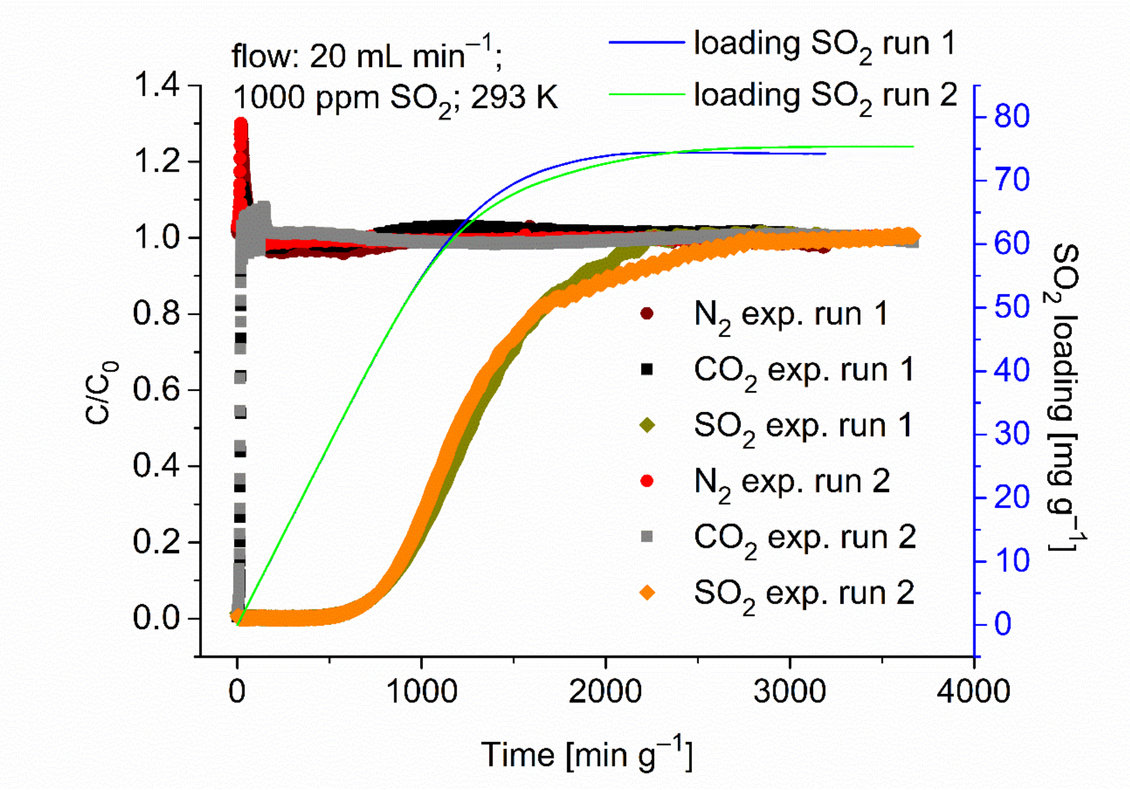

Figure S12. Experimental breakthrough curves of MIL-160 at 293 K with a gas mixture of $N_2/CO_2/SO_2$; 84.0/15.0/0.1; v:v:v (run 1 and 2).

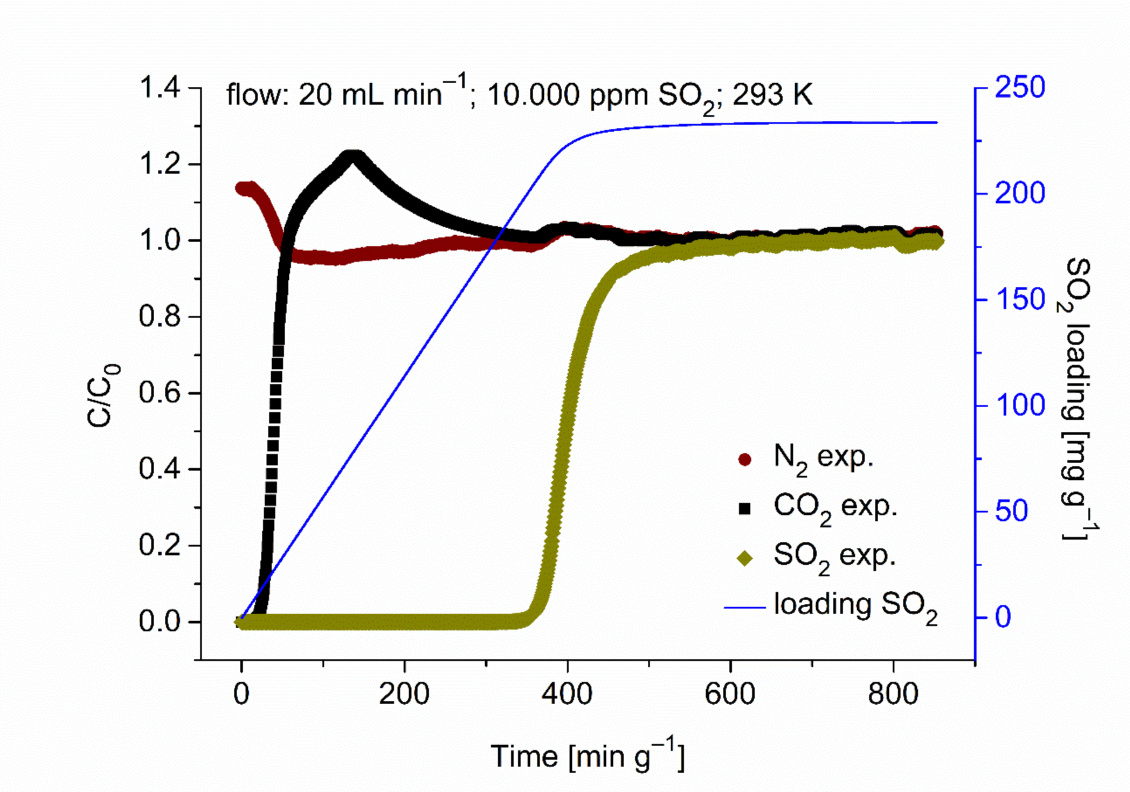

Figure S13. Experimental breakthrough curves of MIL-160 at 293 K with a gas mixture of $N_2/CO_2/SO_2$; 84.0/15.0/1.0; v:v:v.

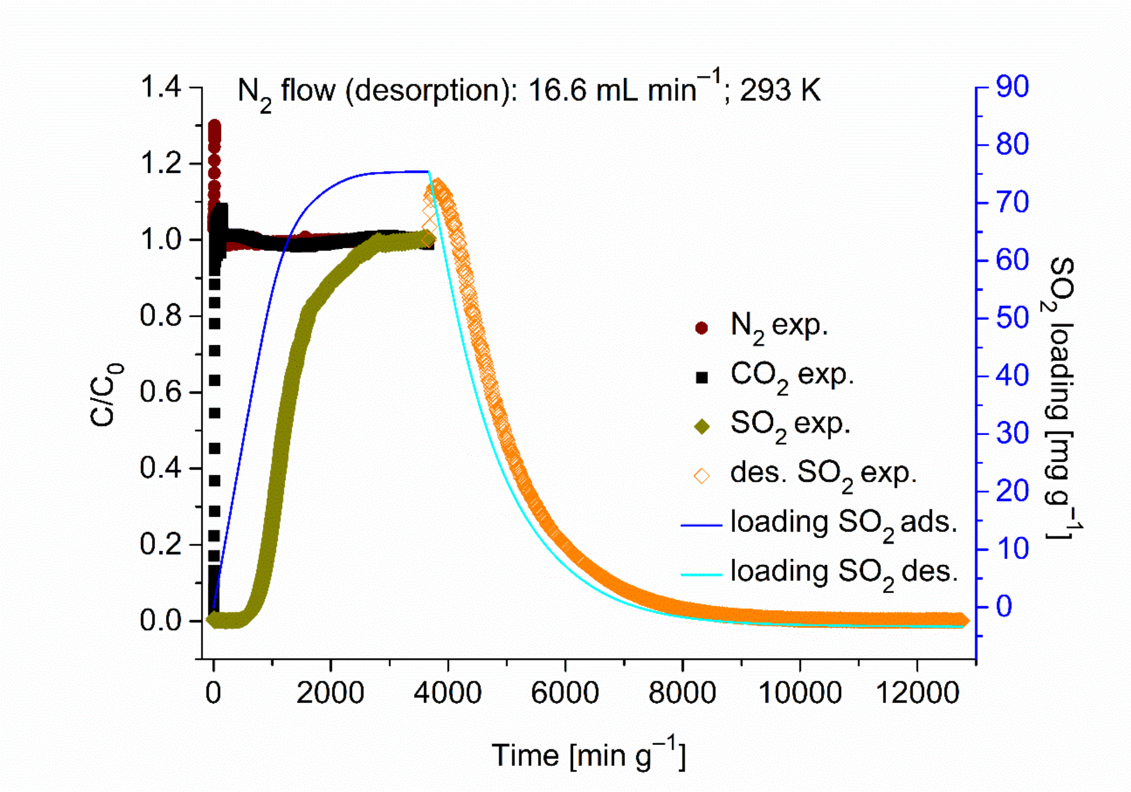

Figure S14. Reversible regeneration of MIL-160 under N$_2$ flow at 293 K.

Table S3. Comparison of maximal loadings under equilibrium or dynamic conditions with a partial pressure of 0.1% and 1% SO$_2$.

Material	SO$_2$-uptake [mmol g^{-1}]				
	Sorption exp. 0.001 bar, 293 K	Sorption exp. 0.01 bar, 293 K	Breakthrough exp. 0.1% SO$_2$, 293 K	Breakthrough exp. 0.1% SO$_2$, 353 K	Breakthrough exp. 1.0% SO$_2$ 293 K
MOF-177	0.07	0.25	-	-	-
NH$_2$-MIL-125(Ti)	0.50	3.0	-	-	-
MIL-160	1.8	4.2	1.17	0.85	3.65

4 Breakthrough simulations

Breakthrough simulations were calculated using 3P sim software calculations are based on a 30 cm high column with an inner diameter of 3 cm, axial dispersion of 50 cm^2 min^{-1} and a continuous gas flow of 20 mL min^{-1}.

Generally mass transfer coefficients in our dispersion model were set to 10 min^{-1} for all gases.

Due to our additional experimental breakthrough measurements for MIL-160 at 293 K and 353 K with flowrates of 20 ml min^{-1} for the ternary gas mixture (N_2/CO_2/SO_2 (84.9/15.0/0.1 v:v:v) we were able to optimize the mass transfer coefficient for SO_2 in our simulation for this specific experiments to 0.005 min^{-1} and the axial dispersion to 20 cm^2 min^{-1}.

4.1 DISPERSED PLUG MODEL

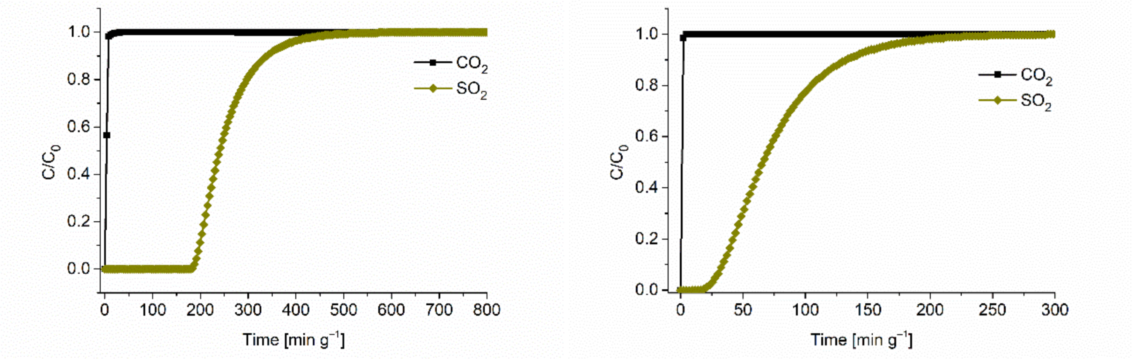

Figure S15. Breakthrough simulations of MIL-160 with CO_2/carrier gas/SO_2; 90/9.75/0.25; v:v:v at 293 (left) and 353 K (right).

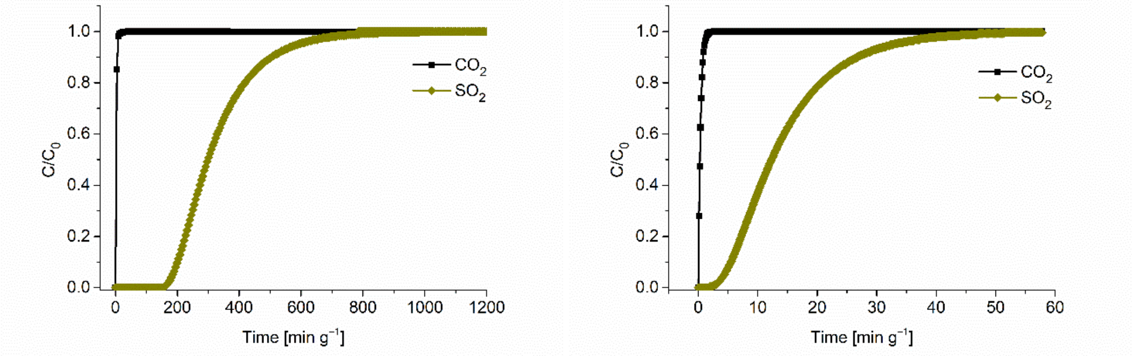

Figure S16. Breakthrough simulations of NH_2-MIL-125(Ti) with CO_2/carrier gas/SO_2; 90/9.75/0.25; v:v:v at 293 (left) and 353 K (right).

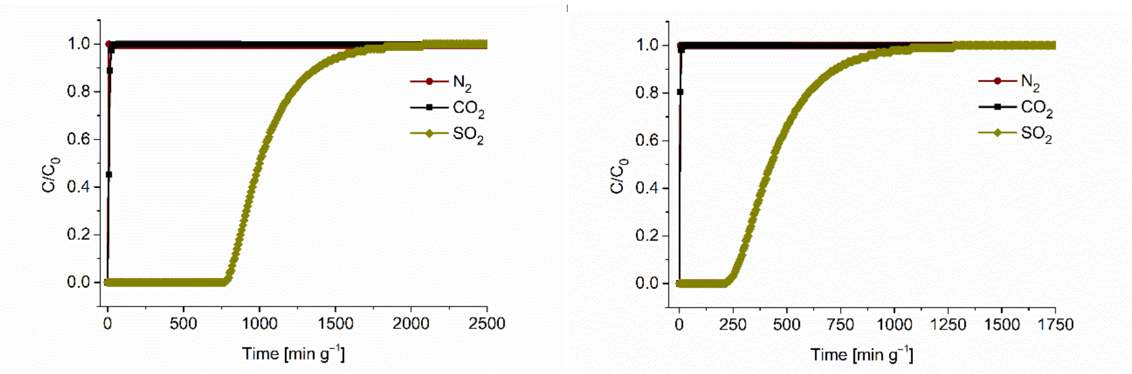

Figure S17. Breakthrough simulations of MIL-160 (left) and NH_2-MIL-125(Ti) (right) with SO_2/CO_2/N_2; 0.1/15.0/84.9; v:v:v at 293 K.

5 DFT calculations

Quantum mechanical calculations for MIL-160 alone and MIL-160 with adsorbed SO_2 were performed using density functional theory (DFT) and the Quantum-Espresso software.[17] The crystal structure of MIL-160 served as starting geometry. Oxygen atoms belonging to water were removed, and hydrogen atoms were added to saturate the furan linker and oxygen atoms forming OH-bridges. The structure was geometry-optimized using the Broyden-Fletcher-Goldfarb-Shanno (BFGS) scheme, ultrasoft Vanderbilt –type pseudoptentials and the generalized gradient approximation (GGA) with Perdew-Burke-Enzerhof (PBE) exchange correlation. To account for dispersion effects, the semi-empirical Grimme D2-correction scheme was applied.[18] Calculations were performed using the Monkhorst pack scheme with a 2 x 2 x 2 k-point mesh, an energy cutoff of 40 Rydberg and a charge cutoff of 400 Rydberg. After geometry optimization of the MIL-160 structure, SO_2 was placed at various locations and the geometries were allowed to fully relax. To compute the binding energy of SO_2, we optimized a single SO_2 molecule in an empty cell of the same size as the MIL-160 structure and under the same conditions stated before. The binding energy was then obtained as the difference between the sum of energies of MIL-160 and SO_2 and the energy of MIL-160 including the adsorbed SO_2 molecule.

6 Stability investigations

Experimental details: Before and after stability tests for dry and humid SO_2 exposure all MOFs were activated as described. For the dry exposure, a SO_2 isotherm was measured. For humid SO_2 exposure a controlled air flow of 2 L min^{-1} was bubbled through a sodium hydrogen sulfite solution (0.4 g $Na_2S_2O_5$ in 100 mL water) in a Schlenk round bottom flask to transport gaseous SO_2 into a humidity chamber (desiccator vessel). The desiccator was equipped with a crystallizing dish filled with saturated sodium chloride solution (80 mL, relative humidity (RH) 75%) and the sample (50 mg). The RH and the amount of SO_2 in the desiccator was monitored with a hygrometer (VWR TH300 hygrometer) and an SO_2-sensor (Dräger Pac 6000 electrochemical sensor), respectively. MIL-160 and NH_2-MIL-125(Ti) were exposed to a humid SO_2 environment at room temperature with 75 ± 6% RH and 35 ± 5 ppm SO_2 for 1 h and 5 h. The unit for humid SO_2 exposure is given by multiplying the concentration by the exposure time.

6.1 N_2-sorption isotherms before and after exposure to dry and humid SO_2

N_2-sorption isotherms were measured on an *Autosorb 6* (QUANTACHROME, Odelzhausen, Germany) instrument at 77 K within a pressure range of $1 \cdot 10^{-2}$-1 bar. Before each experiment samples were activated for at least 3 hours and at a minimum of 373 K under vacuum $<-5 \cdot 10^{-3}$ mbar.

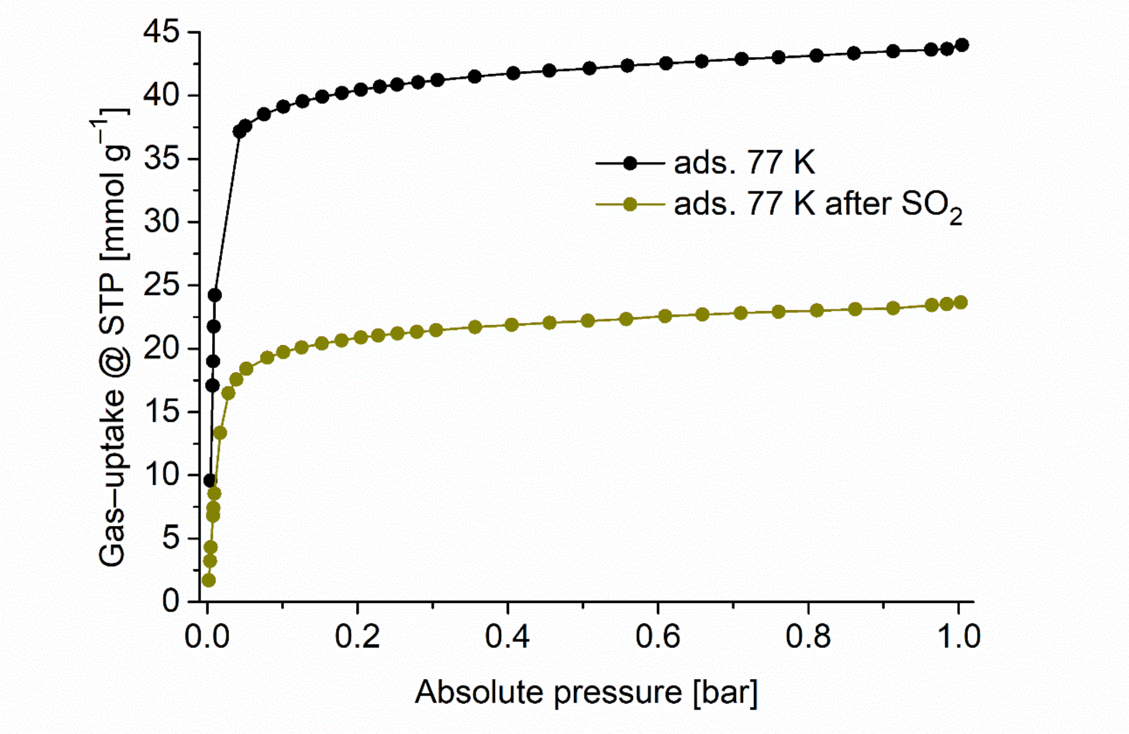

Figure S18. N_2-adsorption isotherms (77 K) of MOF-177 before and after exposure to dry or humid SO_2.

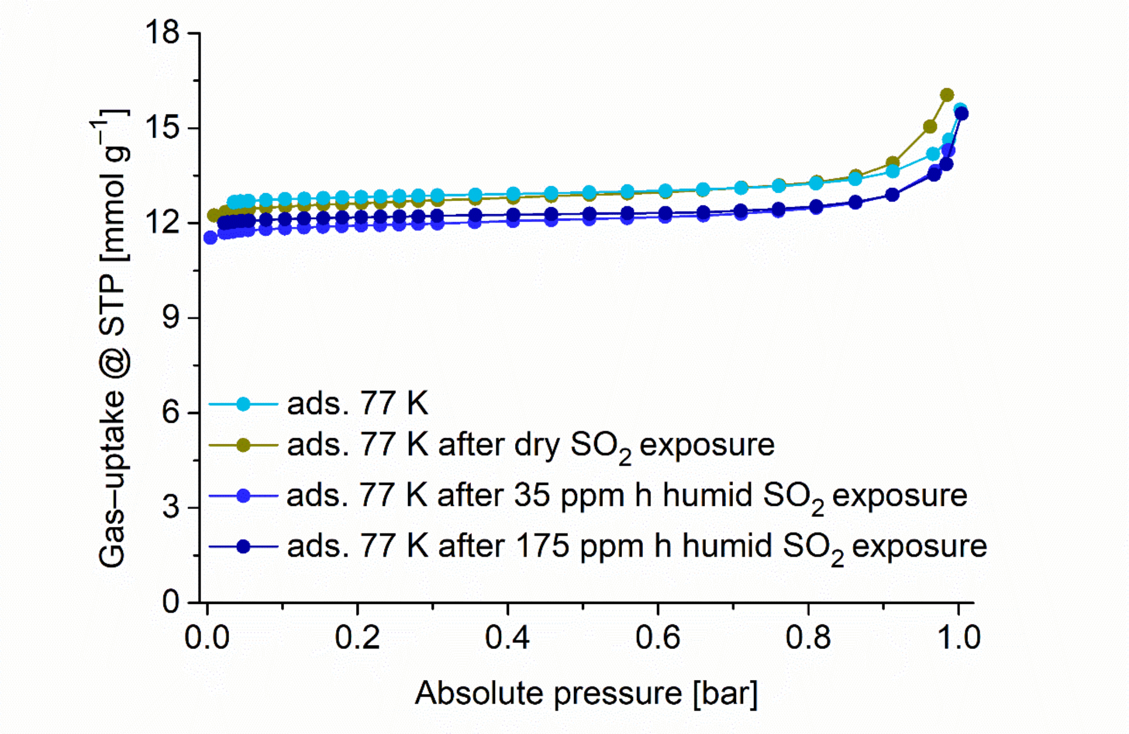

Figure S19. N_2-adsorption isotherms (77 K) of MIL-160 before and after exposure to dry or humid SO_2.

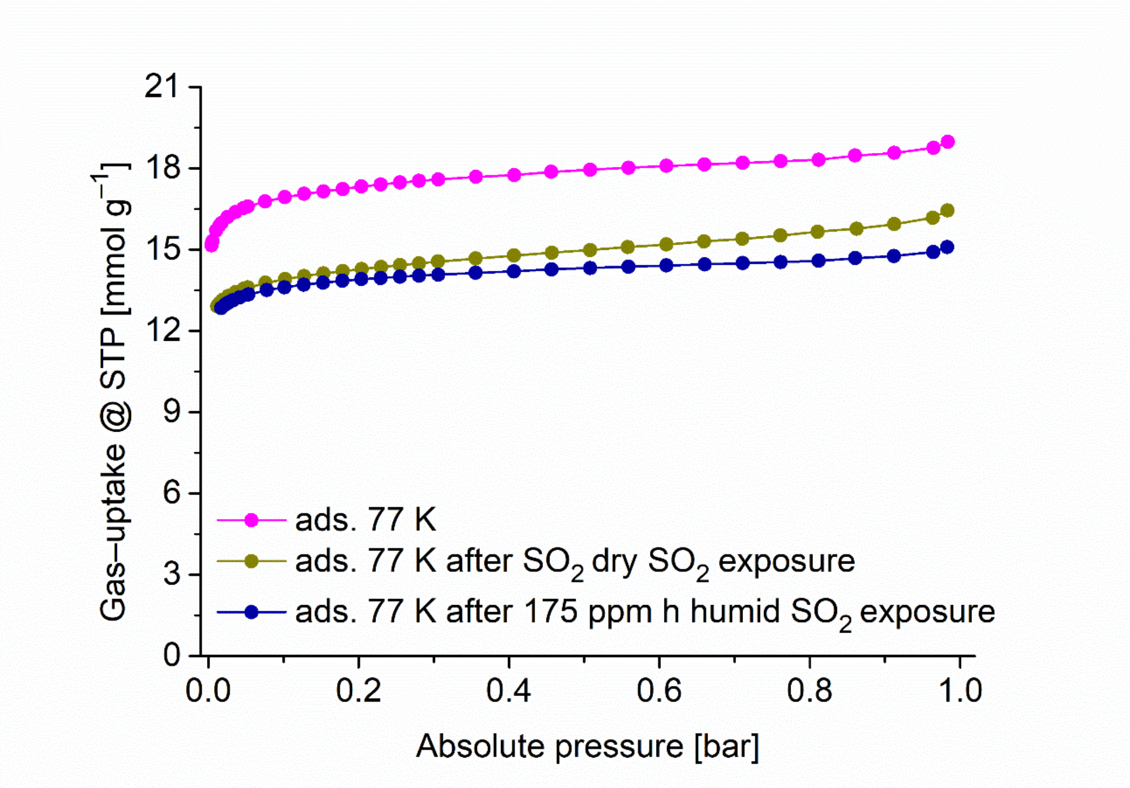

Figure S20. N_2-adsorption isotherms (77 K) of NH_2-MIL-125(Ti) before and after exposure to dry or humid SO_2.

6.2 SO_2-sorption cycling

Between each individual sorption experiment the samples were activated under same conditions.

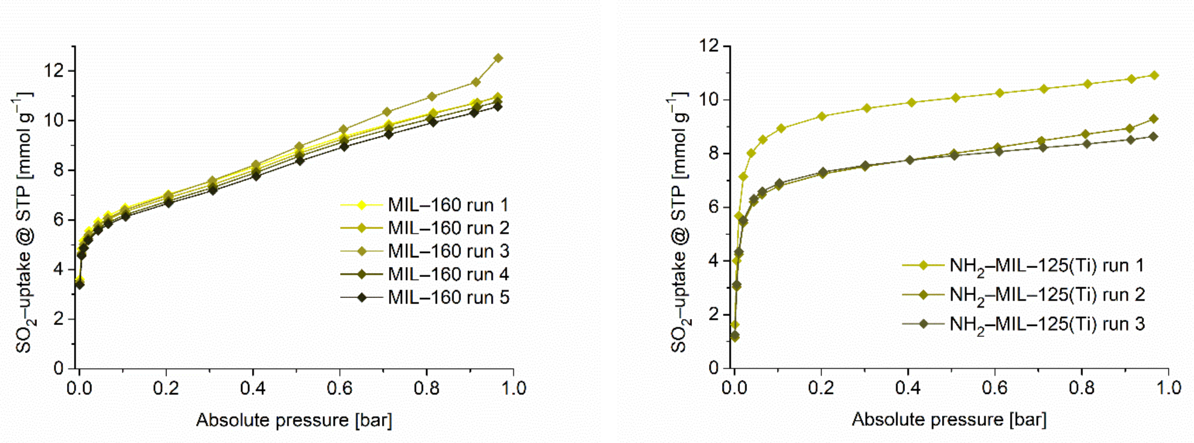

Figure S21. SO_2-sorption recycling of MIL-160 (left) and NH_2-MIL-125(Ti) (right) at 273 K.

Beginning at the third measurement of five cycles for MIL-160 a slightly higher SO_2-uptake was observed due to measurement inaccuracies. The more so as the samples had to be regenerated by heating to 373 K under vacuum and not by pressure-swing desorption due to the noted instrument time-limitations for SO_2 sorption (see Section 2 in Supporting Information).

6.3 PXRD

Powder X-ray diffraction (PXRD) measurements were performed on a Bruker *D2 Phaser* (300 W, 30 kV, 10 mA) at ambient temperatures. As radiation source a Cu-Kα-cathode (λ = 1.54182 Å) between 5° < 2Θ < 50° was used. Diffraction patterns were obtained using a silicon "low background" sample holder.

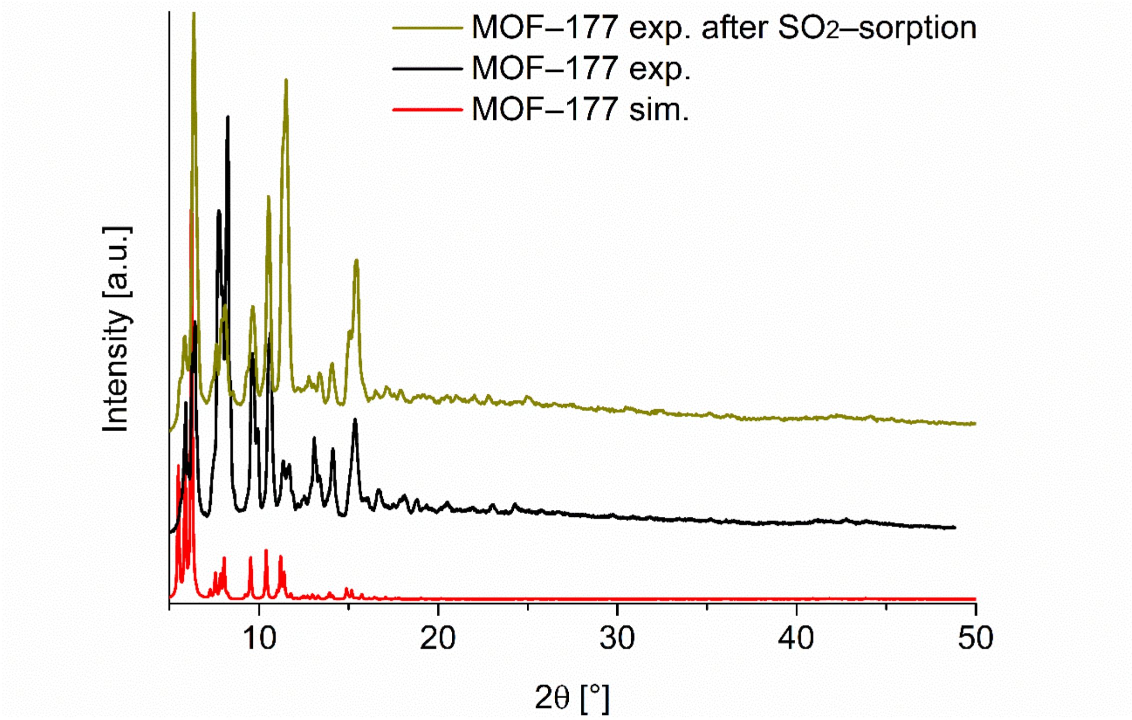

Figure S22. Comparison of PXRD patterns of MOF-177 (sim., based on crystal structure data, CCDC 230642, Reference 19).

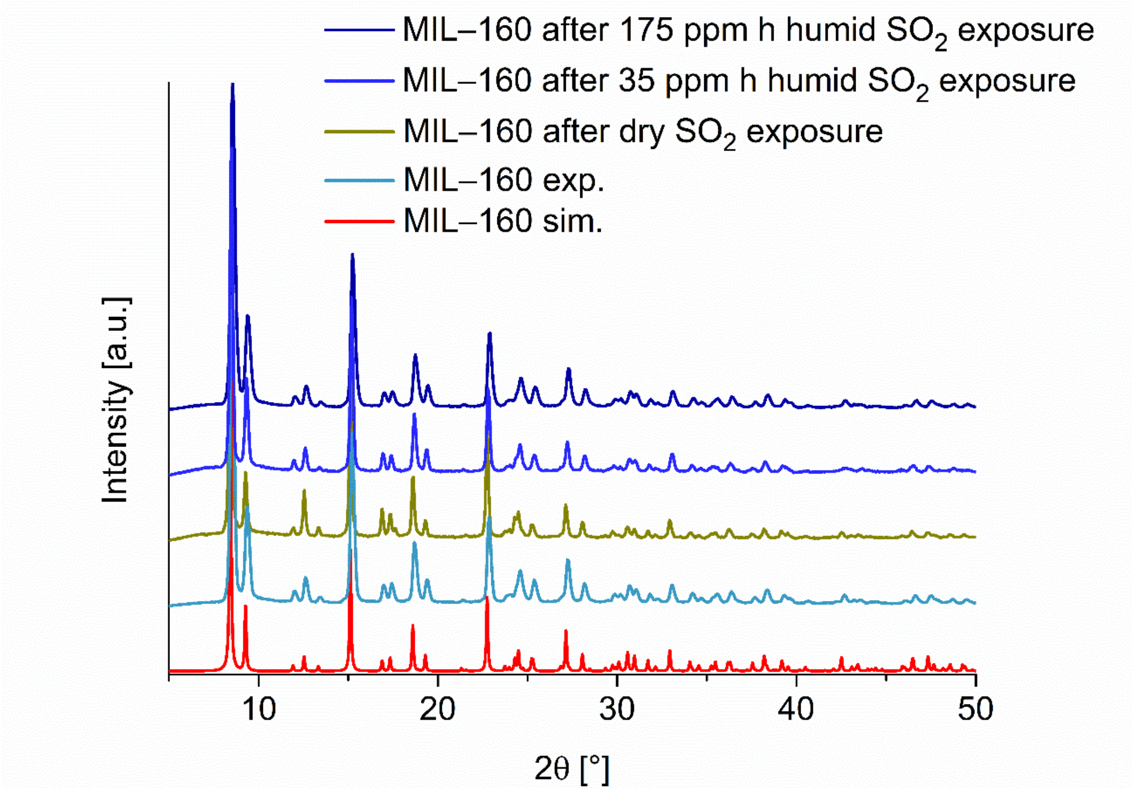

Figure S23. Comparison of PXRD patterns of MIL-160 (sim., based on x-ray data refinement, CCDC 1828694, Reference 9).

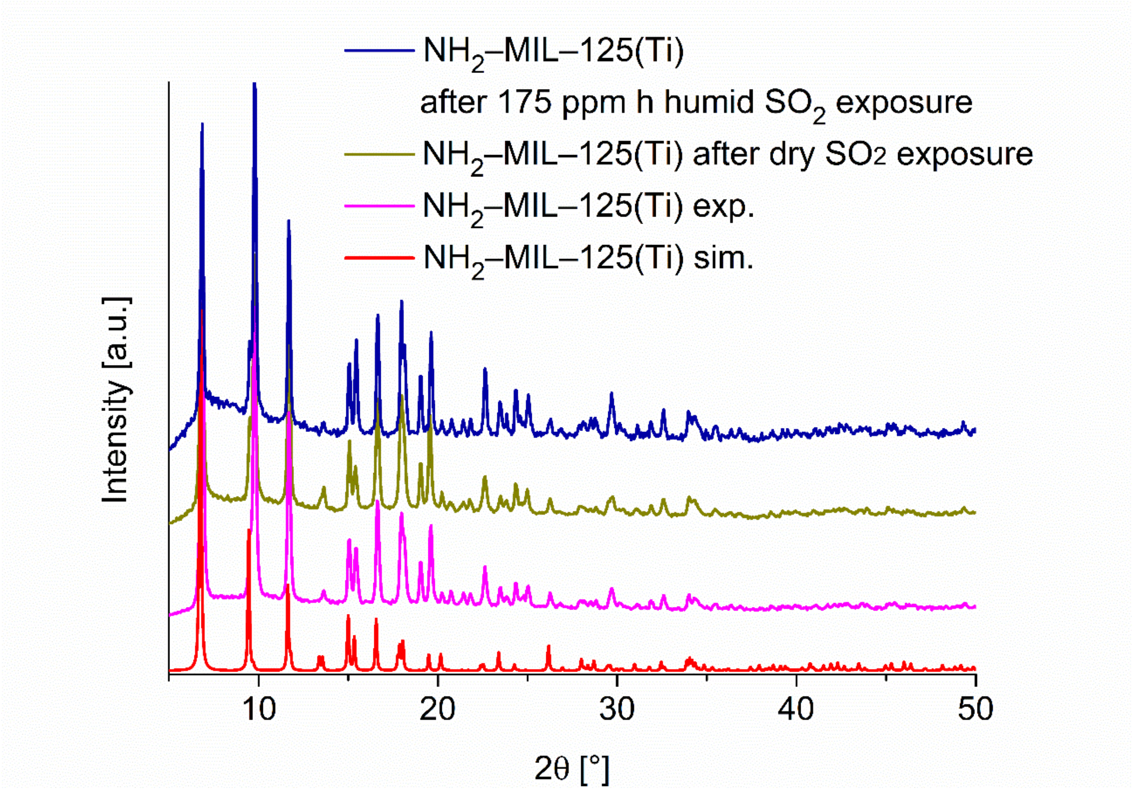

Figure S24. Comparison of PXRD patterns of NH_2-MIL-125(Ti) (sim., based on x-ray data refinement, CCDC 948966, Reference 20).

Table S4. Summary of stability tests for MOF-177, NH_2-MIL-125(Ti) and MIL-160.

Material	BET [m² g⁻¹]	BET after dry SO_2 [m² g⁻¹]	BET after humid SO_2 (35 ppm h at 75% RH) [m² g⁻¹]	BET after humid SO_2 (175 ppm h at 75% RH) [m² g⁻¹]	max. relative SO_2-uptake of multiple runs at 0.2 bar, with first run set to 100%	PXRD after SO_2-exposure
MOF-177	4100	2270	-	-	no multiple runs	changed
NH_2-MIL-125(Ti)	1560	1270	-	1250	100%, 77.7%, 77.9%	unchanged
MIL-160	1170	1170	1120	1130	100%, 98.0%, 99.4%, 96.2%, 94.9%	unchanged

7 Comparison of SO_2 sorption materials with literature

Table S5. Comparison of SO_2-uptake and characteristics of different MOFs.

Material	SO_2-uptake [mmol g^{-1}]			Temp. [K]	BET [m^2 g^{-1}]	Total pore-volume [cm^3 g^{-1}]	Pore width [Å]	Lit.
	0.01 bar	0.1 bar	1 bar					
MOF-177	0.3	1.0	25.7	293	4100	1.51	10.6-11.8[21,22]	this work
NH_2-MIL-125(Ti)	3.0	7.9	10.8	293	1560	0.651	5-8[23]	this work
MIL-160	4.2	5.5	7.2	293	1170	0.460	5[2]	this work
MIL-125(Ti)	-	3[a]	9.8[a]	298	1527	-	-	24
NH_2-MIL-125(Ti)	-	5[a]	9.7[a]	298	1861	-	-	24
MFM-600	-	~3[a]	5.0	298	2281	-	-	25
MFM-601	-	~8[a]	12.3	298	3644	-	-	25
SIFSIX-1-Cu	3.43	8.74	11.01	298	-	-	-	26
SIFSIX-2-Cu-i	4.16	6.01	6.90	298	630	-	-	26
MFM-300(Al)	-	-	8.1, ~5[a]	273, 298	1370	0.375	-	27, 28
MFM-300(In)	-	-	8.28	298	1071	0.419	-	29
MFM-202a	-	3.0	10.2	298	2220	-	-	30
ELM-12	-	1.95	2.73	298	706	0.26	4.3-6.1	31
[Zn_2(oxo-dihbac)$_2$(bipy)]	-	-	10.9	293	47 / 275[c]	0.059/ 0.098[c]	4.5-6.5, 8	32
Ni(bdc)(ted)$_{0.5}$	-	4.54	9.97	298	1783	0.74	7.8	33
Zn(bdc)(ted)$_{0.5}$	-	-	4.41	298	1888	0.84	7.8	33
Mg-MOF-74	-	6.44	8.60	298	1206	-	-	33, 34
FMOF-2	-	-	2.2	298	378	-	-	35
$Co_3[Co(CN)_6]_2$	-	-	2.5	298	712	-	-	36
$Zn_3[Co(CN)_6]_2$	-	-	1.8	298	700	-	-	36
MOF-505	-	-	12.9[a]	298	2216	0.73	8.3, 10.1	37
Ni-DMOF-TM	-	-	4.8[a]	298	940	0.459	-	38

[a] taken from isotherm, [b] at 1.11 bar, [c] emerged from CO_2 isotherm data.

8 References

---

(1) Li, X.; Cheng, F.; Zhang, S.; Chen, J. Shape-Controlled Synthesis and Lithium-Storage Study of Metal-Organic Frameworks Zn_4O(1,3,5-benzenetribenzoate)$_2$. *J. Power Sources* **2006**, *160*, 542–547.

(2) Permyakova, A.; Skrylnyk, O.; Courbon, E.; Affram, M.; Wang, S.; Lee, U.-H.; Valekar, A. H.; Nouar, F.; Mouchaham, G.; Devic, T.; De Weireld, G.; Chang, J.-S.; Steunou, N.; Frère, M.; Serre, C. Synthesis Optimization, Shaping, and Heat Reallocation Evaluation of the Hydrophilic Metal-Organic Framework MIL-160(Al). *ChemSusChem* **2017**, *10*, 1419–1426.

(3) Sohail, M.; Yun, Y.-N.; Lee, E.; Kim, S. K.; Cho, K.; Kim, J.-N.; Kim, T. W.; Moon, J.-H.; Kim, H. Synthesis of Highly Crystalline NH_2-MIL-125 (Ti) with S-Shaped Water Isotherms for Adsorption Heat Transformation. *Cryst. Growth Des.* **2017**, *17*, 1208–1213.

(4) Brandenburg, K.; *Diamond 4.3.1, Crystal and Molecular Structure Visualization*, Crystal Impact - K. Brandenburg & H. Putz GbR: Bonn, 2009.

(5) Feng, Y.; Wang, T.; Li, Y.; Li, J.; Wu, J.; Wu, B.; Jiang, L.; Wang, C. Steering Metallofullerene Electron Spin in Porous Metal-Organic Framework. *J. Am. Chem. Soc.* **2015**, *137*, 15055-15060.

(6) Cadiau, A.; Lee, J. S.; Borges, D. D.; Fabry, P.; Devic, T.; Wharmby, M. T.; Martineau, C.; Foucher, D.; Taulelle, F.; Jun, C.-H.; Hwang, Y. K.; Stock, N.; De Lange, M. F.; Kapteijn, F.; Gascon, J.; Maurin, G.; Chang, J.-S.; Serre, C. Design of Hydrophilic Metal Organic Framework Water Adsorbents for Heat Reallocation. *Adv. Mater.* **2015**, *27*, 4775-4780.

(7) Reinsch, H.; van der Veen, M. A.; Gil, B.; Marszalek, B.; Verbiest, T.; de Vos, D.; Stock, N. Structures, Sorption Characteristics, and Nonlinear Optical Properties of a New Series of Highly Stable Aluminum MOFs. *Chem. Mater.* **2012**, *25*, 17-26.

(8) Fröhlich, D.; Pantatosaki, E.; Kolokathis, P. D.; Markey, K.; Reinsch, H.; Baumgartner, M.; van der Veen, M. A.; de Vos, D. E.; Stock, N.; Papadopoulos, G. K.; Henninger, S. K.; Janiak, C. Water Adsorption Behaviour of CAU-10-H: a Thorough Investigation of its Structure–Property Relationships. *J. Mater. Chem. A* **2016**, *4*, 11859-11869.

(9) Wahiduzzaman, M; Lenzen, D.; Maurin, G.; Stock, N.; Wharmby, M. T. Rietveld Refinement of MIL-160 and its Structural Flexibility Upon H_2O and N_2 Adsorption. *Eur. J. Inorg. Chem.* **2018**, 3626-3632.

(10) Permyakova, A.; Skrylnyk, O.; Courbon, E.; Affram, M.; Wang, S.; Lee, U.-H.; Valekar, A. H.; Nouar, F.; Mouchaham, G.; Devic, T.; De Weireld, G.; Chang, J.-S.; Steunou, N.;

Frère, M.; Serre, C. Synthesis Optimization, Shaping, and Heat Reallocation Evaluation of the Hydrophilic Metal-Organic Framework MIL-160(Al). *ChemSusChem* **2017**, *10*, 1419–1426.

(11) Borges, D. D.; Maurin, G.; Galvao, D. S. Design of Porous Metal-Organic Frameworks for Adsorption Driven Thermal Batteries. *MRS Adv.* **2017**, *2*, 519-524.

(12) Dan-Hardi, D.; Serre, C.; Frot, T.; Rozes, L.; Maurin, Sanchez, C.; Férey, G. A New Photoactive Crystalline Highly Porous Titanium(IV) Dicarboxylate. *J. Am. Chem. Soc.* **2009**, *131*, 10857-10859.

(13) 3P INSTRUMENTS, 3P sim, Version 1.1.0.7, *Simulation and Evaluation Tool for mixSorb*, 3P INSTRUMENTS 2018.

(14) Jeppu, G. P.; Clement, T. P.; A Modified Langmuir-Freundlich Isotherm Model for Simulating pH-Dependent Adsorption Effects. *J. Contam. Hydrol.* **2012**, *129-130*, 46-53.

(15) Turiel, E.; Perez-Conde, C.; Martin-Esteban, A. Assessment of the Cross-Reactivity and Binding Sites Characterisation of a Propazine-Imprinted Polymer Using the Langmuir-Freundlich Isotherm. *Analyst* **2003**, *128*, 137-141.

(16) OriginLab Corporation, OriginPro, Version 9.0.0G., OriginLab Corporation 1991-2012.

(17) Giannozzi, P.; Baroni, S.; Bonini, N.; Calandra, M.; Car, R.;Cavazzoni, C.; Ceresoli, D.; Chiarotti, G. L.; Cococcioni, M.; Dabo, I.; Dal Corso, A.; de Gironcoli, S.; Fabris, S.; Fratesi, G.; Gebauer, R.; Gerstmann, U.; Gougoussis, C.; Kokalj, A.; Lazzeri, M.; Martin-Samos, L.; Marzari, N.; Mauri, F.; Mazzarello, R.; Paolini, S.; Pasquarello, A.; Paulatto, L.; Sbraccia, C.; Scandolo, S.; Sclauzero, G.; Seitsonen, A. P.; Smogunov, A.; Umari, P.; Wentzcovitch, R. M. QUANTUM ESPRESSO: A Modular and Open-Source Software Project for Quantum Simulations of Materials. *J. Phys.: Condens. Matter* **2009**, *21*, 395502, 1-19.

(18) Grimme, S. Semiempirical GGA-Type Density Functional Constructed with a Long-Range Dispersion Correction. *J. Comput. Chem.* **2006**, *27*, 1787–1799.

(19) Chae, H. K.; Siberio-Pérez, D. Y.; Kim, J.; Go, Y.; Eddaoudi, M.; Matzger, A. J.; O´Keeffe, M. Yaghi, O. M. A Route to High Surface Area, Porosity and Inclusion of Large Molecules in Crystals. *Nature* **2004**, *427*, 521–523.

(20) Smalley, A. P.; Reid, D. G.; Tan, J. C.; Lloyd, G. O. Alternative Synthetic Methodology for Amide Formation in the Post-Synthetic Modification of Ti-MIL125-NH_2. *CrystEngComm* **2013**, *15*, 9368-9371.

(21) Saha, D.; Deng, S. Hydrogen Adsorption on Metal-Organic Framework MOF-177. *Tsinghua Sci. Technol.* **2010**, *15*, 363–376.

---

(22) Peterson, G. W.; Mahle, J.; Balboa, A.; Wagner, G.; Sewell, T.; Karwacki, C. J. Defense Technical Information Center: Fort Belvoir, VA, 2008.

(23) Fan, Y.-H.; Zhang, S.-W.; Qin, S.-B.; Li, X.-S.; Qi, S.-H. An Enhanced Adsorption of Organic Dyes onto NH_2 Functionalization Titanium-Based Metal-Organic Frameworks and the Mechanism Investigation. *Microporous Mesoporous Mater.* **2018**, *263*, 120–127.

(24) Mounfield, W. P.; Han, C.; Pang, S. H.; Tumuluri, U.; Jiao, Y.; Bhattacharyya, S.; Dutzer, M. R.; Nair, S.; Wu, Z.; Lively, R. P.; Sholl, D. S.; Walton, K. S. Synergistic Effects of Water and SO_2 on Degradation of MIL-125 in the Presence of Acid Gases. *J. Phys. Chem. C* **2016**, *120*, 27230–27240.

(25) Carter, J. H.; Han, X.; Moreau, F. Y.; da Silva, I.; Nevin, A.; Godfrey, H. G. W.; Tang, C. C.; Yang, S.; Schröder, M. Exceptional Adsorption and Binding of Sulfur Dioxide in a Robust Zirconium-Based Metal-Organic Framework. *J. Am. Chem. Soc.* **2018**, *140*, 15564-15567.

(26) Cui, X.; Yang, Q.; Yang, L.; Krishna, R.; Zhang, Z.; Bao, Z.; Wu, H.; Ren, Q.; Zhou, W.; Chen, B.; Xing, H. Ultrahigh and Selective SO_2 Uptake in Inorganic Anion-Pillared Hybrid Porous Materials. *Adv. Mater.* **2017**, *29*, 1606929.

(27) Yang, S.; Sun, J.; Ramirez-Cuesta, A. J.; Callear, S. K.; David, W. I. F.; Anderson, D. P.; Newby, R.; Blake, A. J.; Parker, J. E.; Tang, C. C.; Schröder, M. Selectivity and Direct Visualization of Carbon Dioxide and Sulfur Dioxide in a Decorated Porous Host. *Nat. Chem.* **2012**, *4*, 887–894.

(28) Han, X.; Godfrey, H. G. W.; Briggs, L.; Davies, A. J.; Cheng, Y.; Daemen, L. L.; Sheveleva, A. M.; Tuna, F.; McInnes, E. J. L.; Sun, J.;Drathen, C.; George, M. W.; Ramirez-Cuesta, A. J.; Thomas, K. M.; Yang, S.; Schröder, M. Reversible Adsorption of Nitrogen Dioxide Within a Robust Porous Metal-Organic Framework. *Nat. Mater.* **2018**, *17*, 691–696.

(29) Savage, M.; Cheng, Y.; Easun, T. L.; Eyley, J. E.; Argent, S. P.; Warren, M. R.; Lewis, W.; Murray, C.; Tang, C. C.; Frogley, M. D; Cinque, G.; Sun, J.; Rudić, S.; Murden, R. T.; Benham, M. J.; Fitch, A. N.; Blake, A. J.; Ramirez-Cuesta, A. J.; Yang, S.; Schröder, M. Selective Adsorption of Sulfur Dioxide in a Robust Metal-Organic Framework Material. *Adv. Mater.* **2016**, *28*, 8705–8711.

(30) Yang, S.; Liu, L.; Sun, J.; Thomas, K. M.; Davies, A. J.; George, M. W.; Blake, A. J.; Hill, A. H.; Fitch, A. N.; Tang, C. C.; Schröder, M. Irreversible Network Transformation in a Dynamic Porous Host Catalyzed by Sulfur Dioxide. *J. Am. Chem. Soc.* **2013**, *135*, 4954–4957.

(31) Zhang, Y.; Zhang, P.; Yu, W.; Zhang, J.; Huang, J.; Wang, J.; Xu, M.; Deng, Q.; Zeng, Z.; Deng, S. Highly Selective and Reversible Sulfur Dioxide Adsorption on a Microporous Metal-Organic Framework via Polar Sites. *ACS Appl. Mater. Interfaces* **2019**, DOI: 10.1021/acsami.9b01423.

(32) Glomb, S.; Woschko, D.; Makhloufi, G.; Janiak, C. Metal-Organic Frameworks with Internal Urea-Functionalized Dicarboxylate Linkers for SO_2 and NH_3 Adsorption. *ACS Appl. Mater. Interfaces* **2017**, *9*, 37419–37434.

(33) Tan, K.; Canepa, P.; Gong, Q.; Liu, J.; Johnson, D. H.; Dyevoich, A.; Thallapally, P. K.; Thonhauser, T.; Li, J.; Chabal, Y. J. Mechanism of Preferential Adsorption of SO_2 into Two Microporous Paddle Wheel Frameworks M(bdc)(ted)$_{0.5}$. *Chem. Mater.* **2013**, *25*, 4653–4662.

(34) Grant Glover, T.; Peterson, G. W.; Schindler, B. J.; Britt, D.; Yaghi, O. M. MOF-74 Building Unit has a Direct Impact on Toxic Gas Adsorption. *Chem. Eng. Sci.* **2011**, *66*, 163–170.

(35) Fernandez, C. A.; Thallapally, P. K.; Motkuri, R. K.; Nune, S. K.; Sumrak, J. C.; Tian, J.; Liu, J. Gas-Induced Expansion and Contraction of a Fluorinated Metal−Organic Framework. *Cryst. Growth Des.* **2010**, *10*, 1037–1039.

(36) Thallapally, P. K.; Motkuri, R. K.; Fernandez, C. A.; McGrail, B. P.; Behrooz, G. S. Prussian Blue Analogues for CO_2 and SO_2 Capture and Separation Applications. *Inorg. Chem.* **2010**, *49*, 4909–4915.

(37) Song, X.-D.; Wang, S.; Hao, C.; Qiu, J.-S. Investigation of SO_2 Gas Adsorption in Metal–Organic Frameworks by Molecular Simulation. *Inorg. Chem. Commun.* **2014**, *46*, 277–281.

(38) Hungerford, J.; Bhattacharyya, S.; Tumuluri, U.; Nair, S.; Wu, Z.; Walton, K. S. DMOF-1 as a Representative MOF for SO_2 Adsorption in Both Humid and Dry Conditions. *J. Phys. Chem. C* **2018**, *122*, 23493-23500.

3.3 High performance MIL-101(Cr)@6FDA-*m*PD and MOF-199@6FDA-*m*PD mixed-matrix membranes for CO_2/CH_4 separation

Alexander Nuhnen, Maximilian Klopotowski, Harold B. Tanh Jeazet, Sara Sorribas, Beatriz Zornoza, Carlos Téllez, Joaquín Coronas, Christoph Janiak

Dalton Trans., **2020**, 49, 1822–1829.

DOI: 10.1039/C9DT03222C

Die Membrantechnologie spielt eine wichtige Rolle bei der Reduktion des Ausstoßes von umweltschädlichen Stoffen und den operativen Kosten von kommerziellen Separationsprozessen. Energieeffiziente Membrantechnologien könnten den Energieverbrauch im Vergleich zu konventionellen Methoden der Gastrennung um bis zu 50 % reduzieren. Aufgrund der begrenzten Leistungsfähigkeit von reinen Polymermembranen in Bezug auf ihre Separationseigenschaften (*upper bound*), steht die Entwicklung von Mixed-Matrix-Membranen in den letzten Jahren im Fokus von vielen wissenschaftlichen Arbeiten. In dieser Arbeit wurden zwei bekannte MOFs, MIL-101(Cr) und MOF-199, synthetisiert und in das Polymer 6FDA-mPD eingebettet. REM/EDX-Aufnahmen zeigten eine exzellente Verteilung der MOF-Partikel in den MMMs und Permeationsstudien mit einem binären Gasgemisch von CO_2/CH_4 (50:50, v:v) zeigten erhöhte Gaspermeabilitäten (bis zu 400 % höher für 24 wt% MIL-101(Cr)@6FDA-mPD MMMs im Vergleich zum reinen Polymer) für beide MMMs abhängig vom zusätzlich eingebrachtem freien Volumen durch die MOF-Partikel. Außerdem konnte die Selektivität der MOF-199@6FDA-mPD-MMMs nahezu verdoppelt werden, wodurch die Permeationseigenschaften der 24 wt% MOF-199@6FDA-mPD-MMMs in die Nähe der Robeson upper bound von 2008 verschoben wurden.

Anteile an der Veröffentlichung:

- Große Teile der experimentellen Arbeiten im Labor und der Durchführung der Analytik, die Auswertung der Ergebnisse, das Erstellen von Abbildungen und Tabellen und maßgebliche Verfassung des Manuskripts. Korrekturen wurden von Herrn Prof. Dr. Janiak und Prof. Dr. Joaquín Coronas vorgenommen.
- Die REM/EDX-Messungen und die Herstellung des Polymers wurden von Herrn Maximilian Klopotowski durchgeführt.
- Harold B. Tanh Jeazet hat das Projekt gestartet, an der Erstellung des Manuskripts mitgewirkt und Teile der MMMs hergestellt.
- Sara Sorribas, Beatriz Zornoza und Carlos Téllez haben die Gaspermeationsmessungen in Spanien durchgeführt

Dalton Transactions

ROYAL SOCIETY OF CHEMISTRY

PAPER

Cite this: *Dalton Trans.*, 2020, **49**, 1822

High performance MIL-101(Cr)@6FDA-*m*PD and MOF-199@6FDA-*m*PD mixed-matrix membranes for CO_2/CH_4 separation†

Alexander Nuhnen,[a] Maximilian Klopotowski,[a] Harold B. Tanh Jeazet,[a] Sara Sorribas,[b] Beatriz Zornoza,[b,c] Carlos Téllez,[b] Joaquín Coronas *[b] and Christoph Janiak *[a]

Received 7th August 2019,
Accepted 13th January 2020

DOI: 10.1039/c9dt03222c

rsc.li/dalton

Combination of the polyimide 6FDA-*m*PD (6FDA = 4,4′-hexafluoroisopropylidene diphthalic anhydride and *m*PD = *m*-phenylenediamine) and crystallites of the metal–organic frameworks (MOFs) MIL-101(Cr) or MOF-199 (HKUST-1, Cu-BTC) produces mixed-matrix membranes (MMMs) with excellent dispersion and compatibility of the MOF particles within the polymer matrix. Permeation tests of a binary CO_2/CH_4 (50/50) gas mixture showed a remarkable increase of CO_2 permeabilities for MIL-101(Cr)@6FDA-*m*PD and significantly higher selectivities for MOF-199@6FDA-*m*PD. The CO_2 permeability increased from 10 (neat polymer) to 50 Barrer for the 24 wt% MIL-101(Cr)@6FDA-*m*PD membrane (with essentially constant selectivity) due to the high pore volume of MIL-101(Cr). The CO_2/CH_4 selectivity increased from 54 to 89 from the neat 6FDA-*m*PD polymer to the 24 wt% MOF-199@6FDA-*m*PD membrane, apparently due to the high CO_2 adsorption capacity of MOF-199.

Introduction

Membrane technology plays an important role in the reduction of the environmental impact and operational costs of industrial separation processes as energy costs increase. As a result, application of membrane technology can help to save energy up to 50% of the production costs.[1,2] As the ratio between equipment size and production capacity decrease, membrane technologies address the requirements of process intensification.[3] Distillation and absorption-based processes are among conventional technologies that require a phase change in the mixture to be separated. This phase change increases significantly the energy loss which may be avoided in the case of membrane gas separation which does not require a phase change.[4] Separation through membranes is mainly based on the size and shape of the molecules to be separated and on their interaction with the membrane material.[5] The commercially applied membrane materials are mostly made from polymers. These are cheaper to produce and easier to process as flat sheet or hollow fiber membranes than inorganic materials.[6]

The most basic requirements for choosing membrane materials are the selectivity and the permeability parameters. These can be mainly used to determine the economic performance of membrane processes.[7] From this point of view, the existing polymeric membrane materials are not optimal: improvement in permeability is always at the expense of selectivity, and *vice versa*.[8] Also plasticization hinders the application of polymeric membranes at high pressures since the swelling and dilatation of the polymer due to high concentration of adsorbates may induce an increase in the mobility of the polymer chains and therefore reduce the membrane selectivity.[6]

To improve the performance of polymeric membranes several solutions have been proposed during the last decades. Various polymers have been modified using different types of inorganic additives such as zeolites, mesoporous silicas, activated carbons, carbon nanotubes and non-porous solids to produce mixed-matrix membranes (MMMs).[7,9–20] MMMs are composite membranes consisting of micro- or nanoparticles of an inorganic or inorganic–organic hybrid material (dispersed phase) incorporated into a polymer matrix (continuous phase). Polymer, filler properties, filler loading and homogeneous dispersion affect the MMM morphology as well as the separation performance.[7,13] The chemical structure, surface chemistry, particle size distribution and aspect ratio are key parameters

---

[a] *Institut für Anorganische Chemie und Strukturchemie, Heinrich-Heine-Universität Düsseldorf, 40204 Düsseldorf, Germany. E-mail: janiak@hhu.de*

[b] *Chemical and Environmental Engineering Department, Instituto de Nanociencia de Aragon, Instituto de Ciencia de Materiales de Aragón (ICMA), Universidad de Zaragoza-CSIC, 50018 Zaragoza, Spain. E-mail: coronas@unizar.es*

[c] *Department of Energy and Environment, Instituto de Carboquímica-ICB-CSIC, Miguel Luesma Castán 4, 50018 Zaragoza, Spain*

† Electronic supplementary information (ESI) available: TGA, PXRDs, SEM-EDX, Maxwell model, permeation data, T_g. See DOI: 10.1039/c9dt03222c

of the filler. MMMs may provide separation properties which can be above the so-called Robeson upper bound.[18]

Recent advances have shifted towards the use of metal organic frameworks (MOFs) as potential fillers in the polymer matrix.[21] MOFs exhibit advantages over zeolites and therefore are potential additives for deep impact in MMM separation properties.[22–27] For example, because of the broad variety of functionalities of organic ligands in MOFs, they can interact strongly with the polymer phase, so that the volume of micro gaps between inorganic and organic phase, which cause loss in selectivity, can be diminished.[12–14] To obtain materials with optimized separation properties a perfect interaction between the two components has to be established for the preparation of MMMs together with a good dispersion avoiding as much as possible filler agglomeration. In addition, MOFs are not only tuneable concerning their chemical groups, but also for their textural properties (pore volume and surface area).[28] Therefore, the MOF effect on the membrane properties can be higher for a given mass loading than that corresponding to conventional fillers. As emphasized in theoretical predictions, the choice of suitable MOF/polymer pairs is necessary for high-performance MMMs in addition to the control of interface morphology.[29]

Different to the studies made on continuous (pure) MOF membranes[24,26,30] we present herein results on the CO_2/CH_4 separation with MMMs of MIL-101(Cr)[31] or MOF-199 (also named HKUST-1 or Cu-BTC)[32] with the polyimide 6FDA-*m*PD (Scheme 1) (6FDA = 4,4′-hexafluoroisopropylidene diphthalic anhydride and *m*PD = *m*-phenylenediamine). The neat polyimide 6FDA-*m*PD is thermally stable until about 500 °C (Fig. S1 in ESI†) and shows excellent mechanical stability.[33] Furthermore, 6FDA-*m*PD features good properties in both permeation and selectivity for CO_2/CH_4 separation processes.[33]

The CO_2 sorption of MOFs has been the subject of intense interest for "carbon capture".[34] MIL-101(Cr) exhibits a moderate CO_2 uptake of 10.5 wt% (1 bar, 293 K),[35] while MOF-199 is one of the best MOFs for CO_2 adsorption with an uptake capacity of 27 wt% (1 bar, 298 K).[36]

Even though it has been shown in the last years that several MOFs are very interesting for the fabrication of MMMs with very attractive separation characteristics (see Table S5 in ESI† for some specific examples),[9,10,12,13] the separation performance of the present study is remarkable. Particularly, we present here MOF-containing gas-separation membranes with technologically attractive properties.

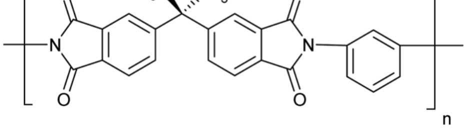

Scheme 1 6FDA-*m*PD repeating unit (6FDA = 4,4′-hexafluoroisopropylidene diphthalic anhydride and *m*PD = *m*-phenylenediamine).

Experimental

Materials and methods

Chromium nitrate nonahydrate ($Cr(NO_3)_2 \cdot 9H_2O$, 99%) hydrofluoric acid (analysis grade), toluene (>99%) and triethylamine (99%) were obtained from Acros Organics. Methanol (99.8%), *m*-phenylenediamine (*m*PD, 99%) and acetic anhydride (>97%) were acquired from fisher scientific. Copper acetate monohydrate $Cu(OAc)_2 \cdot H_2O$, (99%) was purchased from Aldrich. Benzene-1,3,5-tricarboxylic acid (H_3BTC, 99%) and benzene-1,4 dicarboxylic acid (H_2BDC, 98%) were acquired from Aldrich. 4,4′-Hexafluoroisopropylidene diphthalic anhydride (6FDA, >98%) and *N*,*N*-dimethyl acetamide (DMAc, >99%) were obtained from TCI. Dichloromethane (DCM, >99.9%), *N*,*N*-dimethylformamide (DMF, 99.9%) and ethanol (99.9%) were purchased from Prolabo. Gases CO_2 and CH_4 were supplied by Air Liquide (Germany) and used as received (purity 99.995%).

Powder X-ray diffraction patterns (PXRD) were obtained on a Bruker D2 Phaser powder diffractometer with a flat silicon, low background sample holder, at 30 kV, 10 mA for Cu-Kα radiation (λ = 1.5418 Å). In all diffractograms, the most intense reflection was normalized to 1.

Nitrogen sorption isotherms were measured at 77 K using a Quantachrome Autosorb iQ MP gas sorption analyzer. Ultra-high purity (UHP, grade 5.0, 99.999%) nitrogen, and helium gases were used; the latter was used for performing cold and warm free space correction measurements. MIL-101(Cr) and MOF-199 BET surface areas (2770 $m^2 g^{-1}$ and 950 $m^2 g^{-1}$, respectively) and pore sizes were calculated using sample weights after degassing for 2 h at 150 °C with the built-in oil-free vacuum system of the instrument (ultimate vacuum <10^{-8} mbar).

To acquire scanning electron microscopy (SEM) images alone, the MOF particles and the membrane cross-sections were coated with gold. The cross sections were obtained by breaking the membranes after freezing in liquid nitrogen. The coated samples were then imaged using an ESEM Quanta 400 FEG SEM equipped with a secondary electron (SE) detector and operated at 20 keV.

The MIL-101(Cr) microcrystals were coated with palladium and the SEM image was obtained on Zeiss Leo DSM 982 Gemini with field emitter.

SEM images combined with EDX-mapping were recorded with a Jeol JSM-6510LV QSEM Advanced electron microscope with a LAB-6 cathode at 20 keV. The microscope was equipped with a Bruker Xflash 410 silicon drift detector and the Bruker ESPRIT software for EDX analysis. The membrane cross-sections were prepared through freeze-fracturing after immersion in liquid nitrogen and then coated with gold by a Jeol JFC 1200 fine-coater at an approximate current of 20 mA for 20–30 s.

Differential scanning calorimetry (DSC) was measured using a Mettler Toledo DSC 3 with a temperature gradient of 10 K min^{-1} in the temperature range of 20 °C to 400 °C for the determination of the glass temperatures (T_g). All samples were heated four times and cooled 3 times. The glass temperature was determined as the mean of the 2nd and 3rd heating and cooling cycle. The results were analyzed with the STARe SW 16.00 Software.

Synthetic procedures

MIL-101(Cr). MIL-101(Cr) was synthesized according to the previously reported procedure.[31] A typical synthesis involved a solution containing chromium(III) nitrate $Cr(NO_3)_3 \cdot 9H_2O$ (400 mg, 1 mmol), hydrofluoric acid (1 mmol) and 1,4-benzene dicarboxylic acid H_2BDC (164 mg, 1 mmol) in 5 mL of H_2O. The mixture was transferred to the Teflon line in a hydrothermal autoclave which was heated for 6 h at 210 °C and cooled afterwards slowly to room temperature over a time period of 8 h. The mixture was then isolated from the autoclave and the solid separated from the solution through centrifugation (4200 U min^{-1} for 50 min). A significant amount of recrystallized terephthalic acid was present. To eliminate most of the carboxylic acid, the product was dispersed and centrifuged two times in DMF (20 mL), one time in ethanol (10 mL) and one time in water (10 mL). The final product was then dried at room temperature (yield 302 mg, 50%).

MOF-199 (HKUST-1, Cu-BTC). The synthesis was carried out according to the procedure reported by Tranchemontagne *et al.*[32] Benzene-1,3,5-tricarboxylic acid (514 mg, 2.40 mmol) and $Cu(OAc)_2 \cdot H_2O$ (817 mg, 4.37 mmol) were dissolved each in 12 mL of a 1 : 1 : 1 mixture of H_2O/DMF/EtOH. Both solutions were mixed together and the resulting mixture was stirred for about 30 min. After addition of 0.5 mL of triethylamine, the solution was stirred for 6 days. The obtained turquoise suspension was poured on 100 mL of DMF and allowed to stand overnight, afterwards it was centrifuged at 2000 rpm for 99 min and the supernatant was removed. This washing procedure was repeated three times. The product was collected, immersed in 100 mL of CH_2Cl_2, left overnight and centrifuged as given above. This last washing step was also repeated three times and afterwards the product was dried overnight under vacuum (yield: 430 mg, 59%). We choose this synthetic procedure to yield especially small MOF particles in the submicrometer range. Because of the subsequent use in mixed-matrix membranes particle size is of prime importance for a defect free composite membrane.

6FDA-*m*PD. The synthesis was carried out according to the procedure reported by Staudt-Bickel and Koros[33] All monomer materials were purified before the polymerization reaction. 6FDA (4,4′-hexafluoroisopropylidene diphthalic anhydride) was sublimed twice; *m*PD (*m*-phenylenediamine) was recrystallized twice from toluene. The monomers were stored separately under high vacuum. For the synthesis of the polyimide in this study, chemical imidization was performed. In a moisture free flask with nitrogen inlet and magnetic stirrer, the diamine monomer was dissolved in *N*,*N*-dimethyl acetamide (DMAc) and the 6FDA dianhydride dissolved in DMAc was added dropwise at room temperature. The 20–25 wt% solution was stirred 6–8 h. Thereby high molecular polyamic acids were formed. The imidization was performed by the dehydration of the polyamic acids by adding a large excess of triethylamine and acetic anhydride to the reaction mixture and stirring for 2–3 h at 323 K and 10–20 min at 373–383 K. After cooling to room temperature, the highly viscous reaction solution was slowly poured into methanol. The precipitated polyimide (6FDA-*m*PD) was homogenized in a blender; filtered and washed several times with fresh methanol. The obtained polyimide was dried 12 h under vacuum at room temperature and at least 24 h under vacuum at 523 K.

Mixed-matrix membranes. 500 mg of the polymer (6FDA-*m*PD) was dissolved in 7 mL dichloromethane (CH_2Cl_2) and the solution was stirred for 24 h. For an 8 wt% MMM simultaneously 44 mg of the MOF material (MIL-101(Cr) or MOF-199) was suspended in 9 mL CH_2Cl_2 and stirred for 24 h ($44/(500 + 44) \times 100\% = 8\%$). Next the MOF suspension was homogenized by ultrasonication for which the sample was treated three times for 15 min each with an amplitude of 20% by an ultrasonic liquid processor (VCX 750 Sonics, Microtip 630-0419). Then a small portion of the polymer solution was added to the MOF suspension. After further stirring for 24 h, the ultrasonication procedure was repeated. Then the remaining polymer solution was added. Before casting, the dispersion was kept under stirring for one hour. The dispersion was cast into metal rings, 4 cm in diameter, which were placed on a flat stainless-steel surface. All of the casting equipment was placed on top of an adjustable table to assure horizontal alignment during the membrane formation. To prevent contamination by dust particles and to ensure a slow evaporation of the solvent, a funnel was placed upside down over the metal ring and the small opening was covered with filter paper. As soon as all solvent had evaporated, the membrane was removed from the metal ring and the stainless-steel surface by flushing the ring with distilled water. The membrane was finally dried in a vacuum oven at 120 °C and 50 mbar overnight. MMMs with 16 and 24 wt% were produced the same way with 95 mg and 158 mg MOF material (MIL-101(Cr) or MOF-199), respectively. The pure polymer membranes were prepared accordingly and dried the same way.

We also tried to produce MMMs with loadings of above 24 wt% MOF. Unfortunately, the MMMs with filler loadings of above 24 wt% were to brittle for handling and gas separation measurements. The MMMs either broke after casting or while preparing them for the measurement. Therefore, we are not able to prepare defect-free membranes and to present separation performance data of MMMs with filler loadings above 24 wt%.

Gas permeation experiments

Conducted in Spain, Zaragoza. A detailed description of the gas permeation setup can be found elsewhere.[37] The membranes (13.8 cm^2) were placed inside a permeability module composed of two stainless steel parts with a cavity in which a macroporous disk support (20 μm nominal pore size, Mott Corp.) is gripped inside with Viton O-Rings. Mass-flow meter controllers (Alicat Scientific) were used for feed and sweep gas provision to the membrane module. A CO_2/CH_4 (25/25 cm^3 (STP) min^{-1}) mixture stream was fed at 3 bar to the retentate side, while the permeate side was swept with a 2 cm^3 (STP) min^{-1} mass-flow controlled stream of Ar at 1 bar. Gas concentrations in the outgoing stream were analyzed by an Agilent 3000A on-line gas micro-chromatograph equipped with thermal conductivity detector (TCD). Permeability results in Barrer (1×10^{-10} cm^3 (STP) cm (cm^2 s cmHg)$^{-1}$) were obtained once the exit stream of the membrane was stabilized. The real separation selectivity of the mixtures was calculated as the ratio of permeabilities. Permeation measurements were performed at 35 °C controlled by a Memmert UNE 200 oven.

Conducted in Germany, Düsseldorf. Binary gas separation experiments were carried out with a continuous flow permeation system (OSMO inspector, provided by Convergence Industry B.V., 7532 SM Enschede, The Netherlands) with helium as sweep gas and an Agilent 490μGC gas chromatograph to measure the gas concentration in the permeate. The membranes were cut in a round sheet, placed in the permeation module (4.5 cm diameter) and covered by a rubber ring to provide an effective inner diameter of 3.8 cm with an area of 11.3 cm^2. All permeation experiments were performed at 25 °C and with 3 bar transmembrane pressure. The feed gases were mixed in a 50/50 volume flow mixture of CO_2 and CH_4 by two Bronkhorst Coriolis-flow controllers as well as the helium gas stream with a total upstream flow of 160 mL min^{-1}. The downstream is swept with helium at a rate of 1 mL min^{-1} at ambient pressure. The gas concentration in the permeate stream was measured with the Agilent 490μGC with a thermal conductivity detector and a Pora PLOT Q column until steady state (up to 24 h).

Results and discussion

MIL-101(Cr) and MOF-199 were synthesized according to previously reported procedures with product identity established by powder X-ray diffraction (Fig. S2 and S3 in ESI†).[31,32,38,39] BET surface areas were 2770 m^2 g^{-1} and 950 m^2 g^{-1}, respectively. Particles sizes were in the range of 100–400 nm for MIL-101(Cr) and mostly below 100 nm except for some bigger crystals of about 400 nm for MOF-199 (Fig. 1). The prepared MOF particles were used to fabricate membranes with the 6FDA-*m*PD polyimide (see ESI†). From the scanning electron microscopy (SEM) cross-sections of the MOF@6FDA-*m*PD MMMs it is evident that the MOF particles showed excellent adhesion with the polymer matrix as the membrane cross-section morphology reveals the formation of circular cavities and elongated matrix segments with increased plastic deformation of the polymer (Fig. 2). The good interaction of the MOFs with the polymer is favored due to the partial organic nature of the former.

Interfacial voids were absent in the MMMs and MOF crystals were homogeneously distributed in the 6FDA-*m*PD matrix. No particle agglomeration can be observed. The X-ray patterns (Fig. S2 and S3 in ESI†) reveal that most of the main MOF reflections are present in the composite membranes. This also proves that the membrane preparation procedure did not alter the filler crystallinities. Furthermore, SEM images combined with elemental EDX mapping of chromium (MIL-101(Cr)) and copper (MOF-199) of the cross-sections of the MMMs (Fig. S3 and S5†) show also a remarkable homogeneous distribution of the MOF particles in the polymer matrix. Possible defects concerning particle agglomeration or particle sedimentation can thus be eliminated.

The gain of this MMM study is clearly demonstrated from the point of view of gas separation performance for CO_2/CH_4 gas mixtures (related to natural gas upgrading by removal of CO_2). Results of CO_2 and CH_4 gas permeation and separation experiments conducted with pure 6FDA-*m*PD membrane, MIL-101(Cr)@6FDA-*m*PD and MOF-199@6FDA-*m*PD MMMs are shown in Fig. 3 (data in Tables S2 and S3 in ESI†). Two to three membranes of each type were fabricated and every mem-

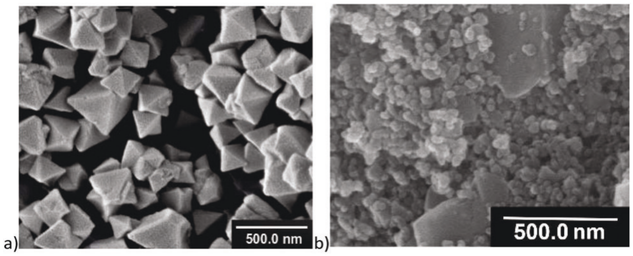

Fig. 1 Scanning electron microscopy (SEM) images of (a) MIL-101(Cr) and (b) MOF-199 nano/microcrystals.

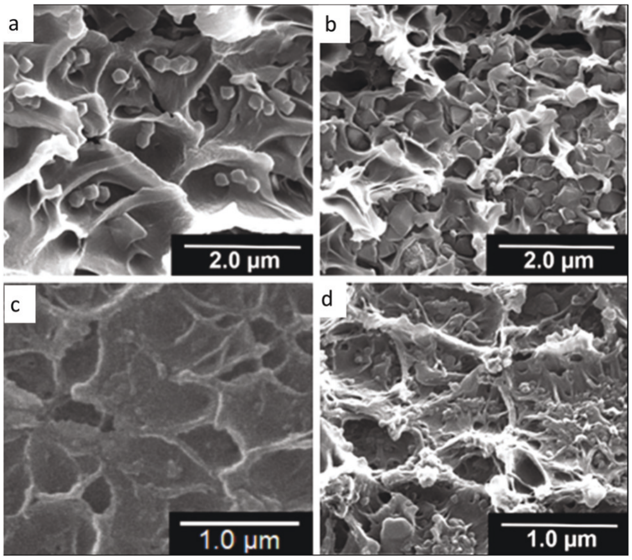

Fig. 2 SEM cross-sections of MOF@6FDA-*m*PD membranes based on 250 mg of 6FDA-*m*PD with different loadings of MOFs: (a) 8 wt% MIL-101(Cr), (b) 24 wt% MIL-101(Cr), (c) 8 wt% MOF-199 and (d) 24 wt% MOF-199.

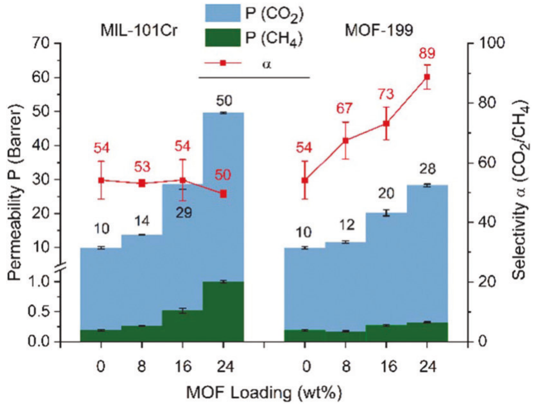

Fig. 3 CO_2/CH_4 permeability and separation performance of pure 6FDA-*m*PD (0 wt% MOF loading), MIL-101(Cr)@6FDA-*m*PD and MOF-199@6FDA-*m*PD MMMs at different MOF loadings. See Tables S2 and S3 in ESI† for experimental details.

brane was measured at least two times to provide reliable error estimates.

The gas separation experiments were performed at 25 °C and 35 °C, 4 and 3 bar feed pressure, respectively, and 50/50 CO_2/CH_4 mixture on MMMs containing 8, 16 and 24 wt% of either MIL-101(Cr) or MOF-199. These mixed-gas separation experiments indicated enhancements in CO_2 permeability with increasing MOF weight percentage in 6FDA-*m*PD. For all MIL-101(Cr)@6FDA-*m*PD MMMs the selectivity approximately remained equal to that of the neat polymer, while MOF-199@6FDA-*m*PD MMMs featured a steady rise in selectivity with increasing amount of MOF. This suggests that the membranes are free of interfacial defects, which otherwise would have led to a distinct decrease on the selectivity. The CO_2 permeability increased from about 10 Barrer for pure 6FDA-*m*PD to 50 or 28 Barrer in MMMs containing 24 wt% of MIL-101(Cr) or MOF-199, respectively. The CO_2/CH_4 selectivity decreased slightly from 54 for pure 6FDA-*m*PD to 50 for 24 wt% MIL-101(Cr)@6FDA-*m*PD MMM and increases significantly to 89 for 24 wt% of MOF-199@6FDA-*m*PD MMM (Fig. 3, data in Tables S2 and S3 in ESI†). Thus, the MMMs made of 6FDA-*m*PD and MIL-101(Cr) or MOF-199 provide a remarkable gas-separation performance enhancement as compared with the pure polyimide with respect to permeability or selectivity, respectively.

The breaking of polymer chain packing and linking due to the presence of fillers leading to an increase in polymer matrix free volume and especially the large porosity of MOFs can explain the permeability improvement in agreement with previous publications related to ZIF-8 or Al-fumarate containing MMMs.[40,41]

A rigidification of polymer chains in the composite membranes does not occur as the T_g, determined by differential scanning calorimetry, decreases slightly for the MOF-199@6FDA-*m*PD MMMs compared to the neat polymer (Table S4†). For MIL-101(Cr)@6FDA-*m*PD MMMs the T_g exhibits no distinct trend for a rigidification or disruption of polymer chains.

For most composite membranes, a constant selectivity is observed with increased MOF loading, as is found here for the MIL-101(Cr)@6FDA-*m*PD MMMs.[10,42] Therefore, the increase in selectivity for MOF-199@6FDA-*m*PD MMMs contrasts with expectations since the used MOFs have large cages and window sizes in their neat, virgin state, and no size exclusion of any gas from CO_2/CH_4 mixtures is likely if the MOF would remain unchanged. According to literature MIL-101(Cr) has cages with diameters of 3.4 nm and hexagonal windows of 1.6 nm diameter.[31] MOF-199 has square channels of 9 × 9 Å with 13 Å across the diagonals.[39]

In some cases, where a selectivity increase has been seen with MOF@polymer composite membranes, the following reasons were given for the increase in selectivity.

- The polymer could be influenced by the filler in such a way, that a chain rigidification takes places which results in a higher T_g for the composite membrane in comparison to the pure polymer membrane. The general correlation of the T_g of the polymer with permeability and selectivity is, that a high T_g goes together with low permeability and high selectivity and *vice versa*.[43]

- The MOF filler could become size discriminating if the polymer chains diffuse through the MOF channels and block them to some degree. This blocking can intensify the molecular sieving property of the MOF and enhance transport of smaller gas molecules relative to the larger ones and thereby induce a higher selectivity.[48]

- MOF fillers, such as ZIF-8, with pore apertures of ∼4 Å feature sieving properties based on their diffusion selectivity even for gas pairs with kinetic diameters of <4 Å if they are properly matched with the polymer matrix.[44]

- The MOF filler could show a very high adsorption affinity for one specific gas and thus increases the transport of this gas through the membrane, which can also result in an increased selectivity.[45,46]

In our case an increase in T_g was clearly not observed, but rather a decrease in the T_g was measured. Thus, the increase in selectivity cannot be due to the change in polymer structure alone. At the same time MOFs by itself, as for example in pure MOF membranes are not known for high selectivities.[47]

The apparent increase in selectivity for the MOF-199 MMMs may be due to the fact, that the polyimide blocked or partially reduced the access to the MOF-199 channels. Whereby the MOF filler becomes more size discriminating, that is exhibits intensified molecular sieving properties through the enhanced transport of smaller gas molecules relative to the larger ones which leads to a higher selectivity. CO_2 and CH_4 have kinetic diameters of 0.33 and 0.38 nm, respectively.

Furthermore, the increase in CO_2/CH_4 selectivity for MOF-199@6FDA-*m*PD MMMs may also be promoted by the high adsorption efficiency of MOF-199 for CO_2 (see above).[36]

Moreover, the good dispersion and non-agglomeration of MOF-199 particles may favor the action of adsorbing CO_2 over CH_4 improving the separation selectivity up to the total loading of 24 wt%.[48] Likewise, an increased selectivity for different MOF-199@polymer MMMs with increasing MOF content was observed. The selectivity increase for MOF-199@poly(vinylidene fluoride) (PVDF) was from 21 to 40 when going from neat PVDF to 15 wt% MOF content.[49] For MOF-199@Matrimid the increase was from 17 to 23 when going from neat Matrimid to 30 wt% MOF content (see also Table S5†).[50] This effect was especially evident for small MOF-199 particles in the nanometer range, which in this study were also used, due to better distribution in the polymer matrix and neglectable formation of voids between MOF particles.[45,51]

The difference in gas separation performances between the fabricated MMMs result from the varying structure and properties of the MOFs. MIL-101(Cr) exhibits a much higher pore volume of about 1.32 $cm^3 g^{-1}$ compared to the pore volume of 0.78 $cm^3 g^{-1}$ of MOF-199. Hence, the density of MIL-101(Cr) is much lower, which leads to a considerably higher volume fraction for the same amount of loaded wt% for MIL-101(Cr) in the MMMs (see eqn (S2), ESI† how ϕ_d is derived from the MOF loading in wt%). Thus, the increase in free volume is more pronounced for the MIL-101(Cr)@6FDA-*m*PD MMMs, which ultimately leads to the higher permeability in comparison to the MOF-199@6FDA-*m*PD MMMs.[41] This observation is in good agreement with the results emerging from the Maxwell model for CO_2, shown in Fig. 4a, which was applied to both types of MMMs.

The Maxwell model with the assumption $P_d \gg P_c$, (eqn (1)) is a highly specialized limiting version of the full Maxwell model, which can be designated as "Maxwell model ∞". This limiting case corresponds essentially to the introduction of infinitely permeable voids with a volume fraction equal to that of the dispersed phase.

$$P_d \gg P_c; \frac{P_{eff}}{P_c} = \frac{1+2\phi_d}{1-\phi_d} \tag{1}$$

The "Maxwell model ∞" with the assumption $P_d \gg P_c$, that is, an infinite high CH_4 permeability of the dispersed, filler phase does not give a good agreement with the experimental data. The latter stays below the predicted line of the "Maxwell model ∞" (Fig. 4b). In reverse conclusion this indicates that the assumption $P_d \gg P_c$ is no longer valid for CH_4 and MOF-199. Instead the relative experimental permeability approaches the Maxwell model with $P_d = P_c$.

Since in pure MOF-199 the CH_4 permeability (from single-gas permeation) was 1000 Barrer, we have to conclude that either pore blocking from polymer chain ends results in discriminating CH_4 from entering the pores or that the excellent adsorption of CO_2 compared to CH_4 in MOF-199 prevents CH_4 from entering the pores (see above).

As Fig. 4 indicates, the filler volume of the 16 wt% MIL-101 (Cr)-6FDA-*m*PD MMMs already surpasses the filler volume of the 24 wt% MOF-199@6FDA-*m*PD MMM and as a consequence the relative permeability of the 16 wt% MIL-101(Cr) MMM already reaches the is the relative permeability of the MOF-199 MMM. In general, one can observe a good match between the predicted values of the "Maxwell model ∞" for the composite membranes and the experimental values. Larger deviations between the model and the experimental values are revealed for higher loadings of a filler volume fraction ϕ_d above 0.4 and

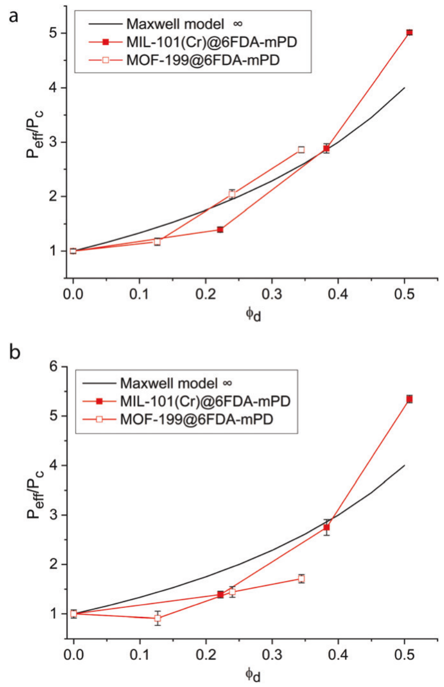

Fig. 4 Relative experimental (a) CO_2 and (b) CH_4 permeabilities (referenced to the permeability P_c of the pure polymer membrane) for MIL-101(Cr)@6FDA-*m*PD MMMs (filled red squares) and MOF-199@6FDA-*m*PD MMMs (hollow red squares) with different filler volume fraction ϕ_d (see eqn (S2), ESI† how ϕ_d is derived from the MOF loading in wt%). The black line gives the relative theoretical gas permeabilities for a porous filler (with permeability $P_d \gg P_c$). Note that for the same wt% of MOF the higher density MOF-199 leads to a lower filler volume fraction (see ESI† for details to the Maxwell model).

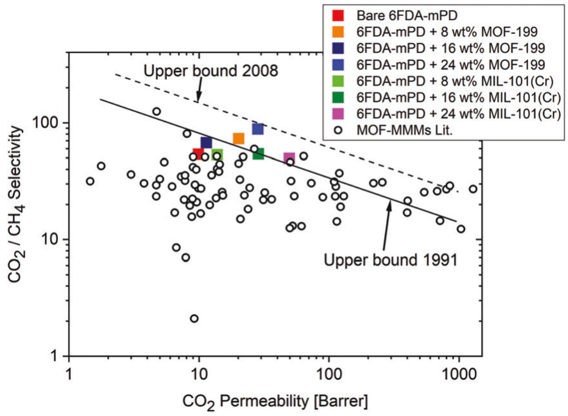

Fig. 5 CO_2/CH_4 separation performance of the studied MOF@6FDA-*m*PD MMMs compared with the results from previously reported MOF MMMs (see Table S5†). The straight lines are the Robeson upper bounds for best polymer separation performances as defined in 1991[8] and 2008.[18]

should result from filler–filler interactions which are not considered in the Maxwell model.[52]

In Fig. 5 we compare the presented results with those previously reported from other MOF-containing MMMs (see Table S5†). The performance of the 6FDA-*m*PD membrane with 8 wt% of MIL-101(Cr) is located in the region considered as commercially unattractive. However, the performance of MOF-199@6FDA-*m*PD MMMs with 24 wt% MOF loading clearly surpasses the polymer upper bound drawn in 1991, and reaches the commercially attractive region. A MOF-199@6FDA-*m*PD membrane with 24 wt% MOF loading exhibits specifically much higher CO_2/CH_4 mixed-gas selectivity (89) than most other MOF-based MMMs, combined with a good CO_2 permeability of 28 Barrer.

Conclusions

In summary, high-performance gas separation mixed-matrix membranes were obtained by combining the polyimide 6FDA-*m*PD and nano- to microcrystalline particles of the MOFs MIL-101(Cr) or MOF-199 (HKUST-1, Cu-BTC). The MOF particles showed good adhesion with the polymer matrix and the resulting membranes were free of interfacial defects. We demonstrated that the MMMs yielded to a substantial increase in CO_2 permeability as well as in CO_2/CH_4 selectivity for the MOF-199@6FDA-*m*PD MMMs. The high permeability increase for the MIL-101(Cr)@6FDA-*m*PD MMMs can be traced to the high pore volume in MIL-101(Cr). The remarkable and unexpected increase in selectivity for the MOF-199 MMMs is reasoned by pore blocking and reduction of the MOF window size through polyimide together with the high adsorption of CO_2 by MOF-199. Still, more investigations are necessary for better elucidation of permeation mechanisms and selectivity properties, the intrinsic gas-transport properties of MOFs, the roles of filler loading, geometry, pore size and the nature of the molecular interactions on preferential adsorption when using MOFs in MMMs.

Conflicts of interest

There are no conflicts to declare.

Acknowledgements

Financial support (MAT2013-40556-R) from the Ministry of Economy and Competitiveness (MINECO) is gratefully acknowledged by JC. The work of CJ was supported by the Federal German Ministry of Education and Research (BMBF) under grant Optimat 03SF0492C. We thank Mrs Alexa Schmitz for TGA and Mr Carsten Schlüsener for SEM/EDX measurements.

Notes and references

1 J. C. Davis, R. J. Valus, R. Eshragi and A. E. Velikoff, *Sep. Sci. Technol.*, 1993, **28**, 463–476.

2 M. G. Buonomenna, *RSC Adv.*, 2013, **3**, 5694–5740.

3 J. C. Charpentier, *Chem. Eng. J.*, 2007, **134**, 84–92.

4 W. J. Koros, *AIChE J.*, 2004, **50**, 2326–2334.

5 J. Coronas and J. Santamaria, *Sep. Purif. Methods*, 1999, **28**, 127–177.

6 M. A. Aroon, A. F. Ismail, T. Matsuura and M. M. Montazer-Rahmati, *Sep. Purif. Technol.*, 2010, **75**, 229–242.

7 T. S. Chung, L. Y. Jiang, Y. Li and S. Kulprathipanja, *Prog. Polym. Sci.*, 2007, **32**, 483–507.

8 L. M. Robeson, *J. Membr. Sci.*, 1991, **62**, 165–185.

9 B. Zornoza, A. Martinez-Joaristi, P. Serra-Crespo, C. Tellez, J. Coronas, J. Gascon and F. Kapteijn, *Chem. Commun.*, 2011, **47**, 9522–9524.

10 J. Dechnik, C. J. Sumby and C. Janiak, *Cryst. Growth Des.*, 2017, **17**, 4467–4488; J. Dechnik, J. Gascon, C. J. Doonan, C. Janiak and C. J. Sumby, *Angew. Chem., Int. Ed.*, 2017, **56**, 9292–9310.

11 O. G. Nik, X. Y. Chen and S. Kaliaguine, *J. Membr. Sci.*, 2012, **413–414**, 48–61.

12 H. B. Tanh Jeazet, C. Staudt and C. Janiak, *Dalton Trans.*, 2012, **41**, 14003–14027; K. Hunger, N. Schmeling, H. B. Tanh Jeazet, C. Janiak, C. Staudt and K. Kleinermanns, *Membranes*, 2012, **2**, 727–763; H. B. Tanh Jeazet and C. Janiak, Metal-Organic Frameworks in Mixed-Matrix Membranes, in *Metal Organic Framework Materials*, ed. L. R. MacGillivray and C. Lukehart, John Wiley & Sons, Ltd, Chichester, UK, 2014, pp. 1–15.

13 B. Zornoza, C. Tellez, J. Coronas, J. Gascon and F. Kapteijn, *Microporous Mesoporous Mater.*, 2013, **166**, 67–78.

14 D. Bastani, N. Esmaeili and M. Asadollahi, *J. Ind. Eng. Chem.*, 2013, **19**, 375–393.

15 G. Dong, H. Li and V. Chen, *J. Mater. Chem. A*, 2013, **1**, 4610–4630.

16 M. J. C. Ordonez, K. J. Balkus, Jr., J. P. Ferraris and I. H. Musselman, *J. Membr. Sci.*, 2010, **361**, 28–37.

17 Y. Dai, J. R. Johnson, O. Karvan, D. S. Sholl and W. J. Koros, *J. Membr. Sci.*, 2012, **401–402**, 76–82; D. Zheng, X. Liu, D. Hu, M. Li, J. Zhang, G. Zeng, Y. Zhang and Y. Sun, *RSC Adv.*, 2014, **4**, 10140–10143; M. G. Buonomenna, W. Yave and G. Golemme, *RSC Adv.*, 2012, **2**, 10745–10773; X. Y. Chen, H. Vinh-Thang, D. Rodrigue and S. Kaliaguine, *RSC Adv.*, 2014, **4**, 12235–12244; S. Sorribas, B. Zornoza, C. Téllez and J. Coronas, *J. Membr. Sci.*, 2014, **452**, 184–192; P. Burmann, B. Zornoza, C. Téllez and J. Coronas, *Chem. Eng. Sci.*, 2014, **107**, 66–75; X. Y. Chen, H. Vinh-Thang, D. Rodrigue and S. Kaliaguine, *Ind. Eng. Chem. Res.*, 2012, **51**, 6895–6906; B. Seoane, J. M. Zamaro, C. Téllez and J. Coronas, *RSC Adv.*, 2011, **1**, 917–922; X. Y. Chen, H. Vinh-Thang, D. Rodrigue and S. Kaliaguine, *RSC Adv.*, 2013, **3**, 24266–24279.

18 L. M. Robeson, *J. Membr. Sci.*, 2008, **320**, 390–400.

19 G. Rebollar-Perez, E. Carretier, N. Lesage and P. Moulin, *Membranes*, 2011, **1**, 80–90.

20 L. Dumee, L. Velleman, K. Sears, M. Hill, J. Schutz, N. Finn, M. Duke and S. Gray, *Membranes*, 2011, **1**, 25–36.

21 P. S. Goh, A. F. Ismail, S. M. Sanip, B. C. Ng and M. Aziz, *Sep. Purif. Technol.*, 2011, **81**, 243–264.

22 B. Seoane, J. Coronas, I. Gascon, M. E. Benavides, O. Karvan, J. Caro, F. Kapteijn and J. Gascon, *Chem. Soc. Rev.*, 2015, **44**, 2421–2454.

23 R. D. Noble, *J. Membr. Sci.*, 2011, **378**, 393–397.

24 J.-R. Li, Y. Ma, M. C. McCarthy, J. Sculley, J. Yu, H.-K. Jeong, P. B. Balbuena and H.-C. Zhou, *Coord. Chem. Rev.*, 2011, **255**, 1791–1823.

25 D. Liu and C. Zhong, *J. Mater. Chem.*, 2010, **20**, 10308–10318.

26 S. T. Meek, J. A. Greathouse and M. D. Allendorf, *Adv. Mater.*, 2011, **23**, 249–267.

27 T.-H. Bae, J. S. Lee, W. Qju, W. J. Koros, C. W. Jones and S. Nair, *Angew. Chem., Int. Ed.*, 2010, **49**, 9863–9866.

28 C. Janiak and J. K. Vieth, *New J. Chem.*, 2010, **34**, 2366–2388.

29 S. Keskin and D. S. Sholl, *Energy Environ. Sci.*, 2010, **3**, 343–351; J. A. Sheffel and M. Tsapatsis, *J. Membr. Sci.*, 2009, **326**, 595–607.

30 S. Aguado, J. Canivet and D. Farrusseng, *J. Mater. Chem.*, 2011, **21**, 7582–7588.

31 G. Férey, C. Mellot-Draznieks, C. Serre, F. Millange, J. Dutour, S. Surble and I. Margiolaki, *Science*, 2005, **309**, 2040–2042.

32 D. J. Tranchemontagne, J. R. Hunt and O. M. Yaghi, *Tetrahedron*, 2008, **64**, 8553–8557.

33 C. Staudt-Bickel and W. J. Koros, *J. Membr. Sci.*, 1999, **155**, 145–154.

34 K. Sumida, D. L. Rogow, J. A. Mason, T. M. McDonald, E. D. Bloch, Z. R. Herm, T.-H. Bae and J. R. Long, *Chem. Rev.*, 2012, **112**, 724–781; Z. Zhang, Y. Zhao, Q. Gong, Z. Li and J. Li, *Chem. Commun.*, 2013, **49**, 653–661; J. Liu, P. K. Thallapally, B. P. McGrail, D. R. Brown and J. Liu, *Chem. Soc. Rev.*, 2012, **41**, 2308–2322; X. Lu, D. Jin, S. Wei, Z. Wang, C. An and W. Guo, *J. Mater. Chem. A*, 2015, **3**, 12118–12132.

35 A. Khutia and C. Janiak, *Dalton Trans.*, 2014, **43**, 1338–1347.

36 A. Ö. Yazaydin, A. I. Benin, S. A. Faheem, P. Jakubczak, J. L. Low, R. R. Willis and R. Q. Snurr, *Chem. Mater.*, 2009, **21**, 1425–1430.

37 B. Zornoza, S. Irusta, C. Tellez and J. Coronas, *Langmuir*, 2009, **25**, 5903–5909; S. Sorribas, B. Zornoza, C. Téllez and J. Coronas, *J. Membr. Sci.*, 2014, **452**, 184–192.

38 T. Zhao, F. Jeremias, I. Boldog, B. Nguyen, S. K. Henninger and C. Janiak, *Dalton Trans.*, 2015, **44**, 16791–16801; A. Herbst, A. Khutia and C. Janiak, *Inorg. Chem.*, 2014, **53**, 7319–7333.

39 S. S.-Y. Chui, S. M.-F. Lo, J. P. H. Charmant, A. G. Orpen and I. D. Williams, *Science*, 1999, **283**, 1148–1150.

40 B. Zornoza, B. Seoane, J. M. Zamaro, C. Téllez and J. Coronas, *ChemPhysChem*, 2011, **12**, 2781–2785.

41 A. Nuhnen, D. Dietrich, S. Millan and C. Janiak, *ACS Appl. Mater. Interfaces*, 2018, **10**, 33589–33600.

42 A. E. Amooghin, S. Mashhadikhan, H. Sanaeepur, A. Moghadassi, T. Matsuura and S. Ramakrishna, *Prog. Mater. Sci.*, 2019, **102**, 222–295.

43 Y. Li, T.-S. Chung, C. Cao and S. Kulprathipanja, *J. Membr. Sci.*, 2005, **260**, 45–55.

44 W. J. Koros and C. Zhang, *Nat. Mater.*, 2017, **16**, 289–297.

45 N. M. Jacques, P. R. E. Rought, D. Fritsch, M. Savage, H. G. W. Godfrey, L. Li, T. Mitra, M. D. Frogley, G. Clinque, S. Yang and M. Schröder, *Chem. Commun.*, 2018, **54**, 2866–2869.

46 R. Abedini, A. Mosayebi and M. Mokhtari, *Process Saf. Environ. Prot.*, 2018, **114**, 229–239.

47 S. Qiu, M. Xue and G. Zhu, *Chem. Soc. Rev.*, 2014, **43**, 6116–6140.

48 H. W. B. Teo, A. Chakraborty and S. Kayal, *Appl. Therm. Eng.*, 2017, **110**, 891–900.

49 E. A. Fejani, H. Mahdavi and A. Tavasoli, *Chem. Eng. Res. Des.*, 2015, **96**, 87–102.

50 S. Basu, A. Cano-Odena and I. F. J. Vankelecom, *Sep. Purif. Technol.*, 2011, **81**, 31–40.

51 R. Lin, L. Ge, H. Diao, V. Rudolph and Z. Zhu, *ACS Appl. Mater. Interfaces*, 2016, **8**, 32041–32049.

52 R. H. B. Bouma, A. Checchetti, G. Chidichimo and E. Drioli, *J. Membr. Sci.*, 1997, **128**, 141–149.

Electronic Supplementary Information (ESI)

High performance MIL-101(Cr)@6FDA-mPD and MOF-199@6FDA-mPD mixed-matrix membranes for CO_2/CH_4 separation

Alexander Nuhnen,[a] Maximilian Klopotowski,[a] Harold B. Tanh Jeazet,[a] Sara Sorribas,[b] Beatriz Zornoza,[b,c] CarlosTéllez,[b] Joaquín Coronas*[b] and Christoph Janiak*[a]

[a] Institut für Anorganische Chemie und Strukturchemie, Heinrich-Heine-Universität Düsseldorf, 40204 Düsseldorf, Germany. E-mail: alexander.nuhnen@uni-duesseldorf.de; Janiak@uni-duesseldorf.de

[b] Chemical and Environmental Engineering Department, Instituto de Nanociencia de Aragon and Instituto de Ciencia de Materiales de Aragón (ICMA), Universidad de Zaragoza-CSIC, 50018 Zaragoza, Spain. E-mail: coronas@unizar.es

[c] Department of Energy and Environment, Instituto de Carboquímica-ICB-CSIC, Miguel Luesma Castán 4, 50018 Zaragoza, Spain.

Email addresses:
alexander.nuhnen@uni-duesseldorf.de, maximilian.klopotowski@hhu.de, tanharold2000@yahoo.fr, sarasr@unizar.es, bzornoza@unizar.es, ctellez@unizar.es, coronas@unizar.es, janiak@uni-duesseldorf.de

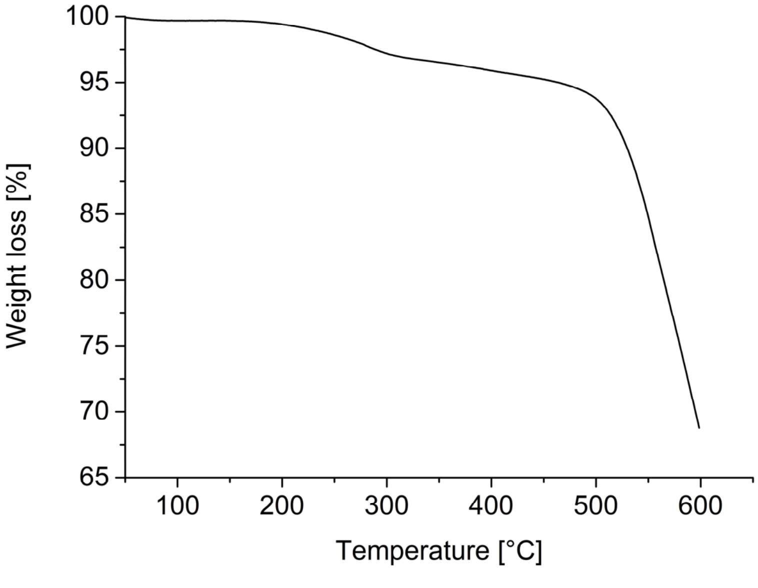

Fig. S1 Thermogravimetric analysis (TGA) curve of pure 6FDA-mPD under nitrogen at a heating flow of 5 K/min.

Table S1 Elemental analysis of MOF-199 and MIL-101(Cr)

	MOF-199 $[Cu_3(btc)_2(H_2O)_3]$		**MIL-101(Cr)** $[Cr_3(O)(OH)(bdc)_3(H_2O)_2]\cdot DMF$	
Atom	**calculated**	**experimental**	**calculated**	**experimental**
C	32.81	35.10	41.03	40.66
H	1.84	1.84	3.06	2.95
N	0	0	1.77	1.52

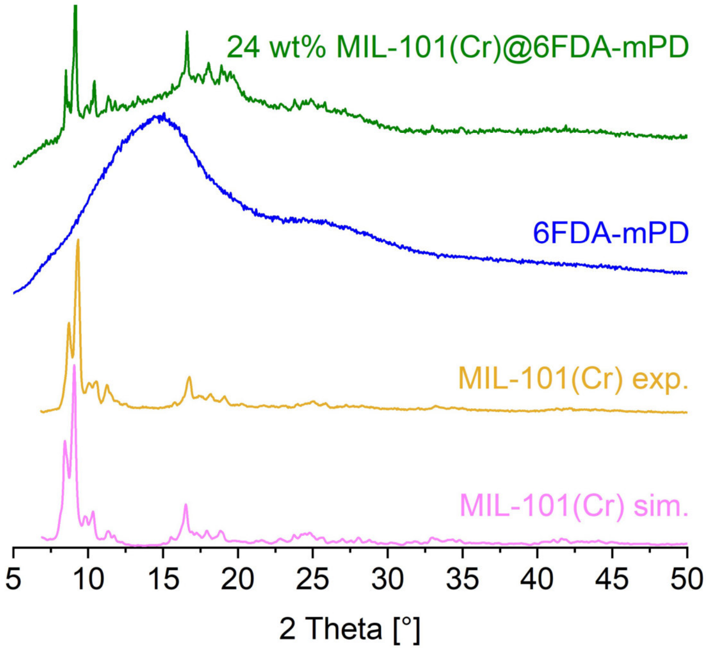

Fig. S2 X ray powder diffraction pattern of MIL-101 (Cr), 6FDA-mPD polyimide and a mixed matrix membrane of 6FDA-mPD with 24 wt% loading of MIL-101 (Cr).

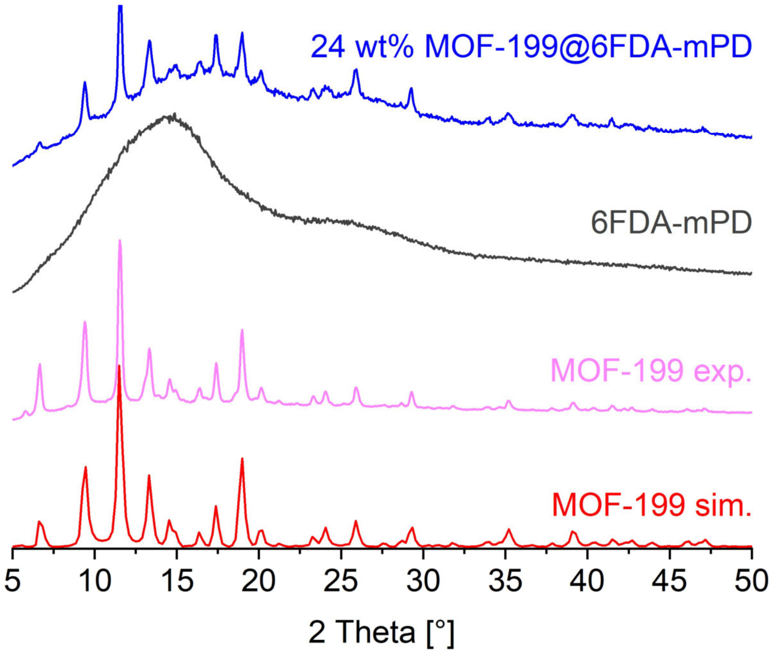

Fig. S3 X ray powder diffraction pattern of MOF-199, 6FDA-mPD polyimide and a mixed matrix membrane of 6FDA-mPD with 24 wt% loading of MOF-199.

SEM images with EDX mapping

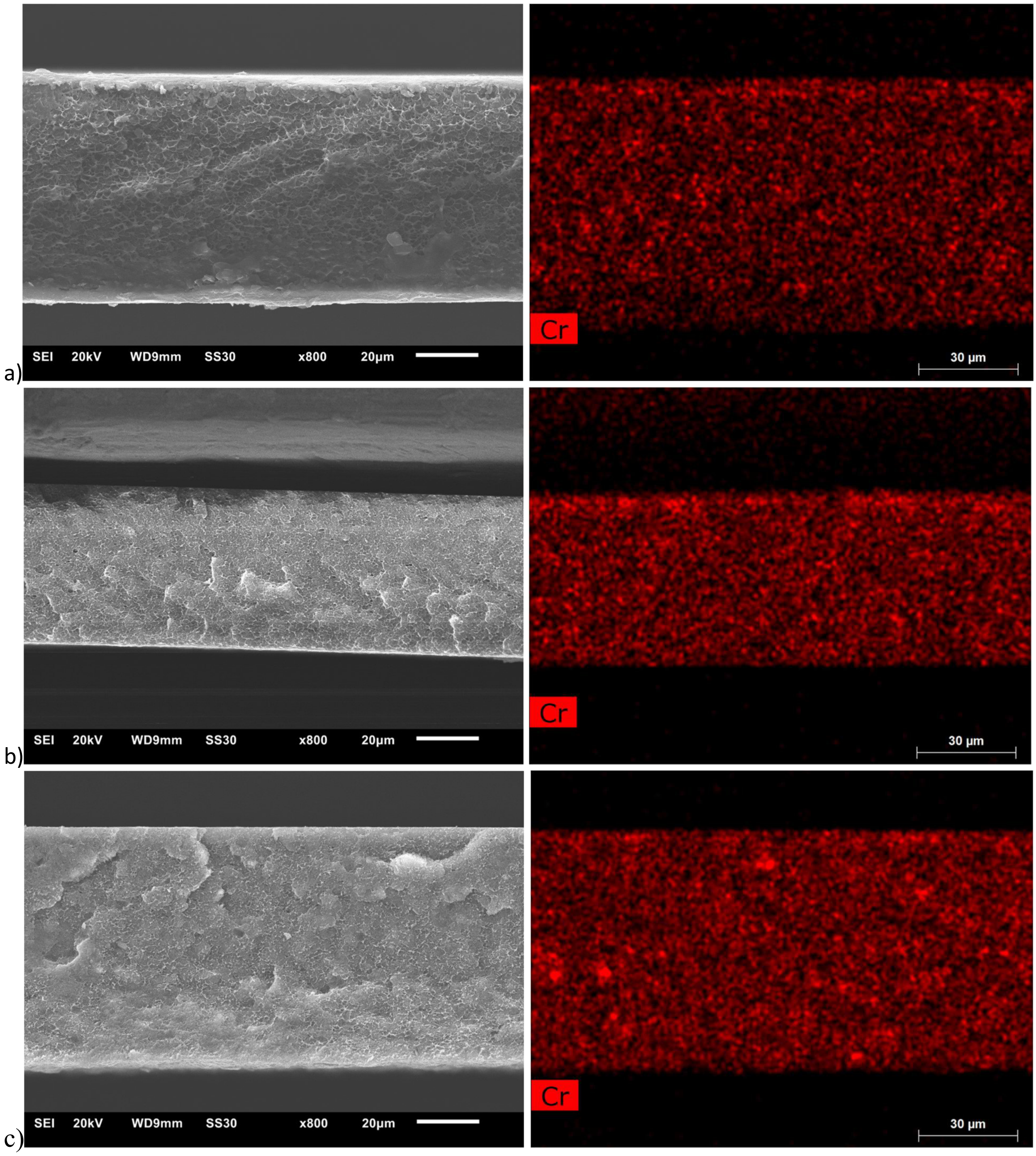

Fig. S4 SEM images combined with SEM/EDX mapping of chromium for cross sections of MMMs of MIL101(Cr)@6FDA-mPD with different loadings of MIL-101(Cr). a) 8 wt% MOF; b) 16 wt% MOF; c) 24 wt% MOF.

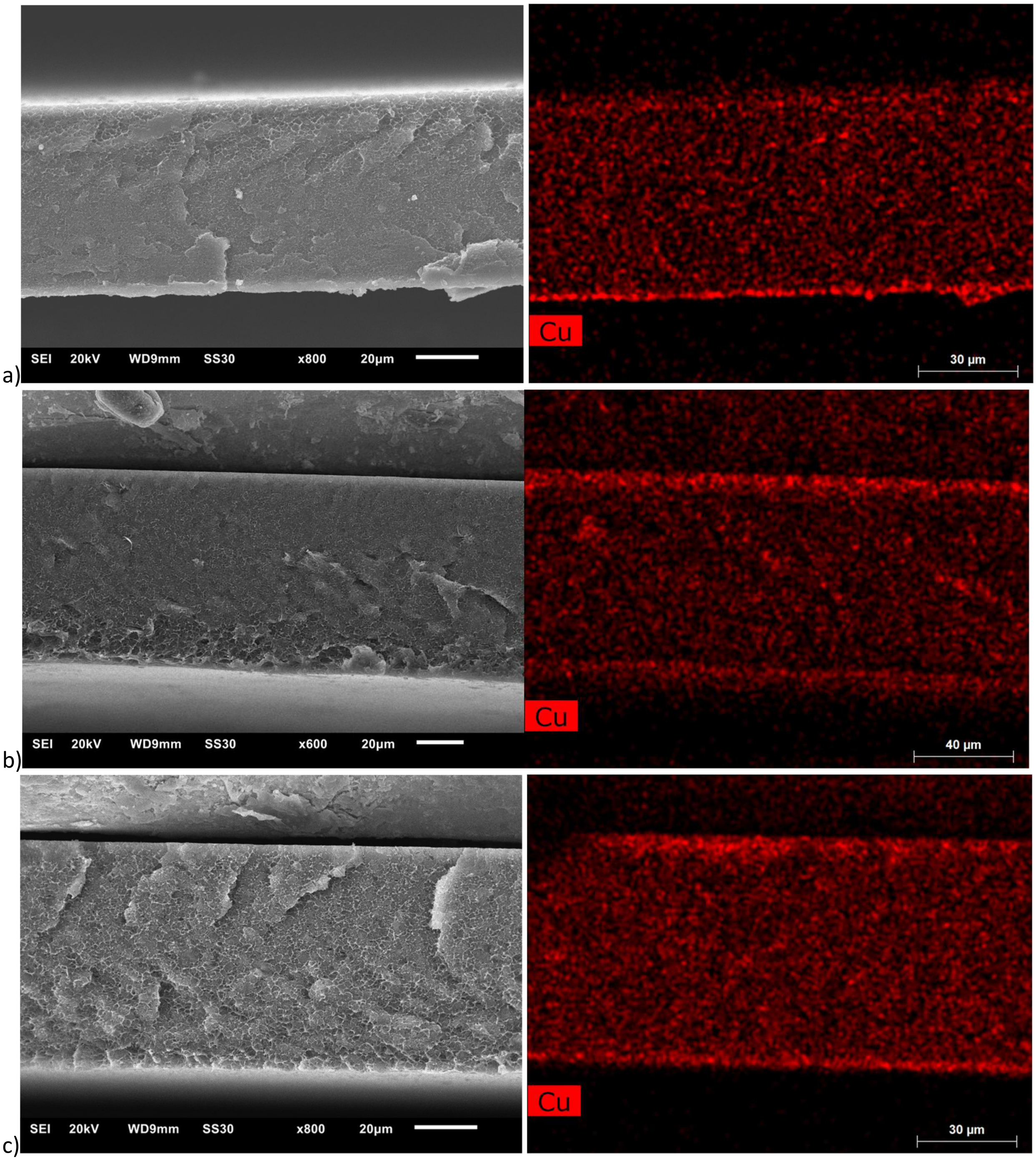

Fig. S5 SEM images combined with SEM/EDX mapping of copper for cross sections of MMMs of MOF-199@6FDA-mPD with different loadings of MOF-199. a) 8 wt% MOF; b) 16 wt% MOF; c) 24 wt% MOF. Note, that for some EDX images copper is detected outside of the membrane cross section, due to reflections from the sample holder which is made of brass.

Maxwell model[1,2,3,4]

The Maxwell model requires no assumption and leads to no conclusion about the gas selectivity of the MMMs. The Maxwell model is solely based on permeability (*P*) and filler volume fraction (ϕ with weight percentage and density) as given in eq. (S1)-(S3). With the Maxwell model it is possible to predict gas permeation through a dense composite membrane. For spherical particles the permeability of the composite membrane P_{eff} can be estimated as follows:

$$\boldsymbol{P_{eff} = P_c \times \frac{P_d + 2P_c - 2\phi_d \times (P_c - P_d)}{P_d + 2P_c + \phi_d \times (P_c - P_d)}} \qquad \text{(S1)}$$

Where, P_c is the continuous phase permeability, P_d is the dispersed phase permeability and ϕ_d is the volume fraction of the filler.

With equation S2 one can calculate the filler volume fraction in the dispersed phase:

$$\boldsymbol{\phi_d = \frac{w_d \,/\, \rho_d}{\frac{w_c}{\rho_c} + \frac{w_d}{\rho_d}}} \qquad \text{(S2)}$$

With w_d and w_c as the weight percentages, ρ_d and ρ_c as the densities of the filler and the polymer.

In cases where the filler exhibits a distinctly higher permeability than the continuous phase ($P_d >> P_c$) equation (S1) can be simplified as follows, which then corresponds to “Maxwell model ∞”:

$$P_d >> P_c;\ \frac{P_{eff}}{P_c} = \frac{1+2\phi_d}{1-\phi_d} \qquad \text{(S3)}$$

This limiting equation (S3) is also given as equation (1) in the main manuscript.
For MOF-199 (HKUST-1) pure MOF membranes were already fabricated and measured several times for their CO_2 and CH_4 permeance.[5]
The experimental CO_2 permeance of roughly 2000x10^{-10} mol m^{-2} s^{-1} Pa^{-1} with a membrane thickness of about 10 µm translates into a CO_2 permeability of about 6000 Barrer = P_d in eq. (S1).
For CH_4 a permeability of about 1000 was measured (permeance ≈ 300x10^{-10} mol m^{-2} s^{-1} Pa^{-1}).
CO_2 permeability of pure 6FDA-mPD, P_c = 10 Barrer.
For MIL-101(Cr), to our best knowledge, no pure MOF membrane was ever produced. But considering that the pore sizes of MIL-101(Cr) are even larger than those of MOF-199 we would expect a similar result.

Table S2 CO_2/CH_4 (50/50 mixture) permeation results on Mixed MIL-101(Cr)@6FDA-mPD membranes.

Membrane				
MIL-101(Cr) loading [wt%]	Membrane thickness [µm]	P (CO_2) [Barrer]	P (CH_4) [Barrer]	α (CO_2/CH_4)
0	44 – 110	9.9 ± 0.4[b]	0.19 ± 0.01[b]	54 ± 6
8	47 – 55	13.8 ± 0.1[a]	0.26 ± 0.00[a]	53 ± 1
16	61 – 74	29 ± 1[b]	0.51 ± 0.04[b]	54 ± 7
24	81 – 85	49.6 ± 0.2[a]	1.00 ± 0.02[a]	50 ± 1

Values are the average and standard deviation of at least two different membrane samples.
[a] experiments performed at 35 °C and ΔP = 2 bar total feed pressure; [b] experiments performed at 25 °C and ΔP = 3 bar total feed pressure.

Table S3 CO_2/CH_4 (50/50 mixture) permeation results on MOF-199@6FDA-mPD membranes.

Membrane		P (CO_2) [Barrer]	P (CH_4) [Barrer]	α (CO_2/CH_4)
MOF-199 loading [wt%]	Membrane thickness [μm]			
0	44 – 110	9.9 ± 0.4^b	0.19 ± 0.01^b	54 ± 6
8	77 – 82	11.4 ± 0.3^b	0.17 ± 0.01^b	67 ± 6
16	99 – 102	20.2 ± 0.9^b	0.27 ± 0.01^b	73 ± 6
24	80 – 87	28.3 ± 0.4^a	0.32 ± 0.01^a	89 ± 4

Values are the average and standard deviation of at least two different membrane samples. [a] experiments performed at 35 °C and ΔP=2 bar total feed pressure; [b] experiments performed at 25 °C and ΔP=3 bar total feed pressure.

Table S4 Glass transition temperatures (T_g) for pure 6FDA-mPD and different weight percentages of MIL-101Cr and MOF-199@6FDA-mPD MMMs.

Material	**T_g [K]**	
6FDA-mPD	300	± 2
8wt% MIL-101Cr@6FDA-mPD MMM	303	± 2
16wt% MIL-101Cr@6FDA-mPD MMM	299	± 4
24wt% MIL-101Cr@6FDA-mPD MMM	302	± 1
8wt% MOF-199@6FDA-mPD MMM	297	± 2
16wt% MOF-199@6FDA-mPD MMM	292	± 1
24wt% MOF-199@6FDA-mPD MMM	294	± 2

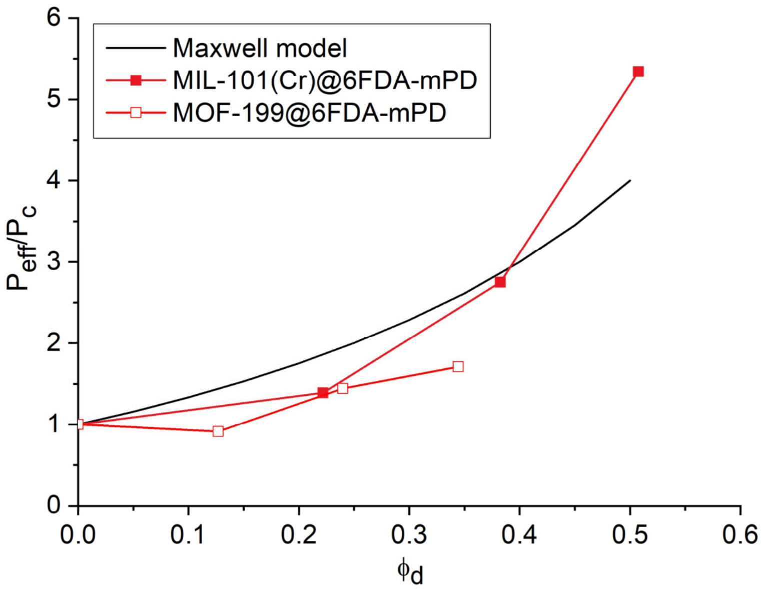

Fig. S6: Relative experimental CH_4 permeabilities (referenced to the permeability P_c of the pure polymer membrane) for MIL-101(Cr)@6FDA-mPD MMMs (filled red squares) and MOF-199@6FDA-mPD MMMs (hollow red squares) with different filler volume fraction ϕ_d. The black line gives the relative theoretical CH_4 permeabilities for a porous (filler permeability $P_d >> P_c$).

Table S5 Gas (CO_2/CH_4) permeation data of mixed-matrix membranes with MOFs from literature.

Polymer[a]	**MOF**	**MOF (wt%)**	**P (CO_2)**[b] **[Barrer]**	**P (CH_4)**[b] **[Barrer]**	**S** [c] **(CO_2/CH_4)**	**Ref.**
Matrimid 5218	MOF-5	*0*	9	0.22	41.7	6
		10	11.1	0.22	51	
		20	13.8	0.34	40.5	
		30	20.2	0.45	44.7	
PSF	Cu-BTC	*0*	6.5	0.3	17	7
		5	7.7	0.3	22	
		10	7.9	1.3	7	
Matrimid 5218	Cu-BPY-HFS	*0*	7.29	0.21	34.7	8
		10	7.81	0.24	31.9	
		20	9.88	0.36	27.6	
		30	10.36	0.38	25.4	
		40	15.06	0.59	25.6	
Matrimid 5218	ZIF-8	*0*	9.52	0.24	39.8	9
		20	9.03	0.18	51.1	
		30	14.23	0.38	38.2	
		40	24.55	0.89	27.8	
		50	4.72	0.05	124.9	
		60	8.08	0.1	80.8	
Matrimid	ZIF-90	*0*	7.8	–	35.5	10
		15	12.5	–	35.6	
6FDA-DAM	ZIF-90B	*0*	400	–	17	
		15	680	–	26	
6FDA-DAM	ZIF-90A	*15*	800	–	27	
PSF	ZIF-8	*16*	12.1	–	19.8*	11
PSF	ZIF-8/S1C	*16*	8.5	–	19.6*	
PSF	HKUST-1	*16*	8.8	–	15.7*	
PSF	HKUST-1/S1C	*16*	8.9	–	22.4*	
PSF	S1C	*16*	9.6	–	20.9*	
PSF	NH_2-MIL-53(Al)	*0*	4.7	0.2	23.5*	12
		8	4.7	0.13	29.3*	
		16	5	0.13	33.0*	
		25	5.4	0.1	46.0*	
		40	10.3	0.64	16.7*	
6FDA-ODA	UiO-66	*0*	14.4	0.33	44.1	13
		25	50.4	1.1	46.1	
6FDA-ODA	NH_2-UiO-66	*25*	13.7	0.27	51.6	
6FDA-ODA	MOF-199	*25*	21.8	0.43	51.2	
6FDA-ODA	NH_2-MOF-199	*25*	26.6	0.45	59.6	

Polymer[a]	**MOF**	**MOF (wt%)**	**P (CO_2)**[b] **[Barrer]**	**P (CH_4)**[b] **[Barrer]**	**S** [c] **(CO_2/CH_4)**	**Ref.**
6FDA-ODA	UiO-67	*25*	20.8	1.4	15	13
Matrimid 5218	MIL-53	*0*	6.2	0.2	28.5*	14
		15	6.7	0.71	8.5*	
	MIL-53-NH_2	*15*	9.2	4.4	2.1*	
Ultem 1000	MIL-53	*0*	1.46	0.037	31.6*	
		15	1.77	0.041	42.8*	
	MIL-53-NH_2	*15*	3	0.083	36.1*	
6FDA/ODA-DAM (1:1)	MIL-53	*0*	54.1	2.3	23.6	
		20	61.5	4.8	13	
	MIL-53-NH_2	*10*	51.2	1.8	31.8	
		20	52.6	3.4	13.1	
		22	50	4.8	12.5	
6FDA/ODA-DAM (1:4)	MIL-53	*0*	130	6.4	23.6	
		25	123	6.9	19.1	
	MIL-53-NH_2	*10*	112	4.5	23.5	
		15	113	4	28.5	
		20	115	8.2	14.3	
PSF	MIL-101(Cr)	*0*	5.6	0.33	16.9	15
		7.5	15.2	0.64	23.9	
		14	22.3	0.93	24	
		19	32	1.26	25.3	
		24	36.2	1.64	22.2	
PES	C15A1	*0.25*	3.01	0.16	18.72	16
	C15A2	*0.25*	9.77	0.29	33.49	
PPO	Cu-BTC	*40*	113.7	3.49	33.5	17
Matrimid	Fe-BTC	*30*	13.5	0.45	30	18
Pebax-2553	ZIF-8	*35*	1287	143	9	19
6FDA-durene	ZIF-8	*33.5*	1552	140	11.06	20
Matrimid	SMBA@CNT	*10*	4.1	0.043	97	21
Cellulose acetate	Ni_2(dobdc)	*23*	3.78	–	30.3*	22
Matrimid		*23*	9.31	–	29.5*	
6FDA-DAT		*15*	63.9	–	51.9*	
6FDA-DAM:DAT		*18*	220	–	30.5*	
6FDA-DAM		*23*	715	–	14.5*	
6FDA-durene		*21*	1035	–	12.3*	

Polymer[a]	MOF	MOF (wt-%)	P (CO_2)[b] [Barrer]	P (CH_4)[b] [Barrer]	S [c] (CO_2/CH_4)	Ref.
6FDA-DAM	ZIF-11	*0*	20.6	-	32.7	23
		10	109.7	-	31.3	
		20	257.5	-	31.0	
		30	73.1	-	30.4	
6FDA-DAM	3D-COF	*0*	540	-	25.5	24
		10	850	-	29.0	
		15	1280	-	27.1	
Pebax-1657	Fe-BTC	*30*	402.7	-	21.5	25
Pebax-1657	$Ni_2(L\text{-}asp)_2bipy$	*20*	120.2	-	37.1	26
	$Ni_2(L\text{-}asp)_2pz$	*20*	89.7	-	23.1	
PVDF	Cu-BTC	*0*	0.915	0.043	21.3	27
		5	1.067	0.043	24.8	
		10	2.002	0.048	41.7	
		15	3.206	0.080	40.1	
PMP	Cu-BTC	*0*	76.1	5.0	15.2	28
		5	88.3	5.2	17.1	
		10	102.5	5.3	19.2	
		15	124.4	5.5	22.7	
		20	143.8	5.9	24.3	

[a] PVAC: poly(vinylacetate); PSF: polysulfone; 6FDA: 6FDA: 2,2-bis(3,4-carboxyphenyl) hexafluoropropane dianhydride, DAM: diaminomesitylene, ODA: 4,4'-oxydianiline; DAT: diamino toluene; PVDF: poly(vinylidene fluoride)

[b] gas permeability

[c] all are ideal selectivities except those marked with (*) which correspond to 50/50 % CO_2/CH_4 mixed gas selectivities

MOF-199 = Cu-BTC

References

---

1 Y. Shen and A. C. Lua, Theoretical and experimental studies on the gas transport properties of mixed matrix membranes based on polyvinylidene fluoride. *AIChE Journal*, 2013, **59**, 4715-4726.

2 S. Rafiq, A. Maulud, Z. Man, M. I. A. Mutalib, F. Ahmad, A. U. Khan, A. L. Khan, M. Ghauri and N. Muhammad, Modelling in mixed matrix membranes for gas separation. *Can. J. Chem. Eng.*, 2015, **93**, 88-95.

3 Z. Sadeghi, M. Omidkhah, M. E. Masoumi and R. Abedini, Modification of existing permeation models of mixed matrix membranes filled with porous particles for gas separation. *Can. J. Chem. Eng.*, 2016, **94**, 547-555.

4 H. B. Tanh Jeazet, T. Koschine, C. Staudt, K. Raetzke and C. Janiak, Correlation of Gas Permeability in a Metal-Organic Framework MIL-101(Cr)-Polysulfone Mixed-Matrix Membrane with Free Volume Measurements by Positron Annihilation Lifetime Spectroscopy (PALS). *Membranes* (Basel), 2013, **3**, 331-353.

5 M. N. Shah, M. A. Gonzalez, M. C. McCarthy and H.-K. Jeong, An Unconventional Rapid Synthesis of High Performance Metal–Organic Framework Membranes. *Langmuir*, 2013, **29**, 7896-7902.

6 E. V. Perez, K. J. Balkus Jr., J. P. Ferraris and I. H. Musselman, *J. Membr. Sci.*, 2009, **328**, 165–173.

7 A. Car, C. Stropnik and K. V. Peinemann, *Desalination*, 2006, **200**, 424–426.

---

8 Y. Zhang, I. H. Musselman, J. P. Ferraris and K. J. Balkus Jr., *J. Membr. Sci*., 2008, **313**, 170–181.

9 M. J. C. Ordonez, K. J. Balkus Jr., J. P. Ferraris and I. H. Musselman, *J. Membr. Sci*., 2010, **361**, 28–37.

10 T.-H. Bae, J. S. Lee, W. Qju, W. J. Koros, C. W. Jones and S. Nair, *Angew. Chem., Int. Ed*., 2010, **49**, 9863–9866.

11 B. Zornoza, B. Seoane, J. M. Zamaro, C. Tellez and J. Coronas, *ChemPhysChem*., 2011, **12**, 2781–2785.

12 Zornoza, B.; Martinez-Joaristi, A.; Serra-Crespo, P.; Tellez, C.; Coronas, J.; Gascon, J.; Kapteijn, F. *Chem. Commun.,* 2011, **47**, 9522–9524.

13 Nik, O.G.; Chen, X.Y.; Kaliaguine, S. *J. Membr. Sci*., 2012, **413–414**, 48–61.

14 X. Y. Chen, H. Vinh-Thang, D. Rodrigue and S. Kaliaguine, *RSC Adv*., 2013, **3**, 24266–24279.

15 H. B. Tanh Jeazet, T. Koschine, C. Staudt, K. Raetzke and C. Janiak, *Membranes*, 2013, **3**, 331–353.

16 N.M. Ismail, A. F. Ismail, A. Mustaffa, *Jurnal Teknologi*, 2014, **69**, 83–87.

17 L. Ge, W. Zhou, V. Rudolph, Z. H. Zhu, *J. Mater. Chem. A*, 2013, **1**, 6350–6358.

18 S. Shahid, K. Nijmeijer, *J. Membr. Sci.,* 2014, **459**, 33–44.

19 V. Nafisi, M.-B. Hägg, *J. Membr. Sci.,* 2014, **459**, 244–255.

20 S. N. Wijenayake, N. P. Panapitiya, S. H. Versteeg, C. N. Nguyen, S. Goel, K. J. Balkus, I. H. Musselman, J. P. Ferraris, *Ind. Eng. Chem. Res*., 2013, **52**, 6991–7001.

21 Y. Liu, D. Peng, G. He, S. Wang, Y. Li, H. Wu, Z. Jiang, *ACS Appl. Mater. Inter.,* 2014, **6**, 13051–13060.

22 J. E. Bachman, J. R. Long, *Energy Environ. Sci.,* 2016, **9**, 2031–2036.

23 M. S. Boroglu, A. B. Yumru, *Sep. Purif. Technol.,* 2016, **173**, 269–279.

24 Y. Yang, K. Goh, P. Weerachanchai, T-H. Bae, *J. Membr. Sci*., 2019, **574**, 235–242.

25 F. Dorosti, A. Alizadehdakhel, *Chem. Eng. Res. Des*., 2018, **136**, 119–128.

26 L. Fan, Z. Kang, Y. Shen, S. Wang, H. Zhao, H. Sun, X. Hu, H. Sun, R. Wang, S. Sun, *Cryst. Growth. Des.,* 2018, **18**, 4365–4371.

[27] E. A. Fejani, H. Mahdavi and A. Tavasoli, *Chem. Eng. Res*. Des., 2015, **96**, 87–102.

[28] R. Abedini, A. Mosayebi and M. Mokhtari, *Process. Saf. Environ.,* 2018, **114**, 229–239.

3.4 A practical guide to calculate the isosteric heat/enthalpy of adsorption via adsorption isotherms in metal-organic frameworks, MOFs

Alexander Nuhnen, Christoph Janiak

Eingereicht zur Publikation bei Chemical Society Reviews am 22.04.2020

Poröse Materialien wie MOFs sind interessante Kandidaten für die Gastrennung und -Speicherung. Ein wichtiger Parameter, um tiefere Einblicke in den Adsorptionsprozess eines Adsorptivs an ein Adsorbens zu erhalten, ist die isostere Adsorptionsenthalpie, ΔHads, welche über die abgegebene/aufgenommene Wärme bei der Anlagerung/Loslösung des Adsorptivs an einem Adsorbens definiert ist. Für die Ableitung der isosteren Adsorptionsenthalpie nach dem Clausius-Clapeyron-Ansatz oder der Virial Analyse müssen zwei Adsorptionsisothermen bei mit geringfügig unterschiedlichen Temperaturabständen (T1, T2) mit $\Delta T \approx$ 10-20 K aufgenommen werden. In diesem Tutorial wird das Verfahren des üblichen Freundlich-Langmuir-Fit / Clausius-Clapeyron-Ansatzes und die Anpassung der Isothermen unter Anwendung der Virial Analyse mit verwendbaren Excel-Tabellen und Origin-Dateien für die anschließende Ableitung von ΔHads vorgestellt. Beispielhafte Adsorptionsisothermen von CO_2, SO_2 und H_2 bei zwei Temperaturen an verschieden MOFs werden analysiert. Die detaillierte rechnerische Beschreibung und der Vergleich des Clausius-Clapeyron-Ansatzes und der Virial Analyse zur Bestimmung von ΔHads skizzieren die Grenzen der beiden Methoden in Bezug auf die verfügbaren experimentellen Daten, insbesondere bei niedrigen Drücken und niedrigen Werten für die Gasaufnahme. Eine wichtige Forderung aus der Analyse der Sorptionsdaten und Anpassung durch die vorliegenden Fit Modelle ist, dass keine Extrapolation über den experimentellen Datenbereich hinaus durchgeführt werden sollte. Die Qualität der wichtigen und zugrundeliegenden Isothermen Anpassungen muss überprüft und mit logarithmisch skalierten *n*/*p*-Isothermen Kurven für die Freundlich-Langmuir-Anpassung im Niederdruckbereich und durch geringe Standardabweichungen für die Koeffizienten in der Virial Analyse sichergestellt werden.

Anteile an der Veröffentlichung:

Auswahl der Daten, Anfertigung der Berechnungen und Schreiben des Manuskripts.

Korrekturen erfolgten von Herrn Prof. Dr. Janiak.

ARTICLE

A practical guide to calculate the isosteric heat/enthalpy of adsorption via adsorption isotherms in metal-organic frameworks, MOFs†‡

Received 00th January 20xx,
Accepted 00th January 20xx

DOI: 10.1039/x0xx00000x

Alexander Nuhnen[a] and Christoph Janiak[a]

Porous materials such as MOFs are interesting candidates for gas separation and storage. An important parameter to gain deeper insights to the adsorption process of an adsorptive on an adsorbent is the isosteric enthalpy of adsorption, ΔH_{ads} which is defined as the heat to be released/required when an adsorptive binds/detaches to the solid surface of an adsorbent. Two adsorption isotherms at different but close temperatures, (T_1, T_2) with $\Delta T \approx$ 10-20 K are the basis to derive the isosteric enthalpy of adsorption through the Clausius-Clapeyron approach or the virial analysis. This tutorial presents the procedure of the common Freundlich-Langmuir fit/ Clausius-Clapeyron approach and the virial fit of the isotherms with usable Excel sheets and Origin files for the subsequent derivation of ΔH_{ads}. Exemplary adsorption isotherms of CO_2, SO_2 and H_2 at two temperatures on MOFs are analyzed. The detailed computational description and comparison of the Clausius-Clapeyron approach and the virial analysis to determine ΔH_{ads} outlines the limitations of the two methods with respect to the available experimental data, especially at low pressure/low uptake values. It is emphasized that no extrapolation beyond the experimental data range should be done. The quality of the important and underlying isotherm fits must be checked and ensured with logarithmic-scale n/p isotherm plots for the Freundlich-Langmuir fit in the low-pressure region and through low standard deviations for the coefficients in the virial analysis.

Key learning points:

- For the enthalpy of adsorption at (close to) zero coverage, ΔH_{ads}^0 low uptake data points in the adsorption isotherm are necessary, and such missing data must not be extrapolated by fitting.
- The often-emphasized enthalpy of adsorption at zero coverage, ΔH_{ads}^0 heavily depends on the isotherm measurement and subsequent fit and calculation details, which should be provided.
- For the value of ΔH_{ads}^0 as well as for the $\Delta H_{ads}(n)$ vs. n plot, the lowest experimental uptake n_{min}, which was included in the isotherm fit for both isotherms, must be given to exclude misleading extrapolation.
- The isotherm fits and subsequent calculation to derive at ΔH_{ads}^0 or $\Delta H_{ads}(n)$ vs. n should not be left to implemented sorption analyzer routines without clear documentation.
- The virial analysis is so far the best isotherm fitting method available, yet the correctness of the virial fit must be ensured through low standard deviations of the obtained virial coefficients.

Introduction

Gas sorption for storage and separation is of continuous interest with porous materials, such as activated carbon, zeolites, silica gel, metal-organic frameworks (MOFs) etc. At the moment, MOFs, which are potentially porous three-dimensional coordination polymers,[1] appear to receive the highest attention for such gas sorption applications as they feature a high functional and composition diversity.[2] MOFs are built from metal ions or metal cluster, connected by multidentate organic ligands and can be tuned in regards to their physiochemical properties depending on their organic and inorganic building blocks.[3] Over the last two decades plenty of studies about gas separation and storage in MOFs have been published.[4,5]

Of interest for gas sorption with MOFs are, e.g., carbon capture and storage (CCS) technologies.[6,7] Furthermore, MOFs with high hydrogen uptake are envisioned for energy storage and as carrier in mobile applications,[8,9] in order to achieve a higher volumetric energy density, which is otherwise only

---

[a] *Institut für Anorganische Chemie und Strukturchemie, Heinrich-Heine-Universität Düsseldorf, D-40204 Düsseldorf Germany. Email: janiak@hhu.de.*

† Electronic Supplementary Information (ESI) available: Details for Clausius-Clapeyron and virial equation, Freundlich-Langmuir fit of n vs. p isotherms, MOF structures, SO_2 Adsorption isotherms of NH_2-MIL-125(Ti) at 273 K and 293 K, Virial analysis for SO_2 isotherms of NH_2-MIL-125(Ti) at 273 K and 293 K with a larger number of a_i and b_i fit parameters, Enthalpy of adsorption for CO_2 on MIL-100(Cr). See DOI: 10.1039/x0xx00000x

‡ In order not to interrupt the flow of reading we have added a glossary for sorption specific terms as Appendix.

accessible under high pressures (up to 700 bar) or cryogenically (cooled to 20 K). By physisorption of supercritical gases, such as dihydrogen in a porous material a liquid-like adsorbate phase (with higher than gas density) is formed. For practical use at operating conditions of 1.5 to 30 bar at 298 K lightweight materials with high adsorption capacities and binding enthalpies of about –15 to –20 kJ mol^{-1} are required.[10,11] Higher H_2 binding enthalpies are achieved by chemisorption of H_2 as in metal hydrides or other materials which store hydrogen through chemical bond formation; there the release is slow and requires heating.[12] Besides, the sorption of CO_2 and H_2, also CH_4 separation and storage draws interest[13] and an effective capture of harmful gases such as SO_2 and NO_x is of growing importance.[14]

In the chemical industry the separation of gas mixtures by pressure swing or thermal swing adsorption at a surface is an established process.[15] The surface is part of the adsorbent; the adsorbed species become the adsorbate. For the separation of two species from a fluid mixture, these two species (assuming the same unrestricted accessibility to the surface) must have different interaction energies with the surface, so that one is preferentially adsorbed over the other. The actual amount adsorbed of adsorbate at a given mass of adsorbent depends on the relative pressure and the temperature together with the adsorbate-adsorbent interaction energy.

We note that for this interaction energy the terms “heat of adsorption”, “isosteric heat of adsorption” both with the symbol Q_{st} and “(isosteric) enthalpy of adsorption, ΔH_{ads}” appear to be used indiscriminately. In most of the MOF literature it is not clearly distinguished between the two expressions of ΔH_{ads} and Q_{st} and they appear to be used interchangeably to describe binding energies. The use of the term “heat of adsorption”, Q_{st} is discouraged since it does not correspond to any well-defined thermodynamic change of state. It has been suggested that the term “isosteric heat” is preferably replaced by the term “isosteric enthalpy of adsorption, ΔH_{ads}”.[16] Q_{st} is a positive quantity and for an adsorption process the enthalpy of adsorption, ΔH_{ads} has to be negative, in short $\Delta H_{ads} = -Q_{st}$.[17,18] The isosteric enthalpy of adsorption, ΔH_{ads} is defined as the heat which is released when an adsorptive binds to a surface.[19] The higher the adsorption enthalpy for an adsorbate-adsorbent pair, the more species will be adsorbed at a given pressure and temperature. The enthalpy of adsorption is released during the adsorption process ($\Delta H_{ads} <$ 0 kJ/mol) and is the reverse of the enthalpy of desorption, ΔH_{des}, which is required for the reverse process of desorption ($\Delta H_{ads} = -\Delta H_{des}$).

Generally, adsorption materials should meet several requirements to be suitable for a sorption application, such as high selectivity, low regeneration energies and high working capacity.[20] Consequently, the enthalpy of adsorption is an important parameter in adsorption processes and is further used to gain deeper insights into the adsorbate-adsorbent interactions. Since ΔH_{ads} depends on the strength of the interaction for an adsorbate-adsorbent pair, it is possible to classify the interactions of the adsorbed species with the adsorbent, e.g. if weak physisorption or strong chemisorption is present. In the same way, ΔH_{ads} can be used to determine the regeneration energies for the desorption of the adsorbate. Regeneration energies are especially important for pressure swing experiments, as the energy required for desorption depends on the binding strength.[21]

Approaches to determine ΔH_{ads} can initially be divided into two types, experiment-based calculations and molecular simulations. The simulated enthalpies of adsorption in the latter are mostly based on isotherms obtained by grand canonical Monte Carlo simulations (GCMS) and calculated via the ensemble fluctuation approach.[22] The experimental procedures can be divided into a direct and indirect approach. In the direct approach, using a calorimetric-volumetric system, it is possible to directly measure the released heat during the adsorption with a calorimeter.[23] Since these systems are very complex and costly, only very few studies use the direct method to determine ΔH_{ads}.[6] The by far most common way to determine the isosteric enthalpy of adsorption as a function of the amount adsorbed (loading) is via the indirect approach using adsorption isotherms. The adsorbate-adsorbent interaction energy is typically assessed indirectly from two adsorption isotherms obtained at close but different temperatures (T_1, T_2) with $\Delta T \approx$ 10-20 K.

Adsorption isotherms are most typically obtained through volumetric gas sorption measurements. For gases such as CO_2, CH_4 and SO_2 isotherms are usually measured at around standard conditions, for example at 273 K and 293 K from 0 to 1 bar (0-101.3 kPa). This is due to the relative high uptake for many MOF materials even at elevated temperatures for these gases, compared to their respective boiling point. H_2 isotherms are mostly collected at 77 K and 87 K, as the overall uptake at higher temperatures is insufficient. These adsorption isotherms form the basis for either the Clausius-Clapeyron approach or the virial analysis to derive the isosteric enthalpy (ΔH_{ads}) or heat (Q_{st}), respectively, of adsorption.

For the Clausius-Clapeyron approach the two adsorption isotherms should be fitted with the same continuous function, e.g. a Freundlich-Langmuir fit, and evaluated for pressure (p)-loading (n) data pairs with the same loading n at each temperature. This is known as the “isosteric” method, based on the use of the Clausius-Clapeyron equation (Eq. 1)[24] (see Section S1, ESI†).

$$\Delta H_{\mathrm{ads}}(n) = -R \cdot \ln\left(\frac{p_2}{p_1}\right)\frac{T_1 \cdot T_2}{(T_2 - T_1)} \qquad (1)$$

(R = ideal gas constant)

The Clausius-Clapeyron equation relates the adsorption heat effects to the temperature dependence of the adsorption isotherm. There are two approximations made in deriving the Clausius-Clapeyron equation, *i*) a negligible molar volume of the adsorbed phase and *ii*) ideal gas behavior of the gaseous phase (see Section S1, ESI†). Thus, the ΔH_{ads} values from this approach can differ from the direct experimental data, especially at higher loadings (vide infra).[24]

For the virial analysis, the isotherms are fitted according to the virial-type equation (Eq. 2), which expresses the pressure p as a function of loading n of a gas (see Section S2, ESI†).

Especially for highly polarized gases such as CO_2 and SO_2 the virial analysis has been used for calculating enthalpies of adsorption.[25,26]

$$p = n \cdot \exp\left(\sum_{i=0}^{m} C_i n^i\right) \qquad (2)$$

In Eq. (2) C_0 is a constant for the adsorbate-adsorbent interaction, C_1, C_2 etc. are constants for the double, triple etc. interactions in the adsorbent field. The constants C_i depend on temperature and the heat of adsorption Q_{st} (not to be mistaken as the *enthalpy of* adsorption, since $\Delta H_{ads} = -Q_{st}$) is given as (Eq. 3)[27]

$$Q_{st}(n) = \left(\sum_{i=0}^{m} \frac{dC_i}{dT} RT^2 n^i\right) \qquad (3)$$

Note that $\Delta H_{ads}(n)$ or $Q_{st}(n)$ is typically given only as ΔH_{ads} or Q_{st} in the literature, but definitely varies with loading. The amount adsorbed (n), i.e., the surface coverage or loading of an adsorbent is important for ΔH_{ads} or Q_{st} calculations. Most materials feature different adsorption sites with different surfaces energies and thus ΔH_{ads} or Q_{st} depends on the surface coverage of the adsorbent. In return, it is possible to illustrate the energetic heterogeneity, that is, elucidate different adsorption sites of a solid surface when ΔH_{ads} or Q_{st} is plotted against the adsorbed amount n.

In the literature most papers dealing with enthalpy of adsorption from the Clausius-Clapeyron or virial approach essentially state the basic formula and only occasionally also give further information, such as the applied fit of the isotherms. Programs that are implemented with the automatic gas sorption measurement devices can provide ΔH_{ads} plots based on two adsorption isotherms at two temperatures. However, the used method may not be apparent from the manual and software and not necessarily available from the company. Thus, the determination of ΔH_{ads} becomes a black-box method, the underlying principle and pitfalls may no longer be evident.

In this work, we focus on the material class of MOFs, which are currently investigated by researchers coming from disciplines such as organic chemistry, crystal engineering, coordination chemistry, synthesis, crystallography, solid-state (zeolite) chemistry and theoretical chemistry. Structural details for all MOF materials included in this study can be found in the ESI†. For example, to improve the above noted H_2 storage by physisorption in MOFs, current research aims to increase the enthalpy of adsorption. At present $\Delta H_{ads}(H_2)$ in most MOFs is typically –5 to –7 kJ mol^{-1}, much lower than the targeted –15 to –20 kJ mol^{-1}. Thus, in such work the determination of the enthalpy of adsorption is fundamental.[9,10,12]

New researchers entering the field of porous materials and especially MOFs may benefit from a detailed description of the various methods to determine the isosteric enthalpy of adsorption, including the weaknesses, strengths and the procedure of the isotherm fitting by the common methods e.g. Freundlich-Langmuir and virial analysis (vide infra). The specific goal of this Tutorial is not only to describe these methods, but to provide usable Excel data sheets with implemented formulae, where the data from gas sorption isotherms can be pasted into, in order to calculate the isosteric enthalpy of adsorption (see Section S3, ESI† for details).

Clausius-Clapeyron approach

via Freundlich-Langmuir fit of *n* vs. *p* isotherms

The two isotherms at two temperatures must be fitted with the same model. At the mentioned conditions most MOFs will exhibit a Freundlich-Langmuir-type isotherm, which can be fitted with the following Freundlich-Langmuir equation (4):

$$n = \frac{a \cdot b \cdot p^c}{1 + b \cdot p^c} \qquad (4)$$

where n is the amount adsorbed (the loading) in mmol g^{-1}, p the pressure in kPa, a is the maximal loading in mmol g^{-1}, b the affinity constant (1/bar) and c the heterogeneity exponent.
In Fig. 1 an example for the Freundlich-Langmuir fit of CO_2 adsorption isotherms for MIL-160 at 273 K and 293 K is depicted.

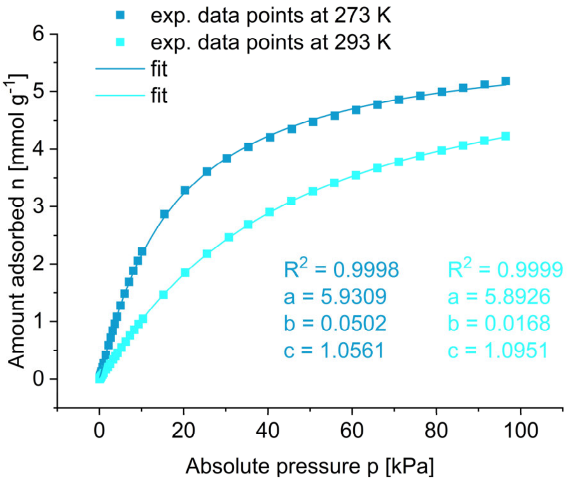

Fig. 1 Freundlich-Langmuir fit for CO_2 adsorption isotherms on MIL-160 at 273 K and 293 K. See ESI† for structure details of MIL-160. Isotherm data taken from reference 28.

A detailed description how to create fitting curves in the program Origin[29] is given in Section S3 and in the pdf slides of the ESI†. Afterwards one has to rearrange the Freundlich-Langmuir equation as follows:

$$p(n) = \sqrt[c]{\frac{n}{a \cdot b - n \cdot b}} \qquad (5)$$

Now one can calculate the pressures p_1 and p_2 for both temperatures T_1 and T_2, respectively at the same loading n by plugging in the respective values for a, b and c derived from the Freundlich-Langmuir fit from Fig. 1. With this approach one can compare the pressures at isosteric conditions, that is at the same uptake of the adsorbate. The fitting routine leads to a continuous sequence of $n|p$ data pairs.

One may wonder why the two $n|p_1$ and $n|p_2$ data pairs could not be directly taken from the experimental data points of the two isotherms: Unless both isotherms were measured with a very large number of data points (concomitant with small pressure intervals) there will not be both pressure values p_1 and p_2 available for the same n. An interpolation or estimation of p

values for a given n value is not practical and not accurate enough. Thus, the fit serves essentially to provide a continuum of $n|p_1$ and $n|p_2$ data pairs or rather $n|p_1|p_2$ data triples.

To get the most reliable data for the isosteric enthalpy of adsorption one should not extrapolate beyond the measured data points, that is to lower or higher uptake and pressure. Such tempting extrapolation should especially not be done to uptakes in the low-pressure region if these data points could not be measured due to limitations in the instrument setup. Note, that low-pressure regimes ($p/p_0 < 0.001$, or $p_{absolute} < 1.0$ mbar) can only be measured if the gas sorption analyzer is fitted with the necessary low-pressure 1 Torr transducer (pressure sensor) and if the instrument is equipped with a turbomolecular pump to provide a low starting pressure.

Therefore, only pressures in the range of the measured gas uptake for both isotherms can and should be calculated. The calculation is provided in the Excel sheet named Ex1 (ESI†).

via straight-line fit of ln*p* vs. *n* isotherms

The $n|p$ data pairs in the measured adsorption isotherms can be transformed into $n|\ln p$ data pairs (Section S3.6, ESI†). We note that in the literature the adsorption isotherms in an 'ln*p* against *n*' plot are then fitted with a straight line ($\ln p = m \cdot n + b$) in a suitable region (Fig. 2, Section S3.7 and S3.8, ESI†).[30] This straight-line or 'ln*p* vs. *n*'-fit approach is mathematically simpler as the Freundlich-Langmuir fit.

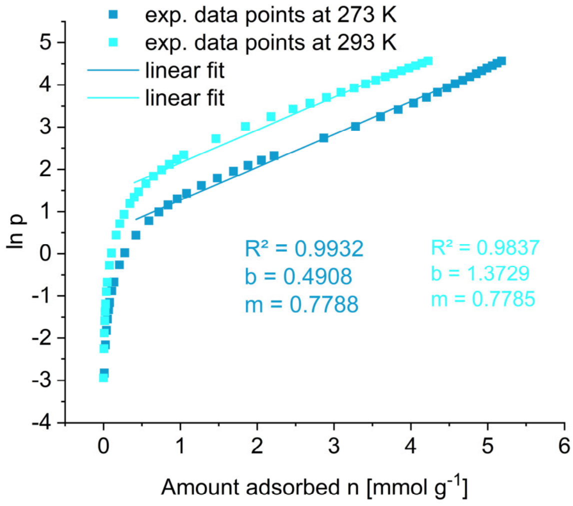

Fig. 2 'lnp against n' plot from the CO_2 adsorption isotherms on MIL-160 at 273 K and 293 K (cf. Fig. 1) with a linear fit approximation in the region of 0.4 < n < maximum uptake. See ESI† for structure details of MIL-160. Isotherm data taken from reference 28.

From the 'ln*p* vs. *n*'-plot in Fig. 2 it is, however, evident that there are only sections where ln*p* against *n* can be approximated by a straight line. For the example in Fig. 2, this is the case from $0.001 < n < 0.1$ or $0.4 < n <$ maximum uptake. The straight-line approximation at the two temperatures then serves to provide a continuum of $n|\ln p_1|\ln p_2$ data triples, yet, only over a limited uptake region, compared with the Freundlich-Langmuir fit.

Only for gases with low affinity to the adsorbent the function of ln*p* against *n* becomes fairly linear over a wider uptake region. However, for most gases adsorbed on MOF materials this straight-line approximation of ln*p* versus *n* is not practical, because of stronger interactions between adsorbate and adsorbent, hence the isotherm has to be fitted by the Freundlich-Langmuir model as described above. For the example in Fig. 2, we use the region of $0.4 < n <$ maximum uptake where, in a first approximation, the two isotherms were fitted by a linear function and then used to derive $\Delta H_{ads}(n)$.

$\Delta H_{ads}(n)$ from ln*p* against 1/*T*

$\Delta H_{ads}(n)$ can be calculated from the derived pressures (p_1, p_2 or $\ln p_1$, $\ln p_2$) at equal loadings (n). Using the $n|p_1|p_2$ or $n|\ln p_1|\ln p_2$ data triples from either the Freundlich-Langmuir or the straight-line fits, respectively, the isosteric enthalpy of adsorption is then calculated by plotting ln*p* against 1/*T* for the isosteric adsorptions, that is, for equal *n* at the two temperatures (Fig. 3). The slope *m* of the straight line with the two data points at $\ln p_1|1/T_1$ and $\ln p_2|1/T_2$ at equal loading *n* will give $\Delta H_{ads}(n)$ according to Eq. (6).[27] For computational details of this calculation approach see Section S3.5 and Excel sheet Ex1 (ESI†).

For didactic purpose, we plotted ln*p* against 1/*T* for 10 loadings *n* in Fig. 3. For computational details of this simplistic calculation approach see Section S3.9 and Excel sheet Ex2 (ESI†).

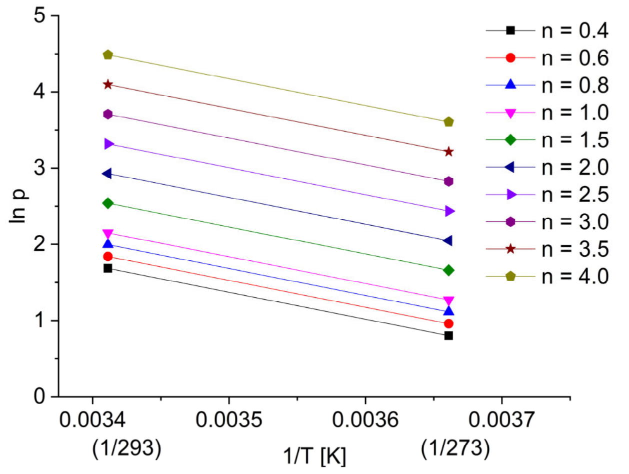

Fig. 3 Isosteric ln*p* against 1/*T* plot for T_1 = 273 K and T_2 = 293 K for 10 different loadings *n* (in mmol g^{-1}) to illustrate the determination of $\Delta H_{ads}(n)$ from the slopes ($m = \Delta H_{ads}(n)/R$) of the straight lines (*R* = universal gas constant) (see also Section S1, ESI†).

$$\Delta H_{ads}(n) = R \cdot m \tag{6}$$

The isosteric enthalpy of adsorption, $\Delta H_{ads}(n)$ from a Freundlich-Langmuir fit of the isotherms and from the straight-line-fit of a 'ln*p* against *n*' plot in the region of $0.4 < n <$ maximum uptake is compared in Fig. 4. Both fit methods give similar results for the isosteric enthalpy of adsorption at high amounts adsorbed, but not for the low-uptake region. The 'ln*p* vs *n* plot' method underestimates $\Delta H_{ads}(n)$ significantly. The slopes of the two straight lines in Fig. 2 were essentially equal which also leads to the special case of a constant ΔH_{ads} that is independent from loading.

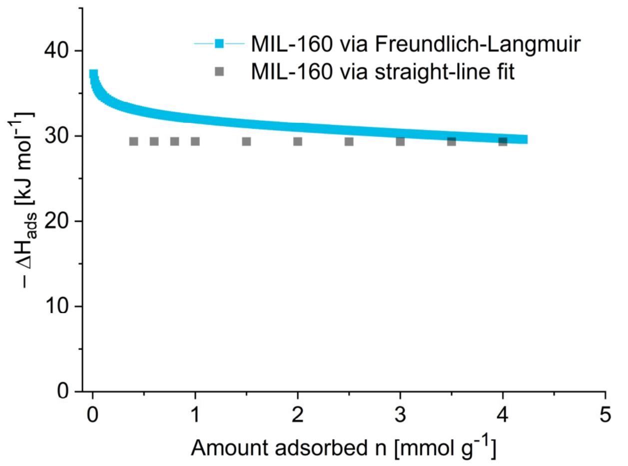

Fig. 4 Isosteric enthalpy of adsorption of CO_2 for MIL-160.The blue curve shows $\Delta H_{ads}(n)$ from a Freundlich-Langmuir fit of the isotherms with n_{min} = 0.01 mmol g^{-1} (Fig. 1). The grey data points represent $\Delta H_{ads}(n)$ derived from the straight-line fit of a 'ln*p* against *n*' plot in the region of 0.4 < *n* < maximum uptake (Fig. 2 and Fig. 3).

ΔH_{ads} describes the strength of the binding energy between adsorbate and adsorbent. It is expected that the value changes with the uptake during the adsorption process. A high enthalpy of adsorption is reasoned by a strong affinity between adsorbate and adsorbent. Typically, the adsorption sites with the highest affinity to the adsorbate species are occupied at low pressure. These adsorption sites correlate with higher (negative) ΔH_{ads} values for very low loadings, as is evident in Fig. 4. The interaction energy for the "first few molecules" is generally called enthalpy of adsorption at zero coverage ($n \rightarrow 0$, $\Delta H_{ads}{}^0$). In the literature often only the value for zero coverage $\Delta H_{ads}{}^0$ is given and discussed. This value of $\Delta H_{ads}{}^0$ can differ distinctly from ΔH_{ads} for the bulk adsorption. Also, the values for $\Delta H_{ads}{}^0$ are often questionable, since mostly not enough experimental data points are collected at such low loadings or they are even just extrapolated through the fitting procedure. After the occupation of the preferred binding sites the enthalpy of adsorption usually declines with increasing uptake. Upon pore filling ΔH_{ads} eventually approaches the interaction energy of the adsorptive molecules, that is, the enthalpy of liquefaction or evaporation, which is 17 kJ mol^{-1} for CO_2. In Fig. 4 ΔH_{ads} is still far from this 17 kJ mol^{-1} because the adsorption isotherms did not reach the pore-filling regime at the highest measured pressure of 100 kPa (Fig. 1).

Careful evaluation of the performance of a porous material should consider the enthalpy of adsorption over the entire adsorption range (not just at zero coverage). At zero to low coverage the magnitude of the isosteric enthalpy of adsorption is largely a function of the binding strength of the strongest binding sites within the material. These (few) high energy sites are, however, rapidly saturated already at low uptake. For the uptake to continue also the remaining sites must have an interaction energy which is above the enthalpy of liquefaction or evaporation.

Virial analysis

For the virial fit the two isotherms measured at two different temperatures are brought into an ln*p* vs. *n* form (Fig. 5, cf. Fig. 2). Equation (7) is then used to fit both isotherms simultaneously, that is with the same(!) fitting parameters a_i and b_j. It is crucial to use the same fitting parameters for both isotherms, hence to compromise in the optimization of the simultaneous fit of both isotherms. Thereby it is important to use as few fitting parameters a_i and b_j as possible.

$$\ln p = \ln n + \frac{1}{T}\sum_{i=0}^{m} a_i n^i + \sum_{i=0}^{m} b_i n^i \qquad (7)$$

In Eq. 7, *p* is the pressure in kPa, *n* is the of total amount adsorbed in mmol/g, *T* is the temperature in K (e.g. 273 K, 293 K), a_i and b_j are the virial coefficients and *m* represents the number of coefficients required to adequately fit the isotherms (see Section S2, ESI†).

As an example, two SO_2 adsorption isotherms at 273 K and 293 K of NH_2-MIL-125(Ti) are shown in Fig. 5 and fitted with Eq. (7).

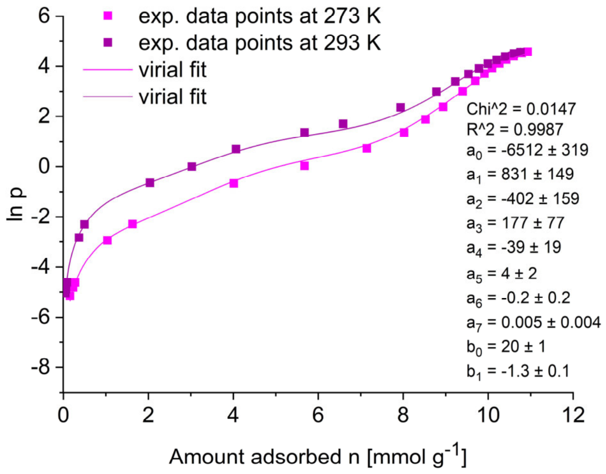

Fig. 5 Virial analysis for SO_2 adsorption isotherms of NH_2-MIL-125(Ti) at 273 K and 293 K with the fitting parameters (virial coefficients) a_i and b_j. The amount adsorbed *n* starts at 0.05 mmol g^{-1} (293 K) and 0.16 mmol g^{-1} (273 K) (see Fig. S4, ESI† for the usual *n* vs *p* isotherm presentation). The virial coefficients a_i have the unit [K·mol^{-i}]. Isotherm data taken from reference 28.

A detailed description how to apply the virial fit in Origin for two isotherms simultaneously is given in the ESI† in the pdf slides. There is no general rule how many virial coefficients a_i and b_j should be used. In practice five *a* (a_0 to a_4) and two *b* parameters (b_0 and b_1) are good starting values for the fit. More parameters should be added until the final fit does not improve anymore. The quality of the fit can be evaluated by comparing R^2 and Chi^2 as well as by visual inspection.

In special cases a reasonable fit with the virial method is not possible. This is, for example, the case when a low uptake regime at the beginning of the isotherm is followed by stepwise uptake behavior with several inflection points in the micropore region as depicted in Fig. 6. We note that the standard linear (*n* vs. *p*) scale diagram of the adsorption isotherm (cf. Fig. S4 and S5, ESI†) will not show such steps very well, whereas a logarithmic *p*-scale or double-logarithmic *n*- and *p*-scale will reveal such steps clearly. In such logarithmic-scale isotherm diagrams a better picture on the microporosity can be derived (Fig. S6 and S7, ESI†).[31] The logarithmic scale of the absolute or relative pressure *p* yields step-like curves in the low-pressure region with the uptake steps related to the filling of pores of a certain size or adsorbent sites of a certain energy. The pressure ranges for these steps depend on the pore sizes or adsorption enthalpies. The linear (*n* vs. *p*) scale with the very steep uptake at very low pressures (p_{abs} < ~10 kPa or p/p_0 < ~0.1) for microporous materials cannot present any uptake steps as the larger pressure region from 10 < p_{abs} < 100 kPa takes up most (90%) of the axis length. The logarithmic scale, on the other hand, expands and presents at over 80% of the axis length the pressure region below 10 kPa. (We note that the fit problem of such uptake steps in the low-pressure region is in principle not limited to the virial fit but also applies to the Freundlich-Langmuir fit. It is just more apparent for the virial fit since it is based on the 'ln*p* vs n' plot with the inherent expansion on the low-pressure region.)

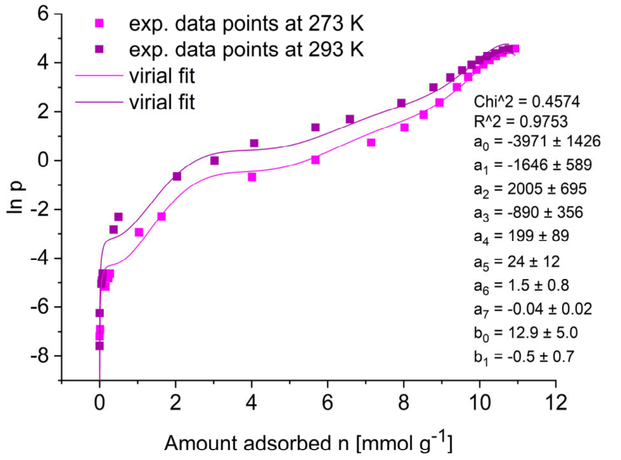

Fig. 6 Virial analysis for SO_2 adsorption isotherms of NH_2-MIL-125(Ti) at 273 K and 293 K with additional low uptake points, starting at n = 0.0002 mmol g^{-1} (see Fig. S5, ESI† for the usual *n* vs *p* isotherm presentation). The virial coefficients a_i have the unit [$K \cdot mol^{-i}$]. Isotherm data taken from reference 28.

The isotherms in Fig. 6 cannot be reliably fitted, even by adding more *a* and *b* parameters (see Fig. S8, ESI† for a fit of Fig. 6 with additional *a* and *b* parameters). Hence, the adsorption data points in the low pressure range had to be excluded to enable a reasonable fit as shown in Fig. 5. As a consequence, this implies that one cannot report a ΔH_{ads} for adsorptions below the range of the used and fitted gas uptake values.

From the virial fit, $\Delta H_{ads}(n)$ is then calculated by multiplying the ideal gas constant *R* with the sum of the a_i coefficients multiplied by the uptake *n* to the power of *i* (Eq. 8) (see the Excel sheet Ex3 (ESI†) for computational details):

$$\Delta H_{ads}(n) = R \cdot \sum_{i=0}^{m} a_i n^i \qquad (8)$$

(See Eq. (S29) in ESI† for Eq. (8) in the form $Q_{st} = -R\Sigma a_i n^i$ as it is normally given in the literature). Note that Eq. (8) will yield a negative value for $\Delta H_{ads}(n)$ from the most important coefficient a_0 being negative. (Furthermore, with the unit of the ideal gas constant *R* of J K^{-1} mol^{-1} and *n* with the unit mol, the virial coefficients a_i must have the unit $K \cdot mol^{-i}$ in order to derive at the unit of (k)J mol^{-1} for ΔH_{ads}.) The isosteric enthalpy of adsorption, $\Delta H_{ads}(n)$, derived from the virial fit shown in Fig. 5, is plotted against the amount adsorbed *n* in Fig. 7. The higher isosteric enthalpy of adsorption for SO_2 compared, for example, to CO_2 (vide supra) or H_2 (vide infra) can be explained by stronger interactions between the polar, permanently dipolar SO_2 molecule and functional groups within the structure of the MOF adsorbent. As expected, a decrease in the enthalpy of adsorption is seen with increased loading as the higher energy binding sites are occupied first. The enthalpy of adsorption for SO_2 at/near zero coverage, $\Delta H_{ads}(n)$ in the amino-functionalized MOF NH_2-MIL-125(Ti) exhibits a value of –53 kJ mol^{-1} (from Eq. (8) with the lowest experimental uptake for both isotherms of n = 0.16 mmol g^{-1} and the a_i given in Fig. 5). Such a high enthalpy of adsorption for amine functionalized MOFs is in good agreement with the literature.[25] Besides functional groups at the linker, open metal sites in MOFs are predestined for high binding-energy interactions with molecules and can exhibit high "zero-coverage" enthalpies of adsorption.[32,33]

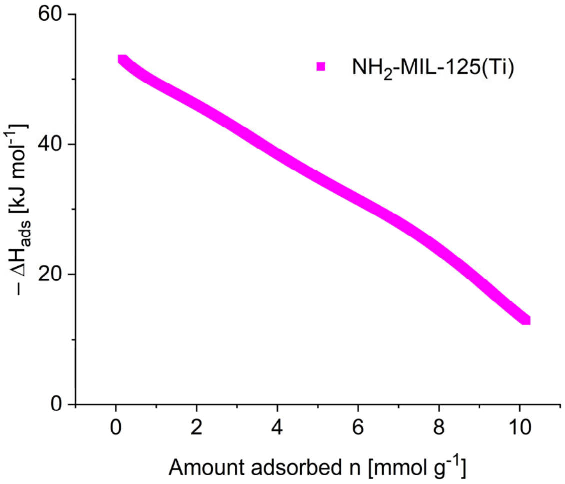

Fig. 7 Isosteric enthalpy of adsorption of SO_2 for NH_2-MIL-125(Ti) from a virial fit of the SO_2 adsorption isotherms at 273 K and 293 K in Fig. 5. The isotherms were fitted from n_{min} = 0.16 mmol g^{-1}. Computational details with Eq (8) are given in the Excel sheet Ex3 (ESI†).

The enthalpy of adsorption at zero (rather very low) coverage (ΔH_{ads}^0) is well approximated by multiplication of the ideal gas constant *R* (8.314 J mol^{-1} K^{-1}) and the first virial coefficient a_0 (Eq. 9):

$$\Delta H_{ads}^{\,0} = R \cdot a_0 \qquad (9)$$

(For very low coverage, $n \ll 1$, if *n* is set to 0, then the products $a_i\, n^i$ will all be 0, except for $a_0 \cdot 0^0 = a_0 \cdot 1$). At the same time, ΔH_{ads}^0 is, however, strongly correlated with the value of the lowest coverage which is included in the virial analysis and is therefore heavily dependent on the measurement and calculation details. This is illustrated with the virial fits in Fig. 5 and 6. From Fig. 5 a_0 = –6511 K gives (with Eq (9)) ΔH_{ads}^0 = –54 kJ mol^{-1}, whereas from Fig. 6 a_0 = –3971 K yields ΔH_{ads}^0 = –33 kJ mol^{-1}. The value for a_0 is the most important of the polynomial coefficients. It is evident that a_0 can be adjusted with the uptake-pressure data points, which are included in the fit. Consequently, reports of record values for the enthalpy of adsorption at zero coverage, ΔH_{ads}^0 should not be accepted without clear documentation how these values were derived. To judge the correctness of the virial fit it is mandatory to take the standard deviations of the coefficients into account. These standard deviations were given for the fits in Fig. 5 and Fig. 6. It is evident that the standard deviations for a_0 and a_1 for the (better) fit in Fig. 5 are significantly smaller than for the (worse) fit in Fig. 6. For a_0 in Fig. 5 the standard deviation is 5%, while for a_0 in Fig. 6 it is 36%. A too large standard deviation renders the fit value meaningless. It must be noted that we are not aware of standard deviations being discussed in virial fits of adsorption isotherms.

Clausius-Clapeyron vs virial analysis

In this section a comparison between the Clausius-Clapeyron approach after Freundlich-Langmuir fitting and the virial analysis is presented for the calculation of the isosteric enthalpy of adsorption. For the comparison we fitted H_2 adsorption isotherms at 77 K and 87 K on HHU-1 with a Freundlich-Langmuir approach and the virial analysis (Fig. 8) as described before. The goodness of isotherm fit in Fig. 8 top and bottom, judged visually and by R^2, seems to be similar for both methods (see also below). As a result, one would expect similar values for the isosteric enthalpy of adsorption. Nevertheless, $\Delta H_{ads}(n)$ calculated from both methods differs significantly as shown in Fig. 9. The most obvious difference in ΔH_{ads} between both models is present at close to zero coverage.

Usually in the literature,[34,35] and also here, the Clausius-Clapeyron approach with Freundlich-Langmuir-fitted isotherms shows a highly increased ΔH_{ads} at low amount adsorbed when compared to the virial analysis (Fig. 9). The accuracy of the Clausius-Clapeyron derived values is however questionable.[36] Enthalpies of adsorption derived from the virial analysis mostly exhibit smaller differences between low uptakes at zero coverage and bulk adsorption, which is considered more reasonable.[36]

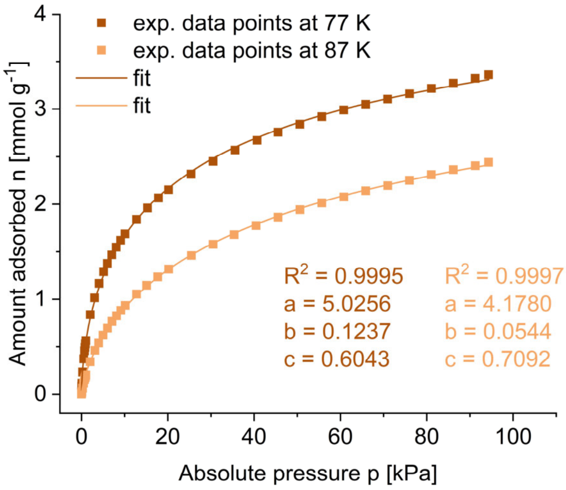

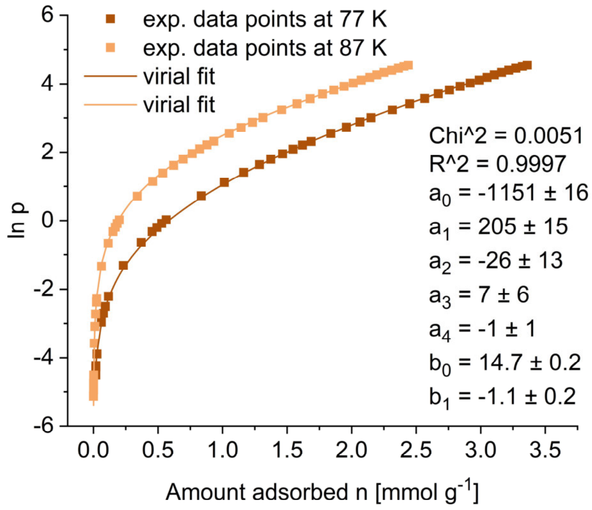

Fig. 8 Freundlich-Langmuir fit (top) and virial analysis (bottom) for H_2 adsorption isotherms on HHU-1 at 77 K and 87 K (see ESI† for structure details of HHU-1). The isotherms were fitted from n = 0.001 mmol g^{-1} (87 K) and n = 0.01 mmol g^{-1}.(77 K). Computational details are given in the Excel sheet Ex4 (ESI†). Note the small standard deviation for a_0 in the virial fit. The virial coefficients a_i have the unit [K·mol^{-i}]. Isotherm data taken from reference 37.

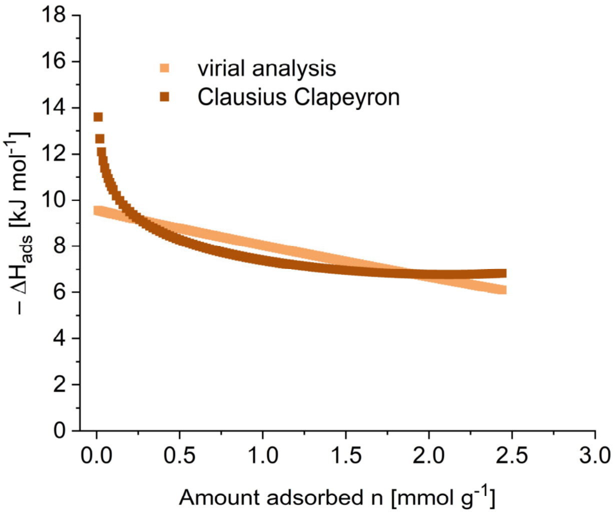

Fig. 9 $\Delta H_{ads}(n)$ calculated from H_2 adsorption isotherms on HHU-1 at 77 K and 87 K from virial analysis and a Freundlich-Langmuir fit together with the Clausius-Clapeyron equation. The isotherms were fitted from n_{min} = 0.01 mmol g^{-1} as lowest common experimental uptake for both isotherms.

ΔH_{ads}^0 for H_2 on HHU-1 derived from the Clausius-Clapeyron equation (–13.6 kJ mol^{-1}) is almost 1.5-fold higher than ΔH_{ads} calculated by virial analysis (–9.6 kJ mol^{-1}). Further, the Clausius-Clapeyron approach leads to an often-seen typical exponential-decay curvature with a high ΔH_{ads}^0, followed by a rapid decrease of the enthalpy of adsorption with increasing loading and an approach of a constant value at higher loadings. Yet, this constant ΔH_{ads} value of here ~–7 kJ mol^{-1} (Fig. 9) for the adsorption of H_2 on HHU-1 is still higher than the enthalpy of evaporation for H_2 (–0.9 kJ mol^{-1} at 20 K) which should be approached in the pore-filling regime with adsorptive-adsorbate interactions. To the contrary, ΔH_{ads} derived from virial analysis shows a moderate heat of adsorption at zero coverage and a rather linear decrease with increased loading.

This difference in $\Delta H_{ads}(n)$ from the Clausius-Clapeyron approach and the virial fit can be rationalized from a closer inspection of the goodness-of-fit at low amounts adsorbed. In the linear-scale n/p or $\ln p/n$ plots in Fig. 8 both fits seemed equally good. However, a logarithmic-scale n/p or $\ln p/n$ plot in Fig. 10 (for the same isotherms as in Fig. 8) reveals that the Freundlich-Langmuir fit for the Clausius-Clapeyron approach deviates significantly for loadings of n below ~0.1 mmol g^{-1}. On the other hand, the virial fit still covers almost all data points of n below ~0.1 mmol g^{-1}.

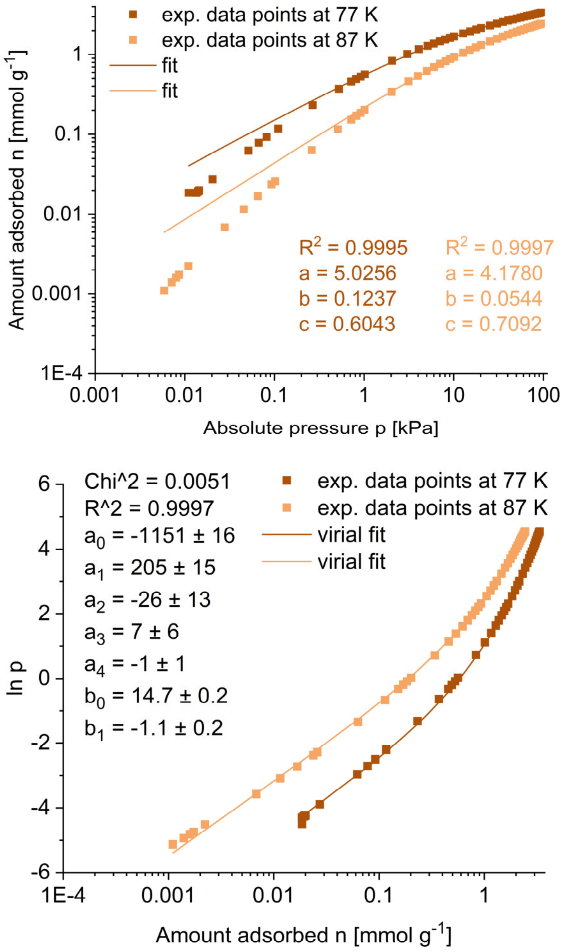

Fig. 10 Logarithmic-scale plots for Freundlich-Langmuir fit (top) and virial analysis (bottom) for H_2 adsorption isotherms on HHU-1 at 77 K and 87 K from Fig. 8.

Yet, the isosteric enthalpies of adsorption from the Clausius-Clapeyron and virial approach are in general very similar, except for low loadings close to zero coverage and at (possible, but discouraged) extrapolation to (not measured) higher loadings (Fig. 9). To conclude which approach is closer to the real values a comprehensive study with experimental data from calorimetric measurements compared to both methods would be needed.

The enthalpy of adsorption can be directly obtained from calorimetric measurements, which is seldom done, however. So far, only very few calorimetric experiments are available for the enthalpy of adsorption of adsorbates for MOFs.[22] To the best of our knowledge we are not aware of calorimetric heat of adsorption values for which at the same time $\Delta H_{ads}(n)$ from *both* the Clausius-Clapeyron approach *and* the virial fit were derived. For the open-metal-site MOF MIL-100(Cr) the enthalpy of adsorption for CO_2 was determined by microcalorimetry[38,] and calculated from adsorption isotherms at 273, 298 and 323 K with a Freundlich-Langmuir fit and Clausius-Clapeyron approach (Fig. S9, ESI†).[39] A close comparison of both curves shows that the ΔH_{ads} values for low coverage match but the values deviate considerably with increasing loading. The empirical values from the isotherm fit lie substantially below the microcalorimetry values (Fig. S9, ESI†). For the MOF HKUST-1 calorimetry and isotherm-fit values (Clausius-Clapeyron) match for low coverage; calorimetry values for higher coverage were not available.[23]

Conclusion

The good quality measurement of two adsorption isotherms at different but close temperatures is a convenient way to derive the isosteric enthalpy of adsorption, ΔH_{ads} as a function of coverage (amount adsorbed), $\Delta H_{ads}(n)$. To be able to obtain reasonable enthalpies at zero coverage, $\Delta H_{ads}{}^0$ the experimental sorption analyzer should be able to operate in low-pressure regimes ($p/p_0 < 0.001$, or $p_{absolute} < 1.0$ mbar) in order to record low-uptake data points. The curve fits of experimental sorption isotherms must not be extrapolated below or above the measured data points, that is, any extrapolation from the isotherm fit is strongly discouraged. The thus determined zero-coverage enthalpy of adsorption, is directly associated with the lowest measured uptake data point. The fitting procedure of the isotherms is of major importance for $\Delta H_{ads}(n)$. The virial analysis is superior over the Freundlich-Langmuir fit/Clausius-Clapeyron approach in order to obtain meaningful $\Delta H_{ads}{}^0$ values. A Freundlich-Langmuir fit may deviate strongly for low-uptake data points, which should be checked in a logarithmic-scale n vs p plot. For a virial fit it is mandatory to ensure low standard deviations of the obtained virial coefficients. In general, the derived isosteric enthalpy of adsorption is only as accurate as the recorded isotherm and the applied fit.

Conflicts of interest

There are no conflicts to declare.

Acknowledgements

We thank Mr. Philipp Brandt and Dr. Jun Liang for reading the manuscript and for valuable suggestions.

Notes and references

Glossary (alphabetic)

Absorption: The term absorption is used, when the species of the adsorptive penetrate the surface layer and enter the dense (not porous) structure of the bulk solid.

Adsorption and Desorption: Physical adsorption, physisorption or in short simply adsorption is the enrichment or adhesion of species from a gas or liquid phase at a solid surface, that is at a solid-gaseous or solid-liquid interface. Desorption is the opposite process of removing the adsorbed species from the surface. The surface is part of the adsorbent; the adsorbed species form the adsorbate (Fig. 11). The forces responsible for adsorbate-adsorbent interactions in physical adsorption start from weak van-der-Waals forces for non-polar gases (solutes) such as Ar and the other noble gases. Other physisorbed species can exert additional attractive forces such as quadrupole-quadrupole (e.g. N_2, CO_2, H_2), dipole-dipole (e.g. SO_2) or hydrogen bonding interactions (e.g. H_2O, NH_3). Finally, chemical adsorption, that is, chemisorption leads to stronger chemical bonds (ionic, covalent, coordinative) between the adsorbed species and the surface (Fig. 12). The maximum possible amount of an adsorbate at a surface is given by the (accessible) surface area of the adsorbent. For systems close to saturation adsorption should be viewed as a pore-filling process rather than adsorbate monolayer formation. Gas (solute) uptake capacity under these saturation conditions is eventually governed by pore volume and not by the surface area or strength of adsorbent–adsorbate interaction. The adsorbed amount is usually based on a unit mass, e.g. 1 gram, of adsorbent, so that the sorption capacities of different materials can be compared.

Adsorbate refers to a two-component system, consisting of the solid adsorbent and the adsorbed molecules (Fig. 11). Often adsorbate is used to mean only the adsorbed species.

Adsorbent is the solid phase with external or internal surface, which is exposed to the gaseous or liquid molecules (Fig. 11).

Adsorptive are the free gaseous or solute molecules, which have not yet been adsorbed onto the surface (Fig. 11).

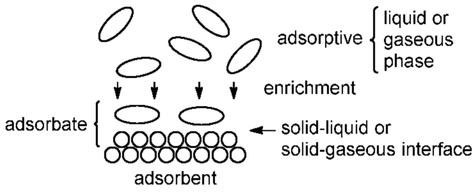

Fig. 11 Schematic illustration of an adsorption process of a gaseous or liquid phase on a solid surface.

Chemisorption and Physisorption: Depending on the interaction strength or binding energy by which molecules are bound onto a surface, one can differentiate between chemisorption or physisorption phenomena. Physisorption is a reversible physical adsorption with low binding energies via van-der-Waals forces (Fig. 12). The adsorption is strongly temperature-dependent, not specific, can form multilayers and shows low enthalpies ("heat") of adsorption. In chemisorption molecules are bound to the surface of the solid by strong "chemical" bonds (ionic, covalent, coordinative and also strong hydrogen bonds) with high enthalpies of adsorption. There is only the formation of a single adsorption layer (monolayer), which occurs less independent of temperature. Chemisorption is specific to the surface characteristics of the adsorbent. An example for chemisorption is the dissociative binding of the adsorptive H_2 as a metal hydride (Fig. 12).

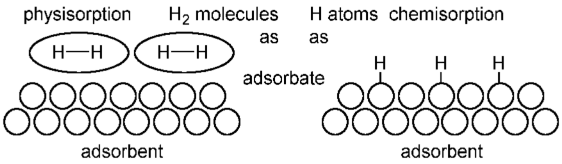

Fig. 12 Illustration of the difference between physi- and chemisorption for the case of the adsorptive H_2.

Desorption: See Adsorption.

Freundlich isotherm: The Freundlich adsorption isotherm is an empirical expression for the quantity of gas (or solute) adsorbed by a solid adsorbent at different pressures:

$$\frac{x}{m} = a \cdot c^{\frac{1}{n}}$$

where *x* is the mass of the adsorbed species, *m* is the mass of the adsorbent, *c* is the equilibrium concentration of adsorbate in solution and *a*, *n* are substance and temperature specific constants (here *n* is not to be mistaken with the amount adsorbed or loading *n*). Due to its exponential nature the Freundlich adsorption isotherm is not valid for high loadings.

Isoster means (here) the same surface coverage, which is equivalent to the same gas uptake or loading (*n*). When the heat of adsorption, ΔH_{ads} is calculated as the ***isosteric*** heat of adsorption, it refers to the same surface coverage, when determined from two adsorption isotherms at two different temperatures.[16]

Isotherms are lines with the same temperature in, e.g., a *p-V* (pressure vs. volume) or a *p-n* (pressure versus uptake) diagram. In adsorption studies *p-n* diagrams are measured and evaluated for surface area and porosity. An isotherm assumes thermodynamic equilibrium between the adsorptive/adsorbate and adsorbent at each $p|n$ data point. The shape and hysteresis for the adsorption and desorption isotherm can be already used to classify materials as micro-meso-macro-porous and also with respect to pore shape.[16]

Enthalpy of adsorption, ΔH_{ads} is defined as the heat to be released when an adsorptive binds to the surface of the adsorbent. The enthalpy of adsorption is the reverse of the enthalpy of desorption, ΔH_{des}, which is required for the reverse process to detach an adsorbate ($\Delta H_{ads} = -\Delta H_{des}$).

Langmuir isotherm: The Langmuir adsorption isotherm is an empirical expression for the quantity of gas (or solute) adsorbed and is based on three main assumptions for the gas-solid interaction: (i) solely single adsorption layer (monolayer) formation, (ii) a homogenous surface, (iii) without interactions of adsorbates on neighboring adsorption sites.

$$\frac{x}{m} = \frac{a \cdot c}{1 + b \cdot c}$$

where *x* is the mass of the adsorbed species, *m* is the mass of the adsorbent, *c* is the equilibrium concentration of adsorbate in the gas or solution phase, *a* is the maximal loading of the adsorbate and *b* is the Langmuir constant.

Porosity refers to the free volume or empty space in a porous material in relation to its total volume. Micro- and Meso-porosity is typically probed by gas sorption under isothermal conditions, e.g., N_2 gas sorption measurements at 77 K which yields *n-p* gas sorption isotherms. For each data point a thermodynamic equilibrium between the adsorptive/adsorbate and adsorbent is assumed. The isotherms are usually evaluated by the Brunauer-Emmett-Teller (BET) method for the accessible specific surface area (in $m^2 g^{-1}$) and/or specific pore volume (in $cm^3 g^{-1}$). Alternatively, Ar (at 87 K), Kr (at 77 K) or CO_2 (between 195 K to ambient temperature) can be used to probe micro- and mesopores. The term "specific" means that the surface area values are based on (referenced to) a unit mass, e.g. 1 gram, of the adsorbent. The pore size is defined as (i) micropores with diameters < 2 nm, (ii) mesopores with diameters between 2 – 50 nm, (iii) macropores with diameters exceeding (>) 50 nm. Pore structures of porous materials can be diverse and consist of different pore sizes and shapes with, e.g., larger cavities and smaller pore windows, which complicates their characterization. Further, the accessibility of pores is only possible if the kinetic diameter of the adsorptive is smaller than the pore or pore window diameter, otherwise the potentially available pores are blocked.

Sorption: If it is not possible to distinguish between absorption and adsorption it is convenient to use the more general term sorption which includes both phenomena. Then one should also use the derived terms sorbent, sorbate and sorptive accordingly (cf. Fig. 11).

Surface coverage is defined as the number of occupied adsorption sites dived by the number of available adsorption sites. Adsorption sites can further be divided into internal and external surface area. The external surface area describes adsorption on the outside of particles, while internal surface area means the surface of all inner pore walls.

References

[1] R. Batten, N. R. Champness, X.-M. Chen, J. Garcia-Martinez, S. Kitagawa, L. Öhrström, M. O'Keeffe, M. P. Suh and J. Reedijk, *Pure Appl. Chem.*, 2013, **85**, 1715–1724.

[2] A. Kirchon, L. Feng, H. F. Drake, E. A. Joseph and H-C. Zhou, *Chem. Soc. Rev.*, 2018, **47**, 8611–8638.

[3] A. E. Baumann, D. A. Bruns, B. Liu and V. S. Thoi, *Commun. Chem*. 2019, **2**, 86.

[4] H. Li, K. Wang, Y. Sun, C. T. Lollar, J. Li and H-C. Zhou, *Mater. Today*, 2018, **21**, 108–121.

[5] B. Li, H.-M. Wen, W. Zhou and B. Chen, *J. Phys. Chem. Lett.*, 2014, **5**, 3468–3479.

[6] K. Sumida, D. L. Rogow, J. A. Mason, T. M. McDonald, E. D. Bloch, Z. R. Herm, T.-H. Bae and J. R. Long, *Chem. Rev.*, 2012, **112**, 724–781.

[7] J. Liu, P. K. Thallapally, B. P. McGrail, D. R. Brown and J. Liu, *Chem. Soc. Rev.*, 2012, **41**, 2308–2322.

[8] A. Ahmed, S. Seth, J. Purewal, A. G. Wong-Foy, M. Veenstra, A. J. Matzger and D. J. Siegel, *Nat. Commun.*, 2019, **10**, 1568–1577.

[9] M. P. Suh, H. J. Park, T. K. Prasad and D.-W. Lim, *Chem. Rev.*, 2012, **112**, 782–835.

[10] K. Sumida, C. M. Brown, Z. R. Herm, S. Chavan, S. Bordiga and J. R. Long, *Chem. Commun.*, 2011, **47**, 1157–1159.

[11] S. K. Bhatia and A. L. Myers, Langmuir, 2006, **22**, 1688–1700.

[12] J. M. Crow, *ChemistryWorld*, 2019, September, p. 48–52.

[13] Y. He, W. Zhou, G. Quian and B. Chen, *Chem. Soc. Rev.*, 2014, **43**, 5657–5678.

[14] X. Han, S. Yang and M. Schröder, *Nat. Rev. Chem.*, 2019, **3**, 108–118.

[15] S. Sircar, *Adsorption Sci. Tech.*, 2001, **19**, 347–366.

[16] M. Thommes, K. Kaneko, A. V. Neimark, J. P. Olivier, F. Rodriguez-Reinso, J. Rouquerol and K. S. W. Sing, *Pure Appl. Chem.*, 2015, **87**, 1051–1069.

[17] D. Nicholson and T. Stubos, Recent Advances in Gas Separation by Microporous Ceramic Membranes, *Membrane Science and Technology*, Elsevier 2000.

[18] J. Rouquerol, F. Rouquerol and K. S. W. Sing, Adsorption by powders and porous solids, Academic Press, San Diego, USA 1999.

[19] S. Sircar and D. V. Cao, *Chem. Eng. Technol.*, 2002, **10**, 945–948.

[20] S. Keskin, T. M. van Heest and D. S. Scholl, *ChemSusChem*. 2010, **3**, 879–891.

[21] H. W. Langmi, J. Ren, B. North, M. Mathe and D. Bessarabov, *Electrochim. Acta*, 2014, **128**, 368–392.

[22] Z. Du, X. Nie, S. Deng, L. Li, S. Zhao, Y. Zhang and J. Zhao, *Micropor. Mesopor. Mater.*, 2020, **298**, 110053.

[23] D. Farrusseng, C. Daniel, C. Gaudillere, U. Ravon, Y. Schuurman, C. Mirodatos, D. Dubbeldam, H. Frost and R. Snurr, *Langmuir*, 2009, **25**, 7383–7388.

[24] H. Pan, J. A. Ritter and P. B. Balbuena, *Langmuir*, 1998, **14**, 6323–6327.

[25] S. Yang, J. Sun, A. J. Ramirez-Cuesta, S. K. Callear, W. I. F. David, D. P. Anderson, R. Newby, A. J. Blake, J. E. Parker, C. C. Tang and M. Schröder, *Nat. Chem*., 2012, **4**, 887–894.

[26] J. H. Carter, X. Huan, F. Y. Moreau, I. da Silva, A. Nevin, H. G. W. Godfrey, C. C. Tang, S. Yang and M. Schröder, *J. Am. Chem. Soc*., 2018, **140**, 15564–15567.

[27] A. G. Bezus, A. V. Kiselev, Z. Sedlacek and P. Q. Du, *Trans. Faraday Soc.*, 1971, **67**, 468–482.

[28] P. Brandt, A. Nuhnen, M. Lange, J. Möllmer, O. Weingart and C. Janiak, *ACS Appl. Mater. Interfaces*, 2019, **11**, 17350–17358.

[29] Origin(Pro), Version *Number* 2019, 9.6.0.172 OriginLab Corporation, Northampton, MA, USA.

[30] D. Ma, J. Zhang, J. Bai and H. Zhang, *Nat. Res.*, 2014, **5**, 782–794.

[31] N. Maes, H.-Y. Zhu and E. F. Vansant, *J. Porous Mater.*, 1995, *2*, 97–105.

[32] Ü. Kökcam-Demir, A. Goldman, L. Esrafili, M. Gharib, A. Morsali, O. Weingart and C. Janiak, *Chem. Soc. Rev.*, 2020, https://doi.org/10.1039/C9CS00609E.

[33] Z. Zhang, Y. Zhao, Q. Gong, Z. Li and J. Li, *Chem. Commun.,* 2013, **49**, 653–661.

[34] Z. Zhao, Z. Li and Y. S. Lin, *Ind. Eng. Chem. Res*., 2009, **48**, 10015–10020.

[35] S. R. Caskey, A. G. Wong-Foy and A. J. Matzger, *J. Am. Chem. Soc.*, 2008, **130**, 10870–10871.

[36] J. L. C. Rowsell and O. M. Yaghi, *J. Am. Chem. Soc.*, 2006, **128**, 1304–1315.

[37] T. J. Matemb Ma Ntep, H. Reinsch, B. Moll, E. Hastürk, S. Gökpinar, H. Breitzke, C. Schlüsener, L. Schmolke, G. Buntkowsky and C. Janiak, *Chem. Eur. J.*, 2018, **24**, 14048–14053.

[38] P. L. Llewellyn, S. Bourrelly, C. Serre, A. Vimont, M. Daturi, L. Hamon, G. De Weireld, J. S. Chang, D. Y. Hong, Y. K. Hwang, S. H. Jhung and G. Férey, *Langmuir*, 2008, **24**, 7245–7250.

[39] J. Yang, H. Bai, F. Zhang, J. Liu, J. Winarta, Y. Wang and B. Mu, *J. Chem. Eng. Data*, 2019, **64**, 5814−5823.

Electronic Supplementary Information (ESI) for

A practical guide to calculate the isosteric heat/enthalpy of adsorption via adsorption isotherms in metal-organic frameworks, MOFs

Alexander Nuhnen and Christoph Janiak

Institut für Anorganische Chemie und Strukturchemie, Heinrich-Heine-Universität Düsseldorf, D-40204 Düsseldorf Germany. Email: janiak@hhu.de

Content

S1. Clausius-Clapeyron equation

The thermodynamic equation (S1)

$$\frac{dp}{dT} = \frac{\Delta H_{ads}}{\Delta V \cdot T} \tag{S1}$$

with
p = vapor pressure
T = absolute temperature in K(elvin)
ΔH_{ads} = (molar) enthalpy of adsorption in kJ mol^{-1}
$\Delta V = V_{ads} - V_g$, difference of the (molar) volume between the final adsorbed phase and the starting gaseous phase

can be approximated
with $\Delta V \approx -V_g$ since the volume of a gas is much higher than the molar volume of the liquid-like adsorbed phase

$$\frac{dp}{dT} = \frac{\Delta H_{ads}}{-V_g \cdot T} \tag{S2}$$

Further, for the gaseous phase of 1 mol an ideal gas behavior (with the equation of state pV = RT) is assumed, and

$$V_g = \frac{RT}{p} \tag{S3}$$

is substituted to give the Clausius-Clapeyron equation:

$$\frac{dp}{dT} = \frac{p \cdot \Delta H_{ads}}{-RT^2} \quad \text{or} \quad \frac{dp}{p} = \frac{\Delta H_{ads}}{-RT^2} dT \tag{S4}$$

(universal gas constant R = 8.314 J K^{-1}·mol^{-1})

If the enthalpy of adsorption is taken as constant over a small temperature interval from T_1 to T_2, the integrated form of the Clausius-Clapeyron equation can be obtained:

$$\ln\frac{p_2}{p_1} = \frac{\Delta H_{ads}}{R}\left(\frac{1}{T_2} - \frac{1}{T_1}\right) \tag{S5}$$

$$\left(\int_{T_1}^{T_2} \frac{1}{T^2} dt = -\frac{1}{T_2} - \left(-\frac{1}{T_1}\right)\right) \tag{S6}$$

The difference of the two quotients can be rewritten:

$$\ln\frac{p_2}{p_1} = \frac{\Delta H_{ads}}{R}\left(\frac{T_1 - T_2}{T_2 \cdot T_1}\right) \tag{S7}$$

or by exchanging T_1 and T_2 in the numerator:

$$\ln\frac{p_2}{p_1} = -\frac{\Delta H_{ads}}{R}\left(\frac{T_2 - T_1}{T_2 \cdot T_1}\right) \tag{S8}$$

From this we obtain Eq. (1) in the manuscript

$$\Delta H_{ads}(n) = -R \cdot \ln\left(\frac{p_2}{p_1}\right)\left(\frac{T_1 \cdot T_2}{T_2 - T_1}\right) \tag{S9}$$

$\Delta H_{ads}(n)$ is typically written as ΔH_{ads} only but as the isosteric heat of adsorption it is a function of the gas uptake (the loading) n. We introduce $\Delta H_{ads}(n)$ here as in the following we will explicitly calculate the isosteric enthalpy of adsorption as a function of loading n.

Note,
(i) when comparing the aforementioned four equations to literature, pay attention to the order of T_1 and T_2 in the difference, which affects the (minus/plus) sign on the right side of the equation.

$$\left(\frac{1}{T_2}-\frac{1}{T_1}\right)=-\left(\frac{1}{T_1}-\frac{1}{T_2}\right)\ and\ \left(\frac{T_1\cdot T_2}{T_2-T_1}\right)=-\left(\frac{T_1\cdot T_2}{T_1-T_2}\right) \tag{S10}$$

(ii) Often the Clausius-Clapeyron equation (1) is written in the literature as

$$Q_{st} = -R\cdot\ln\left(\frac{p_2}{p_1}\right)\left(\frac{T_1\cdot T_2}{T_2-T_1}\right) \tag{S11}$$

The use of the symbol Q_{st} which stands for “isosteric heat of adsorption” is misleading (see Section S2 below), especially if at the same time the minus-sign on the right side of the equation is kept.

From the equation

$$\ln\frac{p_2}{p_1}=\frac{\Delta H_{ads}(n)}{R}\left(\frac{1}{T_2}-\frac{1}{T_1}\right) \tag{S12}$$

$\Delta H_{ads}(n)$ can be obtained from two experimental adsorption isotherms which were measured at two temperatures T_1 and T_2. Note that T_1 and T_2 are different but should be close. Most often a temperature difference of 10-20 K is used.

Each adsorption isotherm consists of $n_i | p_i$ data points. For an equal uptake of n the data triple $n | p_1 | p_2$ is used.
For a given value of n, the data pairs $\ln p_2 | 1/T_2$ and $\ln p_1 | 1/T_1$ define a straight line with the negative slope

$$\frac{\Delta H_{ads}(n)}{R}=\frac{\ln p_2-\ln p_1}{\left(\frac{1}{T_2}-\frac{1}{T_1}\right)}<0 \tag{S13}$$

For an adsorption process $T_2 > T_1$ correlates with $p_2 > p_1$, that is, a higher temperature requires a higher pressure to achieve the same loading n.
Hence, $\ln p_2 > \ln p_1$ and $\ln p_2 - \ln p_1 > 0$ and $1/T_2 < 1/T_1$ or $(1/T_2 - 1/T_1) < 0$.

Adsorption is an exothermic process, thus $\Delta H_{ads}(n) < 0$ kJ mol^{-1} is obtained as required.

For any experimentally measured or interpolated loading n a heat of adsorption $\Delta H_{ads}(n)$ is obtained this way. This allows to plot $\Delta H_{ads}(n)$ as a function of loading n (Fig. 5).

By defining

$$\frac{\Delta H_{ads}(n)}{R}=m=\frac{\ln p_2-\ln p_1}{\left(\frac{1}{T_2}-\frac{1}{T_1}\right)}<0 \tag{S14}$$

one obtains

$$\Delta H_{ads}=R\cdot m<0 \tag{S15}$$

Note,
in the literature the equation

$$Q_{st}=-R\cdot m' \tag{S16}$$

is usually given. This is derived from

$$Q_{st} = -R\cdot\ln\left(\frac{p_2}{p_1}\right)\left(\frac{T_1\cdot T_2}{T_2-T_1}\right) \tag{S17}$$

with the misleading use of Q_{st} (see below) and

$$m' = \ln\left(\frac{p_2}{p_1}\right)\left(\frac{T_1 \cdot T_2}{T_2 - T_1}\right) \tag{S18}$$

This expression can be rewritten to

$$m' = \ln\left(\frac{p_2}{p_1}\right)\left(\frac{T_1 \cdot T_2}{T_2 - T_1}\right) = \frac{\ln p_2 - \ln p_1}{\left(\frac{T_2 - T_1}{T_1 \cdot T_2}\right)} = \frac{\ln p_2 - \ln p_1}{\left(\frac{1}{T_1} - \frac{1}{T_2}\right)} = \frac{\ln p_2 - \ln p_1}{-\left(\frac{1}{T_2} - \frac{1}{T_1}\right)} = -m \tag{S19}$$

and illustrates that $m' > 0$, while $m < 0$.

S2. Virial equation

The virial fit is based on the exponential virial equation:[1,2,3]

$$p = n \cdot \exp\left(\sum_{i=0}^{m} C_i n^i\right) \tag{S20}$$

with p as the pressure and n the amount adsorbed. C_0 is a constant for the adsorbate-adsorbent interaction, C_1, C_2 etc. are constants for the double, triple etc. interactions in the adsorbent field. The constants C_i depend on temperature, according to[2]

$$\frac{dC_i}{dT} RT^2 = Q_i \tag{S21}$$

The heat of adsorption Q_{st} (not to be mistaken as the *enthalpy of* adsorption, ΔH_{ads}) is given as[1]

$$Q_{st} = \left(\sum_{i=0}^{m} \frac{dC_i}{dT} RT^2 n^i\right) = \left(\sum_{i=0}^{m} Q_i n^i\right) \tag{S22}$$

with Q_0 as the heat of adsorption at $n = 0$, that is Q_{st}^0. The other Q_i ($i \neq 0$) are constants having the units $[Q_i] = [(k)J\ mol^{-(i+1)}]$.[1]
If Q_i is taken as independent from temperature (for small ΔT intervals), the integration of Eq. (S21) gives

$$C_i = -\frac{Q_i}{RT} + const = -\frac{Q_i}{RT} + b_i \tag{S23}$$

Substituting Eq. (S23) into Eq. (S20) leads to

$$p = n \cdot \exp\left(\sum_{i=0}^{m}\left(-\frac{Q_i}{RT} + b_i\right) n^i\right) = n \cdot \exp\left(-\sum_{i=0}^{m}\frac{Q_i}{RT} n^i\right) \exp\left(\sum_{i=0}^{m} b_i n^i\right) \tag{S24}$$

or in the logarithmic form

$$\ln p = \ln n - \frac{1}{T}\sum_{i=0}^{m}\frac{Q_i}{R} n^i + \sum_{i=0}^{m} b_i n^i \tag{S25}$$

The substitution

$$a_i = -\frac{Q_i}{R}\ or\ Q_i = -R \cdot a_i \tag{S26}$$

then gives the virial equation in a commonly published form:

$$\ln p = \ln n + \frac{1}{T}\sum_{i=0}^{m} a_i n^i + \sum_{i=0}^{m} b_i n^i \tag{S27}$$

In equation (S27), p is the pressure in kPa, n is the of total amount adsorbed in mmol/g, T is the temperature in K (e.g. 273 K, 293 K), a_i and b_j are the virial coefficients and m represents the number of coefficients required to adequately fit the isotherms.
We note that in order to derive at dimensionless values in the argument of the logarithm (ln) the pressure and amount adsorbed must be divided by their units as in Eq. (S28).

$$\ln\frac{p}{kPa} = \ln\frac{n}{mmol\cdot g^{-1}} + \frac{1}{T}\sum_{i=0}^{m} a_i n^i + \sum_{i=0}^{m} b_i n^i \qquad \text{(S28)}$$

With the units of $[Q_i] = [(k)J\ mol^{-(i+1)}]$ the units of $[a_i]$ are $[K{\cdot}mol^{-i}]$.

From Eq. (S22) and (S26), the uptake-dependent heat of adsorption Q_{st} (as a function of uptake n) is derived as

$$Q_{st}(n) = -R\cdot\sum_{i=0}^{m} a_i n^i \qquad \text{(S29)}$$

and for the approximation of the heat of adsorption at zero (rather very low) coverage, Q_{st}^0

$$Q_{st}^0(n) = -R\cdot a_0 \qquad \text{(S30)}$$

From the negative sign of the most important virial coefficient a_0 (with the unit K(elvin)) this heat of adsorption $Q_{st}(n)$ and Q_{st}^0 will be positive quantities.
Note that the isosteric heat of adsorption $Q_{st}(n)$ is a differential heat and a positive quantity.[4]

Potential problem with the use of Q_{st}

A problem arises if the positive $Q_{st}(n)$ from the virial fit is taken as the same Q_{st} from the Clausius-Clapeyron equation (see above Eq. (S11, S16, S17) from which Q_{st} will be negative), since both quantities will have the opposite sign (besides a somewhat different value).

Therefore, the Clausius-Clapeyron equation should be used and given with the correct (isosteric) enthalpy of adsorption ΔH_{ads} and not with Q_{st}.
Presumably, the misleading (if not wrong) use of Q_{st} in the Clausius-Clapeyron equation was introduced because the magnitude 'heat of adsorption, Q_{st}' was used for the virial equations.

The quantity *isosteric enthalpy of adsorption* ΔH_{ads} is more meaningful than the simple *heat*, Q. Both magnitudes are equal with opposite sign[4]

$$\Delta H_{ads} = -Q_{st} \qquad \text{(S31)}$$

which then correctly relates the negative, exothermic (isosteric) enthalpy of adsorption ΔH_{ads} from the Clausius-Clapeyron equation to the positive (isosteric) heat of adsorption Q_{st} from the virial fit.

S3. Freundlich-Langmuir fit of *n* vs. *p* isotherms

A brief illustration how to set up the Freundlich-Langmuir fit with the program Origin is given in the file “HoA detailed description_origin.pdf”.

S3.1 CO_2 adsorption isotherm data on MIL-160 at 273 K and 293 K (see Origin file Or1):

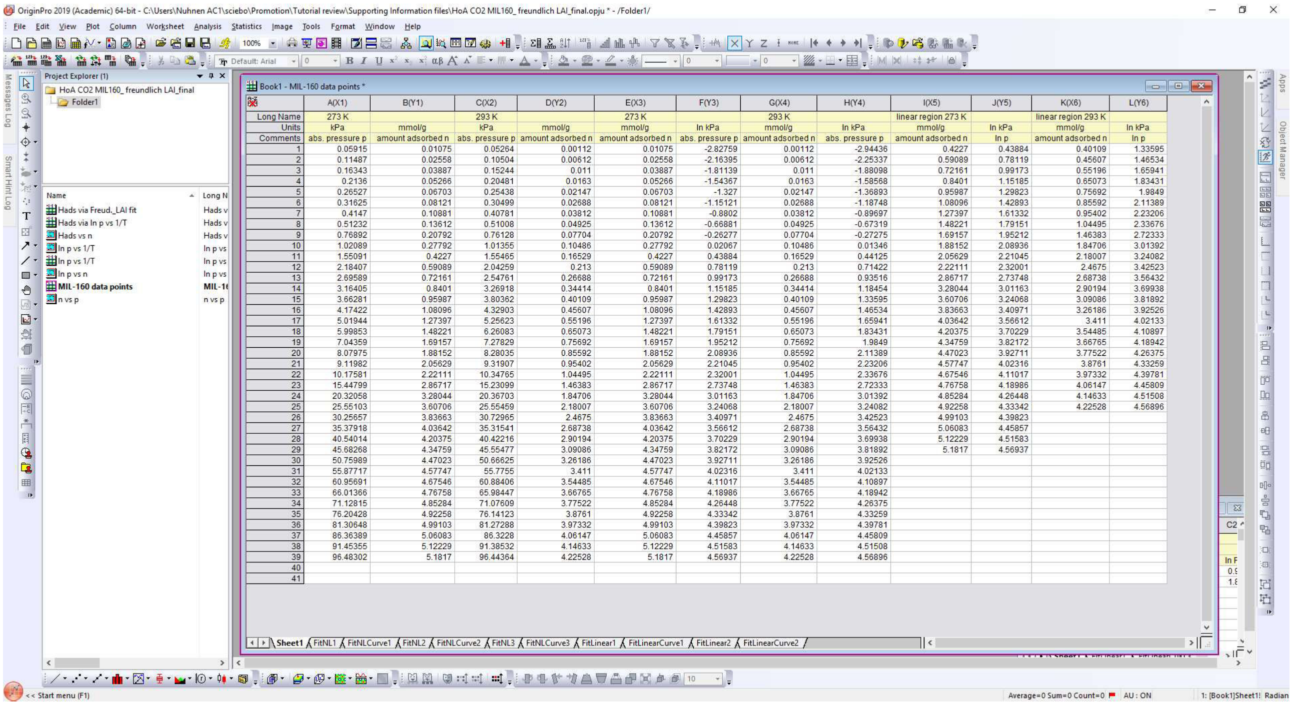

	A(X1)	B(Y1)	C(X2)	D(Y2)	E(X3)	F(Y3)	G(X4)	H(Y4)	I(X5)	J(Y5)	K(X6)	L(Y6)
Long Name	273 K		293 K		273 K		293 K		linear region 273 K		linear region 293 K	
Units	kPa	mmol/g	kPa	mmol/g	mmol/g	ln kPa	mmol/g	ln kPa	mmol/g	ln kPa	mmol/g	ln kPa
Comments	abs. pressure p	amount adsorbed n	abs. pressure p	amount adsorbed n	amount adsorbed n	abs. pressure p	amount adsorbed n	abs. pressure p	amount adsorbed n	ln p	amount adsorbed n	ln p
1	0.05915	0.01075	0.05264	0.00112	0.01075	-2.82759	0.00112	-2.94436	0.4227	0.43884	0.40109	1.33595
2	0.11487	0.02558	0.10504	0.00612	0.02558	-2.16395	0.00612	-2.25337	0.59089	0.78119	0.45607	1.46534
3	0.16343	0.03887	0.15244	0.011	0.03887	-1.81139	0.011	-1.88098	0.72161	0.99173	0.55196	1.65941
4	0.2136	0.05266	0.20481	0.0163	0.05266	-1.54367	0.0163	-1.58568	0.8401	1.15185	0.65073	1.83431
5	0.26527	0.06703	0.25438	0.02147	0.06703	-1.327	0.02147	-1.36893	0.95987	1.29823	0.75692	1.9849
6	0.31625	0.08121	0.30499	0.02688	0.08121	-1.15121	0.02688	-1.18748	1.08096	1.42893	0.85592	2.11389
7	0.4147	0.10881	0.40781	0.03812	0.10881	-0.8802	0.03812	-0.89697	1.27397	1.61332	0.95402	2.23206
8	0.51232	0.13612	0.51008	0.04925	0.13612	-0.66881	0.04925	-0.67319	1.48221	1.79151	1.04495	2.33676
9	0.76892	0.20792	0.76128	0.07704	0.20792	-0.26277	0.07704	-0.27275	1.69157	1.95212	1.46383	2.72333
10	1.02089	0.27792	1.01355	0.10486	0.27792	0.02067	0.10486	0.01346	1.88152	2.08936	1.84706	3.01392
11	1.55091	0.4227	1.55465	0.16529	0.4227	0.43884	0.16529	0.44125	2.05629	2.21045	2.18007	3.24082
12	2.18407	0.59089	2.04259	0.213	0.59089	0.78119	0.213	0.71422	2.22111	2.32001	2.4675	3.42523
13	2.69589	0.72161	2.54761	0.26688	0.72161	0.99173	0.26688	0.93516	2.86717	2.73748	2.68738	3.56432
14	3.16405	0.8401	3.26918	0.34414	0.8401	1.15185	0.34414	1.18454	3.28044	3.01163	2.90194	3.69938
15	3.66281	0.95987	3.80362	0.40109	0.95987	1.29823	0.40109	1.33595	3.60706	3.24068	3.09086	3.81892
16	4.17422	1.08096	4.32903	0.45607	1.08096	1.42893	0.45607	1.46534	3.83663	3.40971	3.26186	3.92526
17	5.01944	1.27397	5.25623	0.55196	1.27397	1.61332	0.55196	1.65941	4.03642	3.56612	3.411	4.02133
18	5.99853	1.48221	6.26083	0.65073	1.48221	1.79151	0.65073	1.83431	4.20375	3.70229	3.54485	4.10897
19	7.04359	1.69157	7.27829	0.75692	1.69157	1.95212	0.75692	1.9849	4.34759	3.82172	3.66765	4.18942
20	8.07975	1.88152	8.28035	0.85592	1.88152	2.08936	0.85592	2.11389	4.47023	3.92711	3.77522	4.26375
21	9.11982	2.05629	9.31907	0.95402	2.05629	2.21045	0.95402	2.23206	4.57747	4.02316	3.8761	4.33259
22	10.17581	2.22111	10.34765	1.04495	2.22111	2.32001	1.04495	2.33676	4.67546	4.11017	3.97332	4.39781
23	15.44799	2.86717	15.23099	1.46383	2.86717	2.73748	1.46383	2.72333	4.76758	4.18986	4.06147	4.45809
24	20.32058	3.28044	20.36703	1.84706	3.28044	3.01163	1.84706	3.01392	4.85284	4.26448	4.14633	4.51508
25	25.55103	3.60706	25.55459	2.18007	3.60706	3.24068	2.18007	3.24082	4.92258	4.33342	4.22528	4.56896
26	30.25657	3.83663	30.72965	2.4675	3.83663	3.40971	2.4675	3.42523	4.99103	4.39823		
27	35.37918	4.03642	35.31541	2.68738	4.03642	3.56612	2.68738	3.56432	5.06083	4.45857		
28	40.54014	4.20375	40.42216	2.90194	4.20375	3.70229	2.90194	3.69938	5.12229	4.51583		
29	45.68268	4.34759	45.55477	3.09086	4.34759	3.82172	3.09086	3.81892	5.1817	4.56937		
30	50.75989	4.47023	50.66625	3.26186	4.47023	3.92711	3.26186	3.92526				
31	55.87717	4.57747	55.7755	3.411	4.57747	4.02316	3.411	4.02133				
32	60.95691	4.67546	60.88406	3.54485	4.67546	4.11017	3.54485	4.10897				
33	66.01366	4.76758	65.98447	3.66765	4.76758	4.18986	3.66765	4.18942				
34	71.12815	4.85284	71.07609	3.77522	4.85284	4.26448	3.77522	4.26375				
35	76.20428	4.92258	76.14123	3.8761	4.92258	4.33342	3.8761	4.33259				
36	81.30648	4.99103	81.27288	3.97332	4.99103	4.39823	3.97332	4.39781				
37	86.36389	5.06083	86.3228	4.06147	5.06083	4.45857	4.06147	4.45809				
38	91.45355	5.12229	91.38532	4.14633	5.12229	4.51583	4.14633	4.51508				
39	96.48302	5.1817	96.44364	4.22528	5.1817	4.56937	4.22528	4.56896				
40												
41												

S3.2 Fit information for the isotherm at 273 K (see Origin file Or1):

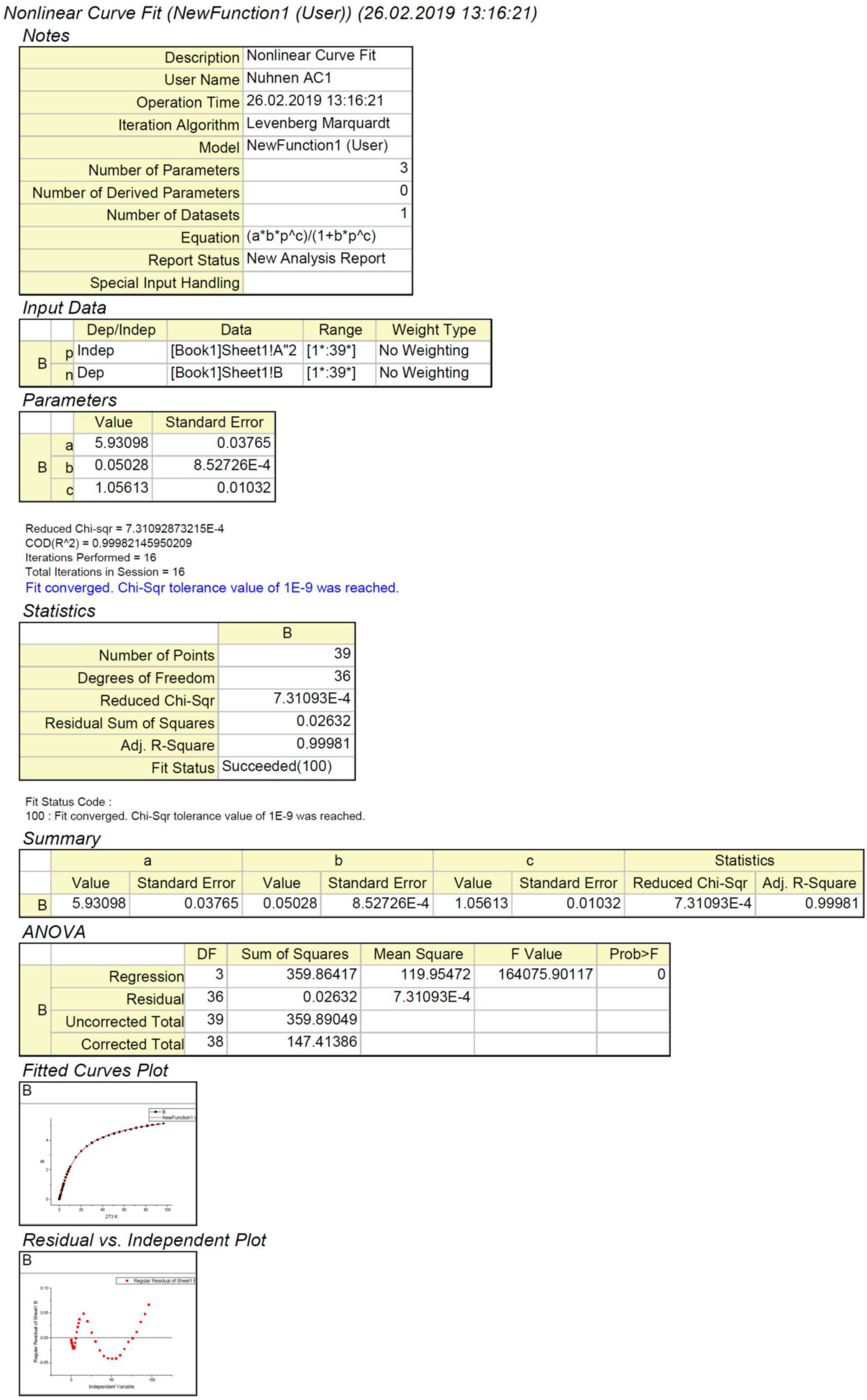

Nonlinear Curve Fit (NewFunction1 (User)) (26.02.2019 13:16:21)

Notes

Description	Nonlinear Curve Fit
User Name	Nuhnen AC1
Operation Time	26.02.2019 13:16:21
Iteration Algorithm	Levenberg Marquardt
Model	NewFunction1 (User)
Number of Parameters	3
Number of Derived Parameters	0
Number of Datasets	1
Equation	(a*b*p^c)/(1+b*p^c)
Report Status	New Analysis Report
Special Input Handling	

Input Data

		Dep/Indep	Data	Range	Weight Type
B	p	Indep	[Book1]Sheet1!A"2	[1*:39*]	No Weighting
	n	Dep	[Book1]Sheet1!B	[1*:39*]	No Weighting

Parameters

		Value	Standard Error
B	a	5.93098	0.03765
	b	0.05028	8.52726E-4
	c	1.05613	0.01032

Reduced Chi-sqr = 7.31092873215E-4
COD(R^2) = 0.99982145950209
Iterations Performed = 16
Total Iterations in Session = 16
Fit converged. Chi-Sqr tolerance value of 1E-9 was reached.

Statistics

	B
Number of Points	39
Degrees of Freedom	36
Reduced Chi-Sqr	7.31093E-4
Residual Sum of Squares	0.02632
Adj. R-Square	0.99981
Fit Status	Succeeded(100)

Fit Status Code :
100 : Fit converged. Chi-Sqr tolerance value of 1E-9 was reached.

Summary

	a		b		c		Statistics	
	Value	Standard Error	Value	Standard Error	Value	Standard Error	Reduced Chi-Sqr	Adj. R-Square
B	5.93098	0.03765	0.05028	8.52726E-4	1.05613	0.01032	7.31093E-4	0.99981

ANOVA

		DF	Sum of Squares	Mean Square	F Value	Prob>F
B	Regression	3	359.86417	119.95472	164075.90117	0
	Residual	36	0.02632	7.31093E-4		
	Uncorrected Total	39	359.89049			
	Corrected Total	38	147.41386			

Fitted Curves Plot

Residual vs. Independent Plot

S3.3 Fit information for the isotherm at 293 K (see Origin file Or1):

Nonlinear Curve Fit (NewFunction1 (User)) (26.02.2019 13:16:57)

Notes

Description	Nonlinear Curve Fit
User Name	Nuhnen AC1
Operation Time	26.02.2019 13:16:57
Iteration Algorithm	Levenberg Marquardt
Model	NewFunction1 (User)
Number of Parameters	3
Number of Derived Parameters	0
Number of Datasets	1
Equation	(a*b*p^c)/(1+b*p^c)
Report Status	New Analysis Report
Special Input Handling	

Input Data

		Dep/Indep	Data	Range	Weight Type
D	p	Indep	[Book1]Sheet1!C"2	[1*:39*]	No Weighting
	n	Dep	[Book1]Sheet1!D	[1*:39*]	No Weighting

Parameters

		Value	Standard Error
D	a	5.89269	0.01733
	b	0.01682	8.43552E-5
	c	1.09519	0.00272

Reduced Chi-sqr = 2.58490693727E-5
COD(R^2) = 0.99999008962444
Iterations Performed = 18
Total Iterations in Session = 18
Fit converged. Chi-Sqr tolerance value of 1E-9 was reached.

Statistics

	D
Number of Points	39
Degrees of Freedom	36
Reduced Chi-Sqr	2.58491E-5
Residual Sum of Squares	9.30566E-4
Adj. R-Square	0.99999
Fit Status	Succeeded(100)

Fit Status Code :
100 : Fit converged. Chi-Sqr tolerance value of 1E-9 was reached.

Summary

	a		b		c		Statistics	
	Value	Standard Error	Value	Standard Error	Value	Standard Error	Reduced Chi-Sqr	Adj. R-Square
D	5.89269	0.01733	0.01682	8.43552E-5	1.09519	0.00272	2.58491E-5	0.99999

ANOVA

		DF	Sum of Squares	Mean Square	F Value	Prob>F
D	Regression	3	191.1773	63.72577	2465302.16	0
	Residual	36	9.30566E-4	2.58491E-5		
	Uncorrected Total	39	191.17823			
	Corrected Total	38	93.89821			

Fitted Curves Plot

D

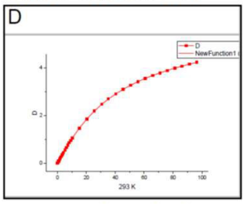

Residual vs. Independent Plot

D

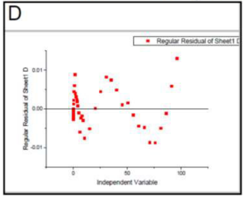

S3.4 Fitted CO_2 adsorption isotherms on MIL-160 at 273 K and 293 K with fit data (see Origin file Or1):

Use these *a*,*b* and *c* parameters, which were derived here from the fitting procedure as input in the Excel data sheet of the next Section S3.5.

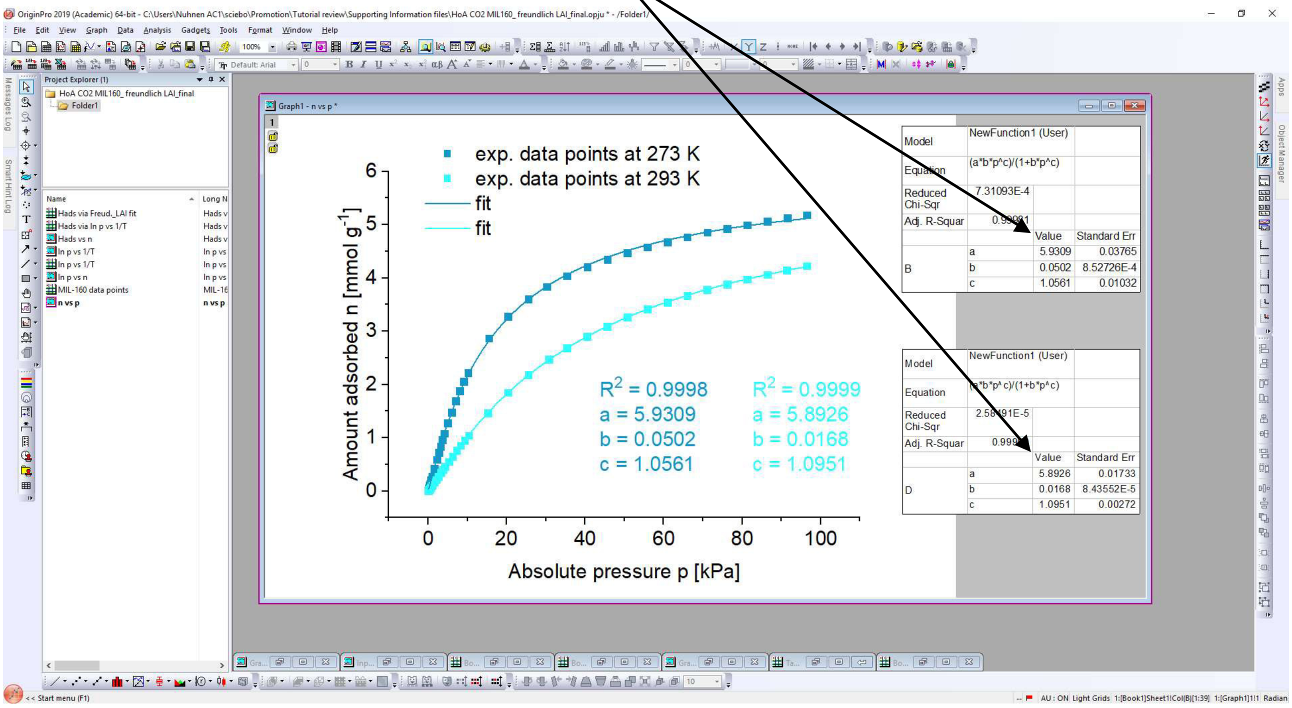

Model	NewFunction1 (User)		
Equation	(a*b*p^c)/(1+b*p^c)		
Reduced Chi-Sqr	7.31093E-4		
Adj. R-Squar	0.99981		
		Value	Standard Err
B	a	5.9309	0.03765
	b	0.0502	8.52726E-4
	c	1.0561	0.01032

Model	NewFunction1 (User)		
Equation	(a*b*p^ c)/(1+b*p^ c)		
Reduced Chi-Sqr	2.58491E-5		
Adj. R-Squar	0.999		
		Value	Standard Err
D	a	5.8926	0.01733
	b	0.0168	8.43552E-5
	c	1.0951	0.00272

S3.5 Excel data sheet Ex1 for continuum of $n|p_1$ and $n|p_2$ data pairs ($n|p_1|p_2$ data triples):

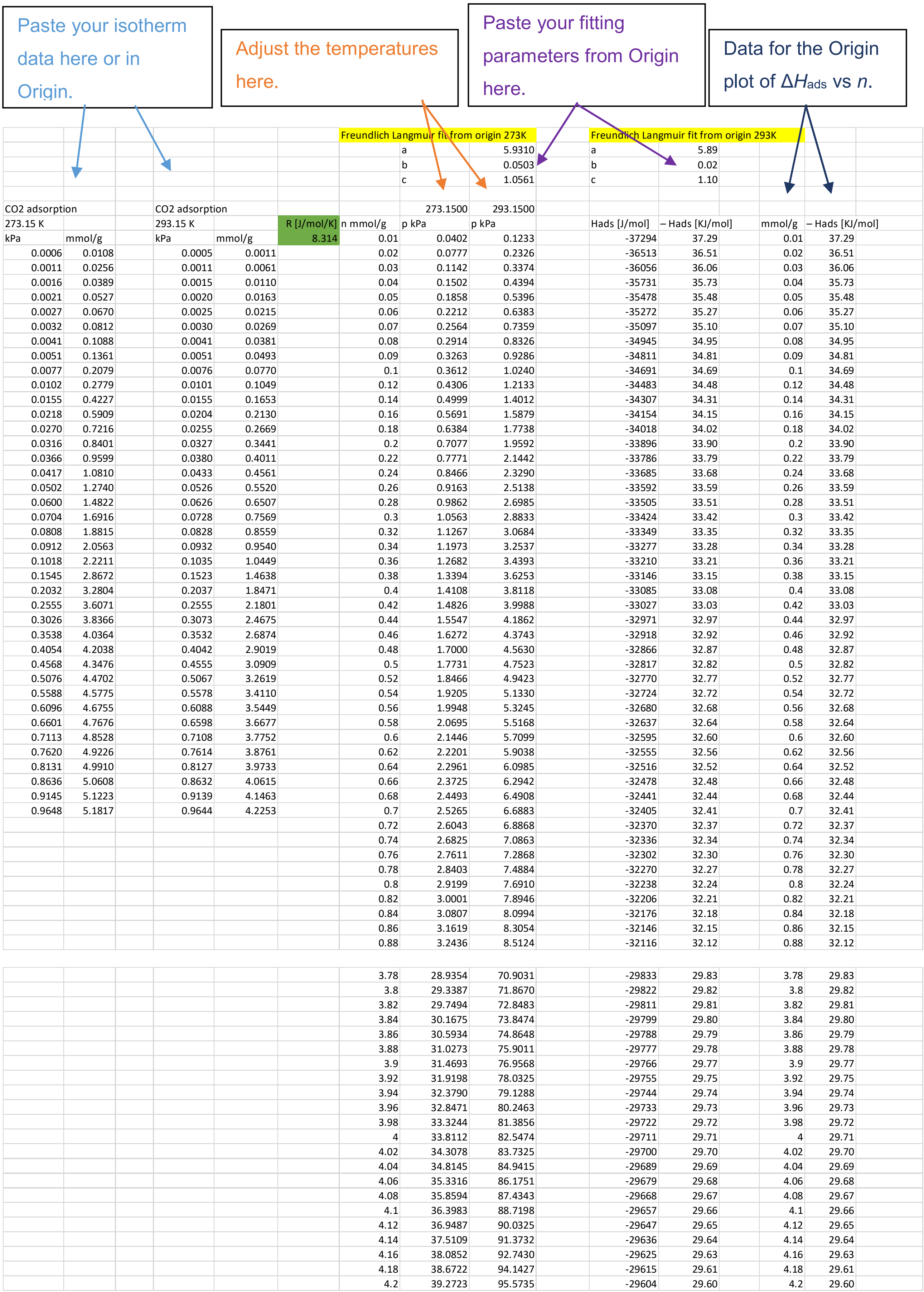

Paste your isotherm data here or in Origin.

Adjust the temperatures here.

Paste your fitting parameters from Origin here.

Data for the Origin plot of ΔH_{ads} vs n.

						Freundlich Langmuir fit from origin 273K				Freundlich Langmuir fit from origin 293K					
							a	5.9310		a	5.89				
							b	0.0503		b	0.02				
							c	1.0561		c	1.10				
CO2 adsorption			CO2 adsorption				273.1500	293.1500							
273.15 K			293.15 K		R [J/mol/K]	n mmol/g	p kPa	p kPa		Hads [J/mol]	– Hads [KJ/mol]		mmol/g	– Hads [KJ/mol]	
kPa	mmol/g		kPa	mmol/g	8.314	0.01	0.0402	0.1233		-37294	37.29		0.01	37.29	
0.0006	0.0108		0.0005	0.0011		0.02	0.0777	0.2326		-36513	36.51		0.02	36.51	
0.0011	0.0256		0.0011	0.0061		0.03	0.1142	0.3374		-36056	36.06		0.03	36.06	
0.0016	0.0389		0.0015	0.0110		0.04	0.1502	0.4394		-35731	35.73		0.04	35.73	
0.0021	0.0527		0.0020	0.0163		0.05	0.1858	0.5396		-35478	35.48		0.05	35.48	
0.0027	0.0670		0.0025	0.0215		0.06	0.2212	0.6383		-35272	35.27		0.06	35.27	
0.0032	0.0812		0.0030	0.0269		0.07	0.2564	0.7359		-35097	35.10		0.07	35.10	
0.0041	0.1088		0.0041	0.0381		0.08	0.2914	0.8326		-34945	34.95		0.08	34.95	
0.0051	0.1361		0.0051	0.0493		0.09	0.3263	0.9286		-34811	34.81		0.09	34.81	
0.0077	0.2079		0.0076	0.0770		0.1	0.3612	1.0240		-34691	34.69		0.1	34.69	
0.0102	0.2779		0.0101	0.1049		0.12	0.4306	1.2133		-34483	34.48		0.12	34.48	
0.0155	0.4227		0.0155	0.1653		0.14	0.4999	1.4012		-34307	34.31		0.14	34.31	
0.0218	0.5909		0.0204	0.2130		0.16	0.5691	1.5879		-34154	34.15		0.16	34.15	
0.0270	0.7216		0.0255	0.2669		0.18	0.6384	1.7738		-34018	34.02		0.18	34.02	
0.0316	0.8401		0.0327	0.3441		0.2	0.7077	1.9592		-33896	33.90		0.2	33.90	
0.0366	0.9599		0.0380	0.4011		0.22	0.7771	2.1442		-33786	33.79		0.22	33.79	
0.0417	1.0810		0.0433	0.4561		0.24	0.8466	2.3290		-33685	33.68		0.24	33.68	
0.0502	1.2740		0.0526	0.5520		0.26	0.9163	2.5138		-33592	33.59		0.26	33.59	
0.0600	1.4822		0.0626	0.6507		0.28	0.9862	2.6985		-33505	33.51		0.28	33.51	
0.0704	1.6916		0.0728	0.7569		0.3	1.0563	2.8833		-33424	33.42		0.3	33.42	
0.0808	1.8815		0.0828	0.8559		0.32	1.1267	3.0684		-33349	33.35		0.32	33.35	
0.0912	2.0563		0.0932	0.9540		0.34	1.1973	3.2537		-33277	33.28		0.34	33.28	
0.1018	2.2211		0.1035	1.0449		0.36	1.2682	3.4393		-33210	33.21		0.36	33.21	
0.1545	2.8672		0.1523	1.4638		0.38	1.3394	3.6253		-33146	33.15		0.38	33.15	
0.2032	3.2804		0.2037	1.8471		0.4	1.4108	3.8118		-33085	33.08		0.4	33.08	
0.2555	3.6071		0.2555	2.1801		0.42	1.4826	3.9988		-33027	33.03		0.42	33.03	
0.3026	3.8366		0.3073	2.4675		0.44	1.5547	4.1862		-32971	32.97		0.44	32.97	
0.3538	4.0364		0.3532	2.6874		0.46	1.6272	4.3743		-32918	32.92		0.46	32.92	
0.4054	4.2038		0.4042	2.9019		0.48	1.7000	4.5630		-32866	32.87		0.48	32.87	
0.4568	4.3476		0.4555	3.0909		0.5	1.7731	4.7523		-32817	32.82		0.5	32.82	
0.5076	4.4702		0.5067	3.2619		0.52	1.8466	4.9423		-32770	32.77		0.52	32.77	
0.5588	4.5775		0.5578	3.4110		0.54	1.9205	5.1330		-32724	32.72		0.54	32.72	
0.6096	4.6755		0.6088	3.5449		0.56	1.9948	5.3245		-32680	32.68		0.56	32.68	
0.6601	4.7676		0.6598	3.6677		0.58	2.0695	5.5168		-32637	32.64		0.58	32.64	
0.7113	4.8528		0.7108	3.7752		0.6	2.1446	5.7099		-32595	32.60		0.6	32.60	
0.7620	4.9226		0.7614	3.8761		0.62	2.2201	5.9038		-32555	32.56		0.62	32.56	
0.8131	4.9910		0.8127	3.9733		0.64	2.2961	6.0985		-32516	32.52		0.64	32.52	
0.8636	5.0608		0.8632	4.0615		0.66	2.3725	6.2942		-32478	32.48		0.66	32.48	
0.9145	5.1223		0.9139	4.1463		0.68	2.4493	6.4908		-32441	32.44		0.68	32.44	
0.9648	5.1817		0.9644	4.2253		0.7	2.5265	6.6883		-32405	32.41		0.7	32.41	
						0.72	2.6043	6.8868		-32370	32.37		0.72	32.37	
						0.74	2.6825	7.0863		-32336	32.34		0.74	32.34	
						0.76	2.7611	7.2868		-32302	32.30		0.76	32.30	
						0.78	2.8403	7.4884		-32270	32.27		0.78	32.27	
						0.8	2.9199	7.6910		-32238	32.24		0.8	32.24	
						0.82	3.0001	7.8946		-32206	32.21		0.82	32.21	
						0.84	3.0807	8.0994		-32176	32.18		0.84	32.18	
						0.86	3.1619	8.3054		-32146	32.15		0.86	32.15	
						0.88	3.2436	8.5124		-32116	32.12		0.88	32.12	

						3.78	28.9354	70.9031		-29833	29.83		3.78	29.83	
						3.8	29.3387	71.8670		-29822	29.82		3.8	29.82	
						3.82	29.7494	72.8483		-29811	29.81		3.82	29.81	
						3.84	30.1675	73.8474		-29799	29.80		3.84	29.80	
						3.86	30.5934	74.8648		-29788	29.79		3.86	29.79	
						3.88	31.0273	75.9011		-29777	29.78		3.88	29.78	
						3.9	31.4693	76.9568		-29766	29.77		3.9	29.77	
						3.92	31.9198	78.0325		-29755	29.75		3.92	29.75	
						3.94	32.3790	79.1288		-29744	29.74		3.94	29.74	
						3.96	32.8471	80.2463		-29733	29.73		3.96	29.73	
						3.98	33.3244	81.3856		-29722	29.72		3.98	29.72	
						4	33.8112	82.5474		-29711	29.71		4	29.71	
						4.02	34.3078	83.7325		-29700	29.70		4.02	29.70	
						4.04	34.8145	84.9415		-29689	29.69		4.04	29.69	
						4.06	35.3316	86.1751		-29679	29.68		4.06	29.68	
						4.08	35.8594	87.4343		-29668	29.67		4.08	29.67	
						4.1	36.3983	88.7198		-29657	29.66		4.1	29.66	
						4.12	36.9487	90.0325		-29647	29.65		4.12	29.65	
						4.14	37.5109	91.3732		-29636	29.64		4.14	29.64	
						4.16	38.0852	92.7430		-29625	29.63		4.16	29.63	
						4.18	38.6722	94.1427		-29615	29.61		4.18	29.61	
						4.2	39.2723	95.5735		-29604	29.60		4.2	29.60	

S3.6 Chosen “linear region” of $n|\ln p$ data pairs of CO_2 adsorption isotherm data on MIL-160 at 273 K and 293 K (see Origin file Or1):

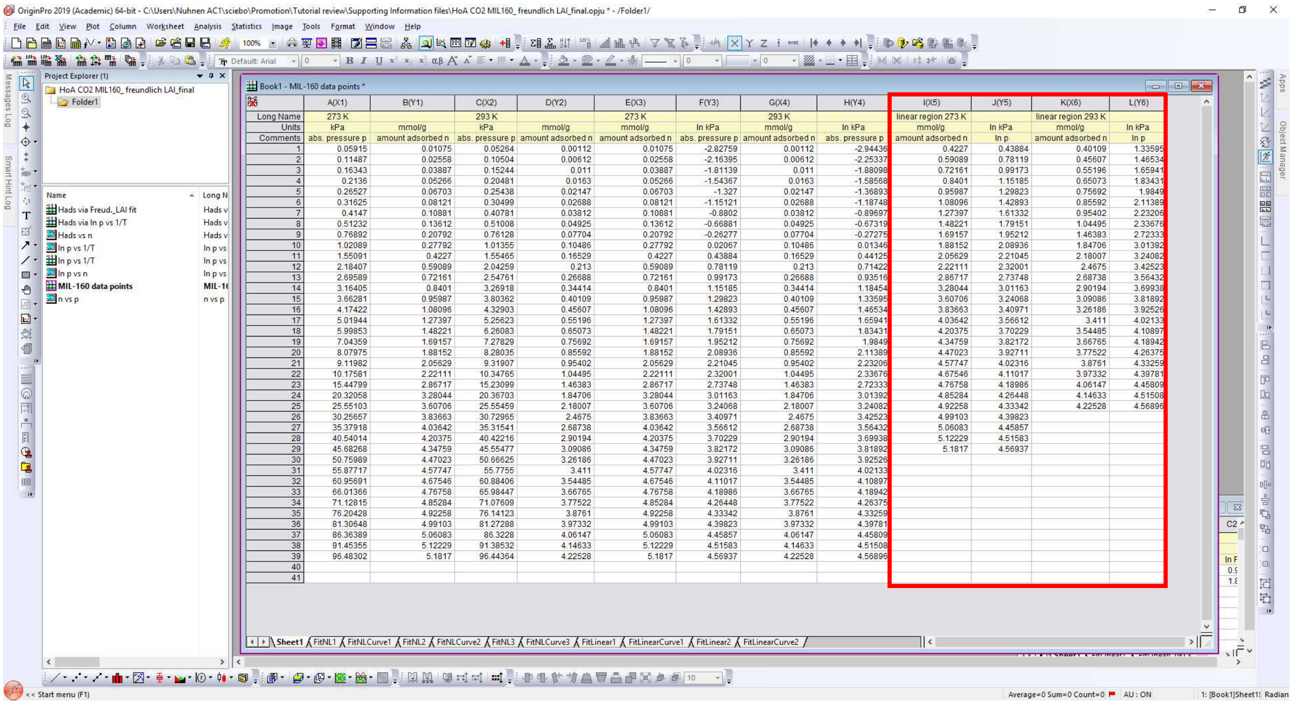

OriginPro 2019 (Academic) 64-bit - C:\Users\Nuhnen AC1\sciebo\Promotion\Tutorial review\Supporting Information files\HoA CO2 MIL160_ freundlich LAI_final.opju * - /Folder1/

Book1 - MIL-160 data points *

	A(X1)	B(Y1)	C(X2)	D(Y2)	E(X3)	F(Y3)	G(X4)	H(Y4)	I(X5)	J(Y5)	K(X6)	L(Y6)
Long Name	273 K		293 K		273 K		293 K		linear region 273 K		linear region 293 K	
Units	kPa	mmol/g	kPa	mmol/g	mmol/g	ln kPa	mmol/g	ln kPa	mmol/g	ln kPa	mmol/g	ln kPa
Comments	abs. pressure p	amount adsorbed n	abs. pressure p	amount adsorbed n	amount adsorbed n	abs. pressure p	amount adsorbed n	abs. pressure p	amount adsorbed n	ln p	amount adsorbed n	ln p
1	0.05915	0.01075	0.05264	0.00112	0.01075	-2.82759	0.00112	-2.94436	0.4227	0.43884	0.40109	1.33595
2	0.11487	0.02558	0.10504	0.00612	0.02558	-2.16395	0.00612	-2.25337	0.59089	0.78119	0.45607	1.46534
3	0.16343	0.03887	0.15244	0.011	0.03887	-1.81139	0.011	-1.88098	0.72161	0.99173	0.55196	1.65941
4	0.2136	0.05266	0.20481	0.0163	0.05266	-1.54367	0.0163	-1.58568	0.8401	1.15185	0.65073	1.83431
5	0.26527	0.06703	0.25438	0.02147	0.06703	-1.327	0.02147	-1.36893	0.95987	1.29823	0.75692	1.9849
6	0.31625	0.08121	0.30499	0.02688	0.08121	-1.15121	0.02688	-1.18748	1.08096	1.42893	0.85592	2.11389
7	0.4147	0.10881	0.40781	0.03812	0.10881	-0.8802	0.03812	-0.89697	1.27397	1.61332	0.95402	2.23206
8	0.51232	0.13612	0.51008	0.04925	0.13612	-0.66881	0.04925	-0.67319	1.48221	1.79151	1.04495	2.33676
9	0.76892	0.20792	0.76128	0.07704	0.20792	-0.26277	0.07704	-0.27275	1.69157	1.95212	1.46383	2.72333
10	1.02089	0.27792	1.01355	0.10486	0.27792	0.02067	0.10486	0.01346	1.88152	2.08936	1.84706	3.01392
11	1.55091	0.4227	1.55465	0.16529	0.4227	0.43884	0.16529	0.44125	2.05629	2.21045	2.18007	3.24082
12	2.18407	0.59089	2.04259	0.213	0.59089	0.78119	0.213	0.71422	2.22111	2.32001	2.4675	3.42523
13	2.69589	0.72161	2.54761	0.26688	0.72161	0.99173	0.26688	0.93516	2.86717	2.73748	2.68738	3.56432
14	3.16405	0.8401	3.26918	0.34414	0.8401	1.15185	0.34414	1.18454	3.28044	3.01163	2.90194	3.69938
15	3.66281	0.95987	3.80362	0.40109	0.95987	1.29823	0.40109	1.33595	3.60706	3.24068	3.09086	3.81892
16	4.17422	1.08096	4.32903	0.45607	1.08096	1.42893	0.45607	1.46534	3.83663	3.40971	3.26186	3.92526
17	5.01944	1.27397	5.25623	0.55196	1.27397	1.61332	0.55196	1.65941	4.03642	3.56612	3.411	4.02133
18	5.99853	1.48221	6.26083	0.65073	1.48221	1.79151	0.65073	1.83431	4.20375	3.70229	3.54485	4.10897
19	7.04359	1.69157	7.27829	0.75692	1.69157	1.95212	0.75692	1.9849	4.34759	3.82172	3.66765	4.18942
20	8.07975	1.88152	8.28035	0.85592	1.88152	2.08936	0.85592	2.11389	4.47023	3.92711	3.77522	4.26375
21	9.11982	2.05629	9.31907	0.95402	2.05629	2.21045	0.95402	2.23206	4.57747	4.02316	3.8761	4.33259
22	10.17581	2.22111	10.34765	1.04495	2.22111	2.32001	1.04495	2.33676	4.67546	4.11017	3.97332	4.39781
23	15.44799	2.86717	15.23099	1.46383	2.86717	2.73748	1.46383	2.72333	4.76758	4.18986	4.06147	4.45809
24	20.32058	3.28044	20.36703	1.84706	3.28044	3.01163	1.84706	3.01392	4.85284	4.26448	4.14633	4.51508
25	25.55103	3.60706	25.55459	2.18007	3.60706	3.24068	2.18007	3.24082	4.92258	4.33342	4.22528	4.56896
26	30.25657	3.83663	30.72965	2.4675	3.83663	3.40971	2.4675	3.42523	4.99103	4.39823		
27	35.37918	4.03642	35.31541	2.68738	4.03642	3.56612	2.68738	3.56432	5.06083	4.45857		
28	40.54014	4.20375	40.42216	2.90194	4.20375	3.70229	2.90194	3.69938	5.12229	4.51583		
29	45.68268	4.34759	45.55477	3.09086	4.34759	3.82172	3.09086	3.81892	5.1817	4.56937		
30	50.75989	4.47023	50.66625	3.26186	4.47023	3.92711	3.26186	3.92526				
31	55.87717	4.57747	55.7755	3.411	4.57747	4.02316	3.411	4.02133				
32	60.95691	4.67546	60.88406	3.54485	4.67546	4.11017	3.54485	4.10897				
33	66.01366	4.76758	65.98447	3.66765	4.76758	4.18986	3.66765	4.18942				
34	71.12815	4.85284	71.07609	3.77522	4.85284	4.26448	3.77522	4.26375				
35	76.20428	4.92258	76.14123	3.8761	4.92258	4.33342	3.8761	4.33259				
36	81.30648	4.99103	81.27288	3.97332	4.99103	4.39823	3.97332	4.39781				
37	86.36389	5.06083	86.3228	4.06147	5.06083	4.45857	4.06147	4.45809				
38	91.45355	5.12229	91.38532	4.14633	5.12229	4.51583	4.14633	4.51508				
39	96.48302	5.1817	96.44364	4.22528	5.1817	4.56937	4.22528	4.56896				
40												
41												

S3.7 Linear fit information for the isotherm at 273 K (see Origin file Or1):

Linear Fit (10.03.2020 12:22:47)

Notes

Description	Perform Linear Fitting
User Name	Nuhnen AC1
Operation Time	10.03.2020 12:22:47
Equation	y = a + b*x
Report Status	Report generated from Data Changed
Weight	No Weighting
Special Input Handling	
Data Filter	No

Input Data

	Input X Data Source	Input Y Data Source	Range
	[Book1]Sheet1!I"273 K"	[Book1]Sheet1!J	[1*:29*]

Parameters

		Value	Standard Error	t-Value	Prob>|t|
J	Intercept	0.49083	0.04285	11.45425	7.14453E-12
	Slope	0.77883	0.01217	64.01305	4.99276E-31

Slope is significantly different from zero (See ANOVA Table).
Standard Error was scaled with square root of reduced Chi-Sqr.
Some input data points are missing.

Statistics

	J
Number of Points	29
Degrees of Freedom	27
Residual Sum of Squares	0.3208
Pearson's r	0.99672
R-Square (COD)	0.99345
Adj. R-Square	0.99321

Summary

	Intercept		Slope		Statistics
	Value	Standard Error	Value	Standard Error	Adj. R-Square
J	0.49083	0.04285	0.77883	0.01217	0.99321

ANOVA

		DF	Sum of Squares	Mean Square	F Value	Prob>F
J	Model	1	48.68715	48.68715	4097.67067	5.00289E-31
	Error	27	0.3208	0.01188		
	Total	28	49.00796			

At the 0.05 level, the slope is significantly different from zero.

Fitted Curves Plot

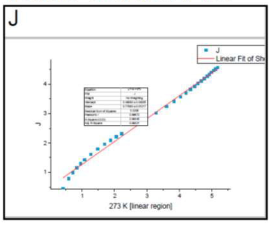

Residual Plots

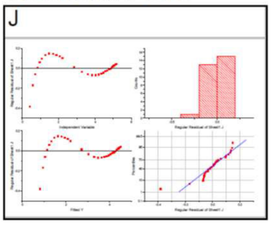

S3.8 Linear fit information for the isotherm at 293 K (see Origin file Or1):

Linear Fit (10.03.2020 12:22:46)

Notes

Description	Perform Linear Fitting
User Name	Nuhnen AC1
Operation Time	10.03.2020 12:22:46
Equation	y = a + b*x
Report Status	Report generated from Data Changed
Weight	No Weighting
Special Input Handling	
Data Filter	No

Input Data

	Input X Data Source	Input Y Data Source	Range
	[Book1]Sheet1!K"293 K"	[Book1]Sheet1!L	[1*:25*]

Parameters

		Value	Standard Error	t-Value	Prob>|t|
L	Intercept	1.37289	0.05644	24.32267	6.53187E-18
	Slope	0.7785	0.02043	38.11202	2.73037E-22

Slope is significantly different from zero (See ANOVA Table).
Standard Error was scaled with square root of reduced Chi-Sqr.
Some input data points are missing.

Statistics

	L
Number of Points	25
Degrees of Freedom	23
Residual Sum of Squares	0.43833
Pearson's r	0.99218
R-Square (COD)	0.98441
Adj. R-Square	0.98373

Summary

	Intercept		Slope		Statistics
	Value	Standard Error	Value	Standard Error	Adj. R-Square
L	1.37289	0.05644	0.7785	0.02043	0.98373

ANOVA

		DF	Sum of Squares	Mean Square	F Value	Prob>F
L	Model	1	27.68213	27.68213	1452.52645	2.73195E-22
	Error	23	0.43833	0.01906		
	Total	24	28.12046			

At the 0.05 level, the slope is significantly different from zero.

Fitted Curves Plot

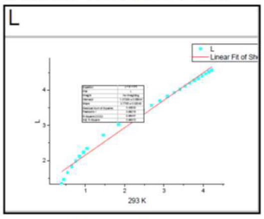

Residual Plots

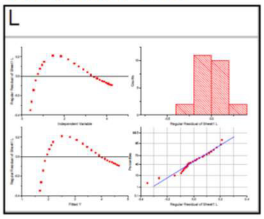

S3.9 Linear fitted CO_2 adsorption isotherms on MIL-160 at 273 K and 293 K with fit data (see Origin file Or1):

Use the slope and intercept derived here from the fitting procedure as input in the Excel data sheet of the next Section S3.10.

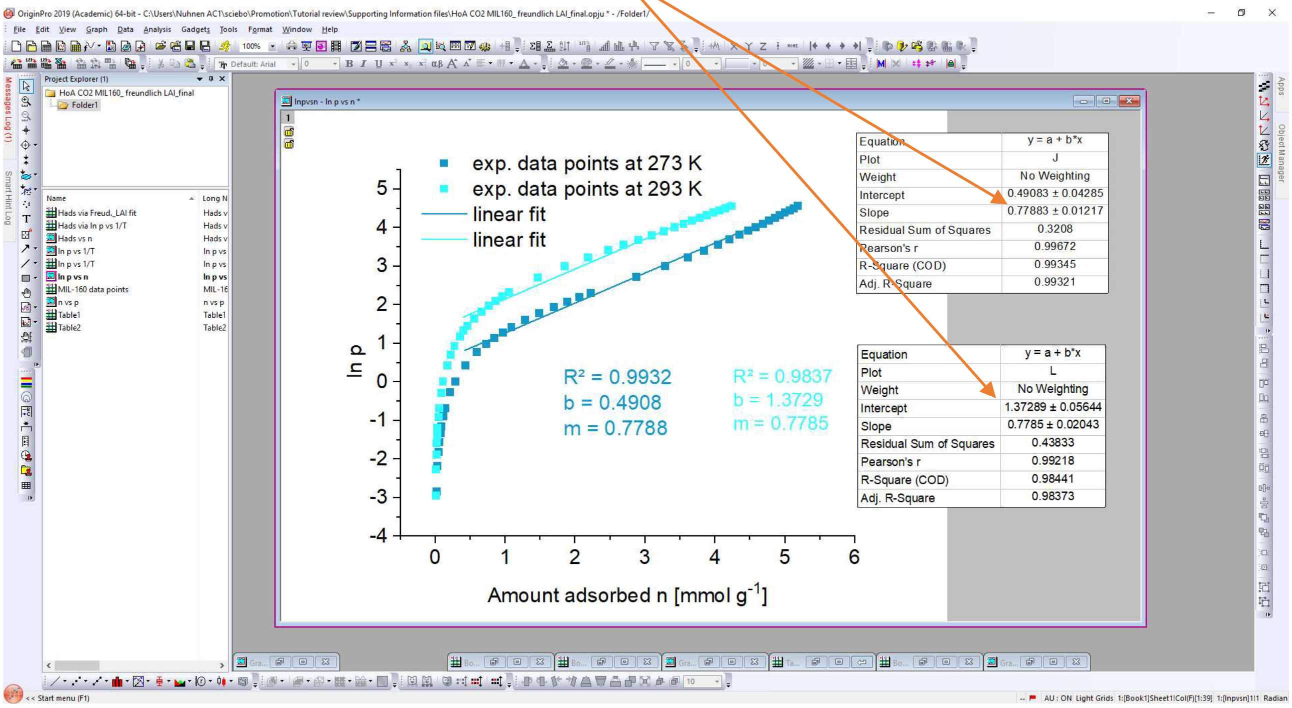

Equation	y = a + b*x
Plot	J
Weight	No Weighting
Intercept	0.49083 ± 0.04285
Slope	0.77883 ± 0.01217
Residual Sum of Squares	0.3208
Pearson's r	0.99672
R-Square (COD)	0.99345
Adj. R-Square	0.99321

Equation	y = a + b*x
Plot	L
Weight	No Weighting
Intercept	1.37289 ± 0.05644
Slope	0.7785 ± 0.02043
Residual Sum of Squares	0.43833
Pearson's r	0.99218
R-Square (COD)	0.98441
Adj. R-Square	0.98373

S3.10 Fit of ln*p* vs1/*T*$_1$ and 1/*T*$_2$ at equal loading *n* (see Origin file Or1):

Use the slope derived here from the fitting of the ln*p* vs 1/*T* plot for a given *n* as input in the Excel data sheet of the next Section S3.11.

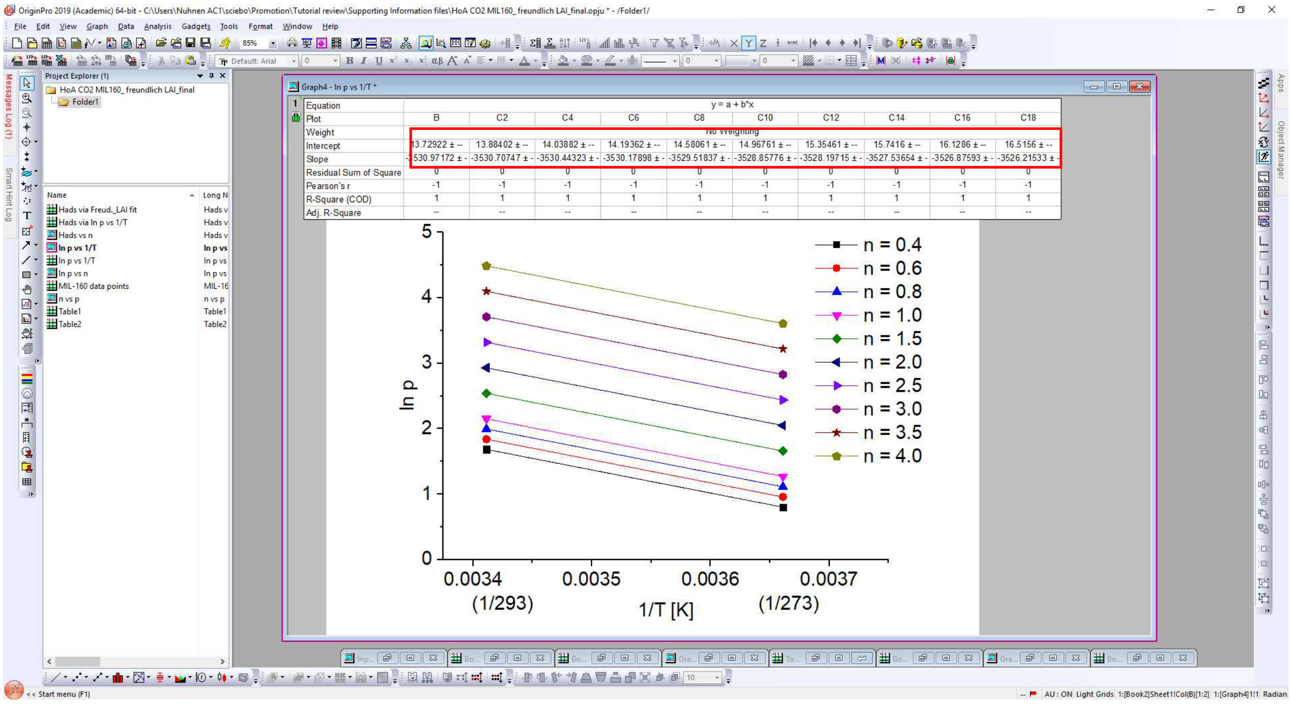

Equation	y = a + b*x									
Plot	B	C2	C4	C6	C8	C10	C12	C14	C16	C18
Weight	No Weighting									
Intercept	13.72922 ± --	13.88402 ± --	14.03882 ± --	14.19362 ± --	14.58061 ± --	14.96761 ± --	15.35461 ± --	15.7416 ± --	16.1286 ± --	16.5156 ± --
Slope	-3530.97172 ± -	-3530.70747 ± -	-3530.44323 ± -	-3530.17898 ± -	-3529.51837 ± -	-3528.85776 ± -	-3528.19715 ± -	-3527.53654 ± -	-3526.87593 ± -	-3526.21533 ± -
Residual Sum of Square	0	0	0	0	0	0	0	0	0	0
Pearson's r	-1	-1	-1	-1	-1	-1	-1	-1	-1	-1
R-Square (COD)	1	1	1	1	1	1	1	1	1	1
Adj. R-Square	--	--	--	--	--	--	--	--	--	--

S3.11 $\Delta H_{ads}(n)$ from lnp_1 | $1/T_1$ and lnp_2 | $1/T_2$ at equal loading n (see Excel sheet Ex2):

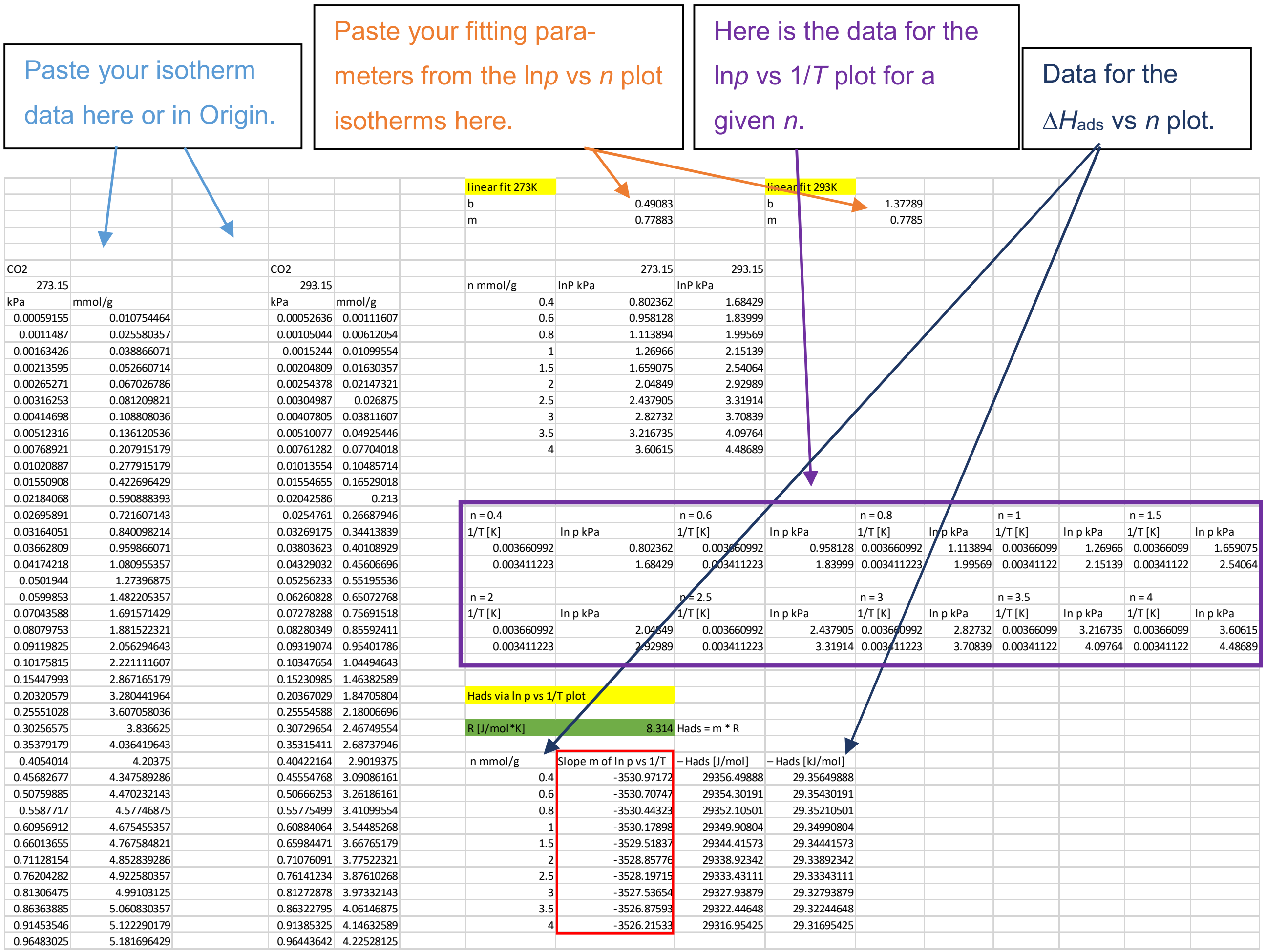

Paste your isotherm data here or in Origin.

Paste your fitting parameters from the ln*p* vs *n* plot isotherms here.

Here is the data for the ln*p* vs 1/*T* plot for a given *n*.

Data for the ΔH_{ads} vs *n* plot.

CO2		CO2	
273.15		293.15	
kPa	mmol/g	kPa	mmol/g
0.00059155	0.010754464	0.00052636	0.00111607
0.0011487	0.025580357	0.00105044	0.00612054
0.00163426	0.038866071	0.0015244	0.01099554
0.00213595	0.052660714	0.00204809	0.01630357
0.00265271	0.067026786	0.00254378	0.02147321
0.00316253	0.081209821	0.00304987	0.026875
0.00414698	0.108808036	0.00407805	0.03811607
0.00512316	0.136120536	0.00510077	0.04925446
0.00768921	0.207915179	0.00761282	0.07704018
0.01020887	0.277915179	0.01013554	0.10485714
0.01550908	0.422696429	0.01554655	0.16529018
0.02184068	0.590888393	0.02042586	0.213
0.02695891	0.721607143	0.0254761	0.26687946
0.03164051	0.840098214	0.03269175	0.34413839
0.03662809	0.959866071	0.03803623	0.40108929
0.04174218	1.080955357	0.04329032	0.45606696
0.0501944	1.27396875	0.05256233	0.55195536
0.0599853	1.482205357	0.06260828	0.65072768
0.07043588	1.691571429	0.07278288	0.75691518
0.08079753	1.881522321	0.08280349	0.85592411
0.09119825	2.056294643	0.09319074	0.95401786
0.10175815	2.221111607	0.10347654	1.04494643
0.15447993	2.867165179	0.15230985	1.46382589
0.20320579	3.280441964	0.20367029	1.84705804
0.25551028	3.607058036	0.25554588	2.18006696
0.30256575	3.836625	0.30729654	2.46749554
0.35379179	4.036419643	0.35315411	2.68737946
0.4054014	4.20375	0.40422164	2.9019375
0.45682677	4.347589286	0.45554768	3.09086161
0.50759885	4.470232143	0.50666253	3.26186161
0.5587717	4.57746875	0.55775499	3.41099554
0.60956912	4.675455357	0.60884064	3.54485268
0.66013655	4.767584821	0.65984471	3.66765179
0.71128154	4.852839286	0.71076091	3.77522321
0.76204282	4.922580357	0.76141234	3.87610268
0.81306475	4.99103125	0.81272878	3.97332143
0.86363885	5.060830357	0.86322795	4.06146875
0.91453546	5.122290179	0.91385325	4.14632589
0.96483025	5.181696429	0.96443642	4.22528125

linear fit 273K			linear fit 293K	
b	0.49083		b	1.37289
m	0.77883		m	0.7785

	273.15	293.15
n mmol/g	lnP kPa	lnP kPa
0.4	0.802362	1.68429
0.6	0.958128	1.83999
0.8	1.113894	1.99569
1	1.26966	2.15139
1.5	1.659075	2.54064
2	2.04849	2.92989
2.5	2.437905	3.31914
3	2.82732	3.70839
3.5	3.216735	4.09764
4	3.60615	4.48689

n = 0.4		n = 0.6		n = 0.8		n = 1		n = 1.5	
1/T [K]	ln p kPa	1/T [K]	ln p kPa	1/T [K]	ln p kPa	1/T [K]	ln p kPa	1/T [K]	ln p kPa
0.003660992	0.802362	0.003660992	0.958128	0.003660992	1.113894	0.00366099	1.26966	0.00366099	1.659075
0.003411223	1.68429	0.003411223	1.83999	0.003411223	1.99569	0.00341122	2.15139	0.00341122	2.54064

n = 2		n = 2.5		n = 3		n = 3.5		n = 4	
1/T [K]	ln p kPa	1/T [K]	ln p kPa	1/T [K]	ln p kPa	1/T [K]	ln p kPa	1/T [K]	ln p kPa
0.003660992	2.04849	0.003660992	2.437905	0.003660992	2.82732	0.00366099	3.216735	0.00366099	3.60615
0.003411223	2.92989	0.003411223	3.31914	0.003411223	3.70839	0.00341122	4.09764	0.00341122	4.48689

Hads via ln p vs 1/T plot

R [J/mol*K]	8.314	Hads = m * R	
n mmol/g	Slope m of ln p vs 1/T	– Hads [J/mol]	– Hads [kJ/mol]
0.4	-3530.97172	29356.49888	29.35649888
0.6	-3530.70747	29354.30191	29.35430191
0.8	-3530.44323	29352.10501	29.35210501
1	-3530.17898	29349.90804	29.34990804
1.5	-3529.51837	29344.41573	29.34441573
2	-3528.85776	29338.92342	29.33892342
2.5	-3528.19715	29333.43111	29.33343111
3	-3527.53654	29327.93879	29.32793879
3.5	-3526.87593	29322.44648	29.32244648
4	-3526.21533	29316.95425	29.31695425

S3.12 Virial fit for SO_2 adsorption isotherms on NH_2-MIL-125(Ti) at 273 K and 293 K in an ln*p* vs *n* plot (see Origin file Or2):

A brief illustration how to set up the virial fit with the program Origin is given in the file “HoA detailed description_origin.pdf”.

Use these a_i and b_i parameters which are derived here from the virial fitting procedure as input in the Excel data sheet of the next Section S3.13.

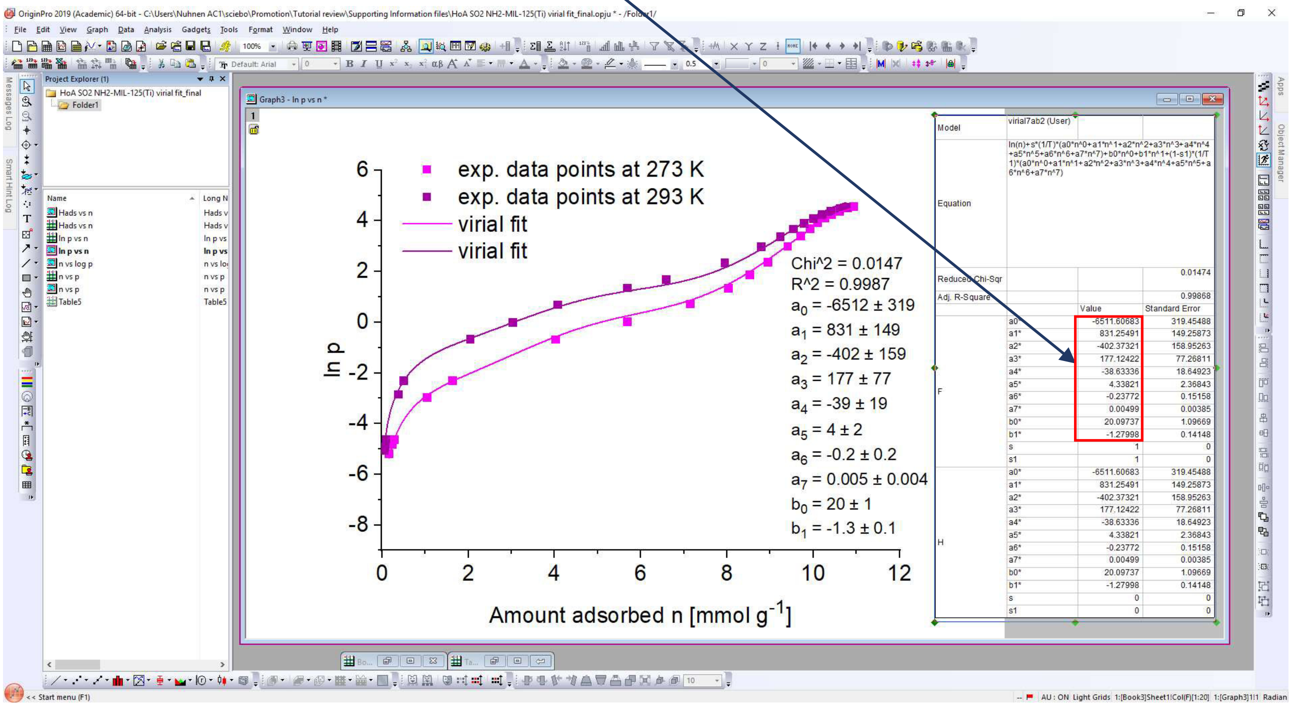

Model	virial7ab2 (User)		
Equation	ln(n)+s*(1/T)*(a0*n^0+a1*n^1+a2*n^2+a3*n^3+a4*n^4+a5*n^5+a6*n^6+a7*n^7)+b0*n^0+b1*n^1+(1-s1)*(1/T1)*(a0*n^0+a1*n^1+a2*n^2+a3*n^3+a4*n^4+a5*n^5+a6*n^6+a7*n^7)		
Reduced Chi-Sqr			0.01474
Adj. R-Square			0.99868
		Value	Standard Error
F	a0*	-6511.60683	319.45488
	a1*	831.25491	149.25873
	a2*	-402.37321	158.95263
	a3*	177.12422	77.26811
	a4*	-38.63336	18.64923
	a5*	4.33821	2.36843
	a6*	-0.23772	0.15158
	a7*	0.00499	0.00385
	b0*	20.09737	1.09669
	b1*	-1.27998	0.14148
	s	1	0
	s1	1	0
H	a0*	-6511.60683	319.45488
	a1*	831.25491	149.25873
	a2*	-402.37321	158.95263
	a3*	177.12422	77.26811
	a4*	-38.63336	18.64923
	a5*	4.33821	2.36843
	a6*	-0.23772	0.15158
	a7*	0.00499	0.00385
	b0*	20.09737	1.09669
	b1*	-1.27998	0.14148
	s	0	0
	s1	0	0

S3.13 $\Delta H_{ads}(n)$ from virial fit for SO_2 adsorption isotherms on NH_2-MIL-125(Ti) at 273 K and 293 K (Excel sheet Ex3):

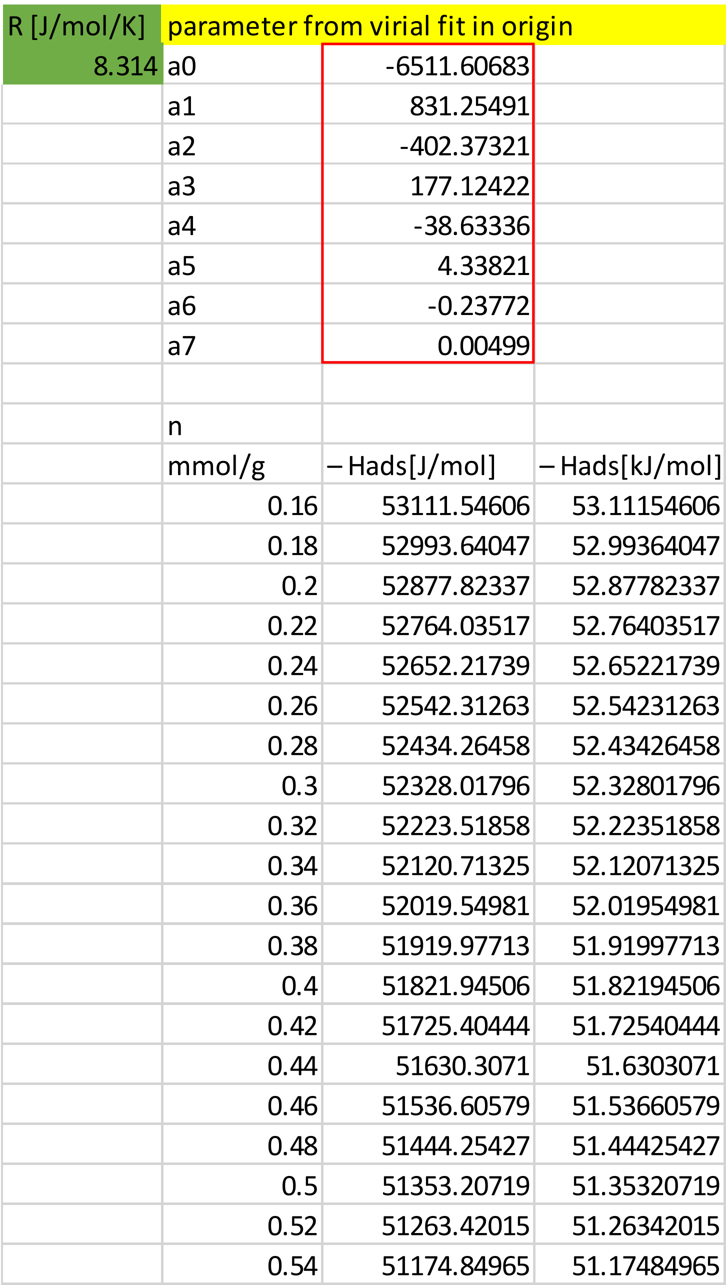

R [J/mol/K]	parameter from virial fit in origin		
8.314	a0	-6511.60683	
	a1	831.25491	
	a2	-402.37321	
	a3	177.12422	
	a4	-38.63336	
	a5	4.33821	
	a6	-0.23772	
	a7	0.00499	
	n		
	mmol/g	– Hads[J/mol]	– Hads[kJ/mol]
	0.16	53111.54606	53.11154606
	0.18	52993.64047	52.99364047
	0.2	52877.82337	52.87782337
	0.22	52764.03517	52.76403517
	0.24	52652.21739	52.65221739
	0.26	52542.31263	52.54231263
	0.28	52434.26458	52.43426458
	0.3	52328.01796	52.32801796
	0.32	52223.51858	52.22351858
	0.34	52120.71325	52.12071325
	0.36	52019.54981	52.01954981
	0.38	51919.97713	51.91997713
	0.4	51821.94506	51.82194506
	0.42	51725.40444	51.72540444
	0.44	51630.3071	51.6303071
	0.46	51536.60579	51.53660579
	0.48	51444.25427	51.44425427
	0.5	51353.20719	51.35320719
	0.52	51263.42015	51.26342015
	0.54	51174.84965	51.17484965

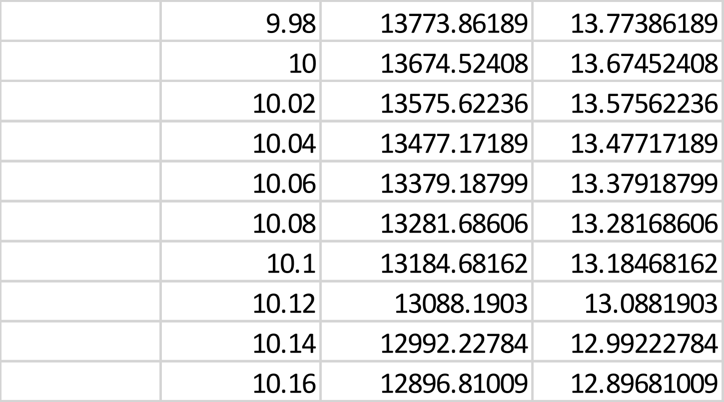

	9.98	13773.86189	13.77386189
	10	13674.52408	13.67452408
	10.02	13575.62236	13.57562236
	10.04	13477.17189	13.47717189
	10.06	13379.18799	13.37918799
	10.08	13281.68606	13.28168606
	10.1	13184.68162	13.18468162
	10.12	13088.1903	13.0881903
	10.14	12992.22784	12.99222784
	10.16	12896.81009	12.89681009

S4. MOF structures

S4.1 MIL-160:

MIL-160 (*Matériaux Institut Lavoisier*) is an Al-MOF, which was described by Cadiau *et al.* in 2015.[5] They obtained the MOF by applying reflux conditions for aqueous solutions of 2,5-furandicarboxylic acid, sodium hydroxide and aluminum chloride. MIL-160 is constructed by cis-µ-OH-connected, vertex-sharing {AlO_6} octahedra, that form helical chains, which are then joined by the linker 2,5-furandicarboxylate (Fig. S1).

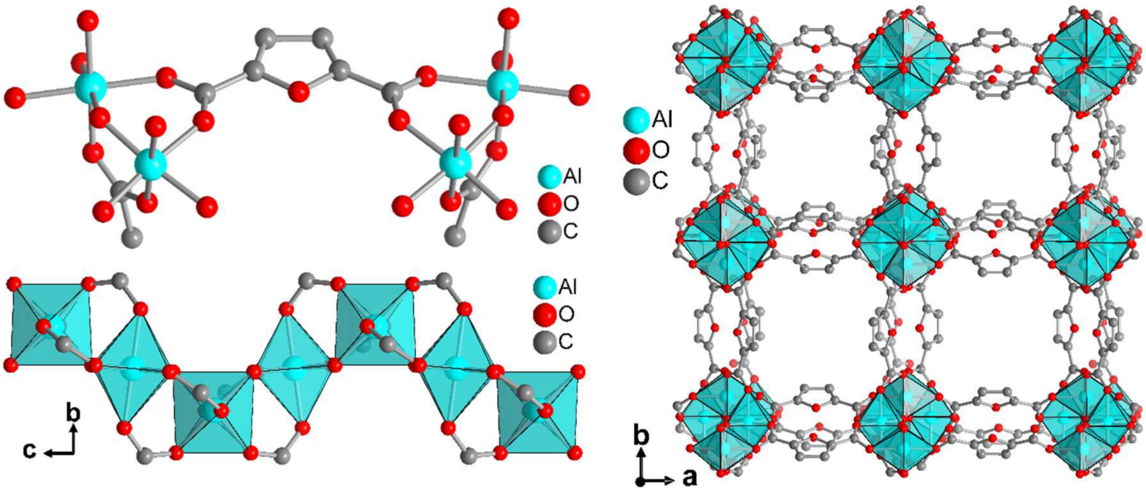

Fig. S1 Structural elements in MIL-160 with extended asymmetric unit, the fourfold helical chain of cis vertex-bridged {AlO_6}-polyhedra as the inorganic building unit, and the 3D framework structure of square-shaped one-dimensional channels. Graphics produced from cif-file for MIL-160 (CSD-Refcode PIBZOS).[6]

MIL-160 consists of chains of {AlO_6}-polyhedra that are surrounded by linker molecules.[5] This results in a chemical formula of $[Al(OH)(O_2C\text{-}C_4H_2O\text{-}CO_2)\ n\ H_2O]_m$ and microporous square-shaped channels of 5 Å edge length.[5,7] The material exhibits a surface area of 1070 $m^2\ g^{-1}$ and a pore volume of 0.40 $cm^3\ g^{-1}$ from $AlCl_3$ and NaOH (theoretically: 1250 $m^2\ g^{-1}$, 0.48 $cm^3\ g^{-1}$),[5] respectively 1150 $m^2\ g^{-1}$ and 0.46 $cm^3\ g^{-1}$, from $Al(OH)(CH_3COO)_2$,7 although very recent theoretical calculations suggested a surface area of 776 $m^2\ g^{-1}$ and a pore volume of 0.45 $cm^3\ g^{-1}$.[8]

The hydrophilic character of the MOF is also due to the heteroatom in the furan moiety of the linker. This resulted in a highly hydrothermally stable material with promising water sorption characteristics. Cadiau *et al.* denoted MIL-160 as the most promising Al-MOF for heat pump applications.[5]

S4.2 NH_2-MIL-125(Ti):

NH_2-MIL-125(Ti) is based on $Ti_8O_8(OH)_4^{12+}$ SBUs and aminoterephthalic acid (H_2N-BDC), and is isostructural to unmodified MIL-125(Ti) (Fig. S2).[9]

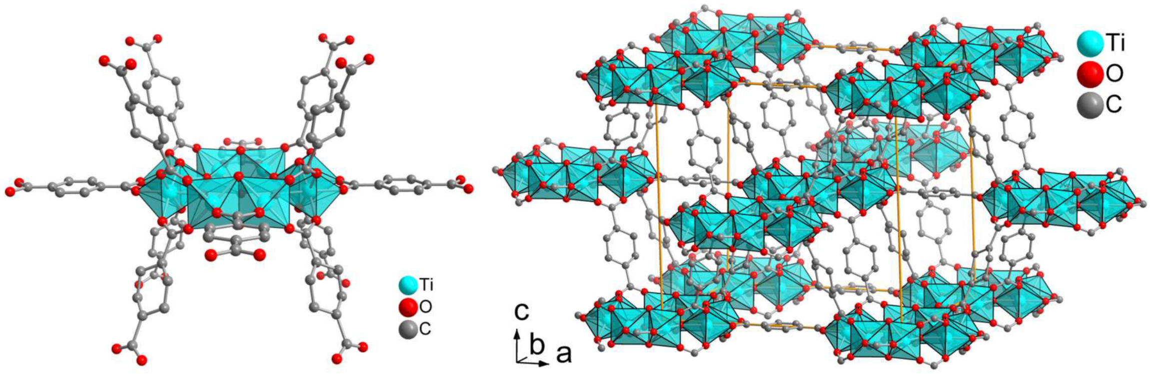

Fig. S2 Structure of titanium terephthalate MIL-125 (isostructural to NH_2-MIL-125(Ti)).[9] The SBU is an eight-membered ring of edge- and vertex-sharing TiO_6 octahedra, which is connected to 12 neighboring SBUs in a body-centered cubic (bcc) packing arrangement. Structure drawn from the deposited cif-file under CCDC 751157 (MIL-125).[9]

Titanium aminoterephthalate, NH_2-MIL-125(Ti) is a hydrophilic MOF, showing a steep rise of the isotherm, and complete water loading at a relative pressure as low as $p/p_0 = 0.2$. Most notably, it is also much more hydrophilic than NH_2-UiO-66, although pore sizes are similar and the linker molecule is the same. The main reason for the increased hydrophilicity of NH_2-MIL-125(Ti) can be explained by the structure of the SBU: Compared to $Zr_6O_4(OH)_4^{12+}$ (679 g/mol), the $Ti_8O_8(OH)_4^{12+}$ cluster (579 g/mol) has a lower formula weight and contains more hydrophilic M^{4+} and O^{2-} ions. From these results, NH_2-MIL-125(Ti) is of strong interest for further examination concerning water sorption for heat transformation.[10]

S4.3 HHU-1 (Zr-ADC):

The reaction of acetylenedicarboxylic acid (H_2ADC) with $ZrOCl_2{\cdot}8H_2O$ in DMF yielded the MOF **HHU-1** of ideal formula $[Zr_6(\mu_3\text{-}O)_4(\mu_3\text{-}OH)_4(ADC)_6]$.[11]·The structure of **HHU-1** was determined from powder diffraction data with a = 17.925(3) Å in space group $Fm\bar{3}m$ using the crystal structure of the terephthalate UiO-66 as a starting point. The UiO-type hexanuclear $[Zr_6O_4(OH)_4]^{12+}$ SBU with the attached ADC linkers and the face-centered cubic (fcc) packing diagram of the **fcu** network are shown in Figure S3. The contact diameters for the surrounding van der Waals radii of the octahedral and tetrahedral cages are about 9.6 Å and 5.8 Å diameter respectively, with a triangular window diameter 4.4 Å.[11]

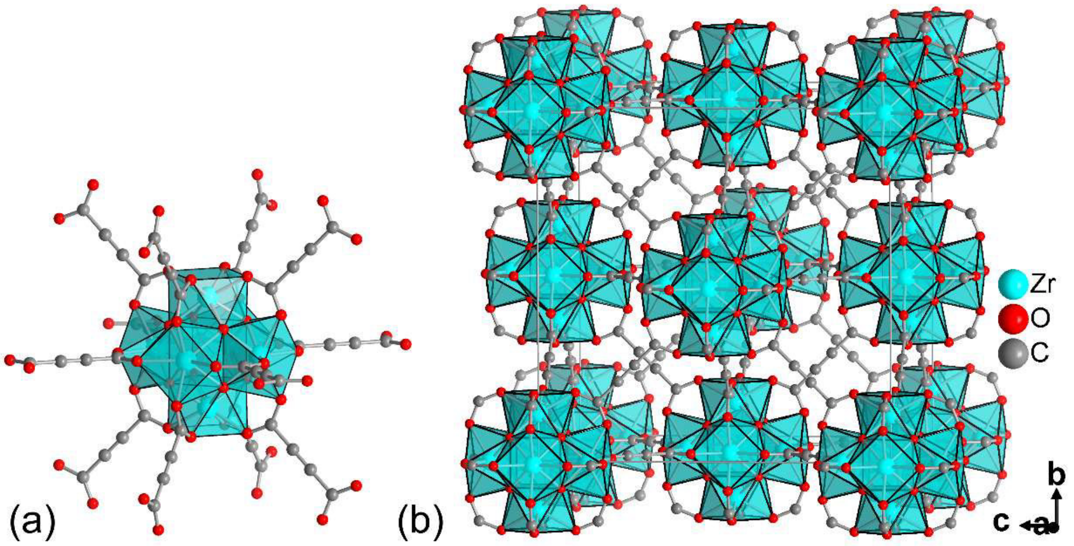

Fig. S3 (a) Secondary building unit of $\{Zr_6(O)_4(OH)_4\}$ with the 12 surrounding and connecting acetylenedicarboxylate linkers and the edge-sharing square-antiprismatic ZrO_8 coordination as polyhedra. (b) fcc packing diagram of the **fcu** framework in **HHU-1**. The refined guest atoms are not shown for clarity.[11]

Water vapor adsorption for **HHU-1** displays a Type Ib isotherm with an early water uptake at $P/P_0 = 0.05$, which indicates a high hydrophilicity, probably due to the small micropores with the synergistic effects of the triple bond C≡C of the ADC linker, and the μ_3-OH and μ_3-O groups on the $[Zr_6O_4(OH)_4]^{12+}$ SBU.[11]

S5. SO_2 adsorption isotherms of NH_2-MIL-125(Ti) at 273 K and 293 K

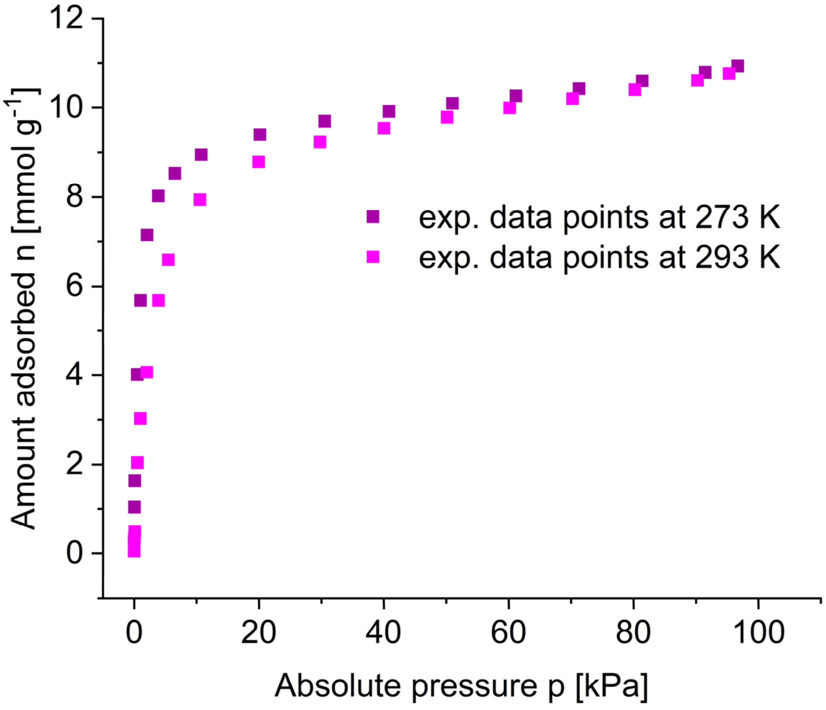

Fig. S4 SO_2 adsorption isotherms of NH_2-MIL-125(Ti) at 273 K and 293 K in a linear-scale *n* vs *p* plot. The amount adsorbed *n* starts at 0.05 mmol g^{-1}.

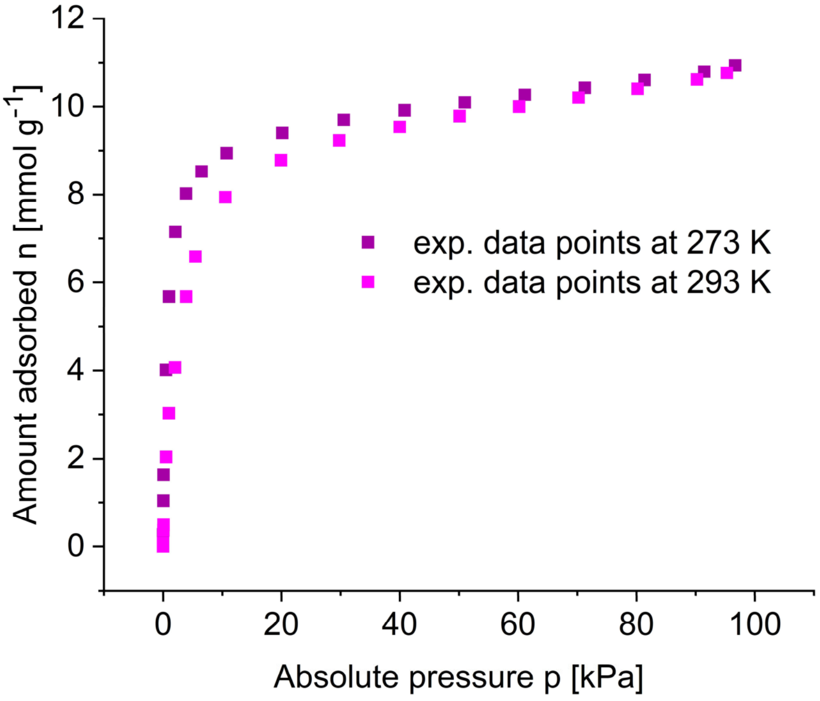

Fig. S5 SO_2 adsorption isotherms of NH_2-MIL-125(Ti) at 273 K and 293 K in a linear-scale *n* vs *p* plot. The amount adsorbed *n* starts at 0.0002 mmol g^{-1}.

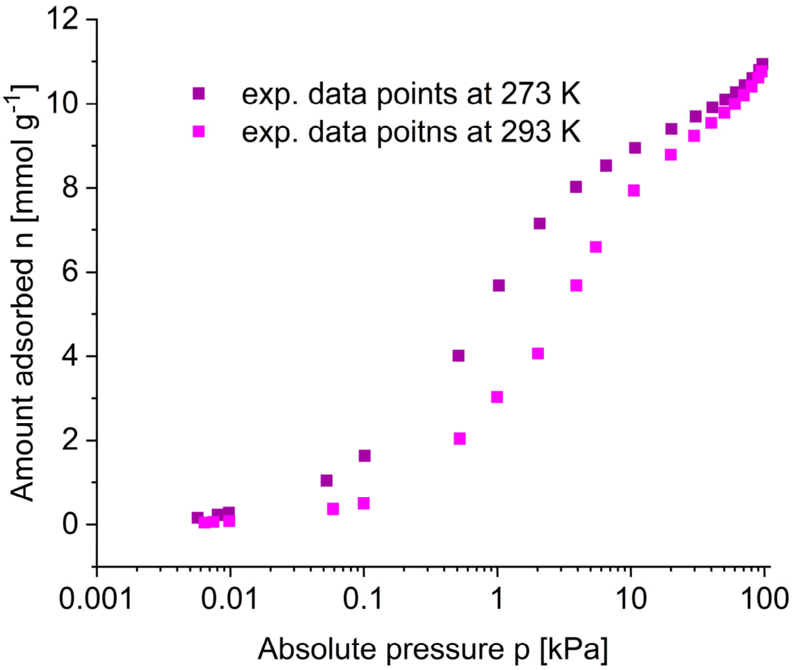

Fig. S6 SO_2 adsorption isotherms of NH_2-MIL-125(Ti) at 273 K and 293 K in a linear *n*- vs logarithmic *p*-scale plot. The amount adsorbed *n* starts at 0.05 mmol g^{-1}.

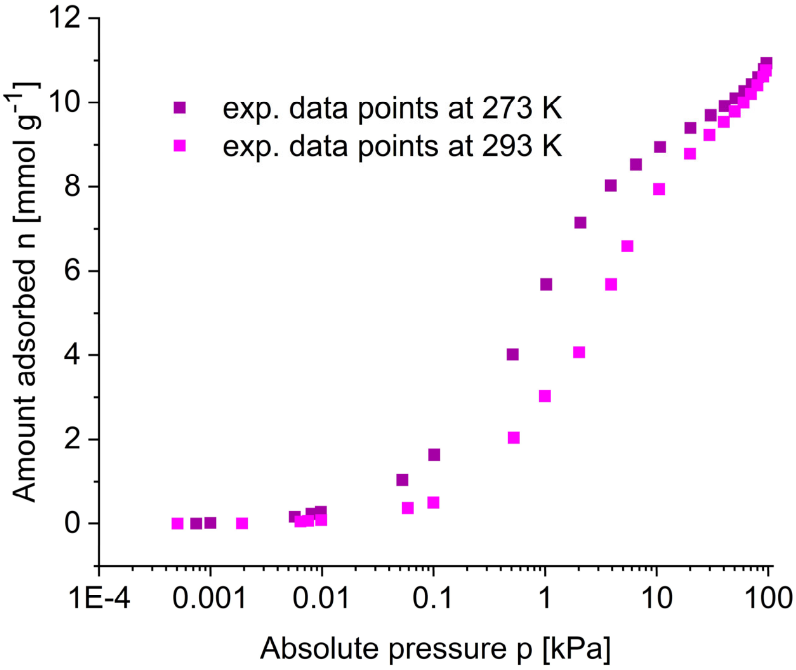

Fig. S7 SO_2 adsorption isotherms of NH_2-MIL-125(Ti) at 273 K and 293 K in a linear *n*- vs logarithmic *p*-scale plot. The amount adsorbed *n* starts at 0.0002 mmol g^{-1}.

S6. Virial analysis for SO_2 isotherms of NH_2-MIL-125(Ti) at 273 K and 293 K with a larger number of a_i and b_i fit parameters

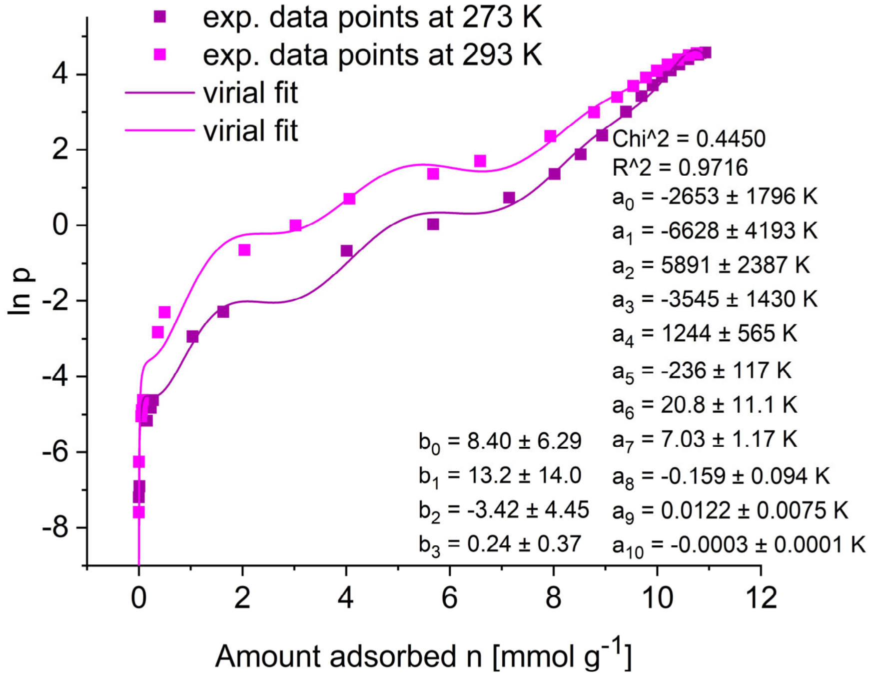

Fig. S8 Virial analysis for SO_2 isotherms of NH_2-MIL-125(Ti) at 273 K and 293 K with additional low uptake points, starting at n = 0.0002 mmol g^{-1} and a larger number of a_i and b_i fit parameters.

S7. Enthalpy of adsorption for CO_2 on MIL-100(Cr)

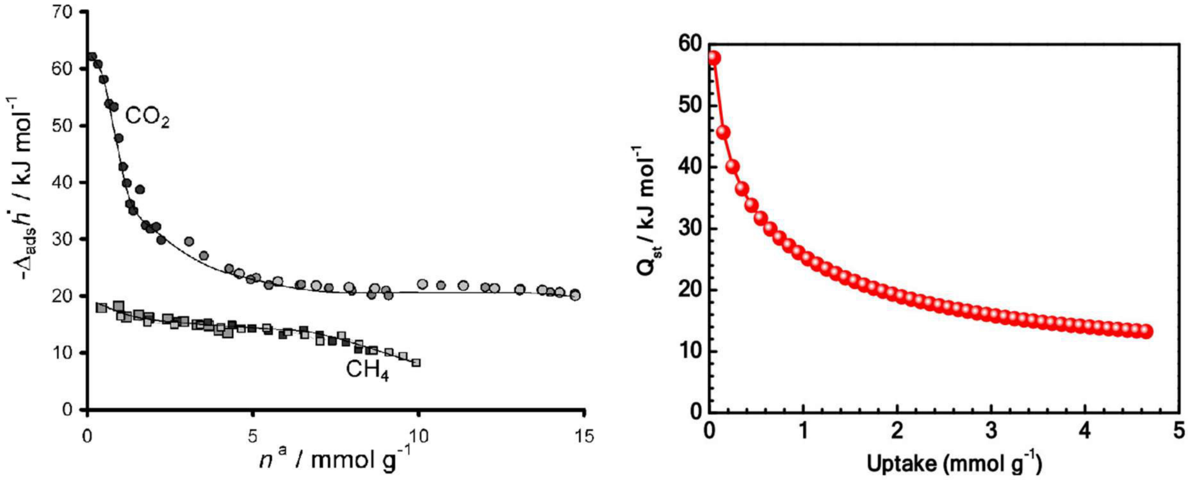

Fig. S9 Enthalpy of adsorption for CO_2 on MIL-100(Cr) determined (left) by microcalorimetry[12] and (right) calculated from adsorption isotherms at 273, 298 and 323 K with a Freundlich-Langmuir fit and Clausius-Clapeyron approach.[13] Left: Reproduced from ref. 12 with permission from the American Chemical Society, copyright 2008. Right: Reproduced from ref. 13 with permission from the American Chemical Society, copyright 2019.

References

---

1 A. G. Bezus, A. V. Kiselev, Z. Sedlacek and P. Q. Du, *Trans. Faraday Soc.*, 1971, **67**, 468–482.

2 N. N. Avgul, A. G. Bezus, E. S. Dobrova and A. V. Kiselev, *J. Coil. Interface Sci.*, 1973, **42**, 486–495.

3 M. Jaroniec and J. A. Jaroniec, *Carbon*, 1977, **15**, 107-111.

4 D. Nicholson and T. Stubos, Recent Advances in Gas Separation by Microporous Ceramic Membranes, in *Membrane Science and Technology*, Elsevier, 2000. J. Rouquerol, F. Rouquerol and K. S. W. Sing, Adsorption by powders and porous solids, Academic Press, San Diego, USA, 1999.

5 A. Cadiau, J. S. Lee, D. D. Borges, P. Fabry, T. Devic, M. T. Wharmby, C. Martineau, D. Foucher, F. Taulelle, C.-H. Jun, Y. K. Hwang, N. Stock, M. F. De Lange, F. Kapteijn, J. Gascon, G. Maurin, J.-S. Chang and C. Serre, *Adv. Mater.*, 2015, **27**, 4775–4780.

6 M. Wahiduzzaman, D. Lenzen, G. Maurin, N. Stock and M.T. Wharmby, *Eur. J. Inorg. Chem.*, 2018, 3626–3632.

7 A. Permyakova, O. Skrylnyk, E. Courbon, M. Affran, S. Wang, U-H. Lee, A. H. Valekar, F. Nouar, G. Mouchaham, T. Devic, G. De Weireld, J.-S. Chang, N. Steunou, M. Frère and C. Serre, *ChemSusChem.*, 2017, **10**, 1419–1426.

8 D. D. Borges, G. Maurin and D. S. Galvao, *MRS Adv.*, 2017, **2**, 519-524.

9 M. Dan-Hardi, C. Serre, T. Frot, L. Rozes, G. Maurin, C. Sanchez and G. Férey, *J. Am. Chem. Soc.*, 2009, **131**, 10857–10859.

10 F. Jeremias, V. Lozan, S. K. Henninger and C. Janiak, *Dalton Trans.*, 2013, **42**, 15967–15973.

11 T. J. Matemb Ma Ntep, H. Reinsch, B. Moll, E. Hastürk, S. Gökpinar, H. Breitzke, C. Schlüsener, L. Schmolke, G. Buntkowsky and C. Janiak, *Chem. Eur. J.*, 2018, **24**, 14048–14053.

12 P. L. Llewellyn, S. Bourrelly, C. Serre, A. Vimont, M. Daturi, L. Hamon, G. De Weireld, J. S. Chang, D. Y. Hong, Y. K. Hwang, S. H. Jhung and G. Férey, *Langmuir*, 2008, **24**, 7245–7250.

13 J. Yang, H. Bai, F. Zhang, J. Liu, J. Winarta, Y. Wang and B. Mu, *J. Chem. Eng. Data*, 2019, **64**, 5814–5823.

3.5 Encapsulation of a Porous Organic Cage into the Pores of a Metal-Organic Framework for Enhanced CO_2 separation

Jun Liang, Alexander Nuhnen, Simon Millan, Hergen Breitzke, Vasily Gvilava, Gerd Buntkowsky, Christoph Janiak

Angew. Chem. Int. Ed., **2020**, 59, 6068–6073.

DOI: 10.1002/anie.201916002

In den letzten Jahrzehnten gab es ein großes Interesse an der Entwicklung von neuartigen porösen Materialien zur selektiven Erfassung und Speicherung von wichtigen Gasen wie CO_2. Unter anderem wurden kristalline Materialien mit ausgedehnten Porenstrukturen wie Zeolithe oder MOFs untersucht. Ferner zeigen auch poröse organische Käfige (*porous organic cages*, POCs) interessante Eigenschaften zur selektiven Gasaufnahme, obwohl POCs häufig nur geringe innere Oberflächen aufweisen. In dieser Arbeit wurde ein einfacher Weg aufgezeigt, um funktionelle, poröse organische Käfige in ein robustes MOF mit Hilfe der Feuchteimprägnation einzulagern. Dabei wurde das poröse organische Molekül cucurbit[6]uril (CB6), dessen Käfigstruktur eine hohe Affinität zu CO_2 zeigt, in die Mesoporen des chrombasierten MIL-101 eingelagert, ohne die Struktur, Morphologie und Stabilität des MOFs zu verändern. Die eingelagerte Menge an CB6 kann durch die Versuchsbedingungen variiert werden. Zudem reduziert sich durch die Einlagerung des mikroporösen CB6 in den Mesoporen von MIL-101 das Mesoporenvolumen, wobei gleichzeitig attraktivere Bindungsstellen für CO_2 in den entstehenden Mikroporen des Kompositmaterials geschaffen werden. Die gesteigerte Affinität zu CO_2 führt zu einer verbesserten CO_2 Aufnahmekapazität und erhöhten CO_2/N_2, CO_2/CH_4-Separationseigenschaften bei niedrigen Drücken für CB6@MIL-101.

Anteile an der Veröffentlichung:

- Hilfestellung bei der Aufnahme der Sorptionsisothermen und der Berechnung der Adsorptionswärmen, IAST-Selektivitäten. Herstellung und Messung der MMMs und Berechnung der Durchbruchskurven mit anschließender Auswertung und Interpretation im Manuskript.
- Die Entwicklung des Konzepts und die maßgebliche Laborarbeit, sowie die Erstellung des Manuskripts wurde von Herrn Dr. Jun Liang durchgeführt. Korrekturen erfolgten von Herrn Prof. Dr. Janiak.
- Herr Simon Millan hat an theoretischen Fragestellungen mitgewirkt.
- Herr Dr. Hergen Breitzke und Herr Prof. Dr. Gerd Buntkowsky haben die Festkörper-NMR Aufnahmen angefertigt.
- Die REM-Aufnahmen wurden von Herrn Vasily Gvilava durchgeführt.

Hybrid Materials **Hot Paper**

Deutsche Ausgabe: DOI: 10.1002/ange.201916002
Internationale Ausgabe: DOI: 10.1002/anie.201916002

Encapsulation of a Porous Organic Cage into the Pores of a Metal–Organic Framework for Enhanced CO_2 Separation

*Jun Liang, Alexander Nuhnen, Simon Millan, Hergen Breitzke, Vasily Gvilava, Gerd Buntkowsky und Christoph Janiak**

Abstract: *We present a facile approach to encapsulate functional porous organic cages (POCs) into a robust MOF by an incipient-wetness impregnation method. Porous cucurbit[6]uril (CB6) cages with high CO_2 affinity were successfully encapsulated into the nanospace of Cr-based MIL-101 while retaining the crystal framework, morphology, and high stability of MIL-101. The encapsulated CB6 amount is controllable. Importantly, as the CB6 molecule with intrinsic micropores is smaller than the inner mesopores of MIL-101, more affinity sites for CO_2 are created in the resulting CB6@MIL-101 composites, leading to enhanced CO_2 uptake capacity and CO_2/N_2, CO_2/CH_4 separation performance at low pressures. This POC@MOF encapsulation strategy provides a facile route to introduce functional POCs into stable MOFs for various potential applications.*

Introduction

There has been intense interest in the development of new porous materials for the selective capture and separation of important gases such as carbon dioxide.[1] In this regard, crystalline materials with extended porous structures such as zeolites,[2] coordination polymers (CPs) or metal–organic frameworks (MOFs),[3,4] and covalent organic frameworks (COFs)[5] are being widely investigated. The tunable pore sizes and high surface areas of these classes of materials make them suitable for trapping various guests. Porous organic molecules such as porous organic cages (POCs)[6] and porous macrocyclic molecules[7] have also been the subject of significant research during the past decade. Yet, it is usually difficult to prepare POC-based materials with high surface areas, and high degrees of gas sorption.[8] At the same time, the unique properties and easy availability of some POCs render them attractive in various fields including gas sorption and separation.[9] One such example is cucurbit[6]uril (CB6; see Scheme 1), which features a barrel-shaped rigid porous structure with only two windows and has been employed in various applications from gas capture to catalysis.[10] However, the application scope of the CB6 cage is limited by its poor solubility, strong intermolecular interactions, high affinity towards metal ions, and low surface area.[11] It is highly desirable to obtain POC-based hybrid materials with high porosity and stability by facile approaches, without sacrificing the inherent properties of the POCs.[12]

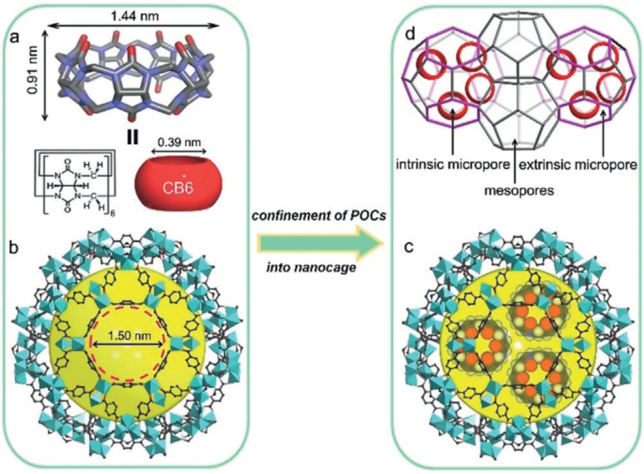

Scheme 1. The host-in-host concept for creating functional hybrid materials by the incorporation of CB6 into Cr-based MIL-101. Schematic views of a) the porous CB6 molecule; b) the mesoporous cage with hexagonal windows in MIL-101; c) CB6 in the larger cage of MIL-101; d) CB6 being selectively doped into the larger cages in MIL-101 while leaving the smaller cages empty. Hexagonal windows in pink. Hydrogen atoms are omitted for clarity.

Traditional strategies to obtain solid porous-organic-molecule-based porous materials can be briefly summarized: 1) Frameworks based on supramolecular bonds or coordination bonds (Figure 1 a);[8d,9a,c,d,13] 2) POCs covalently anchored in porous networks to provide active domains (Figure 1 b);[14] and 3) POCs dispersed as a porous additive in organic

---

[*] Dr. J. Liang, Prof. Dr. C. Janiak
Hoffmann Institute of Advanced Materials
Shenzhen Polytechnic
7098 Liuxian Blvd, Nanshan District, Shenzhen 518055 (China)

Dr. J. Liang, A. Nuhnen, S. Millan, V. Gvilava, Prof. Dr. C. Janiak
Institut für Anorganische Chemie und Strukturchemie
Heinrich-Heine-Universität Düsseldorf
40204 Düsseldorf (Germany)
E-Mail: janiak@uni-duesseldorf.de

H. Breitzke, Dr. G. Buntkowsky
Eduard-Zintl-Institut für Anorganische und Physikalische Chemie
Technische Universität Darmstadt
Alarich-Weiss-Straße 4, 64287 Darmstadt (Germany)

Supporting information and the ORCID identification number(s) for the author(s) of this article can be found under: https://doi.org/10.1002/anie.201916002.

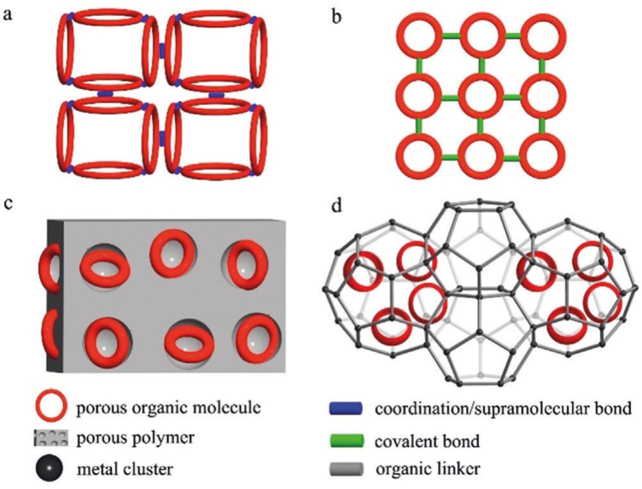

Figure 1. Strategies to generate porous materials containing porous organic molecules as a) neat frameworks, b) covalently anchored docking sites in a network, and c, d) functional guest molecules embedded in a polymer and a MOF, respectively.

polymers (Figure 1c).[15] Although the assembly of POC units directed by metal ions or supramolecular interactions (Figure 1a) is suitable for most POCs to give microporous frameworks, the disadvantages of these materials for practical applications are their low stability, macroscopic size, low surface areas, and polymorph issues.[16] While the covalent anchoring approach is highly programmable (Figure 1b), it requires that the molecules can be readily modified for the required bond formation as elegantly demonstrated by Coskun, Kim, and others.[14] POCs/polymers can also be obtained by physical doping for gas sorption and separation as shown by Cooper and others.[15] Herein, we demonstrate for the first time that a POC can be confined in the pores of a host framework such as a MOF (Figure 1d), and that the inherent properties of both POC and MOF can be combined in the resulting doubly porous hybrid material.

The highly ordered lattice and tunable pore sizes of MOFs have been used to accommodate polyoxometalates,[17] metal complexes,[18] metal–organic polyhedra,[19] metal nanoparticles,[20] and ionic liquids[21] as functional guests. These MOF-based host–guest composites have been obtained by various methods including incipient-wetness impregnation.[22] However, to the best of our knowledge, there is no report on fabricating functional porous hybrids by encapsulating a POC in the pores of a MOF. We demonstrate here that POC@MOF is a new „host-in-host“ system with enhanced performance in CO_2 adsorption and CO_2/N_2, CO_2/CH_4 separation up to 1 bar, a proof of principle for the impetus to develop further POC@MOF materials.

Results and Discussion

As a proof of concept, we used CB6 as the model POC and MIL-101 as the host framework. CB6 has a rigid porous structure with hydrophobic cavities and an outer diameter of 1.44 nm and a height of 0.9 nm (Scheme 1a),[11a] and a high affinity for molecules, such as dihalogens, CO_2, and acetylene through host–guest interactions or hydrogen bonding.[9e,11c,23] MIL-101, a robust MOF created by the Férey group, contains two kinds of mesopores with cage diameters of 2.9 nm and 3.4 nm.[18] The smaller cage has pentagonal windows with an aperture of approximately 1.2 nm, while the larger cage possesses both pentagonal and hexagonal windows with an opening of 1.5 nm (Scheme 1b). As the molecular size (1.44 nm) of CB6 is smaller than the hexagonal window size (1.5 nm), and the inner surface of MIL-101 is more hydrophilic than the outer surface,[19] CB6 molecules could be readily encapsulated in the larger pores of MIL-101 by incipient-wetness impregnation (Scheme 1c). The proper molecular size is, of course, important for the guest impregnation. Cucurbit[8]uril (CB8), with an outer diameter of 1.75 nm and a height of 0.9 nm, proved to be difficult to be encapsulated in MIL-101 by the wet impregnation method (see the Supporting Information for details).

Generally, CB6 was first fully dissolved in hydrochloric acid (37 wt %) solution before being added slowly to the degassed MOF at room temperature. After stirring for enough time to reach diffusion equilibrium, the obtained materials were washed successively with an excess amount of HCl (37 wt %) solution, deionized water, and ethanol (see the Supporting Information for details). Once CB6 has been encapsulated into the MOF pore, the leaching of CB6 could be hindered by the magnitude of the C−H⋯π and π⋯π interactions between CB6 and the terephthalic linkers of MIL-101.[11d] The obtained POC@MOF materials are denoted as CB6@MIL-101-W (W = 19, 29, or 36), where W represents the weight percentage of encapsulated CB6 in the material based on postsynthetic elemental analysis and ^1H NMR spectroscopy of digested samples.

The powder X-ray diffraction (PXRD) patterns of CB6@MIL-101 composites were similar to those of MIL-101 (Figure 2a),[17] indicating the preserved crystalline framework

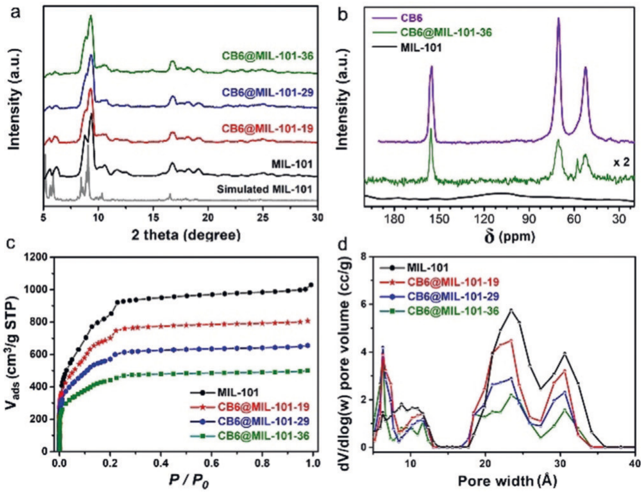

Figure 2. a) PXRD patterns and b) solid-state ^{13}C NMR spectra of the materials. c) N_2 adsorption isotherms at 77 K (see the Supporting Information for desorption isotherms) and d) pore size distributions of MIL-101 and CB6@MIL-101-W (W = 19, 29, 36) based on nonlocal density functional theory (NLDFT) calculations.

during the encapsulation process. Moreover, the intensity of the peaks at around 6° was gradually reduced with increasing CB6 loading, which was attributed to the filling of the MIL-101 pores with CB6. This phenomenon was also observed in previous publications, where the pores of MIL-101 were filled with drugs or polyamines.[24]

The successful encapsulation of CB6 in MIL-101 was supported by Fourier transform infrared (FT-IR) spectroscopy and NMR spectroscopy. The IR spectra of all composites display the characteristic vibration bands of both CB6 and MIL-101 (see the Supporting Information, Figure S2). The relative intensities of the IR bands of CB6 increased upon increasing the amount of CB6 in the composites. The ^{13}C solid-state NMR spectrum of CB6 shows three peaks (Figure 2b) at $\delta = 155.05$, 70.42, and 52.42 ppm, which were attributed to the C=O, CH, and CH_2 groups in CB6.[25] In contrast, solid MIL-101 shows no obvious NMR signals because of the paramagnetic Cr centers.[19] As expected, CB6@MIL-101-36 also shows the characteristic peaks of CB6. The intensities of the resonances are lower than those of neat CB6 because of the dilution of CB6 in the POC@MOF hybrid. Based on the solution ^1H NMR spectra of digested CB6@MIL-101 hybrids (Figures S3–S5), the molar ratio of terephthalic linker to CB6 was matched with the results based on elemental analysis for each sample (Table S1).

Scanning electron microscopy (SEM) analyses of CB6 and CB6@MIL-101 composites showed that the hybrids retained similar particle shapes and sizes (0.5–2 μm) as MIL-101, which are much smaller than that of CB6 crystallites (ca. 100 μm; Figure S6). To investigate if crystallites of CB6 had formed in a mixture with MIL-101 crystallites or if CB6 molecules had adsorbed only on the outer surface of MIL-101 in the composites, leaching experiments were conducted in CsCl/D_2O solution (Figure S7).[26] The CB6@MIL-101 composites did not show any significant loss of CB6, while CB6 bulk crystals underwent ready dissolution. This further supports the effective encapsulation of CB6 into the pores of MIL-101.

To investigate the thermal stabilities of the composites, PXRD patterns were collected for each sample at elevated temperature in air. The results suggest that these composites are stable up to 300 °C, which is in accordance with the thermogravimetric analysis (TGA; Figures S8–S11).

The porosities of CB6, MIL-101, and all composites were investigated by recording nitrogen sorption isotherms at 77 K, showing the expected type Ib isotherms for the MIL-101 materials due to their wider micropores and narrow mesopores (Figures 2c, S12, and S13).[27] The Brunauer–Emmett–Teller (BET) surface areas of CB6, MIL-101, and CB6@MIL-101-W (W = 19, 29, 36) were found to be 185, 3219, 2655, 2117, and 1651 $m^2 g^{-1}$, respectively (Table S2). Compared with pure MIL-101, the surface areas and pore volumes of the composites gradually decreased because of the occupation of the mesopores of MIL-101 with increasing numbers of CB6 molecules (Table S2). Remarkably, CB6@MIL-101-36 still retained a BET surface area of 1651 $m^2 g^{-1}$ with a total pore volume of approximately 0.76 $cm^3 g^{-1}$ (at $P/P_0 = 0.9$), positioning CB6@MIL-101-36 among macrocycle-based materials with the highest porosity ever reported.[9a] The pore size distribution (PSD) of the composites changed with respect to MIL-101. Comparatively more distinct micropores (6 Å) appeared in these hierarchical hybrids and the mesopore volume was lost, which indicated the successful encapsulation of CB6 (Figure 2d). The intrinsic pores of CB6 and the newly formed extrinsic pores between CB6 and the pore walls of MIL-101 should facilitate selective gas sorption and separation processes (Scheme 1d).

To demonstrate that the host-in-host or POC@MOF approach can merge the merits of POCs and MOFs, we investigated the CO_2 and N_2 sorption of CB6, MIL-101, and CB6@MIL-101-W (W = 19, 29, 36) composites up to 1 bar at 293 K (Figure S14). As porous CB6 molecules with high affinity for CO_2 are encapsulated into the pores of MIL-101, these hybrids should show enhanced CO_2 capture and separation performance.[11c,22] Indeed, CB6@MIL-101-W (W = 19, 29, 36) exhibited much higher CO_2 uptake capacities of 68.5, 84.4, and 79.2 $cm^3 g^{-1}$, respectively, than MIL-101 and CB6 (44.3 and 36.7 $cm^3 g^{-1}$, respectively) at 1 bar (Figure 3a).

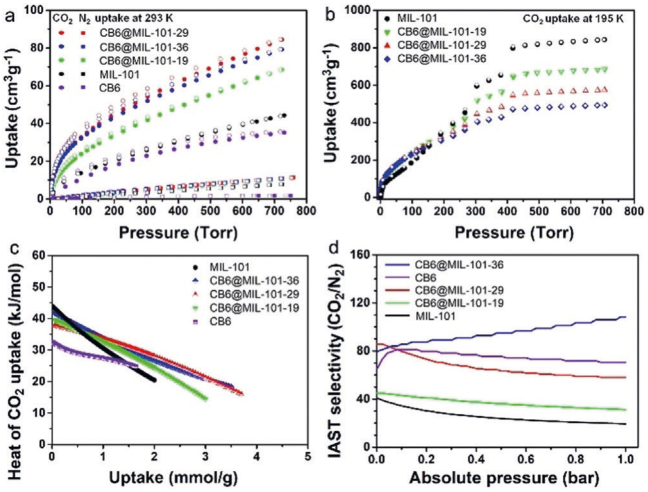

Figure 3. a) CO_2 and N_2 sorption isotherms of CB6, MIL-101, and composites measured up to 1 bar at 293 K. b) CO_2 sorption isotherms of MIL-101 and composites measured up to 1 bar at 195 K. c) Isosteric heats of adsorption (Q_{st}) of CO_2 for the materials. d) CO_2/N_2 selectivity of the materials measured by the IAST technique for a 15:85 (molar ratio) gas mixture of CO_2/N_2 at 293 K.

Notably, the CO_2 adsorption isotherm curves of all hybrids are steeper at low relative pressures than those of CB6 and MIL-101, indicating the higher affinity of these hybrids for CO_2. At the same time, the higher CO_2 uptake demonstrates the CO_2 accessibility of the intrinsic pores of CB6 and the mesopores and extrinsic micropores of CB6@MIL-101 (see Scheme 1d) at ambient conditions. Thereby, the CO_2 sorption studies rule out simple pore blocking by CB6 incorporation into the pore mouths only in MIL-101.

To further confirm this hypothesis, CO_2 adsorption isotherms of MIL-101 and the hybrids were obtained at 195 and 273 K (Figure 3b and Figure S15). The saturated CO_2 uptake capacities of these hybrids at 195 K and 1 bar are lower than that of MIL-101 because of their decreased pore volume (Figure 3b and Table S2). However, all composites show significantly higher uptake at relatively low pressure up to 115 torr (Figure S16), which is the crucial pressure range for potential applications such as post-combustion CO_2 capture. The high affinity for CO_2 is further reflected by the isosteric heat of adsorption (Q_{st}). The Q_{st} values of CO_2 on CB6, MIL-101, and composites were estimated from the CO_2 adsorption data at 273 and 293 K (Figures 3c, S15, and S17–S21). The Q_{st}^0 values were calculated to be 33.2 and 43.9 kJ mol^{-1} for CB6 and MIL-101, respectively, due to the intrinsic pores of CB6 and the coordination of CO_2 onto the Lewis acidic chromium sites in activated MIL-101.[11c,28] The hybrid materials have relatively high Q_{st}^0 values (above 37 kJ mol^{-1}) because of the strong interactions between CO_2 and porous CB6 or Cr^{3+} sites in the composites. The lower Q_{st}^0 value of the CO_2 adsorption on CB6@MIL-101 in comparison to pure MIL-101 might be caused by the „sheltering effect“, which makes some coordinative unsaturated sites (CUSs) unavailable to CO_2. Nevertheless, this is compensated for by CB6 offering more affinity sites and micropores for CO_2, which led to the enhanced uptake up to 1 bar at 293 K. The CO_2 uptake capacity of these composites is comparable or even higher than that of some amine/polyamine-modified MIL-101 materials (Table S4).[29] The strong sorption of CO_2 in CB6@MIL-101 was also confirmed in an FT-IR spectroscopic study. The IR spectrum of CB6@MIL-101-36 taken after exposure to CO_2 at 856 torr shows a CO_2 band at around 2338 cm^{-1} at room temperature, which indicates the interactions between CB6 and CO_2 (Figure S22).[11c] In contrast, the N_2 uptake of all hybrids only increased slightly when the amount of doped CB6 in MIL-101 was gradually increased (Figure 3a).

To simulate flue gas conditions, we calculated the CO_2/N_2 selectivities for CB6, MIL-101, and CB6@MIL-101-W (W = 19, 29, 36) from the N_2 and CO_2 adsorption isotherms using ideal adsorbed solution theory (IAST) for a CO_2/N_2 mixture (15:85) at 293 K (Figure 3d and Figure S23). For post-combustion CO_2 capture, porous sorbents should have both high CO_2 uptake capacities (in the low P/P_0 region) and high CO_2/N_2 selectivity. The IAST values for MIL-101, CB6, and CB6@MIL-101-W (W = 19, 29, 36) were determined to be 19, 70, 31, 58, and 108 at 293 K, respectively. The encapsulation of CB6 into MIL-101 allowed us to introduce CO_2 selectively because of the intrinsic micropores of CB6 and the retained micropores of MIL-101, while losing some of the uptake capacity of the non-selective mesopores of MIL-101. Thus, the combined properties of CB6 and MIL-101 showed a CO_2/N_2 selectivity increase from 31 to 108, upon loading CB6 into MIL-101. We believe that the hydrogen bonding and local dipole/quadrupole interactions between CB6 and CO_2 also play a role in the selectivity increase.[11c] Furthermore, a high concentration of CB6 in MIL-101 is critical to achieving high CO_2/N_2 selectivity. With an increase in the loading amount from 29 to 36 wt %, the selectivity increased to 58 and 108, respectively. A similar „cage effect“ for enhancing CO_2 uptake and separation was also found in porous organic cage based nanoporous polymers by Coskun and co-workers.[14a]

Encouraged by the enhanced CO_2 uptake and CO_2/N_2 selectivity based on IAST predictions, we simulated breakthrough curves with a gas mixture of $N_2/CO_2/He$ (42.5:7.5:50 v/v/v) at 293 K based on the DSLAI-fitted isotherm data of CB6, MIL-101, and composites, respectively (see the Supporting Information for details). The simulated breakthrough plot in Figure S24 shows an immediate rise in the N_2 concentrations at the outlet, indicating the comparably small N_2 sorption capacity of these porous materials under the chosen conditions. In contrast, CO_2 could be retained for about 3 min g^{-1} in CB6 and 4 min g^{-1} in MIL-101, which were close to the experimental breakthrough values (3.32 min g^{-1} and 3.35 min g^{-1}) reported separately for CB6 and MIL-101.[30] For CB6@MIL-101-36 the simulation gave an increased retention time of CO_2 of about 10 min g^{-1}, which is due to its higher uptake capacity and superior CO_2/N_2 selectivity with respect to the individual components under the given conditions. We note, however, that breakthrough experiments would still be part of a non-continuous separation process where the packed column would have to be regenerated by a pressure swing or another procedure. Instead, continuous membrane processes would be advantageous for the envisioned CO_2/CH_4 separation. Hence, we fabricated CB6-, MIL-101-, and CB6@MIL-101-36-based mixed matrix membranes (MMMs) to demonstrate the superiority of the composite MMM in CO_2/CH_4 separation.

The CH_4 sorption and CO_2/CH_4 selectivity investigation of CB6, MIL-101, and CB6@MIL-101-W (W = 19, 29, 36; Figure S25 and Table S2) indicated a slightly enhanced CH_4 sorption for the composite compared with CB6 and MIL-101. This can be traced back to the enhanced composite affinity towards CH_4 based on the Q_{st}^0 values of 18.1, 19.6, 24.2, 25.6, and 26.3 kJ mol^{-1} for MIL-101, CB6, and CB6@MIL-101-W (W = 19, 29, 36), respectively (Figure S25b). Nevertheless, the composites still exhibited an increased CO_2/CH_4 selectivity for a CO_2/CH_4 mixture (2:98) at 1.0 bar over the individual components. The IAST selectivities for CB6, MIL-101, and CB6@MIL-101-W (W = 19, 29, 36) were found to be 12.7, 17, 20, 27, and 29 at 293 K and 1.0 bar (Figure S25d). To further confirm this superiority of the CB6@MIL-101 composites, we fabricated MMMs[15] of 16 wt % CB6, MIL-101, and CB6@MIL-101-36 in Matrimid as the polymer matrix (Figure S34). The membranes were tested for their mixed-gas separation properties in a binary mixture of CO_2/CH_4 (50:50 v/v) at 25 °C and 3 bar transmembrane pressure. Additionally, all MMMs were characterized by SEM imaging and SEM-EDX mapping to confirm the homogeneous distribution of the filler particles in the polymer matrix (Figures S35 and S36).

The MMMs of CB6/Matrimid simultaneously displayed slightly reduced permeability but also slightly increased selectivity for CO_2/CH_4 compared to the neat polymer membrane (Figure S40 and Table S5). The reduction in permeability can be attributed to the almost non-existent pore volume of CB6. Hence, CB6 alone can be considered a nonporous filler with high CO_2 affinity, which leads to the increased selectivity.[31] MIL-101/Matrimid MMMs showed the expected enhanced CO_2 (from 7 Barrer to 16 Barrer) and CH_4 (from 0.2 Barrer to 0.4 Barrer) permeability but no increase in selectivity. The distinct enhancement in permeability can be assigned to the high pore volume of MIL-101. However, the large pores of MIL-101 and mediocre affinity to

CO_2 over CH_4 prevent a favorable adsorption of CO_2 and thus an increase in selectivity. For CB6@MIL-101-36/Matrimid MMMs, an enhancement of the CO_2 permeability to 15 Barrer up from 7 Barrer for the neat polymer membrane was observed. Moreover, the CO_2/CH_4 selectivity improved from 39 to 46. The encapsulation of CB6 in MIL-101 can therefore, as predicted in the IAST model, increase the affinity for CO_2 and lead to a higher selectivity while only slightly reducing the permeability due to the smaller pore volume compared to pure MIL-101 as a filler. Thus, by encapsulating porous CB6 cages in MIL-101, the CO_2 uptake and the CO_2/N_2 and CO_2/CH_4 selectivities of the hybrids can be enhanced.

α-Cyclodextrin (α-CD) was used as another porous organic cage for its comparatively smaller outer diameter (ca. 1.4 nm), which is smaller than the larger window (1.5 nm) of MIL-101, and for its various properties including CO_2 capture to form host/guest inclusion complexes.[32] α-CD was quantitatively merged into the composite by the incipient-wetness impregnation method thanks to its very good water solubility (see the Supporting Information for details). However, it should be noted that compared with cucurbit[6]uril, α-CD has a much lower affinity towards CO_2. This is the reason why a significant CO_2 uptake or separation enhancement was not observed under the current experimental conditions (Tables S6 and S7). Still, these results with α-CD indicate the importance of choosing the right porous organic cage in preparing a targeted POC@MOF composite for a specific application.

Conclusion

In summary, we have confined a porous organic cage into the nanocages of MIL-101 by the incipient-wetness impregnation method, obtaining the host-in-host adsorbent CB6@MIL-101, which showed enhanced performance in selective CO_2 adsorption and separation at low pressures. We believe that the host-in-host concept can be extended to encapsulate a broad range of POCs into porous crystalline materials such as MOFs, either by in situ assembly of host MOFs or by post-impregnation methods. This can lead to advanced porous materials, which could combine the merits (such as tailor-made intrinsic pores for molecule capture and separation,[9b,c] enzymatic catalysis,[33] confinement effects[34]) of porous organic molecules and the tunable, highly ordered architectures of functional MOFs.[3]

Acknowledgements

J.L. acknowledges support from the Hoffmann Institute of Advanced Materials (HIAM), Shenzhen Polytechnic.

Conflict of interest

The authors declare no conflict of interest.

Stichwörter: Cucurbituril · Hybridmaterialien · Kohlendioxid · Metall-organische Gerüste · Poröse organische Käfige

Zitierweise: *Angew. Chem. Int. Ed.* **2020**, *59*, 6068–6073
Angew. Chem. **2020**, *132*, 6124–6129

---

[1] a) A. G. Slater, A. I. Cooper, *Science* **2015**, *348*, aaa8075; b) J. Wang, L. Huang, R. Yang, Z. Zhang, J. Wu, Y. Gao, Q. Wang, D. O'Hare, Z. Zhong, *Energy Environ. Sci.* **2014**, *7*, 3478–3518; c) R. S. Haszeldine, *Science* **2009**, *325*, 1647–1652.

[2] J. Li, A. Corma, J. Yu, *Chem. Soc. Rev.* **2015**, *44*, 7112–7127.

[3] a) H. Furukawa, K. E. Cordova, M. O'Keeffe, O. M. Yaghi, *Science* **2013**, *341*, 1230444; b) Z. Zhang, Z.-Z. Yao, S. Xiang, B. Chen, *Energy Environ. Sci.* **2014**, *7*, 2868–2899; c) K. Sumida, D. L. Rogow, J. A. Mason, T. M. McDonald, E. D. Bloch, Z. R. Herm, T. H. Bae, J. R. Long, *Chem. Rev.* **2012**, *112*, 724–781; d) J. Liu, P. K. Thallapally, B. P. McGrail, D. R. Brown, J. Liu, *Chem. Soc. Rev.* **2012**, *41*, 2308–2322; e) J.-R. Li, Y. Ma, M. C. McCarthy, J. Sculley, J. Yu, H.-K. Jeong, P. B. Balbuena, H.-C. Zhou, *Coord. Chem. Rev.* **2011**, *255*, 1791–1823; f) Y.-S. Bae, R. Q. Snurr, *Angew. Chem. Int. Ed.* **2011**, *50*, 11586–11596; *Angew. Chem.* **2011**, *123*, 11790–11801.

[4] a) K. Adil, Y. Belmabkhout, R. S. Pillai, A. Cadiau, P. M. Bhatt, A. H. Assen, G. Maurin, M. Eddaoudi, *Chem. Soc. Rev.* **2017**, *46*, 3402–3430; b) Y.-B. Huang, J. Liang, X.-S. Wang, R. Cao, *Chem. Soc. Rev.* **2017**, *46*, 126–157; c) C. Janiak, J. K. Vieth, *New J. Chem.* **2010**, *34*, 2366–2388.

[5] a) C. S. Diercks, O. M. Yaghi, *Science* **2017**, *355*, eaal1585; b) S. Kandambeth, K. Dey, R. Banerjee, *J. Am. Chem. Soc.* **2019**, *141*, 1807–1822.

[6] a) G. Zhang, M. Mastalerz, *Chem. Soc. Rev.* **2014**, *43*, 1934–1947; b) M. Mastalerz, *Acc. Chem. Res.* **2018**, *51*, 2411–2422.

[7] a) J. Murray, K. Kim, T. Ogoshi, W. Yao, B. C. Gibb, *Chem. Soc. Rev.* **2017**, *46*, 2479–2496; b) Z. Liu, S. K. M. Nalluri, J. F. Stoddart, *Chem. Soc. Rev.* **2017**, *46*, 2459–2478.

[8] a) G. Zhang, O. Presly, F. White, I. M. Oppel, M. Mastalerz, *Angew. Chem. Int. Ed.* **2014**, *53*, 1516–1520; *Angew. Chem.* **2014**, *126*, 1542–1546; b) M. Mastalerz, M. W. Schneider, I. M. Oppel, O. Presly, *Angew. Chem. Int. Ed.* **2011**, *50*, 1046–1051; *Angew. Chem.* **2011**, *123*, 1078–1083; c) J. Tian, P. K. Thallapally, S. J. Dalgarno, P. B. McGrail, J. L. Atwood, *Angew. Chem. Int. Ed.* **2009**, *48*, 5492–5495; *Angew. Chem.* **2009**, *121*, 5600–5603; d) T. Tozawa, J. T. A. Jones, S. I. Swamy, S. Jiang, D. J. Adams, S. Shakespeare, R. Clowes, D. Bradsaw, T. Hasell, S. Y. Chong, C. Tang, S. Thompson, J. Parker, A. Trewin, J. Bacsa, A. M. Z. Slawin, A. Steiner, A. I. Cooper, *Nat. Mater.* **2009**, *8*, 973–978.

[9] a) A. Chaix, G. Mouchaham, A. Shkurenko, P. Hoang, B. Moosa, P. M. Bhatt, K. Adil, K. N. Salama, M. Eddaoudi, N. M. Khashab, *J. Am. Chem. Soc.* **2018**, *140*, 14571–14575; b) K. J. Hartlieb, J. M. Holcroft, P. Z. Moghadam, N. A. Vermeulen, M. M. Algaradah, M. S. Nassar, Y. Y. Botros, R. Q. Snurr, J. F. Stoddart, *J. Am. Chem. Soc.* **2016**, *138*, 2292–2301; c) R. A. Smaldone, R. S. Forgan, H. Furukawa, J. J. Gassensmith, A. M. Slawin, O. M. Yaghi, J. F. Stoddart, *Angew. Chem. Int. Ed.* **2010**, *49*, 8630–8634; *Angew. Chem.* **2010**, *122*, 8812–8816; d) R. S. Patil, D. Banerjee, C. Zhang, P. K. Thallapally, J. L. Atwood, *Angew. Chem. Int. Ed.* **2016**, *55*, 4523–4526; *Angew. Chem.* **2016**, *128*, 4599–4602; e) S. Lim, H. Kim, N. Selvapalam, K.-J. Kim, S. J. Cho, G. Seo, K. Kim, *Angew. Chem.* **2008**, *120*, 3400–3403; f) E. Li, Y. Zhou, R. Zhao, K. Jie, F. Huang, *Angew. Chem. Int. Ed.* **2019**, *58*, 3981–3985; *Angew. Chem.* **2019**, *131*, 4021–4025.

[10] a) S. J. Barrow, S. Kasera, M. J. Rowland, J. del Barrio, O. A. Scherman, *Chem. Rev.* **2015**, *115*, 12320–12406; b) K. I. Assaf,

W. M. Nau, *Chem. Soc. Rev.* **2015**, *44*, 394–418; c) L. Isaacs, *Chem. Commun.* **2009**, 619–629; d) K. Kim, J. Murray, N. Selvapalam, Y. H. Ko, I. Hwang, *Cucurbiturils: Chemistry, Supramolecular Chemistry and Applications.* World Scientific Publishing Company, Singapore, **2018**.

[11] a) K. Kim, N. Selvapalam, Y. H. Ko, K. M. Park, D. Kim, J. Kim, *Chem. Soc. Rev.* **2007**, *36*, 267–279; b) D. Bardelang, K. A. Udachin, D. M. Leek, J. C. Margeson, G. Chan, C. I. Ratcliffe, J. A. Ripmeester, *Cryst. Growth Des.* **2011**, *11*, 5598–5614; c) H. Kim, Y. Kim, M. Yoon, S. Lim, S. M. Park, G. Seo, K. Kim, *J. Am. Chem. Soc.* **2010**, *132*, 12200–12202; d) X.-L. Ni, X. Xiao, H. Cong, L.-L. Liang, K. Cheng, X.-J. Cheng, N.-N. Ji, Q.-J. Zhu, S.-F. Xue, Z. Tao, *Chem. Soc. Rev.* **2013**, *42*, 9480–9508.

[12] T. Hasell, A. I. Cooper, *Nat. Rev. Mater.* **2016**, *1*, 16053.

[13] a) T. Hasell, S. Y. Chong, K. E. Jelfs, D. J. Adams, A. I. Cooper, *J. Am. Chem. Soc.* **2012**, *134*, 588–598; b) S. Du, C. Hu, J.-C. Xiao, H. Tan, W. Liao, *Chem. Commun.* **2012**, *48*, 9177–9179; c) Q. Li, W. Zhang, O. S. Miljanic, C. H. Sue, Y. L. Zhao, L. Liu, C. B. Knobler, J. F. Stoddart, O. M. Yaghi, *Science* **2009**, *325*, 855–859; d) C. Valente, E. Choi, M. E. Belowich, C. J. Doonan, Q. Li, T. B. Gasa, Y. Y. Botros, O. M. Yaghi, J. F. Stoddart, *Chem. Commun.* **2010**, *46*, 4911–4913.

[14] a) O. Buyukcakir, Y. Seo, A. Coskun, *Chem. Mater.* **2015**, *27*, 4149–4155; b) Y. Zhang, J. Duan, D. Ma, P. Li, S. Li, H. Li, J. Zhou, X. Ma, X. Feng, B. Wang, *Angew. Chem. Int. Ed.* **2017**, *56*, 16313–16317; *Angew. Chem.* **2017**, *129*, 16531–16535; c) M. J. Klemes, Y. Ling, C. Ching, C. Wu, L. Xiao, D. E. Helbling, W. R. Dichtel, *Angew. Chem. Int. Ed.* **2019**, *58*, 12049–12053; *Angew. Chem.* **2019**, *131*, 12177–12181; d) S. Y. Jon, N. Selvapalam, D. H. Oh, J.-K. Kang, S.-Y. Kim, Y. J. Jeon, J. W. Lee, K. Kim, *J. Am. Chem. Soc.* **2003**, *125*, 10186–10187; e) Y. Ahn, Y. Jang, N. Selvapalam, G. Yun, K. Kim, *Angew. Chem. Int. Ed.* **2013**, *52*, 3140–3144; *Angew. Chem.* **2013**, *125*, 3222–3226.

[15] a) J. Dechnik, J. Gascon, C. J. Doonan, C. Janiak, C. J. Sumby, *Angew. Chem. Int. Ed.* **2017**, *56*, 9292–9310; *Angew. Chem.* **2017**, *129*, 9420–9439; b) Y. Cheng, Z. Wang, D. Zhao, *Ind. Eng. Chem. Res.* **2018**, *57*, 4139–4169; c) A. F. Bushell, P. M. Budd, M. P. Attfield, J. T. Jones, T. Hasell, A. I. Cooper, P. Bernardo, F. Bazzarelli, G. Clarizia, J. C. Jansen, *Angew. Chem. Int. Ed.* **2013**, *52*, 1253–1256; *Angew. Chem.* **2013**, *125*, 1291–1294; d) G. Zhu, F. Zhang, M. P. Rivera, X. Hu, G. Zhang, C. W. Jones, R. P. Lively, *Angew. Chem. Int. Ed.* **2019**, *58*, 2638–2643; *Angew. Chem.* **2019**, *131*, 2664–2669.

[16] a) A. I. Cooper, *Angew. Chem. Int. Ed.* **2011**, *50*, 996–998; *Angew. Chem.* **2011**, *123*, 1028–1030; b) A. Avellaneda, P. Valente, A. Burgun, J. D. Evans, A. W. Markwell-Heys, D. Rankine, D. J. Nielsen, M. R. Hill, C. J. Sumby, C. J. Doonan, *Angew. Chem. Int. Ed.* **2013**, *52*, 3746–3749; *Angew. Chem.* **2013**, *125*, 3834–3837.

[17] G. Férey, C. Mellot-Draznieks, C. Serre, F. Millange, J. Dutour, S. Surblé, I. Margiolaki, *Science* **2005**, *309*, 2040–2042.

[18] T. Bogaerts, A. Van Yperen-De Deyne, Y.-Y. Liu, F. Lynen, V. Van Speybroeck, P. Van Der Voort, *Chem. Commun.* **2013**, *49*, 8021–8023.

[19] X. Qiu, W. Zhong, C. Bai, Y. Li, *J. Am. Chem. Soc.* **2016**, *138*, 1138–1141.

[20] Q. Yang, Q. Xu, H.-L. Jiang, *Chem. Soc. Rev.* **2017**, *46*, 4774–4808.

[21] a) Y. Ban, Z. Li, Y. Li, Y. Peng, H. Jin, W. Jiao, A. Guo, P. Wang, Q. Yang, C. Zhong, W. Yang, *Angew. Chem. Int. Ed.* **2015**, *54*, 15483–15487; *Angew. Chem.* **2015**, *127*, 15703–15707; b) I. Cota, F. Fernandez Martinez, *Coord. Chem. Rev.* **2017**, *351*, 189–204.

[22] a) K. A. Kovalenko, V. P. Fedin, *Russ. Chem. Bull.* **2016**, *65*, 1406–1417; b) F. P. Kinik, A. Uzun, S. Keskin, *ChemSusChem* **2017**, *10*, 2842–2863.

[23] H. S. El-Sheshtawy, B. S. Bassil, K. I. Assaf, U. Kortz, W. M. Nau, *J. Am. Chem. Soc.* **2012**, *134*, 19935–19941.

[24] a) P. Horcajada, C. Serre, M. Vallet-Regi, M. Sebban, F. Taulelle, G. Ferey, *Angew. Chem. Int. Ed.* **2006**, *45*, 5974–5978; *Angew. Chem.* **2006**, *118*, 6120–6124; b) Q. Yan, Y. Lin, C. Kong, L. Chen, *Chem. Commun.* **2013**, *49*, 6873–6875.

[25] D. Bardelang, A. Brinkmann, C. I. Ratcliffe, J. A. Ripmeester, V. V. Terskikh, K. A. Udachin, *CrystEngComm* **2014**, *16*, 3788.

[26] A. Day, A. P. Arnold, R. J. Blanch, B. Snushall, *J. Org. Chem.* **2001**, *66*, 8094–8100.

[27] M. Thommes, K. Kaneko, A. V. Neimark, J. P. Olivier, F. Rodriguez-Reinoso, J. Rouquerol, K. S. W. Sing, *Pure Appl. Chem.* **2015**, *87*, 1051–1069.

[28] P. L. Llewellyn, S. Bourrelly, C. Serre, A. Vimont, M. Daturi, L. Hamon, G. D. Weireld, J.-S. Chang, D.-Y. Hong, Y. K. Hwang, S. H. Jhung, G. Férey, *Langmuir* **2008**, *24*, 7245–7250.

[29] A. J. Emerson, A. Chahine, S. R. Batten, D. R. Turner, *Coord. Chem. Rev.* **2018**, *365*, 1–22.

[30] a) J. Tian, J. Liu, J. Liu, P. K. Thallapally, *CrystEngComm* **2013**, *15*, 1528–1531; b) N. A. A. Qasem, N. U. Qadir, R. Ben-Mansour, S. A. M. Said, *J. CO2 Util.* **2017**, *22*, 238–249.

[31] A. Nuhnen, D. Dietrich, S. Millan, C. Janiak, *ACS Appl. Mater. Interfaces* **2018**, *10*, 33589–33600.

[32] a) G. Crini, *Chem. Rev.* **2014**, *114*, 10940–10975; b) T.-L. Neoh, H. Yoshii, T. Furuta, *J. Inclusion Phenom. Macrocyclic Chem.* **2006**, *56*, 125–133; c) J. Szejtli, *Chem. Rev.* **1998**, *98*, 1743–1753.

[33] a) R. Villalonga, R. Cao, A. Fragoso, *Chem. Rev.* **2007**, *107*, 3088–3116; b) Y. Murakami, J. Kikuchi, Y. Hisaeda, O. Hayashida, *Chem. Rev.* **1996**, *96*, 721–758; c) W. L. Mock, T. A. Irra, J. P. Wepsiec, T. L. Manimaran, *J. Org. Chem.* **1983**, *48*, 3619–3620; d) C. Goehry, M. Besora, F. Maseras, *ACS Catal.* **2015**, *5*, 2445–2451.

[34] a) Y. Chen, B. Yu, Y. Cui, S. Xu, J. Gong, *Chem. Mater.* **2019**, *31*, 1289–1295; b) Z. Y. Zhang, Y. Chen, Y. Liu, *Angew. Chem. Int. Ed.* **2019**, *58*, 6028–6032; *Angew. Chem.* **2019**, *131*, 6089–6093.

Manuskript erhalten: 13. Dezember 2019
Akzeptierte Fassung online: 8. Januar 2020
Endgültige Fassung online: 3. Februar 2020

3.6 Synthesis of Nano/Microsized MIL-101Cr Through Combination of Microwave Heating and Emulsion Technology for Mixed-Matrix Membranes

Irina Gruber, Alexander Nuhnen, Arne Lerch, Sandra Niesßing, Maximilian Klopotowski, Annika Herbst, Matthias Karg, Christoph Janiak

Front. Chem., **2019**, 7:777.

DOI: 10.3389/fchem.2019.00777

Diese Publikation beschäftig sich mit der Synthese von nano/micro-MIL-101Cr über ein Emulsionsverfahren unter Mikrowellenbestrahlung und anschließender Verwendung der MOF-Partikel zur Herstellung von MMMs zur Gastrennung. Dazu wurde zunächst nanoMIL-101 mit Partikelgrößen < 100 nm über eine Heptan-in-Wasser-Emulsion mit anionischen Tensiden als Emulgator hergestellt. Anschließend wurden die MOF-Partikel beider Größen in eine Polymermatrix aus Matrimid eingebettet. Gemischtgas-Separationen einer 50:50 v:v Gasmischung von CO_2/CH_4 zeigten überlegende Permeationseigenschaften der 24 wt% nanoMIL-101Cr/Matrimid-MMMs mit einer maximalen Permeabilität von 32 Barrer für CO_2, im Vergleich zu 6 Barrer des reinen Polymers Matrimid und 21 Barrer der höchst möglichen Beladung von 20 wt% mikroMIL-101Cr/Matrimid-MMMs. Jede höhere Beladung der MMMs mit dem Füllstoff in Mikrometergröße führte zu einer extremen Brüchigkeit der Membranen. Die Nanostruktur des MOFs erlaubte in diesem Fallbeispiel eine höhere Beladung mit Füllstoff, wodurch aufgrund von auftretenden Füllstoff-Füllstoff-Wechselwirkungen, Permeabilitäten deutlich oberhalb der vorhergesagten Werte des Maxwell-Modells erreicht werden konnten.

Anteile an der Veröffentlichung:

- Hilfestellung bei der Herstellung der MMMs. Messung der MMMs mit anschließender Auswertung und Modellierung. Verfassung des Absatzes über MMMs im Manuskript.
- Die Entwicklung des Konzepts und die maßgebliche Laborarbeit, sowie die Erstellung des Manuskripts wurde von Frau Irina Gruber durchgeführt. Korrekturen am Manuskript erfolgten von Herrn Prof. Dr. Janiak.
- Herr Arne Lerch und Prof. Dr. Matthias Karg haben die DLS Messungen und deren Interpretation angefertigt.
- Herr Hergen Breitzke und Herr Dr. Gerd Buntkowsky haben die Festkörper NMR Aufnahmen angefertigt.
- Die REM-Bilder wurden von Frau Sandra Nießing und Herrn Maximilian Klopotowski aufgenommen.
- Frau Annika Herbst hat Vorarbeiten bei der Synthese des MOFs beigesteuert

ORIGINAL RESEARCH
published: 19 November 2019
doi: 10.3389/fchem.2019.00777

Synthesis of Nano/Microsized MIL-101Cr Through Combination of Microwave Heating and Emulsion Technology for Mixed-Matrix Membranes

Irina Gruber[1], *Alexander Nuhnen*[1], *Arne Lerch*[2], *Sandra Nießing*[1], *Maximilian Klopotowski*[1], *Annika Herbst*[1], *Matthias Karg*[2] *and Christoph Janiak*[1]*

[1] Institut für Anorganische Chemie und Strukturchemie, Heinrich-Heine-Universität Düsseldorf, Düsseldorf, Germany, *[2] Institut für Physikalische Chemie, Heinrich-Heine-Universität Düsseldorf, Düsseldorf, Germany*

Nano/microsized MIL-101Cr was synthesized by microwave heating of emulsions for the use as a composite with Matrimid mixed-matrix membranes (MMM) to enhance the performance of a mixed-gas-separation. As an example, we chose CO_2/CH_4 separation. Although the incorporation of MIL-101Cr in MMMs is well-known, the impact of nanosized MIL-101Cr in MMMs is new and shows an improvement compared to microsized MIL-101Cr under the same conditions and mixed-gas permeation. In order to reproducibly obtain nanoMIL-101Cr microwave heating was supplemented by carrying out the reaction of chromium nitrate and 1,4-benzenedicarboxylic acid in heptane-in-water emulsions with the anionic surfactant sodium oleate as emulsifier. The use of this emulsion with the phase inversion temperature (PIT) method offered controlled nucleation and growth of nanoMIL-101 particles to an average size of <100 nm within 70 min offering high apparent BET surface areas (2,900 m^2 g^{-1}) and yields of 45%. Concerning the CO_2/CH_4 separation, the best result was obtained with 24 wt.% of nanoMIL-101Cr@Matrimid, leading to 32 Barrer in CO_2 permeability compared to six Barrer for the neat Matrimid polymer membrane and 21 Barrer for the maximum possible 20 wt.% of microMIL-101Cr@Matrimid. The nanosized filler allowed reaching a higher loading where the permeability significantly increased above the predictions from Maxwell and free-fractional-volume modeling. These improvements for MMMs based on nanosized MIL-101Cr are promising for other gas separations.

Keywords: metal-organic framework (MOF), MIL-101Cr, nano/microsized MOF, microwave heating, emulsion, surfactants, mixed-matrix membranes (MMMs)

Edited by:
Yatao Zhang,
Zhengzhou University, China

Reviewed by:
Guillermo Javier Copello,
National Council for Scientific and Technical Research (CONICET), Argentina
Mustapha Soukri,
RTI International, United States

Correspondence:
Christoph Janiak
janiak@uni-duesseldorf.de

Specialty section:
This article was submitted to Chemical and Process Engineering, a section of the journal Frontiers in Chemistry

Received: *11 July 2019*
Accepted: *28 October 2019*
Published: *19 November 2019*

Citation:
Gruber I, Nuhnen A, Lerch A, Nießing S, Klopotowski M, Herbst A, Karg M and Janiak C (2019) Synthesis of Nano/Microsized MIL-101Cr Through Combination of Microwave Heating and Emulsion Technology for Mixed-Matrix Membranes. Front. Chem. 7:777. doi: 10.3389/fchem.2019.00777

INTRODUCTION

Starting at the beginning of the 1990s metal-organic frameworks (MOFs) as new porous materials have been constructed from metal-atom or metal-cluster building blocks and bridging organic linkers (Batten and Robson, 1998). It became possible to produce extended anionic, cationic and neutral porous frameworks with unique pore architectures and functions (Yaghi et al., 1998). However, porosity was to some extent counter-acted when independent one-, two-, and even three-dimensional nets interpenetrated into each other in many solid-state structures of polymeric, hydrogen-bonded nets, and coordination polymers (Batten and Robson, 1998). The existence of building units with different sizes, yet close topologies, resulted into "scalable or isoreticular chemistry" giving predictable frameworks (Férey, 2000). Secondary building units are the metal or cluster entities with their directly coordinating ligand groups. Consideration of the geometric and chemical attributes of the secondary building units and linkers leads to prediction of the framework topology (Eddaoudi et al., 2001). It became quickly apparent, how molecular complexes and clusters can be transformed to extended solids (Yaghi et al., 2000). For chemical and physical functionalities robustness of a metal-organic framework is required in the absence of guest molecules in the cavities. The stability depends mainly on the structural dimensionality of the networks (Kitagawa and Kondo, 1998). MOFs quickly emerged as a competitively investigated class of porous materials (Yaghi et al., 2003). MOFs promise applications in small molecule adsorption and storage (Li et al., 2009), gas and liquid separation (Tanh Jeazet et al., 2012), catalysis (Beyzavi et al., 2015), sensing (Chen et al., 2009), drug delivery (Horcajada et al., 2012), heat transformation, and other applications (Janiak and Henninger, 2013; Azar and Keskin, 2018; Erucar and Keskin, 2018). However, the inherent microporosity of most metal-organic frameworks prevents a fast access of molecules to the internal surface in larger MOF crystallites. A faster access of molecules to the internal surface is desirable for application in gas adsorption/desorption and storage and can be achieved by reduction of the diffusion path length by decreasing the crystal size (Rieter et al., 2006; Lin et al., 2009) or by enlargement of the pore dimensions through defects toward hierarchical micro-meso-macropores (Shen et al., 2015). In this work, we focus on the reduction of the diffusion path length through decrease of the particle size. There are various approaches to control the MOF particle size, for example, microwave-assisted routes (Khan et al., 2011), surfactant-mediated syntheses (Huang et al., 2003), reverse microemulsions (Lin et al., 2009), and sonochemistry (Khan and Jhung, 2015). Among these strategies microwave heating and the use of surfactants have been the most advantageous methods (Khan and Jhung, 2015; Huang et al., 2018). Microwave heating is known to enhance rates of nucleation and crystal growth processes, including acceleration of nucleation over crystal growth (Diring et al., 2010). Moreover, in microwave reactions the required temperatures can be reached within seconds (Galema, 1997) and microwave heating is an "instant on/instant off" energy source, significantly reducing the risk of overheating reactions (Bogdal, 2006).

Most critical was the emulsion technique, through which we tried to achieve two goals: The first one was the reduction of the particle size, the second goal was good yields. As shown in **Table S1**, already published results for MIL-101Cr via microwave heating show particle sizes between 49 and 200 nm. A view on the described yields shows relatively low yields (35-38%) (Khan et al., 2011) or no statement concerning the yield (Wuttke et al., 2015). Emulsions stabilized by surfactants also help to control MOF nucleation and growth through micelles, which can work as nanoreactors (Khan et al., 2010). Emulsions can be differentiated between macroemulsions (= emulsions) and microemulsions (Wu et al., 2017). Macroemulsions are built of dispersed droplets with radii in the range of 1-90 μm, whereas microemulsions are built of dispersed droplets with radii in the range of 5–50 nm (Carr and Shantz, 2005). Both can be further differentiated in direct and reverse emulsions (**Figure 1**, **Figure S6**). Direct emulsions are given from hydrophobic "oil" droplets dispersed in a hydrophilic medium (water) (Salvia-Trujillo et al., 2018), whereas reverse emulsions are formed from water droplets dispersed in a hydrophobic medium (organic solvent, oil). The size of the droplets or micelles depends strongly on the water to surfactant ratio and on the temperature. If a high reaction temperature is required, coalescence of the micelles will occur and especially microemulsions do not remain intact at high temperature (Whitby et al., 2012). Therefore, we speak only generally of emulsions here and do not use the term microemulsion, because droplet sizes vary during the reaction procedure. So far, only reverse microemulsions have been used for the synthesis of MOFs (Rieter et al., 2006) wherein two-micellar systems (different micelles contained either the metal salt or the organic linker) were mixed and the reaction was started through coalescence (Wang et al., 2018). The reaction temperature in reverse microemulsion synthesis for MOFs was between 0 and 120°C (Taylor et al., 2008). There are no reverse emulsion syntheses for MOFs known, where higher temperatures (>180°C) were used.

Two processes are known for generating emulsions with small droplets. The first one is based on high-energy emulsification methods (e.g., ultrasound generators), whereas the second process includes low-energy emulsification methods. Among low energy methods, we can find the most widely used phase inversion temperature (PIT) method which was first described by Shinoda and Saito (1969). Phase inversion of emulsions means the conversion of oil-in-water to water-in-oil system (or vice versa) as shown in **Figure 1** and **Figure S6**. The PIT method is based on the temperature at which the phase transition occurs, such that for example a low temperature favors oil-in-water emulsions and a high temperature favors water-in-oil emulsions (Kale and Deore, 2017). This method leads to a reduction of the interfacial tension of the surfactant, providing droplet fragmentation and inverting the water-in-oil emulsion phase to an oil-in-water emulsion. At the PIT the droplet size and the interfacial tension reaches a minimum. Important information about phase structures in the phase inversion temperature (PIT) range were presented by Benton et al. (1986). Other examples of inversion in the PIT range are "abnormal emulsions." Here, the surfactants are preferentially located in the dispersed phase of an emulsion (Sajjadi et al., 2004). The PIT depends on surfactant concentration (Izquierdo et al., 2002) as well as on the type of oil and the hydrophilic chain length of the surfactants. Therefore, in the case of an oil-in-water emulsion, the stability increases significantly with the chain length of the hydrophile–lipophile group of the surfactant and the emulsion droplets are usually negatively charged because of the selective adsorption of OH^- onto the droplet surfaces (Mei et al., 2011). The PIT method is mostly used in combination with non-ionic surfactants but recent studies have shown that a specific oil emulsion can be

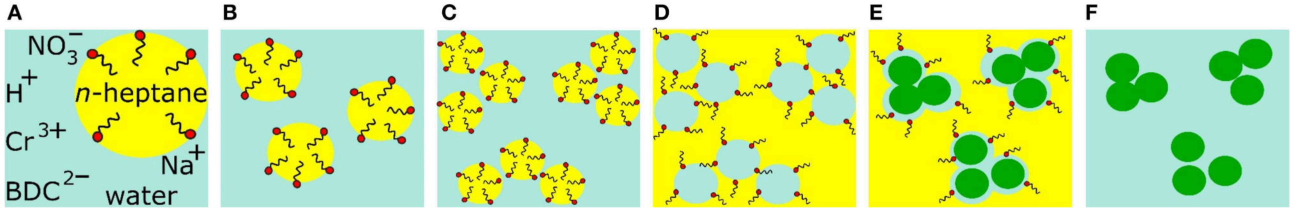

FIGURE 1 | The anticipated direct emulsion mechanism for the formation of nanoMIL-101Cr (depicted as green spheres). BDC^{2-}, benzene-1,4-dicarboxylate; Cr^{3+}, chromium salt; NO_3^-, nitrate ion; and micelles with hydrophobic groups of sodium oleate oriented toward the center of heptane oil droplets (hydrophilic groups = red spheres). MOF precursors are in the aqueous phase **(A)**. At higher temperature, the heptane droplets expand rapidly **(B)**, at the PIT (phase inversion temperature) the size of the heptane droplet reaches a minimum **(C)**, phase inversion occurs **(D)**, reverse micelles work as nanoreactors for nanoMIL-101Cr and in addition coalescence occurs **(E)**, isolated and agglomerated nanoMIL-101Cr particles in water after washing procedure **(F)**.

produced by using combinations of sodium caseinate and Tween 20 (Su and Zhong, 2016). Also, a non-ionic/anionic surfactant blend exhibits a higher PIT than the corresponding non-ionic-only system. This result can be attributed to the hydrophilic nature of anionic surfactants. Kundu et al. (2013) studied the effect on PIT of an oil-in-water emulsion stabilized by anionic surfactant. Moreover, Kale and Deore (2017) also showed the influence on PIT of an oil-in-water emulsions stabilized by an anionic surfactant. Studies also have shown that the formation and properties of emulsions prepared according to the PIT approach can be modulated by using a combination of non-ionic and cationic surfactants. With increasing cationic surfactant concentration not only the PIT increased but also the positive charge on the oil droplets after emulsion formation (Mei et al., 2011). Positively charged oil-in-water emulsions were prepared by Sun et al. by adding a cationic surfactant to the system. The cationic molecules raise the PIT above 100°C (Mei et al., 2011).

One of the most interesting applications of MOFs is their use in mixed-matrix membranes (MMM) (Sorribas et al., 2014). Pure organic polymer membranes are already applied for gas separation processes in industry due to their cost and energy effectiveness, environmentally friendly use, as well as their simple and versatile manufacturing (Seoane et al., 2015). They are used for CO_2 removal from natural gas (natural gas sweetening), hydrogen isolation and recovery, and oxygen and nitrogen enrichment from air (Miricioiu et al., 2019). Membrane technology is becoming more important for CO_2 separation from natural gas as conventional CO_2 absorption and adsorption processes are generally more energy demanding and costly. Pure polymer membranes are the currently used membranes CO_2 separation from natural gas. Because of their low permeability and selectivity, plasticization effects, and low thermal and chemical stability inorganic membranes are seen as the future. The latter feature higher permeability, better selectivity, thermal, and chemical stability. Also, permeability and selectivity of neat polymer membranes are inversely correlated to each other such that a rise in permeability usually results in a loss in selectivity and vice versa. The current maximum selectivity for a given permeability is known as the Robeson upper bound limit (Robeson, 1991, 2008). One possibility to overcome the Robeson upper bound is seen in combining the organic polymer with porous filler particles (e.g., MOFs, zeolites) as an additive in so-called mixed-matrix membranes (Dechnik et al., 2017a). When it comes to mixed-matrix membranes for CO_2/CH_4 separation the choices geared toward application appear to be (functionalized) zeolite/polymer or zeolite/carbon composites (Yeo et al., 2012). Zeolites can be incorporated into membranes but show poor compatibility with organic polymers. Here the MOFs come into play, because they offer some very interesting opportunities in combination with polymers (Liu et al., 2018). Latest advances in MMM research use MOFs as fillers in the polymer matrix based on their well-defined and tuneable nanoporosity (Zornoza et al., 2013). State-of-the art MOF-based MMM work investigates the design and influence of the surface chemistry and texture, particle size, and morphology, and dispersion of the MOF filler particles on the separation properties of the MMMs. For example, particles smaller than <50 nm in size with their defined shape and orientation and their homogeneity known in the membrane are studied to probe the separation properties. Also, effects on polymer rigidity or free volume are quantified and related to changes in permeability. The MOF-MMM work uses also advanced characterization techniques such as tomographic SEM/TEM to better understand the filler-matrix interactions (Dechnik et al., 2017a). For further information on the state-of-the-art on MOF@polymer MMM work the reader is referred to review articles (Tanh Jeazet et al., 2012; Zornoza et al., 2013; Seoane et al., 2015; Dechnik et al., 2017a,c, Amooghin et al., 2019). One of the most investigated polymers for MMMs is Matrimid 5218 (**Figure S3**) which shows high mechanical stability, high chemical resistance, and a good permselectivity (Nuhnen et al., 2018). A trend for the next-generation MMMs follows the incorporation of nanosized fillers (Carreon et al., 2017), as it is supposed that the quality of MMMs increases, due to enhanced distribution, less agglomeration, and reduced sedimentation of nanosized filler particles (Zornoza et al., 2011).

For use in membrane technology MOFs with high water stability are necessary and MIL-101Cr (**Figure S4**) meets the requirement (Janiak and Henninger, 2013). With a view on CO_2/CH_4 separation, the adsorption of CO_2 in MIL-101 is higher than that of CH_4, because of the higher polarization and quadrupole moment of CO_2 (Chowdhury et al., 2012). Moreover, Zhao et al. have achieved with nanosized MIL-101Cr a significant enhancement of CO_2 adsorption compared to bulk MIL-101 due to the "nano-effect" of porous materials for gas adsorption (Zhao et al., 2018). Hence, MIL-101Cr is an appropriate filler in MMMs for CO_2/CH_4 gas separation. To the best of our knowledge, there is no study on the nanoMIL-101Cr in Matrimid (nanoMIL-101Cr@Matrimid) for CO_2/CH_4 mixed-gas separation. In the present work, the formation of nanoMIL-101Cr (corresponds to MOFs with a size in the nano- and lower micrometer range) was achieved by the combined approach of surfactant emulsion and ultrasonication followed by microwave heating. MicroMIL-101Cr (corresponds to MOFs with a size in the middle micrometer range) was synthesized according to the literature (Yang et al., 2010). Subsequently, we show an improved mixed-gas permeation performance of nano- over microMIL-101Cr@Matrimid membranes toward the separation of the binary gas mixture of CO_2 and CH_4.

MATERIALS AND METHODS

Materials

All chemicals were obtained commercially and were used without further purification: $Cr(NO_3)_3 \cdot 9H_2O$ (Acros Organics, 99%), HNO_3 (Grüssing, 65 wt.%), 1,4 benzenedicarboxylic acid (H_2BDC, Acros Organics, >99%), tetramethylammoniumhydroxid (TMAOH, 25 wt.% in water, Sigma Aldrich), sodium oleate (Tokyo Chemical Industry, >97%), hexadecyltrimethylammonium bromide (CTAB, Sigma Aldrich, 95%), Triton X-45 (Sigma Aldrich), Matrimid® 5218 powder (Huntsman, **Figure S3**), n-heptane (Sigma Aldrich, p.a.), DMF (VWR, p.a.), ethanol (VWR, p.a.), and dichloromethane (DCM, Fisher Chemical, 99.9%). All experimental work was performed in air. De-ionized (DI) water was used.

Instrumentation

Powder X-ray diffraction (PXRD) patterns were obtained on a Bruker D2 Phaser powder diffractometer equipped with a flat silicon, low background sample holder using Cu–K_α radiation ($\lambda = 1.5418$ Å, 30 kV, 10 Ma, ambient temperature). With this sample holder at $2\theta < \sim 10°$ the beam spot is strongly broadened so that only a fraction of the reflected radiation reaches the detector; hence lower relative intensities are measured in this range. For all samples 2θ angles between 5 and 50° over a time of 105 min, that is 0.007°/sec, were measured. Simulated patterns of MIL-101Cr were calculated with CCDC Mercury 3.9 program using the single crystal data of MIL-101Cr obtained by Rietveld refinement (CCDC no. 605510, Refcode OCUNAC; Férey et al., 2005). Nitrogen physisorption (N_2) isotherms were obtained with a Nova 4000e from Quantachrome at 77 K. For measuring the isotherms, the MOF powders were loaded into glass tubes and weighted before they were degassed at 150°C for 2 h under vacuum. After that, the glass tubes were weighted again. At last, they were transferred to the analysis port of the sorption analyzer. Apparent Brunauer-Emmett-Teller (BET) surface areas were calculated from the adsorption branch of the nitrogen physisorption isotherms. In this work we refer to the microporous MOF surface areas from Type I isotherms as "apparent BET" based on reference (Thommes et al., 2015), where it is noted that 'the BET-area derived from a Type I isotherm must not be treated as a realistic probe accessible surface area' but 'represents an apparent surface area, which may be regarded as a useful adsorbent "fingerprint."' Non-linear (NL-)DFT calculations for pore size distribution curves were done with the native NovaWin 11.03 software using the "N_2 at 77 K on carbon, slit pore, non-linear density functional theory (NLDFT) equilibrium" model (Gelb et al., 1999). Note that the NL-DFT calculations only yield pore size distributions in the micropore (<2 nm, 20 Å) to low mesopore (<10 nm, 100 Å) regime. BET surface areas and pore volumes (measured at $P \cdot P_0^{-1} = 0.95$) were calculated from N_2 sorption isotherms. Infrared (IR) spectra were obtained with a Bruker FT-IR Tensor 37 in attenuated total reflection (ATR) mode using a diamond crystal in the range 4,000–500 cm^{-1}. Scanning electron microscopic (SEM) images were recorded with a Zeiss DSM 982 and a Jeol JSM-6510LV QSEM Advanced electron microscope with a LAB-6 cathode at 20 keV. The microscope was equipped with a Bruker Xflash 410 silicon drift detector and the Bruker ESPRIT software for EDX analysis. The membrane cross-sections were prepared through freeze-fracturing after immersion in liquid nitrogen. The membrane fractions were mounted on a sample holder (**Figure S1**) and coated with gold by a Jeol JFC 1200 fine-coater at an approximate current of 20 mA for 20–30 s. Dark and light areas around cross-section of membranes depend on mounting on SEM sample holder. Light areas are a consequence of the nearby metal sheet which for stability purpose is screwed close to the membrane (**Figure S1**). Transmission electron microscopy (TEM) micrographs were taken at room temperature with a Zeiss E902 ATEM. Samples were deposited on 200 μm carbon-coated copper grids. The size distribution was calculated from a manual diameter determination over a minimum of 50 isolated particles. Dynamic light scattering (DLS) experiments were conducted with a 3D LS Spectrometer operated in 2D mode (LS Instruments, Fribourg, Switzerland) using a HeNe-laser ($\lambda = 632.8$ nm) with a maximum constant output power of 35 mW as light source. The measurements were performed at scattering angles from $\theta = 30$–$140°$ and at a constant temperature of 25°C, which was achieved by a heat-controlled decalin bath connected to a circulating water bath (Julabo CF31). The light scattered by the sample was detected by two avalanche photodetectors operating in pseudo-cross-correlation mode. For all measurements dust-free, disposable culture tubes made of borosilicate glass (Fisher Scientific, Schwerte, Germany) were used. Samples for light scattering experiments were prepared by redispersion of freeze-dried particles in water using ultrasonication and filtration with a syringe filter (5 μm pore size, PTFE, hydrophobic). Temperature stability was achieved by equilibration of the samples for at least 30 min in the decalin bath before the measurements. All measurements were repeated three times using acquisition times of 60 s each. The resulting intensity-time autocorrelation functions were analyzed by the CONTIN algorithm using the software AfterALV 1.0e (Dullware, Wageningen, the Netherlands) yielding the relaxation rate distributions $G(\Gamma)$. For an angle dependent diffusion analysis the mean relaxation rates Γ of the dominating species in the intensity-weighted $G(\Gamma)$ were plotted vs. the squared scattering vector q^2 to analyze whether translational diffusion is probed.

The polydispersity index (PDI) is given in the figure captions in **Supplementary Material** [calculated according (Kozlov et al., 2017), PDI = (standard deviation/average nanoparticle size)^2]. As a **microwave reactor** a CEM Mars 6 with 55 mL sample tubes (2.1 cm diameter, height 19 cm) was used. Microwave heating was done by pre-setting the desired temperature, maximum power (here 600 W), time ramp to reach the desired temperature and hold time before turning off the microwave heating. During ramping and holding the heating is not continuous but supplied by pulses. A **Sonics vibra-cell** VCX 750 ultrasound generator with Microtip 630-0419, Amplitude 20%) was employed for both emulsion types.

Mixed Gas Permeation

The membranes were placed inside the membrane module composed of two stainless steel parts with a cavity (4.5 cm in diameter) in which a macroporous disk support (20 μm nominal pore size, Mott Corp.) is gripped inside with Viton o-rings. Before the measurement, the membranes were heated for 1 h in a vacuum oven at 150°C for removing residual moisture traces through storage. The composition of the feed gas mixtures and the purge gas flow (sweep gas) were controlled by an **OSMO Inspector** device (Convergence Industry B.V; **Figure S2**). Gas concentrations in the outgoing stream were evaluated by an Agilent 490 μGC on-line **gas micro-chromatograph** equipped with a thermal conductivity detector (TCD). Gas concentrations in the permeate were measured every 30 min until steady state was reached (up to 8 h). Permeability results in Barrer (1 Barrer = 1×10^{-10} cm^3 (STP)cm/(cm^2 s cmHg) were obtained from the concentrations in steady state. The real separation selectivity of the mixtures was calculated as the ratio of the mole fractions of the components in the permeate and the feed stream. Permeation measurements were performed at 25°C controlled by a flexible heating coil. The carrier gas was Helium. After the mixed-gas permeation investigations, the thickness of the membranes was measured at 10 different places using a micrometer screw as a **thickness measuring device**. A binary mixture of CO_2 and CH_4 (50 vol% of CO_2) was used as a feed gas in permeability and selectivity measurements. We note that the natural gas composition is not a 1:1 ratio of CO_2/CH_4. But as the CO_2 in natural gas resources varies from 4 to 50% according to Datta and Sen (2006) it is a good approximation to use a 1:1 (v:v) ratio of CO_2/CH_4. Furthermore, a review from Yeo et al. (2012) shows that most of the studies of membrane technologies regarding CO_2 removal from natural gas are done with feed compositions of equimolar ratios of CO_2/CH_4. There are also other contaminants in natural gas (Faramawy et al., 2016) but they are hardly ever included in CO_2/CH_4 separation studies with MOF@polymer MMMs as such measurements are beyond the scope of the often more fundamental CO_2/CH_4 permselectivity studies.

Permeation experiments were conducted at 25°C, 4 bar feed pressure and 1 bar permeate pressure. The permeability of the membranes was calculated by the following two equations (Abedini et al., 2014):

$$P_{CH_4} = \frac{2.73.15 \times 10^{10} \left(1 - y_{CO_2}\right) VL}{760\, AT\, [\left(1 - x_{CO_2}\right)(P_0 \times 76)/14.7]} \left(\frac{dP}{dt}\right)$$

$$P_{CO_2} = \frac{2.73.15 \times 10^{10} y_{CO_2} VL}{760\, AT\, [\, x_{CO_2}(P_0 \times 76)/14.7]} \left(\frac{dP}{dt}\right)$$

P_{CH4} and P_{CO2} (Barrer): permeability of gases in Barrer;
L (cm): membrane thickness;
T (°C): experiment temperature;
V (cm^3): constant volume vessel;
A (cm^2): membrane surface area;
P_o (cmHg): feed pressure;
(dP/dt): slope of pressure vs. time.

The selectivity was calculated by the following equation:

$$\alpha_{A/B} = \frac{y_A/y_B}{x_A/x_B}$$

x: mole fractions in the feed gas; y: mole fractions in the permeate.

Maxwell Model and Bruggeman Model

The Maxwell model can be used to describe the gas transport through a dense composite membrane (Bouma et al., 1997).

For spherical particles the permeability of the composite membrane P_{eff} can be calculated as follows:

$$P_{eff} = P_c \frac{P_d \cdot (1 + 2\phi_d) + P_c \cdot (2 - 2\phi_d)}{P_d \cdot (1 - \phi_d) + P_c \cdot (2 + \phi_d)}$$

With P_c as permeability of the continuous phase, P_d is the dispersed phase permeability and ϕ_d is the volume fraction of the filler.

In cases where the permeability of the filler is much higher than the permeability of the continuous phase ($P_d >> P_c$) the upper equation can be written as follows:

$$P_d \gg P_c;\ \frac{P_{eff}}{P_c} = \frac{(1 + 2\phi_d)}{(1 - \phi_d)}$$

As in the Maxwell model no filler-filler particle interactions are considered, the model is only valid for low filler loadings up to a volume fraction of about 0.2 for the filler (ϕ_d) (Pal, 2008).

The volume fraction of the filler in the dispersed phase can be calculated as follows:

$$\phi_d = \frac{w_d/\rho_d}{\left(\frac{w_c}{\rho_c}\right) + \left(\frac{w_d}{\rho_d}\right)}$$

Where, w_d and w_c are the weight percentages, ρ_d and ρ_c the densities of the filler (0.451 g^{-1} cm^{-3} for MIL-101Cr) and the polymer (1.17 g^{-1} cm^{-3} for Matrimid), respectively.

The Bruggeman model is based on the effective medium theory and does consider the presence of nearby particles for the permeation properties. Hence, the Bruggeman model is valid for high filler loadings especially.

The permeability for composite membranes can be calculated as follows:

$$(\frac{P_c}{P_{eff}})^{\frac{1}{3}} = (1 - \phi_d) \cdot (\frac{P_d}{P_c} - 1)$$

For fillers with distinctly higher permeabilities compared to the continuous phase ($P_d >> P_c$) the equation simplifies to:

$$P_{eff} = \frac{P_c}{(1-\phi_d)^3}$$

Dynamic Light Scattering

We performed DLS measurements at different scattering angles θ and thus at different magnitudes of the scattering vector q:

$$|\vec{q}| = \frac{4\pi n}{\lambda} \sin\frac{\theta}{2}$$

Here λ corresponds to the wavelength of the incident light and n to the refractive index of the dispersing medium. Analysis of the q-dependence of the relaxation rate Γ allows for a diffusion analysis.

For purely translational diffusion, Γ scales with the square of q:

$$\mathrm{D_t} = \frac{\Gamma}{q^2}$$

The diffusion coefficient $\mathrm{D_t}$ can then be used to calculate the hydrodynamic radius $\mathrm{R_h}$ of the particles in dilute dispersion using the Stokes–Einstein equation (Cao, 2003):

$$R_h = \frac{kT}{6\pi\eta D_t}$$

Here k is the Boltzmann constant, T the absolute temperature and η the solvent viscosity.

Synthesis of NanoMIL 101Cr in Direct Emulsion

The chosen parameters led to positive results using our microwave reactor and the tubes provided for this purpose. It should be mentioned, that other research groups with different microwave reactors/tubes might have used different parameters.

Direct emulsion contains DI water, *n*-heptane, surfactant, HNO_3, and the starting material for MIL-101Cr. First, a solution of H_2BDC (0.33 g, 2 mmol), $Cr(NO_3)_3 \cdot 9H_2O$ (0.80 g, 2 mmol), 5 mL water, and 1.0 equivalent of HNO_3 (with respect to chromium nitrate) were mixed together. This solution was combined with a solution of sodium oleate (0.14 g, 0.34 mmol), 5 mL of water, and ultrasonicated with *n*-heptane (5 mL) for 1 min. The pH value was 4. After the ultrasonication the solution was transferred into microwave ractor tubes with a volume of 55 mL (2.1 cm diameter, height 19 cm). The direct emulsion was heated to 180°C within 30 min and kept at this temperature for 10 min (another batch was kept at 180°C for 40 min). Other direct emulisons were prepared as discribed above but heated to 210°C for 30 min and kept at 210°C for 10 min (another batch for 40 min). After cooling to RT within 15 min the green MIL-101Cr powder was collected by centrifugation and purified as follows: Washing with water (1.00 g MOF to 1.50 L water) by stirring the dispersion for 24 h in order to remove the sodium oleate. Then, the product was washed with hot DMF and hot ethanol two times (2 × 50 mL, 24 h) to remove remaining terephthalic acid. The product was activated under vacuum (50 mbar) at 150°C for 24 h. The reactions were carried out several times to ensure reproducibility. Syntheses without the presence of HNO_3, syntheses by replacing HNO_3 with NaOH (to get pH 7), syntheses without *n*-heptane, and direct emulsion in combination with CTAB and Triton X-45 yielded no MIL-101Cr product.

Attempted Synthesis of NanoMIL 101Cr in Reverse Emulsion

In a one-micellar system, where all reactants are in one micelle, the reaction starts by increasing the temperature or triggering the reaction through other parameters (Anjali and Basavaraj, 2018). Because of the fact that at high temperature micelles coalesce anyway, there is no point in separating the MOF precursors in different micelles at the beginning. Therefore, we suspended all MOF precursors in the same aqueous phase before forming the emulsion (**Figures S5, S6**).

The reverse emulsion experiments were carried out in a water-in-oil emulsion of chromium(III) nitrate non-ahydrate, terephthalic acid, and nitric acid in a PTFE- (Teflon-) lined vessel at 180°C for 70 min reaction time under microwave heating.

A solution of H_2BDC (0.33 g, 2 mmol), $Cr(NO_3)_3 \cdot 9H_2O$ (0.80 g, 2 mmol), 4 mL DI water, and 1.0 equivalent HNO_3 (with respect to chromium nitrate) were mixed together. This solution was combined with a solution of one of the modulators, sodium oleate (1.00 g, 3.28 mmol), CTAB (1.00 g, 2.73 mmol), or Triton X-45 (1.00 g, 2.47 mmol) in 4 mL of DI water and ultrasonicated with *n*-heptane (40 mL) for 1 min. The pH value was 4. After the ultrasonication the solution was dived into three parts and all transferred into microwave ractor tubes with a volume of 55 mL (2.1 cm diameter, height 19 cm). The reaction was initiated by an increase in temperature up to 180°C for 30 min (heating ramp) in closed 55 mL Teflon vessels by microwave heating at 600 W. After finishing the heating ramp the reaction was hold at 180°C for 40 min (dwelling time). Further steps follow the same route mentioned above. It should be mentioned that with lower amounts of sodium oleate the stability of the direct emulsion gets lost and with a higher amount of sodium oleate or with an increase of temperature higher than 210°C only amorphous material was obtained. To verify the relevance of an acidic modulator, we tried to synthesize nanoMIL-101Cr according to the direct emulsion method using NaOH instead of HNO_3. We also tried to synthesize nanoMIL-101Cr according to the direct emulsion method without HNO_3. Also we tried to carry out the synthesis without heptane and just in water with additives. After microwave heating there was no MIL-101Cr material at all. Different variations of direct/reverse emulsions are listed in **Supplementary Material**.

Synthesis of MicroMIL 101Cr With TMAOH (Conventional Synthesis)

The hydrothermal synthesis of MIL-101Cr was adapted from the literature (Yang et al., 2010). H_2BDC (0.332 g, 2 mmol) was added to an alkali solution of 10 mL deionized water (DI water) and tetramethylammonium hydroxide (5 mL, 0.05 mol/L) and stirred at RT for 5 min. $Cr(NO_3)_3{\cdot}9H_2O$ (0.8 g, 2 mmol) was added to the mixture and stirred for 5 min. The resulting mixture was transferred into a 20 ml Teflon-lined autoclave for 24 h at a heating temperature of 180°C. The green powder was collected by repeated centrifugation and thorough washing with 50 mL DMF at 150°C, 50 mL ethanol at 100°C, and 50 mL DI water at 100°C. The product was activated under vacuum at 150°C for 24 h.

Preparation of Matrimid Membranes

For the pure Matrimid membrane a certain amount of polymer and DCM were mixed together and stirred for 24 h. The yellowish solution was not further treated before it was cast into 8 cm diameter metal rings, which were placed on a flat glass surface. Next, the rings were covered with funnels with some paper tissue until the membrane was dry (after ∼1.5 h).

The funnels were used to prevent contamination by dust particles during the evaporation of the solvent and also to control the evaporation rate. As soon as all solvent was evaporated, the membranes were removed from the metal rings and the glass surface by flushing the rings with deionized water. The membranes were kept in a vacuum oven for another 24 h at 150°C and 50 mbar to remove the residual solvent. After the membranes were naturally cooled to ambient temperature they have been tailored to the size of the sample holder (4.5 cm in diameter) and stored in air and RT for characterization and permeation tests. Details for the specific amounts of polymer and solvent are listed in **Table 2**.

We note that the permeability of pure Matrimid membranes is heavily dependent on the thermal pretreatment of the membrane. Ansaloni et al. (2015) have shown that with higher pretreatment temperature the permeability and also the physical aging of Matrimid is continuously reduced. Also, mixed gas experiments often show reduced permeability compared to single gas experiments due to competitive adsorption and diffusion of the gases. In work by Rodenas et al. (2015), similar experimental conditions were applied (temperature 298 K, transmembrane pressure 3 bar, 50/50 gas mixture CO_2/CH_4) and the measured CO_2 permeability was about 6 Barrer as found by us (**Table 3**). Their slightly lower CO_2 permeability is in good agreement with their higher pretreatment temperature of 180°C under dynamic vacuum, when compared to our results.

Preparation of Mixed-Matrix Membranes

For all MMMs nanoMIL-101Cr was used, which was obtained by direct emulsion and sodium oleate (210°C, 70 min). MMMs were fabricated by a dense film casting method using a "priming" technique (Mahajan and Koros, 2002). This technique involves the addition of low amounts of polymer to the MOF-DCM-suspension prior to the incorporation of the particles into the polymer matrix. Priming has shown to support greater affinity between the filler and the polymer, resulting in a symmetric MMM with improved transport properties.

By using the priming technique, a Matrimid-DCM-solution was prepared for each MOF/Matrimid membrane sample (8, 16, and 24 wt.%) and stirred for 24 h. This solution was then combined with an already prepared nanoMIL-101Cr-DCM-suspension in two steps. For the MOF-DCM-suspension a certain amount of MIL-101 was suspended in DCM and stirred for 24 h. Then, the MOF-suspension was sonicated for 15 min with high power ultrasound before stirring it for another 45 min. This procedure was repeated three times. Next, the green suspension was combined with a specific fraction of the previously prepared Matrimid-DCM-solution and stirred again for 24 h (corresponding to the first step of priming). After that, the blend was sonicated for 15 min and stirred for 45 min (here also a repetition of another two times was conducted). Before casting, the leftover Matrimid-DCM-solution was combined with the MOF-DCM-Matrimid-suspension and kept under stirring for 1 h. This final suspension was casted into metal rings. After the solvent was evaporated the membranes were detached, tailored, dried overnight and stored as described above. Details for the specific amounts of MOF, solvent, and polymer are listed in **Table 2**. The experiments were made on mixed-matrix membranes containing 8, 16, and 24 wt.% of MIL-101. Each type of membrane was prepared and measured three times to provide reliable error estimates.

RESULTS AND DISCUSSION

MIL-101Cr Syntheses

MIL-101Cr (MIL = Matériaux de l'Institute Lavoisier) has become one of the most important MOFs (Férey et al., 2005; Zhao et al., 2015).

In order to decrease reaction time and particle size we tested microwave heating in combination with emulsion techniques. Nanosized particles of MIL-101Cr can be synthesized by microwave heating alone (Khan et al., 2011), yet in our hands the use of microwave heating alone did not lead to reproducible results. Although there are syntheses published to obtain MIL-101Cr with microwave heating and water alone, we could not synthesize MIL-101Cr adopting the published procedures for our microwave reactor. Therefore, we tried to adjust the syntheses and used the direct and reverse emulsion technique in combination with microwave heating. With both techniques we were able to obtain MIL-101Cr in our microwave reactor. To the best of our knowledge we present here the first report where microwave heating, emulsions, and ultrasonication are used in combination for the synthesis of MIL-101Cr nano/microparticles, leading to good yields (45%) in short reaction times (∼70 min) without the use of HF or a steel autoclave. Because no HF was used for the syntheses, the formula of the MIL-101Cr framework should be $[Cr_3(O)(OH)(bdc)_3(H_2O)_2]$.

For the stabilization of the emulsions we tested three different surfactants, which are generally utilized for MOF emulsion synthesis (**Figure 2**). Sodium oleate was chosen exemplarily for a monocarboxylic acid and anionic-surfactant, because it should strongly interact with the MOF surface via coordinative bonds and attractive electrostatic forces to open metal sites. This interaction should lead to an adsorption on the MOF surface and inhibits further growth and aggregation (Diring et al., 2010). CTAB was chosen due to its cationic nature and because it is

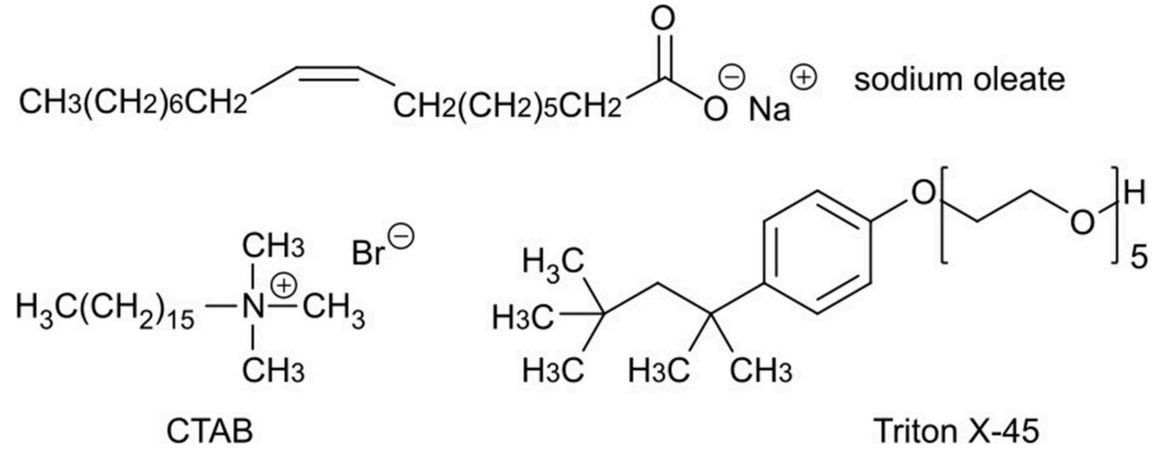

FIGURE 2 | Chemical formulas of the used surfactants sodium oleate, cetyltrimethylammonium bromide (CTAB), and Triton X-45.

known to slow down the nucleation and growth of MOFs (Jiang et al., 2011b). Triton X-45 was tested as a non-ionic surfactant to achieve additional mesoporosity (Du et al., 2016).

The direct and reverse emulsions were employed under identical temperature and reaction time conditions. All experiments were carried out with 2 mmol each of chromium(III) nitrate non-ahydrate and terephthalic acid in a PTFE- (Teflon-) lined vessel at 180–210°C for 40-70 min (see **Supplementary Material**). Using direct emulsion, we mixed the MOF precursors and the surfactant together in a heptane-in-water emulsion; for reverse emulsion in a water-in-heptane emulsion. The emulsions were ultrasonicated before heating, otherwise heptane and water would quickly separate again as bulk phases. Ultrasonication achieved sufficient dispersion of the respective droplets in the continuous phase yielding long-time stable emulsions. Baloch et al. have shown that an increase in ultrasonification time increases the number of *n*-heptane droplets and decreases their average size and the degree of dispersity, hence improves the emulsion quality (Baloch and Hameed, 2005). Once the reaction was finished, the MIL-101Cr powder was purified and activated.

It turned out that only the direct emulsion technique in combination with sodium oleate as surfactant gave reproducible and satisfying yields (45%) together with crystalline products of high apparent BET surface areas around 2,900 $m^2\ g^{-1}$ (**Table 1**). This result may be based on the phase inversion, whereby the oil-in-water emulsion inverts into a water-in-oil emulsion and provides nanoreactors for MOF particles (**Figure 1**). From FTIR-ATR the infrared band assignments of sodium oleate can still be seen in nanoMIL-101Cr but only as a minor contribution (**Figure S7**; Roonasi et al., 2010). Concering the yield we note that in the original synthesis procedure by Férey et al. (2005) the problematic modulator HF was used and a yield of only ~50% was stated after separation of MIL-101Cr from the terephthalic acid. Many small-scale literature syntheses follow this original hydrothermal synthesis procedure with a yield of ~50% (Férey et al., 2005). Hence, yields around 45% are competitive with many literature syntheses of MIL-101Cr. Also, the yields of about 45% are slightly higher than for MIL-101Cr samples synthesized by microwave heating alone (de la Iglesia et al., 2016). The use of microwave heating led to a drastic decrease concerning reaction time (70 min) and temperature (210°C and lower). Attempts to shorten the reaction times to 40 min suffered from a loss in surface area and porosity (García-Márquez et al., 2012; **Table 1**).

For comparison, nanoMIL-101Cr was synthesized via reverse emulsion and microMIL-101Cr via the conventional hydrothermal route as described in **Supplementary Material**. Particles of nanoMIL-101Cr via reverse emulsion were small, but displayed poor porosity characteristics (**Table 1**).

Powder X-ray diffraction (PXRD) confirmed the identity, crystallinity and phase purity of nanoMIL-101Cr synthesized using direct emulsions (**Figure 3A**). It is observed that a higher temperature (210°C) and longer reaction time (70 min) improved crystallinity and porosity (**Table 1**). As Burrows et al. already have described, the broad Bragg reflections of the XRD patterns of the samples are attributed to the small particle size effects, and indeed the lines get broader as the nano/microparticle size decreases (Jiang et al., 2011a). The porosity characteristics were determined from N_2 adsorption-desorption isotherms of the purified and activated nanoMIL-101Cr (**Figure 3B**). The apparent BET surface area could be increased up to 2,900 $m^2\ g^{-1}$ by a 70 min synthesis at 210°C.

The N_2 isotherms of the higher surface area samples after 70 min reaction time are of the Type I(b) up to $p/p_0 \approx 0.4$ with the characteristic step between $0.1 < p/p_0 < 0.2$ due to the presence of the two kinds of microporous windows/mesoporous cages as in pure MIL-101Cr (Férey et al., 2005). For $p/p_0 > 0.4$ the increasing uptake which appears to increase without limit when $p/p_0 = 1$ is the result of unrestricted monolayer-multilayer adsorption due to the macroporous voids in the interparticle space so that the isotherm becomes of Type II (Thommes et al., 2015).

TABLE 1 | Reaction conditions and results for the synthesis of nanoMIL-101Cr.

Conditions,[a] surfactant,[b] temp.	Time[c] (min)	S_{BET}[d] ($m^2 \cdot g^{-1}$)	Size[e] (nm)	V_{pore}[f] ($cm^3 \cdot g^{-1}$)	Yield[g] (%)
Direct emulsion SO (180°C)	40	1,337	<100	0.55	34
Second batch		1,032		0.50	23
SO (180°C)	70	2,269	<100	1.05	43
Second batch		2,400		1.08	30
SO (210°C)	40	1,744	<100	0.73	37
Second batch		1,555		0.75	25
SO (210°C)[h]	70	2,923	<100	1.32	45
Second batch		2,663		1.19	31
Reverse emulsion SO (180°C)	70	561	<100	0.31	36
Second batch		417		0.21	21
CTAB (180°C)	70	862	n.d.	0.42	20
Second batch		706		0.35	33
TX-45 (180°C)	70	401	n.d.	0.21	22
Conventional synthesis (see **Supplementary Material** for details) MicroMIL-101Cr[h]	24 h	2,741	350 ± 70	1.25	64

[a] *All synthesis and other details are given in the Supporting Information. Stated reactions have been carried out in duplicate to ensure reproducibility.*

[b] *SO, sodium oleate; CTAB, cetyltrimethylammonium bromide; TX-45, Triton X-45.*

[c] *Time for heating ramp plus dwelling time.*

[d] *Apparent BET surface area calculated in the pressure range $0.05 < p/p_0 < 0.2$ from N_2 sorption isotherms at 77 K with an estimated standard deviation of $\pm 50\ m^2\ g^{-1}$.*

[e] *Particle size based on SEM pictures, for microMIL-101Cr statistic based on 50 particles.*

[f] *Total pore volume calculated from N_2 sorption isotherms at 77 K ($p/p_0 = 0.4$) for pores ≤3.2 nm.*

[g] *Yield is based on Cr.*

[h] *Used in mixed-matrix membrane fabrication.*

n.d. Not determined.

Hence, we determined the pore volume at $p/p_0 = 0.4$ and not as suggested in the latest IUPAC report for gas sorption at $p/p_0 = 0.95$, in order not to overestimate the pore volume (Thommes et al., 2015). Micrometer sized MIL-101Cr from the literature exhibits the typical Type I(b) isotherm for MIL-101Cr, reaching its plateau at $p/p_0 = 0.4$ (Zhao et al., 2015). Therefore, it is ensured that pore filling is already completed at $p/p_0 = 0.4$. Possibly due to retained surfactant, as mentioned above, the pore volume is smaller than expected. The NL-DFT calculations yielded pore widths largely below ∼25 Å (2.5 nm) (**Figure S8**), which is smaller than the expected 2.9 and 3.4 nm (**Figure S4B**) but match with literature reports (Horcajada et al., 2007) and with our results on microMIL-101Cr from conventional hydrothermal syntheses (**Figure S10**; Huang et al., 2012). With shorter reaction times of 40 min not only does the porosity decrease, but the pore size distributions extent also into the mesopore region (above 20 Å, 2 nm; **Figures S8A,C**). Thus, products from short reaction times seem to have a hierarchically porosity with micropores below 20 Å width and pores sizes between 20 and 100 Å (**Figure S11**).

From reverse emulsion no satisfactory BET surface area, crystallinity and yield could be reached compared to direct emulsion and conventional syntheses. These results may be based on the phase inversion, whereby the water-in-oil emulsion inverts into an oil-in-water emulsion and as a consequence nanoreactors for MOF particles are no longer available (**Figure S6**). From PXRD it is evident that the crystallinities of the samples synthesized in reverse emulsion were all very poor (**Figure 3C**). Still the PXRD patterns with strongly broadened reflections are similar to those for nanosized MIL-101Cr particles reported by other researchers, when using microwave heating or surfactants (**Table S1**). Broad Bragg diffraction peaks may indicate either a low crystallinity or small (nano)particles (de la Iglesia et al., 2016).

Nitrogen sorption experiments of nanoMIL-101Cr from reverse emulsions yield low BET surface areas of $<900\ m^2\ g^{-1}$ and total pore volumes of $<0.2\ cm^3\ g^{-1}$ (**Table 1**, **Figure 3D**). The low porosity values are in accordance with the lower crystallinity deduced from the PXRD patterns and are in about the same range as those for nanosized MIL-101Cr particles reported by other researchers, when using microwave heating or surfactants (see summary in **Table S1**). The nitrogen adsorption isotherms are a combination of Type IV at low p/p_0 (for mesoporous solids) and Type II at high p/p_0 (Thommes et al., 2015), which is characteristic for macrporous solids with interparticular porosity (**Figure S9**). When the reverse emulsion is exposed to high temperature (>100°C), heptane vaporizes and expands rapidly, thereby the surface area of the oil within the water increases and an enhanced contact of surfactant molecules with metal salt and organic linker components occurs. This can lead to further competition concerning the coordination equilibrium on the crystal surface, especially for

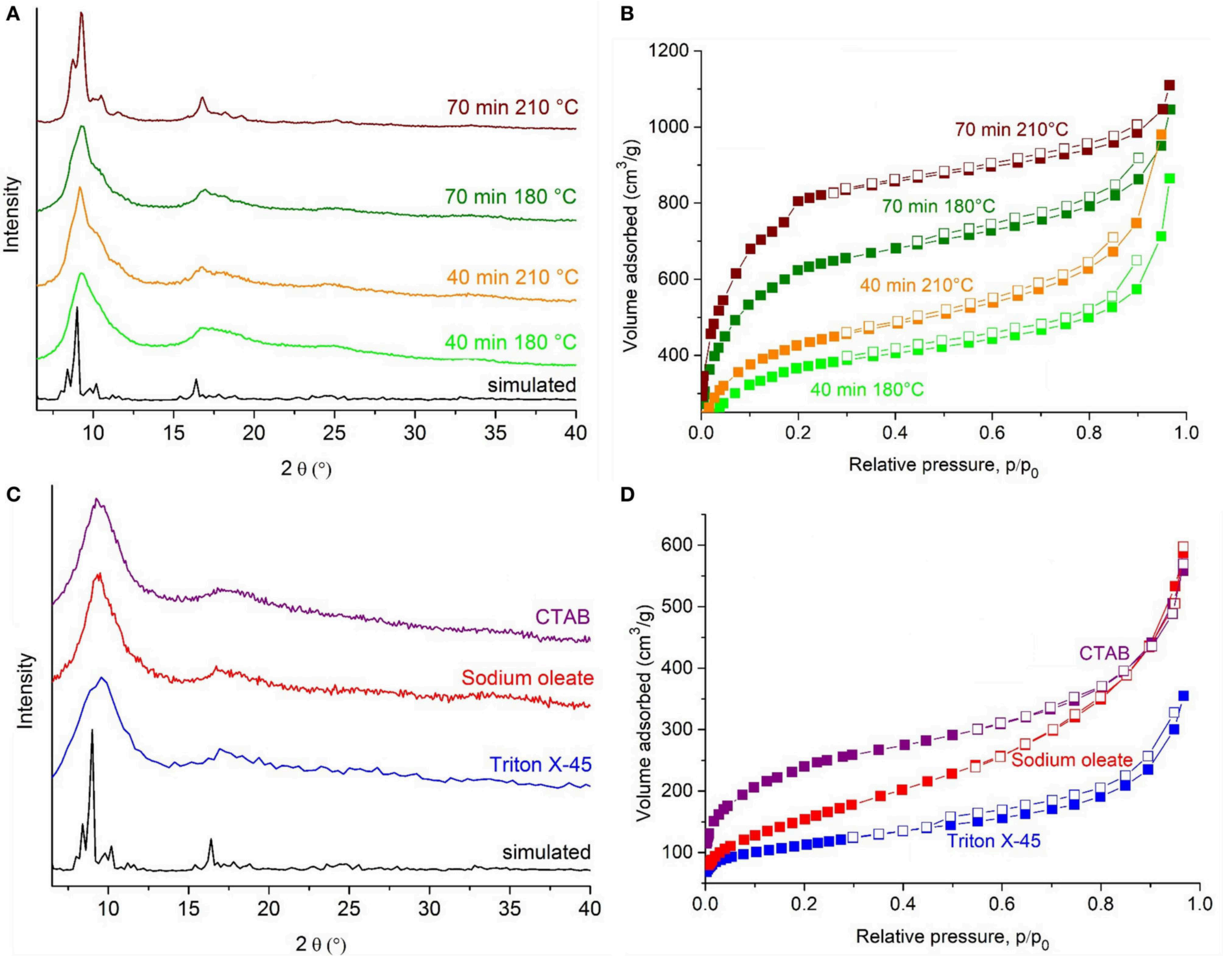

FIGURE 3 | PXRD patterns and N_2 sorption isotherms of nanoMIL-101Cr synthesized in direct emulsion **(A,B)** for 40 min at 180°C (light green), 40 min at 210°C (orange), 70 min at 180°C (dark green), 70 min at 210°C (brown). PXRD patterns and N_2 sorption isotherms of nanoMIL-101Cr synthesized in reverse emulsions **(C,D)** by using sodium oleate (red), CTAB (purple), Triton X 45 (blue). Simulated PXRD pattern based on the cif-file of MIL-101Cr, CCDC number: 605510, (black) (Férey et al., 2005). For the N_2 sorption isotherms the samples were activated at 150°C under vacuum for 12 h. Filled symbols depict adsorption, empty symbols desorption.

the monocarboxylic acid sodium oleate. All reverse emulsion samples show pore size distributions about 1 nm (10 Å) to over 10 nm (100 Å) with a large pore volume fraction, especially for nanoMIL-101Cr from sodium oleate in the lower mesopore region (between 2 and 10 nm) (**Figure 9A**). Yields of MIL-101Cr from reverse emulsion were below 36% (**Table 1**).

The morphology and particle size were assessed by scanning electron microscopic (SEM), transmission electron microscopy (TEM) and dynamic light scattering (DLS). SEM images of MIL-101Cr from direct emulsion with sodium oleate show the formation of nano/microparticles with rather uniform diameters around 100 nm and spherical morphology (**Figure 4**).

TEM images agree with sizes obtained from SEM (**Figures S12, S13**). The TEM-histograms of nanoMIL-101Cr particles (**Figures S12E, S13E**) show that the average particle size and its standard deviation are 73 ± 15 and 86 ± 15 nm diameter for direct emulsion at 210°C for 40 and 70 min reaction time, respectively. TEM images are similar to other TEM images already published by other research groups (Wuttke et al., 2015). For MIL-101 powder gained by reverse emulsion the SEM results, TEM results, and a histogram are shown in **Figures S14, S15**, respectively. For microMIL-101Cr the PXRD, N_2, SEM results, and a histogram are shown in **Figures 5A,B** and **Figure S16**, respectively.

We also used dynamic light scattering (DLS) as a non-destructive ensemble measurement technique to determine the hydrodynamic radius of particles from dilute dispersion. The SEM and TEM images showed aggregates of the small primary particles that may have formed during sample preparation. Since the intensity of scattered light in DLS scales with the diameter at the 6th power, DLS is extremely sensitive to the presence of aggregates or impurities like dust. Indeed, the recorded

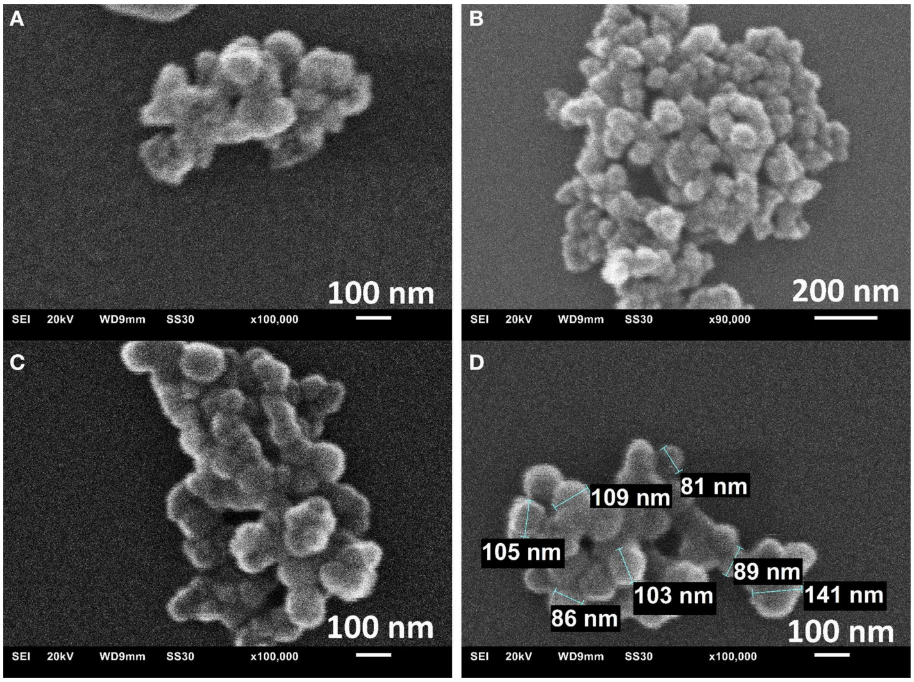

FIGURE 4 | SEM images of the sample prepared in direct emulsion for 40 min at 180°C **(A)**, 70 min at 180°C **(B)** and 70 min at 210°C **(C,D)**.

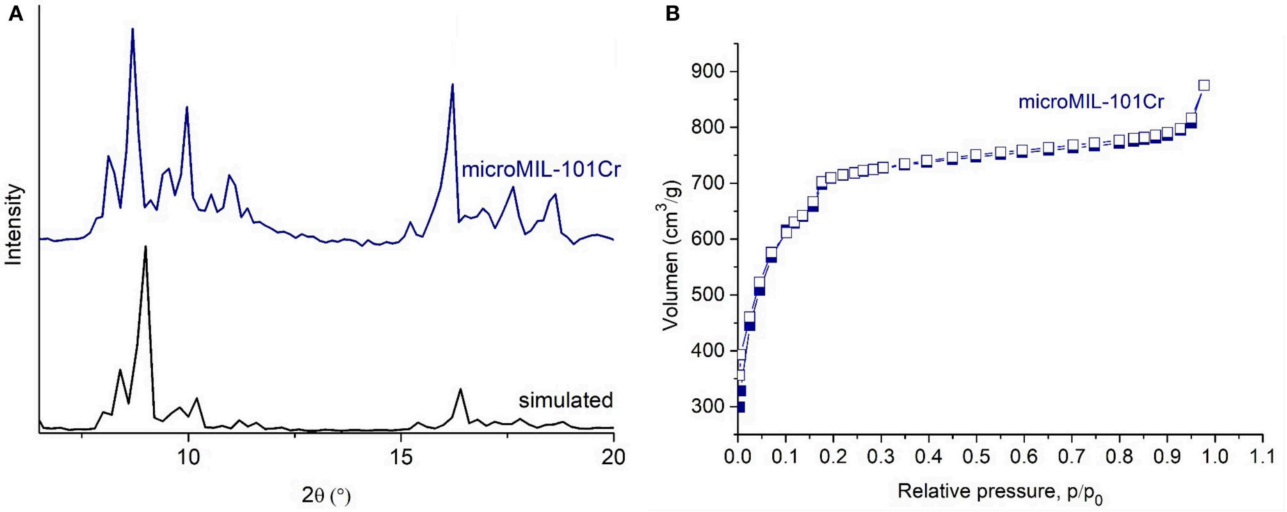

FIGURE 5 | PXRD patterns (navy blue for microMIL-101Cr **(A)**, black for simulated PXRD pattern from the cif-file of MIL-101Cr, CCDC number: 605510) (Férey et al., 2005). N_2 sorption isotherms of microMIL 101Cr **(B)**. Filled symbols depict adsorption, empty symbols desorption.

intensity-time autocorrelation functions and the corresponding distribution functions of the hydrodynamic radii $G(R_h)$ obtained from CONTIN analysis shown in **Figures S17–S23** reveal the presence of small fractions of larger aggregates in all samples. These aggregates appear with average sizes on the order of a few microns. However, we want to note that these larger contributions have low intensities and are clearly not the dominating species in the samples. The diffusion and size of the dominating species [strongest peak in $G(R_h)$] in DLS were analyzed using angle dependent measurements. For each sample we determined the mean relaxation rate and observed a linear dependence on the square of the magnitude of the scattering vector q indicating that we only probe translational diffusion. This allowed us to precisely determine the hydrodynamic radii. For the different nanoMIL-101Cr samples from direct emulsion with sodium oleate DLS gave rather uniform hydrodynamic

TABLE 2 | Weight and mass content of Matrimid and MOF in mixed-matrix membranes.

MOF (wt.%)	Matrimid (g)	DCM (Matrimid) (ml)	MOF [g]	DCM (MOF) (ml)	Matrimid-DCM[a] for priming (ml)
0	0.80	7.0	–	–	–
8	0.80	7.0	0.07	9.0	0.67
16	0.80	7.0	0.15	9.0	1.34
24	0.80	7.0	0.25	9.0	2.01

[a] *Taken from the prepared Matrimid-DCM solution.*

radii between 137 and 155 nm (274–310 nm in diameter). It is also evident that by increasing the reaction temperature from 180 to 210°C or decreasing the reaction time from 70 min to 40 min no significant change of particle size was observed. The determined hydrodynamic radii match nicely to the sizes determined from electron microscopy although slightly smaller values were determined in the latter. This deviation is indeed expected as DLS probes the diffusion of the particles including their solvating shell (Khan et al., 2010).

MIL-101Cr@Matrimid Mixed-Matrix Membrane

The mixed-gas permeation performance of neat Matrimid membranes and MIL-101Cr MMMs were investigated with a binary gas mixture of CO_2 and CH_4. Mixed-gas studies instead of single-gas studies are preferred, since the ideal selectivities from single-gas studies can differ from those of mixed-gases due to gas interaction and plasticization effects (Dechnik et al., 2017b). Plasticization describes the effect that the permeability of both gases increases and the selectivity decreases. This is due to an increase in the segmental motion of polymer chains at high feed pressures caused by the presence of one or more gas sorbates (Wind et al., 2002), CO_2 in particular causes such plasticization, less so CH_4 or N_2. Previous investigations have shown that glassy polymer membranes, including Matrimid, undergo plasticization phenomena only with pressures well above 10 bar (Ismail and Lorna, 2002). No plastization of Matrimid has been reported at a feed pressure of 4 bar where we operated. Comparison of single-gas permeation with CO_2 and CH_4 to mixed-gas permeation with a 50:50 v:v CO_2/CH_4 mixture at otherwise nearly unchanged conditions for a [$Co_4(\mu_4$-$O)(Me_2pzba)_3$]-MOF@Matrimid-MMM revealed only a slightly reduced permeability for the latter mixed-gas measurement. At the used transmembrane pressure of 3 bar plasticization could be ruled out (Dechnik et al., 2017c).

Neat Matrimid membranes and MIL-101Cr@Matrimid MMMs were fabricated with different loadings of the MOF (8, 16, and 20 or 24 wt.%). For comparison, nanoMIL-101Cr from direct emulsion with sodium oleate and microMIL-101Cr from conventional hydrothermal conditions were used to prepare nanoMIL-101Cr@Matrimid MMMs and microMIL-101Cr@Matrimid MMMs, respectively. For the MMM fabrication chosen amounts of MOF and Matrimid (**Table 2**) were first mixed with dichloromethane, DCM, and stirred, before the suspension was casted into metal rings. After covering the rings with funnels and evaporation of the solvent (**Figure S24**), the membranes were detached, tailored, dried and stored. The detailed procedure is described in **Supplementary Material**.

A major difference was already noticed for the preparation of the highly loaded MMMs where it was not possible to produce microMIL-101Cr-MMMs with 24 wt.% MOF because of their extreme brittleness (**Figures S24B,C**). Hence, we could only produce and measure microMIL-101Cr@Matrimid MMMs with 8, 16, and 20 wt.% MOF loading.

The XRD diffractogram of pure Matrimid shows a broad reflection around $2\theta = 20^\circ$ with low intensity based on the semi-crystalline structure (Amooghin et al., 2015). For MMMs, all the intense reflections of MIL-101Cr and the broad reflection of Matrimid can be observed (**Figure S25A**). The MIL-101 reflections confirm that the MOF material were not affected by the preparation of the membranes. For details regarding the infrared analysis of the MMMs see **Figure S26**.

SEM images in combination with energy-dispersive X-ray spectroscopy (EDX) of cross-sections of the membranes confirm the homogeneous distribution of nanoMIL-101Cr particles (**Figure 6**). The uniform distribution is due to the organic-inorganic structure of the MOF filler particles, which disperse well within the continuous polymer phase. SEM images of cross-sections and EDX of the membranes fabricated with conventional synthesized microMIL-101Cr are shown in **Figure S26**. Even larger microMIL-101Cr in Matrimid MMMs lead also to a homogeneous distribution in the polymer matrix.

Mixed-Gas Permeation Performance

The mixed-gas permeation performance of neat Matrimid membranes and mixed-matrix membranes were investigated with a binary gas mixture of CO_2 and CH_4. Before the measurement, the membranes were again heated for 1 h in a vacuum oven at 150°C. The results for the permeability and selectivity for the MIL-101Cr@Matrimid membranes are shown in **Table 3** and **Figure 7**.

Nano- and microMIL-101Cr@Matrimid MMMs show a similar rise in CO_2 and CH_4 permeability with increasing MOF loading. Furthermore, within the measurement error margin the selectivity remains unaltered for all measured MMMs. By comparing our results for CO_2 and CH_4 permeability with already published results (**Table S2**) it can be noticed, that with our nanoMIL-101Cr mixed-matrix membranes we have achieved very high CO_2 and CH_4 permeability results with an almost steady selectivity. By taking into account the results for selectivity of the already published studies it is obvious that their

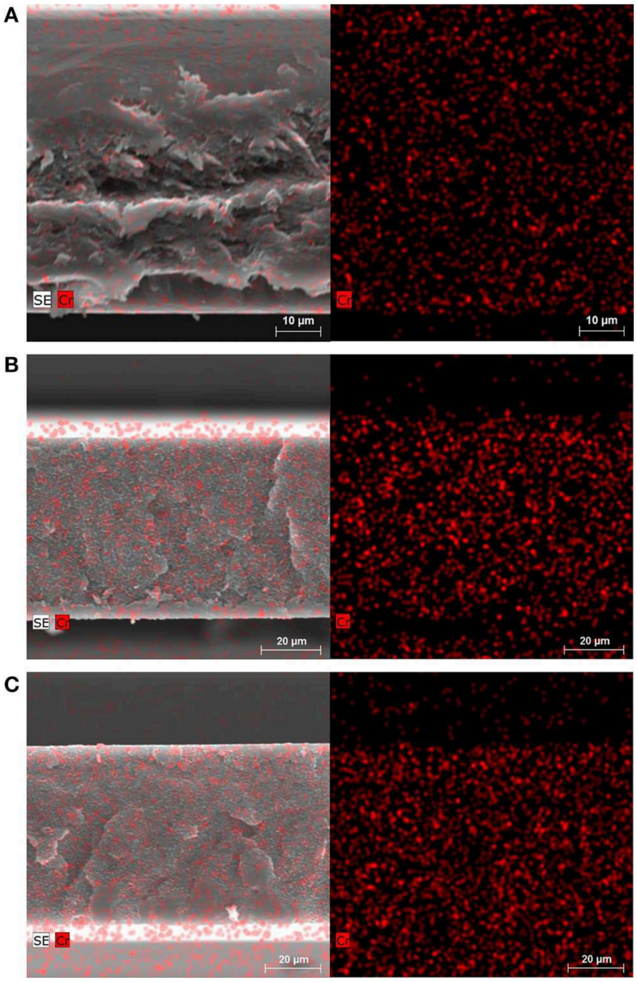

FIGURE 6 | SEM/EDX images of the cross-section of nanoMIL-101Cr@Matrimid membrane with 8 wt.% MOF **(A)**, 16 wt.% MOF **(B)**, and 24 wt.% MOF **(C)**. Left: SEM/EDX images superimposed. Right: EDX element mapping (Cr = red). The bottom of the cross-sections in the image corresponds to the bottom of the membrane when casted. The cross-section of a pure Matrimid membrane is shown in **Figure S25B**. Dark and light areas around cross-section of membranes depend on mounting on SEM sample holder (see **Figure S2**).

selectivity results are sometimes high sometimes low without any correlation concerning the MOF loading. Therefore, the achievement of almost steady selectivity without great changes is worth to be mentioned.

However, we note again that it was not possible to produce MMMs with 24 wt.% microMIL-101Cr. The CO_2 permeability increased from about 6 Barrer for pure Matrimid to over 31 Barrer for the 24 wt.% nanoMIL-101Cr membrane, but to only 21 Barrer for the 20 wt.% microMIL-101Cr membrane. Thus, at 24 wt.% loading of nanoMIL-101Cr, the permeability of the membrane for both gases increased almost five times with respect to the pure Matrimid membrane. However, at 20 wt.% loading of microMIL-101Cr, the permeability for both gases increased only three times with respect to the pure Matrimid membrane. The permeability increase can be traced to the added free fractional volume, which is introduced by the incorporation of the porous MIL-101Cr filler particles. Furthermore, one can observe only a negligible reduction in the CO_2/CH_4 selectivity of around 36 for both MOF variations.

For comparison, single-gas and mixed-gas permeation measurements for CO_2/CH_4 separation of different MOF@Matrimid and MIL-101Cr@polymer MMMs are collected in **Table S2**. The CO_2 permeability and CO_2/CH_4 selectivity of the membranes fabricated in this study together with MOF@Matrimid MMMs from the literature are summarized in a Robeson chart (**Figure 8**). From this chart it is obvious that MMMs with MIL-101Cr@Matrimid compare well in performance with already published results. Yet, the nanoMIL-101Cr-MMM with 24 wt.% surpasses all other MOF@Matrimid MMMs in its CO_2 permeability even though some of these other MOF-MMMs have MOF weight percentages of 30 or even 40 wt.% (Zhang et al., 2008; Perez et al., 2009; Naseri et al., 2015; Rajati et al., 2018).

Modeling

Figure 9 shows the comparison between predicted Maxwell and Bruggeman model (see **Supplementary Material** for details) and experimental relative CO_2 permeabilities for nanoMIL-101Cr@Matrimid MMMs. The very high pore volume of 1.32 $cm^3\ g^{-1}$ for nanoMIL-101Cr results in a low crystal density (0.451 $g^{-1}\ cm^{-3}$) and therefore the values of the weight percentages of 8, 16, and 24 wt.% roughly double when converted into filler volume fraction. Thus, MMMs loaded with 8, 16, and 24 wt.% MOF give a filler volume of 0.18, 0.32, and 0.45, respectively. We note, that for an effective increase in permeability the filler volume fraction (ϕ_d) is of high relevance and is more important than the usually given wt.% loading of the membrane. Further, the filler volume fraction for a highly porous material is largely determined by the free volume (pore volume) of the filler. As found in earlier work (Nuhnen et al., 2018) we can hypothesize again that a high pore volume is decisive for MOFs to yield high permeable MMMs. The relative CO_2 permeabilities for the MMMs with lower filler loadings follow exactly the predicted values for the Maxwell model. This is in good agreement with previous studies, where composite membranes for filler loadings up to 0.2 and even slightly above mostly follow the Maxwell model (Nuhnen et al., 2018). For higher filler loadings above 0.2 the relative CO_2 permeabilities starts to deviate from the Maxwell model and approach the calculated values based on the Bruggeman model. Since the Maxwell model does not consider filler-filler particle interaction, it is not suitable for filler loadings significantly above 0.2. In contrary the Bruggeman model is explicitly used for higher filler loadings in MMMs and also considers the effects of filler-filler particle interactions (Shen and Lua, 2013). Hence, the permeation data displays a good agreement for both models in their respective filler loading range. Relative CH_4 permeabilities show the same trend (**Figure S28**).

A comparison between the predicted Maxwell and Bruggeman model and the experimental relative CO_2 and CH_4 permeabilities for microMIL-101Cr@Matrimid MMMs,

TABLE 3 | Summary of gas permeation properties of nanoMIL-101Cr@Matrimid and MIL-101Cr@Matrimid membranes for a 50:50 v:v gas mixture of CO_2 and CH_4.[a]

MOF	Membrane Thickness[c] (μm)	MIL-101 loading	*P* (CO_2) (Barrer)[b]	*P* (CH_4) (Barrer)[b]	S (CO_2/CH_4)[b]
–	59-60	Pure matrimid	6.6 ± 0.3	0.18 ± 0.01	36 ± 3
NanoMIL-101Cr	68-70	8 wt.%	10.8 ± 0.4	0.28 ± 0.01	39 ± 3
	69-79	16 wt.%	17.0 ± 0.7	0.47 ± 0.02	36 ± 3
	78-88	24 wt.%	31.6 ± 0.2	0.93 ± 0.06	33 ± 2
MicroMIL-101Cr	67-69	8 wt.%	11.6 ± 0.6	0.31 ± 0.01	36 ± 4
	75-75	16 wt.%	15.2 ± 0.3	0.41 ± 0.01	37 ± 2
	70-81	20 wt.%	21.5 ± 0.1	0.58 ± 0.01	37 ± 3

[a] *At 25°C and a feed pressure of 4 bar. Each type of membrane was prepared and measured three times to provide reliable error estimates.*

[b] *Error margins for CO_2 and CH_4 permeabilities were deduced from measurement uncertainties of the three investigated membranes. Error margins for the CO_2/CH_4 selectivity were calculated by error propagation, that is, by summation of the relative errors of the permeabilities.*

[c] *Each membrane was measured at 10 different places using a thickness measuring device.*

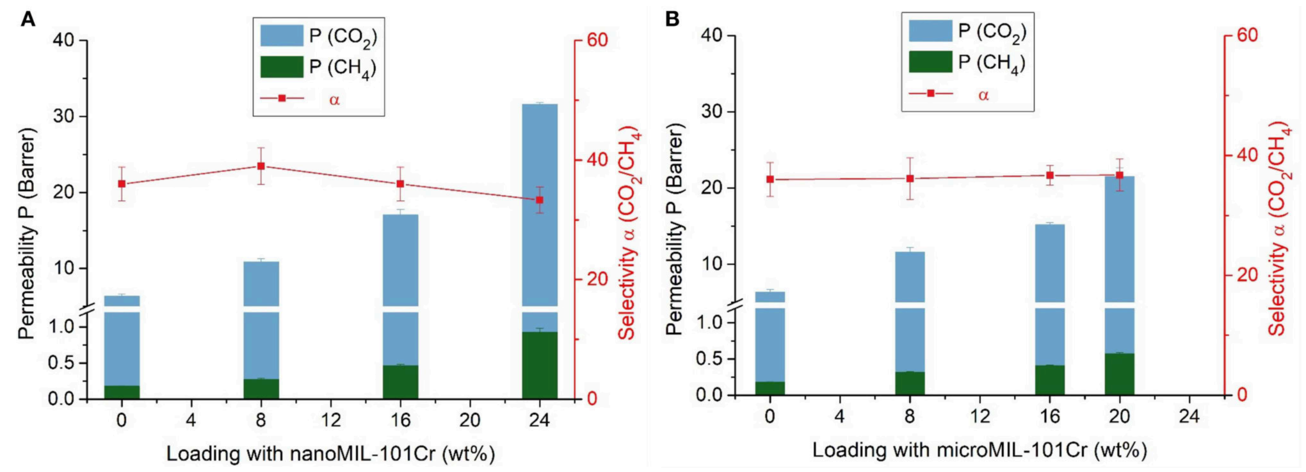

FIGURE 7 | Separation properties of nanoMIL-101Cr@Matrimid **(A)** and microMIL-101Cr@Matrimid **(B)** MMMs with different MOF loadings for a 50:50 v:v gas mixture of CO_2 and CH_4 at 25°C and a feed pressure of 4 bar. Error bars of the permeability correspond to measurement uncertainties of the three investigated membranes; error bars of the selectivity were calculated via error propagation, that is, by summation of the relative errors of the permeabilities.

presented in **Figures S29, S30**, yields slightly different results. For lower filler volumes the experimental data follows the Maxwell model and with rising filler volume it only slightly surpasses the values calculated for the Maxwell model, but does not reach the calculation derived by the Bruggeman model. For the studied MMMs it is observed, that the filler volume fraction, where filler-filler particle interactions influence the permeation performance in a significant manner, is somewhere between 0.35 and 0.45. In this range of the filler volume fraction the permeability starts to rise sharply. This shows in the permeation performance of nanoMIL-101Cr@Matrimid MMMs, which is superior to the regular microMIL-101Cr@Matrimid MMMs, as it is possible to reach higher filler volume fractions to achieve this sharp rise in permeability.

Another way to analyze permeation properties, is to take a look at the so called Free Fractional Volume (FFV). The FFV is defined as the sum of the volume weighted FFV of the polymer and the volume weighted FFV of the filler (Equation 1).

$$(Total)\ FFV = FFV_{polymer} \cdot \phi_c + FFV_{filler} \cdot \phi_d$$

Whereby the FFV of the polymer can be deduced by the Bondi method, which is described in detail in the literature and was determined as 0.17 for Matrimid (Huang et al., 2006; Kanehashi et al., 2015). The FFV of the filler can be calculated by multiplying the pore volume of the MOF, here obtained by nitrogen sorption of nanoMIL-101Cr and microMIL101-Cr, with the density of the MOF, to yield a dimensionless entity. Equation (2) shows the correlation of the FFV and the permeability *P*:

$$P = A_p \cdot \exp^{(-\frac{B_p}{FFV})}$$

After linearization:

$$\lg P = \lg A_p - \frac{B_p}{2.303FFV}$$

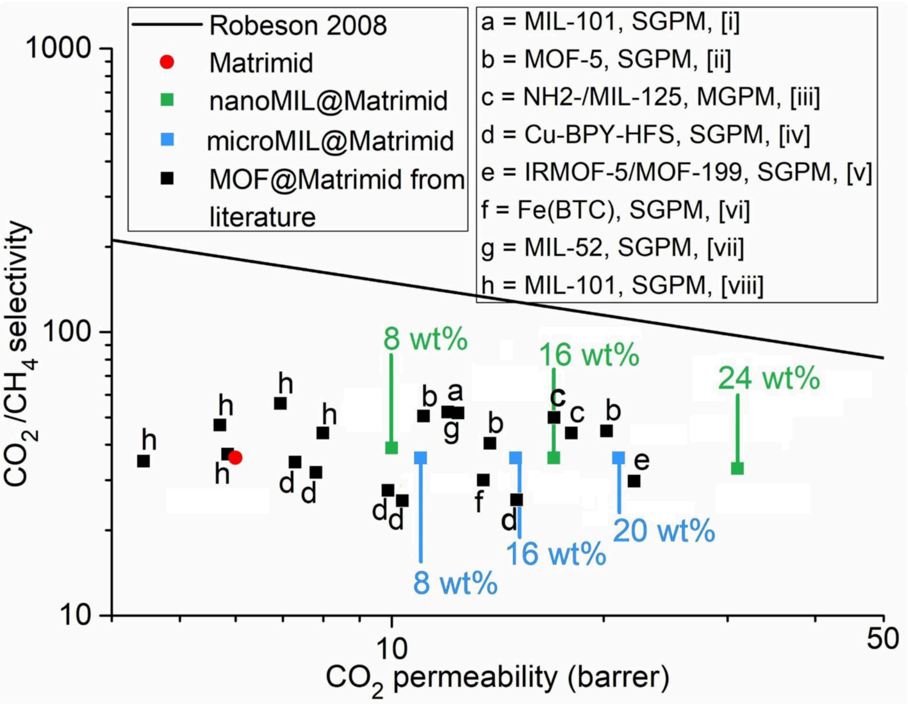

FIGURE 8 | CO_2/CH_4 separation performance of nanoMIL-101Cr@Matrimid (green), microMIL-101Cr@Matrimid (light blue), and neat Matrimid (red) compared with published results for mixed-matrix membranes based on MOF@Matrimid (black). The upper bound for polymer performances as defined by Robeson in 2008 is given as a black line (Robeson, 2008). SGPM = single-gas permeation measurement. MGPM, mixed-gas permeation measurement. References: a, (Rajati et al., 2018); b, (Perez et al., 2009); c, (Anjum et al., 2016); d, (Zhang et al., 2008); e, (Nik et al., 2012); f, (Shahid and Nijmeijer, 2014); g, (Dorosti et al., 2014); and h, (Naseri et al., 2015).

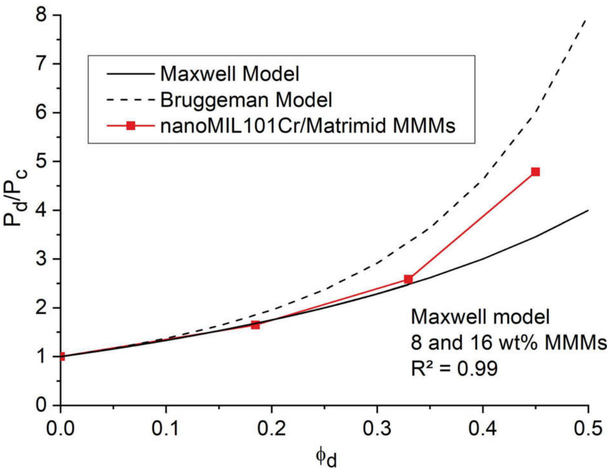

FIGURE 9 | Relative experimental CO_2 permeabilities (referenced to the permeability P_c of the pure polymer membrane) for nanoMIL-101Cr@Matrimid (red curve) with different filler volume fraction ϕ_d. The black solid line gives the theoretical CO_2 permeabilities for porous fillers based on the Maxwell Model and the black dashed line gives the theoretical CO_2 permeabilities for porous fillers based on the Bruggeman Model.

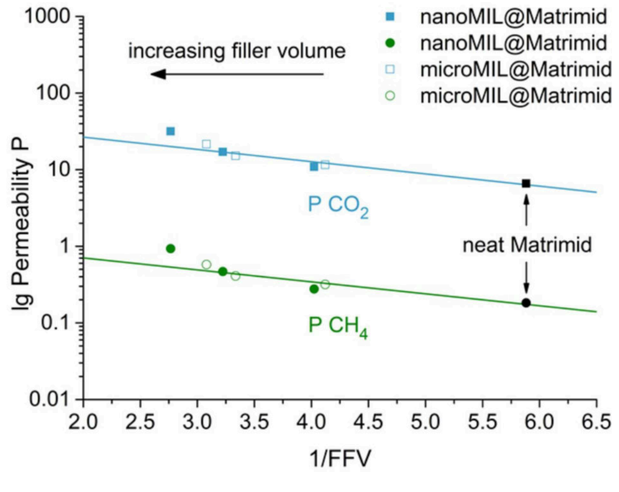

FIGURE 10 | Experimental CO_2 and CH_4 permeabilities of nano- and microMIL-101Cr@Matrimid MMMs as a function of the inverse FFV. The neat polymer has 1/FFV = 5.9, the 20 wt.% microMIL-MMMs has 1/FFV = 3.1, the 24 wt.% nanoMIL-MMM has 1/FFV = 2.8. The added straight lines are intended as guides to the eye.

Hence, lg P plotted against the inverse FFV should give a linear correlation with slope – $B_p/2.303$ and intercept lg A_p. if indeed the FFV determines the permeability. **Figure 10** shows the plot of lg P vs. 1/FFV for the nano- and microMIL-101Cr@Matrimid MMMs. As the FFV rises with increasing filler volume, the inverse FFV decreases. For filler volumes between 0 and 16 wt.% MOF the reduction of the inverse FFV and the rise in permeability show a good linear correlation, displayed by the straight line. The nanoMIL-MMM with 24 wt.% MOF however, has a higher than expected permeability. This is in good agreement with the previous observation that for MMMs with 24 wt.% filler loading a sharp increase in permeability takes place which leads to a significant deviation from the used FFV model. As it seems, similar to the Maxwell model, the FFV model is no longer applicable for MMMs with higher filler loadings, where filler-filler interaction starts to occur. Such filler-filler interaction would add an additional FFV (yielding an even smaller 1/FFV value). A similar effect could be observed in the work of Kanehashi et al. (2015) were they plotted lg*P* vs. 1/FFV for several MOFs and carbons materials. For example, a Cu-BTC MMMs with the highest filler loadings of 30 wt.% showed a distinct increase in CO_2 and CH_4 permeability compared to the given 1/FFV (Kanehashi et al., 2015).

CONCLUSION

In summary, we demonstrated that the size of MIL-101Cr can be adjusted in the nano-micro-range below 100 nm by using microwave heating in combination with a direct emulsion technique, surfactants, and ultrasonication. Direct emulsion with the phase-inversion-temperature method and sodium oleate as surfactant yielded nanoMIL-101Cr particles of <100 nm and high apparent BET-surface areas (2,900 m^2 g^{-1}) in good yields (45%). Furthermore, we observed, that with increasing reaction time and temperature, the particles became more crystalline and showed higher N_2 uptakes, as well as larger total pore volumes. Thereby we prepared nanoMIL-101Cr for application as a filler in mixed-matrix membranes. The use of nanoMIL-101Cr in Matrimid MMMs allowed for the preparation of 24 wt.% filler MMMs compared to a maximum of 20 wt.% for microMIL-101Cr in order to still have a defect-free membrane. The increased filler amount improved the gas permeability. Permeation modeling studies based on the Maxwell model and the free fractional volumes indicate a significant permeability increase beyond the 20 wt.% filler content. Our approach, to surpass the normally obtainable filler wt.% fraction by a nanosized filler in a mechanically still stable membrane, is a promising result with wider implications.

DATA AVAILABILITY STATEMENT

All datasets generated for this study are included in the article/**Supplementary Material**.

AUTHOR CONTRIBUTIONS

IG synthesized, fabricated the nano, microsized MOF as well as the mixed-matrix-membranes, performed, discussed the powder X-ray diffraction, nitrogen physisorption, infrared experiments, and wrote the manuscript. AN performed, discussed the mixed-gas permeation, and wrote the manuscript part concerning the mixed-matrix-membranes. AL performed, discussed the DLS experiments, and results given by the 3D LS spectrometer. SN and MKl performed the scanning electron microscopy, SEM, and EDX analysis. AH contributed the idea of emulsion and microwave heating based synthesis of MIL-101 and ran pilot tests. MKa and CJ proofread and refined the manuscript.

FUNDING

The authors acknowledge the Center for Advanced Imaging (Cai, Heinrich-Heine-University) for access to the TEM instruments and the financial support of the Federal German Ministry of Education and Research (BMBF) in the project Optimat under grant no. 03SF0492C. AL and MK acknowledge financial support from the German Research Foundation (DFG) through the project KA 3880/3-1. The open access publication fee was covered from a library fund at the Heinrich-Heine-Universität Düsseldorf.

SUPPLEMENTARY MATERIAL

The Supplementary Material for this article can be found online at: https://www.frontiersin.org/articles/10.3389/fchem.2019.00777/full#supplementary-material

REFERENCES

Abedini, R., Omidkhah, M., and Dorosti, F. (2014). Highly permeable poly(4-methyl-1-pentyne)/NH_2-MIL 53 (Al) mixed matrix membrane for CO_2/CH_4 separation. *RSC Adv.* 4, 36522-36537. doi: 10.1039/C4RA07030E

Amooghin, A. E., Mashhadikhan, S., Sanaeepur, H., Moghadassi, A., Matsuura, T., and Ramakrishna, S. (2019). Substantial breakthroughs on function-led design of advanced materials used in mixed matrix membranes (MMMs): a new horizon for efficient CO_2 separation. *Progr. Mater. Sci.* 102, 222–295. doi: 10.1016/j.pmatsci.2018.11.002

Amooghin, A. E., Omidkhah, M., and Kargari, A. (2015). Enhanced CO_2 transport properties of membranes by embedding nano-porous zeolite particles into Matrimid®5218 matrix. *RSC Adv*. 5, 8552–8565. doi: 10.1039/C4RA14903C

Anjali, T. G., and Basavaraj, M. G. (2018). Influence of pH and salt concentration on pickering emulsions stabilized by colloidal peanuts. *Langmuir* 34, 13312-13321. doi: 10.1021/acs.langmuir.8b02913

Anjum, M. W., Bueken, B., De Vos, D., and Vankelecom, I. F. (2016). MIL-125(Ti) based mixed matrix membranes for CO_2 separation from CH_4 and N_2. *J. Membr. Sci*. 502, 21–28. doi: 10.1016/j.memsci.2015.12.022

Ansaloni, L., Minelli, M., Giacinti Baschetti, M., and Sarti, G. C. (2015). Effects of thermal treatment and physical aging on the gas transport properties in matrimid. *Oil Gas Sci. Technol.* 70, 367–379. doi: 10.2516/ogst/2013188

Azar, A. N. V., and Keskin, S. (2018). Computational screening of MOFs for acetylene separation. *Front. Chem*. 6:36. doi: 10.3389/fchem.2018.00036

Baloch, M. K., and Hameed, G. (2005). Emulsification of oil in water as affected by different parameters. *J. Colloid Interf. Sci*. 285, 804-813. doi: 10.1016/j.jcis.2004.11.070

Batten, S. T., and Robson, R. (1998). Interpenetrating nets: ordered, periodic entanglement. *Angew. Chem. Int. Ed. Engl.* 37, 1460–1494. doi: 10.1002/(sici)1521-3773(19980619)37:11<1460::aid-anie1460>3.0.co;2-z

Benton, W. J., Raney, K. H., and Miller, C. A. (1986). Enhanced videomicroscopy of phase transitions and diffusional phenomena in oil-water-nonionic surfactant systems. *J. Colloid Interf. Sci*. 110, 363-388. doi: 10.1016/0021-9797(86)90390-5

Beyzavi, M. H., Stephenson, C. J., Liu, Y., Karagiaridi, O., Hupp, J. T., and Farha, O. K. (2015). Metal–organic framework-based catalysts: chemical fixation of CO_2 with epoxides leading to cyclic organic carbonates. *Front. Energy Res*. 2:63. doi: 10.3389/fenrg.2014.00063

Bogdal, D. (2006). *Microwave-Assisted Organic Synthesis*. New York, NY: Elsevier.

Bouma, R. H. B., Checchetti, A., Chidichimo, G., and Drioli, E. (1997). Permeation through a heterogeneous membrane: the effect of the dispersed phase. *J. Membr. Sci*. 128, 141-149. doi: 10.1016/S0376-7388(96)00303-1

Cao, A. (2003). Light Scattering. Recent applications: light scattering, recent applications. *Anal. Lett*. 36, 3185-3225. doi: 10.1081/AL-120026567

Carr, C. S., and Shantz, D. F. (2005). Non-ionic-microemulsion mediated growth of zeolite A. *Microporous Mesoporous Mater*. 85, 284-292. doi: 10.1016/j.micromeso.2005.06.029

Carreon, M., Dahe, G., Feng, J., and Venna, S. R. (2017). "Chapter 1: mixed matrix membranes for gas separation applications," in *World Scientific Series in Membrane Science and Technology: Biological and Biomimetic Applications, Energy and the Environment*, ed M. A. Carreon (Singapore: World Scientific Publishing Co. Pte. Ltd.), 1–57.

Chen, B., Wang, L., Xiao, Y., Fronczek, F. R., Xue, M., Cui, Y., et al. (2009). A luminescent metal–organic framework with lewis basic pyridyl sites for the sensing of metal ions. *Angew. Chem. Int. Ed*. 48, 500-503. doi: 10.1002/anie.200805101

Chowdhury, P., Mekala, S., Dreisbach, F., and Gumma, S. (2012). Adsorption of CO, CO_2 and CH_4 on Cu-BTC and MIL-101 metal organic frameworks: Effect of open metal sites and adsorbate polarity. *Microporous Mesoporous Mater*. 152, 246-252. doi: 10.1016/j.micromeso.2011.11.022

Datta, A. K., and Sen, P. K. (2006). Optimization of membrane unit for removing carbon dioxide from natural gas. *J. Membr. Sci*. 283, 291–300. doi: 10.1016/j.memsci.2006.06.043

de la Iglesia, O., Sorribas, S., Almendro, E., Zornoza, B., Tellez, C., and Coronas, J. (2016). Metal-organic framework MIL-101(Cr) based mixed matrix membranes for esterification of ethanol and acetic acid in a membrane reactor. *Renew. Energ*. 88, 12-19. doi: 10.1016/j.renene.2015.11.025

Dechnik, J., Gascon, J., Doonan, C. J., Janiak, C., and Sumby, C. J. (2017a). Mixed-matrix membranes. *Angew. Chem. Int. Ed*. 56, 9292–9310. doi: 10.1002/anie.201701109

Dechnik, J., Nuhnen, A., and Janiak, C. (2017c). Mixed-matrix membranes of the air-stable MOF-5 analog $[Co_4(\mu_4\text{-}O)(Me_2pzba)_3]$ with mixed-functional pyrazolate-carboxylate linker for CO_2/CH_4 separation. *Cryst. Growth Des*. 17, 4090–4099. doi: 10.1021/acs.cgd.7b00202

Dechnik, J., Sumby, C. J., and Janiak, C. (2017b). Enhancing mixed-matrix membrane performance with metal–organic framework additives. *Cryst. Growth Des*. 17, 4467-4488. doi: 10.1021/acs.cgd.7b00595

Diring, S., Furukawa, S., Takashima, Y., Tsuruoka, T., and Kitagawa, S. (2010). Microwave-assisted synthesis of well-shaped UiO-66-NH_2 with high CO_2 adsorption capacity. *Chem. Mater*. 22, 4531-4538. doi: 10.1021/cm101778g

Dorosti, F., Omidkhah, M., and Abedini, R. (2014). Fabrication and characterization of Matrimid/MIL-53 mixed matrix membrane for CO_2/CH_4 separation. *Chem. Eng. Res. Des*. 92, 2439–2448. doi: 10.1016/j.cherd.2014.02.018

Du, S., Li, F., Sun, Q., Wang, N., Jia, M., and Yu, J. (2016). A green surfactant-assisted synthesis of hierarchical TS-1 zeolites with excellent catalytic properties for oxidative desulfurization. *Chem. Commun*. 52, 3368-3371. doi: 10.1039/C5CC08441E

Eddaoudi, M., Moler, D. B., Li, H., Chen, B., Reineke, T. M., O'Keeffe, M., et al. (2001). Modular chemistry: secondary building units as a basis for the design of highly porous and robust metal-organic carboxylate frameworks. *Acc. Chem. Res*. 34, 319–330. doi: 10.1021/ar000034b

Erucar, I., and Keskin, S. (2018). High-throughput molecular simulations of metal organic frameworks for CO_2 separation: opportunities and challenges. *Front. Mater*. 5:4. doi: 10.3389/fmats.2018.00004

Faramawy, S., Zaki, T., and Sakr, A. A. E. (2016). Natural gas origin, composition, and processing: a review. *J. Natural Gas Sci. Engin*. 34, 34–54. doi: 10.1016/j.jngse.2016.06.030

Férey, G. (2000). Building units design and scale chemistry. *J. Solid State Chem*. 152, 37–48. doi: 10.1006/jssc.2000.8667

Férey, G., Draznieks, C. M., Serre, C., Millange, F., Dutour, J., Surble, S., et al. (2005). A chromium terephthalate-based solid with unusually large pore volumes and surface area. *Science* 309, 2040-2042. doi: 10.1126/science.1116275

Galema, S. A. (1997). Microwave chemistry. *Chem. Soc. Rev*. 26, 233-238. doi: 10.1039/CS9972600233

García-Márquez, A., Demessence, A., Platero-Prats, A. E., Heurtaux, D., Horcajada, P., Serre, C., et al. (2012). Metal-organic framework MIL-101(Cr) based mixed matrix membranes for esterification of ethanol and acetic acid in a membrane reactor. *Eur. J. Inorg. Chem*. 2012, 5165-5174. doi: 10.1002/ejic.201200710

Gelb, L. D., Gubbins, K. E., Radhakrsihan, R., and Sliwinska-Bartowiak, M. (1999). Phase separation in confined systems. *Rep. Prog. Phys*. 62, 1573-1659. doi: 10.1088/0034-4885/62/12/201

Horcajada, P., Gref, R., Baati, T., Allan, P. K., Maurin, G., Couvreur, P., et al. (2012). Metal–organic frameworks in biomedicine. *Chem. Rev*. 112, 1232-1268. doi: 10.1021/cr200256v

Horcajada, P., Surbl,é, S., Serre, C., Hong, D.-Y., Seo, Y.-K., Chang, J.-S., et al. (2007). Synthesis and catalytic properties of MIL-100(Fe), an iron(III) carboxylate with large pores. *Chem. Commun*. 27, 2820-2822. doi: 10.1039/B704325B

Huang, A., Wan, L., and Caro, J. (2018). Microwave-assisted synthesis of well-shaped UiO-66-NH_2 with high CO_2 adsorption capacity. *Res. Bull*. 98, 308-313. doi: 10.1016/j.materresbull.2017.10.038

Huang, L., Wang, H., Chen, J., Wang, Z., Sun, J., Zhao, D., et al. (2003). Synthesis, morphology control, and properties of porous metal–organic coordination polymers. *Microporous Mesoporous Mater*. 58, 105-114. doi: 10.1016/S1387-1811(02)00609-1

Huang, X.-X., Qiu, L.-G., Zhang, W., Yuan, Y.-P., Jiang, X., Xie, A.-J., et al. (2012). Hierarchically mesostructured MIL-101 metal–organic frameworks: supramolecular template-directed synthesis and accelerated adsorption kinetics for dye removal. *CrystEngComm* 14, 1613-1617. doi: 10.1039/C1CE06138K

Huang, Y., Wang, X., and Paul, D. R. (2006). Physical aging of thin glassy polymer films: free volume interpretation. *J. Membr. Sci*. 277, 219–229. doi: 10.1016/j.memsci.2005.10.032

Ismail, A. F. and Lorna, W. (2002). Penetrant-induced plasticization phenomenon in glassy polymers for gas separation membrane. *Sep. Purif. Technol*. 27, 173–194. doi: 10.1016/S1383-5866(01)00211-8

Izquierdo, P., Esquena, J., Tadros, T. F., Dederen, C., Garcia, M. J., and Azemar, N., et al. (2002). Formation and stability of nano-emulsions prepared using the phase inversion temperature method. *Langmuir* 18, 26-30. doi: 10.1021/la010808c

Janiak, C., and Henninger, S. K. (2013). Kühlen mit Sonnenlicht. *Nachr. Chem*. 61, 520-523. doi: 10.1002/nadc.201390159

Jiang, D., Burrows, A. D., and Edler, K. J. (2011a). Size-controlled synthesis of MIL-101(Cr) nanoparticles with enhanced selectivity for CO_2 over N_2. *CrystEngComm* 12, 6916-6919. doi: 10.1039/C1CE06274C

Jiang, D., Mallat, T., Krumreich, F., and Baiker, A. (2011b). Polymer-assisted synthesis of nanocrystalline copper-based metal–organic framework for amine oxidation. *Catal. Commun*. 12, 602-605. doi: 10.1016/j.catcom.2010.12.010

Kale, S. N., and Deore, S. L. (2017). Emulsion micro emulsion and nano emulsion: a review. *Sys. Rev. Pharm*. 8, 39-47. doi: 10.5530/srp.2017.1.8

Kanehashi, S., Chen, G. Q., Scholes, C. A., Ozcelik, B., Hua, C., Ciddor, L., et al. (2015). Enhancing gas permeability in mixed matrix membranes through tuning the nanoparticle properties. *J. Membr. Sci*. 482, 49–55. doi: 10.1016/j.memsci.2015.01.046

Khan, N. A., Haquea, E., and Jhung, S. H. (2010). Rapid syntheses of a metal–organic framework material $Cu_3(BTC)_2(H_2O)_3$ under microwave: a quantitative analysis of accelerated syntheses. *Phys. Chem. Chem. Phys*. 12, 2625-2631. doi: 10.1039/B921558A

Khan, N. A., and Jhung, S. H. (2015). Synthesis of metal-organic frameworks (MOFs) with microwave or ultrasound: rapid reaction, phase-selectivity, and size reduction. *Coord. Chem. Rev*. 285, 11–23. doi: 10.1016/j.ccr.2014.10.008

Khan, N. A., Kang, I. J., Seok, H. Y., and Jhung, S. H. (2011). Facile synthesis of nano-sized metal-organic frameworks, chromium-benzenedicarboxylate, MIL101. *Chem. Eng. J*. 166, 1152-1157. doi: 10.1016/j.cej.2010.11.098

Kitagawa, S., and Kondo, M. (1998). Functional micropore chemistry of crystalline metal complex-assembled compounds. *Bull. Chem. Soc. Jpn*. 71, 1739–1753. doi: 10.1246/bcsj.71.1739

Kozlov, N.K., Natashina, U.A., Tamarov, K.P., Gongalsky, M.B., Solovyev, V.V., Kudryavtsev, A.A., et al. (2017). Recycling of silicon: from industrial waste to biocompatible nanoparticles for nanomedicine. *Mater. Res. Express* 4, 1–6. doi: 10.1088/2053-1591/aa8c33

Kundu, P., Agrawal, A., Mateen, H., and Mishra, I. M. (2013). Stability of oil-in-water macro-emulsion with anionic surfactant: effect of electrolytes and temperature. *Chem. Eng. Sci*. 102, 176-185. doi: 10.1016/j.ces.2013.07.050

Li, J.-R., Kuppler, R. J., and Zhou, H.-C. (2009). Selective gas adsorption and separation in metal–organic frameworks. *Chem. Soc. Rev*. 38, 1477-1504. doi: 10.1039/B802426J

Lin, W., Rieter, W. J., and Taylor, K. M. L. (2009). Modular synthesis of functional nanoscale coordination polymers. *Angew. Chem. Int. Ed*. 48, 650-658. doi: 10.1002/anie.200803387

Liu, G., Chernikova, V., Liu, Y., Zhang, K., Belmabkhout, Y., Shekhah, O., et al. (2018). Mixed matrix formulations with MOF molecular sieving for key energy-intensive separations. *Nat. Mater*. 17, 283–289. doi: 10.1038/s41563-017-0013-1

Mahajan, R., and Koros, W. J. (2002). Mixed matrix membrane materials with glassy polymers. Part 1. *Polym. Eng. Sci*. 42, 1420-1431. doi: 10.1002/pen.11041

Mei, Z., Liu, S., Wang, L., Jiang, J., Xu, J., and Sun, D. (2011). Preparation of positively charged oil/water nano-emulsions with a sub-PIT method. *J. Colloid Interf. Sci*. 361, 565-572. doi: 10.1016/j.jcis.2011.05.011

Miricioiu, M. G., Iacob, C., Nechifor, G., and Niculescu, V.-C. (2019). High selective mixed membranes based on mesoporous MCM-41 and MCM-41-NH_2 particles in a polysulfone matrix. *Front. Chem*. 7:332. doi: 10.3389/fchem.2019.00332

Naseri, M., Mousavi, S. F., Mohammadi, T., and Bakhtiari, O. (2015). Synthesis and gas transport performance of MIL-101/Matrimid mixed matrix membranes. *J. Ind. Eng. Chem*. 29, 249–256. doi: 10.1016/j.jiec.2015.04.007

Nik, O. G., Chen, X. Y., and Kaliaguine, S. (2012). Functionalized metal organic framework-polyimide mixed matrix membranes for CO2/CH4 separation. *J. Membr. Sci*. 4213, 48–61. doi: 10.1016/j.memsci.2012.04.003

Nuhnen, A., Dietrich, D., Millan, S., and Janiak, C. (2018). Role of filler porosity and filler/polymer interface volume in metal–organic framework/polymer mixed-matrix membranes for gas separation. *ACS Appl. Mater. Interfaces* 10, 33589-33600. doi: 10.1021/acsami.8b12938

Pal, R. (2008). Permeation models for mixed matrix membranes. *J. Colloid. Interface Sci*. 317, 191-198. doi: 10.1016/j.jcis.2007.09.032

Perez, E. V., Balkus, J.r,., K. J., and Ferraris, J. P., Musselman, I.H. (2009). Mixed-matrix membranes containing MOF-5 for gas separations. *J. Membr. Sci*. 328, 165–173. doi: 10.1016/j.memsci.2008.12.006

Rajati, H., Navarchian, A. H., and Tangestaninejad, S. (2018). Preparation and characterization of mixed matrix membranes based on matrimid/PVDF blend and MIL-101(Cr) as filler for CO_2/CH_4 separation. *Chem. Eng. Sci*. 185, 92–104. doi: 10.1016/j.ces.2018.04.006

Rieter, W. J., Taylor, K. M. L., An, H., Lin, W., and Lin, W. (2006). Nanoscale metal–organic frameworks as potential multimodal contrast enhancing agents. *J. Am. Chem. Soc*. 128, 9024-9025. doi: 10.1021/ja0627444

Robeson, L. M. (1991). Correlation of separation factor versus permeability for polymeric membranes. *J. Membr. Sci*. 62, 165-185. doi: 10.1016/0376-7388(91)80060-J

Robeson, L. M. (2008). The upper bound revisited. *J. Membr. Sci*. 320, 390-400. doi: 10.1016/j.memsci.2008.04.030

Rodenas, T., Luz, I., Prieto, G., Seoane, B., Miro, H., Corma, A., et al. (2015). Metal–organic framework nanosheets in polymer composite materials for gas separation. *Nat. Mater*. 14, 48–55. doi: 10.1038/NMAT4113

Roonasi, P., Yang, X., and Holmgren, A. (2010). Competition between sodium oleate and sodium silicate for a silicate/oleate modified magnetite surface studied by in situ ATR-FTIR spectroscopy. *J. Colloid Interf. Sci*. 343, 546-552. doi: 10.1016/j.jcis.2009.12.002

Sajjadi, S., Jahanzad, F., and Yianneskis, M. (2004). Catastrophic phase inversion of abnormal emulsions in the vicinity of the locus of transitional inversion. *Colloids Surf. A* 240, 149-155. doi: 10.1016/j.colsurfa.2004.03.012

Salvia-Trujillo, L., Artiga-Artigas, M., Molet-Rodríguez, A., Turmo-Ibarzand, A., and Martín-Belloso, O. (2018). Emulsion-based nanostructures for the delivery of active ingredients in foods. *Front. Sustain. Food Syst*. 2:79. doi: 10.3389/fsufs.2018.00079

Seoane, B., Coronas, J., Gascon, I., Etxeberria Benavides, M., Karvan, O., Caro, J., et al. (2015). Metal–organic framework based mixed matrix membranes: a solution for highly efficient CO_2 capture? *Chem. Soc. Rev*. 44, 2421-2454. doi: 10.1039/C4CS00437J

Shahid, S., and Nijmeijer, K. (2014). High pressure gas separation performance of mixed-matrix polymer membranes containing Highmesoporous FE(BTC). *J. Membr. Sci*. 459, 33–44. doi: 10.1016/j.memsci.2014.02.009

Shen, T., Luo, J., Zhang, S., Luo, X., and Environ, J. (2015). Hierarchically mesostructured MIL-101 metal–organic frameworks with different mineralizing agents for adsorptive removal of methyl orange and methylene blue from aqueous solution. *Chem. Eng*. 3, 1372-1383. doi: 10.1016/j.jece.2014.12.006

Shen, Y., and Lua, A. C. (2013). Theoretical and experimental studies on the gas transport properties of mixed matrix membranes based on polyvinylidene fluoride. *AIChE J*. 59, 4715–4726. doi: 10.1002/aic.14186

Shinoda, K., and Saito, H. (1969). The stability of O/W type emulsions as functions of temperature and the HLB of emulsifiers: the emulsification by PIT-method. *J. Colloid Interface Sci*. 30, 258-263. doi: 10.1016/S0021-9797(69)80012-3

Sorribas, S., Zornoza, B., Téllez, C., and Coronas, J. (2014). Mixed matrix membranes comprising silica-(ZIF-8) core–shell spheres with ordered meso–microporosity for natural- and bio-gas upgrading. *J. Membr. Sci*. 452, 184-192. doi: 10.1016/j.memsci.2013.10.043

Su, D., and Zhong, Q. X. (2016). Lemon oil nanoemulsions fabricated with sodium caseinate and Tween 20 using phase inversion temperature method. *J. Food Eng*. 171, 214-221. doi: 10.1016/j.jfoodeng.2015.10.040

Tanh Jeazet, H. B., Staudt, C., and Janiak, C. (2012). Metal–organic frameworks in mixed-matrix membranes for gas separation. *Dalton Trans*. 41, 14003-14027. doi: 10.1039/C2DT31550E

Taylor, K. M. L., Rieter, W. J., and Lin, W. (2008). Manganese-based nanoscale metal–organic frameworks for magnetic resonance imaging. *J. Am. Chem. Soc*. 130, 14358–14359. doi: 10.1021/ja803777x

Thommes, M., Kaneko, K., Neimark, A. V., Olivier, J. P., Rodriguez-Reinoso, F., Rouquerol, J., et al. (2015). Physisorption of gases, with special reference to the evaluation of surface area and pore size distribution (IUPAC Technical Report). *Pure Appl. Chem*. 87, 1051–1069. doi: 10.1515/pac-2014-1117

Wang, S., McGuirk, C. M., d'Aquino, A., Mason, J. A., and Mirkin, C. A. (2018). Metal–Organic Framework Nanoparticles. *Adv. Mater*. 30, 1-14. doi: 10.1002/adma.201800202

Whitby, C. P., Lotte, L., and Lang, C. (2012). Structure of concentrated oil-in-water pickering emulsions. *Soft Matter* 8, 7784–7789. doi: 10.1039/C2SM26014J

Wind, J. D., Staudt-Bickel, C., Paul, D. R., and Koros, W. J. (2002). The effects of crosslinking chemistry on CO_2 plasticization of polyimide gas separation membranes. *Ind. Eng. Chem. Res*. 41, 6139–6148. doi: 10.1021/ie0204639

Wu, Y. S., Ngai, S. C., Goh, B. H., Chan, K. G., Lee, L. H., and Chuah, L. H. (2017). Anticancer activities of surfactin and potential application of nanotechnology assisted surfactin delivery. *Front. Pharmacol*. 8:761. doi: 10.3389/fphar.2017.00761

Wuttke, S., Braig, S., Prei,ß, T., Zimpel, A., Sicklinger, J., Bellomo, C., et al. (2015). MOF nanoparticles coated by lipid bilayers and their uptake by cancer cells. *Chem. Commun*. 51, 15752-15755. doi: 10.1039/C5CC06767G

Yaghi, O. M., Li, H., Davis, C., Richardson, D., and Groy, T. L. (1998). Synthetic strategies, structure patterns, and emerging properties in the chemistry of modular porous solids. *Acc. Chem. Res*. 31, 474-484. doi: 10.1021/ar970151f

Yaghi, O. M., O'Keeffe, M., and Kanatzidis, M. G. (2000). Design of solids from molecular building blocks: golden opportunities for solid state chemistry. *J. Solid State Chem*. 152, 1–2. doi: 10.1006/jssc.2000.8733

Yaghi, O. M., O'Keeffe, M., Ockwig, N. W., Chae, H. K., Eddaoudi, M., and Kim, J. (2003). Reticular synthesis and the design of new materials. *Nature* 423, 705-714. doi: 10.1038/nature01650

Yang, J., Zhao, Q., Li, J., and Dong, J. (2010). Synthesis of metal–organic framework MIL-101 in TMAOH-$Cr(NO_3)_3$-H_2BDC-H_2O and its hydrogen-storage behavior. *Microporous Mesoporous Mater*. 130, 174-179. doi: 10.1016/j.micromeso.2009.11.001

Yeo, Z. Y., Chew, T. L., Zhu, P. W., Mohamed, A. R., and Chai, S.-P. (2012). Conventional processes and membrane technology for carbon dioxide removal from natural gas: a review. *J. Nat. Gas Chem*. 21, 282–298. doi: 10.1016/S1003-9953(11)60366-6

Zhang, Y., Musselman, I. H., Ferraris, J. P., and Balkus, K. J. Jr. (2008). Gas permeability properties of matrimid (R) membranes containing the metal-organic framework Cu-BPY-HFS. *J. Membr. Sci.* 313, 170–181. doi: 10.1016/j.memsci.2008.01.005

Zhao, T., Jeremias, F., Boldog, I., Nguyen, B., Henninger, S. K., and Janiak, C. (2015). High-yield, fluoride-free and large-scale synthesis of MIL-101(Cr). *Dalton Trans*. 44, 16791-16801. doi: 10.1039/C5DT02625C

Zhao, T., Li, S. H., Shen, L., Wang, Y., and Yang, X. Y. (2018). The sized controlled synthesis of MIL-101(Cr) with enhanced CO_2 adsorption property. *Inorg. Chem. Commun*. 96, 47-51. doi: 10.1016/j.inoche.2018.07.036

Zornoza, B., Gorgojo, P., Casado, C., Tellez, C., and Coronas, J. (2011). Mixed matrix membranes for gas separation with special nanoporous fillers. *Desalin. Water Treat*. 27, 42-47. doi: 10.5004/dwt.2011.2045

Zornoza, B., Tellez, C., Coronas, J., Gascon, J., and Kapteijn, F. (2013). Metal organic framework based mixed matrix membranes: An increasingly important field of research with a large application potential. *Microporous Mesoporous Mater*. 166, 67-78. doi: 10.1016/j.micromeso.2012.03.012

Conflict of Interest: The authors declare that the research was conducted in the absence of any commercial or financial relationships that could be construed as a potential conflict of interest.

4. Zusammenfassung

In einer ersten Arbeit wurde poröses Aluminium Fumarat (Al-Fum) im Submikrometerbereich gemäß der Literatur synthetisiert. Nicht-poröses Al-Fum(DMSO) wurde durch Erhitzen von Al-Fum in DMSO erhalten und mit verschiedenen Methoden charakterisiert. Sowohl die porösen, als auch die nicht-porösen Aluminium Fumarat Füllstoffe, wurden in eine Matrimid-Matrix eingebettet, wodurch die gleiche Füllstoff-Polymer Schnittstelle entstand. REM-Bilder in Kombination mit EDX-Mapping zeigten eine weitgehend homogene Füllstoffverteilung für alle MMMs. Die CO_2/CH_4-Trennleistungen machten entgegengesetzte Effekte für poröse und nicht-poröse Füllstoffe deutlich. MMMs mit dem porösen Füllstoff zeigten einen kontinuierlichen Anstieg von CO_2 und CH_4 Permeabilität, während MMMs mit dem nicht-porösen Füllstoff eine Abnahme der CO_2- und CH_4-Permeabilitäten mit steigendem Füllstoffgehalt aufwiesen. Diese Ergebnisse stimmen gut mit denen des Maxwell Modells überein, das eine Erhöhung der Gas-Permeabilität für poröse Füllstoffe bzw. eine Abnahme für nicht-poröse Füllstoffe vorhersagt. Die Zunahme und die Abnahme der Gas-Permeabilität scheint im Allgemeinen auf den Unterschied im Freien Fraktionellen Volumen (FFV) zurückführbar zu sein, das heißt, auf das erhöhte oder verringerte freie Volumen der Membran durch den Füllstoff. Das Grenzflächen Volumen zwischen Füllstoff und Polymer trägt hingegen nur zu ungefähr 10% des verfügbaren freien Volumens in den MMMs bei. Dies wird am offensichtlichsten in Bezug auf die Gas-Permeations-Ergebnisse der MMMs mit dem nicht-porösen Füllstoff im Vergleich zu dem gemessenem Grenzflächen Volumen. Trotz eines konstanten bis leicht wachsenden Grenzflächen Volumens für höhere Beladungen des nicht-porösen Füllstoffs nehmen die Gas-Permeabilitäten ab. Dies zeigt deutlich den vernachlässigbaren Effekt des Grenzflächen Volumens, sowohl absolut als auch relativ zum FFV. Die organische/anorganische Hybridstruktur der MOF Füllstoffe ermöglicht zudem eine gute Kompatibilität mit dem organischen Polymer, welche entscheidend ist, um fehlerfreie MMMs zu erhalten. Da das FFV entscheidend für die Gas-Permeabilität ist und sowohl vom Polymer als auch vom Füllstoff beeinflusst wird, sollten beide Materialien dementsprechend ausgewählt werden. Eine Erhöhung der Permeabilität erfordert hohe freie Volumina sowohl im Polymer als auch im MOF. Daher ist ein großes Porenvolumen der MOF Füllstoffe für hochpermeable MMMs entscheidend. Im Vergleich mit anderen porösen Füllstoffen wie Zeolithen sollten MOFs nicht nur wegen ihrer besseren Kompatibilität mit organischen Polymeren Zeolithen gegenüber überlegen sein, sondern auch wegen ihrer höheren Porenvolumina. Weiterhin kann eine Abweichung in der Linearität zwischen FFV und Permeabilität ein guter Indikator für eine unzureichende Kompatibilität zwischen MOF und Polymer sein, die schließlich zur Bildung von nicht selektivem Grenzflächen Volumen führt und sich durch einen Anstieg der Permeabilität und teilweisem Verlust der Selektivität bemerkbar macht.

In der Untersuchung von ausgewählten MOFs für die Rauchgasentschwefelung zeigte MOF-177 eine Rekordaufnahme von SO_2 über 25,7 $mmol \cdot g^{-1}$ bei 293 K und 1 bar, erwies sich jedoch als ungeeignet für die Anwendung in der Rauchgasentschwefelung aufgrund seiner chemischen Instabilität und geringen Adsorptionsleistung bei niedrigen Partialdrücken von SO_2. NH_2-MIL-125(Ti) zeigte vielversprechende Eigenschaften in der berechneten Selektivität aus der *ideal adsorbed solution theory* (IAST) und in Durchbruchssimulationen bei Anwendungsbedingungen für die SO_2-Aufreinigung. Die Untersuchung von MIL-160 offenbarte herausragenden Eigenschaften hinsichtlich der SO_2/CO_2-Selektivität, der Durchbruchszeit und Stabilität gegenüber SO_2 unter trockenen und feuchten Bedingungen. Im Durchbruchsexperiment, zeigte MIL-160 eine Rückhaltung von SO_2 für mindestens 500 min g^{-1} aus einer typischen Abgaszusammensetzung der luftbefeuerten Kohleverbrennung, auch bei erhöhten Temperaturen (bis 353 K). In weiteren Studien sollte für praktische Trennanwendungen auf eine frühe Gasaufnahme bei sehr niedrigem Partialdruck geachtet werden, da diese für eine gute Trennleistung von höherer Relevanz ist, als eine hohe Gesamtaufnahme bei höheren Drücken. Das gilt besonders, wenn das Gas, das abgetrennt werden soll, in einer geringen Volumenfraktion vorhanden ist, wie es bei SO_2 im Rauchgas mit weniger als 500 ppm nach der Kalksteinwäsche, der Fall ist. Die IAST-basierte SO_2-Selektivität von MIL-160 gegenüber anderen Gasen (CO_2 und N_2) liegt auf dem Niveau von führenden Benchmark-MOFs. Darüber hinaus weist MIL-160 eine außergewöhnliche chemische Stabilität sowohl unter trockener als auch unter feuchter SO_2-Exposition auf, die MIL-160 zusammen mit der etablierten, günstigen, grünen und leicht skalierbaren Synthese zu einem vielversprechenden Material für die Anwendung in der Rauchgasentschwefelung macht.

In weiterführenden Studien wurden Hochleistungs-MMMs zur Gastrennung durch Kombination des Polyimids 6FDA-mPD und nano- bis mikrokristalliner Partikel der MOFs MIL-101(Cr) oder MOF-199 (HKUST-1, Cu-BTC) erhalten. Die MOF-Partikel zeigten eine gute Kompatibilität mit der Polymermatrix und die resultierenden Membranen waren frei von Grenzflächendefekten. Es wurde gezeigt, dass die MMMs zu einem signifikanten Anstieg in der CO_2-Permeabilität sowie der CO_2/CH_4-Selektivität für die MOF-199@6FDA-mPD-MMMs führten. Die erhebliche Steigerung der Permeabilität für die MIL-101(Cr)@6FDA-mPD-MMMs kann auf das hohe Porenvolumen in MIL-101(Cr) zurückgeführt werden. Die bemerkenswerte und unerwartete Erhöhung der Selektivität für die MOF-199-MMMs wurde anhand der Porenblockierung und Reduzierung der MOF-Fenstergröße durch das Polyimid, zusammen mit der hohen Adsorption von CO_2 durch MOF-199 begründet. Weitere Untersuchungen sind jedoch erforderlich, um eine bessere Aufklärung der Permeations-Mechanismen und der Selektivitäts-Eigenschaften, bezogen auf die intrinsischen Gastransporteigenschaften, die Rolle der Füllstoffbeladung, Geometrie, Porengröße und die Art der molekularen Wechselwirkungen bei der bevorzugten Adsorption, bei der Verwendung von MOFs als Füllstoffe in MMMs, zu erreichen.

Die isostere Adsorptionsenthalpie (ΔH_{ads}) ist ein wichtiger Parameter in Adsorptionsprozessen von porösen Materialien. ΔH_{ads} kann sehr einfach anhand der Messung von zwei Adsorptionsisothermen bestimmt werden und liefert als Funktion der Bedeckung (adsorbierte Menge, n) $\Delta H_{\mathrm{ads}}(n)$ eine Aussage über die Bindungsstärke zwischen Adsorbat und Adsorbens, abhängig von der Beladung. Um plausible Enthalpien bei einer Beladung nahe Null zu erhalten ($\Delta H_{\mathrm{ads}}^0$), sollte der experimentelle Sorptionsanalysator, in Niederdruckregimen ($p/p_0 < 0{,}001$ oder $p_{\mathrm{absolute}} < 1{,}0$ mbar) arbeiten können, um Datenpunkte bei geringer Aufnahme aufzeichnen zu können. Die anschließenden Kurvenanpassungen der experimentellen Sorptionsisothermen dürfen nicht unterhalb oder oberhalb der gemessenen Datenpunkte extrapoliert werden, da die ermittelte Adsorptionsenthalpie $\Delta H_{\mathrm{ads}}^0$ direkt mit dem niedrigsten gemessenen Aufnahmedatenpunkt verbunden ist. Das Anpassungsverfahren der Isothermen ist für die Bestimmung der isosteren Adsorptionsenthalpie essenziell. Die Virial Analyse ist dem Freundlich-Langmuir-Fit/Clausius-Clapeyron-Ansatz überlegen, um aussagekräftige $\Delta H_{\mathrm{ads}}^0$-Werte zu erhalten, weil die Freundlich-Langmuir-Anpassung für Datenpunkte mit geringer Aufnahme stark abweichen kann, ohne dass dies auf Anhieb sichtbar ist. Daher sollte die Qualität der Anpassung in einem logarithmisch-skalierten n gegen p Diagramm überprüft werden. Für eine Virial-Anpassung ist es zwingend erforderlich geringe Standardabweichungen der erhaltenen Virial-Koeffizienten sicherzustellen. Im Allgemeinen kann die abgeleitete isostere Adsorptionsenthalpie nur so genau bestimmt werden, wie die aufgezeichneten Adsorptionsisothermen und die angewendete Anpassung dies ermöglichen. Mit Hilfe dieser Arbeit soll der Leser befähigt werden sinnvolle und nachvollziehbare isostere Adsorptionsenthalpien zu bestimmen, basierend auf eigenen Berechnungen, um nicht von schlecht dokumentierten und undurchsichtigen Adsorptionsenthalpien abgeleitet von der Software der Soprtionsanalysatoren abhängig zu sein.

Abschließend wurde ein poröser organischer Käfig (CB6) über eine Imprägnierungsmethode in die Nanoporen von MIL-101(Cr) eingeschlossen, um das Wirt-in-Wirt-Adsorbens (auf engl. *Host-in-Host adsorbent*) CB6@MIL-101(Cr) zu erhalten. Dieses Kompositmaterial zeigte eine deutlich verbesserte Leistung bezüglich der selektiven CO_2-Adsorption und -Trennung bei niedrigen Drücken. Die Anwendung des Wirt-in-Wirt-Konzepts kann durch die Einlagerung eines breiten Spektrums von POCs, in poröse kristalline Materialien wie MOFs, entweder durch in-situ-Zusammensetzung des Wirts und des MOFs, oder durch Imprägnierungsmethoden, erweitert werden. Dadurch können zukünftig verbesserte, poröse Materialien entstehen, die die Vorzüge aus zwei Materialklassen, wie die maßgeschneiderten intrinsischen Poren zur effektiven Adsorption und spezifischen Trennung von Molekülen der porösen organischen Moleküle und die Robustheit der hochgeordneten Strukturen funktionaler MOFs kombinieren.

Anhang

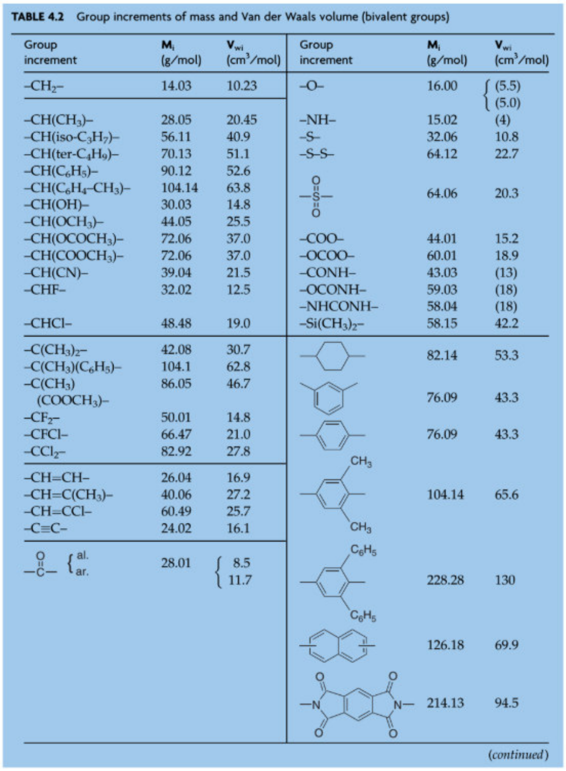

TABLE 4.2 Group increments of mass and Van der Waals volume (bivalent groups)

Group increment	M_i (g/mol)	V_{wi} (cm³/mol)	Group increment	M_i (g/mol)	V_{wi} (cm³/mol)
$-CH_2-$	14.03	10.23	$-O-$	16.00	(5.5) (5.0)
$-CH(CH_3)-$	28.05	20.45	$-NH-$	15.02	(4)
$-CH(iso\text{-}C_3H_7)-$	56.11	40.9	$-S-$	32.06	10.8
$-CH(ter\text{-}C_4H_9)-$	70.13	51.1	$-S-S-$	64.12	22.7
$-CH(C_6H_5)-$	90.12	52.6			
$-CH(C_6H_4-CH_3)-$	104.14	63.8	$-\overset{O}{\overset{\|}{\underset{\underset{O}{\|}}{S}}}-$	64.06	20.3
$-CH(OH)-$	30.03	14.8			
$-CH(OCH_3)-$	44.05	25.5			
$-CH(OCOCH_3)-$	72.06	37.0	$-COO-$	44.01	15.2
$-CH(COOCH_3)-$	72.06	37.0	$-OCOO-$	60.01	18.9
$-CH(CN)-$	39.04	21.5	$-CONH-$	43.03	(13)
$-CHF-$	32.02	12.5	$-OCONH-$	59.03	(18)
			$-NHCONH-$	58.04	(18)
$-CHCl-$	48.48	19.0	$-Si(CH_3)_2-$	58.15	42.2
$-C(CH_3)_2-$	42.08	30.7		82.14	53.3
$-C(CH_3)(C_6H_5)-$	104.1	62.8			
$-C(CH_3)(COOCH_3)-$	86.05	46.7		76.09	43.3
$-CF_2-$	50.01	14.8			
$-CFCl-$	66.47	21.0		76.09	43.3
$-CCl_2-$	82.92	27.8			
$-CH{=}CH-$	26.04	16.9			
$-CH{=}C(CH_3)-$	40.06	27.2		104.14	65.6
$-CH{=}CCl-$	60.49	25.7			
$-C{\equiv}C-$	24.02	16.1			
$-\overset{O}{\overset{\|}{C}}-$ al. ar.	28.01	8.5 11.7			
				228.28	130
				126.18	69.9
				214.13	94.5

(*continued*)

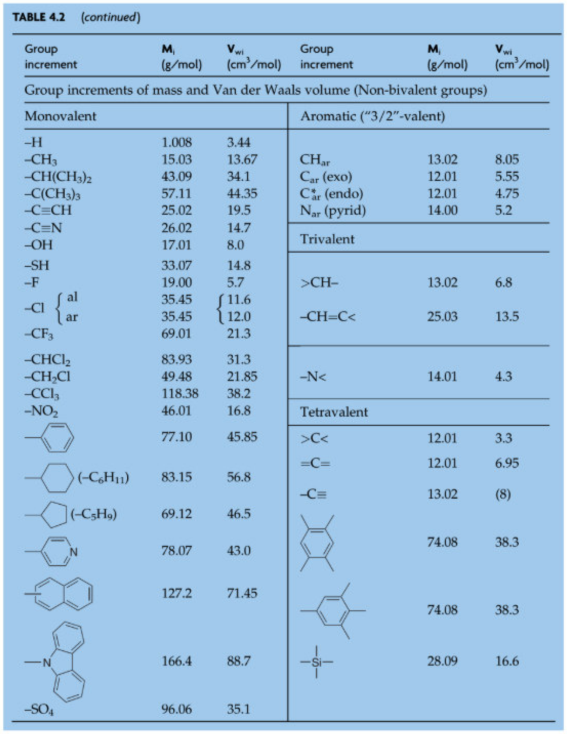

TABLE 4.2 (*continued*)

Group increment	M_i (g/mol)	V_{wi} (cm³/mol)	Group increment	M_i (g/mol)	V_{wi} (cm³/mol)
Group increments of mass and Van der Waals volume (Non-bivalent groups)					
Monovalent			Aromatic ("3/2"-valent)		
$-H$	1.008	3.44			
$-CH_3$	15.03	13.67	CH_{ar}	13.02	8.05
$-CH(CH_3)_2$	43.09	34.1	C_{ar} (exo)	12.01	5.55
$-C(CH_3)_3$	57.11	44.35	C^{*}_{ar} (endo)	12.01	4.75
$-C{\equiv}CH$	25.02	19.5	N_{ar} (pyrid)	14.00	5.2
$-C{\equiv}N$	26.02	14.7			
$-OH$	17.01	8.0	Trivalent		
$-SH$	33.07	14.8			
$-F$	19.00	5.7	$>CH-$	13.02	6.8
$-Cl$ al	35.45	11.6			
ar	35.45	12.0	$-CH{=}C<$	25.03	13.5
$-CF_3$	69.01	21.3			
$-CHCl_2$	83.93	31.3			
$-CH_2Cl$	49.48	21.85	$-N<$	14.01	4.3
$-CCl_3$	118.38	38.2			
$-NO_2$	46.01	16.8	Tetravalent		
	77.10	45.85	$>C<$	12.01	3.3
			$=C=$	12.01	6.95
$(-C_6H_{11})$	83.15	56.8			
			$-C{\equiv}$	13.02	(8)
$(-C_5H_9)$	69.12	46.5			
				74.08	38.3
	78.07	43.0			
	127.2	71.45			
				74.08	38.3
	166.4	88.7		28.09	16.6
$-SO_4$	96.06	35.1			

Abbildung 25: Tabelle der Massen und Volumina ausgewählter Moleküle und chemischer Gruppen, basierend auf Literatur 97. Nachdruck mit Genehmigung von Ref. 97. Copyright 1968 John Wiley and Sons.

Abbildungsverzeichnis

Literaturverzeichnis

[1] W. C. Zeise, *Mag. Pharm.*, **1830**, 35, 105.
[2] L. L. Böhm, *Angew.Chem.*, **2003**,115, 5162–5183.
[3] G. A. Ozin, *Adv. Mater.*, **1992**, 4, 612–649.
[4] E. Davis, *Acc. Chem. Res.*, **1993**, 26, 111–115.
[5] R. M. Barrer, *Proc. R. Soc. Lond. A*, **1938**, 167, 392–420.
[6] E. O. Wigg, A. J. Juhola, *J. Am. Chem. Soc.*, **1949**, 71, 2, 561–568.
[7] M. Hunger, J. Karger, H. Pfeifer, J. Caro, B. Zibrowius, M. Bulow, R. Mostowicz, *J. Chem. Soc.*, *Faraday Trans*. 1, **1987**, 83, 3459–3468.
[8] K. Yamagishi, S. Namba, T. Yashima, *J. Phys. Chem.*, **1991**, 95, 872–877.
[9] B. F. Hoskins, R. Robson, *J. Am. Chem. Soc.,* **1989**, 111, 5962–5964.
[10] B. F. Hoskins, R. Robson, *J. Am. Chem. Soc.,* **1990**, 112, 1546–1554.
[11] O. M. Yaghi, H. Li, *J. Am. Chem. Soc.,* **1995**, 117, 10401–10402.
[12] M. Kondo, T. Yoshitomi, H. Matsuzaka, S. Kitagawa, K. Seki, *Angew. Chem. Int. Ed.,* **1997**, 36, 1725–1727.
[13] S. R. Batten, N. R. Champness, X.-M. Chen, J. Garcia-Martinez, S. Kitagawa, L. Ohrstrom, M. O'Keeffe, M. P. Suh, J. Reedijk, *Cryst. Eng. Comm.,* **2012**, 14, 3001–3004.
[14] S. R. Batten, N. R. Champness, X.-M. Chen, J. Garcia-Martinez, S. Kitagawa, L. Ohrstrom, M. O'Keeffe, M. P. Suh, J. Reedijk, J. *Pure Appl. Chem.,* **2013**, 85*,* 1715–1724.
[15] C. Janiak, J. K. Vieth, *New J. Chem.,* **2010**, 34, 2366–2388.
[16] K. S. W. Sing, *Pure Appl. Chem.,* **1985**, 57, 603–609.
[17] S. S Chui, S. M. Lo, J. P. Charmant, A. G. Orpen, I. D. Williams, *Science,* **1999**, 283, 1148–1150.
[18] O. M. Yaghi, H. Li, M. Eddaoudi, M. O'Keeffe, *Nature,* **1999**, 402, 276–279.
[19] O. M. Yaghi, H. Li, C. Davis, D. Richardson, T. L. Groy, **1998**, Acc. Chem. Res., 31, 474–484.
[20] S. T. Batten, R. Robson, *Angew. Chem. Int. Ed.*, **1998**, 37, 1460–1494.
[21] R. Haldar, N. Sikdar, T. K. Maji, *Materials Today*, **2015**, 18, 97–116.
[22] W. M. Meier, D. H. Olson, "Atlas of Zeolite Structure Types", Butterworths, London, **1987**.
[23] G. Férey, *J. Solid State Chem.,* **2000**, 152, 37–48.
[24] M. Eddaoudi, D. B. Moler, H. Li, B. Chen, T. M. Reineke, M. O'Keeffe, *Acc. Chem. Res.*, **2001**, 34, 319–330.
[25] O. M. Yaghi, M. O'Keeffe, N. W. Ockwig, H. K. Chae, M. Eddaoudi, M., J. Kim, *Nature*, **2003**,423, 705–714.
[26] M. Eddaoudi, J. Kim, N. Rosi, D. Vodak, J. Wachter, M. O'Keeffe, O. M. Yaghi, *Science,* **2002**, 295, 469–472.
[27] Z. Mai, D. Liu, *Cryst. Growth Des.*, **2019**, 19, 7439–7462.
[28] H. Furukawa, Y. B. Go, N. Ko, Y. K. Park, F. J. Uribe-Romo, J. Kim, M. O'Keeffe, O. M. Yaghi, *Inorg. Chem.*, **2011**, 50, 9147–9152.
[29] O. K. Farha, I. Eryazici, N. C. Jeong, B. G. Hauser, C. E. Wilmer, A. A. Sarjeant, R. Q. Snurr, S. T. Nguyen, A. Ö Yazaydın, J. T. Hupp, *J. Am. Chem. Soc.*, **2012**, 134, 15016–15021.
[30] H. Furukawa, N. Ko, Y. B. Go, N. Aratani, S. B. Choi, E. Choi, A. Ö. Yazaydin, R. Q. Snurr, M. O'Keeffe, L. Kim, O. M. Yaghi, *Science,* **2010**, 329, 424–428.
[31] O. K. Farha, O. A. Yazaydin, I. Eryazici, C. D. Malliakas, B. G. Hauser, M. G. Kanatzidis, S. T. Nguyen, R. Q. Snurr, J. T. Hupp, *Nat. Chem.,* **2010**, 2, 944–948.
[32] I. M. Hönicke, I. Senkovska, V. Bon, I. A. Baburin, N. Bönisch, S. Raschke, J. D. Evans, S. Kaskel, *Angew. Chem. Int. Ed.*, **2018**, 57, 13780–13783.
[33] N. Stock, S. Biswas, *Chem. Rev.*, **2012**, 112, 933–969.
[34] O. K. Farha, J. T. Hupp, *Acc. Chem. Res.,* **2010**, 43, 1166–1175.
[35] G. Ferey, C. Mellot-Draznieks, C. Serre, F. Millange, J. Dutour, S. Surble, I. Margiolaki, *Science,* **2005**, 309, 2040–2042.
[36] J. H. Cavka, S. Jakobsen, U. Olsbye, N. Guillou, C. Lamberti, S. Bordiga, K. P. Lillerud, *J. Am. Chem. Soc.,* **2008**, 13850–13851.
[37] Y-R. Lee, J. Kim, W-S. Ahn, *Korean J. Chem. Eng.*, **2013**, 30, 1667–1680.
[38] S. H. Jhung, J. H. Lee. J. S. Chang, *Bull. Korean Chem. Soc.,* **2005**, 26, 880–881.
[39] J. Dechnik, A. Nuhnen, C. Janiak, *Cryst. Growth Des.*, **2017**, 17, 8, 4090–4099.
[40] W. J. Son, J. Kim, J. Kim, W. S. Ahn, *Chem. Commun.*, **2008**, 47, 6336–6338.
[41] U. Mueller, M. Schubert, F. Teich, H. Puetter, K. Schierle-Arndt, J. Pastre, *J. Mater. Chem.*, **2006**, 16, 626–636.

[42] A. Lazuen-Garay, A. Pichon, S. L. James, *Chem. Soc. Rev.,* **2007**, 36, 846–855.
[43] H. B. Tanh Jeazet, C. Staudt, C. Janiak, *Dalton Trans*., **2012**, 41, 14003–14027.
[44] Z. Zhang, Y. Zhao, Q. Gong, Z. Li, J. Li, *Chem. Commun.*, **2013**, 49, 653–661.
[45] K. Sumida, D. L. Rogow, J. A. Mason, T. M. McDonald, E. D. Bloch, Z. R. Herm, T.-H. Bae, J. R. Long, *Chem. Rev*., **2012**, 112, 724–781.
[46] J. Liu, P. K. Thallapally, B. P. McGrail, D. R. Brown, J. Liu, *Chem. Soc. Rev.*, **2012**, 41, 2308–2322.
[47] E. Hastürk, S-J. Ernst, C. Janiak, *Curr. Opin. in Chem. Eng*., **2019**, 24, 26–36.
[48] P. Horcajada, R. Gref, T. Baati, P. K. Allan, G. Maurin, P. Couvreur, G. Férey, R. E. Morris, C. Serre, *Chem. Rev.*, **2011**, 112, 1232–1268.
[49] D. Farrusseng, S. Aguado, C. Pinel, *Angew. Chem. Int. Ed.,* **2009**, 48, 7502–7513.
[50] J. Lee, O. K. Farha, J. Roberts, K. A. Scheidt, S. T. Nguyen, J. T. Hupp, *Chem. Soc. Rev.,* **2009**, 38, 1450–1459.
[51] Z. Hu, B. J. Deibert, J. Li, *Chem. Soc. Rev.,* **2014**, 43, 5815–5840.
[52] R. M. Barrer, F. R. S. Davies, J. A. Davies, *Proc. Roy. Soc. Lond. A.,* **1970**, 320, 289–308.
[53] D. M. Ruthven, *Nat. Phys. Sci*., **1971**, 232, 70–71.
[54] K. S. W. Sing, D. H. Everett, R. A.W. Haul, L. Moscou, R. A. Pierotti, J. Rouqerol, T. Siemieniewska, *Pure Appl. Chem*., **1985**, 57, 4,603–619.
[55] M. Thommes, K. Kaneko, A. V. Neimark, J. P. Olivier, F. Rodriguez-Reinso, J. Rouquerol, K. S. W. Sing, *Pure Appl. Chem*., **2015**, 87, 1051–1069.
[56] S. Brunauer, P. H. Emmett, E. Teller, *J. Am. Chem. Soc.,* **1938**, 60, 309–319.
[57] I. Langmuir, *J. Am. Chem. Soc.,* **1918**, 40, 1361–1403.
[58] J. Rouquerol, P. Llewellyn, F. Rouquerol., *Stud. Surf. Sci. Catal.,* **2007***,* 160, 49–56.
[59] F. Ambroz, T. J. Macdonald, V. Martis, I. P. Parkin, *Small Methods,* **2018**, 1800173.
[60] C. Hackett, K. D. Hammond, Microporous Mesoporous Mater., **2017**, 263, 231–235.
[61] M. Thommes, B. Smarsly, M. Groenewolt, P. I. Ravikovitch, A. V. Neimark, *Langmuir*, **2007**, 22, 756–764.
[62] S. Lowell, J. Shields, M. A. Thomas, M. Thommes, *Porosity and Density*, Springer, **2004**.
[63] J. H. de Boer, B. G. Linsen, T. van der Plas, G. J. Zondervan, *J. Catal*, **1965**, 4, 643–648.
[64] G. D. Halsey, *J. Chem. Phys*., **1948**, 16, 931–937.
[65] A. Galarneau, F. Villemot, J. Rodriguez, F. Fajula, B. Coasne, *Langmuir*, **2014**, 30, 13266–13274.
[66] R. Evans, U. M. B. Marconi, P. Tarzona, *J. Chem. Soc., Faraday Trans. 2*, **1986**, 82, 1763–1787.
[67] L. D. Gelb, K. E. Gubbins, R. Radhakrsihnan, M. Sliwinska-Bartowiak, *Rep. Prog. Phys*., **1999**, 62, 1573–1659.
[68] U.S. Environmental Protection Agency **2017**, Carbon Dioxide Emissions: Consequences of Carbon Emissions for Humans.
[69] Intergovernmental Panel on Climate Change (IPCC), Contribution of working groups I, II and III to the fifth assessment report of the Intergovernmental Panel on Climate Change, Climate Change 2014: Synthesis Report, **2014**, IPCC, Geneva, Switzerland.
[70] Z-Z. Yang, L-N. He, J. Gao, A-H. Liu, B. Yu, *Energy Environ. Sci.,* **2012**, 5, 6602–6639.
[71] K. T. Chue, J. N. Kim, Y. J. Yoo, S. H. Cho, R. T. Yang, *Ind. Eng. Chem. Res*., **1995**, 34, 591–598.
[72] N. Norahim, P. Yaisanga, K. Faungnawakij, T. Charinpanitkul, C. Klaysom, *Chem. Eng. Technol.,* **2018**, 41, 211–223.
[73] X. Lian, L. Xu, M. Chen, C. Wu, B. Huang, Y. Cui, *J. Nanosci. Nanotechnol.,* **2019**, 19, 3059–3078.
[74] K. Sumida, D. L. Rogow, J. A. Mason, T. M. McDonald, E. D. Bloch, Z. R. Herm, T-H. Bae, J. R. Long, *Chem. Rev.,* **2012**, 112, 724–781.
[75] A. K. Qaroush, K. I. Assaf, A. A. Al-Khateeb, F. Alsoubani, E. Nabih, C. Troll, B. Rieger, A. A. F. Eftaiha, *Energy Fuels*, **2017** 31, 8407–8414.
[76] S. Keskin, T. M. van Heest, D. S. Scholl, *ChemSusChem*., **2010**, 3, 879–891.
[77] J. Liu, P. K. Thallapally, B. P. McGrail, D. R. Brown, J. Liu, *Chem. Soc. Rev.,* **2012**, 41, 2308–2322.
[78] A. D. Weirsum, E. Soubeyrand-Lenoir, Q. Yang, B. Moulin, V. Guillerm, M. B. Yahia, S. Bourrelly, A. Vimont, S. Miller, C. Vagner, M. Daturi, C. Guillaume, C. Serre, G. Maurin, P. L. Llewellyn, *Chem. Asian J.*, **2011**, 6, 3270–3280.
[79] Q. Yang, A. D. Wiersum, P. L. Llewellyn, V. Guillerm, C. Serre, G. Maurin, *Chem. Commun*., **2011**, 47, 9603–9605.
[80] D. J. Darensbourg, W-C. Chung, K. Wang, H-C. Zhou, *Acs. Catal*., **2014**, 4, 1511–1515.
[81] Z. Bao; L. Yu, Q. Ren, X. Lu, S. J. Deng, *Colloid Interface Sci*., **2011**, 353, 549–556.
[82] S. Loeb, S. Sourirajan, *Advances in Chemistry,* **1963**, 28, 117–132.
[83] J. M. S. Henis, M.K. Tripodi, *Sep. Sci. Technol.,* **1980**,15, 1059–1068.
[84] P. Bernardo, G. Clarizia, *Chem. Eng. Trans*., **2013**, 32, 1999–2004.

[85] P. Bernardo, E. Drioli, G. Golemme G*, Ind. Eng. Chem. Res.,* **2009**, 48, 4638–4663.
[86] S. C. A. Kluiters, **2004**, Intermediate report EU project MIGREYD NNE5-2001-670, ECN-C-04-102. Ecn.nl/publications.
[87] A. Javid, *Chem Eng J*, **2005**, 112, 219–226.
[88] D. Sieffert, Dissertation, Heinrich-Heine-Universität Düsseldorf, Düsseldorf, Deutschland, **2013**.
[89] S. Li, J. G. Martinek, J. L. Falconer, R. D. Noble, T. Q. Gardner, *Ind. Eng. Chem. Res*., **2005**, 44, 3220–3228.
[90] M. L. Carreon, S. Li, M. A. Carreon, *Chem. Commun*., **2012**, 48,2310–2312.
[91] E. E. McLeay, J. C. Jansen, F. Kapteijn, *Microporous Mesoporous Mater*., **2006**, 90,198–220.
[92] S. P. Nunes, K-V. Pinemann, *Membrane technology in chemical industry*, Wiley-VCH, Weinheim, Deutschland, **2001**.
[93] W. J. Koros, G. K. Fleming, *J. Membr. Sci.,* **1993**, 83, 1–80.
[94] M. Kraume, T. Peters, *Chem. Ing. Tech*., **2005**, 77, 473–485.
[95]A. F. Ismail, K. C. Khulbe, T. Matsuura, *Gas Separation Membranes*, Springer, Heidelberg, Deutschland, **2015**.
[96] R. W. Baker, *Membrane Technology and Application*, Wiley-VCH, Chichester, England, **2004**.
[97] A. Bondi, *Physical Properties of Molecular Crystals, Liquids, and Glasses*, Wiley-VCH, New York, USA, **1968**.
[98] D. W. Van Krevelen, *Properties of Polymers*, Elsevier, Amsterdam, Niederlande, **1990**.
[99] L. Robeson, *J. Membr. Sci*., **1991**, 62, 165–185.
[100] L. Robeson, *J. Membr. Sci*., **2008**, 320, 390–400.
[101] J. Dechnik, J. Gascon, C. J. Doonan, C. Janiak, C. J. Sumby, *Angew. Chem. Int. Ed*., **2017**, 56, 9292–9310.
[102] D. R. Paul, D. R. Kemp, *J. Polym. Sci. Polym. Phys*., **1973**, 41, 79–93.
[103] S. Kulprathipanja, R. W. Neuzil, N. N. Li, Separation of fluids by means of mixed matrix membranes., US patent 4740219,**1988**.
[104] D. Q. Vu, W. J. Koros, S. J. Miller, *J. Membr. Sci*., **2003**, 211, 311–34.
[105] A. Torrisi, C. Mellot-Draznieks, R. G. Bell, *J. Chem. Phys.,* **2010**, 132, 044705.
[106] R. Banerjee, H. Furukawa, D. Britt, C. Knobler, M. O'Keeffe, O. M. Yaghi, *J. Am. Chem. Soc*., **2009**, 131, 3875–3877.
[107] T. C. Merkel, B. D. Freeman, R. J. Spontak, Z. He, I. Pinnau, P. Meakin, A. J. Hill, *Science,* **2002**, 296, 519–522.
[108] J. Ahn, W-J Chung, I. Pinnau, M. D. Guiver, *J. Membr. Sci.,* **2008**, 314, 123–133.
[109] M. Sadeghi, M. A. Semsarzadeh, M. Barikani, M. P. Chenar, *J. Membr. Sci*., **2011**, 376, 188–195.
[110] R. H. B. Bouma, A. Checchetti, G. Chidichimo, E. Drioli, *J. Membr. Sci.,* **1997**, 128, 141–149.
[111] G. Banhegyi, *Colloid Polym. Sci*., **1986**, 264, 1030–1050.
[112] Y. Shen, A. C. Lua, *AIChE J*., **2013**, 59, 4715–4726.
[113] J. M. Duval, Dissertation, University of Twente, Twente, Niederlande, **1995**.
[114] Y. Li, T. S. Chung, C. Cao, S. Kulprathipanja, *J Membr Sci,* **2005**, 260, 45–55.
[115] S. B. Tantekin-Ersolmaz, *J. Membr. Sci*., **2000**, 175, 285–288.
[116] C. Duan, X. Jie, H. Zhu, D. Liu, W. Peng, Y. Cao, J. Appl. Polym. Sci., **2018**, 135, 45728.
[117] R. Mahajan, Dissertation. Univeristy of Texas, Austin, USA, **2000**.
[118] T. S. Chung, L. Y. Jiang, Y. Li, S. Kulprathipanja, *Prog. Polym. Sci*., **2007**, 32, 483–507.
[119] R. M. Barrer, S. D. James, *J. Phys. Chem*., **1960**, 64, 417–421.
[120] I. F. J. Vankelecom, E. Mercks, M. Luts, J. B. Uytterhoeven, *J. Phys. Chem*., **1995**, 99, 13187–13192.
[121] S. Takahashi, D. R. Paul, *Polymer*, **2006**, 47, 7519–7535.
[122] J. Ahn, W-J Chung, I. Pinnau, M. D. Guiver, *J. Membr. Sci.,* **2008**, 314, 123–133.
[123] M. Moaddeb, W. J. Koros, *J. Membr. Sci*., **1997**, 125, 143–163.
[124] Y. Li, T.-S. Chung, C. Cao, S. Kulprathipanja, *J. Membr. Sci*., **2005**, 260, 45–55.
[125] G. Clarizia, C. Algieri, E. Drioli, *Polymer*, **2004**, 45, 5671–5681.
[126] P. S. Goh, A. F. Ismail, S. M. Sanip, B. C. Ng, M. Aziz, *Sep. Purif. Technol*., **2011**, 81, 243–264.
[127] G. Dong, H. Li, V. Chen, *J. Mater. Chem. A*, **2013**, 1, 4610–4630.
[128] W. Li, Z. Yang, G. Zhang, Z. Fan, Q. Meng, C. Shen, C. Gao, *J. Mater. Chem. A*, **2014**, 2, 2110–2118.